universität wien

DISSERTATION / DOCTORAL THESIS

Titel der Dissertation / Title of the Doctoral Thesis

„Establishing criteria to distinguish oil-seep from methane-seep carbonates“

verfasst von / submitted by

MSc. Daniel Smrzka

angestrebter akademischer Grad / in partial fulfilment of the requirements for the degree of

Doktor der Naturwissenschaften

Wien / Vienna, 2017

Studienkennzahl lt. Studienblatt / degree programme code as it appears on the student record sheet:	A 796 605 426
Dissertationsgebiet lt. Studienblatt: / field of study as it appears on the student record sheet:	Erdwissenschaften
Betreut von / Supervisor:	Prof. Dr. Jörn Peckmann

Acknowledgements

This work would not have been started, let alone completed, without the help, support, and guidance of the following people I would like to acknowledge in the following lines.

First and foremost, I thank my supervisor Jörn Peckmann for introducing me to the world of marine geoscience. He initiated the spark of my interest in this subject, into which I delved and never looked back. He encouraged and supported the writing of the PhD proposal that enabled the research of my project. I would like to thank him for encouraging me to publish my master thesis, which introduced me to the world of scientific writing (for real) and the ups and downs of getting manuscripts out there. Finally, thank you for introducing me to many, many people in our scientific field, many of which are and will be of importance in the years to come. The biggest thank you goes to Jennifer, for your guidance and support during my studies and PhD work, for your reliability, good judgement, endless encouragement, and for bringing this whole work into focus. Without you, this journey would be unwritten…thank you.

Many thanks to Daniel Birgel for the many interesting discussions on microbial oil degradation at hydrocarbon seeps, for introducing me to organic geochemistry and biomarker laboratory work. I also thank Bernhard Grasemann and Franz Mikysek for support and assistance in administrative issues.

Without samples there is little to publish. I am indebted to Gerhard Bohrmann for allowing me to work on samples from the Gulf of Mexico. I thank him for letting me participate in RV Meteor cruise M114 to the southern GoM. I thank Heiko Sahling for support during carbonate sampling on board, as well as the MARUM Quest 3000 team and the crew of RV Meteor during that cruise.

In the lab in Vienna I am especially grateful to Claudia Beybel for her patient and professional production of oil-rich carbonate thin sections. I thank Sylvain Richoz for quick and reliable isotope analyses in Graz. In Leoben I am indebted to David Misch, who worked hard on producing data for RAMAN spectra of oil, as well as to Christoph Walkner for rapid trace element determination of hydrocarbons. In the lab in Bremen I am most grateful to Wolfgang Bach, Andreas Klügel, Stefan Sopke, and, above all, Patrick Monien, for his patience, effort, discussions, and excellent support during all measurement campaigns.

To my mother, in loving memory…

Contents

Introduction, aim and scope of this thesis 13

Manuscript 1

Establishing criteria to distinguish oil seep from methane seep carbonates 18

Abstract 19

Introduction 19

Oil seeps versus methane seeps – sampling strategy 21

Material and methods 22

Proxies for identifying ancient oil seeps 22

Summary and conclusions 26

Acknowledgements 27

References 27

Manuscript 2: Carbonate authigenesis at oil seeps: A case study from the southern Gulf of Mexico 30

Abstract 31

Introduction 32

Geologic setting 35

Material and methods 37

Results 51

Characterization and origin of hydrocarbons 85

Anaerobic oxidation of hydrocarbons as a trigger for carbonate authigenesis 89

Chemical environment of carbonate precipitation and the influence of hydrocarbons 94

Conclusions 99

Acknowledgements 100

References 100

Manuscript 3: Trace and rare earth elements in marine authigenic carbonates – Potentials, limitations, and perspectives 111

Abstract 112

Introduction and scope 114

Part 1: Trace and rare earth metals – From seawater to sediments and microbial cycling 117

Part 2: Carbonates as a sink for trace and rare earth metals I – Physicochemical and mineralogical constraints 140

Part 3: Carbonates as a sink for trace and rare earth metals II – The geologic record 147

Part 4: Authigenic carbonates at marine hydrocarbon seeps – An El Dorado for trace and rare earth element application 155

Future perspectives for the use of trace metal proxies in seep research 172

References 175

Summary / Zusammenfassung 201

Appendix 206

Published manuscripts:

Mineralized conduits are part of the uppermost plumbing system of Oligocene methane-seep deposits, Washington State (USA)

Massive asphalt deposits, oil seepage, and gas venting support abundant chemosynthetic communities at the Campeche Knolls, southern Gulf of Mexico

Methane seepage in a Cretaceous greenhouse world recorded by an unusual carbonate deposit from the Tarfaya Basin, Morocco

The only way by which human progress has ever been possible is by relentlessly questioning, doubting, and arguing against established theories, and not to take refuge in the false security of consensus.

-CHRISTOPHER HITCHENS-

Introduction, aim, and scope of this thesis

Methane seeps are sites on the seafloor where hydrocarbon compounds including methane are expulsed from seafloor sediments to bottom waters (Judd and Hovland, 2007). These seafloor seeps deliver reduced compounds from deeper sediments to shallower parts of the sedimentary column and to the seafloor, where they provide chemical energy for chemosynthetic life independent of photosynthesis (Paull et al., 1984, 1985). Since the first discovery of these unusual seafloor ecosystems in the late 1970s, research on hydrocarbon seeps has been ever increasing over the years, and the fundamental principles of geophysics and geochemistry, as well as microbial and macrofaunal ecology are believed to be well understood (Claypool and Kvenvolden, 1983; Brooks et al., 1987a,b). Nonetheless there remain unanswered questions. This thesis aims at a specific aspect of such hydrocarbon seeps, which has not been studied as thoroughly as others with respect to seepage chemistry and biology.

Most of the known hydrocarbon seeps today are dominated by expulsions of reduced fluids that are enriched in methane, and it is believed that the majority of the recognized and identified fossil seep deposits discovered to date have also been methane-dominated seepage sites (Suess, 2014 and references therein). However, more and more hydrocarbon provinces around the globe have been and are being discovered that are not dominated by seepage of methane, but are characterized by a predominance of oil seepage (Kennicutt et al., 1988; MacDonald et al., 2000). Such oil seeps are meanwhile known from almost all modern oceans, as well as from the Black Sea and the Gulf of Mexico (Joye et al., 2004; Körber et al., 2014). Such oil seeps are distinct in character, as the hydrocarbon compounds that are emanated from the seafloor are typically lower to high-molecular weight compounds such as butane, propane, naphthalene, and hexadecane, as well as large complex molecules composed of kerogen and bitumen (MacDonald et al., 2004; Schubotz et al., 2011). It is rather obvious that such seeps influence fluid chemistry, and above all micro- and macrobiology at seeps in different ways than methane-dominated seeps would. It is known from modern observations that community structures of chemosynthetic microorganisms have different tolerance levels for oil, and that macrofaunal assemblages react differently towards the presence or absence of oil, given that many of the compounds emitted at such seepage sites are highly toxic to many marine species (Bergquist et al., 2004; Orcutt et al., 2010).

The effect of oil can be easily investigated at modern seepage sites, as seafloor observations with submersible vehicles can gain much first-hand information, and microbiological sampling is a standard

procedure for environmental samples at such sites. Since the presence or absence of oil has strong and long lasting ecological consequences for chemosynthetic marine life today, it seems logical to assume that oil seepage at ancient seepage sites should have also evoked evolutionary responses and adaptations to oil from macro- and macrofaunal seep communities. The presence of oil possibly influenced the short- and long-term evolutionary development of chemosynthetic life. However, the identification of oil seeps in the rock record is anything but trivial. Most studies that have declared fossil seepage sites as oil seeps have based their arguments on circumstantial evidence such as the presence of bitumen and bitumen-like compounds in thin sections, geochemical signatures such as stable C isotopes, and paleontological considerations (Peckmann et al., 2001, 2007, 2011). However, all of these three methods fall short in one way or another, and cannot provide solid evidence for the presence of oil at ancient seepage sites (Peckmann and Thiel, 2004; Birgel et al., 2011).

Trace and rare earth element geochemistry has been applied for decades to a wide range of geologic materials. The utility of analyzing these elements in marine carbonates has been refined significantly in the past decades, especially due to improved analytical techniques (e.g. Haley and Klinkhammer, 2003). Most trace metal analyses on sediments and authigenic carbonates at modern and ancient hydrocarbon seeps are essentially bulk sampling methods, which can roughly identify and trace key biogeochemical processes in pore waters that lead to precipitation of carbonates and influenced microbial activity of the present communities (e.g. Rongemaille et al., 2011). However, phase-specific analyses allow for a much higher resolution of data that can yield small-scale information on changing environmental conditions over comparably short timescales (Himmler et al., 2010).

This thesis aims to demonstrate how detailed trace element analyses of different early and later diagenetic carbonate cement phases in authigenic carbonates at modern and ancient oil and methane seeps can characterize and distinguish these precipitates derived from ecosystems with varying pore water chemistry and, possibly, microbial community structures that influenced their formation. Utilizing the extensive pool of information compiled over the years on aquatic chemistry of trace metals and their incorporation into carbonate minerals, this work demonstrates how analyses of these elements can unravel the intricate and interdependent abiotic and microbial elemental cycles in modern and ancient marine sediments better than ever before. In addition to this thesis, the appendix features three published manuscripts on modern and ancient cold seeps which emerged as side projects of the PhD. They all focus on hydrocarbon seepage, and are added as the all contribute to this thesis in terms of general content.

However, they are not strictly part of the main questions and aims, which is why they are treated separately.

References

Bergquist, D.C., Fleckenstein, C., Szalai, E., Knisel, J., and Fisher, C.R., 2004, Environment drives physiological variability in the cold seep mussel *Bathymodiolus childressi*: Limnology and Oceanography, v. 49, p. 706–715, doi:10.4319/lo.2004.49.3.0706.

Birgel, D., Feng, D., Roberts, H.H., Peckmann, J., 2011. Changing redox conditions at cold seeps as revealed by authigenic carbonates from Alaminos Canyon, northern Gulf of Mexico. Chem. Geol. 285, 82–96.

Brooks, J. M., Kennicutt, M. C., Bidigare, R. R., Wade, T. L., Powell, E. N., Denoux, G. J., Fay, R.R.,Childress, J.J., Fisher, C.R., Rossman, I., Boland, G., 1987a. Hydrates, oil seepage, and chemosynthetic ecosystems on the Gulf of Mexico slope: An update. Eos, Transactions American Geophysical Union 68, 498–499.

Brooks, J.M., Kennicutt, M.C., Fisher, C.R., Macko, S.A., Childress, J.J., Bidigare, R.R., Vetter, R.D., 1987b. Deep-sea hydrocarbon seep communities: Evidence for energy and nutritional carbon sources. Science New Series 238, 1138–1142.

Claypool, G.E., Kvenvolden, K.A., 1983. Methane and other hydrocarbon gases in marine sediment. Annual Reviews in Earth and Planetary Sciences 11, 299–327.

Haley, B.A., Klinkhammer, G.P., 2003. Complete separation of rare earth elements from small volume seawater samples by automated ion chromatography: method development and application to benthic flux. Mar. Chem. 82, 197–220.

Himmler, T., Bach, W., Bohrmann, G., Peckmann, J., 2010. Rare earth elements in authigenic methane-seep carbonates as tracers for fluid composition during early diagenesis. Chem. Geol. 277, 126–136.

Joye, S.B., Boetius, A., Orcutt, B.N., Montoya, J.P., Schulz, H.N., Erickson, M.J., Lugo, S.K., 2004. The anaerobic oxidation of methane and sulfate reduction in sediments from Gulf of Mexico cold seeps. Chemical Geology 205, 219–238.

Judd, A.G., Hovland, M., 2007. Seabed fluid flow – The impact of geology, biology and the marine environment. Cambridge University Press, 492 p.

Kennicutt, M.C., Brooks, J.M., Bidigare, R.R., Denoux, G.J., 1988. Gulf of Mexico hydrocarbon seep communities—I. Regional distribution of hydrocarbon seepage and associated fauna. Deep Sea Research Part A. Oceanographic Research Papers 35, 1639–1651.

Körber, J. H., Sahling, H., Pape, T., dos Santos Ferreira, C., MacDonald, I., Bohrmann, G., 2014. Natural oil seepage at kobuleti ridge, eastern Black Sea. Mar. Pet. Geol. 50, 68–82.

MacDonald, I.R., Bohrmann, G., Escobar, E., Abegg, F., Blanchon, P., Blinova, V., Brückmann, W., Drews, M., Eisenhauer, A., Han, X., Heeschen, K., Meier, F., Mortera, C., Naehr, T., Orcutt, B., Bernard, B., Brooks, J., de Faragó, M., 2004. Asphalt volcanism and chemosynethetic life in the Campeche Knolls, Gulf of Mexico. Science 304, 999–1002.

MacDonald, I.R., Buthman, D.B., Sager, W.W., Peccini, M.B., Guinasso Jr., N.L., 2000. Pulsed oil discharge from a mud volcano. Geology 28, 907–910.

Paull, C.K., Hecker, B., Commeau, R., Freeman-Lynde, R.P., Neumann, C., Corso, W.P., Golubic, S., Hook, J.E., Sikes, E., Curray, J., 1984. Biological communities at the Florida Escarpment resemble hydrothermal vent taxa. Science 226, 965–967.

Paull, C.K., Jull, A. J.T., Toolin, L.J., Linick, T., 1985. Stable isotope evidence for chemosynthesis in an abyssal seep community. Nature 317, 709–711.

Peckmann, J., Thiel, V., 2004. Carbon cycling at ancient methane–seeps. Chem. Geol. 205, 443–467.

Peckmann, J., Gischler, E., Oschmann, W., Reitner, J., 2001. An Early Carboniferous seep community and hydrocarbon-derived carbonates from the Harz Mountains, Germany. Geology 29, 271–274.

Peckmann. J., Kiel. S., Sandy. M.R., Taylor. D.G., Goedert. J.L., 2011. Mass occurrences of the brachiopod Halorella in late Triassic methane-seep deposits, eastern Oregon. Journal of Geology 119, 207–220.

Peckmann, J., Campbell, K.A., Walliser, O.H., Reitner, J., 2007. A Late Devonian hydrocarbon-seep deposit dominated by dimerelloid brachiopods, Morocco. Palaios 22, 114–122.

Orcutt, B.N., Joye, S.B., Kleindienst, S., Knittel, K., Ramette, A., Reitz, A., Samarkin, V., Treude, T., Boetius, A., 2010. Impact of natural oil and higher hydrocarbons on microbial diversity, distribution, and activity in Gulf of Mexico cold-seep sediments. Deep-Sea Research Part II: Topical Studies in Oceanography 57, 2008–2021.

Rongemaille, E., Bayon, G., Pierre, C., Bollinger, C., Chu, N.C., Fouquet, Y., Riboulot, V., Voisset, M., 2011. Rare earth elements in cold seep carbonates from the Niger delta. Chem. Geol. 286, 196–206.

Schubotz, F., Lipp, J.S., Elvert, M., Kasten, S., Mollar, X.P., Zabel, M., Bohrmann, G., Hinrichs, K.U., 2011. Petroleum degradation and associated microbial signatures at the Chapopote asphalt volcano, Southern Gulf of Mexico. Geochimica et Cosmochimica Acta 75, 4377–4398.

Suess, E., 2014. Marine cold seeps and their manifestations: geological control, biogeochemical criteria and environmental conditions. International Journal of Earth Sciences 103, 1889–1916.

Manuscript 1

Establishing criteria to distinguish oil-seep from methane-seep carbonates

D. Smrzka[1], J. Zwicker[1], A. Klügel[2], P. Monien[2], W. Bach[2], G. Bohrmann[2], J. Peckmann[1,3*]

[1]Department für Geodynamik und Sedimentologie, Erdwissenschaftliches Zentrum, Universität Wien, 1090 Wien, Austria

[2]MARUM Center for Marine Environmental Sciences and Department of Geosciences, University of Bremen, 28359 Bremen, Germany

[3]Institut für Geologie, Universität Hamburg, 20146 Hamburg, Germany

*E-mail: joern.peckmann@uni-hamburg.de

Citation:

Smrzka, D., Zwicker, J., Klügel, A., Monien, P., Bach, W., Bohrmann, G., Peckmann, J., 2016. Establishing criteria to distinguish oil-seep from methane-seep carbonates. Geology 44, 667–670.

Abstract

Hydrocarbon seeps harbor copious chemosynthesis-dependent life, the traces of which are preserved in the fossil record within authigenic carbonates. These environments are mostly characterized by seepage of methane-rich fluids, yet an increasing number of crude oil-dominated seeps have been discovered in recent years. Oil seepage has a profound influence on the local fauna, yet recognizing such seeps in the rock record remains elusive. This study presents new geochemical data that will allow for a more confident identification of ancient oil-seep deposits. Geochemical data from modern and ancient seep limestones reveal that oil-dominated seep carbonates are enriched in rare earth elements and uranium compared to their methane-dominated counterparts. These trace element patterns have the potential to serve as a basis for an improved understanding of the adaptation of chemosynthetic life to oil seepage, and to better constrain the marine carbon cycle in the geologic past.

Introduction

Hydrocarbon seeps today are known from almost all parts of the world, from high to low latitudes and shallow seas to the deep ocean (Suess, 2014, and references therein). Seeps harbor lush ecosystems that depend on chemosynthesis, and have been recognized frequently in the fossil record (Campbell, 2006). The geologic record shows that faunal assemblages and community structures have changed continuously, and that different taxa have dominated hydrocarbon seeps during different periods in Earth's history. For example, dimerelloid brachiopods were abundant at seeps in the Paleozoic and for much of the Mesozoic (Sandy, 2010), whereas late Mesozoic and Cenozoic seeps were dominated by chemosymbiotic bivalves and tubeworms (Kaim et al., 2014).

Fluid composition is an important factor governing the distribution and diversity of seep-dwelling fauna at modern seeps, as varying species have different tolerances and requirements with regard to the emitting chemicals (Levin, 2005). While most modern seeps are dominated by seepage of methane, an increasing number of hydrocarbon provinces have been discovered that are characterized by expulsions of higher hydrocarbons and crude oil (Hornafius et al., 1999; MacDonald et al., 2004; Jones et al., 2014; Körber et al., 2014). The presence of oil is a crucial factor that determines macrofaunal community structure, as it can severely impede life at seeps (cf. Bergquist et al., 2004). However, certain epifaunal bivalves and vestimentiferan tubeworms can cope with larger amounts of oil as opposed to infaunal species (MacDonald et al., 2004). Similarly, dimerelloid brachiopods would have been better adapted to oil seeps than many of the modern and Cenozoic seep-dwelling mollusks due to their epifaunal life style. The presence of oil exerts similar controls on diversity, distribution, and activity of archaeal and bacterial communities (Orcutt et al., 2010), which contribute significantly to mineral authigenesis at oil seeps (Joye et al., 2004).

Despite current effort to better understand the ecology of oil seeps, the confident identification of ancient oil seeps still poses a fundamental problem. Petrography only provides circumstantial evidence for oil seepage such as the presence of metamorphosed crude oil (referred to as impsonite or pyrobitumen; Peckmann et al., 2001, 2007). Although stable carbon isotopes appear to be an obvious tool to discriminate methane from oil seepage, they fall short in many instances due to the unknown degree of mixing between different carbon sources (Peckmann and Thiel, 2004). Lipid biomarker patterns of modern oil-seep carbonates are often typified by unresolvable complex mixtures containing partially

degraded petroleum hydrocarbons, which, however, do not allow to identify microbial oil degradation with certainty (e.g., Naehr et al., 2009). Biomarkers that can be unambiguously ascribed to oil-degrading bacteria have yet to be identified. Furthermore, the biomarker inventory of most known Paleozoic and Mesozoic seep deposits has been erased in the course of burial.

This study presents new tools for identifying ancient oil-seep deposits. This is a big step forward, since the determination of the composition of fluids at seeps is a prerequisite for a reliable reconstruction of the early evolution of chemosynthesis-based ecosystems and the mode of adaptation of their fauna. The new proxy developed here may aid to better constrain the sources and sinks of organic carbon in the marine carbon cycle.

Oil seeps versus methane seeps – sampling strategy

Carbonate samples from modern methane- and oil-dominated seeps were selected and compared to putative ancient counterparts to detect variations in their chemical composition. One locality where prominent seepage of oil occurs today is the Campeche Knolls including the Chapopote asphalt volcano, southern Gulf of Mexico. These knolls are related to buoyancy-driven salt tectonics and feature seepage of gas and crude oil, as well as solidified asphalt and carbonate deposits on the seafloor (Brüning et al., 2010). A putative ancient equivalent is a Late Devonian deposit from Morocco dominated by the dimerelloid brachiopod Dzieduszyckia (Peckmann et al., 2007). The faunal inventory, stable carbon isotope signatures, and the presence of metamorphosed crude oil have been interpreted as circumstantial evidence of oil seepage by Peckmann et al. (2007).

The Makran accretionary prism is an accretionary wedge complex located offshore Pakistan at an active continental margin, where fluid seepage is evidenced by mud volcanoes, mud diapirs, and methane seeps (Bohrmann et al., 2008 and references therein). Crude oil and higher hydrocarbons are absent, making this locality an example for methane-dominated seepage associated with massive gas hydrate deposits close to the seafloor (Römer et al., 2012). As an ancient counterpart, the Oligocene Satsop River (SR4) deposit described by Peckmann et al. (2002) was selected. SR4 limestones exhibit a paragenetic mineral sequence typical for seep carbonates, a seep-specific faunal inventory, and characteristic stable carbon isotope and lipid biomarker patterns (Peckmann et al., 2002; Zwicker et al., 2015), and are interpreted to be methane-dominated seep carbonates lacking influence of oil.

Material and methods

Rock samples from seeps in the southern Gulf of Mexico and Makran were collected with R/V Sonne and R/V Meteor during research cruises SO174 and M74 in 2003 and 2007, respectively (Bohrmann et al., 2004, 2008). Carbonate samples from the Campeche Knolls were collected from the Chapopote asphalt volcano and are described by Naehr et al. (2009). Makran limestones were retrieved at Flare 15 (cf. Himmler et al., 2015). Samples from the Dzieduszyckia and SR4 deposits are detailed by Peckmann et al. (2007) and Peckmann et al. (2002), respectively. In-situ analyses of Mo, Sr, U, Y, and rare earth elements (REEs) as well as Si, Al, Fe, Mn, and Mg were conducted by laser-ablation–inductively coupled plasma–mass spectrometry (LA-ICP-MS) at the Department of Geosciences, University of Bremen, Germany (see the Data Repository1 for details) on 80–100-µm-thick thin sections.

Proxies for identifying ancient oil seeps

Rare earth element geochemistry is a powerful tool that has been applied in recent years to track changes in redox conditions and fluid composition during precipitation of seep carbonates (Feng et al., 2009; Himmler et al., 2010). Carbonates inherit the REE composition of the parent fluid (Webb and Kamber, 2000) and their reliability as a tracer is due to their apparently conservative behavior during early and even late diagenesis (cf. Banner et al., 1988). Seep limestones form as a result of microbially induced changes in pore water chemistry (Ritger et al., 1987), and metal cations including REEs partition into carbonate minerals in relation to their concentration in the parent fluid (Kamber et al., 2004). The resistance of REEs during diagenesis and their uniform incorporation into carbonates suggest that seep limestones reflect the REE patterns of pore waters. As opposed to REEs, there are fewer studies using molybdenum (Mo) and uranium (U) to trace fluid evolution at modern and ancient seeps (e.g., Tribovillard et al., 2013; Hu et al., 2015), most of which use bulk rock or bulk sediment analyses of these elements to constrain their formation history. In spite of our yet limited knowledge on the behavior of these elements at hydrocarbon seeps, Mo and U have been successfully applied in skeletal and diagenetic carbonates to infer the original composition and redox chemistry of ancient waters (Shen and Dunbar, 1995; Voegelin et al., 2009).

To allow a meaningful comparison of data among all studied seep carbonates, element analyses were focused on a pure mineral phase present in all samples. This phase is a clear, banded and botryoidal variety of fibrous aragonite cement (clear aragonite from here on), which is a common constituent of modern and ancient seep limestones (e.g., Savard et al., 1996; Himmler et al., 2010). Clear aragonite in the SR4 deposit is partially recrystallized to calcite, in Dzieduszyckia samples aragonite is completely recrystallized. The phase-specific analytical approach was chosen for two reasons: First, the strong ^{13}C depletion of clear aragonite confirms its ultimate derivation from microbial anaerobic oxidation of methane and higher hydrocarbons (Table 1). Any elements incorporated into clear aragonite should, therefore, reflect pore fluids during active seepage. Second, the choice of this particularly pure carbonate mineral avoids potential contamination by particulate matter, clay minerals, Fe- and Mn-oxides, or a combination of these sources (cf. Bau et al., 1996). This is confirmed by the very low contents of Si, Al, Fe, and Mn that were analyzed together with the trace elements of interest. Indeed, the sum of REEs including yttrium (∑REE+Y), Mo, and U do not correlate among each other, nor do they correlate with any other measured element including Al, Fe, and Mn in any of the samples (see the Data Repository). We put forward the exclusive use of phase-specific trace element analysis as a robust approach to reconstruct the composition and evolution of fluids at hydrocarbon seeps (cf. Himmler et al., 2010).

Seepage system	Oil seep		Methane seep	
Age	Modern	Late Devonian	Modern	Oligocene
Locality	Chapopote	*Dzieduszyckia*	Makran	SR4
$\delta^{13}C$ [‰]	−28.6[a]	−5.8[b]	−54.3[c]	−51.3[d]
∑REE+Y [ppm]	0.797	2.49	0.058	0.360
Mo [ppm]	0.465	0.101	0.961	0.437
U [ppm]	5.08	0.897	2.97	0.164
Mo/U	0.09	0.112	0.323	2.66

Table 1. All data are mean values except ^{13}C values, which are the most negative. Superscripts: a—from Naehr et al. (2009); b—from Peckmann et al. (2007); c—from Himmler et al. (2015); d—from Peckmann et al. (2002). REE—rare earth elements. Isotope ratios are given in per mil relative to Vienna Peedee belemnite. *Chapopote—Gulf of Mexico; Dzieduszyckia—Morocco; Makran—offshore Pakistan; SR4—Satsop River, Washington State (USA) (see text).

Clear aragonite of modern and putative ancient oil-seep limestones was found to be enriched in REEs compared to its counterpart from methane seeps (Fig. 1A). The aqueous behavior of REEs at seeps is partly controlled by particulate and dissolved organic matter (Himmler et al., 2010), which may serve as a significant source of REEs to anoxic pore waters (Haley et al., 2004). The relationship between REEs and organic material in anoxic marine sediments is not straightforward. However, there does seem to be a consensus that organic colloids and ligands, living and dead microbial mats, and other forms of particulate and dissolved organic matter readily complex and passively enrich various trace metals including REEs in natural waters, and that such signatures may be preserved in ancient carbonates (e.g., Tang and Johannesson, 2010a; Corkeron et al., 2012 and references therein). Similarly, the presence of petroleum hydrocarbons in pore waters at oil seeps apparently facilitates complexation and sorption of REEs from pore waters onto these substances. Trace and rare earth metals are in fact preferentially bound to metalloporphyrines of natural oils (Duyck et al., 2007), making crude oil itself a potential additional source of REEs at oil seeps. Our results strongly suggest that the observed ∑REE+Y trend among oil-seep carbonates is related to the presence of crude oil in the parent pore fluids. Due to the lack of correlation of ∑REE+Y to all other measured trace metals and the purity of the analyzed mineral phase, we conclude that pore waters from which clear aragonite precipitated at oil seeps had elevated REE concentrations due to the presence of petroleum hydrocarbons, and that the aragonite cement incorporated and archived this signature during precipitation. Recrystallization of aragonite to calcite may have been a process that contributed to the somewhat higher REE contents of clear aragonite in the oil-derived Dzieduszyckia and the methane-derived SR4 deposits compared to their modern counterparts. More extensive future work will allow to better assess the impact of recrystallization on REE contents. Nevertheless, based on the current data set the applicability of the new proxy is not expected to be compromised by recrystallization of aragonite.

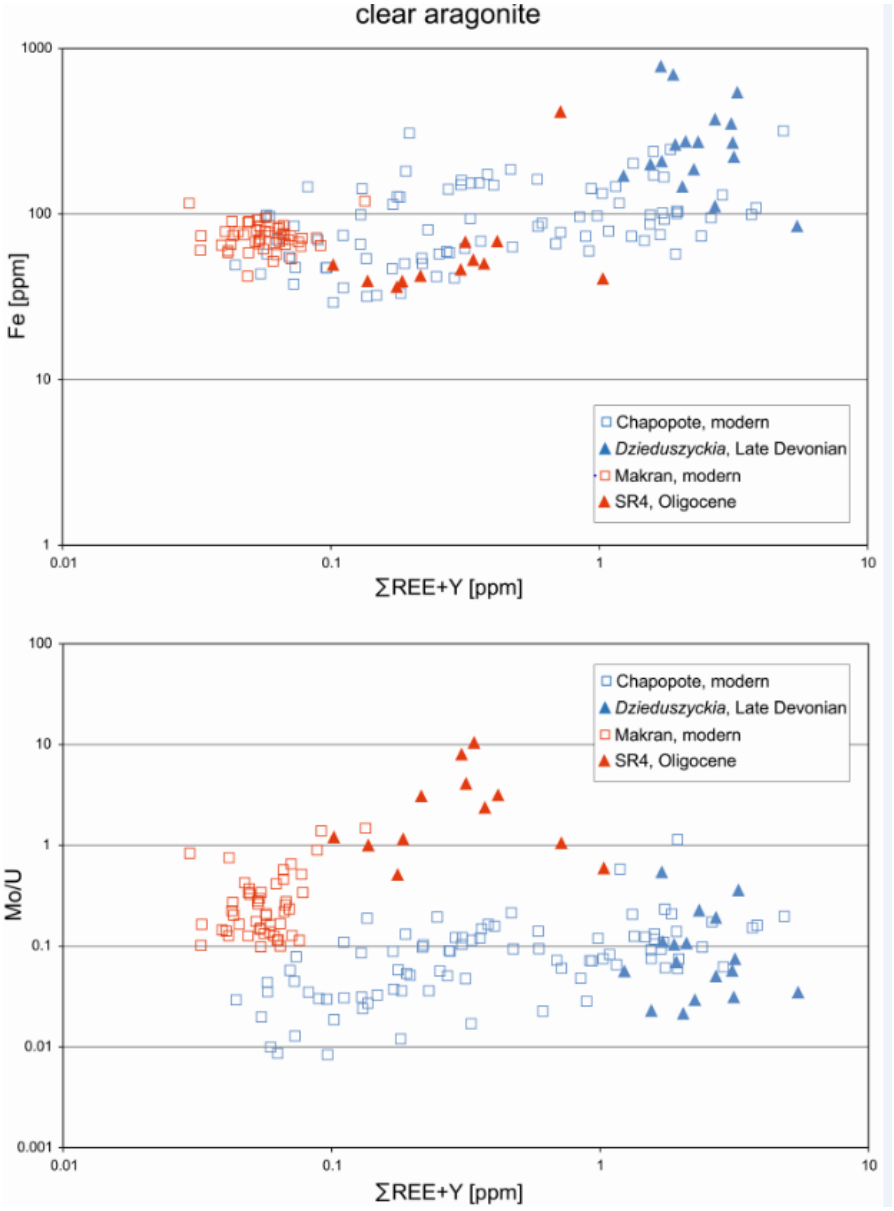


Fig. 1. Phase-specific trace element data for clear aragonite. See text for locations. A: Fe vs. ∑REE + Y (REE—rare earth elements). B: Mo/U ratios versus ∑REE + Y.

Interestingly, Mo/U ratios in clear aragonite of oil-seep carbonates are systematically lower than in the corresponding clear aragonite of methane-seep carbonates (Fig. 1B, Table 1). Molybdenum is enriched in sediments within the sulfate reduction zone at methane seeps, where hydrogen sulfide production facilitates local Mo accumulation (Hu et al., 2015). This should, however, lead to similar enrichments of Mo at oil seeps, where equally vigorous sulfate reduction is known to occur (cf. Joye et al.,

2004). Apparently, redox-dependent scavenging and enrichment of Mo is not the only key to explaining differences in Mo/U ratios in clear aragonite. A significant factor that contributes to the different Mo/U ratios of clear aragonite at the two seep types may be the behavior of U. Uranium input is intimately linked with the flux of particulate organic matter to marine sediments (McManus et al., 2005), as well as with petroleum-bearing reservoir rocks including asphalt- and bitumen-rich deposits (Parnell and Eakin, 1987). Such close association may cause higher U concentrations in pore waters at oil seeps, contributing to the lower Mo/U ratios in oil-seep carbonates. This hypothesis will have to be tested by future work to fully understand the involved mechanisms. A further process that may influence the behavior of U at seeps is reduction of Fe. Soluble U(VI) is reduced to less soluble U(IV) in the iron reduction zone of marine sediments (Morford et al., 2005). This leads to U enrichment and higher U contents of authigenic carbonates forming in the iron reduction zone. REE patterns of pore waters and seep carbonates from the iron reduction zone are typified by enrichment of middle REEs (e.g., Haley et al., 2004; Himmler et al., 2010; Bayon et al., 2011). However, no such enrichment was observed in any of our samples, which renders iron reduction an unlikely mechanism for U enrichment. Irrespective of what causes the different Mo/U ratios of oil- and methane-seep carbonates, this element ratio has great potential to help unraveling the effect of fluid composition on the evolution of chemosynthesis-based fauna at seeps.

Summary and conclusions

This study reveals the potential of combining the phase-specific distribution of REEs, Mo, and U to discern ancient oil seeps from methane seeps. The comparison of modern seep carbonates with their putative ancient counterparts resulted in the recognition of a new proxy that allows for the discrimination of the two different types of seepage in the rock record. Authigenic clear aragonite cement of oil-seep carbonates is enriched in REEs and exhibits systematically lower Mo/U ratios than its counterpart at methane seeps. We suggest that oil-derived carbonate precipitates from fluids with increased REEs and U concentrations, which is in turn related to the presence of petroleum hydrocarbons in the parent fluid. A confident recognition of past oil seepage will help to reevaluate patterns and driving forces of the evolution of chemosynthesis-based metazoan life over geologic time.

Acknowledgements

Thanks to James L. Goedert for providing samples and comments on an early draft, as well as to Dong Feng, Russell Shapiro, and an anonymous reviewer for comments on the manuscript. This research was financed by a Uni:Docs fellowship granted to the first author by the University of Vienna, Austria.

Appendix

In the scope of this study, we have attempted to discern oil- from methane-seep carbonates by comparing bulk rock total carbon and total organic carbon contents, as well as their respective stable carbon isotope values. This effort led to partially counter-intuitive results, indicating that this approach does not allow for such discrimination. Concept, methodology, and results thereof, along with a documentation of the data set on element patterns, are outlined in the Data Repository material.

References

Banner, J.L., Hanson, G.N., and Meyers, W.J., 1988, Rare earth element and Nd isotopic variations in regionally extensive dolomites from the Burlington-Keokuk Formation (Mississippian): Implications for REE mobility during carbonate diagenesis: Journal of Sedimentary Petrology, v. 58, p. 415–432.

Bau, M., Koschinsky, A., Dulski, P., and Hein, J.R., 1996, Comparison of the partitioning behaviours of yttrium, rare earth elements, and titanium between hydrogenetic marine ferromanganese crusts and seawater: Geochimica et Cosmochimica Acta, v. 60, p. 1709–1725, doi:10.1016/0016-7037(96)00063-4.

Bayon, G., Birot, D., Ruffine, L., Caprais, J.-C., Ponzevera, E., Bollinger, C., Donval, J.-P., Charlou, J.-L., Voisset, M., and Grimaud, S., 2011, Evidence for intense REE scavenging at cold seeps from the Niger Delta margin: Earth and Planetary Science Letters, v. 312, p. 443–452, doi:10.1016/j.epsl.2011.10.008.

Bergquist, D.C., Fleckenstein, C., Szalai, E., Knisel, J., and Fisher, C.R., 2004, Environment drives physiological variability in the cold seep mussel *Bathymodiolus childressi*: Limnology and Oceanography, v. 49, p. 706–715, doi:10.4319/lo.2004.49.3.0706.

Bohrmann, G., Schenck S., and Cruise Participants, 2004, Report and preliminary results of R/V *Sonne* cruise SO 174 / OTEGA II, Balboa – Corpus Christi – Miami, 1 October–12 November 2003. Investigations within the BMBF special program "Gashydrate im Geosystem": Geomar report, v. 117, Kiel, Germany IFM–GEOMAR, 130 p.

Bohrmann, G., and Cruise Participants,, 2008, Report and preliminary results of R/V *Meteor* Cruise M74/3, Fujairah–Male. Cold seeps of the Makran subduction zone (Continental Margin of Pakistan): Berichte Fachbereich Geowissenschaften, Universität Bremen, v. 266, 161 p.

Brüning, M., Sahling, H., MacDonald, I.R., Ding, F., and Bohrmann, G., 2010, Origin, distribution, and alteration of asphalts at the Chapopote Knoll, Southern Gulf of Mexico: Marine and Petroleum Geology, v. 27, p. 1093–1106, doi:10.1016/j.marpetgeo.2009.09.005.

Campbell, K.A., 2006, Hydrocarbon seep and hydrothermal vent paleoenvironments and paleontology: Past developments and future research directions: Palaeogeography, Palaeoclimatology, Palaeoecology, v. 232, p. 362–407, doi:10.1016/j.palaeo.2005.06.018.

Corkeron, M., Webb, G.E., Moulds, J., and Grey, K., 2012, Discriminating stromatolite formation modes using rare earth elements geochemistry: Trapping and binding versus in situ precipitation of stromatolites from the Neoproterozoic Bitter Springs Formation, Northern Territory, Australia: Precambrian Research, v.212–213, p. 194–206, doi:10.1016/j.precamres.2012.04.019.

Duyck, C., Miekeley, N., Porto da Silveira, C.L., Aucélio, R.Q., Campos, R.C., Grinberg, P., and Brandão, G.P., 2007, The determination of trace elements in crude oil and its heavy fractions by atomic spectrometry: Spectrochimica Acta. Part B, Atomic Spectroscopy, v. 62, p. 939–951, doi:10.1016/j.sab.2007.04.013.

Feng, D., Chen, D., and Peckmann, J., 2009, Rare earth elements in seep carbonates as tracers of variable redox conditions at ancient hydrocarbon seeps: Terra Nova, v. 21, p. 49–56, doi:10.1111/j.1365-3121.2008.00855.x.

Haley, B., Klinkhammer, G.P., and McManus, J., 2004, Rare earth elements in pore waters of marine sediments: Geochimica et Cosmochimica Acta, v. 68, p. 1265–1279, doi:10.1016/j.gca.2003.09.012.

Himmler, T., Bach, W., Bohrmann, G., and Peckmann, J., 2010, Rare earth elements in authigenic methane-seep carbonates as tracers for fluid composition during early diagenesis: Chemical Geology, v. 277, p. 126–136, doi:10.1016/j.chemgeo.2010.07.015.

Himmler, T., Birgel, D., Bayon, G., Pape, T., Ge, L., Bohrmann, G., and Peckmann, J., 2015, Formation of seep carbonates along the Makran convergent margin, northern Arabian Sea and a molecular and isotopic approach to constrain the carbon isotopic composition of parent methane: Chemical Geology, v. 415, p. 102–117, doi:10.1016/j.chemgeo.2015.09.016.

Hornafius, J.S., Quigley, D., and Luyendyk, B.P., 1999, The world's most spectacular marine hydrocarbon seeps (Coal Oil Point, Santa Barbara Channel, California): Quantification of emissions: Journal of Geophysical Research, v. 104, p. 20703–20711, doi:10.1029/1999JC900148.

Hu, Y., Feng, D., Liang, Q., Xia, Z., Linying, C., and Chen, D., 2015, Impact of anaerobic oxidation of methane on the geochemical cycle of redox-sensitive elements at cold-seep sites of the northern South China Sea: Deep-sea Research. Part II, Topical Studies in Oceanography, v. 122, p. 84–94, doi:10.1016/j.dsr2.2015.06.012.

Jones, D.O.B., Walls, A., Clare, M., Fiske, M.S., Weiland, R.J., O'Brien, R., and Touzel, D.F., 2014, Asphalt mounds and associated biota in the Angolan margin: Deep-sea Research. Part I, Oceanographic Research Papers, v. 94, p. 124–136, doi:10.1016/j.dsr.2014.08.010.

Joye, S.B., Boetius, A., Orcutt, B.N., Montoya, J.P., Schulz, H.N., Erickson, M.J., and Lugo, S.K., 2004, The anaerobic oxidation of methane and sulfate reduction in sediments from Gulf of Mexico cold seeps: Chemical Geology, v. 205, p. 219–238, doi:10.1016/j.chemgeo.2003.12.019.

Kaim, A., Jenkins, R.G., Tanabe, K., and Kiel, S., 2014, Mollusks from late Mesozoic seep deposits, chiefly in California: Zootaxa, v. 3861, p. 401–440, doi:10.11646/zootaxa.3861.5.1.

Kamber, B.S., Bolhar, R., and Webb, G.E., 2004, Geochemistry of late Archaean stromatolites from Zimbabwe: evidence for microbial life in restricted epicontinental seas: Precambrian Research, v. 132, p. 379–399, doi:10.1016/j.precamres.2004.03.006.

Körber, J.H., Sahling, H., Pape, T., dos Santos Ferreira, C., MacDonald, I.R., and Bohrmann, G., 2014, Natural oil seeps at Kobuleti Ridge, eastern Black Sea: Marine and Petroleum Geology, v. 50, p. 68–82, doi:10.1016/j.marpetgeo.2013.11.007.

Levin, L.A., 2005, Ecology of cold seep sediments: Interactions of fauna with flow, chemistry and microbes: Oceanography and Marine Biology - an Annual Review, v. 43, p. 1–46, doi:10.1201/9781420037449.ch1.

MacDonald, I.R., et al., 2004, Asphalt volcanism and chemosynthetic life in the Campeche Knolls: Gulf of Mexico Science, v. 304, p. 999–1002, doi:10.1126/science.1097154.

McManus, J., Berelson, W.M., Klinkhammer, G.P., Hammond, D.E., and Holm, C., 2005, Authigenic uranium: relationship to oxygen penetration depth and organic carbon rain: Geochimica et Cosmochimica Acta, v. 69, p. 95–108, doi:10.1016/j.gca.2004.06.023.

Morford, J.L., Emerson, S.R., Breckel, E.J., and Kim, S.H., 2005, Diagenesis of oxyanions (V, U, Re, and Mo) in pore waters and sediments from a continental margin: Geochimica et Cosmochimica Acta, v. 69, p. 5021–5032, doi:10.1016/j.gca.2005.05.015.

Naehr, T.H., Birgel, D., Bohrmann, G., MacDonald, I.R., and Kasten, S., 2009, Biogeochemical controls on authigenic carbonate formation at the Chapopote “asphalt volcano”, Bay of Campeche: Chemical Geology, v. 266, p. 390–402, doi:10.1016/j.chemgeo.2009.07.002.

Orcutt, B.N., Joye, S.B., Kleindienst, S., Knittel, K., Ramette, A., Reitz, A., Samarkin, V., Treude, T., and Boetius, A., 2010, Impact of natural oil and higher hydrocarbons on microbial diversity, distribution, and activity in Gulf of Mexico cold-seep sediments: Deep-sea Research. Part II, Topical Studies in Oceanography, v 57, p. 2008–2021, doi:10.1016/j.dsr2.2010.05.014.

Parnell, J., and Eakin, P., 1987, The replacement of sandstones by uraniferous hydrocarbons: significance for petroleum migration: Mineralogical Magazine, v. 51, p. 505–515, doi:10.1180/minmag.1987.051.362.05.

Peckmann, J., and Thiel, V., 2004, Carbon cycling at ancient methane-seeps: Chemical Geology, v. 205, p. 443–467, doi:10.1016/j.chemgeo.2003.12.025.

Peckmann, J., Gischler, E., Oschmann, W., and Reitner, J., 2001, An Early Carboniferous seep community and hydrocarbon-derived carbonates from the Harz Mountains, Germany: Geology, v. 29, p. 271–274, doi:10.1130/0091-7613(2001)029<0271:AECSCA>2.0.CO;2.

Peckmann, J., Goedert, J.L., Thiel, V., Michaelis, W., and Reitner, J., 2002, A comprehensive approach to the study of methane-seep deposits from the Lincoln Creek Formation, western Washington State, USA: Sedimentology, v. 49, p. 855–873, doi:10.1046/j.1365-3091.2002.00474.x.

Peckmann, J., Campbell, K.A., Walliser, O.H., and Reitner, J., 2007, A Late Devonian hydrocarbon-seep deposit dominated by dimerelloid brachiopods, Morocco: Palaios, v. 22, p. 114–122, doi:10.2110/palo.2005.p05-115r.

Ritger, S., Carson, B., and Suess, E., 1987, Methane-derived authigenic carbonates formed by subduction-induced pore-water expulsion along the Oregon/Washington margin: Geological Society of America Bulletin, v. 98, p. 147–156, doi:10.1130/0016-7606(1987)98<147:MACFBS>2.0.CO;2.

Römer, M., Sahling, H., Pape, T., Spieß, V., and Bohrmann, G., 2012, Quantification of gas bubble emissions from submarine hydrocarbon seeps at the Makran continental margin (offshore Pakistan): Journal of Geophysical Research: Oceans, v. 117, C10015, doi:10.1029/2011JC007424.

Sandy, M.R., 2010, Brachiopods from ancient hydrocarbon seeps and hydrothermal vents, *in* Kiel, S., ed., The Vent and Seep Biota: Topics in Geobiology 33: New York, Springer, p. 279□314.

Savard, M.M., Beauchamp, B., and Veizer, J., 1996, Significance of aragonite cements around Cretaceous marine methane seeps: Journal of Sedimentary Research, v. 66, p. 430–438, doi:10.1306/D4268365-2B26-11D7-8648000102C1865D.

Shen, G.T., and Dunbar, R.B., 1995, Environmental controls on uranium in reef corals: Geochimica et Cosmochimica Acta, v. 59, p. 2009–2024, doi:10.1016/0016-7037(95)00123-9.

Suess, E., 2014, Marine cold seeps and their manifestations: geological control, biogeochemical criteria and environmental conditions: International Journal of Earth Sciences, v. 103, p. 1889–1916, doi:10.1007/s00531-014-1010-0.

Tang, J., and Johannesson, K.H., 2010, Ligand extraction of rare earth elements from aquifer sediments: Implications for rare earth element complexation with organic matter in natural waters: Geochimica et Cosmochimica Acta, v. 74, p. 6690–6705, doi:10.1016/j.gca.2010.08.028.

Tribovillard, N., Armynot du Chatelet, E., Gay, A., Barbecot, F., Sansjofre, P., and Potdevin, J.L., 2013, Geochemistry of cold seepage-impacted sediments: Per ascensum or per-descensum trace metal enrichment?: Chemical Geology, v. 340, p. 1–12, doi:10.1016/j.chemgeo.2012.12.012.

Voegelin, A.R., Nägler, T.F., Samankassou, E., and Villa, I.M., 2009, Molybdenum isotopic composition of modern and Carboniferous carbonates: Chemical Geology, v. 265, p. 488–498, doi:10.1016/j.chemgeo.2009.05.015.

Webb, G.E., and Kamber, B.S., 2000, Rare earth elements in Holocene reefal microbialites: a new shallow seawater proxy: Geochimica et Cosmochimica Acta, v. 64, p. 1557–1565, doi:10.1016/S0016-7037(99)00400-7.

Zwicker, J., Smrzka, D., Gier, S., Goedert, J.L., and Peckmann, J., 2015, Mineralized conduits are part of the uppermost plumbing system of Oligocene methane-seep deposits, Washington State (USA): Marine and Petroleum Geology, v. 66, p. 616–630, doi:10.1016/j.marpetgeo.2015.05.035.

Manuscript 2

Carbonate authigenesis at oil seeps: A case study from the southern Gulf of Mexico

D. Smrzka[a], J. Zwicker[a], H. Sahling[b] D. Misch[c], C. Walkner[d], W. Bach[b], G. Bohrmann[b], J. Peckmann[a,e]

[a]*Department für Geodynamik und Sedimentologie, Erdwissenschaftliches Zentrum, Universität Wien, 1090 Wien, Austria*

[b]*MARUM Center for Marine Environmental Sciences and Department of Geosciences, University of Bremen, 28359 Bremen, Germany*

[c]*Department of Applied Geosciences and Geophysics, Montanuniversität Leoben, 8700 Leoben, Austria*

[d]*Institut für Allgemeine und Analytische Chemie, Montanuniversität Leoben, 8700 Leoben, Austria*

[e]*Institut für Geologie, Fachbereich Geowissenschaften, Universität Hamburg, 20156 Hamburg, Germany*

Manuscript in preparation for submission to *Sedimentology*

Abstract

Oil seeps from the southern Gulf of Mexico represent natural laboratories where the effect of crude oil seepage on chemosynthetic organisms and carbonate precipitation can be studied first hand. The Bay of Campeche comprises numerous positive seafloor structures such as ridges, crests, and knolls that are known to emit large volumes of liquid hydrocarbons and asphalt deposits that cover the seafloor. Carbonates were sampled during RV Meteor cruise 114 from three newly discovered localities named UNAM Ridge, Mictlan Knoll, and Tsanyao Yang Knoll. Thin section petrography revealed that most samples are pervaded by large amounts of oil and asphalt. Phase-specific $\delta^{13}C$ values range between –30 and –20‰, arguing for oil as the primary carbon source. Raman spectra of oils revealed that hydrocarbons from all sites are very immature, and are most likely sourced from the same reservoir. Trace and rare earth element chemistry of carbonate cement phases show varying patterns, suggesting changing

redox conditions and fluid composition during carbonate precipitation. A comparison of trace elements in carbonates and associated oils argues that liquid hydrocarbons act as an additional source of trace metals to pore waters; a signal that is archived by precipitating carbonate cements. Geochemical modeling using the software code PHREEQC demonstrates how sulfate-dependent oxidation of low- to high-molecular weight hydrocarbons affects carbonate saturation state, and shows how (1) the oxidation state of carbon in hydrocarbon compounds, and (2) oxidation rates of hydrocarbons control carbonate saturation and stability at oil seeps. Crude oil degradation is capable of precipitating carbonate, whose trace metal inventory archives specific elemental patterns that can be assigned to the presence of heavy hydrocarbons such as oils and asphalts in pore waters. This study extends the scope of application of phase-specific trace metal analyses significantly, and suggests that authigenic marine carbonates represent a reliable archive for pore fluid composition.

Introduction

The seepage of hydrocarbons from marine sediments produced by persistent upward migration of oil and gas towards the seafloor represents a poorly confined source of fossil organic carbon in the ocean and the atmosphere (Judd and Hovland, 2007 and references therein). The discharge of hydrocarbons into the water column at cold seeps produces mud volcanoes, brine pools, gas hydrates, and deposits of authigenic minerals (Ritger et al., 1987; Kopf, 2002; Bohrmann et al., 2003). Moreover, seepage supports lush and complex ecosystems based on chemosynthesis that include microbial mats, symbiont-hosted bivalves and tubeworms, filter-feeding shrimp, grazing crabs, and a consortium of archaea and sulfate-reducing bacteria performing the anaerobic oxidation of methane (AOM; Boetius et al., 2000; Sahling et al., 2002; van Dover et al., 2003).

Most seeps at continental margins are dominated by the seepage of biogenic and thermogenic methane, often fueled by the destabilization of gas hydrates (Claypool and Kvenvolden, 1983; Suess et al., 1999; Milkov, 2004). However, an increasing number of hydrocarbon provinces have been discovered characterized not only by seepage of methane, but by expulsions of higher hydrocarbons including various higher, low molecular weight hydrocarbons and crude oil (Estes et al., 1985; Kennicutt et al., 1988a; MacDonald et al., 2000; Kvenvolden and Cooper, 2003; Joye et al., 2004; Körber et al., 2014). Such

hydrocarbon seeps are ideally suited to study the impact of oil seepage on the diversity, activity, and distribution of microbial communities, as well as the role of oil seepage and degradation on carbonate authigenesis (Naehr et al., 2009; Orcutt et al., 2010; Birgel et al., 2011; Schubotz et al., 2011a). The northern Gulf of Mexico (GoM), in particular has served as a natural laboratory for methane and oil seepage over the last decades, and has resulted in a large amount of studies on hydrocarbon and gas seepage, chemosynthetic community structure and diversity, and carbonate formation (Bernard et al., 1976; Pequegnat and Jeffrey, 1979; Paull et al., 1984, 1985; Brooks et al., 1986; Sassen et al., 1993; Aharon et al., 1997; Fischer et al., 2007; Feng et al., 2009a; Roberts et al., 2010).

The interest in studying oil seeps in particular stems in part from the idea that the presence of crude oil at cold seeps may have influenced or even governed the course of macrofaunal evolution of chemosynthetic organisms through geologic time, as the diversity, distribution and life styles of seep dwelling macrofauna today is partly controlled by the composition of seepage fluids (Sibuet and Olu, 1998). Vesicomyid and bathymodiolin bivalves occur almost ubiquitously at modern seeps, whereas solemyids, lucinids and thyasirids do not show such a widespread distribution (Levin, 2005). Moreover, bathymodiolin bivalves exhibit an epibenthic life style as opposed to the endobenthic thyasirids and solemyids (Le Pennec et al., 1995). Crude oil may be an important factor in determining the macrofaunal community structure (cf. Bergquist et al., 2004), whereby certain bivalve species (i.e. epibenthic taxa) and vestimentiferan tubeworms can cope with larger amounts of oil (e.g. MacDonald et al., 2004). Recent studies show that the presence of oil even governs the chemosynthetic symbiosis between cold seep-specific mollusks and their bacterial symbionts (Rubin-Blum et al., 2017). Many of the known Paleozoic and Mesozoic seeps typified by mass occurrences of rhynchonellide brachiopods may have in fact been oil seeps (e.g. Peckmann et al., 2001a, 2007, 2011, 2013). Brachiopods, which seem to have vanished from seep ecosystems in the Early Cretaceous (Campbell and Bottjer, 1995), would have been better adapted to oil seepage than many of the modern and Cenozoic seep-dwelling mollusks due to their epibenthic life style.

Natural oil discharge from the seafloor in modern oceans manifests itself as oil slicks on the sea surface, which can be detected and quantified by airborne remote sensing imaging and from space using radar satellite imagery (Deutsch and Estes, 1980; MacDonald et al., 1993; De Beukelaer et al., 2003). Initial close-hand investigations of these phenomena in the southern GoM were conducted in 2003 when the German research vessel (RV) Sonne – *en route* from Panama and after testing new equipment on

well-documented gas hydrates on the continental slopes of Texas and Louisiana – headed for Mexican waters into the Bay of Campeche and the Yucatan Shelf for the first time (Bohrmann et al., 2004). The findings of this highly successful cruise were quite spectacular: The Bay of Campeche hosts the unusual "Chapopote Asphalt Volcano", characterized by extensive eruptions of liquid heavy hydrocarbons, widespread asphalt flows, seafloor gas hydrate deposits, as well as complex and surprisingly diverse macrofaunal communities able to defy this putatively hostile environment (MacDonald et al., 2004; Sahling et al., 2016; Rubin-Blum et al., 2017). Further investigation of these phenomena continued in the course of R/V Meteor Cruise 67 in 2006 (Weinrebe et al., 2010), which focused on detailed surveying and mapping of asphalt flows, seismic studies, as well as biogeochemical studies on heavy hydrocarbons and authigenic carbonates (Ding et al., 2008, 2010; Naehr et al., 2009; Brüning et al., 2010; Schubotz et al., 2011a,b).

Despite the large scientific and economic interest and intense research conducted on natural oil and gas seeps on the northern GoM continental slope, the southern part of the GoM including the Bay of Campeche has still received comparatively little attention. The most recent visit to this remarkable seafloor site was conducted in 2015 on R/V Meteor Cruise 114, and revealed that oil seepage is more common and widespread in the southern GoM as previously recognized (Sahling and Bohrmann, 2016). Apart from the Chapopote Asphalt Volcano, additional seafloor hills and crests actively emitting gas and liquid oil were discovered, as well as voluminous deposits of gas hydrate, lush chemosynthetic communities, and authigenic carbonates (Sahling et al., 2016). During this cruise the newly discovered sites were thoroughly sampled, including carbonate outcrops from the seafloor. This communication focuses on petrographic and stable isotope characterization of authigenic carbonates sampled from three new seafloor features. We suggest that the voluminous carbonate deposits testify to persistent microbial metabolisms involved in the degradation of crude oil and gas, and that these processes must have been active over long timescales. We apply Raman spectra of oil samples to characterize heavy hydrocarbons within the carbonates. This well-known approach for organic carbon-rich shales and coals has so far not been applied to modern or ancient oil-seep carbonates. High-resolution phase-specific data of trace and rare earth elements (REEs) are presented in order to constrain redox conditions and biogeochemical processes that influenced carbonate precipitation during seepage of oil. These elemental data in concert with geochemical batch modeling of sulfate-dependent oxidation of low- and high-molecular weight

hydrocarbon compounds offer new insights into the mode of carbonate precipitation and its relation to natural crude oil seepage.

Geologic setting

The Gulf of Mexico is a large sedimentary basin covering an area of around 1.5 million km^2. The formation of the basin was initially triggered by a phase of crustal extension that began in the late Triassic. Subsequent ocean spreading and rifting until the middle Jurassic opened the Gulf and massive layers of evaporites were deposited; collectively known today as the Louann Salt (Buffler and Sawyer, 1985; Pindell, 1985; Salvador, 1987). Thermal subsidence in the early Cretaceous provided accommodation space for large sedimentary sequences that were deposited over the evaporites (Watkins and Macrae, 1995). The salt deposits are distributed over the entire northern and southern GoM, suggesting the presence of a large interior sea with limited connection to the neighboring Pacific Ocean (Salvador, 1991). The deposition of large volumes of evaporites ceased in the Late Jurassic due to progressive opening of the Gulf towards the Atlantic Ocean, triggering greater influx and exchange of marine waters (Magoon et al., 2001). In terms of seepage related settings, the GoM can be classified as a passive continental margin where seepage of reduced fluids is associated with sediment loading, differential compaction and salt diapirism. The latter process is especially prominent in the Gulf of Mexico, where salt deposits are overlain by massive successions of continental margin sediments holding enormous reservoirs of hydrocarbons (Sassen et al., 1993; Roberts and Aharon, 1994; Roberts, 2001).

The southern GoM comprises two prominent active salt provinces, the Sigsbee Knolls and the Campeche Knolls. The latter are located on the Campeche Bank, which is composed of a sequence of carbonate and evaporate deposits that was disconnected from the North American Plate during the mid- to late Jurassic (Morán-Zenteno, 1984). The Campeche Bank is part of the Yucatán platform that developed during the mid-Cretaceous (Wilson and Ward, 1993), and has remained tectonically stable over the past 100 Ma. The platform is characterized by large-scale Cretaceous platform margin and ramp carbonate deposits overlain by a massive succession of up to 10 km thick Cenozoic hydrocarbon-rich sediments (Magoon et al., 2001). The Campeche Knolls are a distinct set of positive seafloor features generated by buoyancy-driven salt tectonics that produce a complex network of fluid pathways enabling the migration of hydrocarbons to the seafloor (Fig. 1, Watkins et al., 1978; Salvador, 1991; MacDonald et

al., 2004). These knolls are particularly known for their expulsions of large amounts of gas and heavy hydrocarbons, whereby the latter are manifested as solidified asphalt on the seafloor (MacDonald et al., 2004; Brüning et al., 2010).

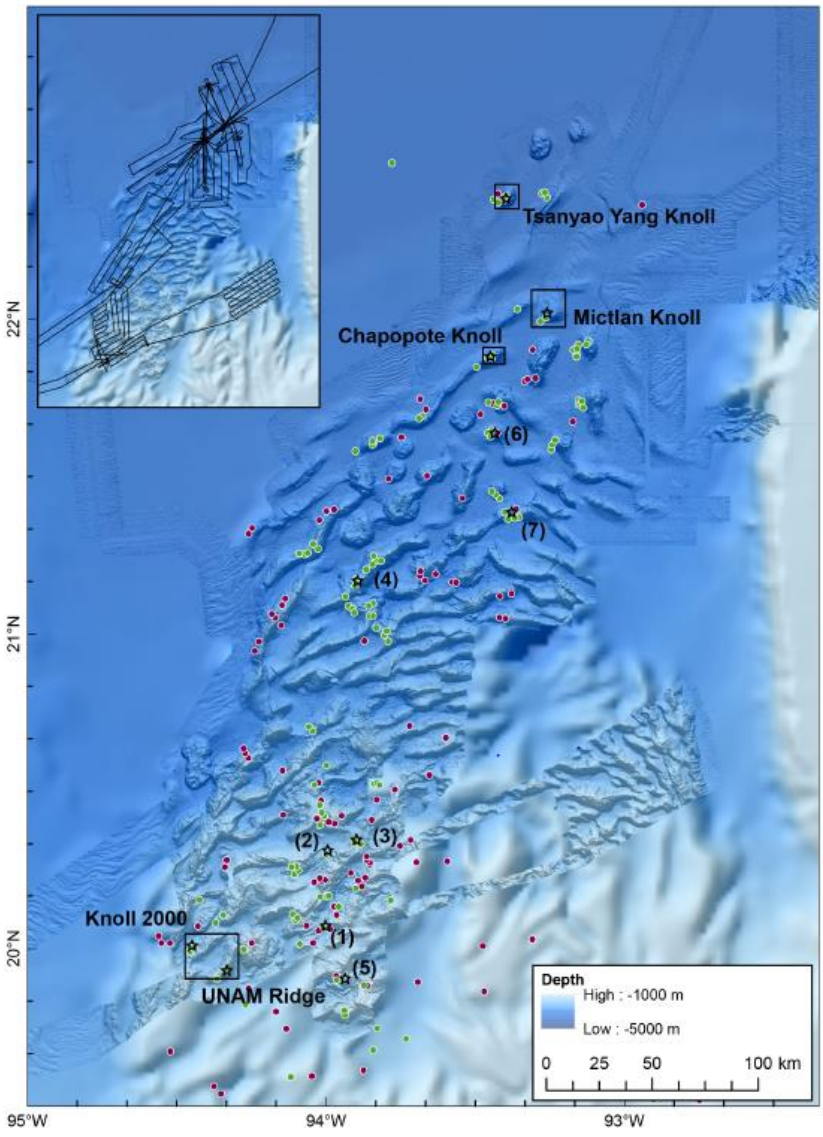


Fig. 1. Study area in the southern Gulf of Mexico, denoting the Chapopote asphalt volcano and associated seafloor structures including UNAM Ridge, Mictlan Knoll, and Tsanyao Yang Knoll (Sahling et al., 2016).

Materials and Methods

Sample collection, organic petrography, and organic geochemistry

Rock samples from seep sites in the southern GoM were collected with R/V Meteor on research cruise M114 in 2015 (Sahling and Bohrmann, 2016). Several samples were collected from recently discovered localities UNAM Ridge, Mictlan Knoll, and Tsangyao Yang Knoll (Sahling et al., 2016). All samples were retrieved with a remotely operated vehicle (ROV) MARUM QUEST 3000 using its Orion manipulator arm. Thin sections (48 x 28 mm) from all samples were prepared by Lab technicians at the University of Vienna. For stable carbon and oxygen stable isotope measurements a total of 37 samples were taken from rock slabs using a hand-held microdrill. The powder samples were reacted with oversaturated 100% orthophosphoric acid at 70 °C in a Kiel II automated reaction system and measured with a Delta Plus isotope-ratio mass spectrometer (Thermoscientific trade mark) at the Institute of Earth Sciences, University of Graz. Reproducibility of replicate analyses for standards (in-house and NBS 19) and sediment samples was better than 1sigma 0.8‰ for $\delta^{13}C$, and 0.15‰ for $\delta^{18}O$. All carbonate isotopic values are quoted relative to the Vienna PeeDee Belemnite (V-PDB).

A qualitative estimation of the fluorescence properties under blue light irradiation was done using a Zeiss microscope. Due to the instable character of bitumen impregnations in the investigated carbonates, bitumen reflectance, fluorescence intensity and spectral distribution could not be obtained. Hence, RAMAN spectra of 3 bitumen samples were measured instead, using a LABRAM (ISA Jobin Yvon) instrument equipped with a frequency-doubled Nd–YAG laser (100 mW source). Wavenumber measurements have an accuracy of 1.62 cm^{-1} at low Dn (Raman shift around 0 cm^{-1}) and 1.1 cm^{-1} at high Dn (around 3000 cm^{-1}). Spectral fitting was done with the open source IFORS software (Keno Lünsdorf, University of Göttingen).

Total organic carbon (TOC) content was determined on 26 subsamples from 5 different rock samples. Subsamples were carefully ground to fine powder using an agate mortar, after which the powder was decalcified by slow addition of 0.1% hydrochloric acid (HCl) until all inorganic carbonate was removed. The remaining material was rinsed with dichloromethane-cleaned water, centrifuged, and dried at 60°C to obtain the non-carbonate residue powder. This powder was then heated to 500°C at a rate of 10°C/min, and subsequently to 1000°C at 70°C/min. A slower rate of heat increase was applied between 0

and 500°C to prevent incineration of the organic-rich material. Total carbon (TC) content was determined by measuring the released CO_2 during heating. A Synthetic Carbon Leco standard was measured prior to sample analyses and a standard deviation of 0.06% was calculated. The TOC content of bulk rock samples was obtained by relating TC content of residue powder to the mass ratio of powder prior to and after decalcification (cf. Smrzka et al., 2016 supplementary material). All TOC data are shown in Table 1.

Locality	Sample	TOC after HCL [%]	TOC whole rock [%]
UNAM Ridge	19317	7.19	45.8
Mictlan Knoll	19336	8.71	50.6
Mictlan Knoll	19327	8.08	50.4
Tsanyao Yang Knoll	19328-4	0.792	29.4
Tsanyao Yang Knoll	19328-8	2.32	33.1

Table 1. Total organic carbon (TOC) of carbonate samples after treatment with hydrochloric acid, and TOC contents of whole rock samples.

Stable isotope geochemistry

Carbonate powders for stable isotope measurements were derived from polished rock slabs using a handheld microdrill at low rotational speed. The powders were reacted with oversaturated 100% orthophosphoric acid at 70 °C in a Kiel II automated reaction system ,and measured with a Delta Plus isotope-ratio mass spectrometer (Thermoscientific trade mark) at the Institute of Earth Sciences, University of Graz. Reproducibility of replicate analyses for standards (in-house and NBS 19) and sediment samples was better than 1 sigma 0.8‰ for $\delta^{13}C$ and 0.15‰ for $\delta^{18}O$. All carbonate isotopic values are quoted relative to VPDB.

Trace and rare earth element geochemistry

In situ analyses of trace element concentrations were carried out by laser-ablation ICP-MS at the Department of Geosciences, University of Bremen, using a NewWave UP 193 solid-state laser coupled to a Thermo-Finnigan Element 2 HR-ICP-MS. Samples and standards were ablated with an irradiance of approximately 1 GW cm^{-2}, spot sizes of 35 to 100 µm, and a laser pulse rate of 5 Hz. Plasma power was

1200 W, helium (approximately 0.8 L min-1) was used as sample gas, and argon (approximately 0.8 L min-1) was subsequently added as make-up gas. All isotopes were analyzed at low resolution with 5 samples in a 20% mass window and a total dwell time of 25 ms for each isotope. Blanks were measured for 25 s prior to ablation. NIST610 glass was analyzed for external calibration after every 8 to 12 samples using the values of Jochum et al. (2011).

For data quantification the Cetac GeoProTM software was used with ^{43}Ca as the internal standard. Because of high Sr concentrations in many samples of this study, the interference of $^{86}Sr^{2+}$ on $^{43}Ca^{2+}$ was corrected for all carbonate analyses using a factor derived from regular analyses of a Sr-rich carbonate standard (MACS-3). Data quality was assessed by regular analyses of USGS reference materials BCR2G and BHVO2G (basaltic glasses) along with the samples. External precision and accuracy for these standards are better than 5% for most elements. For consecutive analyses of NIST614 and NIST616 glasses the precision for most REE is better than 5% at the 1 ppm level, and 14 to 55% at the 0.02 ppm level. As an additional test for the REE and Y, repeated analyses of the glass standards NIST614 (nominal 1 µg/g) and NIST616 (nominal 0.02 µg/g) yielded a precision of about 1-8% and 1-57% (typically around 20%), respectively. As the detection limits of the REE and Y are not well defined owing to their low blanks, we tentatively assigned 0.001 µg/g as the detection limit. For some elements (e.g., Sm, Eu, Lu), such low contents correspond to very few counts per second, which results in relative standard deviations as high as 50%. All element data are shown in Tables 2 and 3 (except for negative values, which are marked as zero), but we note that values below approximately 0.02 ppm are close to the detection limits. For rare earth element patterns, absolute concentrations were normalized to the Post Archean Australian Shale (PAAS) standard, after Taylor and McLennan (1985). Cerium, Europium, and Praseodymium anomalies are calculated from shale-normalized concentrations as follows: $Ce/Ce^* = 3Ce/(2La+Nd)$, $Eu/Eu^* = 3Eu/(2Sm + Tb)$, and $Pr/Pr^* = 2Pr/(Ce + Nd)$. Enrichments in light REEs are calculated as $\sum LREE/\sum REE+Y$, whereby $\sum LREE$ is the sum of concentrations of La to Sm.

Sample preparation and measurement procedures on oil and bitumen were conducted at the Department for Analytical Chemistry, Montanuniversität Leoben, Austria. Bitumen samples were digested in duplicate using a high pressure asher (HPA-S, Anton Paar, Graz, Austria). Subsamples of approx. 0.4 g were digested in quartz vessels during two hours at a temperature of 300 °C and a pressure of approx. 125 bar, using 6 ml concentrated HNO_3 and 0.5 ml 30 % m/m H_2O_2. The digests were filled up to a volume of 50 ml with ultra-pure water, decanted from undissolved solid residues, and diluted ten-fold

again prior to measurement. Measurements were performed according to Walkner et al. (2017) using an Agilent 8800 Triple Quadrupole ICP-MS (Agilent Technologies, Tokyo, Japan), using O_2 and NH_3 (10 % in He) as reaction gasses in order to remove polyatomic interferences affecting some of the measurements. A total of 40 minor and trace elements were quantified using aqueous multi-element standard solutions for external calibration. All element data on hydrocarbons are shown in Tables 4 and 5.

UNAM Ridge															
	Mg	Al	Si	Mn	Fe	Ni	Zn	Sr	Mo	Ba	U	Sb	As	Mg/Sr	Mo/U
Clear aragonite	103	2.53	305	1.07	79.6	0.515	0.456	6000	0.103	9.14	2.52	0.001	0.103	0.017	0.041
	85.1	2.40	194	0.684	72.6	0.132	0.375	6941	0.161	9.77	3.38	0.018	0.055	0.012	0.048
	96.2	1.46	182	0.424	74.4	0.307	0.350	6671	0.073	9.86	2.55	0.010	0.073	0.014	0.029
	116	0.915	182	0.914	89.1	1.25	0.420	6406	0.072	9.81	2.58	0.021	0.095	0.018	0.028
	107	1.95	152	0.428	70.5	0.398	0.348	6340	0.033	10.3	3.04	0.003	0.055	0.017	0.011
	135	7.60	765	0.754	78.8	0.568	0.447	6245	0.093	9.82	2.54	0.005	0.067	0.022	0.037
	137	8.70	878	0.828	76.7	0.340	0.403	7026	0.084	10.6	3.24	0.034	0.086	0.020	0.026
	110	3.15	308	0.983	94.9	0.917	0.396	6400	0.142	10.3	3.16	0.010	0.035	0.017	0.045
	96.2	3.94	177	0.518	83.9	0.194	0.369	6326	0.141	10.2	2.68	0.008	0.015	0.015	0.053
Gray aragonite	205	143	530	3.60	383	1.26	0.95	6923	0.717	14.8	5.53	0.070	0.893	0.030	0.130
	303	437	1412	8.59	703	1.74	2.29	7733	1.31	15.8	6.52	0.002	0.923	0.039	0.202
	212	137	641	4.72	386	0.833	0.90	7671	1.55	16.5	5.40	0.036	0.71	0.028	0.287
	257	195	929	7.64	567	1.24	1.36	7361	1.01	17.3	6.10	0.019	1.21	0.035	0.165
	236	101	523	3.51	248	0.871	0.67	7285	0.528	15.5	5.01	0.024	0.546	0.032	0.105
	215	84	576	3.00	198	1.94	0.70	6892	0.582	14.6	4.96	0.017	0.464	0.031	0.117
Micrite	1216	3989	10716	46.5	2402	2.72	8.59	7688	0.826	25.3	12.4	0.069	0.586	0.158	0.067
	1600	5426	14695	69.5	3093	4.25	11.08	7660	0.936	29.3	13.8	0.081	0.618	0.209	0.068
	1372	4702	12978	59.1	2525	2.97	9.30	7584	0.936	30.9	13.5	0.072	0.650	0.181	0.070
	1349	4182	11436	55.9	2457	3.18	10.65	7728	0.864	27.8	12.1	0.072	0.519	0.175	0.072
	1616	5507	14347	66.2	3048	3.94	11.08	7559	0.975	31.8	12.6	0.074	0.570	0.214	0.078
Mictlan Knoll															
	Mg	Al	Si	Mn	Fe	Ni	Zn	Sr	Mo	Ba	U	Sb	As	Mg/Sr	Mo/U
Clear aragonite	119	0.047	70.0	1.59	79.2	0.297	0.054	6630	0.070	9.88	3.16	0.032	0.077	0.018	0.022
	173	0.055	75.6	2.21	75.6	0.474	0.125	6598	0.195	10.0	3.12	0.001	0.046	0.026	0.063
	145	0.039	76.0	1.87	75.6	0.193	0.072	6604	0.092	10.1	3.38	0.049	0.093	0.022	0.027
	164	0.036	74.4	2.22	71.2	0.134	0.147	6325	0.092	9.78	3.33	0.030	0.148	0.026	0.028
	147	0.105	75.9	1.77	77.5	0.180	0.139	6598	0.111	9.62	3.28	0.011	0.085	0.022	0.034
	130	0.031	72.0	1.38	78.2	0.107	0.131	6792	0.035	9.81	3.07	0.027	0.003	0.019	0.011
	121	0.027	78.9	0.870	78.1	0.375	0.097	6848	0.047	9.48	2.87	0.029	0.088	0.018	0.016
	115	0.006	64.9	0.925	73.6	0.486	0.059	6805	0.056	9.94	2.81	0.003	0.082	0.017	0.020
	141	0.051	77.2	1.30	77.7	0.406	0.026	6720	0.052	10.7	2.25	0.004	0.034	0.021	0.023
	162	0.030	46.3	2.08	76.1	0.194	0.076	6281	0.096	10.5	3.30	0.013	0.054	0.026	0.029
Gray aragonite	206	54.09	503.5	0.731	173	0.725	0.736	6948	0.145	7.16	9.06	0.033	0.448	0.030	0.016
	192	9.84	205.4	0.541	95	0.959	0.519	6767	0.203	7.03	6.09	0.021	0.330	0.028	0.033
	237	4.49	200.8	0.819	281	0.530	0.835	7619	0.152	6.98	8.93	0.010	0.692	0.031	0.017
	379	40.69	1302.8	0.745	218	0.873	1.114	7782	0.318	8.25	6.13	0.037	0.451	0.049	0.052
	221	9.48	306.3	0.557	275	0.814	0.532	6543	0.194	6.34	8.84	0.023	0.727	0.034	0.022
	227	14.59	302.9	0.851	330	1.197	1.087	6870	0.289	6.39	4.49	0.049	0.825	0.033	0.064
	277	12.13	547.7	0.758	478	0.764	1.163	7135	0.226	7.03	3.94	0.063	1.211	0.039	0.057
	331	27.36	515.1	0.709	181	1.161	0.844	8089	0.324	8.29	6.90	0.006	0.547	0.041	0.047
	215	4.17	144	0.590	195	0.289	0.709	6661	0.184	6.43	5.45	0.013	0.585	0.032	0.034
	249	4.61	117	0.557	136	0.628	0.633	6552	0.228	6.49	6.16	0.012	0.40	0.038	0.037
Oil-smeared aragonite	1012	3491	9257	8.48	2093	23.4	4.75	7145	1.64	12.9	11.4	0.093	2.16	0.142	0.144
	358	290	823	2.52	245	6.9	0.926	7313	0.755	8.64	5.36	0.011	0.566	0.049	0.141
	488	182	609	1.78	252	11.5	0.859	7010	0.982	7.41	5.02	0.025	0.797	0.070	0.196
	545	546	1373	5.10	435	21.8	1.38	7266	1.92	7.49	6.13	0.031	0.772	0.075	0.314
	493	645	1907	9.70	548	16.7	1.61	7443	1.50	9.23	5.58	0.022	0.729	0.066	0.268
	415	463	1610	4.64	776	16.7	1.98	7642	1.45	8.50	5.71	0.010	1.46	0.054	0.253
Micrite	3330	11987	35611	16.8	4481	10.8	11.2	7338	0.359	43.2	20.4	0.079	1.12	0.454	0.018
	1290	4676	11787	7.02	1981	4.65	5.15	7128	0.258	18.9	31.2	0.045	1.29	0.181	0.008
	4830	16663	42407	38.9	7500	23.3	16.8	7242	1.09	54.4	19.4	0.170	3.51	0.67	0.056
	15744	73003	175485	101	26533	65.9	68.8	7592	1.25	178	24.5	0.419	4.68	2.07	0.051
	21200	87441	200776	123	31176	78.2	66.2	7845	1.72	205	32.8	0.481	7.25	2.70	0.052
Tsanyao Yang Knoll															
	Mg	Al	Si	Mn	Fe	Ni	Zn	Sr	Mo	Ba	U	Sb	As	Mg/Sr	Mo/U
Clear aragonite	82.5	8.06	317	2.56	77.3	0.091	0.195	9947	0.257	8.24	2.07	0.258	0.117	0.008	0.124
	79.8	1.15	128	0.748	89.1	0.644	0.298	11300	0.628	10.9	2.99	0.069	0.066	0.007	0.210
	50.0	0.231	166	1.10	64.7	b.d.l.	b.d.l.	9904	0.029	7.44	1.62	0.070	0.086	0.005	0.018
	40.6	0.389	165	1.90	72.9	0.813	0.232	11135	0.067	9.43	1.90	0.015	0.059	0.004	0.035
	35.5	0.187	159	2.41	89.7	0.236	0.234	10543	0.185	10.4	1.39	b.d.l.	0.043	0.003	0.133
	32.9	1.37	469	1.65	95.5	0.573	b.d.l.	10526	0.539	7.91	2.26	0.181	0.173	0.003	0.238
	51.8	0.320	181	1.60	94.2	0.038	b.d.l.	12232	0.229	11.0	1.99	0.052	0.041	0.004	0.115
	48.7	0.388	201	2.76	73.3	0.103	b.d.l.	10443	0.074	8.64	1.55	0.043	b.d.l.	0.005	0.048
	38.3	b.d.l.	186	2.20	71.5	0.350	0.057	12055	0.105	8.69	1.98	0.019	0.128	0.003	0.053
	64.7	0.613	151	2.66	80.5	0.566	0.100	10168	0.325	7.64	2.42	0.084	0.117	0.006	0.134
Gray aragonite	205	0.810	156	0.840	68.2	0.794	0.232	9319	0.948	8.26	3.74	0.034	0.300	0.022	0.253
	231	0.764	189	0.559	75.1	0.727	0.110	10712	0.811	9.11	4.09	b.d.l.	0.197	0.022	0.198
	200	0.732	242	0.131	71.1	0.731	0.205	9483	0.495	8.32	3.94	0.020	0.313	0.021	0.126
	168	1.137	185	0.763	76.9	0.705	0.069	9996	0.432	8.21	3.89	0.015	0.301	0.017	0.111
	155	1.422	235	0.803	70.5	0.677	0.181	10683	0.746	8.22	3.37	0.046	0.294	0.015	0.221
	136	0.773	257	0.680	83.2	0.577	0.103	10158	0.568	7.63	3.30	b.d.l.	0.259	0.013	0.172
	125	0.354	172	0.561	63.3	0.637	0.228	10501	0.708	8.30	3.52	b.d.l.	0.142	0.012	0.201
	169	0.216	210	0.652	74.9	0.598	0.233	10761	0.665	9.90	4.02	0.015	0.171	0.016	0.165
	137	0.889	184	0.553	65.7	0.982	0.338	10442	0.567	7.54	3.23	b.d.l.	0.160	0.013	0.176
	131	0.712	168	0.876	68.4	0.501	0.228	11453	1.026	9.06	2.99	0.043	0.123	0.011	0.343
Micrite	16863	12104	27573	176	8069	11.6	19.6	6845	0.630	50.2	18.6	0.256	6.6	2.46	0.034
	16559	14690	37349	157	9440	16.7	25.5	7784	0.595	61.2	17.4	0.209	6.5	2.13	0.034
	22545	12514	29242	203	11899	15.0	29.5	7887	1.14	55.8	19.0	0.331	15.8	2.86	0.060
	20749	15224	33450	178	13953	16.3	28.8	7448	1.46	60.8	17.2	0.373	16.4	2.79	0.085

Table 2. Phase specific trace element contents of carbonates. All values in ppm.

UNAM Ridge

	La	Ce	Pr	Nd	Sm	Eu	Gd	Tb	Dy	Y	Ho	Er	Tm	Yb	Lu	∑REE+Y	∑LREE/∑REE+Y	Y/Ho	Ba/Sm	Ce/Ce*	Log(Ce/Ce*	Eu/Eu*	Pr/Pr*
Clear aragonite	0.002	0.008	0.001	0.006	0.007	0.008	0.003	0.000	0.000	0.037	0.002	0.005	0.000	0.003	0.000	0.081	0.218	22.5	1346	1.12	0.051	8.97	0.642
	0.008	0.006	0.000	0.003	0.005	0.004	0.000	0.000	0.002	0.033	0.000	0.000	0.001	0.007	0.001	0.069	0.211	n.d.	2154	0.493	-0.307	7.00	0.223
	0.004	0.003	0.002	0.004	0.005	0.012	0.002	0.001	0.003	0.027	0.002	0.001	0.001	0.003	0.001	0.071	0.205	n.d.	1895	0.286	-0.544	11.59	2.63
	0.003	0.001	0.001	0.009	0.000	0.001	0.002	0.001	0.005	0.041	0.000	0.000	0.001	0.002	0.001	0.070	0.906	n.d.	n.d.	0.134	-0.873	1.52	1.20
	0.004	0.003	0.002	0.014	0.000	0.002	0.002	0.001	0.003	0.034	0.001	0.000	0.000	0.000	0.000	0.066	0.742	59.8	n.d.	0.210	-0.679	3.74	0.779
	0.017	0.024	0.002	0.013	0.007	0.002	0.003	0.001	0.002	0.047	0.000	0.003	0.000	0.004	0.001	0.125	0.187	n.d.	1460	0.682	-0.166	1.23	0.608
	0.012	0.028	0.004	0.006	0.000	0.008	0.008	0.002	0.004	0.048	0.000	0.003	0.000	0.001	0.000	0.122	0.497	n.d.	n.d.	1.29	0.112	9.50	1.60
	0.009	0.009	0.003	0.003	0.000	0.000	0.000	0.001	0.002	0.039	0.000	0.002	0.001	0.001	0.001	0.070	0	n.d.	n.d.	0.604	-0.219	0.000	2.90
	0.017	0.021	0.003	0.009	0.010	0.016	0.007	0.002	0.009	0.042	0.000	0.003	0.000	0.004	0.000	0.145	0	n.d.	1036	0.658	-0.181	7.96	1.50
Gray aragonite	3.14	3.48	0.753	3.03	0.462	0.091	0.245	0.028	0.168	0.884	0.032	0.078	0.008	0.047	0.005	12.4	0.645	27.5	32.0	0.516	-0.287	1.25	1.28
	2.74	2.73	0.623	2.44	0.486	0.089	0.293	0.038	0.233	1.071	0.037	0.102	0.012	0.078	0.011	11.0	1.13	29.3	32.5	0.478	-0.321	1.10	1.33
	2.71	2.30	0.562	2.16	0.297	0.087	0.234	0.024	0.121	0.798	0.028	0.061	0.007	0.054	0.007	9.45	0.619	28.2	55.5	0.421	-0.376	1.76	1.38
	3.52	4.19	0.810	3.29	0.581	0.131	0.358	0.034	0.203	1.197	0.042	0.116	0.011	0.095	0.013	14.6	0.435	28.4	29.8	0.562	-0.250	1.43	1.23
	1.87	1.79	0.364	1.53	0.291	0.048	0.173	0.023	0.111	0.764	0.019	0.061	0.008	0.041	0.006	7.11	0.000	39.2	53.3	0.469	-0.328	0.993	1.22
	1.89	1.94	0.414	1.84	0.254	0.041	0.155	0.026	0.114	0.744	0.021	0.054	0.007	0.043	0.009	7.55	0.000	34.9	57.4	0.476	-0.322	0.915	1.19
Micrite	1.66	2.93	0.361	1.31	0.321	0.069	0.302	0.044	0.292	1.80	0.061	0.178	0.027	0.169	0.023	9.6	0.916	29.6	78.7	0.879	-0.056	1.11	1.08
	2.51	4.43	0.532	1.92	0.413	0.106	0.395	0.060	0.422	2.84	0.090	0.276	0.041	0.281	0.047	14.4	0.479	31.6	70.9	0.887	-0.052	1.30	1.07
	2.39	3.51	0.469	1.99	0.382	0.113	0.371	0.054	0.334	2.26	0.069	0.203	0.026	0.199	0.033	12.4	0.810	32.9	81.1	0.720	-0.143	1.51	1.03

	1.74	2.95	0.391	1.45	0.340	0.094	0.298	0.048	0.334	1.94	0.063	0.175	0.026	0.185	0.030	10.1	0.000	30.9	81.8	0.831	-0.081	1.42	1.11
	2.50	4.45	0.535	2.12	0.451	0.117	0.440	0.061	0.443	3.15	0.100	0.320	0.054	0.370	0.059	15.2	0.000	31.6	70.6	0.867	-0.062	1.35	1.02

Mictlan Knoll

	La	Ce	Pr	Nd	Sm	Eu	Gd	Tb	Dy	Y	Ho	Er	Tm	Yb	Lu	∑REE+Y	∑LREE/∑REE+Y	Y/Ho	Ba/Sm	Ce/Ce	Ce/Ce*	Eu/Eu*	Pr/Pr*
	0.001	0.000	0.001	0.006	0.014	0.002	0.004	0.000	0.002	0.029	0.000	0.001	0.001	0.002	0.000	0.062	0.349	n.d.	697	0.007	-2.14	0.854	0.770
	0.001	0.001	0.002	0.006	0.000	0.006	0.001	0.001	0.001	0.031	0.001	0.002	0.000	0.003	0.000	0.055	0.170	43.3	n.d.	0.203	-0.693	15.4	1.96
	0.001	0.001	0.000	0.001	0.001	0.002	0.007	0.001	0.002	0.035	0.000	0.001	0.001	0.000	0.000	0.053	0.098	190.6	7268	0.539	-0.268	4.12	0.045
	0.002	0.001	0.001	0.004	0.007	0.002	0.010	0.001	0.000	0.035	0.001	0.001	0.000	0.000	0.001	0.066	0.249	49.0	1317	0.238	-0.623	1.51	1.70
Clear aragonite	0.002	0.000	0.002	0.001	0.000	0.001	0.006	0.000	0.004	0.028	0.000	0.001	0.000	0.006	0.000	0.051	0.092	65.0	n.d.	0.075	-1.12	5.74	11.0
	0.002	0.000	0.001	0.001	0.006	0.003	0.005	0.001	0.003	0.032	0.002	0.002	0.000	0.001	0.002	0.061	0.166	15.1	1577	0.012	-1.91	2.13	4.02
	0.001	0.001	0.000	0.002	0.000	0.003	0.003	0.000	0.002	0.035	0.000	0.000	0.001	0.001	0.000	0.049	0.076	107	n.d.	0.174	-0.759	14.3	0.771
	0.003	0.002	0.001	0.006	0.009	0.001	0.004	0.001	0.001	0.035	0.000	0.001	0.000	0.000	0.001	0.066	0.330	77.7	1057	0.221	-0.655	0.650	1.59
	0.002	0.001	0.001	0.005	0.004	0.004	0.004	0.001	0.000	0.033	0.000	0.001	0.002	0.001	0.000	0.058	0.203	n.d.	3058	0.105	-0.977	5.95	0.772
	0.002	0.000	0.001	0.000	0.000	0.001	0.002	0.000	0.001	0.032	0.000	0.002	0.000	0.000	0.000	0.043	0.080	n.d.	n.d.	0.022	-1.65	5.38	311
	3.55	4.92	0.614	2.28	0.423	0.089	0.295	0.035	0.172	0.804	0.025	0.073	0.007	0.059	0.008	13.4	0.808	32.12	16.9	0.732	-0.135	1.25	1.08
	2.71	3.76	0.471	1.87	0.328	0.072	0.231	0.028	0.151	0.756	0.027	0.060	0.008	0.047	0.005	10.5	0.929	28.16	21.4	0.719	-0.143	1.30	1.04
Gray aragonite	3.25	4.42	0.574	2.14	0.419	0.097	0.277	0.030	0.155	0.619	0.029	0.052	0.005	0.032	0.003	12.1	1.069	21.54	16.7	0.714	-0.146	1.42	1.10
	2.84	4.17	0.505	1.92	0.343	0.071	0.222	0.029	0.141	0.758	0.024	0.061	0.008	0.040	0.007	11.1	0.934	31.98	24.1	0.767	-0.115	1.22	1.05
	3.90	5.52	0.709	2.44	0.356	0.080	0.268	0.030	0.145	0.600	0.022	0.058	0.008	0.030	0.004	14.2	0.748	26.72	17.8	0.754	-0.123	1.34	1.13
	2.97	4.56	0.572	1.96	0.339	0.077	0.240	0.029	0.153	0.812	0.024	0.066	0.009	0.042	0.006	11.9	1.084	33.96	18.8	0.806	-0.093	1.35	1.13

	3.17	4.39	0.564	2.09	0.395	0.084	0.267	0.035	0.197	0.840	0.026	0.063	0.010	0.043	0.006	12.2	0.747	32.38	17.8	0.727	-0.138	1.24	1.09
	3.84	5.59	0.645	2.39	0.395	0.118	0.300	0.037	0.176	0.836	0.031	0.063	0.012	0.055	0.008	14.5	0.678	26.83	21.0	0.776	-0.110	1.72	1.04
	2.73	3.71	0.469	1.85	0.346	0.078	0.256	0.028	0.156	0.623	0.028	0.050	0.008	0.032	0.005	10.36	0.000	22.00	18.6	0.708	-0.150	1.34	1.05
	2.85	3.99	0.504	2.14	0.336	0.098	0.273	0.028	0.197	0.675	0.030	0.055	0.007	0.047	0.004	11.2	0.000	22.26	19.3	0.708	-0.150	1.73	1.01
	3.10	5.73	0.817	3.32	0.704	0.121	0.440	0.047	0.266	1.06	0.041	0.101	0.017	0.115	0.013	15.9	0.860	26.2	18.4	0.830	-0.08	1.07	1.09
	3.88	6.46	0.809	3.59	0.489	0.127	0.323	0.025	0.165	0.676	0.028	0.042	0.003	0.066	0.006	16.7	0.912	23.9	17.7	0.789	-0.10	1.69	0.980
Oil-smeared aragonite	3.00	4.82	0.707	3.03	0.439	0.137	0.339	0.034	0.190	0.545	0.021	0.066	0.006	0.062	0.011	13.4	0.895	25.8	16.9	0.738	-0.13	1.87	1.07
	4.05	6.40	0.907	3.32	0.684	0.127	0.353	0.038	0.169	0.685	0.089	0.092	0.009	0.062	0.013	17.0	0.904	7.7	10.9	0.778	-0.11	1.19	1.15
	4.47	6.71	0.916	3.60	0.663	0.126	0.347	0.046	0.131	0.745	0.025	0.085	0.013	0.070	0.012	18.0	0.911	29.3	13.9	0.743	-0.13	1.17	1.09
	3.86	6.16	0.737	3.04	0.718	0.083	0.337	0.048	0.178	0.728	0.031	0.074	0.006	0.070	0.005	16.1	0.903	23.2	11.8	0.796	-0.10	0.715	0.999
	0.372	0.173	0.072	0.272	0.066	0.020	0.061	0.009	0.047	0.204	0.013	0.029	0.002	0.013	0.002	1.36	0.704	15.3	136	0.237	-0.62	1.572	1.59
	0.206	0.084	0.037	0.167	0.052	0.007	0.038	0.003	0.028	0.140	0.006	0.013	0.001	0.016	0.000	0.786	0.683	22.7	196	0.200	-0.70	-0.792	1.38
Micrite	0.181	0.088	0.036	0.193	0.027	0.010	0.039	0.008	0.037	0.216	0.006	0.022	0.001	0.013	0.001	0.878	0.598	33.3	366	0.22	-0.66	1.301	1.20
	0.268	0.151	0.053	0.215	0.052	0.012	0.047	0.006	0.050	0.212	0.009	0.019	0.004	0.009	0.002	1.11	0.668	24.4	191	0.28	-0.55	1.251	1.47
	0.337	0.150	0.071	0.308	0.060	0.013	0.054	0.005	0.043	0.222	0.008	0.030	0.006	0.036	0.003	1.34	0.689	26.9	163	0.212	-0.67	1.260	1.47

Tsanyao Yang Knoll

	La	Ce	Pr	Nd	Sm	Eu	Gd	Tb	Dy	Y	Ho	Er	Tm	Yb	Lu	∑REE+Y	∑LREE/∑REE+Y	Y/Ho	Ba/Sm	Ce/Ce	Ce/Ce*	Eu/Eu*	Pr/Pr*
	0.036	0.057	0.006	0.056	b.d.l.	b.d.l.	0.023	0.004	0.030	0.355	0.015	0.032	0.002	0.024	0.009	0.648	0.269	23.6	n.d.	0.603	-0.219	2.52	0.540

Clear aragonite	0.123	0.105	0.017	0.093	0.030	0.016	0.052	0.004	0.060	0.430	0.019	0.034	0.004	0.038	0.005	1.031	0.046	23.2	357.3	0.432	-0.364	2.73	0.972
	0.063	0.056	0.007	0.049	b.d.l.	0.003	0.005	0.001	b.d.l.	0.100	0.001	0.013	0.002	b.d.l.	0.001	0.301	0.299	69.8	n.d.	0.445	-0.352	2.18	0.715
	0.014	0.017	0.002	0.011	0.004	b.d.l.	0.002	0.001	0.005	0.066	b.d.l.	0.001	b.d.l.	0.002	b.d.l.	0.124	1.194	n.d.	2334	0.629	-0.201	0	0.678
	0.023	0.037	0.003	0.016	0.011	0.002	0.008	b.d.l.	0.011	0.107	b.d.l.	0.005	b.d.l.	0.006	0.002	0.231	0.300	n.d.	942.1	0.831	-0.081	1.49	0.682
	0.050	0.041	b.d.l.	0.058	b.d.l.	0.004	0.017	0.001	0.017	0.157	0.005	0.013	b.d.l.	0.006	b.d.l.	0.368	0.336	32.6	n.d.	0.357	-0.448	6.63	0.428
	0.020	0.021	0.008	0.015	0.005	b.d.l.	0.015	0.001	0.013	0.166	0.003	0.007	b.d.l.	0.004	b.d.l.	0.279	0.212	52.3	2174	0.511	-0.292	0.726	2.38
	0.035	0.027	0.007	0.023	0.032	b.d.l.	0.003	0.001	0.005	0.069	0.004	0.001	b.d.l.	b.d.l.	b.d.l.	0.207	1.532	18.2	272.1	0.398	-0.400	0.506	1.48
	0.021	0.019	b.d.l.	0.020	b.d.l.	0.002	0.005	b.d.l.	0.004	0.080	b.d.l.	0.010	b.d.l.	0.003	0.001	0.166	0.000	n.d.	n.d.	0.419	-0.378	6.43	0.608
	0.084	0.118	0.011	0.095	0.010	0.006	0.048	0.004	0.020	0.208	0.008	0.017	b.d.l.	0.013	b.d.l.	0.642	0.495	25.0	739	0.617	-0.210	1.97	0.590
Gray aragonite	3.64	6.23	0.679	2.290	0.328	0.049	0.112	0.020	0.083	0.302	0.010	0.021	0.002	0.021	0.001	13.8	1.19	29.0	25.2	0.910	-0.041	0.944	1.05
	4.28	7.31	0.790	2.670	0.375	0.049	0.155	0.012	0.078	0.292	0.013	0.018	0.003	0.021	0.002	16.1	0.987	23.2	24.3	0.910	-0.041	0.909	1.05
	4.69	8.01	0.793	2.567	0.296	0.042	0.106	0.013	0.065	0.255	0.008	0.025	0.004	0.026	0.001	16.9	0.874	33.9	28.1	0.940	-0.027	0.937	1.02
	4.44	7.99	0.691	2.427	0.305	0.023	0.134	0.015	0.051	0.267	0.010	0.022	0.005	0.018	0.001	16.4	1.03	25.6	26.9	0.991	-0.004	0.489	0.911
	4.12	7.27	0.694	2.433	0.252	0.046	0.127	0.022	0.101	0.320	0.009	0.030	0.005	0.009	0.003	15.4	0.500	37.5	32.7	0.953	-0.021	1.07	0.963
	4.94	8.18	0.818	2.643	0.305	0.043	0.176	0.017	0.042	0.256	0.008	0.018	0.003	0.010	0.003	17.5	0.568	30.7	25.0	0.916	-0.038	0.915	1.02
	2.12	3.58	0.372	1.481	0.151	0.035	0.080	0.009	0.028	0.199	0.006	0.012	b.d.l.	0.012	0.001	8.09	0.822	33.6	55.1	0.872	-0.059	1.48	0.950
	2.81	4.75	0.514	1.608	0.246	0.042	0.106	0.007	0.043	0.238	0.013	0.022	0.002	0.023	0.002	10.4	0.562	18.6	40.2	0.921	-0.036	1.18	1.09
	1.89	2.97	0.334	1.321	0.137	0.026	0.079	0.011	0.022	0.192	0.007	0.010	0.001	0.012	b.d.l.	7.01	0	27.9	55.2	0.810	-0.092	1.12	0.991
	1.62	2.80	0.290	1.003	0.141	0.015	0.053	0.009	0.066	0.173	0.005	0.015	0.003	0.004	b.d.l.	6.20	0	33.9	64.3	0.923	-0.035	0.683	1.01

Micrite	5.70	14.0	1.37	4.99	1.25	0.27	1.12	0.210	1.19	7.14	0.244	0.728	0.092	0.646	0.083	38.990	0.515	29.2	40.2	1.18	0.072	1.05	0.965
	4.40	10.5	1.12	3.85	0.817	0.209	1.44	0.137	0.886	6.04	0.168	0.540	0.082	0.535	0.081	30.756	0.676	36.0	74.9	1.15	0.059	1.23	1.03
	4.11	10.1	1.35	3.58	0.912	0.204	0.890	0.149	0.909	7.47	0.200	0.734	0.101	0.618	0.090	31.445	0.000	37.5	61.2	1.19	0.076	1.09	1.31
	4.66	10.4	1.10	3.77	0.897	0.215	1.02	0.166	1.04	8.02	0.245	0.780	0.124	0.732	0.100	33.240	0.626	32.7	67.8	1.10	0.041	1.11	1.03

Table 3. Phase specific rare earth element contents of carbonates. All values in ppm. Ce/Ce* = Cerium anomalies, Eu/Eu* = Europium anomalies, Pr/Pr* = Prasaeodymium anomalies.

Locality	Sample	Al*	P	S*	K*	Ti	V	Cr	Mn	Fe*	Co	Ni	Cu	Zn	As	Se	Rb	Sr*	Ag	Cd	Ba	Re	Pb	Mo	U	Mo/U	V/Ni	V/(V+Ni)
UNAM Ridge	19317	3.11	68.4	0.897	0.515	206	202	74.0	154	1.93	7.16	44.5	35.7	101	45.6	0.861	84.0	0.015	0.038	0.100	51.2	0.042	2.90	5.38	3.30	1.63	4.54	0.820
	19317	1.93	50.3	2.24	0.522	144	244	52.0	92.5	1.34	4.92	47.5	34.6	81.9	23.7	1.63	40.9	0.013	0.121	0.161	41.1	0.092	2.00	5.43	3.60	1.51	5.13	0.837
Mictlan Knoll	19336	1.34	78.1	2.10	0.347	89.9	401	58.4	28.3	0.743	1.80	77.6	15.8	41.2	2.20	0.812	20.2	0.159	0.104	0.034	34.5	0.029	1.92	2.34	3.67	0.637	5.17	0.838
	19327	0.410	129	0.922	0.106	108	85.7	22.5	19.0	0.277	1.11	21.4	14.9	22.4	2.05	0.959	7.89	0.329	0.295	0.326	18.7	0.037	0.609	7.36	10.8	0.680	4.00	0.800

Table 4. Elemental composition of hydrocarbon samples UNAM Ridge and Mictlan Knoll carbonates. All values in ppm except *, which are in g/100g.

Locality	Sample	La	Ce	Pr	Nd	Sm	Eu	Gd	Tb	Dy	Y	Ho	Er	Tm	Yb	Lu	∑REEs+Y	Y/Ho	∑LREE/∑REE	$(Pr/Yb)_{SN}$	Ce/Ce*	log/Ce/Ce*	Eu/Eu*	Pr/Pr*
UNAM Ridge	19317	9.74	17.2	1.947	6.785	1.10	0.201	0.792	0.12	0.722	4.06	0.158	0.454	0.07	0.433	0.063	43.9	25.754	0.839	1.53	0.890	-0.050	0.992	1.11
	19317	5.22	10.3	1.20	4.224	0.688	0.127	0.499	0.076	0.461	2.66	0.102	0.295	0.044	0.283	0.042	26.2	26.021	0.825	1.44	0.953	-0.021	1.01	1.12
Mictlan Knoll	19336	2.08	3.57	0.42	1.509	0.256	0.052	0.191	0.029	0.172	1.00	0.038	0.111	0.017	0.112	0.017	9.58	25.975	0.819	1.29	0.854	-0.068	1.10	1.13
	19327	1.45	2.50	0.306	1.130	0.201	0.042	0.164	0.025	0.154	1.08	0.036	0.106	0.016	0.106	0.017	7.33	29.944	0.762	0.98	0.838	-0.077	1.09	1.12

Table 5. Rare earth element contents of hydrocarbon samples from UNAM Ridge and Mictlan Knoll carbonates. All values in ppm.

Geochemical modeling

The PHREEQC software code (Parkhurst and Appelo, 1999) was used to simulate sulfate-dependent oxidation of a variety of organic compounds, and resulting calcium carbonate precipitation. A simple batch reaction experiment was set up with an input solution of seawater chemistry according to Nordstrom et al. (1979). A starting amount of calcite was added to the sediments of 0.7 moles. Over the course of 1 year various hydrocarbon compounds are added to the batch and reduced with sulfate according to rates and stoichiometry determined from environmental and culture studies of sulfate-reducing bacteria. Oxidation rates of hydrocarbon compounds were recalculated from literature values and are shown in Table 6. Hydrocarbon compounds were added to the batch at given rates, where they equilibrate stepwise with the initial solution producing bicarbonate and hydrogen sulfide while concomitantly reducing sulfate. The phreeqc.dat database file was used for all calculations. Kinetic calcite dissolution and precipitation was enabled by using parameters and rate equations determined by Plummer et al. (1978) as implemented in PHREEQCs phreeqc.dat database file. All solution speciation calculations were conducted at pressures of 300 bars, equivalent of an approximate water depth of 3000 m, (the water depth at which carbonates were sampled cf. Sahling et al., 2016). Formation of gas phases CH_4, CO_2, H_2S, N_2, H_2O, and H_2 was allowed at 300 bars pressure. To assess the influence of varying hydrocarbon oxidation rates with sulfate, all models were run over 1 year with constant increase of oxidation rates (Table 7). An additional set of model runs was conducted where all hydrocarbons are oxidized at the rate of AOM ($4.09*10^{-9}$ moles/L/s) to assess the influence of the oxidation of different hydrocarbons at equal rates on saturation state and precipitation of calcite, as well as on gas production (Table 8).

Oxidation with sulfate	Rate [moles/L/s]	ΔCalcite [g]	ΔSI Calcite	SI Calcite	Effect on $CaCO_3$	pH
Methane[a]	4.09e-9	0.645	0.393	1.47	Precipitation	7.41
Propane[b]	6.50E-10	0.567	0.423	0.687	Precipitation	7.01
Butane[b]	6.50E-10	0.541	0.398	0.611	Precipitation	6.96
n-dodecane[c]	8.44E-09	-2.16	-0.119	-1.27	Dissolution	5.34
Benzene[d]	7.72e-8	-0.916	-0.831	-0.583	Dissolution	6.01
Toluene[e]	1.41e-9	-3.48	-0.526	-1.34	Dissolution	5.39
Xylene[f]	2.50E-08	-3.00	-0.881	-1.14	Dissolution	5.58
Phenanthrene[g]	3.21E-11	0.213	0.543	0.483	Precipitation	7.16
Hexadecane[h]	3.91E-11	-0.051	0.321	-0.115	Precipitation	7.03
Naphthalene[i]	3.85E-11	-0.054	0.251	-0.136	Precipitation	7.08

Table 6. Results from geochemical batch modeling after a run time of 1 year. Hydrocarbon oxidation rates derived from [a]Wallmann et al. (2006), [b]Kniemeyer et al. (2007), [c]Kropp et al. (2000), [d]Musat and Widdel (2008), [e]Beller et al. (1992), [f]Harms et al. (1999), [g]Coates et al. (1996), [h]So and Young (1999), [i]Coates et al. (1997). "ΔCalcite" denotes the net calcite precipitation in grams, "ΔSI Calcite" the change in calcite saturation index over 1 year of simulation, "SI calcite" and pH are given after 1 year of simulation.

Oxidation with sulfate	Rate increase	ΔCalcite [g]	ΔSI Calcite	SI Calcite	Effect on $CaCO_3$	pH
Methane	6x	0.722	0.644	1.49	Precipitation	7.45
Propane	6x	-0.245	-0.408	-0.262	Dissolution	6.25
Butane	6x	-0.413	-0.447	-0.356	Dissolution	6.18
n-dodecane	2x	-1.13	-0.035	-0.631	Dissolution	5.33
Benzene	6x	-3.37	-1.24	-1.24	Dissolution	5.51
Toluene	3x	-3.44	-1.12	-1.20	Dissolution	5.36
Xylene	6x	-3.24	-1.29	-1.15	Dissolution	5.47
Phenanthrene	24x	-0.890	-0.556	-0.571	Dissolution	6.02
Hexadecane	36x	-1.81	-0.445	-0.891	Dissolution	5.78
Naphthalene	48x	-1.97	-0.529	-0.932	Dissolution	5.75

Table 7. Results from geochemical batch modeling after 1 year. Rates were increased stepwise from initial rates shown in Table 6.

Oxidation with sulfate	Rate [moles/L/s]	ΔCalcite [g]	ΔSI Calcite	SI Calcite	Effect on $CaCO_3$	pH
Methane	4.09e-9	0.645	0.393	1.47	Precipitation	7.41
Propane		0.695	-1.14	-0.282	Dissolution	6.24
Butane		-0.865	-1.27	-0.486	Dissolution	6.09
n-dodecane		-2.362	-1.28	-1.00	Dissolution	5.70
Benzene		-2.505	-1.25	-1.03	Dissolution	5.67
Toluene		-2.625	-1.22	-1.06	Dissolution	5.65
Xylene		-2.417	-1.15	-0.988	Dissolution	5.70
Phenanthrene		-2.731	-1.05	-1.07	Dissolution	5.64
Hexadecane		-3.648	-1.03	-1.29	Dissolution	5.47
Naphthalene		-3.212	-1.15	-1.20	Dissolution	5.54

Table 8. Results from geochemical batch modeling after 1 year using rates of methane oxidation from table 6 for all hydrocarbon compounds.

Results

Authigenic carbonate from UNAM Ridge, Mictlan Knoll, and Tsanyao Yang Knoll

The carbonate sample from UNAM Ridge (GeoB 19317) was collected at a water depth of 1287 m. Seafloor outcrops at UNAM Ridge are several meters across and rise up to 2 meters into the water column (Fig. 2A). Closer investigation with the ROV revealed a chaotic rock fabric with an apparently high porosity, suggesting low cohesion of the material. Numerous shell fragments are attached to and cemented by authigenic carbonate. UNAM Ridge carbonates are characterized by a heterogeneous mixture of rock fragments, mud clasts and small, dispersed asphalt pieces intermingled with the carbonaceous matrix (Fig. 2C, D). The rocks are penetrated by small, tubular holes several centimeters deep (Fig. 2B, D). These holes stem from tubeworms using carbonates as substrate for growth while accessing sulfide from the zone of sulfate reduction. This notion is supported by the direct ROV observation of tubeworms dwelling directly within the carbonate (Fig. 2B). Macroscopically, the carbonates can be classified as carbonate breccias, and appear to have cemented a heterogeneous mixture of background sediment and shell fragments during precipitation. The samples show a black, dark brownish to reddish staining (Fig. 2C), which may be due to the oxidation of reduced iron and manganese to Fe– and Mn–(oxy)hydroxide minerals on the surface of the rock upon exposure to oxic seawater.

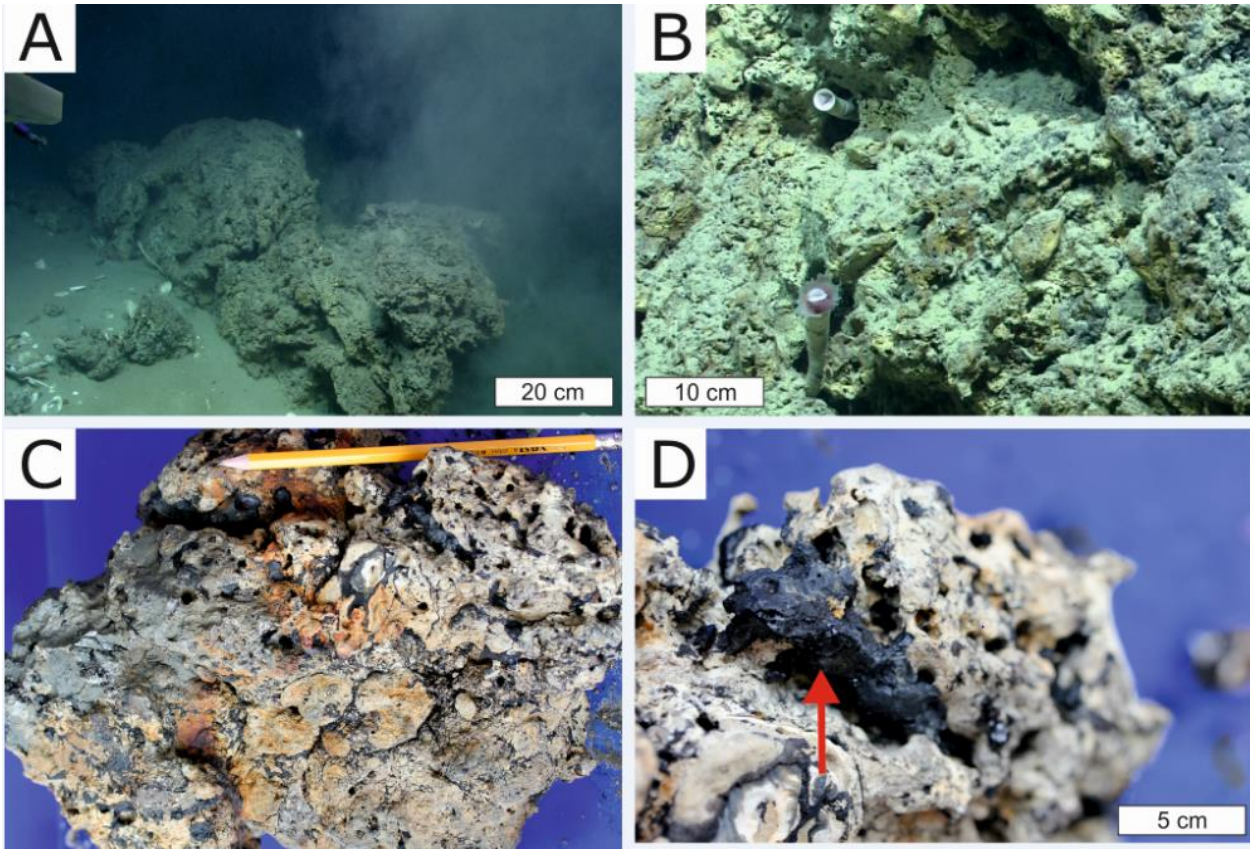


Fig. 2. UNAM Ridge. (A) Large carbonate outcrop on the seafloor, (B) close-up image of the outcrop in (A) showing porous and heterogeneous fabric and tubeworms nesting with small holes and cavities, (C) sample GeoB 19317 featuring heterogeneous fabric of the carbonate breccia, pencil for scale. (D) arrow highlights asphalt pieces interspersed with carbonate of sample GeoB 19317.

Two separate sites were sampled for authigenic carbonates at Mictlan Knoll. The first site was a conspicuous, small circular structure of asphalt embedded the seafloor (Fig. 3A). Within the circular asphalt rim a further rim of whitish authigenic carbonate was clearly visible. A dense cluster of bathymodiolin bivalves and tubeworms nested in the center of this tubular structure, whereas the asphalt surrounding the tube was colonized by sponges and galatheid crabs (Fig. 3A). Carbonate and asphalt are likely connected to larger pieces buried in the sediments. The first sample (GeoB 19327) measures 10-12 cm in length with a matrix of fine, white authigenic carbonate that is pervaded by finely disperse asphalt veins, larger drops and smaller specks (Fig. 3B). Parts of the sample are smeared by liquid oil and asphalt that exhibit a strong smell of heavy petroleum. Thin, entangled tubeworm roots occur within the sample

that are entwined within the carbonate matrix and penetrate the rock in numerous places. The second sample collected from Mictlan Knoll (GeoB 19336) was taken from a distinct positive seafloor features named Hydrate Hill (Sahling et al., 2016). Large and extensive carbonates crop out on all sides of the hill, forming multiple layers of meter-scale pavements stacked atop each other (Fig. 3C). Below the outcropping carbonates there are numerous smaller carbonate slabs and crusts scattered about the entire feature. The collected sample measures around 40 x 30 cm in length and breadth (Fig. 3D). Small chunks and dispersely distributed veins of asphalt pervade the rock. As recognized in previous samples, this piece also features numerous small, tubular holes and indentations. Samples from Mictlan Knoll are much denser and more compact than samples from UNAM Ridge, and are therefore carbonate breccias.

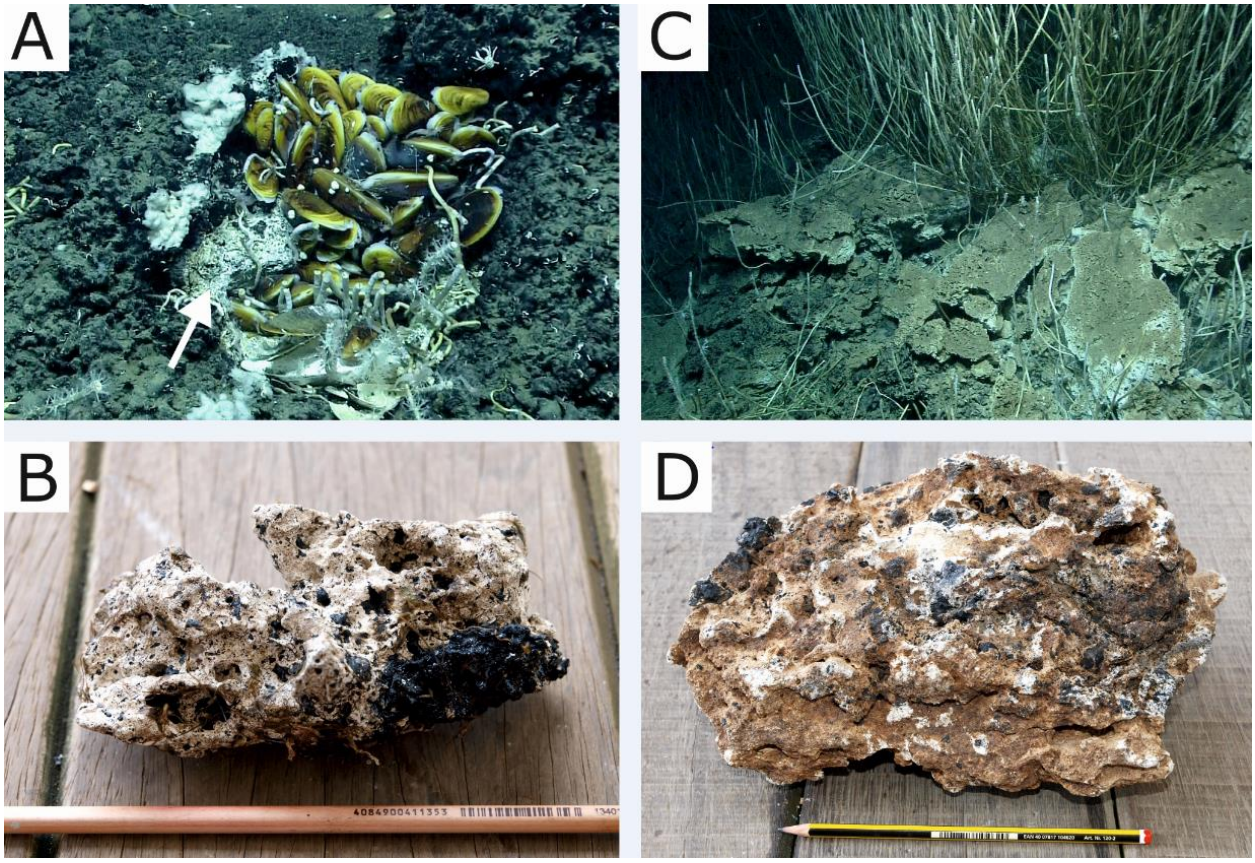


Fig. 3. Mictlan Knoll. (A) small *bathymodiolus* mussel nest with sponges, tubeworms, and galatheid crabs within an asphalt field of active oil and gas seepage, white arrow denotes circular carbonate precipitate GeoB 19327 shown in (B). Mussels are ~20 cm in length for scale (B) Sample GeoB 19327 retrieved from carbonate precipitates shown in (A). Pure, whitish carbonate is interspersed and smeared with fresh, liquid heavy oil, as well as roots of juvenile tubeworms, pencil for scale. (C) Extensive authigenic carbonate pavements at Hydrate Hill among lush fields of tubeworms. Tubeworms are ~ 120cm long for scale. (D) Sample GeoB 19336 collected from site depicted in (C) featuring denser and more compact precipitate littered with small asphalt specks, pencil for scale.

Tsanyao Yang Knoll was the second new Knoll sampled for authigenic carbonates. It is the deepest knoll explored so far in the southern GoM, located in a depth of almost 3400 m (Sahling et al., 2016). Three separate sites were selected for carbonate sampling. The first sample collected (GeoB 19348-4) is located directly at the base of a massive gas hydrate block colonized by bathymodiolin mussels (Fig. 4A). Isolated carbonate fragments collected using the ROV net turned out to be cm-scaled pieces of nearly pure, clear whitish aragonite (Fig. 4B). The small pieces from the net all exhibit a whitish to light gray color and feature very small, mm-sized holes and cavities. The second net sample (GeoB 19348-8) that contained pieces of carbonate was sampled directly atop a tall gas hydrate pillar; around 3 to 4 meters above the seafloor directly next to a vent vigorously emitting large quantities of methane gas (Fig. 4C, Sahling et al., 2016). This sample comprises juvenile tubeworms and mussels directly associated with freshly precipitated carbonate fragments (Fig. 4D). It was possible to reconstruct the orientation of the carbonate pieces, as thin films of bacterial mats were observed on one side of the piece, whereas fine, thin tubeworm roots and juvenile bathymodiolin mussels were attached to the top side of the sample (Fig. 4D).

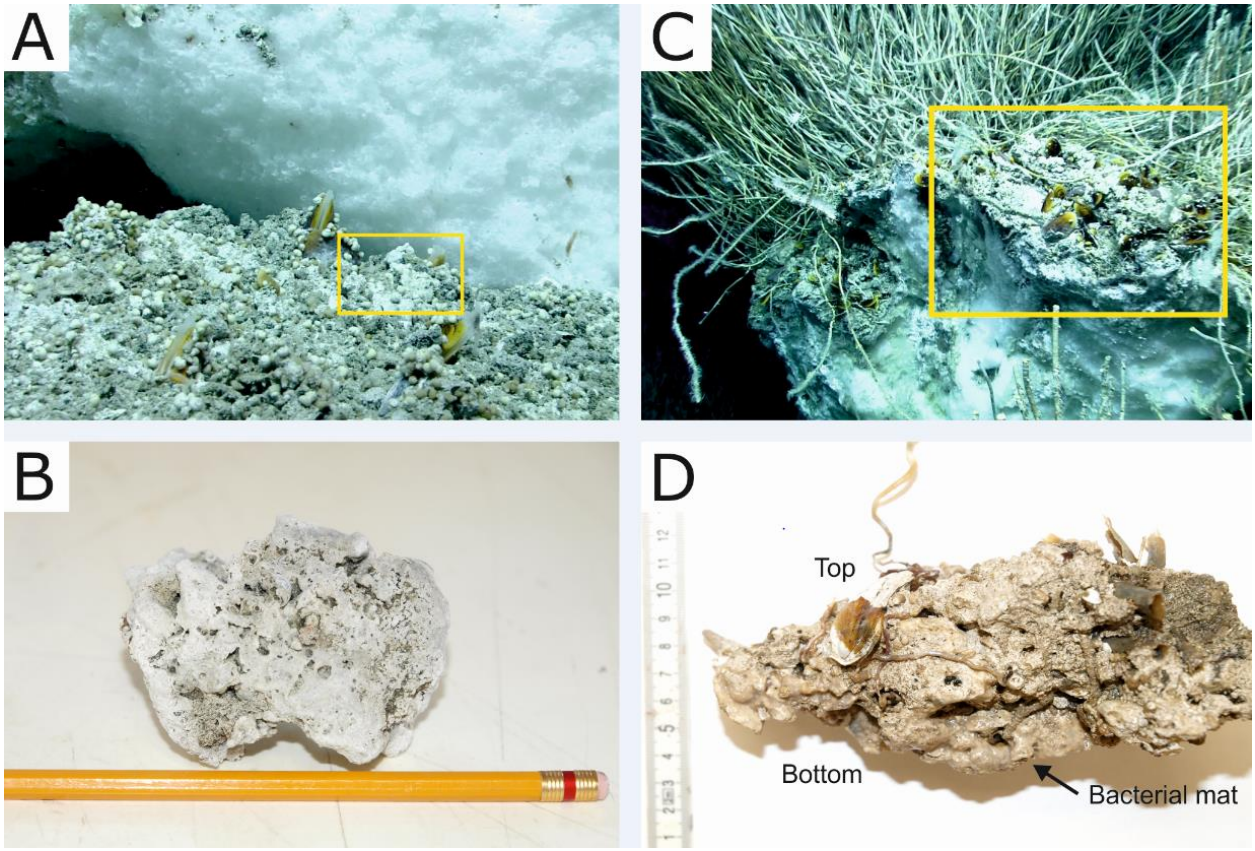


Fig. 4. Tsanyao Yang Knoll. (A) Large piece of gas hydrate among carbonate rubble and *bathymodiolus* mussels, yellow rectangle denotes sampled area, rectangle is ~20 cm in width. (B) Whitish-gray carbonate piece from net sample GeoB 19348-4 collected from yellow rectangle in (A), pencil for scale. (C) Sample location GeoB 19348-8 located atop a large gas hydrate pillar hosting a dense aggregate of tubeworms clusters, *bathymodiolus* mussels, and authigenic carbonate, yellow rectangle denoted location of net sample GeoB 19348-8, rectangle is ~1 m in width. (D) Carbonate sample GeoB 19348-8 collected from yellow rectangle in (C) where original orientation could be reconstructed. Top part of the sample features juvenile mussels and tubeworm roots, bottom part covered by bacterial mats.

Thin section petrography

Micrite (i.e. microcrystalline calcite) and two forms of clear aragonite are the main mineral phases in all samples. Micrite occurs either as fairly homogeneous matrix micrite, or as clotted and peloidal micrite. Aragonite occurs in two varieties, as clear aragonite and gray aragonite. UNAM Ridge exhibits the highest amounts of matrix micrite in relation to total volume and contains abundant nannofossils, primarily planktonic foraminifera that have been subsequently filled by liquid oil (Fig. 5A, B). Clear and gray aragonite is present only in minor amounts, where it is present as rims on the inner fringes of larger cavities (Fig. 5A, B). In places, larger and smaller clasts made up of well-cemented microcrystalline carbonate are held together by clear aragonite. Almost all cavities are filled with liquid oil, which migrated into the rock at a later stage (Fig. 5). Clotted or peloidal micrite is absent from the UNAM Ridge sample.

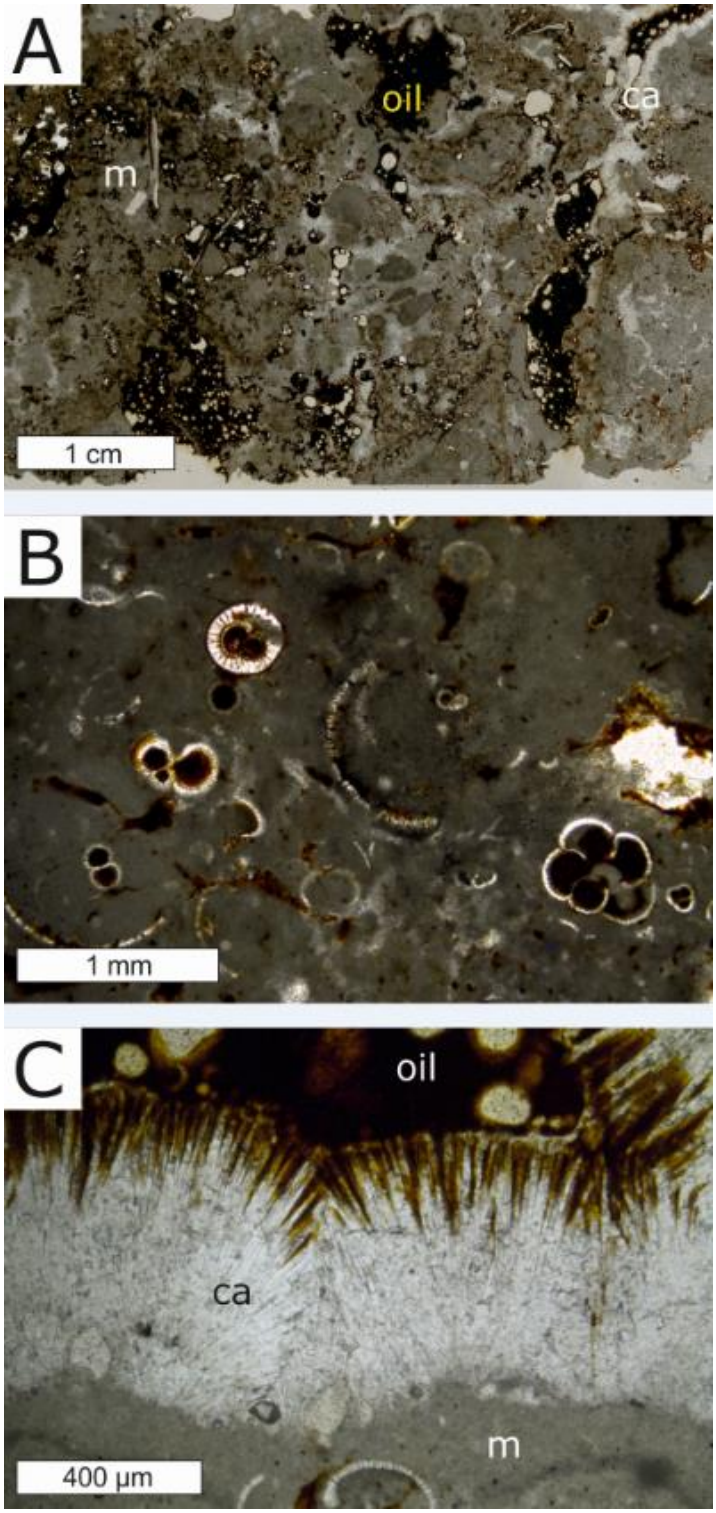


Fig. 5. UNAM Ridge, m = matrix micrite, ca = clear aragonite. (A) thin section scan of sample GeoB 19317 dominated by matrix micrite and large cavities filled by oil. Several cracks filled by clear aragonite. (B) Planktonic formainifera shells filled with oil within matrix micrite. (C) Paragenetic phase sequence of matrix micrite, clear aragonite, and liquid oil.

The two samples from Mictlan Knoll (GeoB 19327 and GeoB 19336) are similar in terms of their mineral paragenesis. Both samples contain matrix micrite, yet in much lower amounts as UNAM Ridge (Fig. 6A, D). GeoB 19336 additionally features abundant peloidal micrite, which is absent in GeoB 19327. Both samples from Mictlan Knoll additionally exhibit gray, diffuse aragonite, which dominates sample GeoB 19327 (Fig. 6B, C, F). This mineral phase is similar to clear aragonite in its appearance, except that botryoids are not as large and as clearly developed. What is most distinguishable is that gray aragonite is covered by gray, diffuse seams and smears, which makes identifying the crystal habit difficult. This seam is distributed unevenly over the aragonite covering it completely in some instances, whereas leaving other areas translucent. In sample GeoB 19327 this grayish aragonite is the volumetrically dominant phase. The macroscopic texture can be described as a matrix of gray aragonite surrounding sporadic occurrences of matrix micrite and clear aragonite. Clear aragonite forms well defined botryoids measuring several hundreds of microns in length that either exists in isolation as rims. This sample contains significant amounts of oil that – as in the UNAM Ridge sample – fills larger cavities where it is preceded by clear or gray aragonite (Fig. 6C). In places the oil covers clear and gray aragonite. Sample GeoB 19336 from Mictlan Knoll is completely devoid of liquid oil. It exhibits large amounts of solid bitumen, which is opaque under the microscope and makes up a quarter of the entire volume in certain thin sections (Fig. 6D). This bitumen is pervaded by fractures possibly derived from post depositional brittle deformation. Furthermore, sample GeoB 19336 is the only one that features bitumen out of all collected rock samples. Micrite is difficult to distinguish from diffuse gray aragonite, and is devoid of any fossils in both Mictlan Knoll samples (Fig. 6E). The other two main phases are clear and gray aragonite, whereby the former shows similar appearance as in sample GeoB 19327 (Fig. 6E, F). Gray aragonite in sample GeoB 19336 occurs as diffuse but recognizable bands (Fig. 6F).

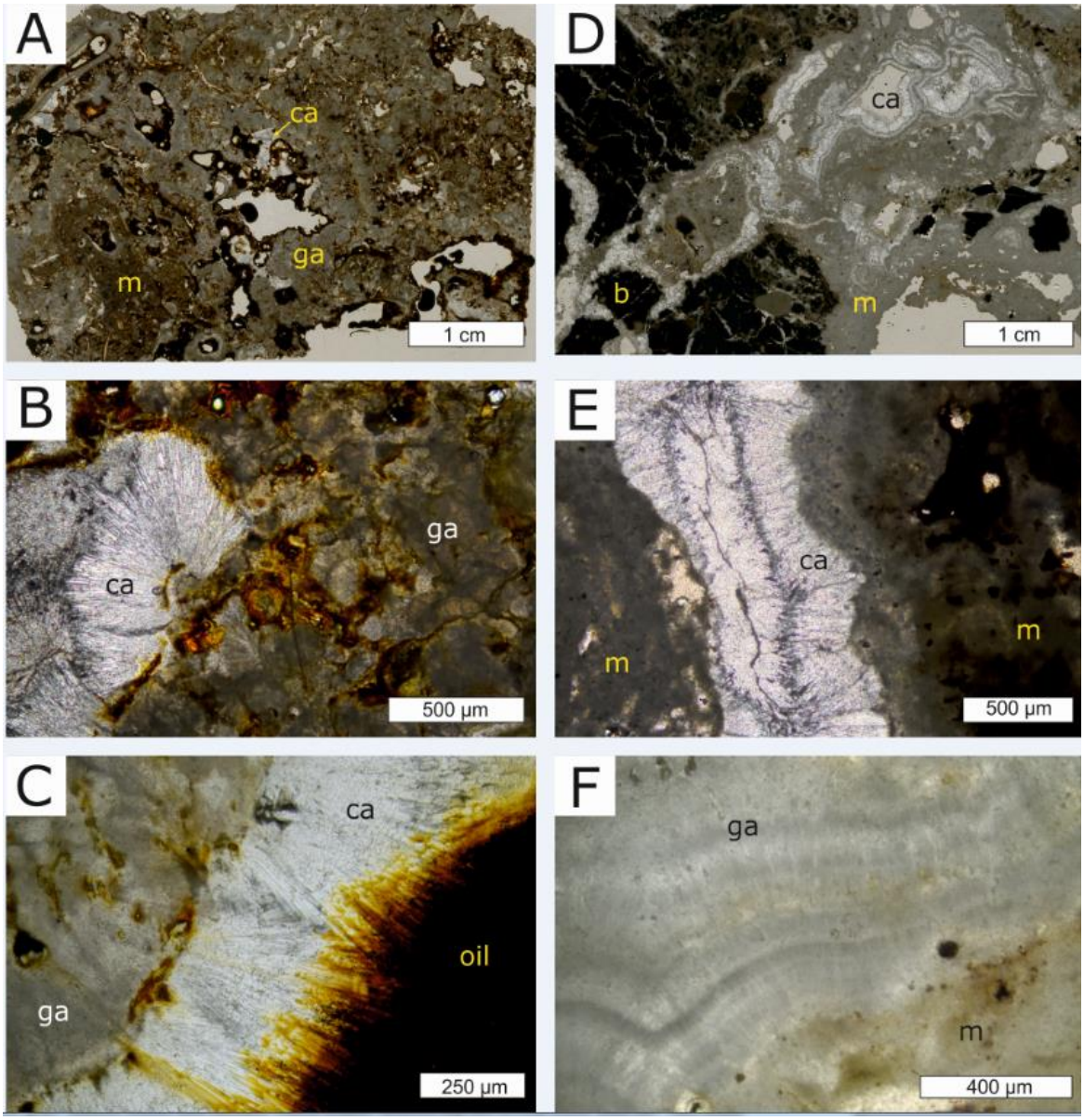


Fig. 6. Mictlan Knoll, m = matrix micrite, ca = clear aragonite, ga = gray aragonite, b = bitumen, A-C = sample GeoB 19327, D-F = sample GeoB 19336. (A) Thin section scan featuring large portions of gray aragonite and matrix micrite. Small cavities are rimmed by clear aragonite, whereas larger ones are filled by liquid oil. (B) Cavitiy completely filled by clear aragonite surrounded by small botryoids of gray aragonite interspersed with liquid oil. (C) Paragenetic phase sequence of gray aragonite, clear aragonite, and liquid oil. (D) Thin section scan showing large solid pieces of opaque bitumen. Cavities are lined with clear aragonite surrounded by matrix micrite. (E) Larger crack filled by clear aragonite surrounded by matrix micrite. (F) Close-up view of gray aragonite and matrix micrite.

Samples from Tsanyao Yang Knoll differ in several respects. They are devoid of liquid oil and bitumen. Sample GeoB 19348-4 is dominated by peloidal micrite and clear aragonite, which together make up the entire rock volume (Fig. 7A). Peloidal micrite forms diffuse clots of various sizes from which clear aragonite radiates into cavities between the micrite (Fig. 7B). Clear aragonite is present as elongated fibrous crystals forming botryoids (Fig. 7B, C). This sample is the only one featuring neither matrix micrite nor clear aragonite. Sample GeoB 19348-8 does not feature peloidal micrite. Instead, it is dominated by matrix micrite that is pervaded by cracks and cavities (Fig. 7D, E), most of which are filled by clear and/or gray aragonite cement (Fig. 7D-F). Numerous long cracks that pervade the entire thin section suggest that it has been ruptured and fractured after cementation. Gray aragonite, in contrast to all other samples, fills cavities and secondary cracks completely (Fig. 7E), and also occurs together with clear aragonite in close proximity (Fig. 7F). In contrast to GeoB 19317 from UNAM Ridge, samples from Mictlan and Tsanyao Yang Knolls are almost devoid for macro or microfossils such as shell fragments or foraminifera.

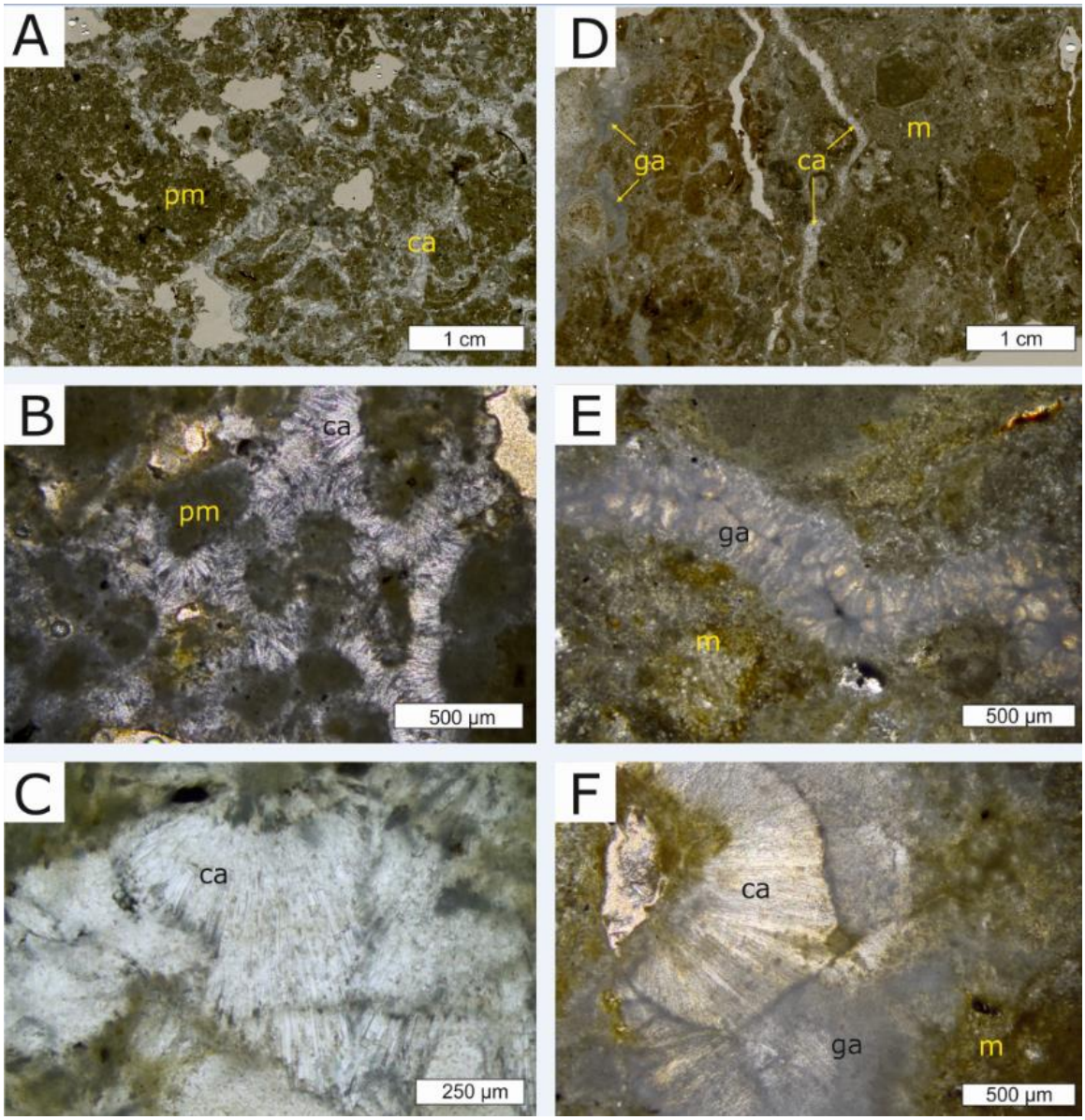


Fig. 7. Tsanyao Yang Knoll. Pm = peloidal micrite, ca = clear aragonite, ga = gray aragonite, m = matrix micrite, A-C = sample GeoB 19348-4, D-F = sample GeoB 19348-8. (A) Thin section scan dominated by peloidal micrite and clear aragonite. (B) Magnified view of clear aragonite radiating into cavities from micritic peloids. (C) Fibrous texture of clear aragonite. (D) Thin section scan showing large portions of matrix micrite penetrated by numerous cracks filled by secondary clear and gray aragonite. (E) Close-up view of a crack filled by diffuse gray aragonite surrounded by matrix micrite. (F) Cavity filled by both clear and gray aragonite.

Organic petrography and geochemistry

Sample GeoB 19317 contains large bitumen stains which host brownish carbonate crystals. Bitumen partly shows a network-like texture under white light irradiation, which might be caused by degassing. Both aggregates with a weak brownish coloration and completely dark fragments occur, with the dark population dominating. A very light greenish fluorescence was observed under blue light irradiation, which seems very uncommon following the general classification scheme of solid bitumen. Both larger bitumen aggregates and smaller, isolated particles in sample GeoB 19336 do not show fluorescence under blue light irradiation. Larger bitumen aggregates partly contain irregularly distributed carbonate needles, and show a network-like internal structure, similar to sample GeoB 19317. Sample GeoB 19348-8 contains bitumen streaks with a brownish coloration. These elongated streaks show a weak brownish fluorescence. Isolated, smaller bitumen particles mostly show no fluorescence under blue light irradiation.

Due to the unstable character of the bitumen impregnations, bitumen reflectance, as well as fluorescence spectra, could not be determined. However, Raman spectra could be obtained for all three samples in order to reveal possible differences in the maturity or geochemical character of the original oil prior to degradation. All three samples show a high grade of disarrangement of the organic bonds, indicated by broad G and D bands at 1350 cm^{-1} and 1600 cm^{-1}, respectively (Fig. 8). Furthermore, the samples show a strong fluorescence background in RAMAN, although this is also related to the relatively high energy of the used laser (532 nm wavelength). In general, spectra of samples from all three locations show similar patterns and peak positions.

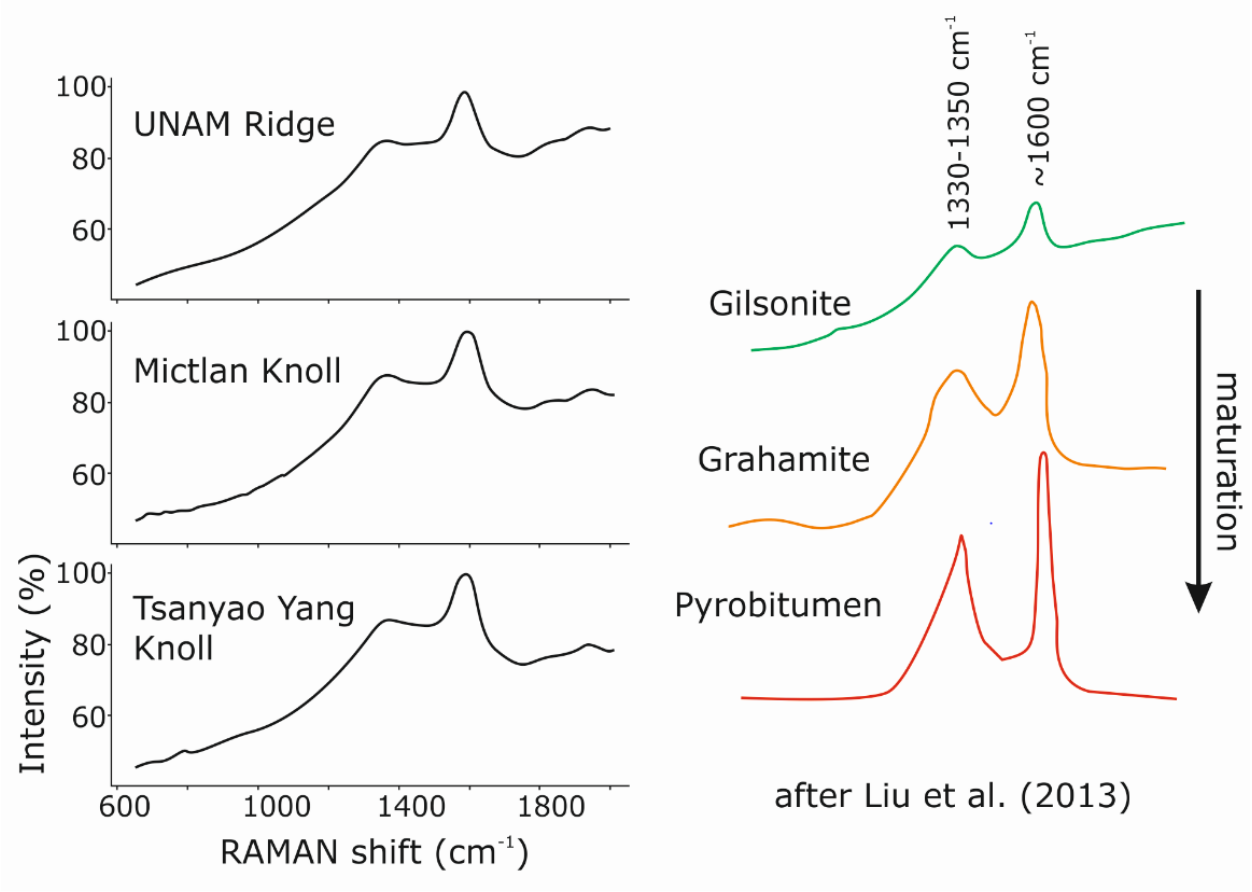


Fig. 8. Raman spectra of hydrocarbons from within carbonates from UNAM Ridge, Mictlan Knoll, and Tsanyao Yang Knoll. Right panel shows three spectra from organic geologic materials gilsonite, grahamite, and pyrobitumen, after Liu et al. (2013).

Total organic carbon of whole rock samples yielded highest average values of 8.71 and 8.08 % TOC for Mictlan Knoll samples GeoB 19336 and GeoB 19327, respectively. UNAM Ridge carbonate samples yielded TOC values of 7.19%, and Tsanyao Yang Knoll samples GeoB 19328-4 and GeoB 19328-8 yielded TOC contents of 0.792 and 2.32, respectively. Pure oil samples yielded TOC contents between 33.1 and 50.6%. All results are shown in Table 1.

Stable isotopes and total organic carbon

Phase-specific $\delta^{13}C$ values of most samples are homogeneous and cluster within −30 and −20‰, whereby $\delta^{18}O$ values range between +3 and +5‰. $\delta^{13}C$ values of clear aragonite and micrite of UNAM Ridge samples are similar, and lie below −25‰. $\delta^{13}C$ values of Mictlan knoll micrites are systematically lower than corresponding clear aragonite, a pattern that is observed for sample GeoB 19348-4 from Tsanyao Yang knoll. In contrast, clear aragonite from Tsanyao Yang sample GeoB 19348-8 is not only more strongly ^{13}C-depleted than corresponding micrite, but also yielded the most negative $\delta^{13}C$ values of all measured samples with a mean value of −31.3‰. $\delta^{18}O$ values of these aragonites also the most positive, which yielded mean values of +4.7‰. All values are shown in a cross plot in Figure 9.

Authigenic carbonates from the Campeche Knolls yield varying amounts of bulk TOC. Both samples from Mictlan Knoll yielded the highest TOC values on average, amounting to 8.7 and 8.1% for sample GeoB 19336 and GeoB 19327, respectively. Samples from Tsanyao Yang Knoll show rather different TOC values. Sample GeoB 19348-4 yielded the lowest TOC values of 0.8%, whereas sample GeoB 19348-8 showed higher values of 2.3 %, still much lower than samples from Mictlan Knoll. Total organic carbon from the UNAM Ridge sample averaged at 7.2%. Samples from Tsanyao Yang Knoll show the lowest non-carbonate fraction of 3.3 and 8.6% for samples GeoB 19348-4 and GeoB 19348-8, respectively, whereas this fraction is higher in UNAM Ridge and Mictlan Knoll samples.

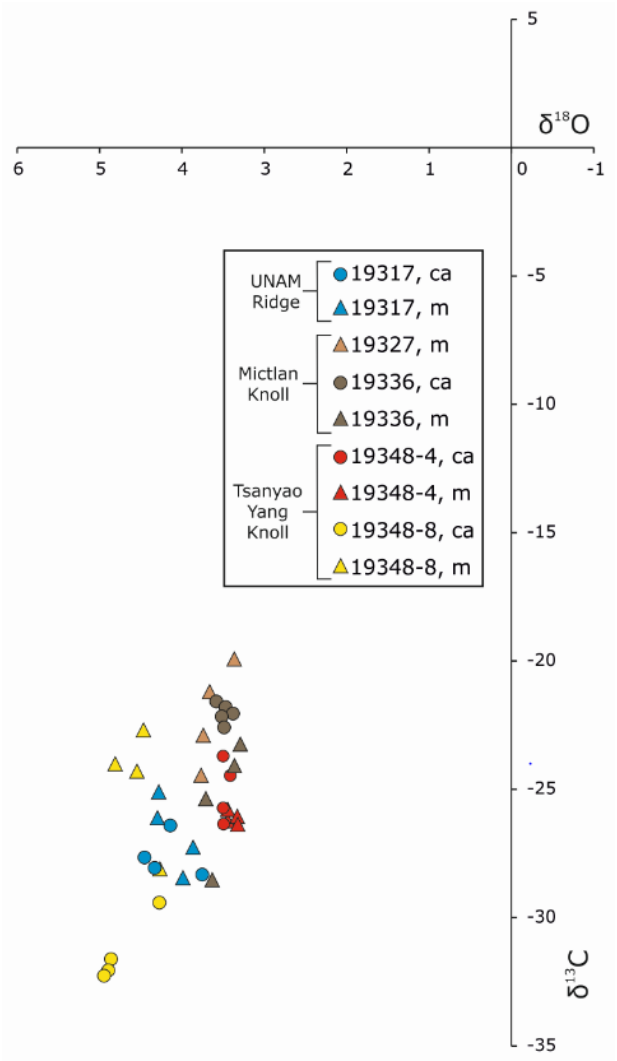


Fig. 9. Stable carbon and oxygen isotope cross plot, ca = clear aragonite, m = microcrystalline calcite.

Trace and rare earth elements

Authigenic carbonates

Clear aragonites from UNAM Ridge and Mictlan Knoll carbonates generally show similar contents of trace and REEs, yet with some minor differences. UNAM ridge has roughly twice as much total REE content as Mictlan Knoll, as well as higher concentrations of Al and Si. Yttrium/Holmium ratios and Pr/Pr* ratios of Mictlan Knoll clear aragonite are significantly higher than in UNAM Ridge clear aragonites. All clear aragonites show enrichments in heavy rare earth elements (HREEs) compared to light rare earth elements (LREEs), with more or less well developed negative Ce anomalies (Figs. 10-12A). Gray aragonites at both sites show the opposite trend, with a distinct enrichment of LREEs over HREEs (Figs. 10-12B). Gray aragonites exhibit higher concentrations of almost all trace metals and REEs than clear aragonite in all samples. Micrite in Mictlan Knoll carbonates has higher concentrations of trace metals and REEs, as well as higher Mg/Sr ratios than micrite from UNAM Ridge carbonates. While UNAM Ridge micrite shows rather smooth HREE enriched patters with a slight positive Eu anomaly, micrite from Mictlan Knoll features flatter PAAS-normalized patterns, with a slight LREE enrichment in several samples (Figs. 10-12C). Mictlan Knoll features an oil-smeared aragonite phase, which exhibits significantly elevated concentrations in all trace and rare earth metals compared to clear aragonites. Similar to gray aragonite, this phase is also characterized by an enrichment of LREEs over HREEs, as well as a positive La anomaly. Plotting Mo/U vs. ∑REE+Y reveals clear differences for clear and gray aragonites at both sites (Fig. 13A). Gray aragonites exhibit elevated ∑REE+Y concentrations, yet Mo/U ratios vary significantly among the phases and localities. The LREE enrichment is clearly dominant in gray and oil smeared aragonites compared to clear aragonites from all sites (Fig. 13B). For comparison, data from the Chapopote asphalt volcan0 and Makran accretionary prism carbonates (cf. Smrzka et al., 2016) are shown. Figure 13 allows drawing two distinct lines between oil-derived and methane-derived aragonite cements, dividing the plot into an oil- and methane-dominated domain, respectively.

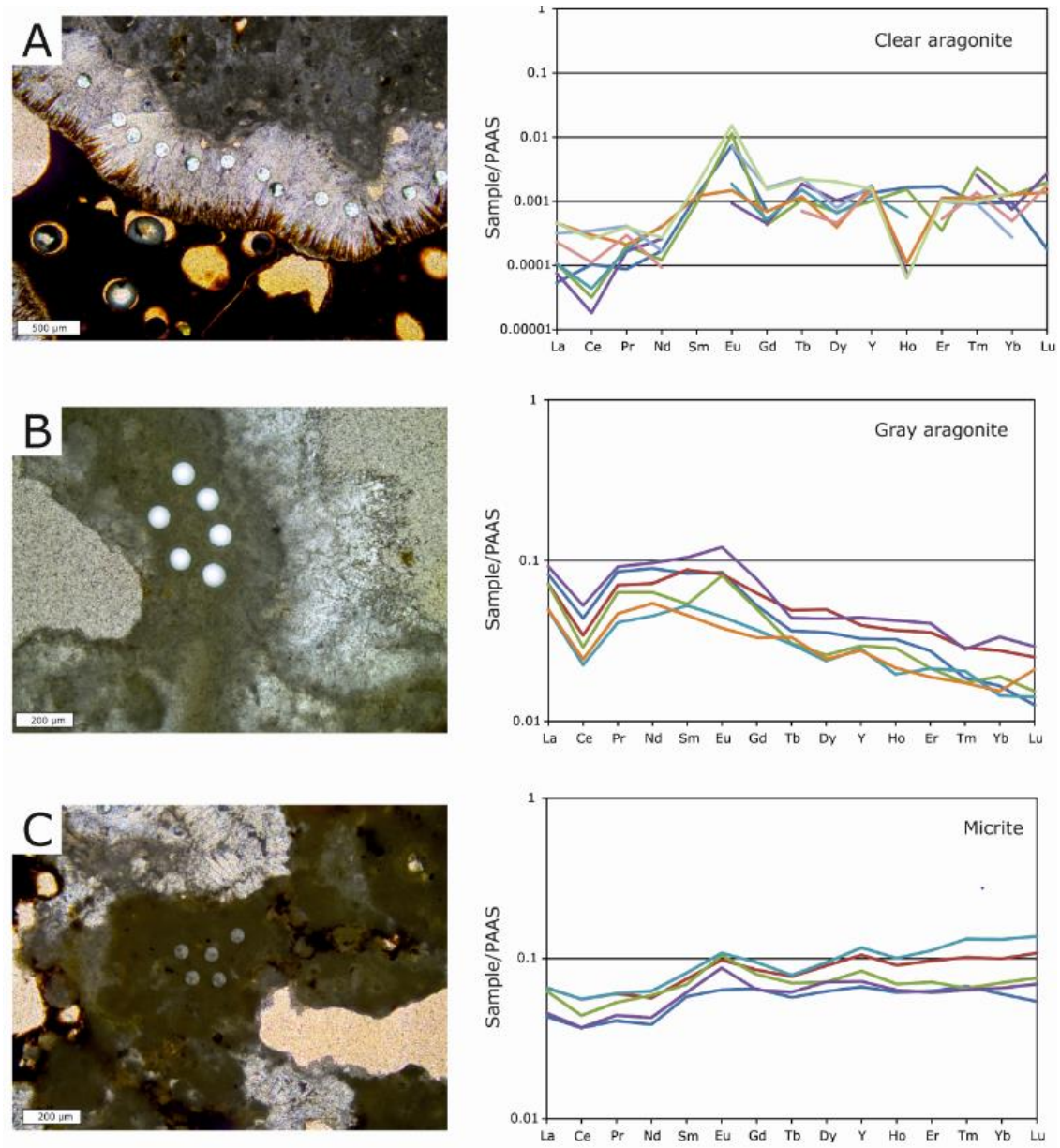


Fig. 10. Results from LA-ICP-MS analyses from UNAM Ridge carbonate. Left panel shows thin sections with ablation craters in (A) clear aragonite, (B) gray aragonite, and (C) micrite. Right panel shows corresponding REE patterns normalized to Post Archean Australian Shale (PAAS, Taylor and McLennan, 1985).

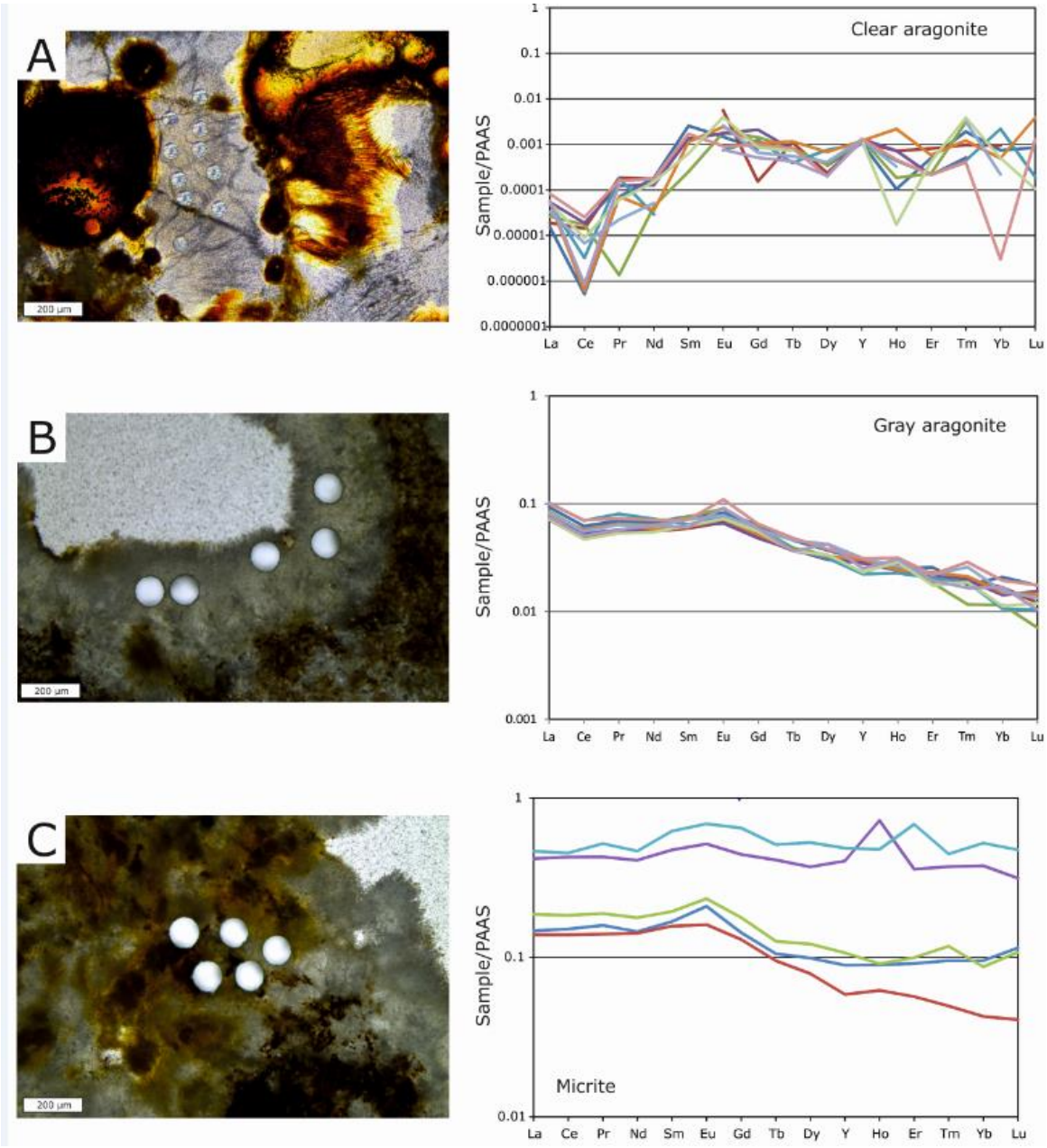


Fig.11. Results from LA-ICP-MS analyses from Mictlan Knoll carbonate. Left panel shows thin sections with ablation craters in (A) clear aragonite, (B) gray aragonite, and (C) micrite. Right panel shows corresponding REE patterns normalized to Post Archean Australian Shale (PAAS, Taylor and McLennan, 1985).

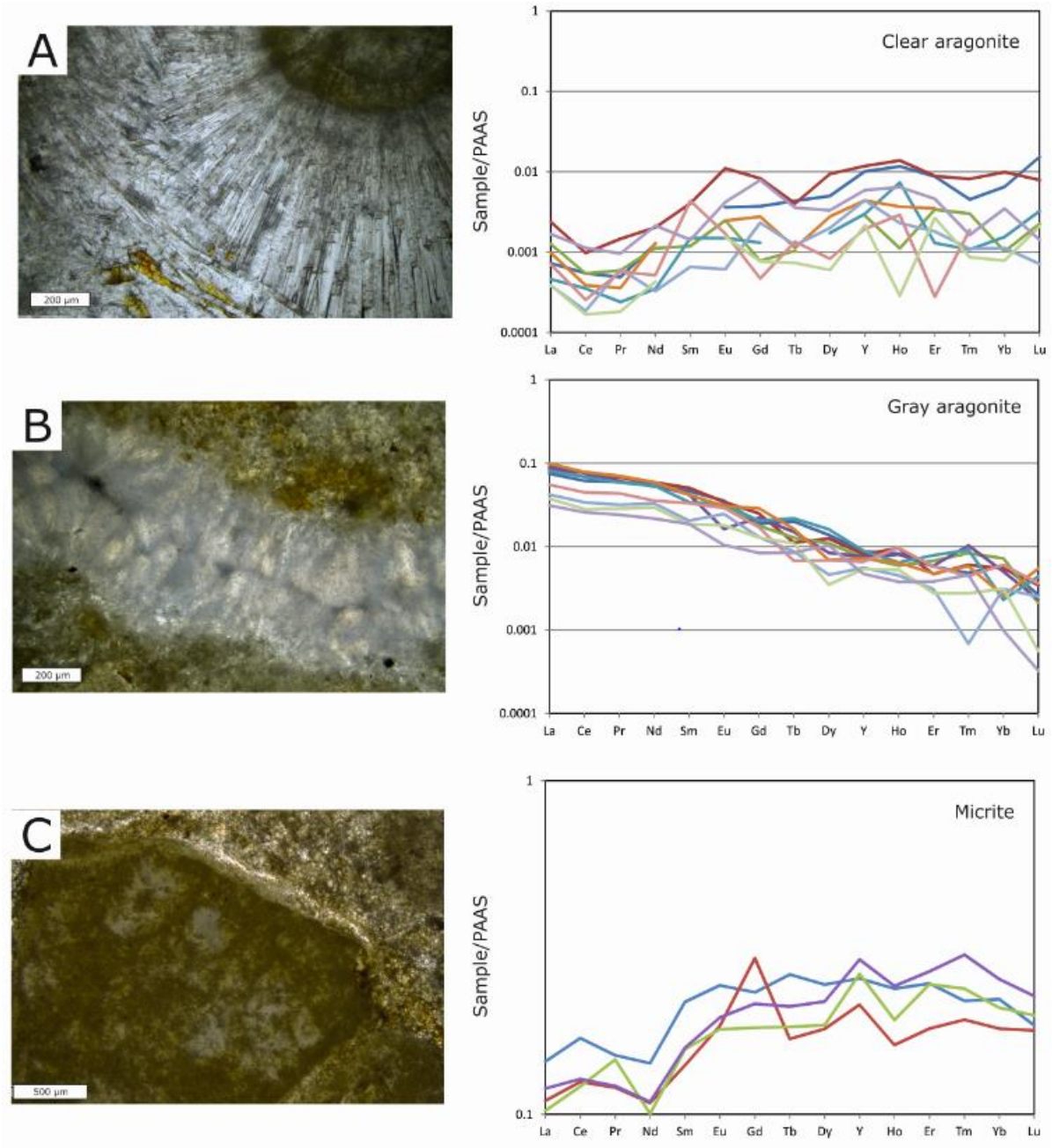


Fig.12. Results from LA-ICP-MS analyses from Tsanyao Yang Knoll carbonate. Left panel shows thin sections of (A) clear aragonite, (B) gray aragonite, and (C) micrite. Right panel shows corresponding REE patterns normalized to Post Archean Australian Shale (PAAS, Taylor and McLennan, 1985).

Plotting the data into a Ce/Ce* vs. Pr/Pr* plot after Bau and Dulski (1996) reveal a large scatter for clear aragonite data, especially values from UNAM Ridge clear aragonite (Fig. 14). The Ce anomalies in clear aragonites from Makran and Chapopote, as well as in UNAM Ridge gray aragonites appear to be real (Fig. 14). However, putative Ce anomalies in gray and oil smeared clear aragonite from Mictlan Knoll are in fact positive La anomalies. Only those data from Chapopote that exhibit clear negative Ce anomalies are plotted. Gray aragonites from Tsanyao Yang Knoll exhibit no anomalies (cf. Fig. 12B), which is why they plot into the center field (I) of the plot (Fig. 14).

Plotting clear and gray aragonite data in a Log(Ce/Ce*) vs. Nd plot after Wright et al. (1987) reveals that most clear aragonite data, except those for Chapopote, are inhomogeneous. Chapopote clear aragonite, as well as Mictlan Knoll gray aragonite plot in the oxic section below a log(Ce/Ce*) cutoff value of −0.1 (Fig. 15A). As mentioned above, only those data from Chapopote are plotted that exhibit clear negative Ce anomalies. Oil smeared aragonites from Chapopote and Mictlan Knoll plot both below and above a log(Ce/Ce*) −0.1. Clear and gray aragonites from Tsanyao Yang Knoll plot in the oxic and anoxic areas of the plot. Microcrystalline calcite from all sites largely plot above the −0.1 value in the anoxic section of the plot (Fig. 15B). Data of clear and gray aragonite show differing trends when their Ce anomalies are plotted vs. shale-normalized Pr/Yb ratios (Fig. 15C). Clear aragonites from Mictlan Knoll, Chapopote, and Makran plot in the seawater-signature area, whereas Ce anomalies are much higher for gray aragonites that plot closer to, but not categorically in the area determining a positive influence from shales (after Oliver and Boyet, 2005). Clear aragonite from Tsanyao Yang Knoll plots slightly above the seawater signature area, whereas gray aragonite plots furthest away from the shale signature area than any of the other gray aragonites (Fig. 15C). Micrite of all samples exhibits Ce/Ce* values closer to unity, and plot closer to the shale-signature area (Fig. 15D). All trace and ∑REE+Y concentration data are shown in Tables 2 and 3.

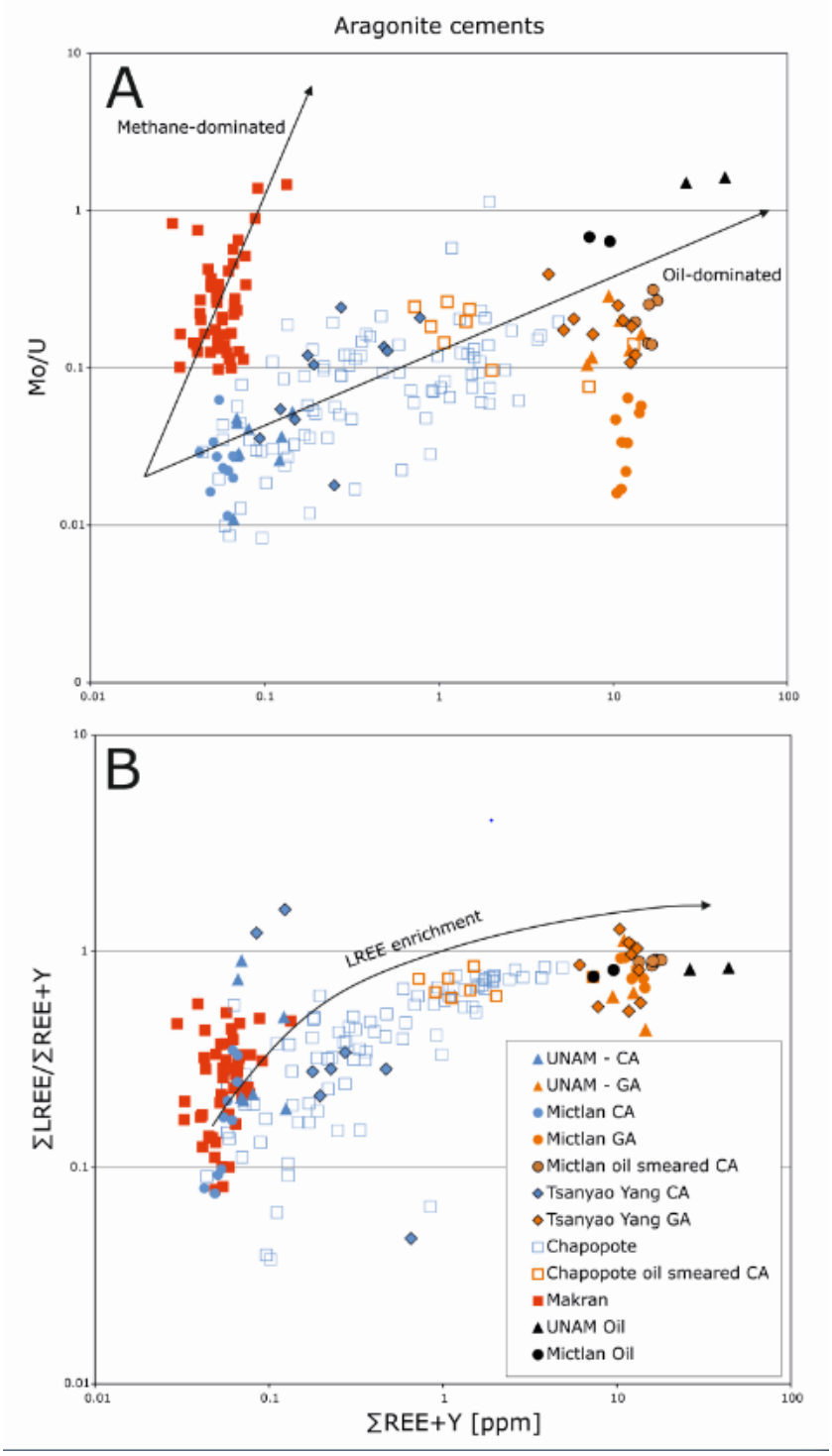


Fig. 13. Trace and REE data from aragonite cements and hydrocarbons, ca = clear aragonite, ga = gray aragonite. Data from Makran and Chapopote clear aragonites calculated from Smrzka et al. (2016). (A) Mo/U ratios vs. ∑REE+Y content (modified from Smrzka et al., 2016), (B) LREE enrichment vs. ∑REE+Y content.

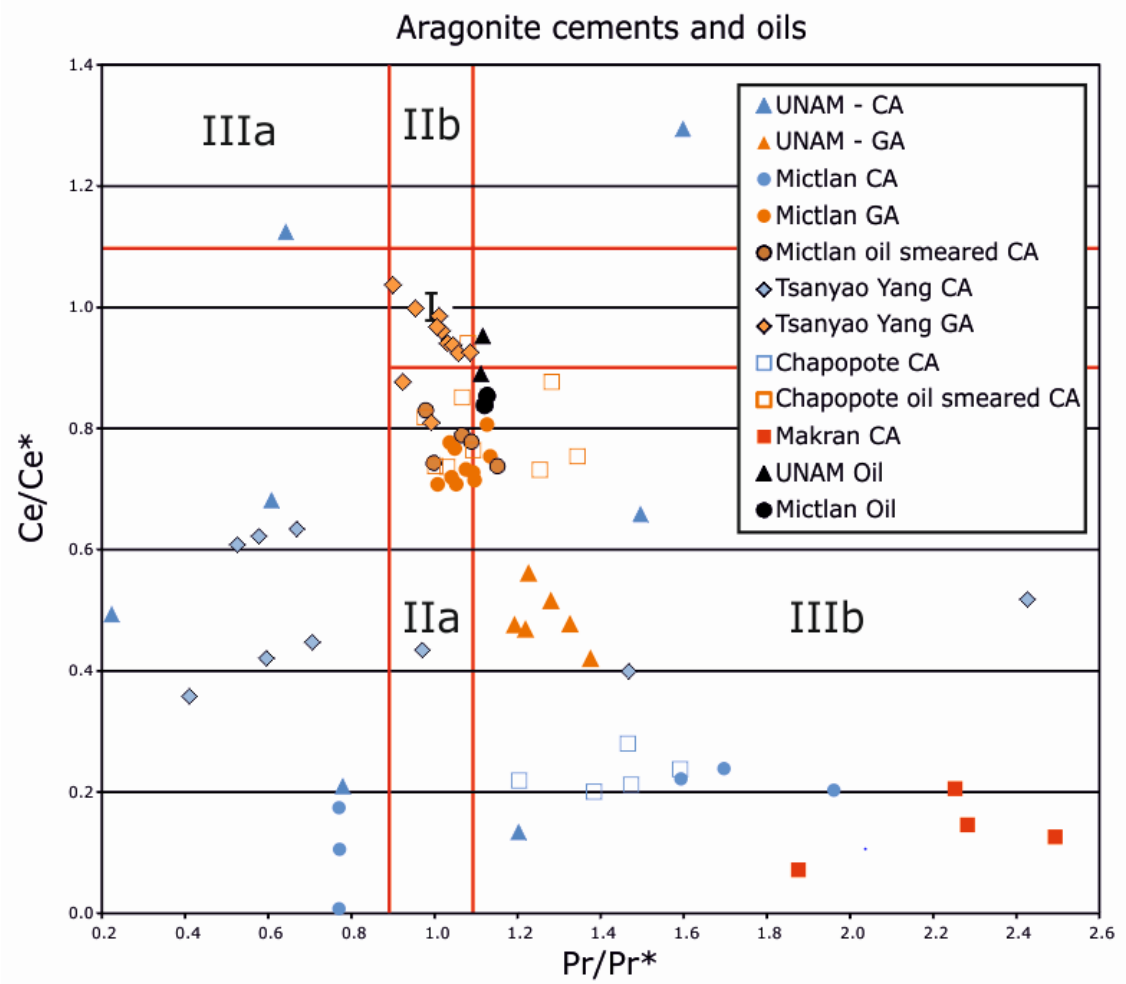


Fig. 14. Cerium and Pr anomalies from aragonite cements and hydrocarbons, ca = clear aragonite, ga = gray aragonite, I = No anomaly, IIa = positive La anomaly, IIb = Negative La anomaly, IIIa = Positive Ce anomaly, IIIb = Negative Ce anomaly, after Bau and Dulski (1996). Data from Makran and Chapopote clear aragonites calculated from Smrzka et al. (2016).

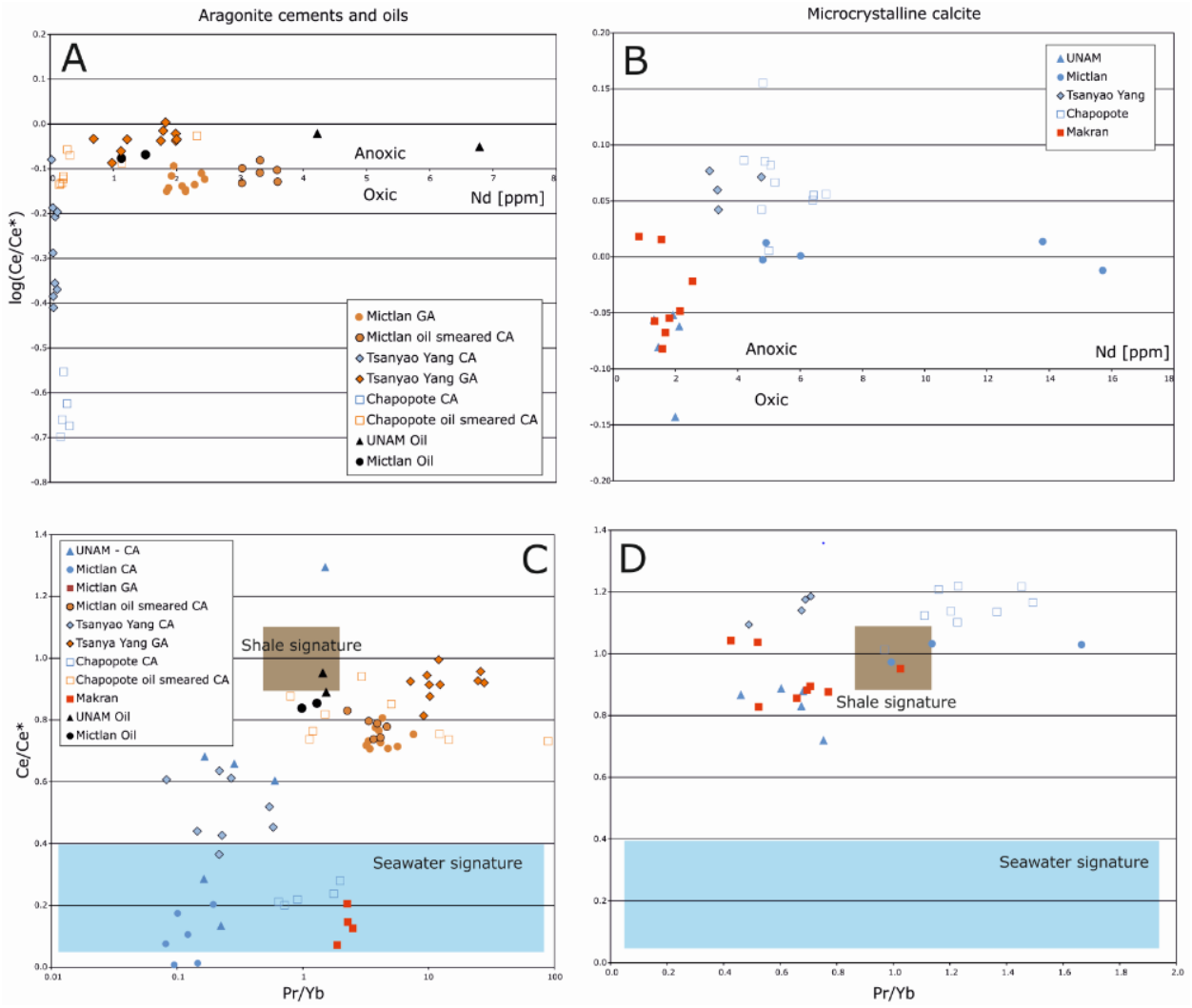


Fig. 15. (A, B) Cerium anomalies vs. Nd concentrations of aragonite cements, micrites, and hydrocarbons after Wright et al. (1987), ca = clear aragonite, ga = gray aragonite. Data from Makran and Chapopote calculated from Smrzka et al. (2016). (C, D) Ce anomalies vs. shale-normalized Pr/Yb ratios of aragonite cements, micrites, and hydrocarbons after Oliver and Boyet (2005), ca = clear aragonite, ga = gray aragonite. Data from Makran and Chapopote calculated from Smrzka et al. (2016).

Hydrocarbons

Four hydrocarbon samples were analyzed for trace and REE content, two from UNAM Ridge, and two from Mictlan Knoll. Both samples are characterized by high concentrations of Al, K, S, Fe, and Sr, which are present in amounts of several weight percent (Table 4). Samples from UNAM Ridge feature higher concentrations of all measured elements except P, V, Sr, Ag, and U compared to samples from Mictlan Knoll. Molybdenum/Uranium ratios and ∑REE+Y contents of UNAM Ridge hydrocarbons are significantly higher than those determined at Mictlan Knoll (Fig. 13A). Vanadium/Nickel ratios are homogeneous between 4 and 5, as are V/(V+Ni) ratios which are in the range of 0.8 (Table 4, Fig. 16). Relative enrichments of LREEs over HREEs are significantly higher than in seawater, as well as in most clear aragonite cements from both sites, and are closer to values determined for gray and oil smeared aragonites (Table 5). Nonetheless, PAAS-normalized REE patterns are flat, and do not show distinct anomalies of La, Ce, or Eu (Fig. 17A). Cerium and Praseodymium anomalies plotted into Figure 14A show that the slightly negative Ce anomalies in all four samples are not real. All hydrocarbon samples plot in the anoxic area, and in the vicinity of the shale-signature area in Figure 15A and C. Trace and rare earth metals in oils show that specific elements including Fe, Ba, Co, Zn, and the ∑REE+Y correlate with Al (Fig. 17B).

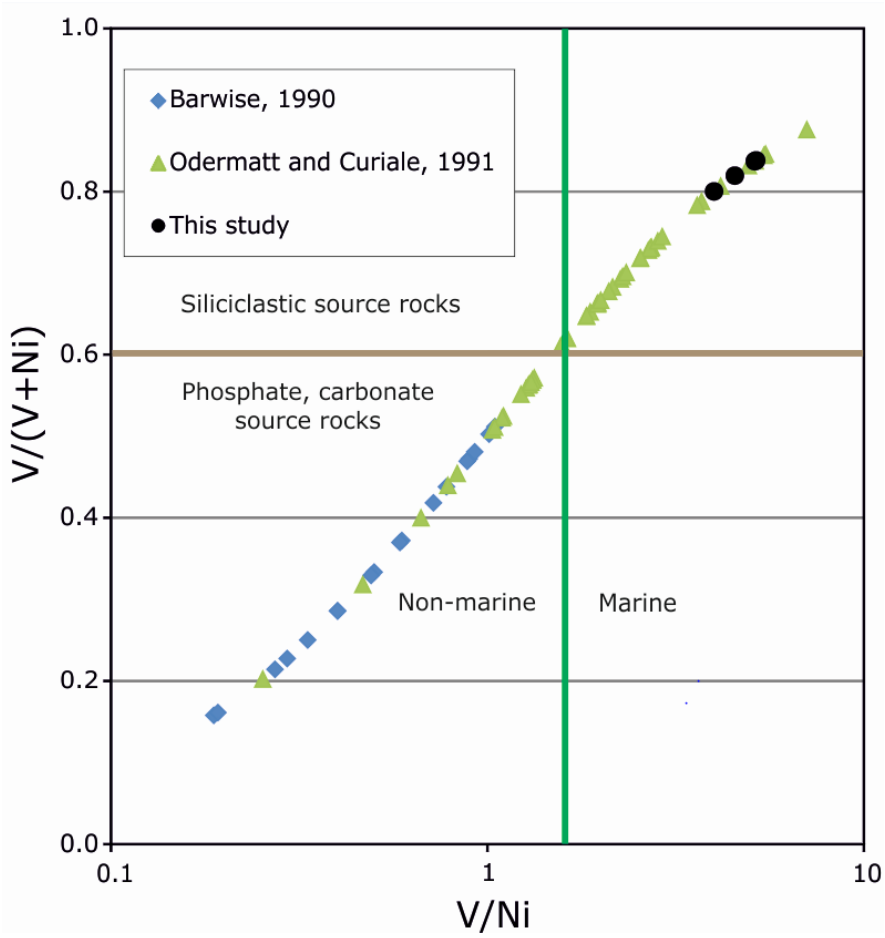


Fig. 16. V/(V+Ni) vs. V/Ni concentration plot of UNAM Ridge and Mictlan Knoll hydrocarbons using data from Barwise (1990) and Odermatt and Curiale (1991). See text for details.

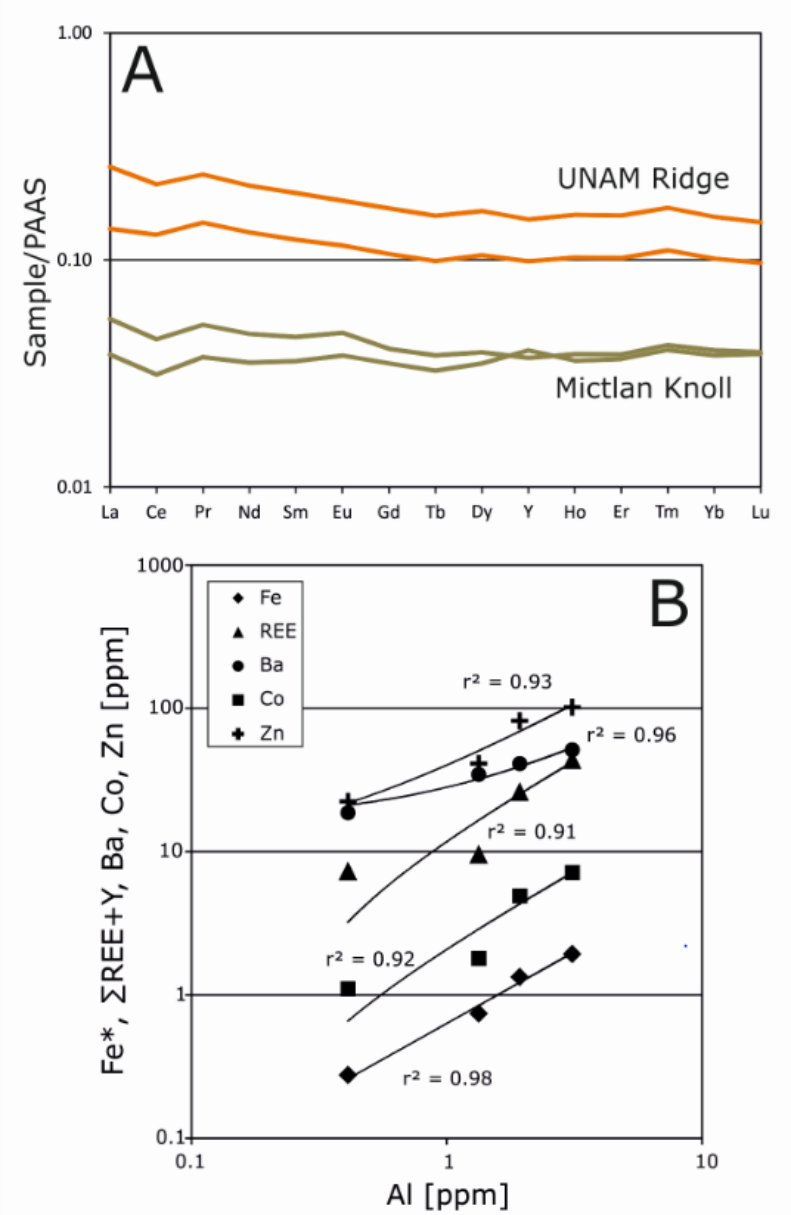


Fig. 17. (A), Shale-normalized REE patterns from UNAM Ridge and Mictlan Knoll hydrocarbon samples. (B), Correlation plot of Al vs. Fe, REEs, Ba, Co, and Zn concentrations. All concentrations in ppm except for Fe which is shown in weight percent.

Geochemical modeling

Results from batch model calculations using the software code PHREEQC highlight the effect of hydrocarbon oxidation with sulfate at measured rates from culture and field studies on carbonate saturation state. Using oxidation rates recalculated from literature values, anaerobic oxidation of methane, propane, butane, phenanthrene, hexadecane, and naphthalene generally favor calcium carbonate precipitation to different degrees. Saturation indices of calcite vary between the model runs, and are generally above zero, favoring precipitation of calcite during oxidation of methane, propane, butane, and hexadecane over 1 year (Fig. 18A, B). Oxidation of Toluene, n-dodecane, xylene, and benzene lead to a decrease in calcite SI, as well as to calcite dissolution (Fig. 18A, C) Larger amounts of calcite precipitate during oxidation of methane, propane, and butane than compared to oxidation of higher hydrocarbons phenanthrene, hexadecane, and naphthalene (Table 6, Fig. 18B). At 300 bars and using hydrocarbon oxidation rates from Table 6 no gases are produced in the model runs. However, methane and carbon dioxide gas reach supersaturation during the oxidation of various compounds (Fig. 19A, B). While oxidation of heavier hydrocarbons does not lead to gas supersaturation, other compounds trigger supersaturation of methane and carbon dioxide gases in pore waters.

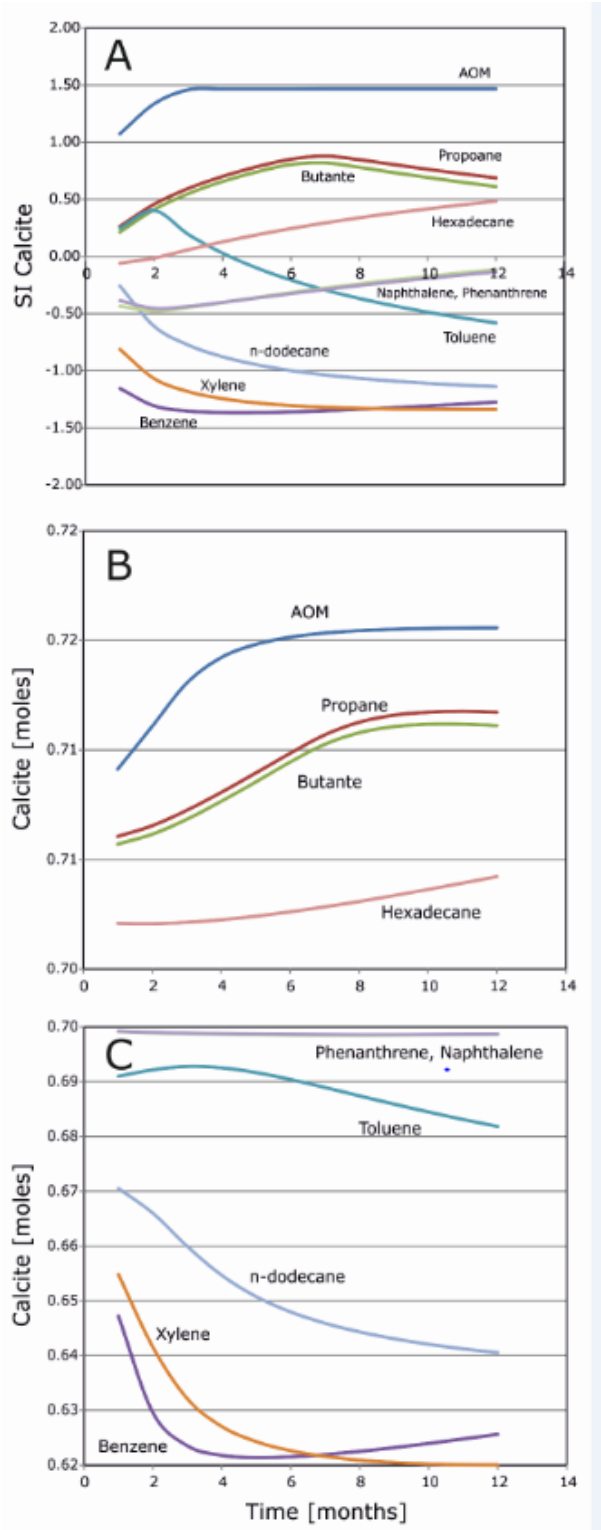


Fig. 18. (A) Saturation index of calcite without calcite precipitation. (B) Calcite precipitation during oxidation of hydrocarbon compounds. (C) Dissolution of calcite during oxidation of hydrocarbon compounds. See text for details.

Increasing oxidation rates of hydrocarbons over 1 year of simulation yields different results (Table 7). Here, all reactions except AOM favor calcite dissolution (Fig. 20A). Applying AOM rates ($4.05*10^{-9}$ moles/L/s, Wallmann et al., 2006) to all compounds changes the model outcome. Here, all but the AOM reaction lead to strong undersaturation and dissolution of calcite (Table 8, Fig. 20B). This modeling setup also affects gas formation, as at higher oxidation rates methane, carbon dioxide, and hydrogen sulfide gas is produced over the course of 1 year of simulation (Fig. 21A-C). Hexadecane, n-dodecane, and phenanthrene produce highest amounts of methane gas, whereby AOM produce almost none (Fig. 21A). Phenanthrene, hexadecane, naphthalene, and n-dodecane oxidation produce for carbon dioxide gas at these rates than other hydrocarbon compounds (Fig. 21B), and the most hydrogen sulfide gas is produced during hexadecane, phenanthrene, and n-dodecane oxidation (Fig. 21C). In contrast, oxidation of low-molecular weight hydrocarbons including methane, propane, and butane produces very little to almost no gas using oxidation rates from Table 6 and 300 bar pressure.

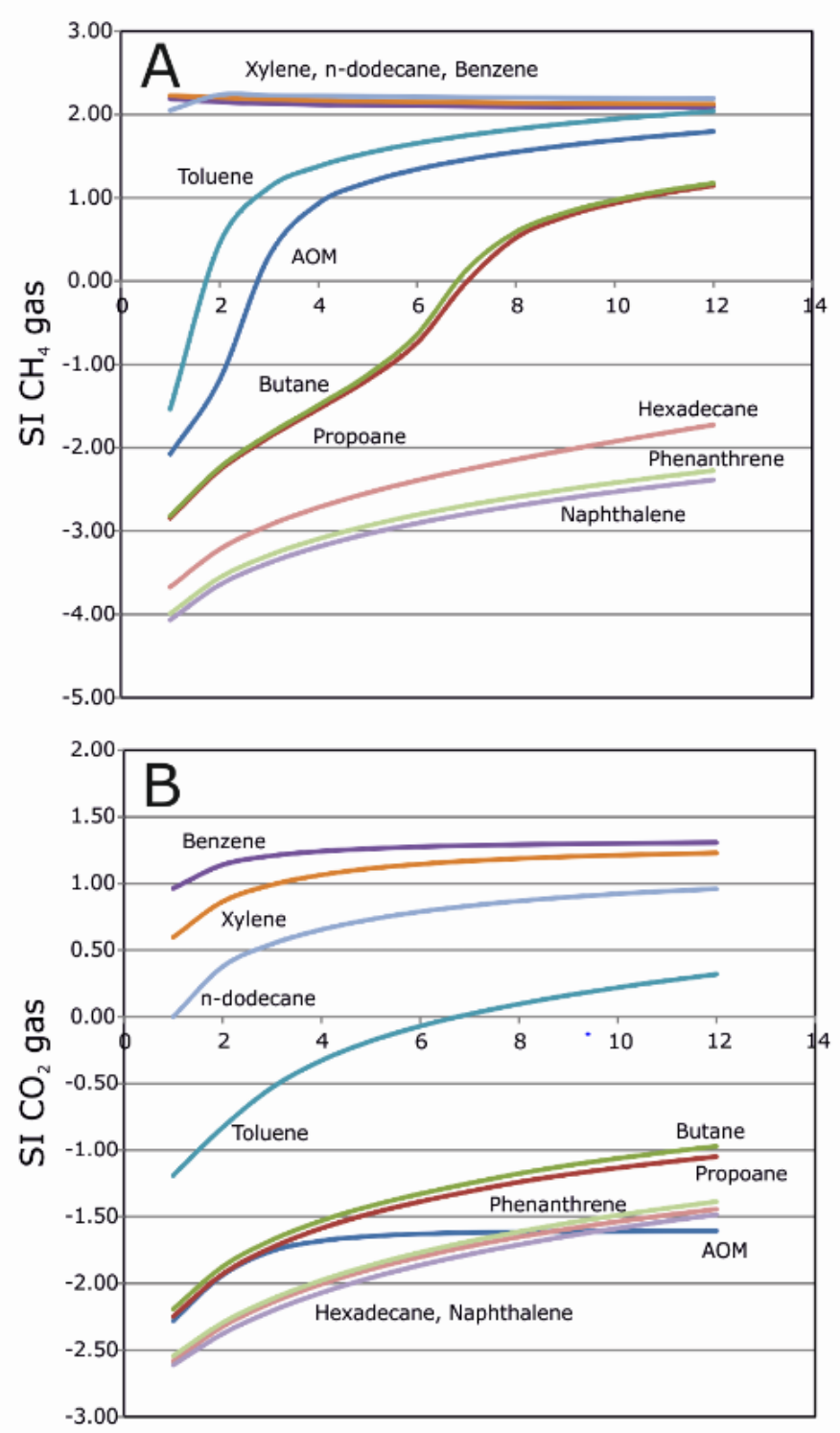


Fig. 19. Saturation indices of CH_4 (A), and CO_2 (B) gas during calcite precipitation using rates shown in Table 6. See text for details.

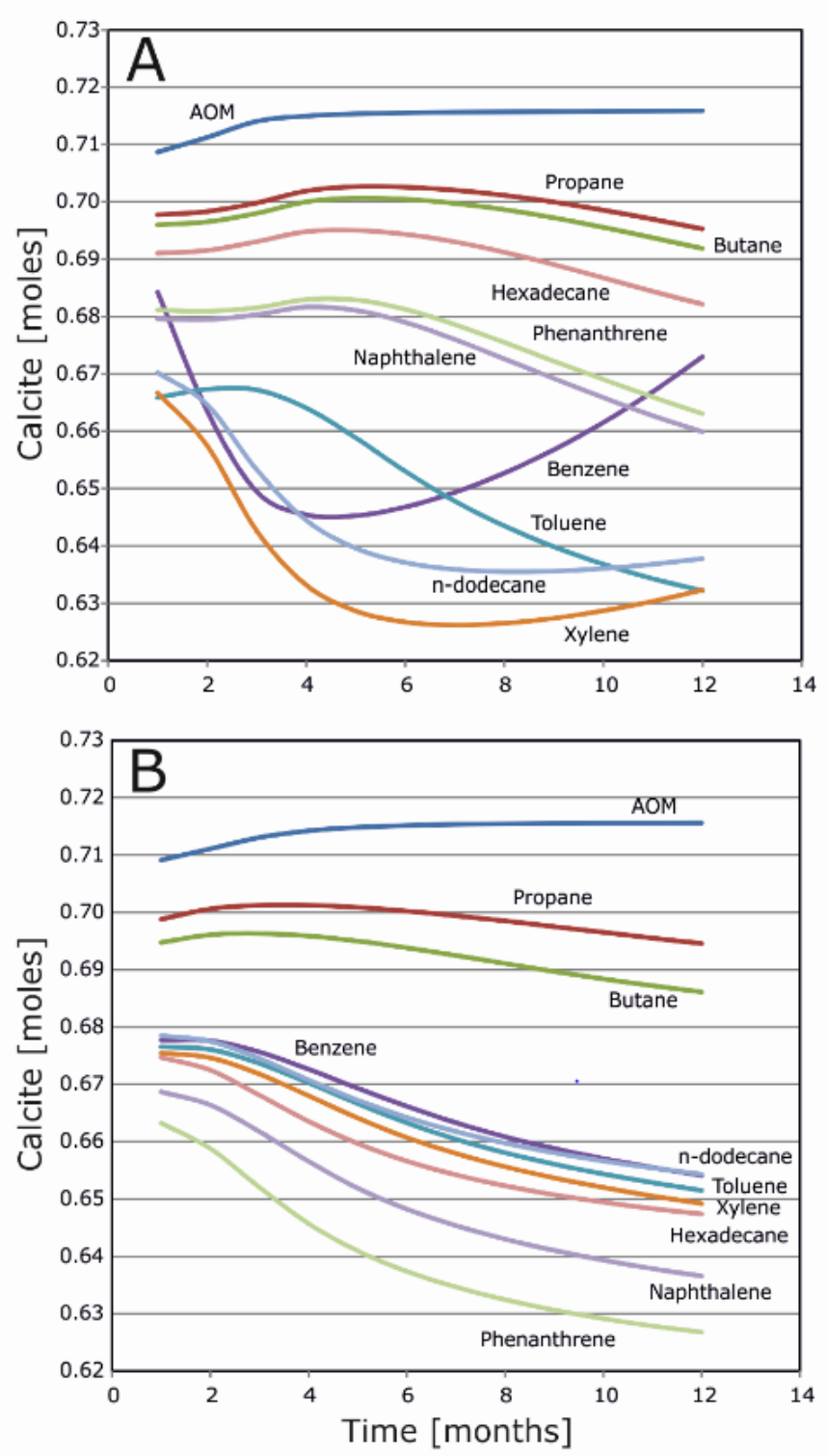


Fig. 20. (A) Calcite precipitation during stepwise increasing rates of hydrocarbon oxidation shown in Table 7. (B) Calcite precipitation and dissolution during hydrocarbon oxidation at constant rates of $4.05*10^{-9}$ moles/L/s (cf. Table 8). See text for details.

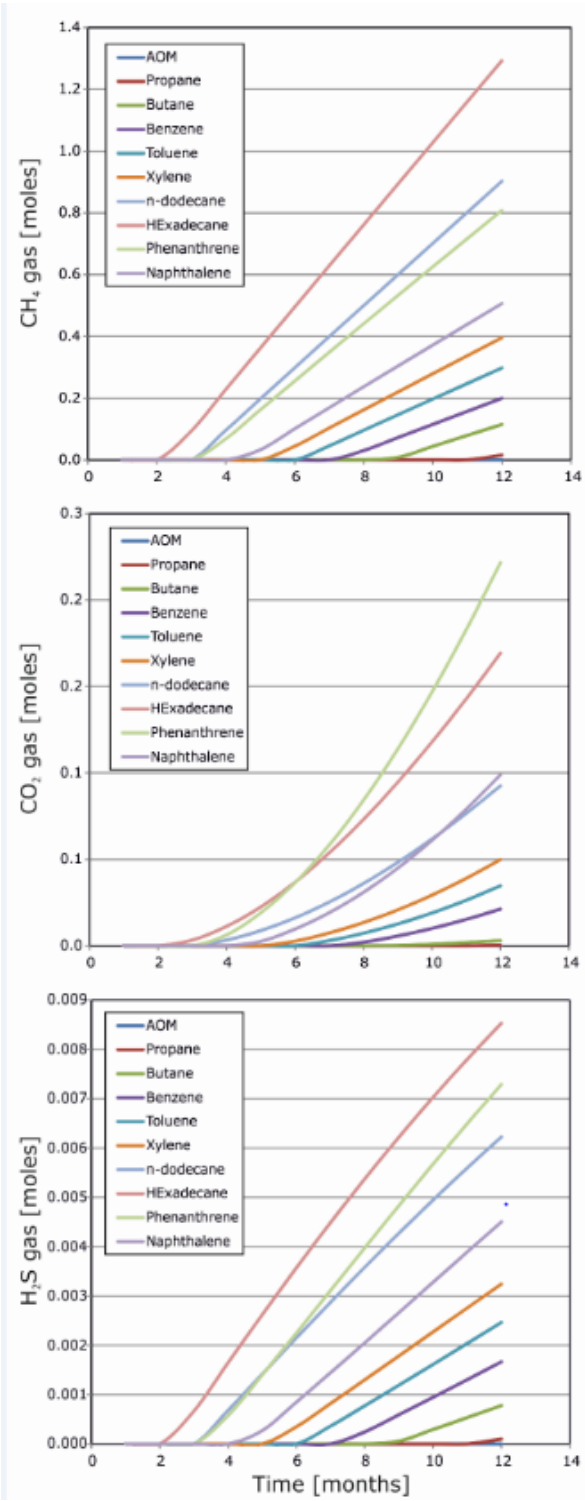


Fig. 21. Evolution of (A) CH_4, (B), CO_2, and (C) H_2S gas composition over time during calcite precipitation and oxidation of hydrocarbons at rates shown in Table 8. See text for details.

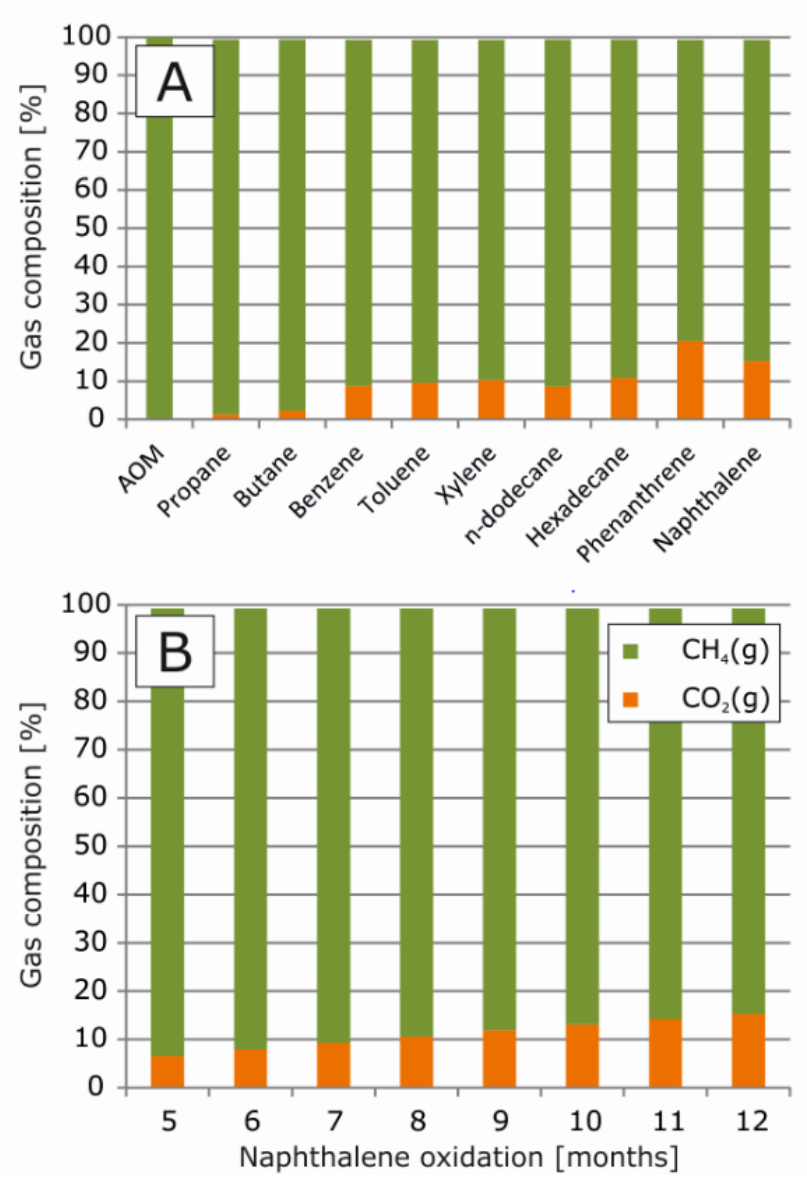


Fig. 22. (A) Green = CH_4, orange = CO_2, gas composition after oxidation of hydrocarbons (methane to naphthalene) using rates from Table 8 after 1 year. (B) Evolution of gas composition during naphthalene oxidation using rates in Table 8. See text for details.

Characterization and origin of hydrocarbons

Constraints on oil maturity

Organic petrography is a well-established and common practice in coal and petroleum geology, and includes the determination of vitrinite reflectance, fluorescence of organic matter, and thermal and conodont alteration indices (Hackley and Cardott, 2016). Vitrinite reflectance focuses on the characterization of macerals – constituents of organic matter such as animal and plant remains in coals and oil shales (Spackman, 1958; Kruszewska, 1989; Peters and Cassa, 1994) – and can yield information on the locations and depths at which oils have accumulated in a reservoir (Stach et al., 1982; van Krevelen, 1993). Bitumen is generated in the process of maturation of deposited organic matter due to the cracking of chemical bonds in kerogen into liquid oil, or from the chemical conversion of oil to gas (Suarez-Ruiz et al., 2012). As the carbonate samples from Campeche Knolls do not contain any macerals of vitrinite, reflectance of solid bitumen was attempted instead. Solid bitumen is a common constituent of organic carbon-rich rocks that appears as vein and cavity fillings, or as dispersed fine-grained material in the rock matrix. Solid bitumen reflectance can be calculated using regression equations to determine the reflectance equivalent from vitrinite reflectance, however this practice has been cautioned due to the difficulty in distinguishing vitrinite from bitumen, variations in reported vitrinite reflectance and citing problems of empirical conversion schemes (Schoenherr et al., 2007; Hackley et al., 2013; Petersen et al., 2013; Zhou et al., 2014). Unfortunately, due to the high instability of the sample material, bitumen reflectance could not yield usable results.

However, Raman spectroscopy of hydrocarbon compounds within thin sections of UNAM Ridge and Mictlan Knoll could be conducted successfully. Raman spectroscopy is a rapid, nondestructive and versatile analytical technique able to identify the structure of organic compounds, and is widely used in Earth Sciences with applications ranging from hydrocarbon exploration (Dubessy et al., 2001) to astrobiology (Winters et al., 2013). Specifically in the material sciences Raman spectroscopy has been employed to organic geologic materials in order to determine the thermal evolution of carboniferous organic material, changes in structural chemistry of organic matter during catagenesis and metagenesis, as well as inferring the biogenicity of putative microfossils as old as the Precambrian (Wopenka and Pasteris, 1993; Kelemen and Fang, 2001; Beyssac et al., 2002; Schopf et al., 2002).

The first-order Raman spectra of the most simple carbon compound found in the rock record, graphite, is characterized by a distinct band at roughly 1600 cm^{-1}. This band has hence been named G (graphite) – band, or O (ordered) – band, as it exists in graphite due its vibration mode, specifically due to in-plane vibrations of aromatic carbon atoms within the graphite structure (Tuinstra and Koenig, 1970). The second band that appears at 1350 cm^{-1} is designated to disordered carbon atoms that are attributed to structural defects within the organic material, and is commonly referred to as D (disordered) band (Tuinstra and Koenig, 1970). Both of these spectra are used as a general basis for the identification of a wide range of organic geologic materials (Roberts et al., 1995; Kelemen and Fang, 2001; Mumm and Inan, 2016). Both the G and the D bands are observable in all investigated carbonate samples, albeit the D bands are only poorly developed. Increasing peak sharpness of both bands has been interpreted as a clear indicator of pressure and temperature alteration of hydrocarbon compounds. Specifically, the progressive disappearance of D bands and decreasing band widths of D and G bands have been assigned to increasing influence of increasing thermal alteration (Jehlička and Beny, 1991; Pasteris and Wopenka, 1991; Yui et al., 1996). As changes in band characteristics are derived from alteration of crystal size and the degree of defects, sharpening and intensification of G and D peaks indicate increasing crystallinity and structural ordering of carbon atoms within the organic material during progressive alteration and burial (Tuinstra and Koenig, 1970; Dillon et al., 1984; Yui et al., 1996). In a set of experiments Zeng and Wu (2007) demonstrated how G and O peak characteristics of kerogen changed significantly from very broad and barely recognizable peaks to increasingly narrower and well defined bands during treatment with high temperatures and pressures, and attributed these changes to progressive ordering of kerogen structure at increasing temperatures. Similar trends for Raman spectra characteristics were also reported for experiments using bitumen, showing how peaks become more defined at higher temperatures (Zhou et al., 2014).

The broad G peaks, and the very poorly developed D peaks in all samples (Fig. 8) argue for low grade alteration and maturation of hydrocarbons archived in authigenic carbonates from the Campeche Knolls. The observed Raman spectra most resemble those of bitumen heated to no more than 400°C (cf. Zhou et al., 2014), or that of gilsonite with very low maturity (cf. Liu et al., 2013). Gilsonite is a specific form of bitumen characterized by high concentrations of Ni petroporphyrins that remain stable due to the absence of severe thermal alteration (Quirke et al., 1979), and has been classified as an asphaltene-rich diagenetic precursor of grahamite and impsonite (Curiale, 1986; Hein, 2006). An early study on the

porphyrine structure in gilsonite suggested that formation temperatures of this bitumen do not exceed 400°C (Sugihara and McGee, 1957), which constitutes the precise temperature limit of Raman spectra for bitumen observed by Zhou et al. (2014) that most closely resemble the spectra of the present samples. Moreover, Liu et al. (2013) compiled Raman spectra of various bitumen species from very low mature gilsonite to pyrobitumen and highly altered anthraxolite. A comparison of the spectra to those compiled by Liu et al. (2013) shows that the spectra of gilsonite bears strongest resemblance to the spectra of the investigated bitumens (Fig. 8). However, the available data set does not allow a robust identification of crude oils as being composed mainly of gilsonite. Specifically, the relatively high sulfur contents of oils, between 0.9 and 2.2 wt%, argues against the presence of large amounts of gilsonite, which is known to exhibit lower sulfur contents (Nciri et al., 2014). The comparison of Raman spectra, however, does suggest that crude oils seeping from seafloor structures at Campeche Knolls experienced very little thermal maturation, and that heavy hydrocarbons from all three localities were sourced from the same reservoir.

Carbon sources and oil migration

Trace metal geochemistry of crude oil has a long history and includes the application of a large number of different techniques (Yen, 1975; Lewan, 1984; Zaki et al., 1989; Lord, 1991; Dreyfus et al., 2005; Ricard et al., 2011). Specifically, the determination of V, Ni, and sulfur is of particular importance as their concentration distribution in crude oils yields valuable information on sources, migration pathways, and modes and intensity of thermal maturation and biological degradation. Vanadium and Ni are primarily bound in natural oils as metalloporphyrins, which were one of the first compounds described to be of a definite biological origin (Treibs, 1934, 1936; Baker and Palmer, 1978). Metalloporphyrins are essentially metallo-organic complexes of V(II) and Ni(II), ultimately derived from chlorophyll and heme pigments, and are present in crude oil mainly as tetrapyrrole complexes (Lewan and Maynard, 1982). Tetrapyrrole complexes have high thermal stability, strong resistance to acid attack and cation exchange reactions (Barnes and Dorough, 1950; Hodgson and Baker, 1957). They are nevertheless highly prone to aerobic degradation in oxic marine sediments, and are only retained to a significant degree in anoxic sediments where they can be preserved on geologic timescales (Lewan and Maynard, 1982). The stability of metalloporphyrins in crude oil enables the use of V and Ni

concentrations as indicators for catagenetic oil formation, maturation of organic matter, and the reconstruction of depositional and environmental conditions (Khuhawar et al., 2012 and references therein).

Although V and Ni concentrations vary somewhat between the studied samples, they are all within the range of oils reported from various source rocks and depositional environments around the world (Lewan and Maynard, 1982; Ali et al., 1983; Fabec and Ruschak, 1985; Barwise, 1990). Several early studies categorized V/Ni ratios of varying types of crude oils and bitumens according to the preferential enrichment of these two elements within specific source materials. Crude oils and kerogens with a dominance of V over Ni concentrations have been categorized as marine kerogen, as Ni is preferably dominant in oils generated from terrestrial and lacustrine source rocks. Low Ni/V ratios below 0.5 are indicative of being sourced from phytoplankton in organic matter deposited in marine carbonates or siliciclastics under conditions with high sulfur availability. On the other hand, high Ni/V ratios are designated for crude oils generated by higher land plant material from angiosperms and gymnosperms, as well as leaf waxes derived from non-marine lacustrine environments with low sulfur availability (Barwise, 1990). Ni/V ratios of all measured oil samples are all in the order of 0.2, confirming a clear marine origin of organic matter within the oils as opposed to terrestrial organic material. In a similar fashion Odermatt and Curiale (1991) found that oils with V/(V+Ni) ratios around 0.5 and below stem from phosphatic shale- carbonates, whereas oils with ratios above 0.6 were derived predominantly from siliceous lithofacies (cf. Odermatt and Curiale, 1991 their Fig. 8). Crude oils seeping from Campeche Knolls yield fairly homogeneous V/(V+Ni) ratios of around 0.8, suggesting that these oils stem from, or were influenced by, siliciclastic source rocks. V/Ni ratios in oils also yield constraints on their age. Increasing V/Ni ratios with increasing age were first determined by Ali et al. (1983), who determined V/Ni values between 2.8 and 3.1 for Cretaceous, and 3.8 and 4.4 for Jurassic oils. Many of the hydrocarbon source rocks in the southern GoM are Oxfordian limestones interbedded with gray shales and siltstones to Kimmeridgian argillaceous oolitic limestones with shales, dolomites, and bentonites (Salvador, 1991), from which oils seep into younger, Cretaceous, platform and shelf carbonate reservoir rocks where they are efficiently trapped (McFarlan and Menes, 1991; Sohl et al., 1991; Magoon et al., 2001). Vanadium/Nickel ratios of oils lie between 4.0 and 5.1, which would fit to Jurassic-age source rocks (cf. Ali et al., 1983), and V/(V+Ni) ratios argue for bedded shales and siltstones as source rocks for the Campeche Bay oils.

Anaerobic oxidation of hydrocarbons as a trigger for carbonate authigenesis

Petrography and isotope geochemistry

Most of the known modern and ancient marine hydrocarbon seep deposits worldwide are associated with the anaerobic oxidation of methane (AOM) in sediments performed by a consortium of archaea and bacteria (Boetius et al., 2000; Aloisi et al., 2002; Peckmann and Thiel, 2004; Campbell, 2006). However, the impact of microbial anaerobic degradation of higher hydrocarbons and crude oils on carbonate precipitation is less well assessed. Numerous studies from the northern Gulf of Mexico hydrocarbon seeps have shown that expulsion of liquid oil is no impediment to the development of lush chemosynthetic macrofaunal communities (Kennicutt et al., 1988a; Sassen et al., 1993), and can be decisive in the precipitation of authigenic carbonates (Brooks et al., 1986; Formolo et al., 2004; Joye et al., 2004; Mansour and Sassen, 2011; Bian et al., 2013). Oil seepage significantly impacts local macro and microfauna at seeps, and is a governing factor in the distribution of archaeal and bacterial microbial communities (Orcutt et al., 2010).

The southern GoM is a comparably less well studied area, yet carbonate precipitation at the Chapopote asphalt volcano shows that similar geomicrobiological processes operate in all parts of the Gulf. Aragonite cements and microcrystalline calcites are common phases in modern and ancient seep carbonates, and their phase-specific $\delta^{13}C$ values are well-established tracers for methane seepage and its biological oxidation (Beauchamp and Savard, 1992; Savard et al., 1996; Peckmann et al., 2002, 2003; Naehr et al., 2007). Mineral paragenesis at all new studied sites from the Campeche Knolls is similar: they all exhibit a matrix of heterogeneous micrite, followed by aragonite cements that precipitated along the inner walls of cracks and cavities. Nevertheless, there are differences. UNAM Ridge carbonates crop out as large meter-scale boulders on the seafloor, which is unusual for seep carbonates as AOM is considered to be confined to anoxic (pore) waters. However, methane-derived carbonates are known to precipitate into the water column under specific circumstances. The Black Sea in particular features large columnar carbonate precipitates that grow into anoxic bottom waters, and studies have shown that such conditions are highly favorable for hosting anaerobic methane metabolizing microbial communities outside the sediments (Peckmann et al., 2001b; Michaelis et al., 2002; Reitner et al., 2005; Treude et al., 2007). Ephemeral anoxic conditions due to enhanced primary production in surface waters have also been

inferred for carbonate chimney formation in bottom waters of the Mediterranean Sea (Bayon et al., 2013) and from the oxygen minimum zone (OMZ) on the Makran continental shelf (Himmler et al., 2015, 2016). Excluding the hydrographically exceptional Black Sea, and the locally confined OMZs, Teichert et al. (2005) suggested a model for carbonate buildups into oxic seawater by the formation of channels surrounded by anaerobic microbial consortia within emanating reducing fluids, and argued that such a formation mechanism enables the growth of meter-tall carbonate structures into oxic seawater. Such a formation mechanism would render carbonate precipitation into bottom waters feasible in almost all hydrographic and tectonic settings.

UNAM Ridge carbonates, however, do not exhibit features of carbonates growing into anoxic water column. Rock samples are partially brecciated (Fig. 2C) and feature large micritic clasts and fragments that almost certainly formed below within the sediments. It is likely that these carbonates were exposed after precipitation by winnowing, seafloor erosion, pockmark formation, or a combination of these mechanisms. However, sample GeoB 19348-8 from Tsanyao Yang Knoll features carbonate fabrics that could argue for partial growth in the water column. These precipitates were collected from the top of a large gas hydrate structure (Fig. 4C, see also Sahling et al. 2016 their Fig. 4B, C), and grew among a densely populated chemosynthetic community of mytilid bivalves and vestimentiferan tubeworms fueled by high rates of bubble emissions from the gas hydrate (Sahling et al., 2016). The lower part of these carbonates featured microbial mats (Fig. 4D) that most likely grew within the rhizosphere of tubeworms, which were still attached to the carbonate. This growth mechanism resembles carbonates precipitating in the direct vicinity of tubeworms in seafloor sediments, except that Tsanyao Yang Knoll carbonates precipitated exposed to seawater on top of gas hydrate, where oxygen from seawater was possibly mitigated by biological chemosynthetic activity and vigorous methane flux. Migration pathways for vigorously seeping gas sourced from the gas hydrate below are evidenced by large cracks (Fig. 7D), which were then filled by aragonite cement (Fig. 7E, F).

Mean $\delta^{13}C$ values of asphalts from Chapopote carbonate samples were determined at –27.8‰ (Smrzka et al., 2016 supplementary material), which is in the order of magnitude determined for heavy hydrocarbon compounds from other parts of the GoM (Mansour and Sassen, 2011; Zhang et al., 2003). Stable C isotope values of aragonite cements and micrite cluster between –30 and –20‰ (Fig. 9), suggesting that most of the carbon for carbonate formation was sourced from heavy hydrocarbon and crude oil degradation (Roberts and Aharon, 1994; Joye et al., 2004; Naehr et al., 2009; Mansour and

Sassen, 2011). Clear aragonite cement from sample GeoB 19348-8 growing on the gas hydrate edifice at Tsanyao Yang Knoll exhibits slightly lower $\delta^{13}C$ values than other samples (Fig. 9). This signature agrees with the visible absence of oil in the sample (Figs. 4D, 7D-F), as well as with the interpretation that this sample was more strongly influenced by seepage and oxidation of biogenic methane from gas hydrates, which usually features more negative $\delta^{13}C$ values than heavy hydrocarbons (Whiticar, 1999). However, $\delta^{13}C$ values of carbonates sourced from biogenic methane usually exhibit highly negative $\delta^{13}C$ values beyond –40‰ and even lower (Ritger et al., 1987; Greinert et al., 2001; Himmler et al., 2015). The exposure to surrounding seawater bicarbonate may have diluted more negative $\delta^{13}C$ values in this sample, and may have been an additional carbon source for carbonate authigenesis.

Geochemical modeling

Three decades of microbiological studies have confirmed that, specifically sulfate reducing bacteria not only tolerate, but actively oxidize and metabolize low- to high-molecular weight organic compounds to end products such as methane and carbon dioxide (Grbic-Galic and Vogel, 1987; Lovley and Lonergan, 1990; Ackersberg et al., 1991; Beller et al., 1992; Edwards et al., 1992; Coates et al., 1996; Heider et al., 1999; Widdel and Rabus, 2001). Although a large body of evidence suggests that microbial oxidation of hydrocarbon compounds fuels carbonate precipitation in the GoM (Joye et al., 2004; Naehr et al., 2009; Mansour and Sassen, 2011), it is not clear which compounds are oxidized at what rates, and how they affect carbonate alkalinity and saturation state. Geochemical studies of oily sediments, asphalt, and seeping crude oil from Chapopote confirm that hydrocarbons are heavily biodegraded (Schubotz et al., 2011a), suggesting that metabolic products of microbial degradation influence carbonate saturation and precipitation at the Campeche Knolls. Highly degraded heavy oils were also reported from northern GoM oil seeps (Kennicutt et al., 1988b), arguing for widespread and active microbial utilization of high-molecular weight hydrocarbons throughout the GoM. Not all oxidation reactions of hydrocarbon with sulfate necessarily lead to carbonate supersaturation, which can be estimated by considering oxidation rates for microbial hydrocarbon degradation (Table 6 and references therein). The large variation in oxidation rates available from microbiological studies makes it difficult to assess the true degradation rates of hydrocarbon compounds in marine sediments, as most studies have been conducted either in culture, or as field studies on anthropogenically polluted sediments (e.g. Rabus et al., 1996; Harayama et

al., 1999; Tang et al., 2005; Miralles et al., 2007). Nevertheless, information from these studies can be still considered a first-order approximation of anaerobic oxidation of hydrocarbons in pristine marine sediments.

Of the many compounds used in the batch models, C1 to C5 hydrocarbons including propane and butane are confirmed to be present in gas inclusions from asphalts and gas hydrates sampled at Chapopote (Klapp et al., 2010; Schubotz et al., 2011a). However, it is likely that most compounds considered here are present within Campeche Knoll sediments and oils, as they are all common constituents at crude oil seeps worldwide. Heavier hydrocarbon compounds such as phenanthrene, hexadecane, and naphthalene are degraded at lower rates than low-molecular weight organic compounds methane, propane, and butane (Zhang and Young, 1997; Galushko et al., 1999; Kniemeyer et al., 2003, 2007; Maillachevuru and Pathan, 2009). This leads to large differences in carbonate saturation state over time, where rapid oxidation of benzene and xylene leads to carbonate dissolution, and slower oxidation of naphthalene and phenanthrene favors carbonate precipitation (Fig.18). Not only the reducing state of carbon in the hydrocarbon compounds, but especially degradation rates exert a major influence on carbonate saturation state in aqueous solution. Enhancement of degradation rates leads to drastic drops in carbonate saturation in all model runs except during AOM (Fig. 20A). The sensitivity towards carbon oxidation state is shown in Figure 20B, where most compounds favor carbonate dissolution at higher rates (Tables 7, 8). Given the wide range of reported reduction rates of propane and butane (Kniemeyer et al., 2007), benzene (Kazumi et al., 1997; Musat and Widdel, 2008; Laban et al., 2009), toluene (Beller et al., 1992; Kleinsteuber et al., 2008), xylene (Edwards et al., 1992; Harms et al., 1999), phenanthrene (Rothermich et al., 2002; Coates et al., 1996; Tang et al., 2005), and naphthalene (Rockne and Strand, 1998; Coates et al., 1997; Galushko et al., 1999) by sulfate reducing bacteria, the range of oxidation rates considered by the model setups can be understood in terms of changing environmental conditions in the sediments that would directly affect metabolic conversion rates of bacteria. Precipitation rates of carbonate at Campeche Knolls are inferred from results in Table 6 to be on the order of a few tens of thousands of years to precipitate several kilograms of carbonate. This quantity is similar to numerical modeling results by Luff and Wallmann (2003), who suggested that meter-scale carbonate pavements could precipitate over a period of only a few tens of thousands of years.

An important factor in assessing carbonate saturation from batch modeling is the consideration of gas phases. At an ambient pressure of 300 bars most oxidation rates of hydrocarbons are too low to

overcome the high pressure, although many of the considered reactions reach saturation with respect to methane and carbon dioxide (Fig. 19). Gases are produced and emitted at high rates from seafloor sediments as shown by submersible investigations at Campeche Knolls (MacDonald et al., 2004; Sahling et al., 2016). Recent analyses of gas compositions of free gas and gas trapped within authigenic carbonates at Mictlan Knoll and UNAM Ridge showed that significant quantities of gas are also entrapped within precipitated carbonates (Blumenberg et al., 2017). However, increasing oxidation rates, or a combination of simultaneous oxidation reactions (which is most certainly the case in Campeche Knolls sediments), can overcome the pressure constraints and produce free gas of varying composition (Fig. 21). The CH_4/CO_2 and CH_4/H_2S ratios of gases produced decrease during oxidation of high-molecular weight compounds phenanthrene, naphthalene, hexadecane, and n-dodecane compared to the oxidation of methane, pentane and butane where almost no CO_2 and H_2S gas is produced (Figs. 21, 22). Moreover, progressive and increasing rates of heavy hydrocarbon oxidation decrease these ratios as shown for naphthalene in Figure 22B. The suppression of calcite precipitation during model runs slightly increases these ratios, as some CO_2 is sequestered into the calcite during precipitation. Given the low amounts of calcite that form during the model runs (around 0.5 grams of calcite per year, Tables 6-8) these low differences are expected. MacDonald et al. (2004) found that gases sampled from oily sediments exhibited CH_4/CO_2 ratios of almost 1, whereas gases sampled from gas hydrate only featured traces of CO_2 gas. The tendency that more CO_2 gas is produced in relation to CH_4 where much oil is present in in accord with modeled gas compositions (Fig. 22A).

To summarize, modeling results show that the only reaction to precipitate carbonate in all model setups is AOM, and that carbonate precipitation at Campeche Knolls is governed by oxidation rate of hydrocarbons and the oxidation state of carbon within these compounds. Oxidation rates and carbon oxidation state also control gas formation and govern gas composition, whereby oxidation of low-molecular weight compounds such as methane, propane, and butane favor carbonate precipitation and the formation of CH_4-rich gases. The tendency of higher-molecular weight compounds to saturate carbonate strongly depends on oxidation rate: low rates mostly favor carbonate precipitation, whereas higher rates can rapidly shift the balance towards carbonate dissolution.

Chemical environment of carbonate precipitation and the influence of hydrocarbons

Carbonate cements as an archive for hydrocarbon-derived trace metals

All clear aragonites feature the lowest content of all measured elements, the lowest Mg/Sr, as well as lowest Mo/U ratios (Table 2). Such low concentrations have been reported for this phase in previous studies (Himmler et al., 2010; Smrzka et al., 2016), and argue for highly pure aragonites that have experienced only very little, if any, conversion to magnesian calcite. Moreover, low contents of Al, Si, Mn, and Fe, and the lack of correlation between these elements and other trace metals and REEs suggest that clear aragonite ∑REE+Y contents are authigenic, and can be regarded as being uninfluenced by significant contamination by clay minerals or Mn/Fe oxides. Shale-normalized REE patterns of clear aragonites resemble shale-normalized patterns of modern seawater, as some samples feature negative Ce anomalies and HREE enrichments. These REE patterns of clear aragonites are in stark contrast to gray aragonites, which yield much higher concentrations of all elements, as well as clear LREE enrichments and less well developed negative Ce anomalies (Figs. 10-12).

The differences in clear and gray aragonite cements from UNAM Ridge, Mictlan Knoll, and Tsanyao Yang Knoll carbonates are discussed in terms of data plots in Figure 13. Smrzka et al. (2016) suggested a Mo/U vs. ∑REE+Y plot as a tool to distinguish methane from oil seepage-derived authigenic carbonate cements, by plotting element data of a methane-dominated seep from the Makran accretionary prism (Himmler et al., 2010, 2015) vs. an oil-dominated seep from the Chapopote asphalt volcano. Samples with relatively high Mo/U ratios (> 0.1) and/or ∑REE+Y contents beyond 0.1 ppm are interpreted as being derived from, or influenced by, the presence of oil in parent fluids. Element data from Makran and Chapopote aragonites from Smrzka et al. (2016) are plotted into Figure 13A and B to show how the aragonite phases from this study fit into the scheme of oil vs. methane derived carbonates. Both clear and gray aragonite cements from all carbonate samples exhibit higher ∑REE+Y contents and lower Mo/U ratios as samples from Makran (Fig. 13A). Assuming that crude oil constitutes an additional and significant source of trace and REEs to pore waters that may be incorporated into precipitating carbonate cements (cf. Smrzka, 2016), these patterns are explained by the equally higher Mo/U of UNAM Ridge hydrocarbons (Fig. 13A). The enrichment of LREEs in gray aragonites is accompanied by slight LREE enrichment in crude oils (Fig. 17A), as they plot in the same segment in Figure 13B. Moreover,

Mo/U ratios and LREE enrichment in oil smeared aragonites from Chapopote and Mictlan Knoll plot closer in the oil-dominated and LREE enriched areas of Figure 13A and B, respectively. These results suggest a strong genetic connection between specifically gray aragonite cements and liquid oils at Campeche Knolls.

Correlations between Al and Fe, Ba, Co, and Zn (Fig. 17B) suggest that these elements are to a large extent sourced from residual fragments of Fe-bearing alumosilicate minerals entrapped within the oils (as has also been put forward by Duyck et al., 2002). Appreciable amounts of other trace metals including As, Cu, Mo, and U are common constituents of natural crude oils, where they are typically enriched within the asphaltene fraction (Filby, 1994; Duyck et al., 2002, 2008; Dreyfus et al., 2005; Gondal et al., 2010). Specifically U has long been associated with petroleum seepage and occurrence, and has been linked to the reducing environments in which migrating hydrocarbons trigger the precipitation of insoluble uraninite (Goldhaber et al., 1978; Curiale et al., 1983; Schumacher, 1996). In some cases petroleum hydrocarbons exhibit U contents of several hundreds of ppm, thus constituting an additional source of U to pore waters of ancient and modern sediments (Parnell and Eakin, 1987). There have been comparably little studies on Mo contents in crude oils and bitumens, however, given the importance of this metal as a catalytic enzyme for metabolism (e.g. Kisker et al., 1997; Schwarz et al., 2009) it is reasonable to assume that Mo contents in oil are at least in part derived from marine primary producers.

Light REEs and U are enriched in organic materials including colloids, organic particulates, and even cell walls of bacteria (De Baar et al., 1985; Tang and Johannesson, 2003; McManus et al., 2005; Ozaki et al., 2006). In the case of gray aragonite cement from UNAM Ridge, featuring negative Ce anomalies, an additional strong correlation of U with Fe and Mn in this phase is worth noting. Iron and U are strongly coupled cycles in natural waters, and frequently accumulate together in marine sediments (Morford and Emerson, 1999; Nameroff et al., 2002). Additionally, there is a strong microbiological coupling between Fe and U, as dissimilatory Fe reduction with U(VI) yields catabolic energy for microbes (Lovely et al., 1991). Although no evidence exists that Fe and U are part of microbial metabolisms at seeps, aragonite cements at seeps precipitate due to the remineralization of methane and organic matter, the latter of which may indeed by a source of both elements for this phase. Crude oil has also been shown to contain significant amounts of LREEs (McIntire, 2014). Both organic matter and crude oil remineralization would efficiently release trace and REEs from organic compounds, and were then incorporated into gray aragonite cement.

The most prominent difference between clear and gray aragonites is their ∑REE+Y contents and REE patterns. Although they both show geochemical signs of heavy hydrocarbon influence, they were affected to different degrees. Clear aragonite possibly precipitated in the presence of increasing amounts of dissolved and particulate organic carbon and higher-molecular weight hydrocarbons in the pore fluids. Seawater-like REE patterns of this cement argue for a certain degree mixing of seawater with pore water during precipitation (cf. Feng et al., 2009b; Birgel et al., 2011). Gray aragonite, on the other hand, shows no signs of seawater influence, and is more directly influenced by organic matter-rich sedimentary pore waters. The diffuse, gray veneer that covers this phase (Figs. 6B, F, 7E, F) could be the source of increased concentrations of trace and rare earth metals in this phase, and is possibly related to the presence of oil and/or other organic matter-rich compounds. Moreover, gray aragonite cements as observed in this study have not yet been reported from seeps dominated by methane (e.g. Peckmann et al., 2001a; Teichert et al., 2005; Himmler et al., 2015), suggesting that gray aragonite and its diffuse veneer may be genetically related to the presence of oil. The trace element data set at hand suggests that carbonate cements precipitating at oil seeps are strongly influenced by fluid composition, and show clear distinctions to methane seeps that are devoid of oil.

Ce anomalies – Constraining redox conditions during carbonate formation

The origin of negative Ce anomalies in aragonite cements is somewhat puzzling, although they are not uncommon in modern and ancient seep carbonates (cf. Feng et al., 2009b; Himmler et al., 2010; Rongemaille et al., 2011; Jakubowicz et al., 2015). The authenticity of Ce anomalies using a Ce/Ce* vs. Pr/Pr. plot is assessed (Fig. 14), revealing the Ce anomalies from Makran and Chapopote clear aragonites, and gray aragonites from UNAM Ridge are true negative Ce anomalies. Data from UNAM Ridge and Mictlan Ridge clear aragonites scatter strongly across the plot, delivering ambiguous results. Only few of the data from Makran and Chapopote are shown here due to the very large scatter in the data. Negative Ce anomalies of Mictlan Knoll gray and oil-smeared aragonites appear to be positive La anomalies instead of negative Ce anomalies. Both negative Ce and positive La anomalies have been attributed to reflect oxygenated marine seawater (Elderfield and Greaves, 1982). Cerium is oxidized in oxic waters to insoluble Ce(IV), which can be catalyzed by Mn-oxides and scavenged from seawater by both Mn- and Fe(oxy)hydroxides (Moffett, 1990; German and Elderfield, 1990; Bau, 1999). However, the behavior in

sedimentary pore waters in which carbonate cements precipitated is not straightforward. Various effects have been invoked to explain the development of negative Ce anomalies in putative anoxic environments, including high pH and dissolved carbonate concentrations, and interactions with dissolved organic material such as humic substances (Pourret et al., 2008; Himmler et al., 2010; Hu et al., 2014). In the case of aragonites featuring authentic negative Ce anomalies an ephemeral influence of seawater diffusing into sediments, as well as dynamic seepage rates may argue for the influence of oxygenated seawater at the time of precipitation (cf. Feng et al., 2009b). As AOM is an obligatory anaerobic process, however, the locus of precipitation of cements is most likely within anoxic sedimentary pore waters, possibly close to the sediment-water interface where seawater may have temporarily influenced Ce redox chemistry. Cerium anomalies of clear and gray aragonite cements and micrite yield conflicting information when plotted against Nd concentrations. Wright et al. (1987) studied ancient phosphates to show how log(Ce/Ce*) values below and above −0.1 argue for oxic and anoxic formation conditions, respectively. Aragonite cement log(Ce/Ce*) values from Campeche Knoll carbonates plot below and above −0.1, whereby Chapopote clear aragonite cement with the clearest Ce anomalies plot very far below this values. Gray aragonite cements from UNAM Ridge, Mictlan and Tsanyao Yang Knolls cluster around this value between −0.2 and zero (Fig. 15A). Micrite on the other hand plots in the anoxic domain of the plot (Fig. 15B). Although trace and ∑REE+Y contents within gray aragonites featuring both negative Ce and positive La anomalies are high, and strong inter-elemental correlations of Al, Fe, and Mn in these phases, there are no detectable correlation between these elements and the REEs. This important observation suggests that REE anomalies, as well as LREE enrichments in gray aragonites are not caused by contamination of Fe and Mn(oxy)hydroxides or clay minerals. Oliver and Boyet (2005) distinguished a shale- from a seawater signature in microbial carbonates based Ce anomalies and Pr/Yb ratios. Figure 15C demonstrates clear differences in precipitation conditions of clear and gray aragonites cements in all studied samples, although the spread in data is significant. All clear aragonites plot into the seawater-signature area of the plot below Ce/Ce* = 0.4, whereas gray aragonites plot in the vicinity of the shale-signature area. However, due to their conspicuous LREE enrichment gray aragonites are further from the shale-signature area than hydrocarbons, which plot almost within unity in the center of the plot. Microcrystalline calcites, on the other hand, all plot far from the seawater-signature area, and spread across a larger interval of Pr/Yb ratios around the shale signature area (Fig. 15D). At this point, the most careful interpretation of this counter-intuitive signal in rocks derived from strictly anoxic pore waters is a

combination of interactions of Ce with dissolved organic and inorganic carbon and oils (cf. Pourret et al., 2008; Himmler et al., 2010; Kim et al., 2012). Possibly, gray aragonites covered in diffuse veneers were more strongly associated with microbial mineralization of organic matter and/or oil in the rocks, or that the oils themselves are responsible for its cryptocrystalline texture and delivered increasing amounts of trace metals to the locus of precipitation. This would account for the non-seawater-like REE patterns, as well as higher contents in trace metals than clear aragonite.

A synthesis of results

High resolution elemental analyses of trace elements in cements can therefore yield specific information on redox state of parent fluids of each phase, as well as estimate concentrations of organic matter and/or heavy hydrocarbons during cement precipitation. It can be concluded that samples from UNAM Ridge and Mictlan Knoll originally formed within the sediment as evidenced by petrographic observations, as well as their trace element patterns which show a strongly shale-derived signature. Clear aragonite and gray aragonite cements precipitated in pore fluids of different composition. The former formed in shallow sediments during early diagenesis with possible influence of diffusing oxygenated seawater as suggested by seawater-type shale-normalized REE patterns. Gray aragonites formed from fluids saturated by large amounts of dissolved and/or particulate organic matter, as well as heavy hydrocarbons that additionally enriched parent fluids with other trace elements within the oils themselves. Stable isotopes suggest that the carbon source of all carbonate phases at all sites was predominantly derived from the anaerobic oxidation of crude oils and asphalts, possibly some smaller amounts of carbon derived from AOM and DIC from seawater in the case of Tsanyao Yang carbonates. Aragonite cement-specific Ce anomalies are of limited use, yet may yield information on the redox state of formation waters if ∑REE+Y content of carbonate phases is high enough.

Conclusions

The comprehensive data set from oils seeping from southern GoM sediments, and the influence of microbial degradation on carbonate precipitation can be summarized as follows:

- Crude oils seeping from Campeche Bay ridges and knolls are of low maturity, and are sourced from one reservoir
- Carbonate saturation at oil seeps is governed by the oxidation state of carbon, and rate of their oxidation with sulfate
- Trace and rare earth metal inventories of carbonate cements are reliable archives for varying redox conditions and fluid composition
- Phase-specific trace element data can reveal detailed formation history of aragonite cements, suggesting that these environments are highly dynamic

High-resolution trace and REE data from aragonite cements precipitating at oil seeps from Campeche Knolls highlight the ability of authigenic chemical sediments to archive information on fluid composition and redox conditions. Crude oils of low maturity are present in prominent amounts at UNAM Ridge, Mictlan Knoll, and Tsanyao Yang Knoll, and have contributed to carbonate formation at Campeche Knolls. The rates of microbial oxidation of specific hydrocarbon compounds with sulfate in southern GoM sediments are unknown, yet applying rates determined from culture and field studies to a batch model can help to assess their influence on carbonate and gas formation. Numerical batch modeling suggests that sulfate-dependent oxidation of many common hydrocarbon compounds generally favor carbonate precipitation, yet this assumption strongly depends on the oxidation state of carbon in the respective compounds, and the rates at which they are oxidized. Gas production and its composition is also determined by these two parameters. Trace and REE patterns of aragonite cements testify to a strong influence of organic matter- and oil-rich pore waters during precipitation. This study strengthens the notion that authigenic carbonates archive redox conditions and fluid composition of parent fluids. The latter point is of significance with respect to changing community structures of micro- and macrofaunal chemosynthetic communities at hydrocarbon seeps over geologic time, as their evolution may have been partially controlled by variations in composition of seeping fluids. A systematic application of trace and

rare earth metals to Phanerozoic, and even Proterozoic, limestones may broaden our understanding and perception of the evolution of chemosynthesis-based life throughout Earth's history.

Acknowledgements

The authors thank Patrick Monien and Andreas Klügel (both University of Bremen) for analytical support during trace and rare earth element analyses, Petra Körner (University of Vienna) for organic carbon determination in carbonate and crude oil samples, Sylvain Richoz (Lund University) for stable carbon isotope measurements, and the scientific team, captain and crew of RV Meteor and the MARUM ROV QUEST 3000 team aboard cruise M114 for outstanding support and sampling. This project was co-funded by a Uni:Docs fellowship from the University of Vienna awarded to Daniel Smrzka, and by funding from the Austrian Academy of Sciences (ÖAW) through a doctoral fellowship awarded to the Jennifer Zwicker.

References

Ackersberg, F., Bak, F., Widdel, F., 1991. Anaerobic oxidation of saturated hydrocarbons of CO_2 by a new type of sulfate-reducing bacterium. Archives of Microbiology 156, 5–14.

Aharon, P., Schwarcz, H.P., Roberts, H.H., 1997. Radiometric dating of submarine hydr carbon seeps in the Gulf of Mexico. Geological Society of America Bulletin 109, 568–579.

Ali, M.F., Bukhari, A., Saleem, M., 1983.). Trace metals in crude oils from Saudi Arabia. Industrial & engineering chemistry product research and development 22, 691–694.

Aloisi, G., Bouloubassi, I., Heijs, S.K., Pancost, R.D., Pierre, C., Damsté, J.S., Gottschal, J.C., Forney, L.J., Rouchy, J.M., 2002. CH_4-consuming microorganisms and the formation of carbonate crusts at cold seeps. Earth and Planetary Science Letters 203, 195–203.

Baker, E.W., Palmer, S.E., 1978. Geochemistry of porphyrins. In: Dolphin, D. (Ed.), The Porphyrins, vol. 1. Academic Press, New York, pp. 486–552.

Barnes, J.W., Dorough, G.D., 1950. Exchange and Replacement Reactions of α, β, γ, δ-Tetraphenyl-metalloporphins1. Journal of the American Chemical Society 72, 4045–4050.

Barwise, A.J.G., 1990. Role of nickel and vanadium in petroleum classification. Energy & Fuels 4, 647–652.

Bau, M., 1999. Scavenging of dissolved yttrium and rare earths by precipitating iron oxyhydroxide: Experimental evidence for Ce oxidation, Y-Ho fractionation, and lanthanide tetrad effect. Geochimica et Cosmochimica Acta 63, 67–77.

Bau,M., Dulski, P., 1996. Distribution of yttrium and rare-earth elements in the Penge and Kuruman iron-formations, Transvaal Supergroup, South Africa. Precambrian Research, 79, 37–55.

Bayon, G., Dupré, S., Ponzevera, E., Etoubleau, J., Chéron, S., Pierre, C., Mascle, J., Boetius, A., De Lange, G.J., 2013. Formation of carbonate chimneys in the Mediterranean Sea linked to deep-water oxygen depletion. Nature Geoscience 6, 755–760.

Beauchamp, B., Savard, M., 1992. Cretaceous chemosynthetic carbonate mounds in the Canadian Arctic. Palaios, 434–450.

Beller, H.R., Reinhard, M., Grbic-Galic, D., 1992. Metabolic by-products of anaerobic toluene degradation by sulfate-reducing enrichment cultures. Applied and Environmental Mircobiology 58, 3192–3195.

Bergquist, D.C., Fleckenstein, C., Szalai, E., Knisel, J., Fisher, C.R., 2004. Environment drives physiological variability in the cold seep mussel *Bathymodiolus childressi*. Limnology and Oceanography 49, 706–715.

Bernard, B.B., Brooks, J.M., Sackett, W.M., 1976. Natural gas seepage in the Gulf of Mexico. Earth and Planetary Science Letters 31, 48–54.

Beyssac, O., Goffé, B., Chopin, C., Rouzaud, J.N., 2002. Raman spectra of carbonaceous material in metasediments: a new geothermometer. Journal of metamorphic Geology 20, 859–871.

Bian, Y., Feng, D., Roberts, H. H., Chen, D., 2013. Tracing the evolution of seep fluids from authigenic carbonates: Green Canyon, northern Gulf of Mexico. Marine and Petroleum Geology 44, 71–81.

Birgel, D., Feng, D., Roberts, H.H., Peckmann, J., 2011. Changing redox conditions at cold seeps as revealed by authigenic carbonates from Alaminos Canyon, northern Gulf of Mexico. Chemical Geology 285, 82–96.

Blumenberg, M., Pape, T., Seifert, R., Bohrmann, G., Schlömer, S., 2017. Can hydrocarbons entrapped in seep carbonates serve as gas geochemistry recorder? Geo-Marine Letters, 1-9, doi 10.1007/s00367-017-0522-6.

Boetius, A., Ravenschlag, K., Schubert, C.J., Rickert, D., Widdel, F., Gleseke, A., Amann, R., Jørgensen, B.B., Witte, U., Pfannkuche, O., 2000. A marine microbial consortium apparently mediating anaerobic oxidation of methane. Nature 407, 623–626.

Bohrmann, G., Ivanov, M., Foucher, J.-P., Spiess, V., Bialas, J., Greinert, J., Weinrebe, W., Abegg, F., Aloisi, G., Artemov, Y., Blinova, V., Drews, M., Heidersdorf, F., Krabbenhöft, A., Klaucke, I., Krastel, S., Leder, T., Polikarpov, I., Saburova, M., Schmale, O., Seifert, R., Volkonskaya, A., Zillmer, M., 2003. Mud volcanoes and gas hydrates in the Black Sea: new data from Dvurechenskii and Odessa mud volcanoes. Geo-Marine Letters 23, 239–249.

Bohrmann, G., Schenck S., and cruise participants, 2004. Report and preliminary results of R/V Sonne cruise SO 174 / OTEGA II, Balboa – Corpus Christi – Miami, 1 October - 12 November 2003. Investigations within the BMBF special program "Gashydrate im Geosystem". Geomar report 117, IFM – GEOMAR, Kiel 2004, 130 p.

Buffler, R.T., Sawyer, D.S.,1985. Distribution of crust and early history, Gulf of Mexico basin. Gulf Coast Association of Geological Societies Transactions 35, 333–344

Brooks, J.M., Cox, B., Bryant, W.R., Kennicutt, M.C., 1986. Association of gas hydrates and oil seepage in the Gulf of Mexico. Organic Geochemistry 10, 221–234.

Brüning, M., Sahling, H., MacDonald, I.R., Ding, F., Bohrmann, G., 2010. Origin, distribution, and alteration of asphalts at Chapopote Knoll, Southern Gulf of Mexico. Marine and Petroleum Geology 27, 1093–1106.

Campbell, K.A., 2006. Hydrocarbon seep and hydrothermal vent paleoenvironments and paleontology: past developments and future research directions. Palaeogeography, Palaeoclimatology, Palaeoecology 232, 362–407.

Campbell, K.A., Bottjer, D.J., 1995. *Peregrinella*: an early Cretaceous cold-seep-restricted brachiopod. Paleobiology 21, 461–478.

Claypool, G.E., Kvenvolden, K.A., 1983. Methane and other hydrocarbon gases in marine sediment. Annual Reviews in Earth and Planetary Sciences 11, 299–327.

Coates, J.D., Anderson, R.T., Lovley, D.R., 1996. Oxidation of polycyclic aromatic hydrocarbons under sulfate-reducing conditions. Applied and Environmental Microbiology 62, 1099–1101.

Coates, J.D., Woodward, J., Allen, J., Philip, P., Lovley, D.R., 1997. Anaerobic degradation of polycyclic aromatic hydrocarbons and alkanes in petroleum-contaminated marine harbor sediments. Applied and Environmental Microbiology 63, 3589–3593.

Curiale, J.A., 1986. Origin of solid bitumens, with emphasis on biological marker results. Organic Geochemistry 10, 559–580.

Curiale, J.A., Bloch, S., Rafalska-Bloch, J., Harrison, W.E., 1983. Petroleum-related origin for uraniferous organic-rich nodules of southwestern Oklahoma. American Association of Petroleum Geologists Bulletin 67, 588–608.

De Baar, H.H.W., Brewer, P.G., Bacon, M.P., 1985. Anomalies in rare earth distributions in seawater: Gd and Tb. Geochimica et Cosmochimica Acta 49, 1961–1969.

De Beukelaer, S.M., MacDonald, I.R., Guinnasso, N.L., Murray, J.A., 2003. Distinct side-scan sonar, RADARSAT SAR, and acoustic profiler signatures of gas and oil seeps on the Gulf of Mexico slope. Geo-Marine Letters 23, 177–186.

Deutsch, M., Estes, J.E., 1980. Landsat detection of oil from natural seeps. Photogrammetric Engineering and Remote Sensing 46, 1313–1322.

Dillon, R.O., Woollam, J.A., Katkanant, V., 1984. Use of Raman scattering to investigate disorder and crystallite formation in as-deposited and annealed carbon films. Physical Review B 29, 3482–3488.

Ding, F., Spiess, V., Brüning, M., Fekete, N., Keil, H., Bohrmann, G., 2008. A conceptual model for hydrocarbon accumulation and seepage processes around Chapopote asphalt site, southern Gulf of Mexico: From high resolution seismic point of view. Journal of Geophysical Research 113, 1–15.

Ding, F., Spiess, V., MacDonald, I.R., Brüning, M., Fekete, N., Bohrmann, G., 2010. Shallow sediment deformation styles in north-western Campeche Knolls, Gulf of Mexico and their controls on the occurrence of hydrocarbon seepage. Marine and Petroleum Geology 27, 959–972.

Dreyfus, S., Pecheyran, C., Magnier, C., Prinzhofer, A., Lienemann, C.P., Donard, O.F.X., 2005. Direct trace and ultra-trace metals determination in crude oil and fractions by inductively coupled plasma mass spectrometry. In: Elemental Analysis of Fuels and Lubricants: Recent Advances and Future Prospects. ASTM International.

Dubessy, J., Buschaert, S., Lamb, W., Pironon, J., Thiéry R., 2001. Methane-bearing aqueous fluid inclusions: Raman analysis, thermodynamic modelling and application to petroleum basins. Chemical Geology 173, 193–205.

Duyck, C., Miekeley, N., Fonseca, T.C., Szatmari, P., Neto, S., 2008. Trace element distributions in biodegraded crude oils and fractions from the Potiguar Basin, Brazil. Journal of the Brazilian Chemical Society 19, 978–986.

Duyck, C., Miekeley, N., da Silveira, C.L.P., Szatmari, P., 2002. Trace element determination in crude oil and its fractions by inductively coupled plasma mass spectrometry using ultrasonic nebulization of toluene solutions. Spectrochimica Acta Part B: Atomic Spectroscopy 57, 1979–1990.

Edwards, E.A., Wills, L.E., Reinhard, M., Grbic-Galic, D., 1992. Anaerobic degradation of toluene and xylene by aquifer microogranisms under sulfate-reducing conditions. Applied and Environmental Microbiology 58, 794–800.

Elderfield, H., Greaves, M.J., 1982. The rare earth elements in seawater. Nature 296, 214–219.

Estes, J.E., Crippen, R.E., Star, J.L., 1985. Natural oil seep detection in the Santa Barbara Channel, California, with shuttle imaging radar. Geology 13, 282–284.

Fabec, J.L., Ruschak, M.L., 1985. Determination of nickel, vanadium, and sulfur in crudes and heavy crude fractions by inductively coupled argon plasma atomic emission spectrometry and flame atomic absorption spectrometry. Analytical Chemistry 57, 1853–1863.

Feng, D., Chen, D., Roberts, H.H., 2009a. Petrographic and geochemical characterization of seep carbonates from Bush Hill (GC 185) gas vent and hydrate site of the Gulf of Mexico. Marine and Petroleum Geology 26, 1190–1198.

Feng, D., Chen, D., Peckmann, J., 2009b. Rare earth elements in seep carbonates as tracers of variable redox conditions at ancient hydrocarbon seeps. Terra Nova 21, 49–56.

Filby, R.H., 1994. Origin and nature of trace element species in crude oils, bitumens and kerogens: implications for correlation and other geochemical studies. Geological Society, London, Special Publications 78, 203–219.

Fisher, C., Roberts, H., Cordes, E., Bernard, B., 2007. Cold seeps and associated communities of the Gulf of Mexico. Oceanography 20, 118–129.

Formolo, M.J., Lyons, T.W., Zhang, C., Kelley, C., Sassen, R., Horita, J., Cole, D.R., 2004. Quantifying carbon sources in the formation of authigenic carbonates at gas hydrate sites in the Gulf of Mexico. Chemical Geology 205, 253–264.

Galushko, A., Minz, D., Schink, B., Widdel, F., 1999. Anaerobic degradation of naphthalene by a pure culture of a novel type of marine sulphate-reducing bacterium. Environmental Microbiology 1, 415–420.

German, C.R., Elderfield, H., 1990. Application of the Ce anomaly as a paleoredox indicator: the ground rules. Paleoceanography 5, doi:10.1029/PA005i005p00823.

Goldhaber, M.B., Reynolds, R.L., Rye, R.O., 1978. Origin of a South Texas roll-type uranium deposit, II: sulfide petrology and sulfur isotope studies: Economic Geology 73, 1690–1703.

Gondal, M.A., Siddiqui, M.N., Nasr, M.M., 2009. Detection of trace metals in asphaltenes using an advanced laser-induced breakdown spectroscopy (LIBS) technique. Energy & Fuels 24, 1099–1105.

Grbić-Galić, D., Vogel, T.M., 1987. Transformation of toluene and benzene by mixed methanogenic cultures. Applied and Environmental Microbiology 53, 254–260.

Greinert, J., Bohrmann, G., Suess, E., 2001. Gas hydrate-associated carbonates and methane-venting at Hydrate Ridge: classification, distribution, and origin of authigenic lithologies. Natural gas hydrates: Occurrence, distribution, and detection, 99–113.

Hackley, P.C., Cardott, B.J., 2016. Application of organic petrography in North American shale petroleum systems: A review. International Journal of Coal Geology 163, 8–51.

Hackley, P.C., Ryder, R.T., Trippi, M.H., Alimi, H., 2013. Thermal maturity of northern Appalachian Basin Devonian shales: insights from sterane and terpane biomarkers. Fuel 106, 455–462.

Hagemann, A., Leefmann, T., Peckmann, J., Hoffmann, V. E., Thiel, V., 2013. Biomarkers from individual carbonate phases of an Oligocene cold-seep deposit, Washington State, USA. Lethaia 46, 7–18.

Harayama, S., Kishira, H., Kasai, Y., Shutsubo, K., 1999. Petroleum biodegradation in marine environments. Journal of Molecular Microbiology and Biotechnology 1, 63–70.

Harms, G., Zengler, K., Rabus, R., Aeckersberg, F., Minz, D., Rosselló-Mora, R., Widdel, F., 1999. Anaerobic oxidation of *o*-xylene, *m*-xylene, and homologous alkylbenzenes by new types of sulfate-reducing bacteria. Applied and Environmental Microbiology 65, 999–1004.

Heider, J., Spormann, A.M., Beller, H.R., Widdel, F., 1998. Anaerobic bacterial metabolism of hydrocarbons. FEMS Microbiology Reviews 22, 459-473.

Hein, F.J., 2006. Heavy oil and oil (tar) sands in North America: an overview & summary of contributions. Natural Resources Research 15, 67–84.

Himmler, T., Bach, W., Bohrmann, G., Peckmann, J., 2010. Rare earth elements in authigenic methane-seep carbonates as tracers for fluid composition during early diagenesis. Chemical Geology 277, 126–136.

Himmler, T., Bayon, G., Wangner, D., Enzmann, F., Peckmann, J., Bohrmann, G., 2016. Seep-carbonate lamination controlled by cyclic particle flux. Scientific Reports 6, 37439.

Himmler, T., Birgel, D., Bayon, G., Pape, T., Ge, L., Bohrmann, G., Peckmann, J., 2015. Formation of seep carbonates along the Makran convergent margin, northern Arabian Sea and a molecular and isotopic approach to constrain the carbon isotopic composition of parent methane. Chemical Geology 415, 102–117.

Hodgson, G.W., Baker, B.L., 1957. Vanadium, nickel, and porphyrins in thermal geochemistry of petroleum. American Association of Petroleum Geologists Bulletin 41, 2413–2426.

Hu, Y., Feng, D., Peckmann, J., Roberts, H.H., Chen, D., 2014. New insights into cerium anomalies and mechanisms of trace metal enrichment in authigenic carbonate from hydrocarbon seeps. Chemical Geology 381, 55–66.

Jakubowicz, M., Dopieralska, J., Belka, Z., 2015. Tracing the composition and origin of fluids at an ancient hydrocarbon seep (Hollard Mound, Middle Devonian, Morocco): A Nd, REE, and stable isotope study. Geochimica et Cosmochimica Acta 156, 50–74.

Jehlička, J., Bény, C., 1992. Application of Raman microspectrometry in the study of structural changes in Precambrian kerogens during regional metamorphism. Organic Geochemistry 18, 211–213.

Jochum, K.P., Weis, U., Stoll, B., Kuzmin, D., Yang, Q., Raczek, I., Jacob, D.E., Stracke, A., Birbaim, K., Frick, D.A., Günther, D., and Enzweiler, J., 2011. Determination of reference values for NIST SRM 610-617 glasses following ISO guidelines. Geostandards and Geoanalytical Research 35, 397–429.

Joye, S.B., Boetius, A., Orcutt, B.N., Montoya, J.P., Schulz, H.N., Erickson, M.J., Lugo, S.K., 2004. The anaerobic oxidation of methane and sulfate reduction in sediments from Gulf of Mexico cold seeps. Chemical Geology 205, 219–238.

Judd, A.G., Hovland, M., 2007. Seabed fluid flow – The impact of geology, biology and the marine environment. Cambridge University Press, 492 p.

Kazumi, J., Caldwell, M.E., Suflita, J.M., Lovely, D.R., Young, L.Y., 1997. Anaerobic degradation of benzene in diverse anoxic environments. Environmental Science and Technology 31, 813–818.

Kelemen, S.R., Fang, H.L., 2001. Maturity trends in Raman spectra from kerogen and coal. Energy & fuels 15, 653–658.

Kennicutt, M.C., Brooks, J.M., Bidigare, R.R., Denoux, G.J., 1988a. Gulf of Mexico hydrocarbon seep communities—I. Regional distribution of hydrocarbon seepage and associated fauna. Deep Sea Research Part A. Oceanographic Research Papers 35, 1639–1651.

Kennicutt, M.C., Brooks, J.M., Denoux, G.J., 1988b. Leakage of deep reserved petroleum to the near surface of the Gulf of Mexico continental slope. Marine Chemistry 24, 39–59.

Khuhawar, M.Y., Mirza, M.A., Jahangir, T.M., 2012. Determination of metal ions in crude oils. In: Crude oil emulsions-Composition stability and characterization. Intech.

Kim, J.-H. Torres, M.E., Haley, D.A., Kastner, M., Pohlman, J.W., Riedel, M., Lee, Y.-J., 2012. The effect of diagenesis and fluid migration on rare earth element distribution in pore fluids of the northern Cascadia accretionary margin. Chemical Geology 291, 152–165.

Kisker, C., Schindelin, H., Rees, D.C., 1997. Molybdenum-cofactor–containing enzymes: structure and mechanism. Annual Review of Biochemistry 66, 233–267.

Klapp, S.A., Bohrmann, G., Kuhs, W.F., Murshed, M.M., Pape, T., Klein, H., Techmer, K.S., Heeschen, K.U., Abegg, F., 2010. Microstructures of structure I and II gas hydrates from the Gulf of Mexico. Marine and Petroleum Geology 27, 116–125.

Kleinsteuber, S., Schleinitz, K.M., Breitfeld, J., Harms, H., Richnow, H.H., Vogt, C., 2008. Molecular characterization of bacterial communities mineralizing benzene under sulfate-reducing conditions. FEMS Microbial Ecology 66, 143–157.

Kniemeyer, O., Fischer, T., Wilkes, H., Glöckner, F.O., Widdel, F., 2003. Anaerobic degradation of ethylbenzene by a new type of marine sulfate-reducing bacterium. Applied and Environmental Microbiology 69, 760–768.

Kniemeyer, O., Musat, F., Sivert, S.M., Knittel, K., Wilkes, H., Blumenberg, M., Michaelis, W., Classen, A., Bolm, C., Joye, S.M., Widdel, F., 2007. Anaerobic oxidation of short-chain hydrocarbons by marine sulphate-reducing bacteria. Nature 449, 898–902-

Kopf, A.J., 2002. Significance of mud volcanism. Reviews of Geophysics 40, 1-52.

Körber, J.H., Sahling, H., Pape, T., dos Santos Ferreira, C., MacDonald, I.R., Bohrmann, G., 2014. Natural oil seeps at Kobuleti Ridge, eastern Black Sea. Marine and Petroleum Geology 50, 68–82.

Kropp, K.G., Davidova, I.A., Suflita, J.M., 2000. Anaerobic oxidation of *n*-dodecane by an addition reaction in a sulfate-reducing bacterial enrichment culture. Applied and Environmental Microbiology 66, 5393–5398.

Kruszewska, K., 1989. The use of reflectance to determin maceral composition and reactive-inert ratio of coal components. Fuel 68, 753–757.

Kvenvolden, K.A., Cooper, C.K., 2003. Natural seepage of crude oil into the marine environment. Geo-Marine Letters 23, 140–146.

Laban, N.A., Selesi, D., Jobelius, C., Meckenstock, R.U., 2009. Anaerobic benzene degradation by gram-positive sulfate-reducing bacteria. FEMS Microbial Ecology 66, 300–311.

Le Pennec, M., Beninger, P.G., Herry, A., 1995. Feeding and digestive adaptations of bivalve molluscs to sulphide-rich habitats. Comparative Biochemisrty and Physiology Part A: Physiology 111, 183–189.

Levin, L.A., 2005. Ecology of cold seep sediments: interactions of fauna with flow, chemistry and microbes. Oceanography and Marine Biology: An Annual Review 43, 1–46.

Lewan, M.D., 1984. Factors controlling the proportionality of vanadium to nickel in crude oils. Geochimica et Cosmochimica Acta 48, 2231–2238.

Lewan, M.D., Maynard, J.B., 1982. Factors controlling enrichment of vanadium and nickel in the bitumen of organic sedimentary rocks. Geochimica et Cosmochimica Acta 46, 2547–2560.

Liu, D., Xiao, X., Tian, H., Min, Y., Zhou, Q., Cheng, P., Shen, J., 2013. Sample maturation calculated using Raman specrtroscopic parameters for solid organics: Methodology and geological applications. Chin. Sci. Bull. 58, 1285–1298.

Lord, C.J., 1991. Determination of trace metals in crude oil by inductively coupled plasma mass spectrometry with microemulsion sample introduction. Analytical Chemistry 63, 1594–1599.

Lovley, D.R., Lonergan, D.J., 1990. Anaerobic oxidation of toluene, phenol, and p-cresol by the dissimilatory iron-reducing organism, GS-15. Applied and Environmental Microbiology 56, 1858–1864.

Lovley, D.R., Phillips, E.J.P., Gorby, Y.A., Landa, E.r., 1991. Microbial reduction of uranium. Nature 350, 413–416.

Luff, R., Wallmann, K., 2003. Fluid flow, methane fluxes, carbonate precipitation and biogeochemical turnover in gas hydrate-bearing sediments at Hydrate Ridge, Cascadia Margin: numerical modeling and mass balances. Geochimica et Cosmochimica Acta 67, 3403–3421.

MacDonald, I.R., Bohrmann, G., Escobar, E., Abegg, F., Blanchon, P., Blinova, V., Brückmann, W., Drews, M., Eisenhauer, A., Han, X., Heeschen, K., Meier, F., Mortera, C., Naehr, T., Orcutt, B., Bernard, B., Brooks, J., de Faragó, M., 2004. Asphalt volcanism and chemosynethetic life in the Campeche Knolls, Gulf of Mexico. Science 304, 999–1002.

MacDonald, I.R., Buthman, D.B., Sager, W.W., Peccini, M.B., Guinasso Jr., N.L., 2000. Pulsed oil discharge from a mud volcano. Geology 28, 907–910.

MacDonald, I.R., Guinasso, N.L., Ackleson, S.G., Amos, J.F., Duckworth, R., Sassen, R., Brooks, J.M., 1993. Natural oil slicks in the Gulf of Mexico visible from space. Journal of Geophysical Research 98, 16351–16364.

Magoon, L.B., Hudson, T.L., Cook, H.E., 2001. Pimienta-Tamabra(!) – a giant supercharged petroleum system in the southern Gulf of Mexico, onshore and offshore Mexico. In: Bartolini, C., Biuffler, R.T., Cantu-Chapa, A., (Eds.), The Western Gulf of Mexico Basin: Tectonics, Sedimentary Basins, and Petroleum Systems. American Association of Petroleum Geologists Bulletin Memoir, 83–125.

Maillacheruvu, K.Y., Pathan, I.A., 2009. Biodegradation of naphthalene, phenanthrene, and pyrene under anaerobic conditions. Journal of Environmental Science and Health, Part A 44, 1315–1326.

Mansour, A.S., Sassen, R., 2011. Mineralogical and stable isotopic characterization of authigenic carbonate from a hydrocarbon seep site, Gulf of Mexico slope: possible relation to crude oil degradation. Marine Geology 281, 59–69.

McFarlane, E., Menes, E.S., 1991. The Gulf of Mexico Basin. The Geology of Northern America. Geological Society of America, 181–204.

McIntire, M.C., 2014. Rare earth elements (REE) in crude oil in the Lansing-Kansas City formations in central Kansas: potential indications about their sources, locally derived or long-distance derived (Doctoral dissertation, Kansas State University).

McManus, J., Berelson, W.M., Klinkhammer, G.P., Hammond, D.E., Holm, C., 2005. Authigenic uranium: relationship to oxygen penetration and organic carbon rain. Geochimica et Cosmochimica Acta 69, 95–108.

Michaelis, W., Seifert, R., Nauhaus, K., Treude, T., Thiel, V., Blumenberg, M., Knittel, K., Gieseke, A., Peterknecht, K., Pape, T., Boetius, A., Amann, R., Jorgensen, B.B., Widdel, F., Peckmann, J., Pimenov, N.V., Gulin, M.B., 2002. Microbial reefs in the Black Sea fueled by anaerobic oxidation of methane. Science 297, 1013–1015.

Milkov, A.V., 2004. Global estimates of hydrate-bound gas in marine sediments: How much is really out there? Earth Science Reviews 66, 183–197.

Miralles, G., Nérini, D., Manté, C., Acquaviva, M., Doumenq, P., Michotey, V., Nazaret, S., Betrand, J.C., Cuny, P., 2007. Effects of spilled oil on bacterial communities of Mediterranean coastal anoxic sediments chronically subjected to oil hydrocarbon contamination. Microbial Ecology 54, 646–661.

Moffett, J.W., 1990. Microbially mediated cerium oxidation in seawater. Nature 345, 421–423.

Morán-Zenteno, D.J., 1984. Geology of the Mexican Republic. American Association of Petroleum Geologists Bulletin 39, 160 p.

Morford, J.L., Emerson, S.R., 1999. The geochemistry of redox sensitive trace metals in sediments. Geochimica et Cosmochimica Acta 63, 1735–1750.

Mumm, A.S. Inan, S., 2016. Microscale organic maturity determination of graptolites using Raman spectroscopy. International Journal of Coal Geology 162, 96–107.

Musat, F., Widdel, F., 2008. Anaerobic degradation of benzene by a marine sulfate-reducing enrichment culture, and cell hybridization of the dominant phylotype. Environmental Microbiology 10, 10–19.

Naehr, T.H., Birgel, D., Bohrmann, G., MacDonald, I.R., Kasten, S., 2009. Biogeochemical controls on authigenic carbonate formation at the Chapopote “asphalt volcano”, Bay of Campeche. Chemical Geology 266, 399–411.

Naehr, T.H., Eichhubl, P., Orphan, V.J., Hovland, M., Paull, C.K., Ussler, W., Lorensen, T.D., Greene, H.G., 2007. Authigenic carbonate formation at hydrocarbon seeps in continental margin sediments: a comparative study. Deep Sea Research Part II: Topical Studies in Oceanography 54, 1268–1291.

Nameroff, T.J., Balistrieri, L.S., Murray, J.W., 2002. Suboxic trace metal geochemistry in the eastern tropical North Pacific. Geochimica et Cosmochimica Acta 66, 1139–1158.

Nciri, N., Song, S., Kim, N., Cho, N., 2014. Chemical characterization of gilsonite bitumen. Journal of Petroleum & Environmental Biotechnology 5, doi.org/10.4172/2157-7463.1000193.

Nordstrom, D.K., Plummer, L.N.,Wigley, T.M.L.,Wolery, T.J., Ball, J.W., Jenne, E.A., Bassett, R.L., Crerar, D.A., Florence, T.M., Fritz, B., Hoffman, M., Holdren, G.R., Jr., Lafon, G.M., Mattigod, S.V., McDuff, R.E., Morel, F., Reddy, M.M., Sposito, G., Thrailkill, J., 1979, A comparison of computerized chemical models for equilibrium calculations in aqueous systems. In: Jenne, E.A., (Ed.), Chemical modeling in aqueous systems—Speciation, sorption, solubility, and kinetics: Series 93, American Chemical Society, 857–892.

Odermatt, J.R., Curiale, J.A., 1991. Organically bound metals and biomarkers in the Monterey Formation of the Santa Maria Basin, California. Chemical Geology 91, 99–113.

Oliver, N., Boyet, M., 2005. Rare earth and trace elements of microbialites in Upper Jurassic coral- and sponge-microbialite reefs. Chemical Geology 230, 105–123.

Orcutt, B.N., Joye, S.B., Kleindienst, S., Knittel, K., Ramette, A., Reitz, A., Samarkin, V., Treude, T., Boetius, A., 2010. Impact of natural oil and higher hydrocarbons on microbial diversity, distribution, and activity in Gulf of Mexico cold-seep sediments. Deep-Sea Research Part II: Topical Studies in Oceanography 57, 2008–2021.

Ozaki, T., Suzuki, Y., Nankawa, T., Yoshida, T., Ohnuki, T., Kimura, T., Francis, A.J., 2006. Interactions of rare earth elements with bacteria and organic ligands. Journal of Alloys and Compounds 408–412, 1334–1338.

Parkhurst, D.L., Appelo, C.A.J., 1999. A User's Guide to PHREEQC (version 2) — A Computer Program for Speciation, Batch-reaction, One-dimensional Transport and Inverse Geochemical Calculations. U.S. Geological Survey, Denver Colorado. 326 p.

Parnell, J., Eakin, P., 1987. The replacement of sandstones by uraniferous hydrocarbons: significance for petroleum migration. Mineralogical Magazine 51, 505–515.

Pasteris, J.D., Wopenka, B., 1991. Raman spectra of graphite as indicators of degree of metamorphism. The Canadian Mineralogist 29, 1–9.

Paull, C.K., Hecker, B., Commeau, R., Freeman-Lynde, R.P., Neumann, C., Corso, W.P., Golubic, S., Hook, J.E., Sikes, E., Curray, J., 1984. Biological communities at the Florida Escarpment resemble hydrothermal vent taxa. Science 226, 965–967.

Paull, C.K., Jull, A. J.T., Toolin, L.J., Linick, T., 1985. Stable isotope evidence for chemosynthesis in an abyssal seep community. Nature 317, 709–711.

Peckmann, J., Thiel, V., 2004. Carbon cycling at ancient methane–seeps. Chemical Geology 205, 443–467.

Peckmann, J., Campbell, K.A., Walliser, O.H., Reitner, J., 2007. A Late Devonian hydrocarbon-seep deposit dominated by dimerelloid brachiopods, Morocco. Palaios 22, 114–122.

Peckmann, J., Gischler, E., Oschmann, W., Reitner, J., 2001a. An Early Carboniferous seep community and hydrocarbon-derived carbonates from the Harz Mountains, Germany. Geology 29, 271–274.

Peckmann, J., Goedert, J.L., Heinrichs, T., Hoefs, J., Reitner, J., 2003. The Late Eocene 'Whiskey Creek' methane-seep deposit (western Washington State). Facies 48, 241–254.

Peckmann, J., Goedert, J.L., Thiel, V., Michaelis, W., Reitner, J., 2002. A comprehensive approach to the study of methane-seep deposits from the Lincoln Creek Formation, western Washington State, USA. Sedimentology 49, 855–873.

Peckmann. J., Kiel. S., Sandy. M.R., Taylor. D.G., Goedert. J.L., 2011. Mass occurrences of the brachiopod Halorella in late Triassic methane-seep deposits, eastern Oregon. Journal of Geology 119, 207–220.

Peckmann, J., Sandy, M.R., Taylor, D.G., Gier, S., Bach, W., 2013. An Early Jurassic brachiopod-dominated seep deposit enclosed by serpentinite, eastern Oregon, USA. Palaeogeography, Palaeoclimatology, Palaeoecology 390, 4-16.

Peckmann, J., Reimer, A., Luth, U., Luth, C., Hansen, B.T., Heinicke, C., Hoefs, J., Reitner, J., 2001b. Methane-derived carbonates and authigenic pyrite from the northwestern Black Sea. Mar. Geol. 177, 129–150.

Pequegnat, W.E., Jeffrey, L.M., 1979. Petroleum in deep benthic ecosystems of the Gulf of Mexico and Caribbean Sea. Contributions in Marine Science 22, 63–75.

Peters, K.E., Cassa, M.R., 1994. Applied Source Rock Geochemistry: Chapter 5: Part II. Essential Elements, 93–120.

Petersen, H.I., Schovsbo, N.H., Nielsen, A.T., 2013. Reflectance measurements of zooclasts and solid bitumen in Lower Paleozoic shales, southern Scandinavia: correlation to vitrinite reflectance. International Journal of Coal Geology 114, 1–18.

Pindell, J.L., 1985. Alleghenian reconstruction and subsequent evolution of the Gulf of Mexico, Bahamas, and Proto-Caribbean. Tectonics 4, 1–39.

Plummer, L.N., Wigley, T.M.L., Parkhurst, D.L., 1978. The kinetics of calcite dissolution in CO_2-water systems at 5 degrees to 60 degrees C and 0.0 to 1.0 atm CO_2. American Journal of Science 278, 179–216.

Pourret, O., Davranche, M., Gruau, G., Dia, A., 2008. New insights into cerium anomalies in organic-rich alkaline waters. Chemical Geology 251, 120–127.

Quirke, J.M.E., Eglinton, G., Maxwell, J.R., 1979.. Petroporphyrins. 1. Preliminary characterization of the porphyrins of gilsonite. Journal of the American Chemical Society 101, 7693–7697.

Rabus, R., Fukui, M., Wilkes, H., Widdel, F., 1996. Degradative capacities and 16S rRNA-targeted whole-cell hybridization of sulfate-reducing bacteria in an anaerobic enrichment culture utilizing alkylbenzenes from crude oil. Applied and Environmental Microbiology 62, 3605–3613.

Rabus, R., Nordhaus, R., Ludwig, W., Widdel, F., 1993. Complete oxidation of toluene under strictly anoxic conditions by a new sulfate-reducing bacterium. Applied and Environmental Microbiology 59, 1444–1451.

Reitner, J., Peckmann, J., Blumenberg, M., Michaelis, W., Reimer, A., Thiel, V., 2005. Concretionary methane-seep carbonates and associated microbial communities in Black Sea sediments. Palaeogeography, Palaeoclimatology, Palaeoecology 227, 18–30.

Ricard, E., Pécheyran, C., Ortega, G.S., Prinzhofer, A., Donard, O.F., 2011. Direct analysis of trace elements in crude oils by high-repetition-rate femtosecond laser ablation coupled to ICPMS detection. Analytical and Bioanalytical Chemistry 399, 2153–2165.

Ritger, S., Carson, B., Suess, E., 1987. Methane-derived authigenic carbonates formed by subduction-induced pore-water expulsion along the Oregon/Washington margin. Bulletin of the Geological Society of America 98, 147–156.

Roberts, H., 2001. Fluid and gas expulsion on the northern Gulf of Mexico continental slope: mud-prone to mineral-prone responses. In: Paull, C.K., Dillon, W.P., (Eds.), Natural Gas Hydrates: Occurrence, Distribution, and Detection. American Geophysical Union, Washington DC, USA, 145–161.

Roberts, H.H., Aharon, P., 1994. Hydrocarbon-derived carbonate buildups of the northern Gulf of Mexico continental slope – a review of submersible investigations. Geo-Marine Letters 14, 135–148.

Roberts, H.H., Feng, D., Joye, S.B., 2010. Cold-seep carbonates of the middle and lower continental slope, northern Gulf of Mexico. Deep-Sea Research II 57, 2040–2054.

Roberts, S., Tricker, P. M., Marshall, J. E. A., 1995. Raman spectroscopy of chitinozoans as a maturation indicator. Organic Geochemistry 23, 223–228.

Rockne, K.J., Strand, S.E., 1998. Biodegradation of bicyclic and polycyclic aromatic hydrocarbons in anaerobic enrichments. Environmental Science and Technology 32, 3962–3967.

Rongemaille, E., Bayon, G., Pierre, C., Bollinger, C., Chu, N.C., Fouquet, Y., Riboulot, V., Voisset, M., 2011. Rare earth elements in cold seep carbonates from the Niger delta. Chemical Geology 286, 196–206.

Rothermich, M.M., Hayes, L.A., Lovely, D.R., 2002. Anaerobic, sulfate-dependent degradation of polycyclic aromatic hydrocarbons in petroleum-contaminated harbor sediments. Environmental Science and Technology 36, 4811–4817.

Rubin-Blum, M., Antony, C. P., Borowski, C., Sayavedra, L., Pape, T., Sahling, H., Bohrmann, G., Kleiner, M., Redmond, M.C., Valentine, D.L., Dubilier, N., 2017. Short-chain alkanes fuel mussel and sponge *Cycloclasticus* symbionts from deep-sea gas and oil seeps. Nature Microbiology 2, 17093, DOI: 10.1038/nmicrobiol.2017.93.

Sahling, H., Bohrmann, G., 2016. Natural hydrocarbon seepage in the southern Gulf of Mexico – Cruise No. M114 – February 12 – March 28, 2015 – Kingston (Jamaica) – Kingston (Jamaica). METEOR-Berichte, M114, 52 pp., DFG-Senatskommission für Ozeanographie, DOI:10.2312/cr_m114.

Sahling, H., Rickert, D., Lee, R.W., Linke, P., Suess, E., 2002. Macrofaunal community structure and sulfide flux at gas hydrate deposits from the Cascadia convergent margin, NE Pacific. Marine Ecology Progress Series 231, 121-138.

Sahling, H., Rubin Blum, M., Borowski, C., Escobar-Briones, E., Gaytán Caballero, A., Hsu, C.-W., Loher, M., MacDonald, I.M., Marcon, Y., Pape, T., Römer, M., Schubotz, F., Smrzka, D., Wegener, G., Bohrmann, G., 2016. Massive asphalt deposits, oil seepage, and gas venting support abundant chemosynthetic communities at the Campeche Knolls, southern Gulf of Mexico. Biogeosciences 13, 4491–4512.

Salvador, A., 1987. Late Triassic–Jurassic paleogeography and origin of Gulf of Mexico basin. American Association of Petroleum Geologists Bulletin 71, 419–451.

Salvador, A., 1991. The Gulf of Mexico Basin. The Geology of Northern America. Geological Society of America, 131–180.

Sassen, R., Brooks, J.M., Kennicutt III, M.C., MacDonald, I.R., Guinasso Jr., N.L., 1993. How oil seeps, discoveries relate in deepwater Gulf of Mexico. Oil & Gas Journal 91, 64–69.

Sassen, R., Roberts, H.H., Carney, R., Milkov, A.V., DeFreitas, D.A., Lanoil, B., Zhang, C., 2004. Free hydrocarbon gas, gas hydrate, and authigenic minerals in chemosynthetic communities of the northern Gulf of Mexico continental slope: relation to microbial processes. Chemical Geology 205, 195–217.

Savard, M.M., Beauchamp, B., Veizer, J., 1996. Significance of aragonite cements around Cretaceous marine methane seeps. J. Sed. Res. 66, 430–438.

Schoenherr, J., Littke, R., Urai, J.L., Kukla, P.A., Rawahi, Z., 2007. Polyphase thermal evolution in the Infra-Cambrian Ara Group (South Oman Salt Basin) as deduced by maturity of solid reservoir bitumen. Organic Geochemistry 38, 1293–1318.

Schopf, J.W., Kudryavtsev, A.B., Agresti, D.G., Wdowiak, T.J., Czaja, A.D., 2002. Laser–Raman imagery of Earth's earliest fossils. Nature 416, 73–76.

Schubotz, F., Lipp, J.S., Elvert, M., Kasten, S., Mollar, X.P., Zabel, M., Bohrmann, G., Hinrichs, K.U., 2011a. Petroleum degradation and associated microbial signatures at the Chapopote asphalt volcano, Southern Gulf of Mexico. Geochimica et Cosmochimica Acta 75, 4377–4398.

Schubotz, F., Lipp, J.S., Elvert, M., Hinrichs, K.-U., 2011b. Stable carbon isotopic compositions of intact polar lipids reveal complex carbon flow patterns among hydrocarbon degrading microbial communities at the Chapopote asphalt volcano. Geochimica et Cosmochimica Acta 75, 4399–4415.

Schumacher, D., 1996. Hydrocarbon-induced alteration of soils and sediments. In: Schumacher, D., Armans, M.A., (eds.), Hydrocarbon migration and its near-surface expression, American Association of Petroleum Geologists Menoir 66, 71–89.

Schwarz, G., Mendel, R.R., Ribbe, M. ., 2009. Molybdenum cofactors, enzymes and pathways. Nature 460, 839–847.

Sibuet, M., Olu, K., 1998. Biogeography, biodiversity and fluid dependence of deep-sea cold-seep communities at active and passive margins. Deep-Sea Research II 45, 517–567.

Smrzka, D., Zwicker, J., Klügel, A., Monien, P., Bach, W., Bohrmann, G., Peckmann, J., 2016. Establishing criteria to distinguish oil-seep from methane-seep carbonates. Geology 44, 667–670.

So, C.M., Young, L.Y., 1999. Isolation and characterization of a sulfate-reducing bacterium that anaerobically degrades alkanes. Applied and Environmental Microbiology 65, 2969–2976.

Sohl, N.F., Martinez, E.R., Salmeron-Urena, P., Soto-Jaramillo, F., 1991. The Gulf of Mexico Basin. The Geology of Northern America. Geological Society of America,205–244.

Spackman, W., 1958. The maceral concept and the study of modern environments as a means of understanding the nature of coal. Trans. N. Y. Acad. Sci. Series II 20, 411–423.

Stach, E., Mackowsky, M.-T., Teichmüller, M., Taylor, G.H., Chandra, D., Teichmüller, R., 1982. Stach's Textbook of Coal Petrology, third Revised and Enlarged Edition. Berlin- Stuttgart, Gebrüder Borntraeger, 535 p.

Suarez-Ruiz, I., Flores, D., Mendonca Filho, J.G., Hackley, P.C., 2012. Review and update of the applications of organic petrology: Part 1, geological applications. International Journal of Coal Geology 99, 54–112.

Suess, E., Torres, M.E., Bohrmann, G., Collier, R.W., Greinert, J., Linke, P., Rehder, G., Trehu, A., Wallmann, K., Winckler, G., Zuleger, E., 1999. Gas hydrate destabilization: enhanced dewatering, benthic material turnover and large methane plumes at the Cascadia convergent margin. Earth and Planetary Science Letters 170, 1–15.

Sugihara, J.M., McGee, L.R., 1957. Porphyrins in Gilsonite. The Journal of Organic Chemistry 22, 795–798.

Tang, J., Johannesson, K.H., 2003. Speciation of rare earth elements in natural terrestrial waters: Assessing the role of dissolved organic matter from the modeling approach. Geochimica et Cosmochimica Acta 67, 2321–2339.

Tang, Y.J., Carpenter, S., Deming, J., Krieger-Brockett, B., 2005. Controlled release of nitrate and sulfate to enhance anaerobic bioremediation of phenanthrene in marine sediments. Environmental Science and Technology 39, 3368–3373.

Taylor, S.R., McLennan, S.M., 1985. The Continental Crust: Its composition and evolution. Blackwell, Malden, Mass.

Teichert, B.M., Bohrmann, G., Suess, E., 2005. Chemoherms on Hydrate Ridge—unique microbially-mediated carbonate build-ups growing into the water column. Palaeogeography, Palaeoclimatology, Palaeoecology, 227, 67–85.

Treibs, A., 1934. Chlorophyll und Häminderivate in bituminösen Gesteinen, Erdölen, Erdwachsen und Asphalten. Annalen der Chemie 510, 42–62.

Treibs, A., 1936. Chlorophyll und Häminderivate in organischen Mineralstoffen. Angewandte Chemie 49, 682–686.

Treude, T., Orphan, V., Knittel, K., Gieseke, A., House, C.H., Boetius, A., 2007. Consumption of methane and CO_2 by methanotrophic microbial mats from gas seeps of the anoxic Black Sea. Applied and Environmental Microbiology 73, 2271–2283.

Tuinstra, F., Koenig, J.L., 1970. Raman spectrum of graphite. The Journal of Chemical Physics 53, 1126–1130.

van Dover, C.L., Aharon, P., Bernhard, J.M., Caylor, E., Doerries, M., Flickinger, W., Gilhooly, W., Goffredi, S.K., Knick, K.E., Macko, S.A., Rapoport, S., Raulfs, E.C., Ruppel, C., Salerno, J.L., Seitz, R.D., Sen Gupta, B.K., Shank, T., Turnipseed, M., Vrijenhoek, R., 2003. Blake Ridge methane seeps: characterization of a soft-sediment, chemosynthetically based ecosystem. Deep Sea Research I 50, 281–300.

van Krevelen, D.W., 1993. Coal: Typology, Physics, Chemistry, Constitution. third ed. Elsevier, Amsterdam, 979 p.

Walkner, C., Gratzer, R., Meisel, T., Bokhari, S.N.H., 2017. Multi-element analysis of crude oils using ICP-QQQ-MS. Organic Geochemistry, 103, 22–30.

Wallmann, K., Drews, M., Aloisi, G., Bohrmann, G., 2006. Methane discharge into the Black Sea and the global ocean via fluid flow through submarine mud volcanoes. Earth and Planetary Science Letters 248, 545–560.

Watkins, J.S., Ladd, J.W., Buffler, R.T., Shaub, F.J., Houston, M.H., Worzel, J.L., 1978. Occurrence and evolution of salt in deep Gulf of Mexico. In: Framework, Facies and Oil-Trapping Characteristics of the Upper Continental Margin, Bouma, A.H., Moore, G.T., Coleman, J.M., (Eds.), American Association of Petroleum Geologists Bulletin 7, 43– 65.

Watkins, J.S., Macrae, G., 1995. Bipolar simple-shear rifting responsible for distribution of mega-salt basins in Gulf of Mexico? In: Travis, C.J., et al. (Eds.), Gulf Coast Section SEPM Foundation Sixteenth Annual Research Conference, Program with Papers, 297–305.

Weinrebe, W., Bohrmann, G., Spiess, V., 2010. Fluid Seepage of Chile and in the Southern Gulf of Mexico – Cruise No. M67 – February 20 – April 25, 2006 – Talcahuano (Chile) – Bridgetown (Barbados). METEOR-Berichte, M67, 110 pp, DFG-Senatskommission für Ozeanographie, DOI:10.2312/cr_m67.

Whiticar, M J., 1999. Carbon and hydrogen isotope systematics of bacterial formation and oxidation of methane. Chemical Geology 161, 291–314.

Widdel, F., Rabus, R., 2001. Anaerobic biodegradation of saturated and aromatic hydrocarbons. Current Opinion in Biotechnology 12, 259–276.

Wilson, J.L., Ward, W.C., 1993. Early Cretaceous carbonate platforms of Northeastern and East-Central Mexico. In: Simo, T., Scott, R.W., Masse, J.-P. (Eds.), Cretaceous Carbonate Platforms. American Association of Petroleum Geologists Bulletin Memoir 56, 35–49.

Winters, Y.D., Lowenstein, T.K., Timofeeff, M.N., 2011. Identification of carotenoids in ancient salt from Death Valley, Saline Valley and Searles Lake, California, using laser Raman spectroscopy. Astrobiology 13, 1065–1080.

Wopenka, B., Pasteris, J.D., 1993. Structural characterization of kerogens to granulite-facies graphite: applicability of Raman microprobe spectroscopy. American Mineralogist 78, 533–557.

Wright, J., Schrader, H., Holser, W.T., 1987. Paleoredox variations in ancient oceans recorded by rare earth elements in fossil apatite. Geochimica et Cosmochimica Acta 51, 631–644.

Yen, 1975. Role of Trace Metals in Petroleum. Ann Arbor Science Publishers, 221 p.

Yui, T.F., Huang, E., Xu, J., 1996. Raman spectrum of carbonaceous material: a possible metamorphic grade indicator for low-grade metamorphic rocks. Journal of Metamorphic Geology 14, 115–124.

Zaki, N.S., Barbooti, M.M., Baha-Uddin, S.S., Hassan, E.B., 1989. Determination of trace metals and their distribution in heavy crude oil distillates (350°C+) by atomic absorption spectrophotometry. Applied Spectroscopy 43, 1257–1259.

Zeng, Y., Wu, C., 2007. Raman and infrared spectroscopic study of kerogen treated at elevated temperatures and pressures. Fuel 86, 1192–1200.

Zhang, X., Young, L.Y., 1997. Carboxylation as an initial reaction in the anaerobic metabolism of naphthalene and phenanthrene by sulfidogenic consortia. Applied and Environmental Microbiology 63, 4759–4764.

Zhang, C.L., Pancost, R.D., Sassen, R., Qian, Y., Macko, S.A., 2003. Archaeal lipid biomarkers and isotopic evidence of anaerobic methane oxidation associated with gas hydrates in the Gulf of Mexico. Organic Geochemistry 34, 827–836.

Zhou, Q., Xiao, X., Pan, L., Tian, H., 2014. The relationship between micro-Raman spectral parameters and reflectance of solid bitumen. International Journal of Coal Geology 121, 19–25.

Manuscript 3

Trace and rare earth elements in marine authigenic carbonates – Potentials, limitations, and perspectives

D. Smrzka [a], D. Feng [b], T. Himmler [c], J. Zwicker [a], Y. Hu, D. Chen [d], W. Bach[c], J. Peckmann [a,e]

[a] *Department of Geodynamics and Sedimentology, University of Vienna, 1090 Vienna, Austria*

[b] *Key Laboratory of Marginal Sea Geology, South China Sea Institute of Oceanology, Chinese Academy of Sciences, Guangzhou 510301, China*

[c] *MARUM — Center for Marine and Environmental Sciences and Department of Geosciences, University of Bremen, 28334 Bremen, Germany*

[d] *Shanghai Engineering Research Center of Hadal Science and Technology, College of Marine Sciences, Shanghai Ocean University, Shanghai 201306, China*

[e] *Institute of Geology, University of Hamburg, 20146 Hamburg, Germany*

Manuscript in preparation for submission to *Earth Science Reviews*

Abstract

Trace and rare earth elements are present in varying concentrations in the modern ocean, and many of them are essential for marine life. Many of these elements are actively cycled in seawater and deposited on the seafloor where they can become enriched in marine sediments depending on local hydrography, redox conditions, and biological activity. Trace and rare earth metals are increasingly used for paleoenvironmental analysis in the Earth Sciences, and frequently analyzed repositories for these

elements include banded and granular iron formations, and organic carbon-rich black shales. Marine carbonates are the most widespread deposits that contain appreciable amounts of these elements today, and have successfully yielded information on past and present Earth surface conditions and processes from the Neoproterozoic to the Phanerozoic up to the present. It is well established that carbonate minerals including calcite, aragonite, and dolomite readily adsorb and incorporate trace and rare earth metals during precipitation. Although experimental results have not always yielded unambiguous results, laboratory studies on carbonate precipitation and dissolution in the presence of dissolved trace metals have generally confirmed the strong tendency of carbonate minerals to accumulate and retain trace metals, making them attractive sources for information on biogeochemical processes through geologic time. Nonetheless, drawbacks of using the elemental chemistry of marine carbonates as paleoproxies exist due to recrystallization or dissolution during early diagenesis and later burial. These processes can affect trace metal concentration in marine carbonates, possibly leading to alteration or even a complete loss of their original elemental composition. Assessing the degree and effect of post-depositional alteration of marine carbonates is challenging, yet not unattainable, and can be archived by comparing and combining element ratios, stable isotopes, thin section petrography, and lipid biomarkers. Apart from marine carbonates, whose carbon source stems primarily from seawater or from the remains of shelly macrofauna, authigenic hydrocarbon seepage-derived carbonates in seafloor sediments are the direct product of anaerobic microbial mineralization of methane. These carbonates only form due to the presence of active microbial communities mediating the anaerobic oxidation of methane and hydrocarbons in the subseafloor. As such, methane-seep carbonates are exceptional archives whose trace and rare earth element content can yield surprisingly detailed information on biogeochemical processes including Fe and Mn-reduction, sulfate reduction, and methanogenesis, as well as information on seepage intensity and magnitude and extent of fluid flux. Trace and rare earth elements in authigenic carbonates serve as excellent proxies in these highly dynamic environments shaped by physical fluid seepage and biological chemosynthesis, and can record both aspects in an equally reliable manner. We attempt to synthesize all aspects of this review into a comprehensive study covering trace metal cycling, incorporation into carbonate, postdepositional diagenetic processes, and the potentials and limitations of these deposits as tracers for past environmental processes.

Introduction and scope

Trace metals in the ocean have been a subject of research for decades, and a large body of work has accumulated over the years on this topic. Trace metal input to the oceans originates from multiple sources that include seafloor and shelf sediments, hydrothermal vents, rivers, and wind-derived particles (Martin et al., 1976; Martin and Whitfield, 1983; Duce et al., 1991; Metz and Trefry, 2000). Trace metals that are deposited on the seafloor and become enriched in seafloor sediments may be ultimately derived from the same sources including seawater itself. Trace metals are removed from oxic seawater by inorganic reactions that involve oxide minerals. Similarly, the REEs are adsorbed by oxide phases not only in oxic, but even in denitrifying conditions, and returned to solution via reductive dissolution of the host oxides at lower Eh. Not all trace metals are enriched to the same degree under similar conditions, and, redox conditions alone do not always control trace metal enrichment in sediments. As the main source of many trace metals to the sediments is seawater, the rate of trace metal enrichment can depend on bottom water renewal rates and residence time. The hydrography of the basin can, in certain cases, be the controlling factor for trace metal enrichment.

The first geologic materials that were analyzed for their trace metal content were crude oils, which were studied primarily for economic purposes (Karchmer and Gunn, 1952; Milner et al., 1952; Hodgson, 1954; Gamble and Jones, 1955). Several years later, organic-rich shales became the first ancient marine deposits whose enrichments of trace metals were analyzed systematically and interpreted within the framework of geochemistry, paleoceanography and paleoclimate (Tourtelot 1956, Le Riche, 1959; Swanson and Swanson, 1961; Calvert and Price, 1970; Vine and Tourtelout, 1970; Holland, 1979; Brumsack, 1986). The fact that many trace metals are redox sensitive, and that redox conditions are the driving force of trace metal accumulation in sediments has led to a large amount of studies using trace metals as proxies for ancient environments as far back as the Archean, and are meanwhile applied in almost all modern and ancient geologic materials (Algeo and Rowe, 2012; Robbins et al., 2016 and references therein). In particular, the recognition of the importance of biological cycling of trace metals in the oceans has greatly influenced our perception on how these elements behave in shallow and deep waters, and how they are distributed and transported from the photic zone to the seafloor (Sunda, 1989; Bruland et al., 1991; Morel et al., 1991; Morel and Price, 2003). As almost all trace metals participate in

biological cycling in the water column, the utility of trace metals in tracing water column processes such as upwelling, primary production, and organic matter export to the seafloor has received ever increasing attention.

The most reliable and widely used archives for trace metals, especially for the Archean and the Proterozoic, include iron formations, black shales, cherts, and sedimentary pyrite (Poulton et al., 2004a; Malvia et al., 2005; Scott et al., 2008; Large et al., 2014). However, the largest and most widely distributed geological repositories for trace metals in the Neoproterozoic, and certainly in the Phanerozoic, are marine carbonates, which are highly prone to accumulate these elements at Earth surface conditions. They have proven useful in yielding information on the evolution of Earth surface conditions through geologic time as they archive global and regional events including glaciation, the expansion of multicellular life, large-scale methane seepage, and the chemical evolution and oxygenation of the oceans (Hoffmann et al., 1998; Jabobsen and Kaufman, 1999; Jiang et al., 2003; Kah et al., 2004; Kasemann et al., 2005; Knauth and Kennedy, 2009). The first attempts to analyze marine carbonate deposits for trace element contents in terms of reconstructing ancient environments dates back to the 1960s, shortly after the first successful studies on marine black shales (Graf, 1962; Ingerson, 1962; Weber, 1964; Flügel and Wedepohl, 1967). In the following decades, trace metal geochemistry of carbonates has evolved into a standard procedure, especially since the continuous improvement of analytical techniques and instruments allowing more precise measurements (Chester and Hughes, 1967; Ohde et al., 1978; Tessier et al., 1979; Shen and Boyle, 1988; Perkins et al., 1991). One of the major drawbacks, however, in using carbonates as archives for past geochemical processes is their tendency for post-depositional alteration in the course of diagenesis and burial, which hampers their use as paleoenvironmental archives compared to iron formations or black shales (Derry, 2010; Grotzinger et al., 2011; Schrag et al., 2013).

One of the fundamental assumptions is that trace metals are incorporated into carbonate minerals in a known, or at least predictable, ratio, so as to allow for a reliable reconstruction of ancient environmental conditions. Most of these assumptions have been made based on the outcome of experimental work, in which mostly calcite is precipitated under controlled conditions while taking up and releasing trace metals to a solution of fixed composition in the process. With growing understanding of the behavior of trace metals in water and their incorporation into calcite from experimental studies, the analysis and interpretation of trace and rare earth metals in natural carbonates has become increasingly refined. In combination with other geochemical proxies including stable isotope geochemistry or lipid

biomarkers, more information on past geologic processes can be derived from the combination of these methods than by any one method alone. Moreover, the quality of data is being improved increasingly due to continuous developments in measurement technology and accuracy, as well as in the development of standard materials.

This review comes at a time where more is data and information on trace and rare earth metals in natural carbonates is produced than ever before. The vast amounts of literature on this subject calls for a current status summary of the potentials and limitations of trace element geochemistry in ancient and modern carbonates. In a sense, this review picks up where Tribovillard et al. (2006) left off over a decade earlier, in which they compiled a compact and highly readable overview on the uses of trace metals as paleoproxies. This review will omit some of the major metals involved in marine cycling such as Mg, Ca, Sr, Fe, and Mn, yet will focus more on trace metals that have not received as much attention as some of the more traditional trace metals. These metals include Ge, As, Sb, and Se, but also the rare earth elements, which are gaining increasing popularity from environmental geosciences to studies reconstructing ancient Earth. This review is an attempt to represent carbonate minerals as reliable, long-term repositories for trace and rare earth metals over geologic time.

This article provides a comprehensive source to sink overview, structured into four parts: (1) the behavior of trace and rare earth elements in seawater and marine sediments, (2) the incorporation of these elements into carbonates, (3) the applicability of trace metals in carbonates as traces for past and present biogeochemical processes, and (4) a detailed assessment on the element geochemistry of marine authigenic hydrocarbon-seepage derived carbonates. The emphasis lies on marine carbonates, specifically on seep carbonates, as these form in chemically and physically highly dynamic environments that cover all aspects of how redox-sensitive trace and rare earth metals can be put to use effectively.

Part 1: Trace and rare earth metals – From seawater to sediments and microbial cycling

Initiated by the pioneering work over half a century ago on the distribution of trace metals in seawater (Goldberg, 1954, 1957; Hitchcock and Starr, 1954; Krauskopf, 1956; Richards, 1956), the knowledge on the chemical composition of the ocean and its distribution of trace metals has grown immensely. With the early development of techniques for accurate determination of the concentration and speciation of trace metals in seawater (Fabricand et al., 1962; Lal et al., 1964; Burrell, 1967; Riley and Taylor, 1968), marine sediments (Hirst, 1962; Schutz and Turekian, 1965; Turekian and Imbrie, 1966; Bender and Schultz, 1968; Chester and Messiha-Hanna, 1970), and interstitial sedimentary pore waters (Brooks et al., 1968, 1970; Presley and Kaplan, 1968; Presley et al., 1972; Duchart et al., 1973) these data enabled a new perspective on yet largely unknown processes that proceed in marine sediments. It is not so much the aim to provide a complete compilation of all studies on the details of trace element geochemistry, but to offer an understanding of their behavior in order for us to use them as tracers of paleoprocesses. The first part of this review will give an overview on what is known on the physicochemical behavior on trace metals in seawater and marine pore waters, as well as assessing their relevance for biological cycling.

Molybdenum

Among the redox-sensitive trace metals, Mo is possibly the best studied of them all. The dominant Mo species in oxic seawater is molybdate, which is efficiently reduced and subsequently enriched in sediments in the presence of various dissolved sulfur species (Helz et al., 1996; Vorlicek et al., 2004; Helz et al., 2011). Molybdenum is primarily transferred from the water column to sediments via diffusion from seawater, and sorption onto Fe and Mn oxides (Zheng et al., 2000). Organic matter in particular acts as a potent agent for Mo enrichment in sediments, as it is itself a carrier phase of Mo and produces sulfide via its microbial decomposition (Piper and Perkins, 2004). Due to its close association with dissolved sulfides, molybdenum does not accumulate efficiently under denitrifying conditions. This distinguishes its behavior from other trace elements including Cd, Cr, V, Re, Zn and U, and has led to associate high Mo content in sediments to lower redox potentials and high sulfide concentrations (Algeo and Lyons, 2006).

Strongly euxinic water bodies in which molybdate is completely converted to tetramolybdate are the most potent environments for the accumulation of Mo in sediments (Neubert et al., 2008; Herrmann et al., 2012).

Like other trace metals Mo behavior in oxic water is controlled by coprecipitation and adsorption onto (oxy)hydroxide minerals, in particularly Mn-oxides (Algeo and Rowe, 2012; Scott and Lyons, 2012). The importance of Mn-oxides in cycling and temporary and permanent enrichments of Mo has been investigated in detail (Morford and Emerson, 1999; Gobeil, 2007; Scott and Lyons, 2012). Coprecipitaiton and adsorption renders Mn(oxy)hydroxides the single most important sink for Mo in oxic environments. Morford et al. (2005) noted concomitant increases in Mo and Mn concentrations in sediments, implying active cycling of Mo and Mn-oxides due to adsorption of the former to the latter. However, this co-cycling does not necessarily produce permanent Mo enrichments in sediments, which is why this relationship is not useful to decipher modes of Mo enrichment in geologic time. Permanent Mo storage is more strongly dependent on dissolved sulfide that produce thiomolybdates, which can sequester and store Mo efficiently over geologic timescales (Scott and Lyons, 2012). Molybdenum enrichment can therefore be linked directly to either sulfate-reducing sediments, or yield information on water mass chemistry and paleohydrography if correlated with other parameters such as Fe-content and TOC (cf. Algeo and Lyons, 2006). This makes Mo unique in its applicability to interpret ancient environments when combined with variations of TOC, Fe, or U content (Algeo and Tribovillard, 2009; Algeo and Rowe, 2012). Molybdenum removal occurs deeper in the sedimentary column than other trace metals such as U and Re (Morford and Emerson, 1999; Morford et al., 2009), and is typically enriched at lower redox potentials than these elements where its uptake rate is significantly faster than that of U (cf. Tribovillard et al., 2012). A second significant sink for Mo in anoxic marine sediments is pyrite, to which molybdate and thiomolybdate adsorb readily and form stable complexes that can be irreversibly retained by pyrite (Bostick et al., 2003).

Culture and field studies have shown that dissolved Mo can influence microbial metabolism. An early study by Bertine (1973) suggested that microbial molybdate reduction coupled to either nitrate or sulfate reduction might occur in anaerobic sediments. However, no concrete evidence for such metabolisms has yet been put forward. Canfield and Des Marais (1991) showed aerobic sulfate reduction to be inhibited by the presence of molybdate, as is the consumption of thiosulfate by chemolithoautotrophic bacteria (Visscher et al., 1992). On the other hand, molybdate seems to have little to no effect on the rates of Mn and U reduction (Burdige and Nealson, 1985; Finneran et al., 2002). Later

studies demonstrated a close coupling of Mo with sulfate-reducing bacteria (Tucker et al., 1997, 1998), where it functions as an important constituent for the synthesis of enzymes. Direct molybdate reduction has been inferred to account for selective Mo enrichment in black shales (Biswas et al., 2009). However, in marine sulfidic sediments where thiomolybdate species are abundant and lead to enrichment of Mo in sediments, higher Mo concentrations may render microbial cycling of Mo an unimportant mechanism due to its toxicity to microbes at elevated concentrations (cf. Lloyd, 2003).

Uranium

The most abundance U species in oxic seawater and intermediate to high pH are ternary, soluble U-Ca-Mg-carbonate complexes (Morford and Emerson, 1999; Endrizzi and Rao, 2014; Cumberland et al., 2016). Uranium transport from surface to bottom waters and to the sediment is controlled primarily by (1) redox conditions in the absence of oxygen, and (2) organic carbon flux rate (McManus et al., 2005, 2006). The main removal mechanism of U from seawater to sediments is diffusion, followed by biological or physicochemical reduction close to or at the sediment-water interface (Legeleux et al., 1994; Morford et al., 2009). It is preferably reduced under Eh conditions typical for the sediment-water interface, and accumulates most effectively in the upper few centimeters below the seafloor (cf. McManus et al., 2005; Morford et al., 2009). Physicochemical reduction of U(VI) proceeds very slowly in the absence of catalysts (Swarzenski et al., 1999). However, U reduction does occur abiotically when ferrous iron is concomitantly oxidized (Boland et al., 2014) and may be catalyzed by the specific adsorption of uranyl to ferrous iron at circumneutral pH (Liger et al., 1999). In the absence of complexing ligands, dissolved U can be passively occluded by Fe-oxide mineral coatings (Duff et al., 2002). Additional mobilization of U is induced by humic acids, and to lesser extent fulvic acids, which cause dissolution of reduced U in sediments (Luo and Guo, 2009).

Uranium enrichment occurs at different redox potentials than other redox-sensitive trace metals such as Mo, and is easily remobilized if sedimentary redox conditions fluctuate frequently from reducing to oxidizing and vice versa (Algeo and Maynard, 2008). Several studies have noted that U enrichment clearly occurs above the zone where sulfate reduction is favored, directly below the oxygen penetration depth (Crusius and Thomson, 2000). Zheng et al. (2002) argued that sediments dominated by sulfate reduction are as ineffective in accumulating authigenic U than sediments where Fe reduction dominates,

implying that U behavior is decoupled from dissolved sulfide (cf. Nameroff et al., 2002). Rosenthal et al. (1995) also noted U enrichment to occur only below the zone of Fe enrichment, and spread over a large depth interval in the sediment (see also Thomson et al., 1998). However, there is a general agreement that Fe and U accumulation occurs under similar conditions, due to the coupled cycling of these two elements (Morford and Emerson, 1999; Nameroff et al., 2002; Zheng et al., 2002). Although there is no known nutritional benefit of U for microbes, dissimilatory Fe reduction coupled to U(VI) is a viable catabolic energy source for microbial growth (Lovley et al., 1991).

The importance of Fe in physicochemical cycling of U is reflected by its equal relevance for microbiological U metabolisms. Both Fe and U reduction may co-occur in the presence of sulfate-reducing bacteria, and have indeed been linked to these and other microbial communities (Lovley et al., 1993; Swarzenski et al., 1999; Frederickson et al., 2000; Behrens and Van Cappellen, 2005). Laboratory studies have shown that U and sulfate reduction can both be performed by sulfate reducing bacteria, and proceed at different rates without influencing or inhibiting each other (Lovley and Phillips, 1992; Spear et al., 2000). Reduction of U by bacteria is not solely controlled by enzymatic catalysis by the bacteria themselves, but also by U speciation that determines its toxicity. Decreasing U reduction rates have been observed with increasing Ca and DIC concentrations, which are in turn dependent on pH of ambient waters that can significantly decrease microbial U reduction rates (Ulrich et al., 2011).

Cadmium, Nickel, Copper, and Zinc

The distribution of Cd in seawater is similar to that of phosphorus, and shows surface water depletion and deep water enrichment (Boyle et al., 1976). Cadmium has a particularly intimate relationship with U, as both elements are associated with particulate organic matter and are largely unaffected by dissolved sulfide in pore waters (Piper and Perkins, 2004). Its high concentration in phytoplankton and organic debris, and very low concentration in terrigenous material has rendered Cd a useful tracer for primary productivity and sedimentation rates (Gendron et al., 1996; Piper and Dean, 2002). Cadmium may form insoluble Cd-sulfide precipitates if sulfide is present (Jacobs et al., 1985; Rosenthal et al., 1995), and is not incorporated into pyrite as many other trace metals (Huerta-Diaz and Morse, 1992). Nevertheless, its rate of enrichment is not controlled by the extent of sulfide availability in pore waters (cf. Sundby et al., 2004). Marine sediments with very shallow oxygen penetration depths may

enrich both U and Cd, while excluding other trace metals such as Mn, V, and Mo (Morford and Emerson, 1999). In contrast to U, however, Cd is mostly concentrated in narrow intervals below the oxidation front, as oxidative remobilization affects U more strongly than Cd (Rosenthal et al., 1995; Gobeil et al., 1997). Moreover, Cd is primarily enriched in, and released to sediments by decomposing organic matter, whereby U is mainly sourced directly by diffusion from seawater (Nameroff et al., 2002).

Cadmium is highly toxic, and does not partake in active cycling by microorganisms as far as we know (e.g. Vig et al., 2003). Microbes can, however, passively enrich and release Cd via sorption and desorption (White and Gadd, 1998; Pagnanelli et al., 2010), yet it remains unknown to which degree this process is relevant for Cd cycling in marine sediments.

Nickel is an important micronutrient for phytoplankton growth in the surface ocean, and is liberated from sinking organic matter in the water column (Calvert and Pedersen, 1993; Dupont et al., 2010). Nickel is mostly co-enriched in anoxic sediments along with Cd, Co, Zn, and Cu, and incorporated into pyrite (Huerta-Diaz and Morse, 1992). However, Ni behavior in pore waters is distinct from most other trace metals in that it is largely unaffected by changing redox conditions, and cannot by itself identify the onset of sulfate reduction (Jacobs and Emerson, 1982; Jacobs et al., 1985). Nickel partakes in biological cycling as it is a key enzyme for methanogenic archaea that can potentially yield important information on present and past microbial methane cycling in the water column and marine sediments (Hausinger, 1997; Kida et al., 2001; Scheller et al., 2012).

Similarly to Ni, Cu also has significant importance as a nutrient for marine plankton and is a required constituent for several enzymes. Copper and Ni show similar behavior in anoxic sediments, in that they are both strongly complexed by dissolved organic matter, transferred as such to the sediments, released to pore waters by remineralization of organic matter, and subsequently incorporated into iron sulfides (Donat et al., 1994; Morse and Luther, 1999; Algeo and Maynard, 2004). Nonetheless, its high concentration in biogenic particles and strong enrichments above the terrigenous fraction makes Cu a useful tracer for organic carbon remineralization via denitrification and/or sulfate reduction (Widerlund, 1996; Piper and Perkins, 2004). The usefulness of Cu in tracing diagenetic processes has be attempted by combining Cu with other metals such as Mn, Cr, and V, but also with carbon content of sediments (Jung et al., 1996; Widerlund, 1996; Piper and Perkins, 2004).

Zinc is one the most important trace metals in biological cycling, particularly for eukaryotes, and shows a nutrient type profile in the modern oceans with distinct surface water depletion (Bruland, 1980;

Vallee and Auld, 1993; Zhao et al., 2014). Zinc is mostly co-enriched with Cu, Ni, and Cd in marine sediments. Similarly to Cu and Ni, Zn forms strong complexes with, and is concentrated in, organic matter (Bruland, 1989). Like Cd, it is not preferably incorporated into pyrite, and is released to pore waters primarily by remineralization of organic matter via aerobic or anaerobic metabolisms (Morse and Luther, 1999; Algeo and Maynard, 2004). Nickel and Zn have shown to be incorporated into Fe(II) solid products during bacterial Fe reduction, which may act as an additional sink of these metals (Cooper et al., 2000; Parmar et al., 2001).

Rhenium

Rhenium is one of the most potent and reliable tracers of anoxic conditions in the environment, and is strongly enriched in most marine sediments. This is due to its very low crustal concentrations, its sensitivity towards redox potential, and its high preservation potential during sedimentation and burial (Koide et al., 1986; Crusius et al., 1996; Morford and Emerson, 1999; Crusius and Thomson, 2002). Rhenium is supplied to the oceans primarily by rivers, and its behavior is conservative in seawater (Anbar et al., 1993; Colodner et al., 1993). Rhenium is neither scavenged in oxic waters by Fe or Mn(oxy)hydroxides nor by particulate organic matter, and its input to the sediment is primarily controlled by diffusion (Colodner et al., 1993). Recently, however, Helz and Dolor (2012) proposed Re coprecipitation onto Fe-Mo-S solid solution particles as an additional mechanism of Re delivery to sediments in euxinic basins. Rhenium has been employed in combination with other trace elements such as Cd, U and Mo to distinguish between oxic, suboxic, and anoxic conditions (Crusius et al., 1996; Russell and Morford, 2001; Nameroff et al., 2002). Rhenium enrichment is greater in reducing sediments than most other trace metals. Its behavior at the sediment-water interface is similar to that of U, and it is not incorporated into pyrite in sulfate reducing conditions like Mo (Koide et al., 1987; Crusius and Thomson, 2000). In contrast to Mo, Re content is rarely significant in pyrite, and is instead typically enriched in organic matter (Ravizza et al., 1991; Selby and Creasar, 2003). In its insensitivity towards dissolved sulfide and sedimentation rates, Re shows some similarities to Cd. Sundby et al. (2004) argued that very slow reaction kinetics are a key to understanding accumulation rates and distribution of both Cd and Re. Rhenium is most sensitive towards Eh, suggesting that its removal occurs at shallower sediment depths than most trace metals (Morford et al., 2005).

Although experimental results have shown that active microbial cycling of Re is unlikely (Dolor et al., 2009), microbial remineralization of organic material in sediments may release and mobilize Re in sulfidic sediments (cf. Helz and Adelson, 2013).

Vanadium

Vanadium is an essential nutrient for phytoplankton in the surface ocean, as it forms the metal centers of numerous enzymes necessary for metabolic processes (Nalewajko et al., 1995; Moore et al., 1996). As V exists in three possible oxidation states it is of particular interest to geochemists, as it can be used to trace biogeochemical processes in the water column and sediments (Wanty and Goldhaber, 1992). Like for many other trace metals, V speciation depends on pH and redox conditions. In the surface ocean V is mostly present as vanadate (Calvert and Pedersen, 1993). Vanadium is depleted in the photic zone compared to deeper waters, which confirms its important role in biological cycling in the ocean (Collier, 1984). Apart from biological uptake, physicochemical processes such as sorption and scavenging by particles have been observed to control the distribution of V in oxygenated waters. Vanadium is associated with both Fe and Mn oxide particles, and all three elements correlate well in various marine environments (e.g. Rudnicki and Elderfield, 1993; Auger et al., 1999). Vanadium adsorption onto sinking particles followed by diffusion is the most important process that delivers V to marine sediments (Trefry and Metz, 1989; Prange and Kremling, 1985; Brumsack, 1986). Several studies have confirmed a strong enrichment of V in reducing sediments (Emerson and Huested, 1991; Thomson et al., 1998). Oxidized V(V) and V(IV) species are efficiently reduced to V(III) in the presence of free hydrogen sulfide, and can subsequently precipitate as insoluble V-precipitates (Wanty and Goldhaber, 1992).

Due to its strong relationship with hydrogen sulfide, V enrichments are often reported in turn with Mo enrichments, and both elements are often co-enriched in anoxic sediments. Nonetheless, there are some differences in their behavior. Vanadium enrichment has been reported in carbonaceous marine shales, where its origin has been attributed to the presence and dissolution of V-porphyrins, and chlorophyll pigments (Premovic et al., 1986). There is a strong correlation between V and organic matter, which also forms strong complexes with V in solution (Breit and Wanty, 1991). An important factor is that unlike Mo, V accumulates preferably in the organic matter fraction of sediments, and not in sulfidic minerals such as pyrite (cf. Algeo and Maynard, 2004). These authors also suggested that V enrichment

occurs earlier than Mo enrichment in black shales, which renders V a useful indicator of past oxic-suboxic transitions that can record subtle changes in redox potential if used together with other trace metals. Vanadium has also been used in combination with Ni to assess levels of anoxia in black shales (Wenger and Baker, 1986), as well as to classify and distinguish the maturity and character of bitumen and other heavy hydrocarbons (Lewan and Maynard, 1982; Barwise, 1990).

Although various microorganisms are tolerant towards V, and have shown to reduce vanadate in culture experiments (Lyalikova and Yurkova, 1992; Carpentier et al., 2003), it is questionable if microbial V cycling plays a relevant role in marine sediments. However, it has been shown that archaeal methanogenesis may be in fact inhibited if V(V) is concomitantly reduced (Zhang et al., 2014).

Cobalt and Chromium

Cobalt forms stable inorganic complexes with chloride in oxic seawater, as well as organic complexes with organic particulate matter (Zhang et al., 1990; Vega and Van den Berg, 1997). It is used as a micronutrient for phytoplankton in seawater, and is associated and cycled primarily with Mn-oxides (Knauer et al., 1982; Johnson et al., 1988; Saito and Moffett, 2002; Stockdale et al., 2010). Cobalt forms insoluble sulfide phases in suboxic sediments and has been shown to correlate with phosphate, suggesting concomitant biological uptake of both elements (Saito et al., 2004). Moreover, Co can be incorporated into pyrite in low amounts, although its affinity for iron sulfides is lower than most other trace metals (Morse and Luther, 1999). Although biogeochemical cycling of Co plays an important role in the ocean (Bown et al., 2011), the use of Cobalt as a proxy for authigenic processes has been cautioned. The main reasons are its high mobility in anoxic sediments, and that its contribution to authigenic minerals in sediments is mainly derived from terrigenous particles (Kremling, 1983; Tribovillard et al., 2006). Chromium exists in aqueous solutions as Cr(VI) and Cr(III), whereby the latter forms strongly inert, stable, and highly insoluble complexes (Pettine et al., 1998a). Chromate can be reduced efficiently in aqueous solution by organic matter and dissolved Fe, as well as an increase in pH (Buerge and Hug, 1997; Pettine et al., 1998a; Schlautman and Han, 2001). In sulfidic pore waters Cr reduction is additionally catalyzed in the presence of Cu, Cd, and Zn, which form ion pairs with chromate that are reduced more effectively (Pettine et al., 1998b). In contrast to most trace metals Cr does not co-precipitate with Fe sulfides due to its very slow reaction with dissolved sulfides (Morse and Luther, 1999).

Microbial Cr reduction is a relevant process in remediation strategies, yet it does not play an important role in Cr cycling in pristine marine sediments (Lovley, 1993; Lloyd, 2003 and references therein). Similar to Co, most of the Cr in sediments is associated with the terrigenous alumosilicate fraction, and its use in interpreting authigenic and biological processes in marine sediments is therefore limited (Brumsack, 1989; Tribovillard et al., 2006).

Arsenic, Antimony, and Selenium

Arsenic is used and cycled as a micronutrient by phytoplankton in ocean surface waters (Andreae and Froelich, 1984: Middelburg et al., 1988), although its toxicity towards marine life is well documented (Maher and Butler, 1988). Arsenate and arsenite are the two most common species in oxic and anoxic waters, respectively (Andreae, 1979; Brannon and Patrick, 1987), whereby redox potential and pH are the two main parameters governing speciation (Smedley and Kinniburgh, 2002). Soluble arsenic sulfur complexes are key species in controlling redox reactions between arsenite and arsenate in sulfidic waters (Wilkin et al., 2003). Stauder et al. (2005) demonstrated the oxidation of As(III) to As(V) and elemental As, attributing these observations to the high affinity of As(III) to the presence of sulfur. Thioarsenic species possibly participate in adsorption and redox reactions in marine sediments, and can even control the behavior of other trace metals. Clarke and Helz (2000) suggested that even very low concentrations of As may control Cu behavior in sulfidic sediments, where stable Cu-As-S complexes determine bioavailability and mobility of Cu. Apart from its interaction with sulfur species, As behavior is influenced by Fe and Mn (oxy)hydroxides in oxic waters, as well as by Fe sulfides in reducing waters. The most important process governing the first relationship is physical sorption of As onto oxides, which is strongly dependent on As speciation, pH, and redox potential (Edenborn et al., 1986; Belzile, 1988). Iron oxides may be the most important carrier phase for As from the water column to pore waters, as particulate As is only very weakly bound to sinking organic detritus (Andreae, 1979; Sullivan and Aller, 1996). Both arsenate and arsenite have a high sorption affinity for Mn and Fe-(oxy)hydroxides, whereby arsenite sorbs more strongly at high As concentrations and vice versa (Pierce and Moore, 1982; Peterson and Carpenter, 1986). Arsenic is actively cycled near or at the zone of Fe-reduction close to the sediment-water interface (Edenborn et al., 1986; Widerlund and Ingri, 1995; Chaillou et al., 2003), where its behavior is mimics that of phosphorus (cf. Mucci et al., 2000). Apart from oxide minerals, natural organic

matter can act as a potent mobilizer of reduced arsenite in sedimentary pore waters (Redman et al., 2002). Iron sulfide minerals such as pyrite and arsenopyrite are considered the most effective long-term sinks for As in sulfidic sediments due to the high affinity of As towards dissolved sulfide (Belzile and Lebel, 1986; Moore et al., 1988; Vink, 1996; Morse and Luther, 1999).

The importance microbes for the distribution and cycling of As has only been documented comparably recently (see Stolz et al., 2006 for a review). Respiration of arsenate in oxic waters can liberate As from Fe-oxide minerals; a process that has also been confirmed for anaerobic, saline environments (Zobrist et al., 2000; Oremland et al., 2005).

Antimony occurs either as Sb(V) in oxic waters, or as Sb(III) in anoxic waters (Filella et al., 2002a), although its true speciation in anoxic waters is still unclear. Both Sb(V) and Sb(III) exist in oxic and anoxic solutions to significant amounts (Bertine and Lee, 1983; Cutter, 1991). Oxidation of Sb(III) to Sb(V) is thought to occur rather slow in oxic waters, but can be catalyzed by bacteria (Bertine and Lee, 1983). Antimony is removed from surface waters mainly via particulate scavenging by Fe oxides (Andreae and Froelich, 1984; Cutter and Cutter, 1998), as it has no known nutritional benefit for any living organism (Filella et al., 2009). Therefore, the primary pathway which transfers Sb from the water column to sediments is through physicochemical adsorption onto Fe and Mn oxides (Belzile et al., 2001; Filella et al., 2002b; Leuz et al., 2006). The behavior of Sb in anoxic waters is less well known. However, it is relatively certain that Sb is immobilized in alkaline, reducing, sulfide-rich solutions where it forms insoluble thiocomplexes (Bertine and Lee, 1983; Andreae and Froelich, 1984). Antimony removal possibly occurs relatively close to the redox boundary by adsorption onto Mn and Fe (oxy)hydroxides (Spencer et al., 1993; Chaillou et al., 2008), and can be immobilized by Fe-sulfides during diagenesis slightly above the zone of U accumulation (Thomson et al., 1993, 1998). Experimental work has confirmed that Sb-sulfur compounds are highly stable under strongly alkaline, sulfidic pore waters, and that Sb solubility may be controlled by Fe sulfide minerals (Chen et al., 2003). Apart from sulfides, organic matter may play an important role in Sb mobility and cycling in anoxic marine sediments. Crecelius et al. (1975) suggested that up to 10% of naturally occurring, sedimentary Sb and As could be bound to organic matter, and later experimental work has shown that even this value is most likely an underestimation (e.g. Buschmann and Sigg, 2004; Tella and Pokrosvki, 2009).

Microbiological volatilization and methylation of Sb are known to occur (Bentley and Chasteen, 2002), and combined Sb and As oxidation have been observed in aerobic algae, confirming that the

structural similarities between these two elements influence their biogeochemical cycling (Lehr et al., 2007). However, there is to date no evidence for active microbial cycling in soils and terrestrial sediments, much less in marine sediments (Filella et al., 2007). In this respect, Sb differs strongly from As and Se, which both partake in active microbiological cycling. It can be concluded, with respect to what is known to date, that microbial metabolisms do not actively affect distribution and enrichment of Sb in marine sediments.

Selenium exists mostly as selenate Se(VI) or selenite Se(IV) in oxic waters, and as elemental Se or reduced selenide (II) in anoxic waters (Cutter, 1978, 1982). Selenate and selenite are considered to be highly soluble and mobile, whereas elemental Se and selenide are much less soluble (Seby et al., 2001). Selenium is required and taken up by phytoplankton in surface waters, and therefore shows a nutrient-like behavior in seawater (Measures and Burton, 1980; Hu et al., 1996). It is actively cycled in the photic zone, and transported to the seafloor as particulate organic selenide on sinking detritus (Cutter and Bruland, 1984). Physicochemical processes involving Se are highly dependent on its speciation. Selenate and selenite sorb efficiently onto Fe oxides, whereas only selenite adsorbs well onto hydroxyapatite (Monteil-Rivera et al., 2000; Rovira et al., 2008). Iron (oxy)hydroxides and phosphorus may therefore play important roles in Se cycling in marine sediments, as is the case for As (cf. Mucci et al., 2000; Duc et al., 2003). The relationship between Fe and Se cycling in marine sediments has been discussed by Thomson et al. (1995, 1998). These authors suggested the use of Se not only with Fe, but also with Iodine to pinpoint the location of the redox boundary and inferred Se accumulation either by organic selenide compounds, or through Se diffusion from bottom waters. It still remains unclear which phases constitute a long-term sink for Se in marine sediments. A likely candidate is pyrite, which can kinetically catalyze Se reduction to selenide and incorporate Se in suboxic sediments (Bruggeman et al., 2005).

Selenium plays an active role in bacterial cycling in a wide range of environments, from freshwater to hypersaline solutions (Stolz and Oremland, 1999). Anaerobic bacteria and archaea are capable of dissimilatory Se reduction combined with organic matter and/or H_2 oxidation, with and without sulfate (Stolz et al., 2006 and references therein). Selenate and selenite reduction is thought to occur at shallower depths than sulfate reduction, and that nitrate and Mn(IV) are the preferred electron acceptors (Oremland et al., 1989; Steinberg et al., 1992). Further, Zehr and Oremland (1987) showed that sulfate may even inhibit selenate reduction. If these microbial processes are of any relevance to Se cycling and/or enrichment in pristine marine sediments is unknown. Due to the variety of biological pathways in

which Se evidently participates it can be regarded as a trace element that has the potential as a tracer for chemical and biological processes in marine sediments. Together with As, Se chemistry of marine sediments requires more work to estimate the relevance of biological cycling for Se distribution and enrichment.

Germanium

Germanium is present in seawater as inorganic and organic methylated species. Although the latter are much more abundant than the former, inorganic species are more reactive and participate in physicochemical and biological processes (Lewis et al., 1989). Inorganic Ge distributions closely resemble those of Si: both elements are taken up by planktonic silicifying organisms, transferred, and subsequently released back to deeper waters and sediments at a constant ratio (Froelich and Andreae, 1981; Andreae and Froelich, 1984). Germanium is transported to sedimentary pore waters by sinking siliceous biogenic particles, mostly diatoms (McManus et al., 2003 and references therein). The correlation of Ge and Si in the water column is interrupted by decoupling of both elements during diagenesis (Hammond et al., 2000), possibly due to interference with Fe oxides and/or sulfide (cf. Murnane et al., 1989; McManus et al., 2003). King et al. (2000) suggested that Ge enrichment in reducing sediments is associated with authigenic Fe or U, slightly above the zone of Fe reduction. Tribovillard et al. (2011) compared Ge enrichment to Mo and U enrichment in several localities. They found that Ge enrichment in sediments only occurs alongside Mo and U enrichment, albeit to a much lower degree. Likely long-term sinks for Ge in marine sediments encompass clay minerals and inorganic particulates (El Wardani, 1958), or possibly iron sulfide phases such as pyrite (Murnane et al., 1989). Aside a few studies, not much is known on the behavior of Ge in marine sediments during early and late diagenesis.

Although experimental work has shown that Ge may be accumulated actively by certain bacteria strains under specific conditions (Chmielowski and Klapcinska, 1985; Van Dyke et al., 1989), it is likely that microbial cycling does not influence Ge distribution in marine sediments as it has no known nutritional function in microbial cycling in nature (Slawson et al., 1992).

Rare earth elements

General features and the practice of normalization

The rare earth elements (REEs) are a series of fifteen elements with atomics numbers 57 to 71 from La to Lu. They are often referred to as the lanthanides, a term that refers to the first element in the series, Lanthanum. The REEs have similar chemical properties, which is why they are mostly referred to as a group rather than by themselves. Their 4f electron shells are progressively filled from La through to Lu, with a concomitant decrease in ionic radius with increasing atomic number (Elderfield et al., 1988). All of the REEs are trivalent except for Ce and Eu, which can have multiple redox states. Sources of REEs to the modern oceans include rivers, seafloor hydrothermal vents, and atmospheric dust, whereby rivers constitute by far the largest source on a global scale (De Baar et al., 1985a; Greaves et al., 1994; Holser, 1997). The concentrations of REEs generally increase steadily from surface waters to deep waters, resembling the nutrient-like profiles of many trace metals (Bertram and Elderfield, 1993; German et al., 1995).

Although the REEs constitute a homogeneous series of elements, small systematic changes in behavior that progress from La to Lu cause inter-element concentration changes in aqueous and solid phases during physical and biological processes. These effects are referred to as fractionation, and makes the individual REEs and the series as a whole a powerful tool to trace biogeochemical processes and to reconstruct ancient environmental conditions. However, the REEs only disclose their full potential when normalized to a reference standard of choice. This practice allows an assessment of the deviation of the REE abundance in a given sample from a chosen standard. The natural abundance of REEs in all materials is governed by the Oddo-Harkins effect, which results from different nuclei stabilities with odd and even atomic numbers produced during nucleosynthesis (Schmitt et al., 1963). As a result, REEs in environmental samples show pronounced see-saw or herringbone-type distributions (Piper and Bau, 2013). Normalization of REEs in samples to a given standard eliminates this effect, and converts the herringbone distribution patterns to smooth curves that can be conveniently compared amongst each other. Although there are many standard reference materials in use, the most commonly used standard for normalizing REE concentrations in seawater and marine sediments is the Post Archaean Australian Shale (PAAS, McLennan, 2001). The composition of the source material for this standard consists of

weathered and recycled, terrigenous material derived from the continental crust and compiled in the literature (e.g. Wedepohl, 1971, 1995; Nance and Taylor, 1976; Taylor and McLennan, 1985). The coherent chemical behavior of the REE series is reflected in the similar abundance of the REEs in PAAS compared to further references materials that also represent felsic, siliciclastic source materials such as the World Shale Average (WSA), the Upper Continental Crust (UCC), and North American Shale Composite (NASC, Gromet et al., 1984; Rudnick and Gao, 2003).

Rare earth elements in seawater

As normalization allows for a convenient inter-element comparison of the REEs, the REE series has been categorized into three subgroups: the light, middle, and heavy REEs (LREEs, MREEs, and HREEs from hereon) according to their increasing atomic weight. Fractionation of the REEs in seawater occurs due to subtle differences in chemical properties, solution chemistry, and REE interactions between solution and particulate phases (Sholkovitz et al., 1994). All REEs are strongly complexed by ligands, and only a very small portion of total REEs is present as free ions in natural waters (Millero, 1992; Lee and Byrne, 1993). The stability of the REE complexes with potential ligands can be estimated using Pearson's rule (Pearson, 1963), which predicts that hard, covalent cations will interact with hard anions in solution to produce strong ionic bonds. The REEs are considered to be hard ions, whose hardness increases with increasing charge-to-radius ratios from La to Lu (Williams-Jones et al., 2012). In the modern oceans the major fraction of the dissolved REEs is present as carbonate complexes, which is the result of the high carbonate content of seawater (Sholkovitz et al., 1994). The complexation with carbonate ions increases systematically with decreasing ionic radius across the REE series, confirming Pearson's rule and producing a strong and characteristic fractionation in seawater (Cantrell and Byrne, 1987; Lee and Byrne, 1992).

Accurate determination of REEs in natural waters improved significantly with the advent of more sophisticated analytical techniques, as well as the development of abundance standards for trace and rare earth metals in the late 70s and 80s (Nance and Taylor, 1976; Potts et al., 1981; De Baar, 1983; Elderfield and Greaves, 1983; Greaves et al., 1988) It has since been well established that, on a global scale, the REE content in seawater increases significantly with depth, except for specific areas in the vicinity of rivers which are a substantial source of REEs to the surface ocean (Goldberg et al., 1963; Martin et al., 1976;

Elderfield et al., 1990; Sholkovitz et al., 1999; Yang and Haley, 2016). This pattern emerges due to preferential REE scavenging by organic and non-organic particles in the shallow ocean, and subsequent transport to the deep where the REEs are released by particle dissolution (Garcia-Solsona et al., 2014; Osborne et al., 2015; Zheng et al., 2016). The two dominant REE-carbonate complexes in seawater are [REE]CO3+ and [REE](CO3)2- species, whose distribution depends more strongly on pH than on REE atomic weight. Luo and Byrne (2004) showed that between a pH of 6 and 8 the [REE]CO3+ complex dominates REE speciation, and that the [REE](CO3)2- complex is dominant at a pH above 8. Less important compounds that complex REE ions in seawater include organic matter, oxalates, sulfates, phosphates, and silicic acid (Lee and Byrne, 1992; Shijf and Byrne, 2004; Akagi, 2013). The strong complexation of the HREEs by carbonate ligands in seawater results in a pronounced PAAS-normalized enrichment of HREEs over LREEs. As interactions between lanthanides and ligands are mostly ionic in character they are governed by Coulombs law, which predicts stability of complexes with the smaller HREE ions under Earth surface conditions. Hydroxides have a relatively weak preference for HREE, sulfate complexes have no major preference of either LREEs or HREEs, and carbonate complexes are strongly HREE selective in ambient seawater (cf. Lee and Byrne, 1992). However, the characteristic PAAS-normalized HREE-enriched pattern of seawater is not merely the result of complexation with carbonate and other ions, but from a constant competition between complexation and physical adsorption (Elderfield et al., 1988). Elderfield and Greaves (1982) suggested that LREEs are more efficiently removed by scavenging in surface waters than HREEs, and are thus less concentrated in seawater than the HREEs. More recent studies have corroborated this observation, arguing that HREEs are associated with hard particulates as opposed to the LREEs, which are more reactive towards particulate matter (Hathorne et al., 2015).

Scavenging by Fe and Mn(oxy)hydroxides is a major process that selectively fractionates REEs in the modern ocean (Klinkhammer et al., 1983; De Baar et al., 1985a; German and Elderfield, 1989). Scavenging proceeds via adsorption on the metal oxide surfaces that results in a modification of the REE distribution in the parent solution, which may cause positive anomalies of Y, La, Ga, and Lu (Bau, 1999). Specific REEs are adsorbed more strongly to Fe and Mn oxides than others. The MREEs show a peculiar affinity towards Mn oxides, whereas the LREEs are adsorbed more strongly to Fe oxides due to the strong complexation constants of HREE towards carbonate ions (Koeppenkastrop and De Carlo, 1993; Pattan et al., 2005). In a recent study Schijf et al. (2015) suggested that REE scavenging in the upper ocean is

controlled by the large availability of organic and particulate detrital particles including Mn- and Fe(oxy)hydroxides, whereas scavenging in the deep ocean is mainly controlled by Mn(oxy)hydroxide particles. Scavenging of the REEs by mineral surfaces is a pH dependent process whose relevance is reduced by high carbonate concentrations that hold the HREEs in solution (Quinn et al., 2006). Enrichment of MREEs has also been attributed to the presence of phosphates, in particular due to weathering of phosphate minerals (e.g. Hannigan and Sholkovitz, 2001). Similar to complexation, adsorption of REEs onto particulate phases is also governed by Coulombs law and is expected to be more efficient for the smaller HREEs, which would lead to LREE enrichment in sorption-dominated systems and HREE enrichment is expected in complexation-dominated systems (Bau, 1991).

Interactions with organic matter

Of all the interactions between REEs in solution and particulate matter, their relation towards organic matter is perhaps the most complicated. Organic complexes with REEs can show a surprising variation in aqueous stability, and can produce strong inter-element fractionation depending on the behavior and attributed of the respective ligand (Wood, 1993; Byrne and Li, 1995; Sonke and Salters, 2006). In circumneutral waters REEs are usually bound to humic substances (Pourret et al., 2006). The presence of abundant organic substances in solution can result in strong competition for REE complexation, and even disrupt sorption processes that would otherwise occur (Pourret et al., 2008; Davranche et al., 2008). However, these competitive sorption effects decrease rapidly with increasing pH and carbonate content, where complexation with carbonate ions take over control on REE distribution (Pourret et al., 2007; Tang and Johannesson, 2010b). The LREEs are complexed more strongly by humic acids that the MREEs and HREEs in circumneutral waters; a trend that is reversed at more acidic pH (Tang and Johannesson, 2003). Similar trends have been observed for REEs in estuaries and terrestrial waters, where the LREEs are complexed by organic colloids in river estuaries where freshwater is mixed with seawater (De Baar et al., 1985b) Gadolinium anomalies in seawater have been attributed to strong Gd complexation with organic matter, which is highly stable in seawater compared to the neighboring REEs (Zhang and Nozaki, 1998). In solutions where dissolved organic matter content is low, sorption reactions involving other solid phases become more relevant for REE fractionation. Positive correlations of dissolved organic matter in river waters and REEs, and the preferential sorption of Ce(IV) to organic

colloids further suggests and intimate relationship of organic matter with the REEs (Pourret et al., 2008; Freslon et al., 2014).

Apart from adsorption onto dead organic matter, rare earth metals can also be taken up by bacteria, where passive adsorption or biosorption is the most relevant mechanism (Andres et al., 2003). Organic compounds such as proteins, polysaccharides, and extrapolymeric substances (EPS) can preferentially sorb and fractionate REEs, although experimental results have been conflicting. Experiments conducted by Takahashi et al. (2005, 2010) showed preferential HREE adsorption onto bacterial cell walls owing to their strong affinity to phosphate surface groups. This enrichment was only observed at a pH lower than that prevailing in seawater or sedimentary pore waters. Contrary to these results Ozaki et al. (2006) showed preferential sorption of the light REEs and Eu onto soil bacteria. Moriwaki and Yamamoto (2013) found that siderophores and other organic acids exert a similar control on REE sorption as surface phosphate groups. They further suggested an increasing importance of carbonate complexes as opposed to phosphate complexes at increasing pH, but could not discern which REEs are most affected by different complexing agents due to their similar chemical behavior. As most studies have been conducted on soil bacteria under pH conditions lower than that of seawater or marine sedimentary pore waters, little is known about these processes involving marine bacterial communities in sedimentary porewaters.

Cerium

Cerium is a unique lanthanide in that it can occur in more than one redox state in aqueous solutions (Goldberg et al., 1963; Sholkovitz and Elderfield, 1988). In oxygenated natural waters Ce(III) can be oxidized to the less soluble Ce(IV), resulting in a fractionation from the other trivalent REEs. This fractionation results in anomalous Ce concentrations within the lanthanide series, either in the solution from which it oxidized, or within the phase acting as the sink for oxidized Ce(IV). These deviant Ce concentrations are referred to as the Cerium anomalies, and are a measure of fractionation of Ce from the other REEs that can only be achieved by redox chemistry (Henderson, 1984). The Ce anomaly is a typical feature of modern seawater, which features a well-developed negative Ce anomaly (Elderfield and Greaves, 1982; De Baar et al., 1985a). Several processes have been put forward to explain this Ce distribution, including abiotic Ce oxidation during scavenging onto oxides, and microbial Ce oxidation

(Moffett, 1990; Sholkovitz et al., 1994). In most cases, the parent solutions exhibit negative Ce anomalies, as dissolved Ce(III) is removed by oxidation to insoluble Ce(IV) (German and Elderfield, 1990). This oxidation is strongly catalyzed by Mn-(oxy)hydroxides with high surfaces areas, which can even act as a sink for Ce(IV) (Loges et al., 2012). Although Fe-oxides may also scavenge Ce(IV) from solutions under certain conditions, Mn oxides are considered to be the most significant carrier phase of Ce(IV) (Bau, 1999; Ohta and Kawabe, 2001). The oxidation of Ce(III) and reduction of Ce(IV) is strongly pH dependent in marine waters, whereas Eh may be more effective across the redoxcline in pore waters (cf. De Baar et al., 1988). Although the behavior of Ce in oxic waters is relatively straightforward, this is not the case for sedimentary pore waters. Particulate organic material plays a key role in the distribution of Ce(III) and Ce(IV). This is due to the strong complexation between organic matter and Ce, which can produce negative Ce anomalies in solutions in the absence of oxygen. Specifically high pH and dissolved carbonate concentrations may lead to preferential Ce adsorption, which leads to negative Ce anomalies in solution and simultaneous positive anomalies in humic substances (Pourret et al., 2008; Morgan et al., 2012).

The strong complexation of all REEs by organic material may also lead to decreased sorption of REEs onto other potential carrier phases such as oxides or carbonates. Davranche et al. (2008) found that collectively bound REEs to humic acids cannot be sorbed onto other materials such as oxides, which – in the specific case of Ce – would inhibit oxidation of Ce on the oxide surface. As a consequence, any Ce anomaly is suppressed by humate complexes holding Ce(III) in solution. Similarly, Leybourne and Johannesson (2008) noted a lack of Ce anomalies in DOC-rich stream waters, attributing it to strongly bound Ce(III) to organic material. Aside from humic substances, other solid phases exhibit negative Ce anomalies. Positive Ce anomalies are uncommon in natural environments compared to negative anomalies, and have mostly been reported from alkaline lake waters (cf. Möller and Bau, 1993), and have not yet been reported in marine sedimentary pore waters.

Europium

Europium is the only other lanthanide apart from Ce that exhibits active redox chemistry. Unlike Ce however, its redox behavior is more strongly governed by pH and temperature (Bau and Möller, 1992). Acidic, high-temperature fluids increase the mobility of Eu(II), which is also the dominant in strongly reducing conditions (Elderfield et al., 1988). At Earth surface conditions, however, Eu behaves more like the other trivalent REEs. An exception to this may be highly alkaline, reducing lake and marine pore waters (Sverjensky, 1984). The strong temperature dependence on Eu speciation is an important factor that distinguishes Eu behavior from that of Ce (cf. Bau, 1991), and why Eu anomalies can be interpreted with more confidence in marine waters and sediments. Europium anomalies in seawater have been used to establish a record of hydrothermal input versus other sources of REEs to seawater (Elderfield et al., 1988; Goldstein and Jacobsen, 1988). Seawater features a slight positive Eu anomaly, which may result from river waters where such anomalies are generated by weathering of sulfide and preferential mobilization of Eu relative to the other REEs (Leybourne and Johannessson, 2008; Xu and Han, 2009).

Europium is known to interact with bacteria in soils, where it adsorbs onto cell walls in the presence of organic ligands (Ozaki et al., 2006), however it is unclear how relevant this behavior is in marine sediments.

Yttrium and Holmium

Although Y is not part of the lanthanide series, it is often measured and reported concomitantly with the REEs, as its behavior in natural waters is very similar to that of its geochemical twin, Ho. This behavior results from their comparable ionic radii, identical charge, and similar stability constants of carbonate complexation in seawater (Zhang et al., 1994; Bau, 1999). Despite these similarities, Y and Ho fractionate strongly in solution via several processes that include scavenging by particulate matter and Fe oxides (Nozaki et al., 1997; Bau, 1999). Fractionation of Y from Ho results its different hydrolysis behavior, which is more similar to that of Sm and Eu than Ho. Further, Y is a harder ion and is more weakly complexed than Ho, whose bonding is more electrostatic in character (Klugness and Byrne, 2000). The difference in covalency between Y and Ho associated with ligand exchange between the two elements, as well as the absence of electrons in the Y 4f electron shell are possibly the two major traits that produce

Y-Ho fractionation in solution (cf. Nozaki et al., 1997; Choppin, 2002; Tanaka et al., 2008). Yttrium also fractionates from Ho during scavenging onto particles. The affinity of Y for Fe-oxides is lower than that of Ho, and fractionation increases with increasing pH (Bau et al., 1996). Bau and Dulski (1999) showed that Y behaves conservatively during mixing of hydrothermal fluids and seawater, whereas the other REEs including Ho are scavenged by Fe (oxy)hydroxides.

Rare earth elements in marine sedimentary pore waters

There are much fewer studies on REE abundance and behavior in marine pore waters than studies on REEs in the water column of the ocean. This could be due to analytical difficulties in determining pore water REE concentrations as opposed to measurements in the water column (Piper, 1974). The advancement of new analytical techniques has only relatively recently lead to a new surge of studies on REEs in seawater and marine sedimentary pore waters (Haley and Klinkhammer, 2003; Rousseau et al., 2013; Zheng et al., 2014; Behrens et al., 2016; Fisher and Kara, 2016). That modern marine sediments are generally enriched in REEs compared to ocean bottom waters has been known long before measurements of REEs in sedimentary pore waters could be conducted (Wildeman and Haskin, 1965; Haskin et al., 1966; Chaudhuri and Cullers, 1979; Elderfield et al., 1981). In the first ever study on REEs in marine pore waters – published over 20 years after the first pore water studies on trace metals – Elderfield and Sholkovitz (1987) showed that not only do REE concentrations increase with depth; they also progressively lose their seawater-type pattern in favor of flatter, LREE and MREE-enriched shale-normalized patterns. This study demonstrated the strong control of diagenetic remobilization of REE-bearing phases such as phosphates, Fe and Mn oxides, and organic matter over the distribution and concentration of REEs in marine pore waters. This notion was confirmed in subsequent studies who applied various graphical methods to depict REE fractionation such as element-element plots and normalizing REEs not only o PAAS, but also to mean sediment and deeper pore water REE concentrations (Sholkovitz et al., 1989). The main mechanism resulting in pore water REE enrichment is the transport of REEs to the sediment via metal oxides and particulate organic matter. In the course of diagenesis, cycling of minerals and organic matter subsequently release their REEs to pore waters to such a degree that porewaters have even been inferred to act as a source of REEs to bottom waters (Elderfield and Greaves, 1982).

Since the late 1980s, numerous of follow-up studies have attempted to untangle the various diagenetic processes involved in sedimentary REE cycling in order to attribute specific reactions to the mobility of certain REEs that produce diagnostic REE patterns. Sholkovitz et al. (1992) found that the LREEs are cycling much more efficiently than the HREEs, a behavior that also applies for unusual pore waters such as anoxic brines (cf. Schijf et al., 1995). Generally, those processes that govern REE behavior in the water column such as adsorption onto particulate phases and complexation by inorganic and organic ligands are responsible for REE patterns in the sediment (cf. Haley and Klinkhammer, 2003). A comprehensive study on various REE patterns in marine sediments was conducted by Haley et al. (2004), who showed that varying enrichments of HREE, MREE, and LREEs can indeed by linked to a specific process during diagenesis. Additionally, the cycling of organic matter in marine sediments by microbial processes has been stressed to release significant amounts of REEs to pore waters (Freslon et al., 2014).

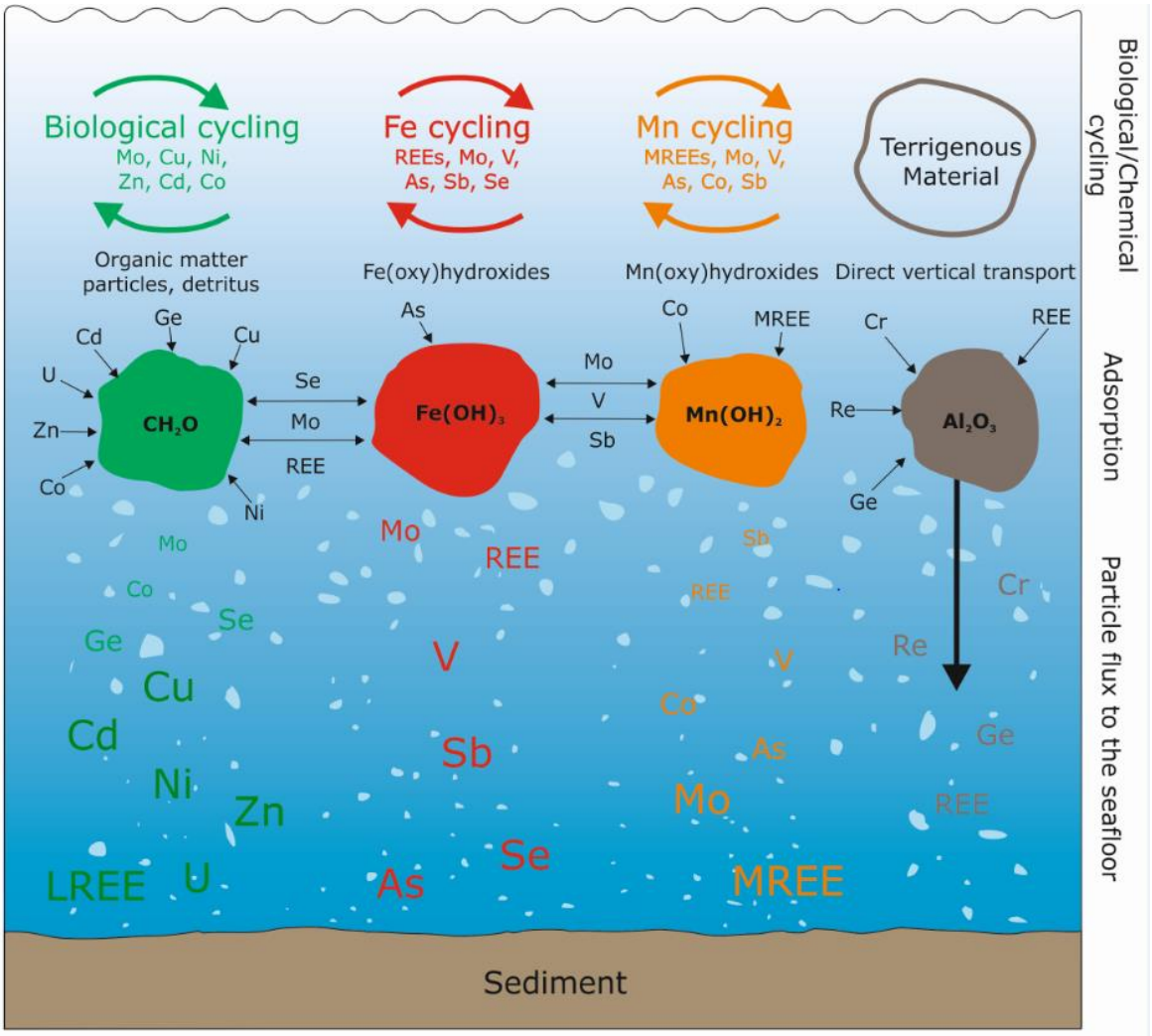


Fig. 1. Schematic illustration of trace element cycling, sorption, and transport in the water column to the seafloor. Four solid phases involved in cycling and vertical transport are considered: organic matter (green), Fe(oxy)hydroxides (red), Mn (oxy)hydroxides (orange), and terrigenous material (brown). Elements are cycled in the photic zone by marine life and hydroxide phases, after which they adsorb trace metals and transport them to the seafloor as particle rain. Terrigenous phases are not involved in surface water cycling. Although all solids exhibit concentrations of all elements, the focus here is on which elements are the most relevant for the respective phase. The size of the elements denotes the importance of organic matter, Fe and Mn oxides, and terrigenous particles on flux of the respective element to the seafloor. No scale implied.

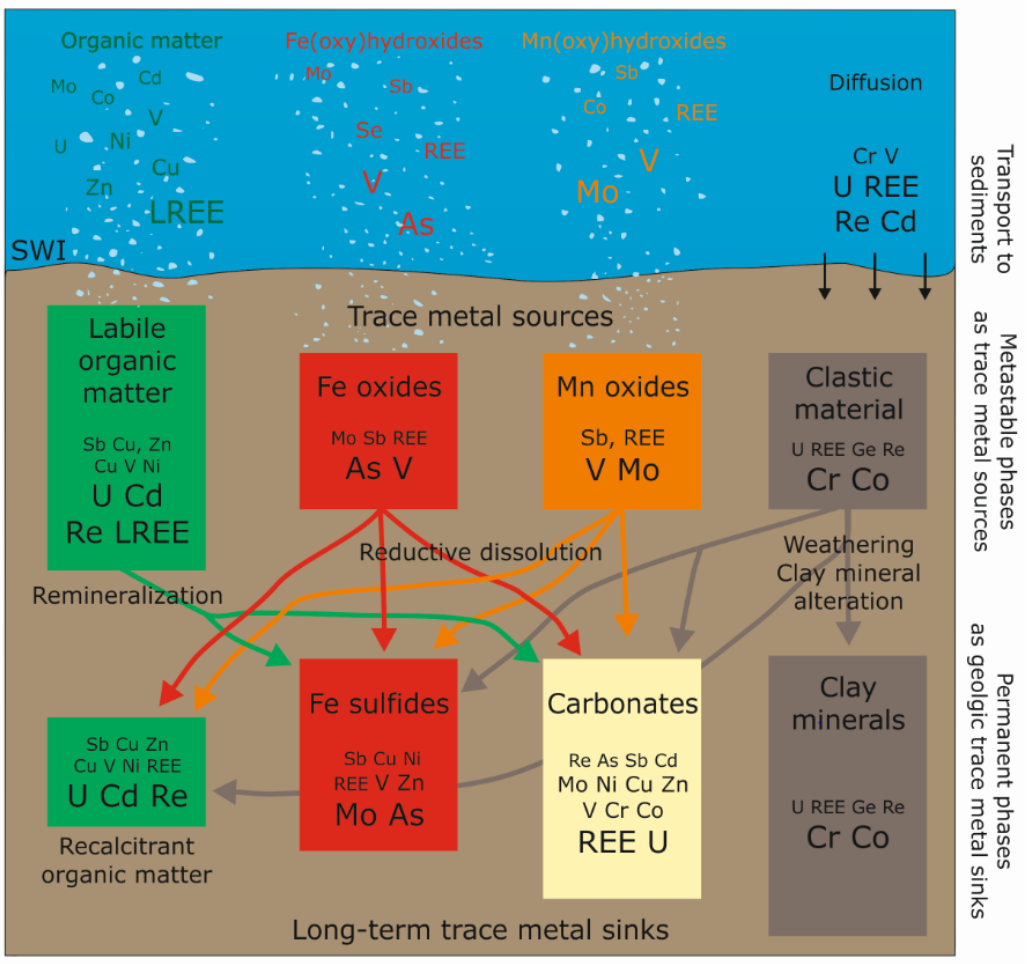


Fig. 2. Schematic illustration of trace element sources and pathways in marine sediments, SWI = sediment water interface. Organic matter and Fe- and Mn(oxy)hydroxides particles, and diffusion from seawater deliver trace metals to sedimentary pore waters where they are distributed among four main sources (top rectangles): organic matter (green), Fe oxides (red), Mn oxides (orange), and siliciclastic alumosilicate clay minerals (brown). During diagenesis organic matter is remineralized, oxides undergo reductive dissolution in the absence of free oxygen, and clay minerals undergo transformation and weathering, releasing their trace metals to pore waters. These dissolved metals are transferred to one of four main sinks (bottom rectangles): recalcitrant organic matter (green), Fe sulfides (red), carbonates (white), and clay minerals (brown). The size of letters denotes the importance of the respective transport process, source, and sink materials for the respective element. The size of top and bottom rectangles denotes their importance as a source or a sink for the respective elements. Arrows denote important transport paths of trace elements between their sources and their long-term sinks. No scale implied.

Part 2: Carbonates as a sink for trace and rare earth metals I – Physicochemical and mineralogical constraints

The first part of this review focused on the behavior of trace and rare earth elements in natural waters from source to sink, that is, from the surface ocean to marine sediments. For carbonate petrologists – and petrologists in general –this is a logical place to start when reviewing why and how these elements accumulate where mineral formation takes place. The second step is to focus on the mechanisms of how carbonate minerals incorporate and archive these metals, in order for us to analyze them to gain information on past geologic processes. Geochemical analysis of marine biogenic and non-biogenic carbonates has yielded much information on a large variety of topics ranging from chemical oceanography to the marine carbon cycle and climate change (e.g. Berger, 1983; Sandberg, 1983; Archer and Maier-Reimer, 1994; Millero, 2007). The research over the years has shown that understanding and quantifying the thermodynamics and kinetics of carbonate formation and dissolution, as well as incorporation of major elements including Ca, Mg, Sr, Fe, and Mn are the foundation and a prerequisite in tackling any of the aforementioned issues (Morse and MacKenzie, 1990; Andersson and MacKenzie, 2013 and references therein). Consequently, the practice of analyzing major element contents of marine carbonates has been harnessed into a powerful tool that is applicable to almost all geological and oceanographical settings (Kinsman, 1978; Brand and Veizer, 1980; Land, 1980; Veizer, 1983). We will omit the major elements including Ca, Mg, Sr, Fe, and Mn from the following discussion, as the literature concerning the geochemistry of these elements in carbonates is vast and not the main focus of this review. The next two sections summarize the modes and mechanisms of trace and rare earth metal incorporation into carbonate minerals, followed by several examples of case studies that utilize these elements to establish concepts and interpretations on the genesis of Holocene corals and microbialites to Neoproterozoic non-biogenic carbonates.

Trace and rare earth metal incorporation into carbonates – Modes and mechanisms

Trace metals

Carbonate minerals are highly prone to incorporate significant amounts of trace and rare earth metals (Veizer, 1983). Calcite precipitation and dissolution reactions act both as a sink and as a source of trace metals in natural environments, and depend on their concentrations in solution (Hardstad and Stipp, 2007). Uptake of trace metals by calcite not only occurs during growth, but also during dissolution and when the mineral is in equilibrium with surrounding solution (Lorens, 1981; Stipp et al., 1992). Most of our knowledge on trace metal incorporation into carbonate minerals stems from laboratory studies, in which chemical parameters are determined to predict and model interactions between dissolved components and the solid phase. Rimstidt et al. (1998) summarized these parameters, which include distribution coefficients, mineral surface area, mineral precipitation and/or growth rate, and aqueous concentrations of metal ions (cf. Lorens, 1981; Paquette and Reeder, 1995). The vast majority of studies have concentrated on calcite, as opposed to aragonite or dolomite. Calcite can easily adsorb and substitute trace metal ions for Ca^{2+} and Mg^{2+} in its lattice, resulting in the common observation that natural carbonates are almost never present as pure $CaCO_3$ (Dromgoole and Walter, 1989; Burton, 1993).

The two main mechanisms that are responsible for the trace metal content of carbonate minerals are coprecipitation and adsorption (Zachara et al., 1991; Paquette and Reeder, 1995). Coprecipitation refers to the uptake and active incorporation of ions into the mineral during growth, and may be influenced by growth rate and surface structure (Reeder et al., 1999). Although much experimental work has been conducted to derive predictable distribution coefficients for trace element substitution in carbonate minerals, reliable or robust data that predict partitioning behavior are difficult to attain. This results from the multitude of factors influencing incorporation including precipitation rate, metal ion concentrations in solution, and competitive behavior of trace metal amongst each other (Morse and Bender, 1990). Carbonate minerals can incorporate different metal ions to varying degrees depending on their crystal structure. The calcium ion occupies a unique octahedral site within the calcite lattice, which results in ready substitution of ions that also occur in this coordination in calcite such as Co, Zn, and Fe. Larger ions such as Sr and U have a higher coordination number, and preferably incorporate into the octahedral crystal structure of aragonite (Parekh et al., 1977; Reeder et al., 1999; Morse et al., 2007).

Metal adsorption on the mineral surface is the second major process leading to trace metal incorporation into calcite. Experimental studies on the sorption behavior of ions on calcite have shown that it depends primarily on solution chemistry and pH (Franklin and Morse, 1983; Davis et al., 1987; Zachara et al., 1991). Adsorption of cations on carbonate minerals is related to their size relative to the Ca^{2+} ion that is substituted within the lattice, and proceeds as a multiple-step process with initial rapid surface uptake followed by slower removal from solution (Comans and Middelburg, 1987; Stipp and Hochella, 1991). The initial rapid chemical adsorption of cations onto the mineral leads to progressive enrichment of trace metals at the surface, which is an important first step towards actual incorporation into the lattice during crystal growth (Watson, 1996). Adsorption of cations generally increases with decreasing ionic radius and occurs as free metal ions in the case of most divalent cations, or as complexed aqueous species in the case of trivalent ions (McBride, 1979; Zachara et al., 1988; Cheng et al., 1999).

Uranium – An "all-rounder" in paleoenvironmental analysis of carbonates

Certain trace metals have received more attention with respect to mineral incorporation than others, depending on their utility for geologic applications, as geochemical tracers, or their relevance in environmental pollution. Uranium is one of the best studied trace metals regarding its relationship to calcite and aragonite, which has resulted from its applicability as a chronometer, thermometer, and an indicator of past ocean anoxia and carbonate ion concentrations (Hamelin et al., 1991; Min et al., 1995; Shen and Dunbar, 1995; De Carlo et al., 2015) It is well established that U is less compatible within the rhombohedral conformation of calcite than in the orthorhombic form of aragonite (Reeder et al., 2000), and that U incorporation into lattices depends strongly on its speciation. Uranyl (U(VI)) substitution is easier in aragonite than in calcite, where it requires a change in coordination that may lead to disruptions of the calcite lattice (Kelly et al., 2003). Uranium partitioning into calcite further depends on pH and precipitation rate as shown by Meece and Benninger (1993), who demonstrated decreasing distribution coefficients for U into calcite at increasing pH and precipitation rate (but see Gabitov et al. 2008 for contrasting results). As soon as U incorporation into calcite is achieved it can be efficiently immobilized and stored there for millions of years (Reeder et al., 2001). Less studies have been conducted on the incorporation of reduced U(IV) into carbonates. Uranium(IV) can be accommodated easier into calcite than uranyl due to its smaller size, leading to high concentrations of U in natural carbonates from

reducing environments (Sturchio et al., 1998). However, high concentrations of dissolved Ca^{2+} have shown to inhibit the rate of U reduction through the formation of large Ca-U-CO_3 complexes, which may reduce the U(IV) uptake rate by carbonates precipitating in reducing waters (Brooks et al. 2003).

Not all have received the same attention – Relevant, yet understudied trace metals

Arsenic incorporation into calcite has received some attention, though not as extensively as U. Arsenic is a trivalent ion, and its incorporation is more complex than incorporation and isomorphic substitution of Ca^{2+} by divalent cations of similar size (Curti et al., 2005). As with U, arsenic speciation governs its incorporation into minerals, as arsenate and arsenite behave differently in solution. Arsenate competes strongly with bicarbonate complexes during adsorption onto calcite, whereby decreasing alkalinity facilitates arsenate accumulation on the mineral surface (Sø et al., 2009). Arsenate is incorporated via adsorption of As(V)-oxyanions at the calcite surface, possibly substituting for carbonate groups in the lattice (Cheng et al., 1999; Alexandratos et al., 2007). Arsenite appears to be more readily incorporated than arsenate, and forms solid solution series with calcite similar to Cd. Coprecipitation of arsenite with calcite has been observed in experiments that imply that dissolved arsenite availability and mobility is severely limited by calcite precipitation (Román-Ross et al., 2006).

Surprisingly little work has been done regarding adsorption and incorporation of Mo into calcite, given this elements importance in paleoeanographic studies (see section 2). The overwhelming majority of studies on Mo involve the adsorption and desorption of various Mo species onto oxide minerals in soils, which is a strongly pH dependent process (McKenzie, 1983; Goldberg and Forster, 1998). Molybdate has a high adsorption affinity for negatively charged surfaces of Fe and Al oxides such as goethite and gibbsite, although other ions including arsenate, selenate, phosphate, and sulfate may compete efficiently for adsorption (cf. Manning and Goldberg, 1996; Wu et al., 2001). It is feasible that similar behavior controls Mo sorption onto carbonate minerals.

Certain trace metals behave differently than others in the vicinity of the mineral surface. Zachara et al. (1991) found that Cd and Mn dehydrate upon contact with the surface, whereas Zn, Co, and Ni remain hydrated and possibly partition into the lattice as hydrated complexes. Zinc and Cu are incorporated differently into calcite than Co, Cd, or Mn, as they form mononuclear inner-sphere adsorption complexes before substituting for Ca^{2+} in the surface layer of the mineral (Elzinga and Reeder,

2002). Zinc in particular adsorbs very strongly onto calcite at high pH and low Ca^{2+} activities where it subsequently substitutes for Ca^{2+} in the calcite lattice (Zachara et al., 1988; Cheng et al., 1998). This behavior is complicated by complexation with dissolved species such as Cl, which can significantly decrease Zn partitioning into the solid phase (Temmam et al., 2000). Similar complexation behavior has also been observed for Cu, whose adsorption and incorporation into calcite is influenced by organic humic acid complexes (Lee et al., 2005). Cadmium has a high affinity for adsorption onto calcite, which proceeds rapidly and results in a strong tendency to partition into calcite (McBride, 1980; Tesoriero and Pankow, 1996). Cadmium is so effectively substituted for Ca^{2+} that solid solution series exist between $CdCO_3$ and calcite (Hoffmann and Stipp, 2001). Nonetheless, phosphate and sulfate ions can reduce the capacity for Cd sorption; a process that is particularly relevant in seawater and marine pore waters (van der Weijden et al., 1997). Moreover, calcite recrystallization and Cd sorption decrease with increasing pH and dissolved Mg^{2+} content (Davis et al., 1987).

In contrast to Zn and Cd, Ni is only moderately incorporated into calcite. Nickel forms more stable complexes in solution than Zn or Cd, which prevent rapid dehydration and impede rapid Ni incorporation into calcite (Hoffmann and Stipp, 2001). However, Ni does partition into calcite in proportion to its concentration in solution, yet at a much slower rate than other trace metals (cf. Lakshtanov and Stipp, 2007). Cobalt incorporation is preceded by adsorption of Co^{2+} onto both aragonite and calcite where it substitutes for Ca^{2+}, although its affinity is much higher for calcite (Kornicker et al., 1985; Katsikopoulos et al., 2008). Xu et al. (1996) observed a strong pH dependency of Co^{2+} adsorption onto calcite, with higher Co concentrations on the mineral surface at higher pH. Even low concentrations of Co^{2+} in solution may actively influence the growth habit of minerals during precipitation (Braybrooke et al., 2002).

Rare earth elements in carbonates – An exercise in discrepancy

The REEs partition into carbonates via similar processes as those outlined above for the trace elements. Not all aspects of REE incorporation into carbonates will be discussed in depth here, as other reviews have recently covered this topic in greater detail (see Debruyne et al., 2016). Carbonate minerals including calcite and aragonite, but also dolomite, act as efficient repositories for REEs on geologic time

scales due to their ability to accommodate significant amounts of REEs in their lattice, and modes and mechanisms by which they achieve this will be summarized below.

Most of what is known on REE partitioning into carbonates is derived from laboratory studies, and the overwhelming majority of these have focused on calcite. Although experimental efforts have not yielded consensual results for the relevant parameters (e.g. Liu and Byrne, 1998 vs. Ohta and Kawabe, 2000), the fundamental mechanisms and their importance has been constrained fairly well. Incorporation of REEs in calcite proceeds via coprecipitation and adsorption, and depends on REE concentration and the nature of their complexation in solution. As with most minerals the calcite surface is negatively charged, and adsorption of trivalent positively charged REE ions proceeds quickly and efficiently. However, carbonate ions do not participate in the REE-adsorption processes. Rather, hydroxo-complexes are involved in the attachment of lanthanide ions onto the surface, highlighting the importance of REE complexation (Sawada et al., 2005). The role of complexation was investigated by Terakado and Masuda (1988), who suggested that REE partitioning into calcite more strongly controlled by REE complexation in solution rather than by the crystal structure of the mineral. Zhong and Mucci (1995) showed that REE uptake by calcite is rapid at first and slows down with progressing mineral growth, and appears to be largely independent of precipitation rate (cf. Toyama and Terakado, 2014). Furthermore, the LREEs are more effectively partitioned into calcite, which was attributed to increased competition for crystal sites at higher REE concentrations with an increasing preference for the better fitting LREEs. This would reflect retention of the HREEs by aqueous carbonate complexes. Highly charged cations such as the REEs have large adsorption coefficients, which may account for the minimal to nonexistent effect of precipitation rate on REE distribution coefficients.

Precipitation rate does not necessarily affect the rate of incorporation of the REEs into calcite in such a way as it would affect other trace metals with lower charge (Wang and Xu, 2001). Fractionation during partitioning into calcite has also been observed for Y and Ho. Fractionation of these two elements in natural waters has been attributed to the difference of bonding covalence associated with ligand exchange between Y and Ho (see section 1). The same mechanism applies to their fractionation during incorporation into minerals. Yttrium-Holmium fractionation occurs during reactions of REE-carbonate complexes with dissolved carbonate ions during the incorporation of $REE(CO_3)^{2-}$ complexes into calcite (Tanaka et al., 2008). This leads to a more rapid uptake of Ho compared to Y, although they are both strongly partitioned into calcite (Qu et al., 2009). The significance and influence of aqueous complexation

for REE uptake by calcite was further stressed by Tanaka et al. (2004), who showed a direct dependency of partitioning coefficients on the degree of REE-carbonate complexation in solution. Most Ca^{2+}-bearing minerals are enriched with REEs relative to other solid phases due to the ease of REE substitution for Ca^{2+}. It is important to note that the LREEs adopt a different local coordination within calcite than the HREEs, which reflects differences in charge compensation during substitution of the trivalent REEs for divalent Ca (cf. Elzinga et al., 2002). This substitution leads to an excess of charge in the vicinity of the substitute ion, in this case REE^{3+} that may be compensated by charge-balanced substitution of other ions such as Na^{2+} or hydroxylated forms of REE^{3+} (Withers et al., 2003; Marques Fernandes et al., 2008; Voigt et al., 2017). The mode of REE substitution in the calcite lattice is still a matter of debate, and has led to several studies focusing on Eu in particular. Stipp et al. (2003) showed strong adsorption and uptake of Eu by calcite, and argued that REE uptake by calcite is not limited by its uptake capacity, but by REE availability in solution (see also Lakshtanov and Stipp, 2004). Curti et al. (2005) suggested different substitution mechanisms at high and low pH during incorporation of Eu into calcite, leading to coordination rearrangements and changes in mineral solubility at different pH.

Aside from lattice properties and charge compensation mechanisms, the incorporation of REEs in particular seems to enact an influence on the habit of the growing carbonate crystal. Barker and Cox (2011) demonstrated varying growth of acicular and rhombohedral calcite crystals dependent on REE/Ca ratios of the parent solution, as well as increasing REE content within calcite during growth. Similar results were derived by Maskenskaya et al. (2015), who could also verify the influence of crystal habit on REE distribution patterns in calcite. Their study further showed that uptake of LREEs is stronger than for HREEs (as suggested by Zhong and Mucci (1995)), if the parent solution has equal concentrations of all REEs, and slow precipitation conditions favor diffusion and adsorption of REE ions to the mineral surface.

Although not all trace and rare earth metals are separately reviewed here, their adsorption and incorporation behavior into carbonates is similar. Adsorption onto the mineral surfaces is usually the first step, where their concentration is increased in the vicinity or directly at the surface compared to the surrounding parent solution. In a second, usually slower step, they are subsequently incorporated into the mineral lattice during precipitation. Differences in speciation, valency, size, and in the tendency to form aqueous complexes with inorganic and organic ligands produce minor variations in the capacity of carbonates to incorporate and hold trace metals. Carbonate minerals, especially calcite, can be considered

long-term repositories of lanthanides and actinides that are more effectively incorporated into calcite than other trace metals (cf. Sabau et al., 2014), and only complete mineral dissolution leads to an effective loss of trace metals from the mineral lattice (Stipp et al., 2006). This is a useful aspect to consider when interpreting trace metal contents of natural carbonates. The next part of this review will detail the applicability of trace and rare earth metals to natural carbonates in the rock record, and will reveal that interpretation of these metals in terms of reconstructing ancient environments is not at all straightforward despite experimental evidence and present-day observations.

Part 3: Carbonates as a sink for trace and rare earth metals II – The geologic record

The question of preservation

Two assumptions inevitably need to be made in order to use trace and rare earth metals as proxies in ancient carbonates: (1) trace metals are partitioned into the solid phase with a constant ratio that reflects their concentrations in the parent fluid, and that (2) already partitioned elements are not removed or added during diagenesis. The first supposition is much easier to assert than the second, as it can be tested with relative confidence in laboratory experiments outlined in the previous section. The second, however, cannot be affirmed experimentally, which is why post depositional alteration of rocks and its effect on their element content is an issue that is addressed in most case studies. Early studies on diagenetic carbonates focused on the recrystallization of aragonite to calcite with concomitant decrease of Sr and increase of Mg (e.g. Berner, 1966). Later studies enabled to establish a relationship between early and later diagenetic carbonate phases and their trace element content, revealing that certain elements become systematically enriched in the course of equilibration with diagenetic fluids (Brand and Veizer 1980).

Since the earliest work dedicated to trace and REEs in ancient and modern carbonates there has been an ongoing debate if, and to what degree, these metals are preserved in carbonates over geologic timescales. The notion that carbonate minerals represent a stable archive for trace and REEs is highly tempting, and has been anticipated long before experimental work partially corroborated this idea

(Friedman, 1969; Veizer et al., 1971; Parekh et al., 1977). The study of Banner et al. (1988) is a definite step forward in resolving the question of the effect of diagenesis on trace metal contents of sedimentary carbonates. In a systematic study on dolomite they showed how post-marine diagenesis does not affect REE systematics, and how recrystallization of dolomite does not alter REE patterns. Similar conclusions can be drawn from experimental studies suggesting that carbonate minerals such as calcite, aragonite, and dolomite must dissolve completely in order to alter their REE contents (Terakado and Masudo, 1988; Zhong and Mucci, 1995). Banner and Hanson (1990) further argued for the importance of the water to rock (W:R) ratio during diagenesis, which can reset distribution coefficients of trace elements due to the varying degrees of water-rock interactions. As the W:R ratio during diagenesis exerts direct influence on the exposure time of fluids with carbonates, this increased reaction time can indeed alter the REE or trace metal content of carbonates (Bellanca et al., 1997; Tanaka et al., 2003; Tanaka and Kawabe, 2006). Fluid circulation is considered an even more important factor with respect to REE stability in carbonates than elevated temperatures (Cherniak, 1998) or dolomitization (Miura and Kawabe, 2000; Kucera et al., 2009; Wang et al., 2014). In some cases, however, even high W:R ratios do not affect REE contents, particularly if dissolution and reprecipitation of carbonates is rapid and dissolved elements re-enter secondary minerals (Bau and Alexander, 2006; Allwood et al., 2010). The argument for preservation of primary signals from W:R ratios has also been suggested in studies of carbonate shell material that experienced diagenesis and burial (Azmy et al., 2011; Zaky et al., 2015). The possibility that REE patterns in authigenic ancient minerals can be preserved and can withstand diagenetic alteration without substantial change has also been put forward for other geologic materials including cherts and phosphates (McArthur and Walsh, 1984; Wright et al., 1987; Murray et al., 1990, 1992; Grandjean-Lécuyer et al., 1993), as well as iron formations (Fryer, 1983; Jacobsen et al., 1988; Derry and Jacobsen, 1990; Bau and Möller, 1992; Bau and Dulski, 1996).

Nevertheless, the idea that REEs are largely unaffected by post-depositional processes has been challenged. A case study of Mid-Proterozoic laminated shales and carbonates demonstrated the mobility redistribution of REEs during diagenesis (Schieber, 1988), argued for diffusion of LREEs from shales and preferential enrichment in limestones during diagenesis. Johannesson et al. (2006) pointed out the sensitivity of REEs towards post-depositional mobilization, fractionation during precipitation, and the ease of contamination of primary signature. Studies of REEs in modern stromatolites have further noted the difficulty of applying these metals as tracers of abiotic vs. biotic activity, as microbial activity

fractionated REE during adsorption and uptake from parent fluids (Johannesson et al., 2014; Censi et al., 2015). As of today, no solid method has yet been put forward that can unambiguously determine the extent of post-depositional alteration. However, some attempts have been made to establish proxies of the degree diagenetic influence, particularly concerning the REE content of ancient carbonates.

Primary or altered signals? Attempts to solve an enduring dilemma

The calls for caution in the interpretation of trace and REEs in ancient limestones have encouraged the search for proxies to assess diagenetic influence, and detect external sources of potential contamination. The most obvious and simple method to recognize the above factors is to calculate correlation coefficients of the elements in question to elements considered to be indicative of minerals of a definite terrestrial or terrigenous origin. Trace elements used for such correlations include Th, Zr, Sc (Chester and Aston, 1976), Co (Tribovillard et al., 2006), Ti, and Al (Calvert and Pedersen, 1993; Tribovillard et al., 1994; Van der Weijden, 2002; Kryc et al., 2003), as well as combination of specific element pairs such as U-Th, Fe-Cr, Rb-Cs or Zr-Hf (Dulski et al., 1977). Thus, correlations of a given trace element or REE with either one or a combination of one of these elements can be considered as being derived from terrigenous material. The same principle of correlation can be applied by correlating trace and REEs to Fe or Mn, as Fe- and Mn(oxy)hydroxides are known to scavenge and subsequently release trace and REEs as discussed previously. However, inter-elemental correlation is only one of several methods to estimating the degree of alteration of trace and REEs in carbonates. The correlation between Fe-isotopes and total REE content has been put forward as an argument for the survival of primary REE contents in ancient carbonates (Von Blanckenburg et al., 2008).

Apart from inter-elemental correlations between trace metals and specific metal isotopes, the REEs offer a wider range of possibilities to identify post-depositional alteration of trace metal contents in carbonates. Setting aside the possibility that the shale-normalized REE content of seawater changed over geologic time (Shields and Webb, 2004; Lécuyer et al., 2004), the REE composition of seawater can be used as a first-order approximation of what compositions and patterns of unaltered carbonates should yield. Modern seawater REE systematics can by summarized by:

1. Positive La, Gd, Lu, and Y anomalies in shale-normalized patterns

2. Negative Ce anomalies

3. HREE enrichment

4. Superchondritic Y/Ho ratios

Therefore, any significant or observable deviation in REE systematics from the above traits can be viewed in terms of an unoriginal or non-primary signal that is suspect of diagenetic or post-depositional alteration. Modification of primary REE patterns during diagenesis is the most obvious and concerning issue hampering the REE interpretation of ancient carbonates, and several approaches have been suggested to detect and circumvent erroneous conclusions:

1. Sr-Nd isotopes

Strontium is more mobile in fluids than Nd during diagenesis, and correlations between isotopes of these two elements have been suggested as being indicative of primary, unaltered signals (Kamber and Webb, 2001). Depending on the questions posed and the geologic setting of the studied samples, Sr and Nd isotopes can be either superfluous or essential in determining the degree of alteration of carbonates.

2. Shale-normalized Dy/Sm ratios above unity, and correlations between Ce anomalies and Dy/Sm and total REE contents.

Shields and Stille (2001) suggested this correlation as a means to estimate of MREE enrichment and the potential influence of diagenesis accompanying the generation of MREE enrichment in the samples.

3. Correlations of Eu with any other REE (Shields and Stille, 2001; Bolhar et al., 2004).

4. Correlations of ^{34}S and Ce anomalies

5. Positive La and Y anomalies assigned to subsurface weathering

6. No correlation between Y/Ho and Ce anomaly (Bolhar and Van Kranendonk, 2007).

7. MREE enrichments indicative of P or Fe-oxide contribution (Haley et al., 2004; Baldwin et al., 2011)

8. Correlation of Eu anomaly to Sm/Yb ratio as indicator of hydrothermal influence (Kamber and Webb, 2001)

9. Correlation of Fe and REEs combined with low Fe/REE ratios as indicators for diagenetic Fe enrichment (Nothdurft et al., 2004)

10. Correlation of Ce anomalies with Nd (Holser, 1997)

11. Arching effect, MREE bulge, 2Gd/(La+Lu) after Holser, (1997)

Enrichment factors – Towards a uniform comparability

Perhaps the most important element to discern various input sources is Al, which is neither affected by biological nor diagenetic processes. Aluminum has emerged as the element of choice to quantify terrigenous and detrital fractions of trace metals in sediments by normalizing their content to its content in natural samples; a practice that yields relative concentrations in natural samples compared to a predetermined standard of choice. These values are known as enrichment factors (EFs) of a given element. The concept of calculating enrichment factors for trace metals in the environment stems from research on anthropogenic pollution studies of heavy metals, and has been put to use since the late 1960s (Müller, 1969; Bruland et al., 1974; Lantzy and MacKenzie, 1979; Hakanson, 1980; Hilton et al., 1985; Salomons and Förstner, 1984). The application of trace metal EFs for paleoenvironmental analysis in pristine marine sediments and shales is a comparably younger field of research (see Brumsack, 2006 for a review). As elegant and convenient the calculation of EFs may be, there are caveats of which one must be aware of during interpretation. Enrichment factors are easily over- or underestimated if they are not considered together with total concentrations of the respective elements and Al. Ideally, information on the composition of background material is required to correctly assess trace metal EFs in sediments. Van der Weijden (2002) summarized the issues concerning Al normalization of trace metal data. In certain cases, normalization of trace metal data using Al should be cautioned, or avoided altogether. These include sediments with very low Al content, or an excess of Al content over other elements that are associated with the terrigenous fraction including Co, Cs, Ga, Li, Rb, Ta, Th, and Sc (see also Tribovillard et al., 2006).

From modern corals to Archaean stromatolites – A brief overview

Specific carbonate minerals can be assigned to particular redox zones in marine sediments, which control the distribution of trace metals in sediments and, thus, thermodynamic stability of carbonate minerals (Coleman, 1985; Barnaby and Rimstidt, 1989). These early studies focused mainly on major elements in carbonates such as Mg, Sr, Fe, and Mn, which are effective at assessing the degree of recrystallization, progressive diagenesis and redox zonation. Much of the basic concepts and understanding on REEs in natural carbonates have been established by the analysis of modern corals in the 1990s. Sholkovitz and Shen (1995) linked REE uptake into corals to their complexation with carbonate in seawater, concluding that REEs are taken up by the mineral in proportion to their concentration in seawater. This notion had already been put forward a decade earlier by Shaw and Wasserburg (1985), who claimed that "REEs in primary carbonate are derived from seawater". This recognition of the utility of trace and REEs in corals has led to a wealth of literature, which was again revived around the year 2000 by the study of Webb and Kamber (2000), who developed a new proxy based on REE contents in corals. Subsequent studies on corals have confirmed that REEs are indeed taken up from seawater in a predictable ratio, and can thus be used as a relatively reliable proxy to interpret ancient environmental conditions (Fallon et al., 2002; Agaki et al., 2004; Nothdurft et al., 2004; Wyndham et al., 2004; Cabioch et al., 2006).

Although corals offer a potentially more robust and reliable trace and REE archive, post-depositional processes including diagenesis and neomorphism of carbonate minerals contribute to contamination and alteration of primary signals (Webb et al., 2009). The promising results and interpretations enabled by the pioneering work on corals encouraged the use of trace and REEs to reconstruct environmental conditions much further back in geologic time (although this practice has been explicitly cautioned see Holser, 1997). Two of these types of carbonates are Neoproterozoic marine carbonates, and Archean microbialites. Both bear some resemblance to hydrocarbon-seepage derived authigenic carbonates in their mode and environment of formation, and trace and REEs have been applied to all three types of carbonates in order to unravel essentially the same types of processes.

The record of Neoproterozoic carbonate successions has yielded valuable information on redox conditions of ancient oceans, large-scale climatic shifts, oxygenation of the atmosphere and the concomitant evolution of marine life, whereby most of these processes have been inferred based on high-

resolution carbon and oxygen isotope stratigraphy (Karhu and Holland, 1996; Buick et al., 1998; Lindsay and Brasier, 2001; Bekker et al., 2003; Melezhik et al., 2007; Guo et al., 2009; Och and Shields-Zhou 2012; Lyons et al., 2014). Trace and REEs are being increasingly applied to these ancient deposits to retain additional and more detailed information on specific environmental conditions and biogeochemical processes. Many known Neoproterozoic carbonates were deposited in proximity to continental margins, where river water or meltwater from deglaciation affected the chemistry of fluids from which the carbonates precipitated. Trace and REEs have been used with some success in discerning marine from a terrestrial water input, and to assess the influence of both sources (Mazumdar et al., 2003; Zhao et al., 2009; Zhao and Zheng, 2013). A combination of Y/Ho ratios, and correlations of trace and REEs with Ti, Zr, Sc, and Th have been suggested to estimate the magnitude of terrestrial input to parent fluids (Frimmel, 2009; Huang et al., 2009; Hohl et al., 2015a), as well as employing Eu anomalies to trace hydrothermal input (Meyer et al., 2012; Xiong et al., 2014). In a similar manner, enrichments or depletions of trace metals Mo, U, and V have been applied in such ancient carbonates to evaluate the prevailing redox potentials to reconstruct ancient sulfur cycling (Armstrong-Atlin et al., 2010; Meyer et al., 2012: Hohl et al., 2015b), as well as using Ce anomalies in assessing the degree of oxygenation of ancient waters (Komiya et al., 2008; Zhao et al., 2009; Nagarajan et al., 2011; Ling et al., 2013).

The more relevant types of carbonates in the framework of this review are microbialites, which include modern and ancient stromatolites. Microbial carbonates are of great interest for geologists and biologists alike, as they represent unique archives of the most ancient forms of life on Earth (Burne and Moore, 1987; Gehling, 1999; Grotzinger et al., 2000; Allwood et al., 2006; Altermann et al., 2006; Schopf et al., 2007; Riding, 2011). The record of Proterozoic microbial carbonates, and of stromatolites in particular, has been studied using sedimentological tools, petrography, and detailed isotope stratigraphy in order to unravel the onset of microbial life in Earth's history, as well as pinpointing the time frame and direction of their evolution in the light of major geological changes including Neoproterozoic oxygenation events, global and regional glaciation, and putative large-scale emissions of greenhouse gases to the atmosphere (Knoll et al., 1993; Grey and Corkeron, 1998; Grotzinger and Knoll, 1999; Kennedy et al., 2001; Corsetti and Grotzinger, 2005; Fairchild and Kennedy, 2007; Flannery and Walter, 2012). Generally, microbial carbonates have higher trace and REE contents than corals or abiotically produced marine carbonates. This can either be seen as an impediment or an asset. Elevated concentrations can be a priori assigned to progressive diagenetic enrichment (Scherer and Seitz, 1980; Shaw and Wasserburg,

1985; Holser, 1997). Nevertheless, microbialites have been regarded as superior element repositories compared to corals, as element fractionation due to biologically controlled carbonate formation can be excluded (e.g. Webb and Kamber, 2000). Certain trace and REEs such as V, Cr, Mo, and Ba have been employed to infer the degree of biogenicity in modern microbial mats and stromatolites, and to discriminate between microbial from skeletal or abiotic carbonate (Webb and Kamber, 2004; Kamber and Webb, 2007; Valdivieso-Ojedo et al., 2014; Censi et al., 2015; Li et al., 2017). Similar to studies on Neoproterozoic marine carbonates, the influence of terrestrial input from erosion or river water, and the influence of seawater on microbialite formation has been successfully discerned by trace and REEs (Van Kranendonk et al., 2003; Bolhar et al., 2004; Cabioch et al., 2006; Bolhar and Van Kranendonk, 2007). Trace and REEs have also been used to assess the water depth of microbialites formation (Kamber et al., 2014), as well as to estimate the degree of direct microbial involvement in carbonate precipitation (Kamber and Webb, 2001; Corkeron et al., 2012).

This chapter briefly summarized the potentials, the limitations, and possible pitfalls of using trace and REEs in certain types of modern and ancient marine carbonates for (paleo)environmental analyses. The next section ties in with microbial carbonate deposits, yet focuses on an unusual type of microbial carbonate that has gained significant attention in recent years, specifically as a sink and an archive for trace and REEs that may even be considered being of global relevance.

Part 4: Authigenic carbonates at marine hydrocarbon seeps – An El Dorado for trace and rare earth metal application

The unique character of hydrocarbon seepage-derived authigenic carbonate deposits in marine sediments lies in a factor that is often overlooked. Seep carbonate deposits are often described as – or included into the term of – microbialites, yet this inclusion implies that both types of carbonate are either formed by similar or even the same mechanisms, or that they are derived from the same source of carbon. However, microbialites receive their carbon largely from seawater DIC including marine cements, coral skeletons, sponge bodies, bryozoans, and other metazoan remains, (Bosence and Bridges, 1985; Flajs et al., 1995; Neuweiler et al., 1996; Riding, 2002), whereas the main carbon source for seep carbonates is organic carbon derived from microbial mineralization of methane and organic matter in sediments (Ritger et al., 1987; Paull et al., 1992; Peckmann et al., 1999; Greinert et al., 2001). This difference is most evident when comparing phase-specific or bulk rock $\delta^{13}C$ values of reefal microbialites (Montaggioni and Camoin, 1993; Camoin et al., 1999; Heindel et al., 2010), mud mound microbialites (Wendt et al., 1997; Neuweiler et al., 1999; Elrick and Snider, 2002; Calner et al., 2010), and seep carbonates. Hydrocarbon seep carbonates display the lowest $\delta^{13}C$ values of all known marine limestones, demonstrating that their main carbon source stems from a combination of methane and higher molecular weight organic compounds, mixed with minor amounts of bicarbonate from seawater (Peckmann and Thiel, 2004). In this respect, seep carbonates can be viewed as the "true" microbialites, as their formation is directly involved with – and even only possible due to – microbial metabolic activity in seafloor sediments.

The reasons why trace and rare earth element studies on authigenic seep carbonates are enjoying an ever-growing popularity is obvious: They constitute deposits capable of archiving a wide range of abiotic element cycling processes, as well as many microbial metabolic processes that proceed in marine sediments. As most modern seep carbonates are located at or close to the seafloor, they can yield additional information on bottom water process such as diffusive and advective element flux to and from sediments, sedimentation rates, seafloor weathering, and winnowing. Redox reactions below the seafloor can be conveniently classified according to their energy yield for microorganisms, and can hence be divided into the following zones:

Oxygen reduction

Nitrate reduction

Manganese reduction

Iron reduction

Sulfate reduction

Methanogenesis

Acetogenesis

Fermentation

This geochemical zonation of subseafloor sediments is well established and has been substantiated by pore water chemistry data (Froelich et al., 1979), as well as by free energy considerations and redox potentials (Fenchel and Jørgensen, 1977). As authigenic seep carbonates are produced as a direct result of AOM they are, strictly speaking, associated with the zone of sulfate reduction. However, as shallow marine sediments are highly dynamic environments, carbonates precipitating in the sulfate reduction zone are bound to be affected by any one, or a combination of, the redox processes outlined above. Therefore, their chemical properties are guaranteed of tracing multitudes of interdependent physicochemical and biogeochemical processes that partake in the cycling of carbon, sulfur, iron, and manganese.

Apart from oxic processes at seeps such as aerobic methanotrophy and aerobic sulfide oxidation triggering carbonate corrosion and dissolution (Cai et al., 2006; Birgel and Peckmann, 2008; Himmler et al., 2008), seep carbonates precipitate in a strictly anoxic environment. The following part of this review will summarize the processes that shape, and have shaped, modern and ancient cold seep environments, and how which trace and rare earth metals can help to trace and constrain these processes. However, before addressing the interpretation thereof, we provide an overview of how these elements are best extracted from natural samples in order to allow for reliable (paleo)environmental reconstructions.

Determining metals in carbonates – Analytical approaches

Two types of analytical approaches in determining trace and REE content of have so far been applied to cold seep carbonates. The first and by far the most widely used method is dissolving sample powder and measuring element contents in solvents, which are then analyzed by solution inductively coupled plasma mass spectrometry (ICP-MS). Bulk carbonate samples are leached either partially or completely using various acids of different strengths that attack specific components of the bulk material. The most commonly used acids during this procedure are acetic, nitric, hydrochloric, and hydrofluoric acids used in varying proportions, whereby the first two are more suitable for carbonates, and hydrofluoric acid combinations are more effective in dissolving silicates. Detailed knowledge of the samples prior to dissolution, including mineral and total inorganic and organic carbon content of samples, and information on host sediments is a prerequisite in deciding which leaching method to use. Depending on whether authigenic seep carbonates or background sediments are analyzed, sequential leaching in the former and complete leaching in the latter case is recommended. Rongemaille et al. (2011) tested various leaching methods on bulk carbonate samples at varying temperatures, and gave a clear recommendation for the use of weak nitric acid (5%) for carbonate dissolution over a time frame of 24 hours under constant agitation. As more and more studies using varying leaching methods from bulk sediments and carbonate samples are being published, several of these focus on sequential leaching. Zhang et al. (2015) recommend acetic acid (5%) for REE analyses in bulk carbonates in order to prevent non-carbonates from contaminating the measurements. A sequential leaching protocol using nitric acid during pre-leaching and main leaching is endorsed by Tostevin et al. (2016). The reconstruction of (micro)environments in which seep carbonates precipitated can only be reliably performed if element concentrations of host and/or external non-carbonate material remain unaffected during the leaching process. In our view, bulk sediment analysis of modern or ancient seep sites is only of limited use in the reconstruction of ancient environments, as the temporal (and in some cases even spatial) relationship between the marine sediment and geomicrobiological processes is not always straightforward. Authigenic carbonates on the other hand, being a direct result of these processes, are much more reliable repositories. Therefore, it is recommended that careful sequential leaching using a pre-leaching step and a main leaching step in preferably nitric or acetic acid – as put forward by Zhang et al. (2015) and Tostevin et al. (2016) – is required when analyzing bulk methane seep carbonate samples.

The second method to analyze trace and rare earth metals in modern and ancient seep carbonates is laser ablation ICP-MS. Compared to solution ICP-MS this practice has rarely been used so far for seep carbonates although it constitutes a well-established and highly promising tool in determining elemental concentrations in natural carbonates (Pearce et al., 1992; Woodhead et al., 2004; Hathorne et al., 2007; Schöne et al., 2010; Jochum et al., 2012). Although several wavelengths of lasers are used in the earth sciences (see Liu et al., 2013 for a review), a wavelength of 193 nm is possibly the most suitable for carbonates as it produces more uniform ablation yields and exhibits reduced matrix effects compared to lasers of larger wavelengths (Günther and Heinrich 1999; Guillonge et al., 2003; Sylvester, 2008). For LA-ICP-MS analyses of limestones thin sections of a standard size (48 x 28 mm) are used. Modern carbonates are generally softer than ancient samples, so the thickness should be at least 80 to 100 μm depending on the age. Clear advantages of LA-ICP-MS over solution ICP-MS are the convenient and rapid sample preparation, high micrometer-scale accuracy, and rapid measurement times. Moreover, seep limestones are usually composed of several carbonate mineralogies and clearly identifiable carbonate phases, which reflect different formation conditions. Himmler et al. (2010) showed for the first time how phase-specific trace and REE analyses of seep carbonates yielded notable variations in REE content within different aragonite and calcite cements, confirming different environmental conditions of precipitation. Moreover, from a statistical point of view, laser ablation allows for a much higher amount of data points that can be statistically analyzed.

Despite its advantages, the use of LA-ICP-MS bears certain drawbacks. Most studies analyzing carbonates or carbonate-rich materials use the ^{43}Ca isotope as an internal standard for raw data quantification (Himmler et al., 2010; Chen et al., 2011), meaning that for normalization at least one element (in this case Ca) must be known beforehand (Longerich et al., 1996). For very pure carbonates, a concentration of 40% for Ca may be assumed, although this disregards carbonate solid solutions of Ca with Mg or Sr carbonates. Liu et al. (2016) recently suggested an internal standard-independent scheme to circumvent this issue based on calculation of an ablation yield correction factor. Other possibilities are to simply measure Ca using electron microprobe or X-ray fluorescence, and use the measured values for quantification. The high Sr content in many modern and some seep carbonates may further lead to measurement issues and overestimation of this element, which can however be corrected during raw data evaluation (Woodhead et al., 2004; Fietzke et al., 2008; Vroon et al., 2008).

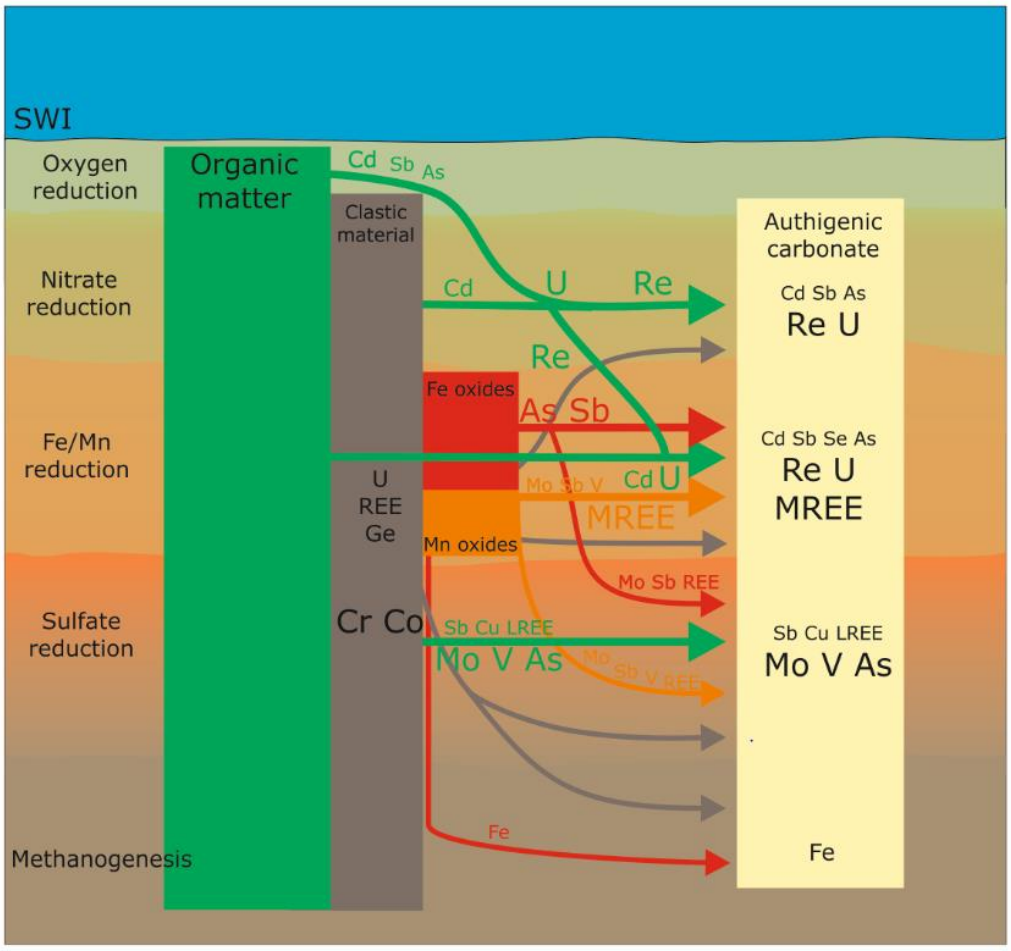


Fig. 3. Schematic illustration of trace metal flux from sources to carbonates during diagenesis, SWI = sediment water interface. Trace elements sources are denoted by rectangles and include organic matter (green), clastic material (brown), Fe oxides (red), Mn oxides (orange) and are mobilized to different degrees in specific redox zones of marine sediments. Rectangle size (top to bottom) shows the relevance of the source in the course of diagenesis. Arrows denote element flux. Arrow colors indicate the source of elements: green = organic matter, gray = clastic material, red = Fe oxides, orange = Mn oxides. Arrow thickness symbolizes the importance of flux of specific elements from a certain source in a redox zone to the authigenic carbonate sink. See text for details. No scale implied.

Constraining the cold seep environment I – Redox processes

The use of trace and rare earth metals to constrain redox processes at cold seeps has come a long way in the past decade. As summarized in part one of this review, the behavior of trace and REEs in natural waters is to a large part governed by redox state, pH, and by the chemical composition of the parent solution. The advantages of using redox-sensitive elements in constraining these processes are, therefore, obvious. Constraining the cold seep environment includes the reconstruction of redox and mineralization processes that lead to the formation of various carbonate minerals that we can analyze today, as well as reconstructing present-day or sub-recent events that shape hydrocarbon seeps.

Considering that the precipitation of seep carbonates requires the sulfate-dependent anaerobic oxidation of methane, the use of Ce anomalies in constraining anoxic conditions has been applied in several modern and ancient seep limestones (Feng et al., 2009a,b, 2013, 2014; Ge et al., 2010; Himmler et al., 2010; Rongemaille et al., 2011; Bayon et al., 2013; Jakubowicz et al., 2015). However, in the light of the results of these and other studies it appears that negative or positive Ce anomalies are insufficient to reliably trace oxygen content or the redox state of pore waters by themselves, particularly in ancient seep carbonates. Firstly, negative Ce anomalies in seawater, which result from oxygenated conditions, are prone to alteration amidst the redox processes within sedimentary pore waters. This is even more the case for progressive diagenesis and burial. Feng et al. (2009a) attributed negative Ce anomalies in some of their samples to an influence of seawater oxygenation. Although correlations between Dy/Sm and Ce/Ce* have been attributed to diagenetic alteration (Shields and Stille 2001), an absence of such correlation neither necessarily implies an original seawater signature, nor does it strictly imply the presence of oxygenated fluids. The interpretation of Ce anomalies is complicated by the observation that oxygenation is not the sole cause of negative Ce anomalies, but that alkalinity and interactions with organic matter may cause similar signals (Pourret et al., 2008; Himmler et al., 2010; Kim et al., 2012). To date, it is not possible to constrain the mechanisms producing Ce anomalies at modern of ancient seeps with reasonable certainty (cf. Himmler et al., 2010). However, varying Ce anomalies in a set of samples can argue for changing redox conditions during carbonate precipitation, which can be expected given the dynamic nature of modern seep environments (Feng et al., 2008, 2013 ; Ge et al., 2010). The combination of Ce anomalies with other tools such as lipid biomarkers (Birgel et al., 2011), other REEs such as Nd (Elderfield and Pagett, 1986; Wright et al., 1987; Ge et al., 2010), or trace element ratios such as V/Cr and

Ni/Co (cf. Palomares et al., 2012) may be a more solid approach in constraining the extent of oxygenation than the use of Ce anomalies by themselves.

Attempts to trace redox processes related to Fe and Mn (oxy)hydroxide reduction at cold seeps typically involve the use of enrichments of the MREEs, which can be quantified using Dy/Sm ratios (cf. Shields and Stille, 2001). The so-called MREE-bulge pattern has been attributed to the reductive dissolution of Fe and/or Mn(oxy)hydroxides, which preferentially release MREEs to pore waters (Haley et al., 2004; Himmler et al., 2013). Although diagenetic alteration also causes MREE enrichment in ancient apatites and conodonts (Grandjean-Lécuyer et al., 1993; Bright et al., 2009), it is unclear if this interpretation is also applicable to carbonates, as they incorporate REEs to a different degree than phosphates (Wright et al., 1987; Zhong and Mucci, 1995). Moreover, results by Freslon et al. (2014) showed that organic matter can also act as an additional source of MREEs to pore waters. Whether or not MREE enrichment is derived from progressive diagenesis or from the release of Fe and Mn(oxy)hydroxides during early diagenesis can be tested by additionally comparing Mg/Sr ratios or La/Yb ratios of the samples (cf. Elderfield and Pagett, 1986). Distinguishing the pools of REEs released by organic matter or by Fe or Mn oxides is a more challenging task. As Fe and Mn are not incorporated to the same degree as REEs into carbonate minerals, correlations between these elements are of little help. Analysis of the redox state of Fe and Mn in host sediments of seep carbonates could assess the degree of the reductive dissolution of oxides, whose reactivity can vary significantly in marine sediments (Canfield et al., 1992; Poulton et al., 2004). Such a conclusion was reached by Crémière et al. (2016) who compared MREE enrichments in seep carbonates to pyrite distribution in combination with Y/Ho ratios.

The most straightforward approach in discerning the Fe or Mn reduction zone from the sulfate reduction zone is by Mo/U ratios. As outlined in part 1 of this review, Mo and U behave differently in marine sediments due to (1) the scavenging effect of the sulfur cycle on Mo, and (2) the behavioral link of U to Fe reduction. These differences result in fractionation of Mo and U in sediments, which is particularly useful in studying modern and ancient hydrocarbon seep sites. According to what has been observed so far concerning Mo and U enrichments in marine continental margin sediments, Mo should be strongly enriched in the sulfate reduction zone compared to U, which should be present in higher concentrations in the Fe reduction zone. Indeed, modern methane seep carbonates are enriched in both Mo and U, although Mo enrichments are significantly higher (Sato et al., 2012; Hu et al., 2014, 2015b; Pierre et al., 2014; Liang et al., 2017). That sulfate reduction produces a fractionation of Mo from U

enrichments at seeps appears to be a correct assessment, yet is it possible to distinguish sulfate-dependent AOM from organoclastic sulfate reduction (OSR) that occurs in most marine sediments? Himmler et al. (2013) argue that HREE-enriched pore water patterns at cold seeps are a consequence of OSR instead of AOM, as remineralization of organic matter releases LREE preferentially over HREEs, and the oxidation of methane does not. During OSR the LREEs can be rapidly re-associated with organic colloids that keep them in solution, thus producing HREE-enriched patterns (cf. Haley et al., 2004). The question then arises of how to discern this effect from simple HREE enrichment patterns by carbonate complexation in oxygenated seawater. If the processes of LREE re-association and carbonate complexation by increased alkalinity – in seawater or in pore waters – cannot be distinguished, then this line of argument needs additional support, such as a systematic assessment of the degree of HREE enrichment of pore waters compared to ocean bottom waters above hydrocarbon seeps. Chen et al. (2016) argue that OSR should enrich Co, Cu, Ni, Zn, and V in addition to Mo in organic carbon-poor sediments, whereby AOM only enriches Mo which is most strongly affected by sulfide production. The question arises if an environment with pore waters of such trace metal distribution remains static enough over time for this pattern to be archived by authigenic carbonate precipitation. Should this be the case, then trace metal ratios can indeed be used to confidently trace redox zonation in modern and ancient seeps, as well as constraining the depth of the respective zones (cf. Li et al., 2016).

The Fe content of carbonates has been used as a measure of distinguishing the methanogenic zone of marine sediments from the shallower zones of Fe and sulfate reduction. One of the first studies applying Fe contents of non-marine carbonates in combination with $\delta^{13}C$ values presented a scheme to distinguish sulfate reduction from methanogenic zone (Curtis et al., 1977); a suggestion corroborated by Irwin et al. (1977). This concept was refined by later studies suggesting that increasing Fe content compared to Mn in authigenic carbonates to be a measure of depth of precipitation, arguing for a stronger influence of fluids typified by methanogenesis than sulfate reduction (Coleman, 1985, 1993). Non marine, as well as marine carbonate cements may contain several thousands of ppm Fe and Mn, and attempts have been made to infer redox conditions and redox potentials, suggested they reflect Eh conditions prevailing during various stages of cementation (Frank et al., 1982; Barnaby and Rimstidt, 1989). In marine sediments where abundant sulfate derived from seawater is available, sulfide produced by sulfate reduction preferably reacts with dissolved Fe to precipitate iron sulfide minerals including amorphous Fe-monosulfide, followed by pyrite and greigite (Wilkin and Barnes, 1996; Raiswell and Canfield, 2012).

Consequently, elevated Fe content in fluids – and carbonates precipitating from these fluids – are enriched in Fe where sulfate is exhausted. This effect has led to the interpretation that carbonates with significant concentrations of Fe must have formed from almost sulfide free pore waters, which are characteristic of the zone of methanogenesis (Coleman, 1993). This interpretation of Fe content in carbonate cements, in combination with phase-specific $\delta^{13}C$ values can distinguish the methanogenic zone from the iron or sulfate reduction zones at cold seeps (Stakes et al., 1999; Pierre et al., 2014; Hu et al., 2015a; Zwicker et al., 2015).

Constraining the cold seep environment II – Fluid composition

Alkalinity is a key parameter that governs carbonate precipitation at methane seeps (Ritger et al., 1987), and varies strongly in time and space depending on methane flux rate (Luff and Wallmann, 2003; Wallmann et al., 2006). Cerium anomalies are affected by organic matter mineralization, as dissolving organic particulates effectively complex and adsorb the LREEs including Ce, producing negative Ce anomalies in the residual fluids (Pourret et al., 2008). As alkalinity is directly controlled by the mineralization of organic matter, Ce anomalies have been put forward as a measure for alkalinity changes and gradients at modern methane seeps (Himmler et al., 2010; Rongemaille et al., 2011). However, as discussed previously, Ce anomalies are problematic to interpret and can be assigned to a multitude of processes including organic matter remineralization, mixing by pore fluids with oxygenated seawater, and changes from oxic to anoxic conditions (Hu et al., 2014, Franchi et al., 2015; Jakubowicz et al., 2015).

Mineralization of organic matter plays a key role in the precipitation of seep carbonates. In one of the first studies of its kind, Haley et al. (2004) put forward that REE patters showing distinct enrichments of the HREEs over LREEs may be linked to a particulate organic carbon (POC) source of REEs. They argued how the ratio of HREEs to LREEs reflect changing dynamics of organic matter remineralization, and how a high ratios may reflect preferential HREE complexation with DOC coupled with a tendency of the LREE to re-adsorb to POC. Their model demonstrated how POC acts as a primary carrier of REEs in marine sediments where active microbial mineralization takes place, and how such resulting REE patterns of pore waters can inverse or alter the typical REE patterns assigned to oxygenated seawater. This pioneering work has since served as a solid basis for interpreting REEs in pore waters and carbonates at cold seeps. Various carbonate cement types linked to different modes of precipitation at

seeps include banded and botryoidal aragonite cement, as well as a cryptocrystalline, brownish-yellowish form of cement (Peckmann et al., 2003, Hagemann et al., 2012). It has been speculated that the latter cement is more strongly involved in direct precipitation of carbonate by microbial mats, and may contain increased contents of organic matter (Leefmann et al., 2008; Hagemann et al., 2012). As discussed by Haley et al. (2004), the LREEs may be preferentially absorbed by POC compared to the HREEs, and new, yet published data on phase specific REE from modern and ancient cold seep carbonates gathered by the Vienna Sedimentology Group seem to suggest that REEs can be used to distinguish carbonate cements with increased contents of organic matter from those cements who have higher contents of inorganic carbon. On these grounds it has been put forward that yellow cryptocrystalline aragonite cements at modern and ancient methane seeps (cf. Peckmann et al., 2003; Leefmann et al., 2008; Himmler et al., 2010) may indeed be mineralized remnants of biofilms, possibly even representing fossilized microbial AOM communities. Distinguishing the mode of precipitation of carbonate cements in microbialites has been attempted using enrichments of LREEs over HREEs, yet this method is not unambiguous (Frimmel, 2009; Corkeron et al., 2012). Moreover, experimental studies have so far yielded contrasting results with respect to the complexation of REEs by organic substances. Kamijo et al. (1998) suggested that terrestrial soil microbes preferentially scavenge LREEs from solution, whereas Takahashi et al. (2005, 2007) provided evidence for HREE enrichment onto cell walls. The question of microbial interaction with REEs in solution is further complicated as no studies have yet been conducted that investigate REE interaction with marine microbial communities.

Residence times and circulation of DOM in marine pore waters may affect REE concentrations in sediment depths of up to several tens of meters (Kim et al., 2012). In the context of DOM the results presented by Pourret et al. (2008) have been inferred to assign Ce anomalies to fluctuations of specifically humic acid concentrations in sedimentary pore waters. Several case studies have since argued that negative Ce anomalies can also be caused in anoxic waters by preferential adsorption of Ce(IV) onto humic acids, leaving the residual waters depleted in Ce(IV) (Pourret et al., 2008; Himmler et al., 2010; Kim et al., 2012; Franchi et al., 2015). However, as stated previously, Ce anomalies by themselves cannot be used with certainty to assess the degree of organic matter influence, much less the concentrations of DOM in ancient pore waters.

Many modern hydrocarbon seep sites are dominated by the presence of high molecular weight organic compounds and crude oils (Kennicutt et al., 1988; MacDonald et al., 2000; Joye et al., 2004;

Naehr et al., 2009; Birgel et al., 2011; Körber et al., 2014). Hydrocarbon seeps typified by voluminous expulsions of crude oil can strongly affect local micro- and macrofauna, and produce unique habitats for distinct crude oil-tolerant fauna (MacDonald et al., 2004; Orcutt et al., 2010; Sahling et al., 2016). Differences in oil- and methane-dominated hydrocarbon seeps today can be easily assessed by submersible investigations, yet this distinction is not as straightforward in the geologic record. In an attempt to define proxies that may allow for a reliable distinction between the two types of seepage, Smrzka et al. (2016) found that modern and putative ancient oil seep carbonates are characterized by low Mo/U ratios, as well as higher total contents of REEs. This study provided first promising results, yet more systematic work needs to be conducted to solidify these findings.

Constraining the cold seep environment III –Seepage in space and time

Within the context of this review, constraining seepage dynamics is concerned with how trace and rare earth metal contents of different carbonate minerals can yield information to determine the rate and persistence of fluid flux, seepage variability and spatial distribution, the position of the sulfate-methane transition zone (SMTZ) in the sedimentary column, and diagenetic evolution at modern and ancient seep sites. This is valuable information of the dynamics of methane seepage, AOM, the position of the SMTZ through time, and can be used to infer estimates of global methane budgets. Prior to the application of trace and REEs to address these issues, major element chemistry and mineralogy of carbonates provided a useful approach. Several studies have compared Mg/Sr ratios of carbonates as a measure of diagenetic progression, burial, and recrystallization of aragonite to calcite in the course of diagenesis (Ritger et al., 1987; Savard et al., 1996; Campbell et al., 2002; Buggisch and Krumm, 2005; Peckmann et al., 2007; Leefmann et al., 2008; Joseph et al., 2013). High resolution studies of Mg, Sr, Ca, Mn, and Fe contents in concert with mineralogical investigations have enabled to track temporal and spatial changes in methane seepage, and to detect ancient horizons where AOM occurred. Downcore trace metal analyses have enabled to recognize precipitation events within specific sedimentary horizons at seeps, which can point to carbonate authigenesis within a certain depth intervals in a sedimentary core using Sr/Ca and Mg/Ca ratios, as well as to fossil AOM horizons in seep sediments (Bayon et al., 2007). Nöthen and Kasten (2011) demonstrated how temporal and spatial changes in methane seepage can be deduced by geochemical and mineralogical signatures preserved in seep carbonates. They argued that active and persistence of seepage

and AOM can be inferred from layers for aragonite and high-Mg calcite in the sedimentary column. These approaches have also been applied with success to ancient seep deposits, where systematic assessments of elemental ratios of Sr, Ca, Mn, and Fe can aid in determining the extent of recrystallization, burial, and to constrain the influence of deep fluids (Joseph et al., 2013). In a similar fashion, late diagenesis at hydrocarbon seeps has been traced using REEs. In a comparative approach, Feng et al. (2009a) demonstrated how late stage diagenetic processes produce negative correlations between Ce anomalies and Dy/Sm ratios, as well as positive correlations between total REE contents and Ce anomalies.

Seepage dynamics play an important role in the geomicrobiology of ancient and modern cold seeps. It has been suggested that the temporal variability of fluid flux is archived by REEs and trace element patterns of authigenic carbonates (Feng et al., 2010). Varying contents in REEs in seep carbonates may result in precipitation rates of minerals, which are in turn related to seepage intensity. Based on this assumption, Ge et al. (2010) suggested that low REE contents in seep carbonates could be the result of precipitation in a low flux environment. Total REE content is usually determined by which phase is analyzed, and specific carbonate cements yield higher content than others (cf. Himmler et al., 2010). Variations in Ce anomalies in seep limestones have been interpreted as changing redox conditions, which are in turn caused by variations in gas and fluid flux (Feng et al., 2013). Such lines of argument can be solidified by combining REEs with trace metals, and comparing these contents to the mineralogy of the respective sample. High-Mg calcite at seeps has yielded high contents of REEs, Mo, U, and Cd, suggesting low seepage flux at some depth below the sediment-water interface (Feng and Chen, 2015). High Mo contents of seep sediments and carbonates may also indicate high sulfate flux promoting high rates of AOM and sulfide production, which can then be stored efficiently as thiomolybdate in pyrites (Hu et al., 2015b). The utility of Mo is valuable in constraining flux rates at seeps, as it is one of only a few trace metals that directly respond to variations of seepage flux intensity. Uranium has also been shown to produce moderate enrichments at seeps in response to increase seepage flux in suboxic sediments (Chen et al., 2016), and Ba – Mo enrichments have been assigned to transient seepage activity at modern seeps (Hu et al., 2017). Seawater influence at seeps is traceable using Y/Ho ratios, and can likewise provide clues to seepage intensities. Suprachondritc, seawater-like Y/Ho ratios archived in carbonates suggest that precipitation took place in waters dominated or at least influenced by seawater and thus close to the SWI, arguing against high flux rates (Himmler et al., 2010).

Being able to identify the depth and extent of the SMTZ at ancient and modern seeps can give important indications on past seepage dynamics that may yield information on the future behavior of seepage systems today. Barite and carbonate enrichments have been used to trace the shift of the SMTZ, and systematic application of metal ratios have been applied to identify fossil horizons of AOM (Nöthen and Kasten, 2011). As the depth of the SMTZ is closely linked to seepage rates, trace and REEs can likewise be used to trace the depth of paleo-SMTZs (cf. Li et al., 2016). Peketi et al. (2012) proposed C-S-Mo systematics in marine sediments as a potential tool to identify paleo-SMTZs and sulfide seepage events by attributing Mo enrichment peaks in sedimentary profiles to pulses of elevated H_2S production associated with AOM and methane seepage.

Modes and sources of enrichment – External, authigenic, and scavenging processes

From what this review has covered so far, it seems clear that, at least on a local scale, cold seep carbonates are an effective sink for trace and rare earth elements (Himmler et al., 2013; Lemaitre et al., 2014). Yet the question remains on the origins of trace and rare earth metals, and by what first order means they can be enriched in cold seep sediments and authigenic carbonates. We can distinguish three modes, or sources, of enrichment at cold seeps: (1) external enrichment, (2) enrichment via scavenging processes, and (3) authigenic enrichment. At first glance these three types of enrichment may seem to cover one or two of the same processes. However, the following section will elucidate how and why such a distinction can be helpful when addressing the issue of separating them. All three modes of enrichment examine the process of delivering trace and rare earth metals to marine sedimentary pore waters. External enrichment denotes the addition of metals to pore waters from a source other than those that are in direct contact with pore waters, such as marine sediments. Further, with respect to hydrocarbon seeps, external sources are strictly non-seepage specific processes that add to the element input of pore waters. These external sources include the water column above the seep, hydrothermal exhalations in the vicinity of the seep, particle flux to the seafloor, and freshwater input from rivers. Anthropogenic input from water and sediment pollution are excluded here, as we are only considering pristine sediments.

External enrichment

As outlined above, the water column above sediments is by far the largest external source of trace and rare earth metals to marine sediments. The same is true for sites of hydrocarbon seepage, yet although dominant, seawater itself does not constitute such a dominant source for these metals as is the case for sedimentary pore waters unaffected by methane seepage. The most obvious method of distinguishing a REE pool derived from seawater is comparing total REE contents of a sample to its Y/Ho ratios, analyzing REE patterns with respect to typical signals for seawater, and to scan for possible contamination by correlation of total REE contents to elements diagnostic for terrigenous sources such as Al, Ti, or Sc. Rare earth element patterns in authigenic carbonate that mimic that of oxygenated seawater, have suprachondritic Y/Ho ratios and do not correlate with the above mentioned elements, are very likely to be sourced from bottom waters. Additionally, one can scan for indicators of diagenetic modification of the respective REE content using one or several of the approaches outlined in section 1.

Hydrothermal input of trace metals to the ocean is relevant on a global scale (Douville et al., 1999), yet its impact can vary strongly on a local scale. Detecting significant hydrothermal input of trace and/or REEs in seep deposits is a comparably unambiguous procedure, as it relies on the most prominent tool to detect this source: Eu anomalies (Bau, 1991; Leybourne and Johannesson, 2008; Allwood et al., 2010). Strong Eu anomalies have been interpreted as being hydrothermal in origin over decades of research, and have likewise been adopted to trace the influence and mixing of hydrothermal fluids with either seawater or pore water at hydrocarbon seeps (Kim et al., 2012; Franchi et al., 2015; Jakubowicz et al., 2015).

Although riverine input constitutes the largest source of trace and rare earth metals to the oceans (Holser, 1997; Abbott et al., 2015), only in very few cases does this external source of enrichment play a role at seeps. Although REEs can be of great use in tracing river discharge in corals and microbial carbonates (cf. Sholkovitz and Shen, 1995; Frimmel, 2009; Huang et al., 2009), considering rivers as a potentially relevant source for trace and rare earth metals at seeps has so far been a minor issue. However, if the geological setting allows for such an interpretation, REEs can be used to trace freshwater input to the seep (cf. Novikova et al., 2015).

Particle flux to the seafloor, i.e. the effect of primary production, can always be regarded as a relevant source of trace and rare earth metals to cold seep sediments, provided the oceanographic setting

allows for significant particle rain onto the seepage site. Surprisingly, only one study to date used Ni/Al and Cu/Al ratios as palaeoproductivity proxies to determine the influence of productivity on the generation of suboxic conditions (Li et al., 2016). If a cold seep is located below an upwelling zone, it can be of interest to detect particle flux to seafloor sediments to pore waters, and to scan for these signals in authigenic carbonates using trace element ratios and correlations (cf. Rosenthal et al., 1995; Piper and Perkins, 2004; Nameroff et al., 2002; Piper and Perkins, 2004; Tribovillard et al., 2006).

Scavenging processes

As outlined in a previous section of the review, scavenging of dissolved trace and rare earth metals from seawater by metal oxides and/or organic particles is a major process that governs the behavior and fractionation of trace and REEs. At cold seeps, however, scavenging of these elements exerts a direct influence on the efficiency and the degree of additional input of trace and REEs from seawater to the sediment. In what was possibly the first study on the effect of emanating seepage fluids on trace metal distribution and behavior within the vicinity of active seeps, Bayon et al. (2011) showed how the input of reduced Fe-rich waters into oxygenated bottom waters above an active seep triggers the precipitation of Fe(oxy)hydroxides in the water column. Due to the observed concentration anomalies of dissolved Fe, Mn, and also REEs, they suggested that the actively formed Fe(oxy)hydroxide phases during seepage are responsible for scavenging REEs from seawater, which settle back to the seafloor where they can be released by reductive dissolution during early diagenesis. Although the oxidation of Fe to form oxides is much faster than for Mn, Fe oxidation rates directly above an active seep are somewhat sluggish due to the complexation of organic ligands and the reduced nature of the fluids (Lemaitre et al., 2014). Nonetheless, it has been confirmed that hydrocarbon seeps constitute a significant, albeit local source of dissolved Fe to the ocean, and can thereby lead to measureable depletions of trace and rare earth metals in bottom waters. This intriguing discovery that seepage of reduced fluids actively scavenges REEs from surrounding seawater lead to subsequent investigations on the processes, which has been termed the "particulate shuttle process" by Tribovillard et al. (2013, although the term shuttle has previously been used to describe trace element behavior in anoxic basins of the Black and Baltic Seas, see Dellwig et al., (2010)). These authors expanded the idea of REE scavenging to enrichments of other metals including As, Sb, Mo, U, Cu, and Ni, and put forward three hypotheses on how certain metals can be actively enriched

in seafloor sediments that are enabled by processes that only operate at active cold hydrocarbon seeps. The sorption of newly formed Fe and Mn oxides that are subsequently transferred to sediments and reduced can account for enrichments of Mo, As, Sb, but not U, and V, which do not sorb well onto these metal oxide phases. They concluded that the particulate shuttle only accounts for the enrichment of those metals that adsorb efficiently onto metal oxides. The selective enrichment of the particulate shuttle would likewise explain trace metal enrichments at mud volcanoes, where the exact same enrichment patterns (Mo, As, and Sb, but no U) have been documented (see also Cangemi et al., 2010). In a subsequent study, Hu et al. (2014) confirmed the idea of a selective particulate shuttle process that lead to systematic enrichments of Mo, Sb, and As, but not of U.

Authigenic seep-related enrichment

This mode of enrichment focuses on physical, chemical and biological processes that operate exclusively at hydrocarbon seeps, and are not found elsewhere in marine sediments. These processes include physical transport of deep, reduced fluids towards the seafloor, and the oxidation of hydrocarbons and methane contained in these fluids. Fluid seepage at passive continental margins is governed by tectonic processes, sediment loading, sea-level changes, and thermohaline convection (Suess, 2014 and references therein), which act in concert or separately to squeeze deep fluids towards the seafloor. Cold seeps can be active over long periods of time, and provide a stable and reliable source of energy for chemosynthesis (Paull et al., 1984; Kulm et al., 1986; Wallmann et al., 1997; Van Dover et al., 2003; Judd and Hovland 2007). The reduced fluids have been in contact with deeper sedimentary successions, and are often enriched in hydrocarbons and trace metals. Strictly speaking, fluid ascension and import of trace and rare earth metals from the deep can be considered an external source, yet the process of seepage is in itself a defining factor of marine cold seeps. Especially seepage from submarine mud volcanoes is prone to delivering warm fluids loaded with trace metals to shallow sediments, and physical transport of ascending fluids have been invoked to enrich cold seep environments in Fe, Sr, Ba, Zn, Cu, Mn As, and Sb (Nath et al., 2008; Liu et al., 2009; Cangemi et al., 2010). Distinguishing the input of trace metals from ascending deep fluids has been attempted using Nd isotopes, which has proved to be a potent tracer for migrating fluids that have interacted with deep sedimentary reservoirs at ancient and modern cold seeps (Piepgras

and Wasserburg, 1985; Jakubowicz et al., 2015), although cold seeps do not represent a relevant Nd source to the modern ocean (Bayon et al., 2011).

The most important reaction that defines the water chemistry at cold seep environments is AOM, which produces bicarbonate and sulfide from methane and sulfate. Specifically, the production of sulfide will have strong effects on the distribution and speciation of dissolved trace metals in the pore waters as outlined in section 1. However, microbial sulfate reduction is a process that is almost ubiquitous in the modern ocean, and the seepage of methane- or hydrocarbon-rich fluids is not a prerequisite for the production of sulfide in sedimentary porewaters (Jørgensen, 1982; Canfield, 1989; Bowles et al., 2014). The intense sulfide production at sites of vigorous seepage creates an ideal environment for the accumulation of trace metals prone to be scavenged by dissolved reduced sulfur species, as well as sulfide precipitates such as pyrite. Authigenic enrichment linked to oxidation of methane and high molecular weight hydrocarbons is similar to enrichments of trace and REEs associated directly with fluid composition described earlier. However, authigenic seep-related enrichment distinguishes between fluid composition, and the processes that occur due to the chemical composition of the fluids such as AOM. Hydrocarbon compounds themselves add trace and REEs to solution, yet their subsequent dissolution produces sulfides that scavenge and archive these elements for the geologic record.

Future perspectives for the use of trace metal proxies in seep research and beyond

Follow-up studs based on this thesis

The immediate follow-up studies inspired by the outcomes and results of this thesis include a highly promising data set derived from yellow aragonite cements within Oligocene to Carboniferous seep limestones. Several deposits feature yellow aragonite cements, which is a cryptocrystalline, highly irregular variation of aragonite cement partially recrystallized into calcite in some of the samples. Phase-specific trace and REE geochemistry revealed that the better preserved yellow aragonite (i.e. determined by very low Mg/Sr ratios) features distinct shale-normalized enrichments of the LREEs over the HREEs. Such signatures are highly uncommon for any marine limestones, as most feature shale-normalized REE patterns that resemble seawater (HREE enriched patterns), or feature flat shale-normalized patterns suggesting contamination from surrounding clay minerals derived from the host sediment. Moreover, recrystallized yellow aragonites to calcite (i.e. determined by very high Mg/SR ratios) do not show such LREE enrichments. Rather, they are typified by flat to slightly HREE enriched REE patterns. These systematic patterns are interpreted in that LREE enriched patterns in well preserved yellow aragonites are remnants of fossilized microbial mats that have retained LREE-enriched signatures. This data set further demonstrated that recrystallization of aragonite cements to calcite do not necessarily preserve REE patterns, and that cautious examination is always recommended when interpreting REE data from ancient limestones.

The second study that is currently in progress is a systematic solution-ICP-MS study on several ancient brachiopod-dominated seep deposits derived from North America, Europe, Africa, and Asia, spanning from the Late Devonian to the Oligocene. All of these deposits may have been potential sites of ancient oil seepage through the Phanerozoic; an interpretation that has so far relied on circumstantial evidence and paleontological considerations. This systematic approach using trace and REEs will test this hypothesis, and will either confirm of reject the notion that some, or all, of these deposits were in fact oil seeps. Based on the extensive data set and the resulting interpretation from trace and REEs, a new assessment on macrofaunal ecology and evolution of chemosysmthesis-based life through geologic time can be made, which would be a big step forward in our understanding of these highly unique ecosystems

that operate independent of sunlight. This study demonstrates the relevance of trace element geochemistry of fossil hydrocarbon seep carbonates beyond the scope of the geosciences.

As can be seen from the application opportunities for trace and rare earth metals in authigenic carbonates outlined above, this area of research has come a long way in the past 20 years. Especially in the past couple of years the amounts of studies reporting new data on metal concentrations and possible proxies in seep carbonates shows how much potential is still available, and how much is still left to be explored. This final chapter addresses unanswered questions and how to tackle them, and outlines some areas of research that should be focused on more deeply so as to improve the effectiveness of trace metal geochemistry as a tool for reconstructing ancient environments.

Much information has been gathered over the past decades on the aquatic chemistry of trace metals, particularly on their behavior in marine waters of higher salinity. This information greatly aids our understanding and interpretation of these metals with respect to ancient marine environments. However, their behavior with respect to microbiology has been comparatively understudied. This statement is not necessarily valid to all trace metals, as some trace metals have generally received more attention than others. The reason for the rather unevenly distributed focus of scientific research is obvious, as some metals have direct consequences on human activity, health, and can severely affect our environment. Unsurprisingly, elements such as As, U, and Cr have received more attention than other trace metals due to such concerns. There is a need for more detailed applied research on other trace metals that are of more relevance to reconstructing ancient environments and to explore their full potency as geochemical proxies in Earth's history. The most relevant studies to be undertaken in coming years should focus on cultivation studies of marine archaea and bacteria and their passive and active interactions with relevant trace metals, most notably Mo, U, REEs, Ni, V, Sb, and Se. Some information, particularly in the case of U, is available to date, yet most studies have been conducted on terrestrial freshwater microbial communities. Although cultivating anaerobic marine microbial consortia is a demanding task, it is nonetheless possible, and studies with a strong focus on trace metal adsorption, desorption, passive enrichment and active metabolic utilization and cycling of trace metals could yield valuable information with respect to the research questions addressed by this thesis.

Research outlook

Further research outlooks could address the question of the modes and mechanisms of trace metal – carbonate mineral interactions. Very much information has been gathered, particularly with respect to the REE in this issue, and experimental studies have yielded solid, yet also ambiguous and contradictory results as outlined in part two of the last manuscript. This complex issue can however be addressed more thoroughly by conducting series of systematic experimental studies exploring all the relevant factors governing trace metal incorporation into carbonate minerals. This is, of course, a time consuming labor intensive and costly undertaking, yet only a systematic approach can yield more detailed information on how specific trace metals are taken up and archived by natural carbonates. Specific trace metals such as Mo, Ni, Cu, Sb, Se, and As have received comparably little attention with respect to these research questions. Particularly in the case of Mo – which can be regarded as one of the most important trace metals in geochemical proxy research – hardly any studies have been conducted at all concerning its incorporation into carbonate minerals. There is much potential in such experimental studies, which can be regarded as the most important basis for our understanding of the complex interplay of trace elements in solution and trace elements in solid phases.

As outlined in part four of the third manuscript of this thesis, cold seep carbonates are rewarding in terms of trace metal geochemistry, as they form within highly dynamic environments where a multitude of biogeochemical processes occur simultaneously that can all be traced – to different degrees – by trace metal geochemistry. Most of the information derived for the interpretation of trace metal contents in carbonates and their host sediments stem from laboratory experimental work as outlined above. Yet, many of the aspects that have so far been addressed by studies focusing on trace metal chemistry at modern and ancient hydrocarbon seeps could also be applied in a systematic way to other, similar types of carbonate deposits in the rock record. Some of these deposits – that include Proterozoic and Phanerozoic cap carbonates – have already been touched upon in part three of manuscript three. Systematic analysis of trace metal contents and ratios, combined with C and O stable isotope geochemistry, lipid biomarkers, carbonate-associated sulfate, and stable isotopes of more unconventional metals such as Mo, V, and Ni could yield more detailed and valuable information on depositional environments, redox conditions, and modes of formation of many carbonate deposits whose origins and modes of formation are not as well understood as is the case for hydrocarbon seep carbonates. As an

outlook put forward by this thesis, it can be of great value for future projects and endeavors to apply trace metals to carbonates under different questions and problems as posed by seep carbonates.

References

Abbott, A.N., Haley, B.A., McManus, J., Reimers, C.E., 2015. The sedimentary flux of dissolved rare earth elements to the ocean. Geochim. Cosmochim. Ac. 154, 186–200.

Agaki, T., Hashimoto, Y., Fu, F.-F., Tsuno, H., Tao, H., Nakano, Y., 2004. Variation of the distribution coefficients of rare earth elements in modern coral-lattices: Species and site dependencies. Geochim. Cosmochim. Ac. 68, 2265–2273.

Akagi, T., 2013. Rare earth element (REE)-silicic acid complexes in seawater to explain the incorporation of REEs in opal and the "leftover" REEs in surface water: New interpretations of dissolved REE distribution profiles. Geochim. Cosmochim. Ac. 113, 174–192.

Alexandratos, V.G., Elzinga, E.J., Reeder, R.J., 2007. Arsenate uptake by calcite: macroscopic and spectroscopic characterization of adsorption and incorporation mechanisms. Geochim. Cosmochim. Ac. 71, 4172–4187.

Algeo, T.J., Lyons, T.W., 2006. Mo-total organic carbon covariation in modern anoxic marine environments: Implications for analysis of paleoredox and paleohydrographic conditions. Paleoceanography 21, PA1016, doi:10.1029/2004PA001112.

Algeo, T.J., Maynard, J.B., 2004. Trace-element behavior and redox facies in core shales of Upper Pennsylvanian Kansas-type cyclothems. Chem. Geol. 206, 289–318.

Algeo, T. J., Maynard, J.B., 2008. Trace-metal covariation as a guide to water-mass conditions in ancient anoxic marine environments. Geosphere 4, 872–887.

Algeo, T.J., Rowe, H., 2012. Paleoceanographic applications of trace-metal concentrations data. Chem. Geol. 324–325, 6–18.

Algeo, T.J., Tribovillard, N., 2009. Environmental analysis of paleoceanographic systems based on molybdenum-uranium covariation. Chem. Geol. 268, 211–225.

Allwood, A.C., Kamber, B.S., Walter, M.R., Burch, I.W., Kanik, I., 2010. Trace elements record depositional history of an Early Archean stromatolitic carbonate platform. Chem. Geol. 270, 148–163.

Allwood, A.C., Walter, M.R., Kamber, B.S., Marshall, C.P., Burch, I.W., 2006. Stromatolite reef from the Early Archaean era of Australia. Nature 441, 714–718.

Altermann, W., Kazmierczak, J., Oren, A., Wright, D.T., 2006. Cyanobacterial calcification and its rock-building potential during 3.5 billion years of Earth history. Geobiology 4, 147–166.

Anbar, A.D., Creaser, R.A., Papanastassiou, D.A., Wasserburg, G.J., 1993. Rhenium in seawater: Confirmation of generally conservative behavior. Geochim. Cosmochim. Ac. 56, 4099–4103.

Andersson, A.J., MacKenzie, F.T., 2013. The marine carbon system and ocean acidification during Phanerozoic time. Geochem. Persp. 2, 1–227.

Andreae, M.O., 1979. Arsenic speciation in seawater and interstitial waters: The influence of biological-chemical interactions on the chemistry of a trace element. Limnol. Oceanogr. 24, 440–452.

Andreae, M.O., Froelich, P.N., 1984. Arsenic, antimony, and germanium biogeochemistry in the Baltic Sea. Tellus 38B, 101–117.

Andres, Y., Texier, A.C., Le Cloirec, P., 2003. Rare earth element removal by microbial biosorption: a review. Environ. Technol. 24, 1367–1375.

Archer, D., Maier-Reimer, E., 1994. Effect of deep-sea sedimentary calcite preservation on atmospheric CO_2 concentration. Nature 367, 260–263.

Armstrong-Atlin, J.S., Verma, S.P., Madhavarju, J., Lee, Y.I., Ramasamy, S., 2003. Geochemistry of Upper Miocene Kudankulam Limstones, Southern India. Int. Geol. Rev. 45, 16–26.

Auger, Y., Bodineau, L., Leclercq, S., Wartel, M., 1999. Some aspects of vanadium and chromium chemistry in the English Channel. Cont. Shelf Res. 19, 2003–2018.

Azmy, K., Brand, U., Sylvester, P., Gleeson, S.A., Logan, A., Bitner, M.A., 2011. Biogenic and abiogenic low-Mg calcite (bLMC and aLMC): Evaluation of seawater-REE composition, water masses and carbonate diagenesis. Chem. Geol. 280, 180–190.

Baldwin, G.J., Thurston, P.C., Kamber, B.S., 2011. High-precision rare earth element, nickel, and chromium chemistry of chert microbands pre-screened with in-situ analysis. Chem. Geol. 285, 133–143.

Banner, J.L., Hanson, G.N., 1990. Calculation of simultaneous isotopic and trace element variations during water-rock interaction with applications to carbonate diagenesis, Geochim. Cosmochim. Ac. 54, 3123–3137.

Banner, J.L., Hanson, G.N., Meyers, W.J., 1988. Rare earth element and Nd isotopic variations in regionally extensive dolomites from the Burlington-Keokuk Formation (Mississippian): Implications for REE mobility during carbonate diagenesis. J. Sed. Petrol. 54, 415–432.

Barker, S.L.L., Cox, S.F., 2011. Oscillatory zoning and trace element incorporation in hydrothermal minerals: insights from calcite growth experiments. Geofluids 11, 48–56.

Barnaby, R.J., Rimstidt, J.D., 1989. Redox conditions of calcite cementation interpreted from Mn and Fe contents of authigenic calcites. J. Geol. Soc. Bull. 101, 795–804.

Barwise, A.J.G., 1990. Role of nickel and vanadium in petroleum classification. Energ. Fuel. 4, 647–652.

Bau, M., 1991. Rare-earth element mobility during hydrothermal and metamorphic fluid-rock interaction and the significance of the oxidation state of europium. Chem. Geol. 93, 219–230.

Bau, M., 1999. Scavenging of dissolved yttrium and rare earths by precipitating iron oxyhydroxide: Experimental evidence for Ce oxidation, Y-Ho fractionation, and lanthanide tetrad effect. Geochim. Cosmochim. Ac. 63, 67–77.

Bau, M., Alexander, B., 2006. Preservation of primary REE patterns without Ce anomaly during dolomitization of Mid-Paleoproterozoic limestone and the potential reestablishment of marine anoxia immediately after the “Great Oxidation Event”. S. Afr. J. Geol. 109, 81–86.

Bau, M., Dulski, P., 1996. Distribution of yttrium and rare-earth elements in the Penge and Kuruman iron formations, Transvaal Supergroup, South Africa. Precambrian Res. 79, 37–55.

Bau, M., Dulski, P., 1999. Comparing yttrium and rare earths in hydrothermal fluids from the Mid-Atlantic Ridge: implications for Y and REE behavior during near-vent mixing and for the Y/Ho ratio of Proterozoic seawater. Chem. Geol. 155, 77–90.

Bau, M., Möller, P., 1992. Rare earth element fractionation in metamorphogenic hydrothermal calcite, magnesite and siderite. Min. Petrol. 45, 231–246.

Bau, M., Koschinsky, A., Dulski, P., Hein, J.R., 1996. Comparison of the partitioning behaviours of yttrium, rare earth elements, and titanium between hydrogenetic marine ferromanganese crusts and seawater. Geochim. Cosmochim. Ac. 60, 1709–1725.

Bayon, G., Birot, D., Ruffine, L., Caprais, J.-L, Ponzevera, E., Bollinger, C., Donval, J.-P., Charlou, J.-L., Voisset, M., Grimaud, S., 2011. Evidence for intense REE scavenging at cold seeps from the Niger Delta margin. Earth Planet. Sci. Lett. 213, 443–452.

Bayon, G., Dupré, S., Ponzevera, E., Etoubleau, J., Chéron, S., Pierre, C., Mascle, J., Boetius, A., de Lange, G.J., 2013. Formation of carbonate chimneys in the Mediterranean Sea linked to deep-water oxygen depletion. Nat. Geosci. 6, 755–760.

Bayon, G., Pierre, C., Etoubleau, J., Voisset, M., Cauquil, E., Marsset, T., Sultan, N., Le Drezen, E., Fouquet, Y., 2007. Sr/Ca and Mg/Ca ratios in Niger Delta sediments: Implications for authigenic carbonate genesis in cold seep environments. Mar. Geol. 241, 93–109.

Behrends, T., Van Cappellen, P., 2005. Competition between enzymatic and abiotic reduction of uranium(VI) under iron reducing conditions. Chem. Geol. 220, 315–327.

Behrens, M.K., Muratli, J., Pradoux, C., Wu, Y., Böning, P., Brumsack, H.-J., Goldstein, S.L., Haley, B., Jeandel, C., Paffrath, R., pena, L.D., Schnetger, B., Pahnke, K., 2016. Rapid and precise analysis of rare earth elements in small volumes of seawater – Method and intercomparison. Mar. Chem. 186, 110–120.

Bekker, A., Karhu, J.A., Eriksson, K.A., Kaufman, A.J., 2003. Chemostratigraphy of Paleoproterozoic carbonate successions of the Wyoming Craton: tectonic forcing of biogeochemical change? Precambrian Res. 120, 279–325.

Bellanca, A., Masetti, D., Neri, R., 1997. Rare earth elements in limestone/marlstone couplets from the Albian-Cenomanian Cismon section (Venetian region, northern Italy): assessing REE sensitivity to environmental changes. Chem. Geol. 141, 141–152.

Belzile, N., 1988. The fate of arsenic in sediments of the Laurentian Trough. Geochim. Cosmochim. Ac. 52, 2293–2302.

Belzile, N., Lebel, J., 1986. Capture of arsenic by pyrite in near-shore marine sediments. Chem. Geol. 54, 279–281.

Belzile, N., Chen, Y.-W., Wang, Z., 2001. Oxidation of antimony (III) by amorphous iron and manganese oxyhydroxides. Chem. Geol. 174, 379–387.

Bender, M.L., Schultz, C., 1969. The distribution of trace metals in cores from a traverse across the Indian Ocean. Geochim. Cosmochim. Ac. 33, 292–297.

Bentley, R., Chasteen, T.G., 2002. Microbial methylation of metalloids: arsenic, antimony, and bismuth. Microbiol. Mol. Biol. Rev. 66, 250–271.

Berger, W.H., 1983. Increase of carbon dioxide in the atmosphere during deglaciation: the coral reef hypothesis. Naturwissenschaften 69, 87–88.

Berner, R.A., 1966. Chemical diagenesis of some modern carbonate sediments. Am. J. Sci. 264, 1–36.

Bertine, K.K., 1973. The deposition of molybdenum in anoxic waters. Mar. Chem. 1, 43–53.

Bertine, K.K., Lee, D.S., 1983. Antimony content and speciation in the water column and interstitial waters of Saanich Inlet. In: Wong, C.S., Boyle, E., Bruland, K.W., Burton, J.D., Goldberg, E.D. (Eds.), Trace Metals in Sea Water. NATO Adv. Res. Inst., Plenum, New York, 21–38.

Bertram, C.J., Elderfield, H., 1993. The geochemical balance of the rare earth elements and neodymium isotopes in the oceans. Geochim. Cosmochim. Ac. 57, 1957–1986.

Birgel, D., Peckmann, J., 2008. Aerobic methanotrophy at ancient marine methane seeps: A synthesis. Org. Geochem. 39, 1659–1667.

Birgel, D., Feng, D., Roberts, H.H., Peckmann, J., 2011. Changing redox conditions at cold seeps as revealed by authigenic carbonates from Alaminos Canyon, northern Gulf of Mexico. Chem. Geol. 285, 82–96.

Biswas, K.C., Woodards, N.A., Xu, H., Barton, L.L., 2009. Reduction of molybdate by sulfate-reducing bacteria. Biometals 22, 131–139.

Bolhar, R., Van Kranendonk, M.J., 2007. A non-marine depositional setting fort he northern Fortescue Group, Pilbara Craton, inferred from trace element geochemistry of stromatolitic carbonates. Precambrian Res. 155, 229–250.

Bolhar, R., Kamber, B.S., Moorbath, S., Fedo, C.M., Whitehouse, M.J., 2004. Characterization of early Archaean chemical sediments by trace element signatures. Earth Planet. Sci. Lett. 222, 43–60.

Bosence, D.W.J., Bridges, P.H., 1985. A review of the origin and evolution of carbonate mud-mounds. Spec. Publ. Int. Ass. Sediment. 23, 3–9.

Bostick, B.C., Fendorf, S., Helz, G.R., 2003. Differential adsorption of molybdate and tetrathiomolybdate on pyrite (FeS_2). Environ. Sci. Technol. 37, 285–291.

Bowles, M.W., Mogollón, J.M., Kasten, S., Zabel, M., Hinrichs, K.-U., 2014. Global rates of marine sulfate reduction and implications for sub-sea-floor metabolic activities. Science 344, 889–891.

Bown, J., Boye, M., Baker, A., Duvieillbourg, E., Lacan, F., Le Moigne, F., Planchon, F., Speich, S., Nelson, D.S., 2011. The biogeochemical cycle of dissolved cobalt in the Atlantic and the Southern Ocean south off the coast of South Africa. Mar. Chem. 126, 193–206.

Boyle, E.A., 1976. On the marine geochemistry of cadmium. Nature 263, 42–44.

Brand, U., Veizer, J., 1980. Chemical diagenesis of a multicomponent carbonate system – 1: trace elements. J. Sed. Petrol. 50, 1219–1236.

Brannon, J.M., Patrick, W.H., 1987. Fixation, transformation, and mobilization of arsenic in sediments. Environ. Sci. Technol. 21, 450–459.

Braybrooke, A.L., Heywood, B.R., Jackson, R.A., Pitt, K., 2002. Parallel computational and experimental studies of the morphological modification of calcium carbonate by cobalt. J. Cryst. Growth, 243, 336–344.

Breit, G.N., Wanty, R.B., 1991. Vanadium accumulation in carbonaceous rocks: A review of geochemical controls during deposition and diagenesis. Chem. Geol. 91, 83–97.

Bright, C.A., Cruse, A.M., Lyons, T.W., MacLeod, K.G., Glascock, M.D., Ethington, R.Y., 2009. Seawater rare-earth element patterns preserved in apatite of Pennsylvanian conodonts? Geochim. Cosmochim. Ac. 73, 1609–1624.

Brooks, S.C., Fredrickson, J.K., Carroll, S.L., Kennedy, D.W., Zachara, J.M., Plymale, A.E., Kelly, S.D., Kemner, K.M., Fendorf, S., 2003. Inhibition of bacterial U(VI) reduction by calcium. Environ. Sci. Technol. 37, 1850–1858.

Brooks, R.R., Kaplan, I.R., Peterson, M.N.A., 1969. Trace element composition of Red Sea geothermal brine and interstitial water. In: Hot brines and recent heavy metal deposits in the Red Sea. Springer Berlin Heidelberg, 180-203.

Brooks, R.K., Presley, B.J., Kaplan, I.R., 1968. Trace elements in the interstitial waters of marine sediments. Geochim. Cosmochim. Ac. 32, 397–414.

Bruland, K.W., 1980. Oceanographic distributions of cadmium, zinc, nickel, and copper in the North Pacific. Earth Planet. Sci. Lett. 47, 176–198.

Bruland, K.W., 1989. Complexation of zinc by natural organic-ligands in the Central North Pacific. Limnol. Oceanogr. 34, 269–285.

Bruland, K.W., Bertine, K., Koide, M., Goldberg, E.D., 1974. History of metal pollution in southern California coastal zone. Environ. Sci. Technol. 8, 425–432.

Bruland, K.W., Donat, J.R., Hutchins, D.A., 1991. Interactive influences of bioactive trace metals on biological production in oceanic waters. Limnol. Oceanogr. 36, 1555–1577.

Brumsack, H.-J., 1986. The inorganic geochemistry of Cretaceous black shales (DSDP Leg 41) in comparison to modern upwelling sediments from the Gulf of California. In: Summerhayes, C.P., Shackleton, N.J., (Eds.), North Atlantic Paleoceanography. Geol. Soc., Spec. Publ. 2l, 447–462.

Brumsack, H.-J., 1989. Geochemistry of recent TOC-rich sediments form the Gulf of California and the Black Sea. Geol. Rund. 78, 851–882.

Brumsack, H.-J., 2006. The trace metal content of recent organic carbon-rich sediments: Implications for Cretaceous black shales formation. Palaegeogr. Palaeocl. 232, 344–361.

Bruggeman, C., Maes, A., Vancluysen, J., Vandemussele, P., 2005. Selenite reduction in Boom clay: Effect of FeS_2, clay minerals, and dissolved organic matter. Environ. Poll. 137, 209–221.

Buerge, I.J., Hug, S.J., 1997. Kinetics and pH dependence of Chromium(VI) reduction by iron(II). Environ. Sci. Technol. 31, 1426–1432.

Buggisch, W., Krumm, S., 2005. Palaeozoic cold seep carbonates from Europe and North Africa – an integrated isotopic and geochemical approach. Facies 51, 566–583.

Buick, I.S., Uken, R., Gibson, R.L., Wallmach, T., 1998. High-$\delta^{13}C$ Paleoproterozoic carbonates from the Transvaal Supergroup, South Africa. Geology 26, 875–878.

Burdige, D.J., Nealson, K.H., 1985. Microbial manganese reduction by enrichment cultures from coastal marine sediments. Appl. Environ. Microbiol. 50 (2), 491–497.

Burne, R.V., Moore, L.S., 1987. Microbialites: Organosedimentary deposits of benthic microbial communities. Palaios 2, 241–254.

Burrell, D.C., 1967. Trace elements in marine waters by atomic absorption spectrophotometry. Anal. Chim. Ac. 38 447–455.

Burton, E.A., 1993. Controls on marine carbonate cement mineralogy: review and reassessment. Chem. Geol. 105, 163–179.

Buschmann, J., Sigg, L., 2004. Antimony(III) binding to humic substances: Influence of pH and type of humic acid. Environ. Sci. Technol. 38, 4535–4541.

Byrne, R.H., Li, B., 1995. Comparative complexation behavior of the rare earths. Geochim. Cosmochim. Ac. 59, 4575–4589.

Cabioch, G., Camion, G., Webb, G.E., Le Cornec, F., Molina, M.G., Pierre, C., Joachimksi , M.M., 2006. Contribution of microbialites to the development of coral reefs during the last deglacial period: Case study from Vanuatu (South-West Pacific). Sed. Geol. 185, 297–318.

Cai, W.-J., Chen, F., Powell, E.N., Walker, S.E., Parson-Hubbard, K.M., Staff., G.M., Wang, Y., Ashton-Alcox, K., Callender, W.R., Brett, C.E., 2006. Preferential dissolution of carbonate shells driven by petroleum seep activity in the Gulf of Mexico. Earth Planet. Sci. Lett., 248, 227–243.

Calner, M., Lehnert, O., Joachimski, M., 2010. Carbonate mud-mounds, conglomerates, and sea-level history in the Katian (Upper Ordovician) of central Sweden. Facies 56, 157–172.

Calvert, S.E., Pedersen, T.F., 1993. Geochemistry of recent oxic and anoxic marine sediments – implications for the geological record. Mar. Geol. 113, 67–88.

Calvert, S.E., Price, N.B., 1970. Minor metal contents of recent organic-rich sediments off South West Africa. Nature 227, 593–595.

Camoin, G.F., Gautret, P., Montaggioni, L.F., Cabioch, G., 1999. Nature and environmental significance of microbialites in Quaternary reefs: the Tahiti paradox. Sed. Geol. 126, 271–304.

Campbell, K.A., Farmer, J.D., Des Marais, D., 2002. Ancient hydrocarbon seeps from the Mesozoic convergent margin of California: carbonate geochemistry, fluids and palaeoenvironments. Geofluids 2, 63–94.

Canfield, D.E., 1989. Sulfate reduction and oxic respiration in marine sediments: implications for organic carbon preservation in euxinic environments. Deep-Sea Res. A. 121–138.

Canfield, D.E., Des Marais, D.J., 1991. Aerobic sulfate reduction in microbial mats. Science 251, 1471–1473.

Canfield, D.E., Raiswell, R., Bottrell, S. 1992. The reactivity of sedimentary iron minerals toward sulfide. Am. J. Sci. 292, 659–683.

Cangemi, M., Di Leonardo, R., Bellanca, A., Cundy, A., Neri, R., Angelone, M., 2010. Geochemistry and mineralogy of sediments and authigenic carbonates from the Malta Plateau, Strait of Sicily (Central Mediterranean): Relationships with mud/fluid release from a mud volcano system. Chem. Geol. 276, 294–308.

Cantrell, K.J., Byrne R.H., 1987. Rare earth element complexation by carbonate and oxalate ions. Geochim. Cosmochim. Ac. 51, 597–605.

Carpentier, W., Sandra, K., De Smet, I., Brigé, A., De Smet, L., Van Beeumen, J., 2003. Microbial reduction and precipitation of vanadium by *Shewanella oneidensis*. Appl. Environ. Microbiol. 69, 3636–3639.

Censi, P., Cangemi, M., Brusca, L,. Madonia, P., Saiano, F., Zuddas, P., 2015. The behavior of rare-earth elements, Zr and Hf during biologically-mediated deposition of silica-stromatolites and carbonate-rich microbial mats. Gondwana Res. 27, 209–215.

Chaillou, G., Schäfer, J., Anschutz, P., Lavaux, G., Blanc, G., 2003. The behaviour of arsenic in muddy sediments of The Bay of Biscay (France). Geochim. Cosmochim. Ac. 67, 2993–3003.

Chaillou, G,. Schäfer, J., Blanc, G., Anschutz, P., 2008. Mobility of Mo, U, As, an Sb within modern turbidites. Mar. Geol. 254, 171–179.

Chaudhuri, S., Cullers, R.S., 1979. The distribution of rare-earh elements in deeply buried Gulf Coast sediments. Chem. Geol. 24, 327–338.

Chen, Y.W., Deng, T.L., Filella, M., Belzile, N., 2003. Distribution and early diagenesis of antimony species in sediments and porewaters of freshwater lakes. Environ. Sci. Technol. 37, 1163–1168.

Chen, F., Hu, Y., Feng, D., Zhang, X., Cheng, S., Cao, J., Lu, H., Chen, D., 2016. Evidence of intense methane seepages from molybdenum enrichments in gas hydrate-bearing sediments of the northern South China Sea. Chem. Geol. 443, 173–181.

Chen, L., Liu, Y., Hu, Z., Gao, S., Zong, K., Chen, H., 2011. Accurate determinations of fifty-four major and trace elements in carbonate by LA-ICP-MS using normalization strategy of bulk components as 100%. Chem. Geol. 284, 283–295.

Cheng, L., Fenter, P., Sturchio, N.C., Zhong, Z., Bedzyk, M.J., 1999. X-ray standing wave study or arsenite incorporation at the calcite surface. Geochim. Cosmochim. Ac. 63, 3153–3157.

Cheng, L., Sturchio, N.C., Woicik, J.C., Kemner, K.M., Lyman, P.F., Bedzyk, M.J., 1998. High-resolution structural study of zinc ion incorporation at the calcite cleavage surface. Surf. Sci. Lett. 415, L976–L982.

Cherniak, D.J., 1998. REE diffusion in calcite. Earth Planet. Sci. Lett. 160, 273–287.

Chester, R., Aston, S.R., 1976. The geochemistry of deep-sea sediments. In: Chemical Oceanography, (Riley, J.P., Chester, R., Eds.), Academic Press, New York, 281-390.

Chester, R., Hughes, M.J., 1967. A chemical technique for the separation of ferro-manganese minerals, carbonate minerals and adsorbed trace elements from pelagic sediments. Chem. Geol. 2, 249-262.

Chester, R., Messiha-Hanna, R.G., 1970. Trace element partition patterns in North Atlantic deep-sea sediments. Geochim. Cosmochim. Ac. 34, 1121–1128.

Chmielowski, J., Klapcinska, B., 1985. Bioaccumulation of Germanium by *Pseudomonas putida* in the presence of two selected substrates. Appl. Environ. Microbiol. 51, 1099–1103.

Choppin, G.R., 2002. Covalency in f-element bonds. J. Alloy. Compd. 344, 55–59.

Clarke, M.B., Helz, G.R., 2000. Metal – thiometalate transport of biologically active trace elements in sulfidic environments. 1. Experimental evidence for copper thioarsenite complexing. Environ. Sci. Technol. 34, 1477–1482.

Coleman, M.L., 1985. Geochemistry of diagenetic non-silicate minerals: kinetic considerations. Phil. Trans. R. Soc. Lon. A 315, 39–56.

Coleman, M.L., 1993. Microbial processes: control on the shape and composition of carbonate concretions. Mar. Geol. 113, 127–140.

Collier, R.W., 1984. Particulate and dissolved vanadium in the North Pacific Ocean. Nature 309, 441–444.

Colodner, D., Sachs, J., Ravizza, G., Turekian, K., Edmond, J., Boyle, E., 1993. The geochemical cycle of rhenium: a reconnaissance. Earth Planet. Sci. Lett. 117, 205–221.

Comans, R.N.J., Middelburg, J.J., 1987. Sorption of trace metals on calcite: Applicability of the surface precipitation model. Geochim. Cosmochim. Ac. 51, 2587–2591.

Cooper, D.C., Picardal, F., Rivera, J., Talbot, C., 2000. Zinc immobilization and magnetite formation via ferric oxide reduction by *Shewanella putrefaciens 200*. Environ. Sci. Technol. 34, 100–106.

Corkeron, M., Webb, G.E., Moulds, J., Grey, K., 2012. Discriminating stromatolite formation modes using rare earth elements geochemistry: Trapping and binding versus in situ precipitation of stromatolites from the Neoproterozoic Bitter Springs Formation, Northern Territory, Australia. Precambrian Res. 212–213, 194–206.

Corsetti, F.A., Grotzinger, J.P., 2005. Origin and significance of tube structures in Neoproterozoic post-glacial cap carbonates: example from Noonday Dolomite, Death Valley, United States. Palaios 20, 348–362.

Crecelius, E.A., Bothner, M.H., Carpenter, R., 1975. Geochemistries of arsenic, antimony, mercury, and related elements in sediment of Puget Sound. Environ. Sci. Technol. 9, 325–333.

Crémière, A., Lepland, A., Chand, S., Sahy, D., Kirsimäe, K., Bau, M., Whitehouse, M.J., Noble, S.R., Martma, T., Thorsnes, T., Brunstad, H., 2016. Fluid source and methane-related diagenetic processes recorded in cold seep carbonates from the Alvheim channel, central North Sea. Chem. Geol. 432, 16–33.

Crusius, J., Thomson, J., 2000. Comparative behavior of authigenic Re, U, and Mo during reoxidation and subsequent long-term burial in marine sediments. Geochim. Cosmochim. A. 64, 2233–2242.

Crusius, J., Calvert, S., Pedersen, T., Sage, D., 1996. Rhenium and molybdenum enrichments in sediments as indicators of oxic, suboxic and sulfidic conditions of deposition. Earth Planet. Sci. Lett. 145, 65–78.

Cumberland, S.A., Douglas, G., Grice, K., Moreau, J.W., 2016. Uranium mobility in organic matter-rich sediments: A review of geological and geochemical processes. Earth-Sci. Rev. 159, 160–185.

Curti, E., Kulik, D.A., Tits, J., 2005. Solid solutions of trace Eu(III) in calcite: Thermodynamic evaluation of experimental data over a wide range of pH and pCO_2. Geochim. Cosmochim. Ac. 69, 1721–1737.

Curtis, C.D., Burns, R.G., smith, J.V., 1977. Sedimentary geochemistry: environments and processes dominated by involvement of an aqueous phase. Phil. Trans. R. Soc. Lon. A 286, 353–372.

Cutter, G.A., 1978. Species determination of selenium in natural waters. Anal. Chim. Ac. 98, 59–66.

Cutter, G.A., 1982. Selenium in reducing waters. Science 217, 829–831.

Cutter, G.A., 1991. Dissolved arsenic and antimony in the Black Sea. Deep-Sea Res. 38, 825–843.

Cutter, B.A., Bruland, 1984. The marine biogeochemistry of selenium: A re-evaluation. Limnol. Oceanogr. 29, 1179–1192.

Cutter, G.A., Cutter, L.S., 1998. Metalloids in the high latitude North Atlantic Ocean: Sources and internal cycling. Mar. Chem. 61, 25–36.

Davis, J.A., Fuller, C.C., Cook, A.D., 1987. A model for trace metal sorption processes at the calcite surface: Adsorption of Cd^{2+} and subsequent solid solution formation. Geochim. Cosmochim. Ac. 51, 1477–1490.

Davranche, M., Pourret, O., Gruau, G., Dia, A., Jin, D., Gaertner, D., 2008. Competitive binding of REE to humic acids and manganese oxide: Impact of reaction kinetics on development of cerium anomaly and REE adsorption. Chem. Geol. 247, 154–170.

De Baar, H.J.W., 1983. The marine geochemistry of the rare earth elements. PhD thesis, Woods Hole Oceanographic Institotution, 283 p.

De Baar, H.J.W., Bacon, M.P., Brewer, P.G., Bruland, K.W., 1985a. Rare earth elements in the Atlantic and Pacific oceans. Geochim. Cosmochim. Ac. 49, 1943–1959.

De Baar, H.H.W., Brewer, P.G., Bacon, M.P., 1985b. Anomalies in rare earth distributions in seawater: Gd and Tb. Geochim. Cosmochim. Ac. 49, 1961–1969.

De Baar, H.J.W., German, C.R., Elderfield, H., Van Gaans, P., 1988. Rare earth element distribution in anoxic waters of the Cariaco Trench. Geochim. Cosmochim. Ac. 52, 1203–1219.

Debryune, D., Hulsbosch, N., Muchez, P., 2016. Unraveling rare earth element signatures in hydrothermal carbonate minerals using a source-sink system. Ore Geol. Rev. 72, 232–252.

De Carlo, T.M., Gaetani, G.A., Holcomb, M., Cohen, A.L., 2015. Experimental determination of factors controlling U/Ca of aragonite precipitated from seawater: Implications for interpreting coral skeleton. Geochim. Cosmochim. Ac. 162, 151–165.

Dellwig, O., Leipe, T., März, C., Glockzin, Pollehne, F., Schnetger, B., Yakushev, E.V., Böttcher, M.E., Brumsack, H.-J., 2010. A new particulate Mn-Fe-P-shuttle at the redoxcline of anoxic basins. Geochim. Cosmochim. Ac. 74, 7100–7115.

Derry, L.A., 2010. A burial diagenesis origin for the Ediacaran Shuram–Wonoka carbon isotope anomaly. Earth Planet. Sci. Lett. 294, 152–162.

Derry, L.A., Jacobsen, S.B., 1990. The chemical evolution of Precambrian seawater: evidence from REEs in banded iron formations. Geochim. Cosmochim. Ac. 54, 2965–2977.

Dolor, M.K., Gilmour, C.C., Helz, G.R., 2009. Distinct microbial behavior of Re compared to Tc: evidence against microbial Re fixation in aquatic sediments. Geomicrobiol. J. 26, 470–483.

Donat, J.R., Lao, K.A., Bruland, K.W., 1994. Speciation of dissolved copper and nickel in South San Franscisco Bay: a multi-method approach. Anal. Chim. Ac. 284, 547–571.

Douville, E., Bienvenu, P., Charlou, J.L., Donval, J.P., Fouquet, Y., Appriou, P., Gamo, T., 1999. Yttrium and rare earth elements in fluids from various deep-sea hydrothermal systems. Geochim. Cosmochim. Ac. 63, 627–643.

Dromgoole, E.L., Walther, L.M., 1990. Iron and manganese incorporation into calcite: Effects of growth kinetics, temperature and solution chemistry. Chem. Geol. 81, 311–336.

Duc, M., Lefevre, G., Fedoroff, M., Jeanjean, J., Rouchand, J.C., Monteil-Rivera, F., Domunceau, J., Milonjic, S., 2003. Sorption of selenium anionic species on apatites and iron oxides from aqueous solutions. J. Environ. Radioactiv. 70, 61–72.

Duce, R.A., Liss, P.S., Merrill, J.T., Atlas, E.L., Buat-Menard, P., Hicks, B.B., Miller, J.M., Prospero, J.M., Arimoto, R., Church, T.M., Ellis, W., Galloway, J.N., Hansen, L., Jickells, T.D., Knap, A.H., Reinhardt, K.H., Schneider, B., Soudino, A., Tokos, J,J., Tsunogai, S., Wollast, R., Zhou, M., 1991. The atmospheric input of trace species to the world ocean. Glob. Biogeochem. Cycl. 5, 193–259.

Duchart, P., Calvert, S.E., Price, N.B., 1973. Distribution of trace metals in the pore waters of shallow water marine sediments. Limnol. Oceanogr. 18, 605–610.

Duff, M.C., Coughlin, J.U., Hunter, D.B., 2002. Uranium co-precipitation with iron oxide minerals. Geochim. Cosmochim. Ac. 66 (20), 3533–3547.

Dulski, P., Parekh, P., Möller, P., 1977. Resolution of the two phases of limestones with respect to their trace element contents. J. Radioanal. Nucl. Chem. 38, 315–325.

Dupont, C.L., Buck, K.N., Palenik, B., Barbeau, K., 2010. Nickel utilization in phytoplankton assemblages from contrasting ocean regimes. Deep Sea Res. I. 57, 553–566.

Edenborn, H.M., Belzile, N., Mucci, A., Lebel, J., Silverberg, N., 1986. Observations on the diagenetic behavior of arsenic in a deep coastal sediment. Biogeochemistry 2, 359–376.

Elderfield, H., Hawkesworth, C.J., Greaves, M.J., Calvert, S.E., 1981. Rare earth element geochemistry of oceanic ferromanganese nodules and associated sediments. Geochim. Cosmochim. Ac. 45, 513–528.

Elderfield, H., Greaves, M.J., 1982. The rare earth elements in seawater. Nature 296, 214–219.

Elderfield, H., Greaves, M.J., 1983. Determination of the rare earth elements in sea water. In: Trace Metals in Sea Water, Springer US., 427-445.

Elderfield, H., Pagett, R., 1986. Rare earth elements in ichthyoliths: variations with redox conditions and depositional environment. In: Riley, J.P. (Ed), Sciences of the Total Environment, 175–197.

Elderfield, H., Sholkovitz, E.R., 1987. Rare earth elements in the pore waters of reducing nearshore sediments. Earth Planet. Sci. Lett. 82, 280–288.

Elderfield,H., Upstill-Goddard, R., Sholkovitz, E.R., 1990. The rare earth elements in rivers, estuaries, and coastal seas and their significance to the composition of ocean waters. Geochim. Cosmochim. Ac. 54, 971–991.

Elderfield, H., Whitfield, M., Burton, J.D., Bacin, M.P., Liss, P.S., 1988. The oceanic chemistry of the rare-earth elements. Phil. Trans. R. Soc. Lon. A 325, 105–126.

Elrick, M., Snider, A.C., 2002. Deep-water stratigraphic cyclicity and carbonate mud mound development in the Middle Cambrian Marjum Formation, House Range, Utah, USA. Sedimentology 49, 1021–1047.

El Wardani, 1958. Marine geochemistry of germanium and the origin of Pacific pelagic clay minerals. Geochim. Cosmochim. Ac. 15, 237–254.

Elzinga, E.J., Reeder, R.J., 2002. X-ray absorption spectroscopy study of Cu^{2+} and Zn^{2+} adsorption complexes at the calcite surface: Implications for site-specific metal incorporation preferences during calcite crystal growth. Geochim. Cosmochim. Ac. 66 (22), 3943–3954.

Elzinga, E.J., Reeder, R.J., Withers, S.H., Peale, R.E., Mason, R.A., Beck, K.M., Hess, W.P., 2002. EXAFS study of rare-earth element coordination in calcite. Geochim. Cosmochim. Ac. 66, 2875–2885.

Emerson, S,R., Huested, S.S., 1991. Ocean anoxia and the concentrations of molybdenum and vanadium in seawater. Mar. Chem. 34, 177–196.

Endrizzi, F., Rao, L., 2014. Chemical speciation of uranium(VI) in marine environments: complexation of calcium and magnesium ions with $[(U_2)(CO_3)_3]^{4-}$ and the effect on the extraction of uranium from seawater. Chem. Eur. J. 20, 14499–14506.

Fabricand, B.P., Sawyer, R.R., Ungar, S.G., Adler, S., 1962. Trace metal concentrations in the ocean by atomic absorption spectroscopy. Geochim. Cosmochim. Ac. 26, 1023–1027.

Fairchild, I.J., Kennedy, M.J., 2007. Neoproterozoic glaciation in the Earth System. J. Geol. Soc. 164, 895–921.

Fallon, S.J., White, J.C., McCulloch, M.T., 2004. *Porites* corals as recorders of mining and environmental impacts: Misima Island, Papua New Guinea. Geochim. Cosmochim. Ac. 66, 45–62.

Fenchel, T.M., Jørgensen, B.B., 1977. Detritus food chains of aquatic ecosystems: The role of bacteria. In: Alexander, M. (ed), Advances in Microbial Ecology, 1, Plenum Press, NY, 1–58.

Feng, D., Chen, D., 2015. Authigenic carbonates from an active cold seep of the northern South China Sea: New insights into fluid sources and past seepage activity. Deep-Sea Res. II 112, 74–83.

Feng, D., Chen, D., Peckmann, J., 2009a. Rare earth elements in seep carbonates as tracers of variable redox conditions at ancient hydrocarbon seeps. Terra Nova 21, 49–56.

Feng, D., Chen, D., Roberts, H.H., 2008. Sedimentary fabrics in the authigenic carbonates from Bush Hill: implication for seabed fluid flow and its dynamic signature. Geofluids 8, 301–310.

Feng, D., Chen, D., Roberts, H.H., 2009b. Petrographic and geochemical characterization of seep carbonate from Bush Hill (GC 185) gas vent and hydrate site of the Gulf of Mexico. Mar. Petrol. Geol. 26, 1190–1198.

Feng, D., Chen, D., Peckmann, J., Bohrmann, G., 2010. Authigenic carbonates from methane seeps of the northern Congo fan: Microbial formation mechanism. Mar. Petrol. Geol. 27, 748–756.

Feng, D., Lin, Z., Bian, Y., Chen, D., Peckmann, J., Bohrmann, G., Roberts, H.H., 2013. Rare earth elements of seep carbonates: Indication for redox variations and microbiological processes at modern seep sites. J. Asian Earth Sci. 65, 27–33.

Feng, D., Roberts, H.H., Joye, S.B., Heydari, E., 2014. Formation of low-magnesium calcite at cold seeps in an aragonite sea. Terra Nova 26, 150–156.

Fietzke, J., Liebetrau, V., Günther, D., Gürs, K., Hameter, K., Zumholz, K., Hansteen, T.H., Eisenhauer, A., 2008. An alternative data acquisition and evaluation strategy for improved isotope ratio precision using LA-MC-ICP-MS applied to stable and radiogenic strontium isotopes in carbonates. J. Anal. At. Spectrom. 23, 955–961.

Filella, M., Belzile, N., Chen, Y.W., 2002a. Antimony in the environment: a review focused on natural waters II. Relevant solution chemistry. Earth-Sci. Rev. 59, 265–285.

Filella, M., Belzile, N., Chen, Y.-W., 2002b. Antimony in the environment: a review focused on natural waters I. Occurrence. Earth-Sci. Rev. 57, 125–176.

Filella, M., Belzile, N., Chen, Y.-W., 2007. Antimony in the environment: a review focused on natural waters III. Microbiota relevant interactions. Earth-Sci. Rev. 80, 195–217.

Filella, M., Williams, P.A., Belzile, N., 2009. Antimony in the environment: knowns and unknowns. Environ. Chem. 6, 95–105.

Finneran, K. T., Anderson, R.T., Nevin, K.P., Lovley, D.R., 2002. Potential for bioremediation of uranium-contaminated aquifers with microbial U(VI) reduction. Soil Sed. Contam. 11, 339–357.

Fisher, A., Kara, D., 2016. Determination of rare earth elements in natural water samples – A review of sample separation, preconcentrations and direct methodologies. Anal. Chim. Ac. 935, 1–29.

Flajs, G., Vigener, M., Keupp, H., Meischner, D., Neuweiler, F., Paul, J., Reitner, J., Warnke, K., Weller, H., Dingle, P., Hensen, C., Schäfer, P., Gauret, P., Leinfelder, R.P., Hüssner, H., Kaufmann, B., 1995. Mud mounds: A polygenetic spectrum of fine-grained carbonate buildups. Facies 32, 1–69.

Flannery, D.T., Walter, M.R., 2012. Archean tufted microbial mats and the Great Oxidation Event: new insights into an ancient problem. Austral. J. Earth Sci. 59, 1–11.

Flügel, H.W. Wedepohl, K.H., 1967. Die Verteilung des Strontiums in oberjurassischen Karbonatgesteinen der nördlichen Kalkalpen. Contrib. Mineral. Petrol. 14, 229–249.

Franchi, F., Hofmann, A., Cavalazzi, B., Wilson, A., Barbieri, R., 2015. Differentiating marine vs hydrothermal processes in Devonian carbonate mounds using rare earth elements (Kess Kess mounds, Anti-Atlas, Morocco). Chem. Geol. 409, 69–86.

Frank, J.R., Carpenter, A.B., Oglesby, T.W., 1982. Cathodoluminscence and composition of calcite cement in the Taum Sauk limestone (Upper Cambrian), southeast Morocco. J. Sed. Res. 52, 631–638.

Franklin, M.L., Morse, J.W., 1983. The interaction of manganese(II) with the surface of calcite in dilute solutions and seawater. Mar. Chem. 12, 241–254.

Fredrickson, J.K., Zachara, J.M., Kennedy, D.W., Duff, M.C., Gorby, Y.A., Shu-mei, W.L., Krupka, K.M., 2000. Reduction of U (VI) in goethite (α-FeOOH) suspensions by a dissimilatory metal-reducing bacterium. Geochim. Cosmochim. Ac. 64, 3085–3098.

Freslon, N., Bayon, G., Toucanne, S., Bermall, S., Bollinger, C., Chéron, S., Etoubleau, J., Germain, Y., Khripounoff, A., Ponzervera, E., Rouget, M.-L., 2014. Rare earth elements and neodymium isotopes in sedimentary organic matter. Geochim. Cosmochim. Ac. 140, 177–198.

Friedman, G.M., 1969. Trace elements as possible environmental indicators in carbonate sediments. In: Friedman, G.M., (Ed.), Depositional Environments in Carbonate Rocks: Soc. Econ. Paleontologists Mineralogists, Spec. Publ. No. 14, 193–200.

Frimmel, H.E., 2009. Trace element distribution in Neoproterozoic carbonates as palaeoenvironmental indicator. Chem. Geol. 258, 338–353.

Froelich, P.N., Andreae, M.O., 1981. The marine geochemistry of germanium: Ekasilicon. Science 213, 205–207.

Froelich, P.N., Klinkhammer, G.P., Bender, M.L., Luedtke, N.A., Heath, G.R., Cullen, D., Dauphin, P., Hammond, D., Hartman, B., Maynard, V., 1979. Early oxidation of organic matter in pelagic sediments of the eastern equatorial Atlantic: Suboxic diagenesis. Geochim. Cosmochim. Ac. 43, 1075–1090.

Fryer, B.J., 1983. Part B. Rare earth elements in iron-formation. Develop. Precambr. Geol. 6, 345–358.

Gabitov, R.I., Gaetani, G.A., Watson, E.B., Cohen, A.L., Ehrlich, H.L., 2008. Experimental determination of growth rate effect on U^{6+} and Mg^{2+} partitioning between aragonite and fluid at elevated U^{6+} concentration. Geochim. Coscmochim. Ac. 72, 4058–4068.

Gamble, L.W., Jones, W.H., 1955. Determination of trace metals in petroleum. Anal. Chem. 27, 1456–1459.

Garcia-Solsona, E., Jeandel, C., Labatut, M., Lacan, F., Vance, D., Chavagnac, V., Pradoux, C., 2014. Rare earth elements and Nd isotopes tracing water mass mixing and particle-seawater interactions in the SE Atlantic. Geochim. Cosmochim. Ac. 125, 351–372.

Ge, L., Jiang, S.-Y., Swennen, R., Yang, T., Yang, J.-H., Wu, N.-Y., Liu, J., Chen, D.-H., 2010. Chemical environment of cold seep carbonate formation on the northern continental slope of South China Sea: Evidence from trace and rare earth element geochemistry. Mar. Geol. 277, 21–30.

Gehling, J.G., 1999. Microbial mats in terminal Proterozoic siliciclastics: Ediacaran death masks. Palaios 14, 40–57.

Gendron, A., Silverberg, N., Sundby, B., Lebel, J., 1996. Early diagenesis of cadmium and cobalt in sediments of the Laurentian Trough. Geochim. Cosmochim. Ac. 50, 741–747.

German, C.R., Elderfield, H., 1989. Rare earth elements in Saanich Inlet, British Columbia, a seasonally anoxic basin. Geochim. Cosmochim. Ac. 53, 2561–2571.

German, C.R., Elderfield, H., 1990. Application of the Ce anomaly as a paleoredox indicator: the ground rules. Paleoceanography 5, doi:10.1029/PA005i005p00823.

German, C.R., Masuzawa, T., Greaves, M.J., Elderfield, M., Edmond, J.M., 1995. Dissolved rare earth elements in the Southern Ocean: Ce oxidation and the influence of hydrography. Geochim. Cosmochim. Ac. 59, 1551–1558.

Gobeil, C., MacDonald, R.W., Sundby, B., 1997. Diagenetic separation of cadmium and manganese in suboxic continental margin sediments. Geochim. Cosmochim. Ac. 61, 4647–4654.

Goldberg, E.D., 1954. Marine geochemistry 1. Chemical scavengers of the sea. J. Geol. 62, 249–265.

Goldberg, E.D., 1957. Biogeochemistry of trace metals. Geol. Soc. Am. Mem. 67, 345–358.

Goldberg, E.D., Koide, M., Schmitt, R.A., Smith, R.H., 1963. Rare earth distributions in the marine environment. J. Geophys. Res. 68, 4209–4217.

Goldberg, S., Forster, H.S., 1998. Factors affecting molybdenum adsorption by soils and minerals. Soil Sci. 163, 109–114.

Goldstein, S.J., Jacobsen, S.B., 1988. Rare earth elements in river waters. Earth Planet. Sci. Lett. 89, 35–47.

Graf, D.L., 1962. Minor element distribution in sedimentary carbonate rocks. Geochim. Cosmochim. Ac. 26, 849–856.

Grandjean-Lécuyer, P., Feist, F., Albarede, F., 1993. Rare earth elements in old biogenic apatites. Geochim. Cosmochim. Ac. 57, 2507–2514.

Greaves, M.J., Elderfield, H., Klinkhammer, G.J., 1988. Determination of the rare earth elements in natural waters by isotope-dilution mass spectrometry. Anal. Chim. Ac. 218, 265–280.

Greaves, M.J., Statham, P.J., Elderfield, H., 1994. Rare earth element mobilization from marine atmospheric dust into seawater. Mar. Chem. 46, 255–260.

Greinert, J., Bohrmann, P., Suess, E., 2001. Gas hydrate-associated carbonates and methane-venting at Hydrate Ridge: Classification, distribution, and origin of authigenic lithologies. Natural Gas Hydrates: Occurrence, Distribution, and Detection, Geophys. Monogr. 124, 99–113.

Grey, K., Corkeron, M., 1998.. Late Neoproterozoic stromatolites in glacigenic successions of the Kimberley region, Western Australia: evidence for a younger Marinoan glaciation. Precambrian Res. 92, 65–87.

Gromet, L.P., Haskin, L.A., Korotev, D.L., Dymek, R.F., 1984. The “North American shale composite”: Its compilation, major and trace element characteristics. Geochim. Cosmochim. Ac. 48, 2469–2482.

Grotzinger, J P., Knoll, A.H., 1999. Stromatolites in Precambrian carbonates: evolutionary mileposts or environmental dipsticks?. Ann. Rev. Earth Planet. Sci. 27, 313–358.

Grotzinger, J.P., Fike, D.A., Fischer, W. W., 2011. Enigmatic origin of the largest-known carbon isotope excursion in Earth's history. Nat. Geosc. 4, 285–292.

Grotzinger, J.P., Watters, W.A., Knoll, A.H., 2000. Calcified metazoans in thrombolite-stromatolite reefs of the terminal Proterozoic Nama Group, Namibia. Paleobiology 26, 334–359.

Guillong, M., Horn, I., Günther, D., 2003. A comparison of 266 nm, 213 nm and 193 nm produced from a single solid state N:YAG laser for laser ablation ICP-MS. J. Anal. At. Spectrom. 18, 1224–1230.

Günther, D., Heinrich, C.A., 1999. Comparison of the ablation behaviour of 266 nm Nd:YAG and 193 nm ArF excimer lasers for LA-ICP-MS analysis. J. Anal. At. Spectrom. 14, 1369–1374.

Guo, Q., Strauss, H., Kaufman, A.J., Schröder, S., Gutzmer, J., Wing, B., Baker, M.A., Bekker, A., Jin, Q., Kim, S.-K., Farquhar, J., 2009. Reconstructing Earth's surface oxidation across the Archean-Proterozoic transition. Geology 37, 399–402

Hakanson, L. 1980. Ecological risk index for aquatic pollution control, a sedimentological approach. Water Res. 14, 975–1001.

Haley, B.A., Klinkhammer, G.P., 2003. Complete separation of rare earth elements from small volume seawater samples by automated ion chromatography: method development and application to benthic flux. Mar. Chem. 82, 197–220.

Haley, B.A., Klinkhammer, G.P., McManus, J., 2004. Rare earth elements in pore waters of marine sediments. Geochim. Cosmochim. Ac. 68, 1265–1279.

Hamelin, B., Bard, E., Zindler, A., Fairbanks, R.G., 1991. $^{234}U/^{238}U$ mass spectrometry of corals: how accurate is the U-Th age of the last interglacial period? Earth Planet. Sci. Lett. 106, 169–180.

Hammond, D.E., McManus, J., Berelson, W.M., Meredith, C., Klinkhammer, G.P., Coale, K.H., 2000. Diagenetic fractionation of Ge and Si in reducing sediments: The missing Ge sink and a possible mechanism to cause glacial/interglacial variations in oceanic Ge/Si. Geochim. Cosmochim. Ac. 64, 2453–2465.

Hannigan, R.E., Sholkovitz, E.R., 2001. The development of middle rare earth element enrichments in freshwaters: weathering of phosphate minerals. Chem. Geol. 175, 495–508.

Harstad, A.O., Stipp, S.L.S., 2007. Calcite dissolution: Effects of trace cations naturally present in Iceland spar calcites. Geochim. Cosmochim. Ac. 71, 56–70.

Haskin, L.A., Wildeman, T.R., Frey, F.A., Collins, K.A., Keedy, C.R., Haskin, M.A., 1966. Rare earths in sediments. J. Geophys. Res. 71, 6091–6105.

Hathorne, E.C., James, R.H., Savage, P., Alard, O., 2007. Physical and chemical characteristics of particles produced by laser ablation of biogenic calcium carbonate. J. Anal. At. Spectrom. 23, 240–243.

Hathorne, E.C., Stichel, T., Brück, B., Frank, M., 2015. Rare earth element distribution in the Atlantic sector of the Southern Ocean: The balance between particle scavenging and vertical supply. Mar. Chem. 177, 157–171.

Hausinger, R.P., 1997. Metallocenter assembly in nickel-containing enzymes. J. Biol. Inorg. Chem. 2, 279–286.

Heindel, K., Birgel, D., Peckmann, J., Kuhnert, H., Westphal, H., 2010. Formation of deglacial microbialites in coral reefs off Tahiti (IODP 310) involving sulfate-reducing bacteria. Palaios 25, 618–635.

Henderson, P., 1984. General geochemical properties and abundances of the rare earth elements. In: Henderson, P. (Ed.), Rare Earth Element Geochemistry, 1–32. Elsevier.

Helz, G.R., Adelson, J.M., 2013. Trace element profiles in sediments as proxies of dead zone history; rhenium compared to molybdenum. Environ. Sci. Technol. 47, 1257–1264.

Helz, G.R., Dolor, M.K., 2012. What regulates rhenium deposition in euxinic basins? Chem. Geol. 304–305, 131–141.

Helz, G.R., Bura-Nakic, E., Mikac, N., Ciglenecki, I., 2011. New model for molybdenum behavior in euxinic waters. Chem. Geol. 284, 323–332.

Helz, G.R., Miller, C.V., Charnick, J.M., Mosselmans, J.F.W., Pattrick, R.A.D., Garner, C.D., Vaughan, D.J., 1996. Mechanism of molybdenum removal from the sea and its concentration in black shales: EXAFS evidence. Geochim. Cosmochim. Ac. 60, 3631–3642.

Herrmann, A.D., Kendall, B., Algeo, T.J., Gordon, G.W., Wasylenki, L.E., Anbar, A.D., 2012. Anomalous molybdenum isotope trends in Upper Pennsylvanian euxinic facies: Significance for use of δ^{98}Mo as a global marine redox proxy. Chem. Geol. 324–325, 87–98.

Hilton, J., Davison, W., Ochsenbein, U., 1985. A mathematical model for analysis of sediment core data. Implications for enrichment factor calculations and trace metal transport mechanisms. Chem. Geol. 48, 281–291.

Himmler, T., Bach, W., Bohrmann, G., Peckmann, J., 2010. Rare earth elements in authigenic methane-seep carbonates as tracers for fluid composition during early diagenesis. Chem. Geol. 277, 126–136.

Himmler, T., Brinkmann, F., Bohrmann, G., Peckmann, J., 2008. Corrosion patterns of seep-carbonates from the eastern Mediterranean Sea. Terra Nova 23, 206–212.

Himmler, T., Haley, B.A., Torres, M.E., Klinkhammer, G.P., Bohrmann, G., Peckmann, J., 2013. Rare earth element geochemistry in cold-seep pore waters of Hydrate Ridge, northeast Pacific Ocean. Geo-Mar. Lett. 33, 369–379.

Hirst, D.M., 1962. The geochemistry of modern sediments from the Guld of Paria – II the location and distribution of trace elements. Geochim. Cosmochim. Ac. 26, 1147–1187.

Hitchcock, R.D., Starr, W.L., 1954. Spectrographic techniques as applied to the analysis of sea water. Appl. Spectr. 8, 5–17.

Hodgson, G.W., 1954. Vanadium, nickel, and iron trace metals in crude oils of western Canada. Am. Assoc. Petrol. Geol. Bull. 38, 2537–2554.

Hoffman, P.F., Kaufman, A.J., Halverson, G.P., Schrag, D.P., 1998. A Neoproterozoic Snowball Earth. Science 281, 1342–1346.

Hoffmann, U., Stipp, S.L.S., 2001. The behavior of Ni^{2+} on calcite surfaces. Geochim. Cosmochim. Ac. 65, 4131–4139.

Hohl, S.V., Becker, H., Gamper, A., Jiang, S.-Y., Wiechert, U., Yang, J.-H., Wie, H.-Z., 2015a. Secular changes of water chemistry in shallow-water Ediacaran ocean: Evidence from carbonates at Xiaofenghe, Three Gorges area, Yangtze Platform, South China. Precambrian Res. 270, 50–79.

Hohl, S.V., Becker, H., Herzlieb, S., Guo, Q., 2015b. Multiproxy constraints on alteration and primary compositions of Ediacaran deep-water carbonate rocks, Yangtze Platform, South China. Geochim. Cosmochim. Ac. 163, 262–278.

Holland, H.D., 1979. Metals in black shales; a reassessment. Econom. Geol. 74, 1676–1680.

Holser, W.T., 1997. Evaluation of the application of rare-earth elements to paleoceanography. Palaegeogr. Palaeocl. 132, 309–323.

Hu, Y., Chen, L., Feng, D., Liang, Q., Xia, Z., Chen, D., 2017. Geochemical record of methane seepage in authigenic carbonates and surrounding host sediments: A case study from the South China Sea. J. Asian Earth Sci. 138, 51–61.

Hu, Y., Feng, D., Chen, L., Zheng, G., Peckmann, J., Chen, D., 2015a. Using iron speciation in authigenic carbonates from hydrocarbon seeps to trace redox conditions. Mar. Petrol. Geol. 67, 111–119.

Hu, Y., Feng, D., Liang, Q., Xia, Z., Linying, C., Chen, D., 2015b. Impact of anaerobic oxidation of methane on the geochemical cycle of redox-sensitive elements at cold-seep sites of the northern South China Sea. Deep-Sea Res. II 122, 84–94.

Hu, Y., Feng, D., Peckmann, J., Roberts, H.H., Chen, D., 2014. New insights into cerium anomalies and mechanisms of trace metal enrichment in authigenic carbonate from hydrocarbon seeps. Chem. Geol. 381, 55–66.

Hu, M., Yang, Y., Martin, J.-M., Yin, K., Marrison, P.J., 1996. Preferential uptake of Se(IV) over Se(VI) and the production of dissolved organic Se by marine phytoplankton. Mar. Environ. Res. 44, 225–231.

Huang, J., Chu, X.-L., Chang, H.-J., Feng, L.-J., 2009. Trace element and rare earth element of cap carbonate in Ediacaran Doushantuo Formation in Yangtze Gorges. Chin. Sci. Bull., doi:10.1007/s11434-009-0305-1.

Huerta-Diaz, M.A., Morse, J.W., 1992. Pyritization of trace metals in anoxic marine sediments. Geochim. Cosmochim. Ac. 56, 2681–2702.
Ingerson, E., 1962. Problems of the geochemistry of sedimentary carbonate rocks. Geochim. Cosmochim. Ac. 26, 815–847.
Irwin, H., Curtis, C., Coleman, M., 1977. Isotopic evidence for source of diagenetic carbonates formed during burial of organic-rich sediments. Nature 269, 209–213.
Jacobs, L., Emerson, S., 1982. Trace metal solubility in an anoxic fjord. Earth Planet. Sci. Lett. 60, 237–252.
Jacobs, L., Emerson, S., Skei, J., 1985. Partitioning and transport of metals across the O_2/H_2S interface in a permanently anoxic basin, Framvaren Fjord, Norway. Geochim. Cosmochim. Ac. 49, 1433–1444.
Jacobsen, S.B., Kaufman, A.J. 1999. The Sr, C and O isotopic evolution of Neoproterozoic seawater. Chem. Geol. 161, 37–57.
Jacobsen, S.B., Pimentel-Klose, M.R., 1988. A Nd isotopic study of the Hamersley and Michipicoten banded iron formations: the source of REE and Fe in Archean oceans. Earth Planet. Sci. Let. 87, 29–44.
Jakubowicz, M., Dopieralska, J., Belka, Z., 2015. Tracing the composition and origin of fluids at an ancient hydrocarbon seep (Hollard Mound, Middle Devonian, Morocco): A Nd, REE, and stable isotope study. Geochim. Cosmochim. Ac. 156, 50–74.
Jiang, G., Kennedy, M.J., Christie-Blick, N., 2003. Stable isotopic evidence for methane seeps in Neoproterozoic postglacial cap carbonates. Nature, 426, 822–826.
Jochum, K.P., Weis, U., Stoll, B., Kuzmin, D., Yang, Q., Raczek, I., Jacob, D.E., Stracke, A., Birbaim, K., Frick, D.A., Günther, D., and Enzweiler, J., 2011. Determination of reference values for NIST SRM 610-617 glasses following ISO guidelines: Geostand. Geoanal. Res. 35, 397–429.
Johannesson, K.H., Hawkins, D.L.J., Cortés, A., 2006. Do Archean chemical sediments record ancient seawater rare earth element patterns? Geochim. Cosmochim. Ac. 70, 871–890.
Johannesson, K.H., Telfeyan, K., Chevis, D.A., Rosenheim, B.E., Leybourne, M.I., 2014. Rare earth elements in stromatolites — 1. Evidence that Modern terrestrial stromatolites fractionate rare earth elements during incorporation from ambient waters. Evolution of Archean Crust and Early Life. Springer, 385–411.
Johnson, K.S., Stout, P.M., Berelson, W.M., Sakamoto-Arnold, C.M., 1988. Cobalt and copper distributions in the waters of Santa Monica Basin, California. Nature 332, 527–530.
Jørgensen, B.B., 1982. Mineralization of organic matter in the sea bed—the role of sulphate reduction. Nature 296, 643–645.
Joseph, C. Campbell, K.A., Torres, M.E., Martin, R.A., Pohlman, J.W., Riedel, M., Rose, K., 2013. Methane-derived authigenic carbonates from modern and paleoseeps on the Cascadia margin: Mechanisms of formation and diagenetic signals. Palaegeogr. Palaeocl. 390, 52–67.
Joye, S.B., Boetius, A., Orcutt, B.N., Montoya, J.P., Schulz, H.N., Erickson, M.J., Lugo, S.K., 2004. The anaerobic oxidation of methane and sulfate reduction in sediments from Gulf of Mexico cold seeps. Chem. Geol. 205, 219–238.
Judd, A.G., Hovland, M., 2007. Seabed fluid flow – The impact of geology, biology and the marine environment. Cambridge University Press, 492 p.
Jung, H.-S., Lee, C.-B., Cho, Y.-G., Kang, J.-K., 1996. A mechanism for the enrichment of Cu and depletion of Mn in anoxic marine sediments, Banweol Intertidal Flat, Korea. Mar. Poll. Bull. 32, 782–787.
Kah, L.C., Lyons, T.W., Frank, T.D., 2004. Low marine sulphate and protracted oxygenation of the Proterozoic biosphere. Pap. Geosci. 99, 834–838.
Kamber, B.S., Webb, G.E., 2001. The geochemistry of late Archaean microbial carbonate: Implications for ocean chemistry and continental erosion history. Geochim. Cosmochim. Ac. 65, 2509–2525.
Kamber, B.S., Webb, G.E., 2007. Transition metal abundances in microbial carbonate: a pilot study based on in situ LA-ICP-MS analysis. Geobiology 5, 375–389.
Kamber, B.S., Bolhar, R., Webb, G.E., 2004. Geochemistry of late Archaean stromatolites from Zimbabwe: Evidence for microbial life in restricted epicontinental seas. Precambrian Res. 132, 379–399.
Kamber, B.S., Webb, G.E., Gallagher, M., 2014. The rare earth element signal in Archaean microbial carbonate: information on ocean redox and biogenicity. J. Geol. Soc. Lon. 171, 745–763.
Kamijo, M., Suzuki, T., Kawai, K., Murase, H., 1998. Accumulation of yttrium by *Variovorax paradoxus*. J. Fermen. Bioen. 86, 564–568.
Karchmer, J.H., Gunn, E.L., 1952. Determination of trace metals in petroleum fractions. Anal. Chem. 24, 1733–1741.
Karhu, J.A., Holland, H.D., 1996. Carbon isotopes and the rise of atmospheric oxygen. Geology 24, 867–870.
Kasemann, S.A., Hawkesworth, C.J., Prave, A.R., Fallick, A.E., Pearson, P.N., 2005. Boron and calcium isotope composition in Neoproterozoic carbonate rocks from Namibia: evidence for extreme environmental change. Earth Planet. Sci. Lett. 231, 73–86.
Katsikopoulos, D., Fernandez-Gonzalez, A., Prieto, A.C., Prieto, M., 2008. Co-crystallization of Co(II) with calcite: Implications for the mobility of cobalt in aqueous environments. Chem. Geol. 254, 87–100.

Kelly, S.D., Newville, M.G., Cheng, L., Kemner, K.M., Sutton, S.R., Fenter, P., Sturchio, N.C., Spötl, C., 2003. Uranyl incorporation in natural calcite. Environ. Sci.Technol. 37, 1284–1287.

Kennedy, M.J., Christie-Blick, N., Sohl, L.E., 2001. Are Proterozoic cap carbonates and isotopic excursions a record of gas hydrate destabilization following Earth's coldest intervals? Geology 29, 443–446.

Kennicutt, M.C., Brooks, J.M., Denoux, G.J., 1988. Leakage of deep, reservoired petroleum to the near surface on the Gulf of Mexico continental slope. Mar. Chem. 24, 39–59.

Kida, K., Shigematsu, T., Kijima, J., Numaguchi, M., Mochinaga, Y., Abe, N., Morimura, S., 2001. Influence of Ni^{2+} and Co^{2+} on methanogenic activity and the amounts of coenzymes involved in methanogenesis. J. Biosci. Bioeng. 91, 590–595.

Kim, J.-H. Torres, M.E., Haley, D.A., Kastner, M., Pohlman, J.W., Riedel, M., Lee, Y.-J., 2012. The effect of diagenesis and fluid migration on rare earth element distribution in pore fluids of the northern Cascadia accretionary margin. Chem. Geol. 291, 152–165.

King, S.L., Froelich, P.N., Jahnke, R.A., 2000. Early diagenesis of germanium in sediments of the Antarctic South Atlantic: In search of the missing Ge sink. Geochim. Cosmochim. Ac. 64, 1375–1390.

Kinsman, D.J.J., 1978. Interpretation of Sr^{2+} concentrations in carbonate minerals and rocks. J. Sed. Res. 39 , 486–508.

Klinkhammer, G., Elderfield, H., Hudson, A., 1983. Rare earth elements in seawater near hydrothermal vents. Nature, 305, 185–188.

Klungness, G.D., Byrne, R.H., 2000. Comparative hydrolysis behavior of the rare earths and yttrium: the influence of temperature and ionic strength. Polyhedron 19, 99–107.

Knauer, G.A., Martin, J.H., Gordon, R.M., 1982. Cobalt in north-east Pacific waters. Nature, 297, 49–51.

Knauth, L.P., Kennedy, M.J. 2009. The late Precambrian greening of the Earth. Nature 460, 728–732.

Knoll, A.H., Fairchild, I.J., Swett, K., 1993. Calcified microbes in Neoproterozoic carbonates: implications for our understanding of the Proterozoic/Cambrian transition. Palaios 8, 512–525.

Koeppenkastrop, D., De Carlo, E.H., 1993. Uptake of rare earth elements from solution by metal oxides. Environ.Sci. Technol. 27, 1796–1802.

Koide, M., Hodge, V.F., Yang, J.S., Goldberg, E.D., 1987. Determination of rhenium in marine waters and sediments by graphite furnace atomic absorption spectroscopy. Anal. Chem. 59, 1802–1805.

Koide, M., Hodge, V.F., Yang, J.S., Stallard, M., Goldberg, E.G., Calhoun, J., Bertine, K.K., 1986. Some comparative marine chemistries of rhenium, gold, silver and molybdenum. Appl. Geochem. 1, 705–714.

Komiya, T., Hirata, T., Kitajima, K., Yamamoto, S., Shibuya, T., Sawaki, Y., Ishikawa, T., Shu, D., Li, Y., Han, J., 2008. Evolution of the composition of seawater through geologic time, and its influence on the evolution of life. Gondwana Res. 14, 159–174.

Körber, J. H., Sahling, H., Pape, T., dos Santos Ferreira, C., MacDonald, I., Bohrmann, G., 2014. Natural oil seepage at kobuleti ridge, eastern Black Sea. Mar. Pet. Geol. 50, 68–82.

Kornicker, W.A., Morse, J.W., Damasceno, R.N., 1985. The chemistry of Co^{2+} interaction with calcite and aragonite surfaces. Chem. Geol. 53, 229–236.

Krauskopf, K.B., 1956. Factors controlling the concentrations of thirteen rare metals in sea-water. Geochim. Cosmochim. Ac. 9, 1–32.

Kremling, K., 1983. The behavior of Zn, Cd, Cu, Ni, Co, Fe, and Mn in anoxic Baltic waters. Mar. Chem. 13, 87–108.

Kryc, K.A., Murray, R.W., Murray, D.W., 2003. Al-to-oxide and Ti-to-organic linkages in biogenic sediment: relationships to paleo-export production and bulk Al/Ti. Earth Planet. Sci. Lett. 211, 125–141.

Kučera, J., Cempírek, J., Dolníček, Z., Muchez, P., Prochaska, W., 2009. Rare earth elements and yttrium geochemistry of dolomite from post-Variscan vein-type mineralization of the Nízký Jeseník and Upper Silesian Basins, Czech Republic. J. Geochem. Expl. 103, 69–79.

Kulm, L.D., Suess, E., Moore, J.C., Carson, B., Lewis, B.T., Ritger, S., Kadko, D., Thornburg, T., Embley, R., Rugh, W., Massoth, G.J., Langseth, M., Cochrane, G.R., Scamman, R.L., 1986. Oregon subduction zone: Venting, fauna and carbonates. Science 231, 561–566.

Lakshtanov, L.Z., Stipp, S.L.S., 2007. Experimental study of nickel(II) interaction with calcite: Adsorption and coprecipitation. Geochim. Cosmochim. Ac. 71, 3686–3697.

Lal, D., Arnold, J.R., Somayajulu, B.L.K., 1964. A method for the extraction of trace elements from sea water. Geochim. Cosmochim. Ac. 28, 1111–1117.

Land, L.S., 1980. The isotopic and trace element geochemistry of dolomite: the state of the art. SEPM Spec. Publ. 28, 87–110.

Lantzy, R.J., MacKenzie, F.T., 1979. Atmospheric trace metals: global cycles and assessment of man's impact. Geochim. Cosmochim. Ac. 43, 511–525.

Large, R.R., Halpin, J.A., Danyushevsky, L.V., Maslennikov, V.V., Bull, S.W., Long, J.A., Gregory, D.D., Lounejeva, E., Lyons, T.W., Sack, P.J., McGoldrick, P.J., Claver, C.R., 2014. Trace element content of sedimentary pyrite as a new proxy for deep-time ocean-atmosphere evolution. Earth Planet. Sci. Lett. 389, 209–220.

Le Riche, H.H., 1959. The distribution of certain trace elements in the Lower Lias of southern England. Geochim. Cosmochim. Ac. 16, 101–122.

Lécuyer, C., Reynard, B., Grandjean, P., 2004. Rare earth element evolution of Phanerozoic seawater recorded in biogenic apatites. Chem. Geol. 204, 63–102.

Lee, J.H., Byrne, R.H., 1992. Examination of comparative rare earth element complexation behavior using linear free-energy relationships. Geochim. Cosmochim. Ac. 56, 1127–1137.

Lee, J.H., Byrne, R.H., 1993. Complexation of trivalent rare earth elements (Ce, Eu, Gs, Tb, Yb) by carbonate ions. Geochim. Cosmochim. Ac. 57, 295–302.

Lee, Y.J., Elzinga, E.J., Reeder, D.J., 2005. Cu(II) adsorption at the calcite-water interface in the presence of natural organic matter: kinetic studies and molecular-scale characterization. Geochim. Cosmochim. Ac. 69 (1), 49–61.

Leefmann, T., Bauermeister, J., Kronz, A., Liebetrau, V., Reitner, J., Thiel, V., 2008. Miniaturized biosignature analysis reveals implications for the formation of cold seep carbonates at Hydrate Ridge (off Oregon, USA). Biogeosciences 5, 731–738.

Legeleux, F., Reyss, J.-L., Bonte, P., Organo, C., 1994. Concomitant enrichments of uranium, molybdenum and arsenic in suboxic continental margin sediments. Oceanol. Ac. 17 (4), 417–429.

Lehr, C.R., Kashyap, D.R., McDermott, T.R., 2007. New insights into microbial oxidation of antimony and arsenic. Appl. Environ. Microbiol. 73 (7), 2386–2389.

Lemaitre, N., Bayon, G., Ondréas, H., Caprais, J.-C., Freslon, N., Bollinger, C., Rouget, M.-L., de Prunelé, A., Ruffine, L., Olu-Le Roy, K., Sarthou, G., 2014. Trace element behavior at cold seeps and the potential export of dissolved iron to the ocean. Earth Planet Sci. Lett. 404, 376–388.

Leuz, A.-K., Mönch, H., Johnson, C.A., 2006. Sorption of Sb(III) and Sb(V) to goethite: Influence on Sb(III) oxidation and mobilization. Environ. Sci. Technol. 40, 7227–7282.

Lewan, M.D., Maynard, J.B., 1982. Factors controlling enrichment of vanadium and nickel in the bitumen of organic sedimentary rocks. Geochim. Cosmochim. Ac. 46, 2547–2560.

Lewis, B.L., Andreae, M.O., Froelich, P.N., 1989. Sources and sinks of methylgermanium in natural waters. Mar. Chem. 27, 179–200.

Leybourne, M.I., Johannesson, K.H., 2008. Rare earth elements (REE) and yttrium in stream waters, stream sediments, and Fe-Mn oxyhydroxides: Fractionation, speciation, and controls over REE+Y patterns in the surface environment. Geochim. Cosmochim. Ac. 72, 5962–2983.

Liang, Q., Hu, Y., Feng, D., Peckmann, J., Chen, L., Yang, S., Liang, J., Tao, J., Chen, D., 2017. Authigenic carbonates from newly discovered active cold seeps on the northwestern slope of the South China Sea: Constraints on fluid sources, formation environments, and seepage dynamics. Deep-Sea Res. I 124, 31–41.

Li, F., Yan, X., Burne, R.V., Chen, Z.-Q., Algeo, T.J., Zhang, W., Gan, Y., Xie, S., 2017. Paleo-seawater REE compositions and microbial signatures preserved in laminae of Lower Triassic ooids. Palaelgeogr. Palaeoclim. in press.

Li, N., Feng, D., Chen, L., Wang, H., Chen, D., 2016. Using sediment geochemistry to infer temporal variation of methane flux at a cold seep in the South China Sea. Mar. Petrol. Geol. 77, 835–845.

Liger, E., Charlet, L., Van Cappellen, P., 1999. Surface catalysis of uranium(VI) reduction by iron(II). Geochim. Cosmochim. Ac. 63 (19/20), 2939–2955.

Lindsay, J.F., Brasier, M.D., 2002. Did global tectonics drive early biosphere evolution? Carbon isotope record from 2.6 to 1.9 Ga carbonates of Western Australian basins. Precambrian Res. 114, 1–34.

Ling, H.-F., Chen, X., Li, D., Wang, D., Shields-Zhou, G.A., Zhu, M., 2013. Cerium anomaly variations in Ediacaran-earliest Cambrian carbonates from the Yangtze Gorges area, South China: Implications for oxygenation of coeval shallow seawater. Precambrian Res. 225, 110–127.

Liu, C.-C., Jean, J.-S., Nath, B., Lee, M.-K., Hor, L.-I., Lin, K.-H., Maity, J.P., 2009. Geochemical characteristics of the fluids and muds from two southern Taiwan mud volcanoes: Implications for water-sediment interaction and groundwater arsenic enrichment. Appl. Geochem. 24, 1793–1802.

Liu, Y., Hu, Z., Gao, S., Günther, D., Xu, J., Gao, C., Chen, H., 2016. In situ analysis of major and trace elements of anhydrous minerals by LA-ICP-MS without applying an internal standard. Chem. Geol. 257, 34–43.

Liu, Y., Hu, Z., Li, M., Gao, S., 2013. Applications of LA-ICP-MS in the elemental analyses of geologic samples. Chin. Sci. Bull. 58, 3863–3878.

Lloyd, J.R., 2003. Microbial reduction of metals and radionuclides. FEMS Microbiol. Rev. 27, 441–425.

Loges, A., Wagner, T., Barth, M., Bau, M., Göb, S., Markl, G., 2012. Negative Ce anomalies in Mn oxides: The role of Ce^{4+} mobility during water-mineral interaction. Geochim. Cosmochim. Ac. 86, 296–317.

Longerich, H.P., Jackson, S.E., Gunther, D., 1996. Laser ablation inductively coupled plasma mass spectrometric transient signal data acquisition and analyte concentration calculation. J. Anal. At. Spectrom. 11, 899–904.

Lorens, R.S., 1981. Sr, Cd, Mn and Co distribution coefficients in calcite as a function of calcite precipitation rate. Geochim. Cosmochim. Ac. 45, 553–561.

Lovley, D.R., 1993. Dissimilatory metal reduction. Ann. Rev. Microbiol. 47, 263–290.

Lovley, D.R., Phillips, E.J.P., Gorby, Y.A., Landa, E.r., 1991. Microbial reduction of uranium. Nature 350, 413–416.

Lovley, D.R., Phillips, E.J.P., 1992. Reduction of uranium by *Desulfovibrio desulfuricans*. Appl. Environ. Microbiol. 58, 850–856.

Lovley, D.R., Roden, E.E., Phillips, E.J.P., Woodward, J.C., 1993. Enzymatic iron and uranium reduction by sulfate-reducing bacteria. Mar. Geol. 113, 41–53.

Luff, R., Wallmann, K., 2003. Fluid flow, methane fluxes, carbonate precipitation and biogeochemical turnover in gas hydrate-bearing sediments at Hydrate Ridge, Cascadia Margin: Numerical modeling and mass balances. Geochim. Cosmochim. Ac. 67, 3403–3421.

Luo, Y.-R., Byrne, E.H., 2004. Carbonate complexation of yttrium and the rare earth elements in natural waters. Geochim. Cosmochim. Ac.68, 691–699.

Luo, W., Guo, B., 2009. Dissolution and mobilization of uranium in a reduced sediment by natural humic substances under anaerobic conditions. Environ. Sci. Technol. 43, 152–156.

Lyalikova, N.N., Yurkova, N.A., 1992. Role of microorganisms in vanadium concentration and dispersion. Geomicrobiol. J. 10, 15–26.

Lyons, T. W., Reinhard, C.T., Planavsky, N.J., 2014. The rise of oxygen in Earth's early ocean and atmosphere. Nature 506, 307–315.

MacDonald, I.R., Buthman, D B., Sager, W.W., Peccini, M.B., Guinasso, N.L., 2000. Pulsed oil discharge from a mud volcano. Geology 28, 907–910.

MacDonald, I.R., Bohrmann, G., Escobar, E., Abegg, F., Blanchon, P., Blinova, V., Brückmann, W., Drews, M., Eisenhauer, A., Han, X., Heeschen, K., Meier, F., Mortera, C., Naehr, T., Orcutt, B., Bernard, B., Brooks, J., de Faragó, M., 2004. Asphalt volcanism and chemosynethetic life in the Campeche Knolls, Gulf of Mexico. Science 304, 999–1002.

Maher, W., Butler, E., 1988. Arsenic in the marine environment. Appl. Organomet. Chem. 2, 191–214.

Manning, B.A., Goldberg, S., 1996. Modeling competitive adsorption of arsenate with phosphate and molybdate on oxide minerals. Soil Sci. Soc. Am. J. 60, 121–131.

Marques Fernandes, M., Schmidt, M., Stumpf, T., Walther, C., Bosbach, D., Klenze, R., Fanghänel, T., 2008. Site-selective time-resolved laser fluorescence spectroscopy of Eu3+ in calcite. J. Coll. Interf. Sci. 321, 323–331.

Maliva, R.G., Knoll, A.H., Simonson, B.M., 2005. Secular change in the Precambrian silica cycle: insights from chert petrology. Geol. Soc. Am. Bull. 117, 835–845.

Martin, J.M., Whitfield, M., 1983. The significance of the river input of chemical elements to the ocean. In: Trace metals in sea water, Springer US., 265–296.

Martin, J.M., Hogdahl, O., Philippot, J.C., 1976. Rare earth element supply to the Ocean. J. Geopys. Res. 81, 3119–3124.

Maskenskaya, O.M., Drake, H., Mathurin, F.A., Åström, M.E., 2015. The role of carbonate complexes and crystal habit on rare earth element uptake in low-temperature calcite in fractured crystalline rock. Chem. Geol. 391, 100–110.

Mazumdar, A., Tanaka, K., Takahashi, T., Kawabe, I., 2003. Characteristics of rare earth element abundances in shallow marine continental platform carbonates of Late Neoproterozoic successions from India. Geochem. J. 37, 277–289.

McArthur, J.M., Walsh, J.N., 1984. Rare-earth geochemistry of phosphorites. Chem. Geol. 47, 191–220.

McBride, M.B., 1979. Chemisorption and precipitation of Mn^{2+} at $CaCO_3$ surfaces. Soil Sci. Soc. Amer. J. 41, 693–698.

McBride, M.B., 1980. Chemisorption of Cd^{2+} on calcite surfaces. Soil Sci. Soc. Amer. J. 44 (1), 26–28.

McKenzie, R.M., 1983. The adsorption of molybdenum on oxide surfaces. Aust. J. Soil Res. 21 (4), 505–513.

McManus, J., Berelson, W.M., Klinkhammer, G.P., Hammond, D.E., Holm, C., 2005. Authigenic uranium: relationship to oxygen penetration and organic carbon rain. Geochim. Cosmochim. Ac. 69 (1), 95–108.

McManus, J., Berelson, W.M., Severmann, S., Poulson, R.L., Hammond, D.E., Klinkhammer, G.E., Holm, C., 2006. Molybdenum and uranium geochemistry in continental margin sediments: Paleoproxy potential. Geochim. Cosmochim. Ac. 70 (18), 4643–4662.

McManus, J., Hammond, D.E., Cummins, K., Klinkhammer, G.P., Berelson, W.M., 2003. Diagenetic Ge-Si fractionation in continental margin environments: Further evidence for a nonopal Ge sink. Geochim. Cosmochim. Ac. 67 (23), 4545–4557.

McLennan, S.M., 2001. Relationships between the trace element composition of sedimentary rocks and upper continental crust. Geochem. Geophys. Geosys. 2, Paper number 2000GC000109.

Measures, C.I., Burton, J.D., 1980. The vertical distribution and oxidation states of dissolved selenium in the Northeast Atlantic Ocean and their relationship to biological processes. Earth Planet. Sci. Lett. 46, 385–396.

Meece, D.E., Benninger, L.K., 1993. The coprecipitation of Pu and other radionuclides with $CaCO_3$. Geochim. Coscmochim. Ac. 57, 1447–1458.

Melezhik, V.A., Huhma, H., Condon, D.J., Fallick, A.E., Whitehouse, M.J., 2007. Temporal constraints on the Paleoproterozoic Lomagundi-Jatuli carbon isotopic event. Geology 35, 655–658.

Metz, S., Trefry, J.H., 2000. Chemical and mineralogical influences on concentrations of trace metals in hydrothermal fluids. Geochim. Cosmochim. Ac. 64, 2267–2279.

Meyer, E.E., Quicksall, A.N., Landis, J.D., Link, P.K., Bostrick, B.C., 2012. Trace and rare earth elemental investigation of a Sturtian cap carbonates, Pocatello, Idaho: Evidence for ocean redox conditions before and during carbonate deposition. Precambrian Res. 192–195, 89–106.

Middelburg, J.J., Hoede, D., Van der Sloot, H.A., Van der Weijden, C.H., Wijkstra, J., 1988. Arsenic, antimony and vanadium in the North Atlantic Ocean. Geochim. Cosmochim. Ac. 52, 2871–2878.

Millero, F.J., 1992. Stability constants for the formation of rare earth inorganic complexes as a function of ionic strength. Geochim. Cosmochim. Ac. 56, 3123–3132.

Millero, F.J., 2007. The marine inorganic carbon cycle. Chem. Rev. 107, 308–341.

Milner, O.I., Glass, J.R., Kirchner, J.P., Yurick, A.N., 1952. Determination of trace metals in crudes and other petroleum oils. Anal. Chem. 24, 1728–1732.

Min, G.R., Edwards, R.L., Taylor, F.W., Recy, J., Gallup, C.D. Beck, J.W. 1995. Annual cycles of U/Ca in coral skeletons and U/Ca thermometry. Geochim. Cosmochim. Ac. 59, 2025–2042.

Miura, N., Kawabe, I., 2000. Dolomitization of limestone with $MgCl_2$ solution at 150°C: Preserved original signatures of rare earth elements and yttrium as marine limestone. Geochem. J. 34, 223–227.

Moffett, J.W., 1990. Microbially mediated cerium oxidation in seawater. Nature 345, 421–423.

Möller, P., Bau, M., 1993. Rare earth patterns with positive Ce anomaly in alkaline waters from Lake Van, Turkey. Earth Planet. Sci. Lett. 117, 671–676.

Montaggioni, L.F., Camoin, G.F., 1993. Stromatolites associated with coralgal communities in Holocene high-energy reefs. Geology 21, 149–152.

Monteil-Rivera, F., Fedoroff, M., Jeanjean, J., Mineral, L., Barthes, M.-G., Dumonceau, J., 2000. Sorption of selenite (SeO_3^{2-}) on hydroxyapatite: an exchange process. J. Colloid. Interf. Sci. 221, 291–300.

Moore, J.N., Ficklin, W.H., Johns, C., 1988. Partitioning of arsenic and metals in reducing sulfidic sediments. Environ. Sci. Technol. 22, 432–437.

Morel, F.M.M., Price, N.M., 2003. The biogeochemical cycles of trace metals in the oceans. Science 300, 944–947.

Morel, F.M., Hudson, R.J., Price, N.M., 1991. Limitation of productivity by trace metals in the sea. Limnol. Oceanogr. 36, 1742–1755.

Moore, R.M., Webb, R., Tokarczyk, R., Wever, R., 1996. Bromoperoxidase and iodoperoxidase enzymes and production of halogenated methanes in marine diatom cultures. J. Geophys. Res. 101, 20899–20908.

Morford, J.L., Emerson, S.R., 1999. The geochemistry of redox sensitive trace metals in sediments. Geochim. Cosmochim. Ac. 63, 1735–1750.

Morford, J.L., Emerson, S.R., Breckel, E.J., Kim, S.H., 2005. Diagenesis of oxyanoins (V, U, R, and Mo) in pore waters and sediments from a continental margin. Geochim. Cosmochim. Ac. 69, 5021–5032.

Morford, J.L., Martin, W.R., Carney, C.M., 2009. Uranium diagenesis in sediments underlying bottom waters with high oxygen content. Geochim. Cosmochim. Ac. 73, 2920–2937.

Morgan, B., Rate, A.W., Burton, E.D., Smirk, M.N., 2012. Enrichment and fractionation of rare earth elements in FeS- and organic-rich estuarine sediments receiving acid sulfate soil drainage. Chem. Geol. 308–309, 60–73.

Moriwaki, H., Yamamoto, H., 2013. Interactions of microorganisms with rare earth ions and their utilization for separation and environmental technology. Appl. Microbiol. Biotechnol. 97, 1–8.

Morse, J.W., Bender, M.L., 1990. Partition coefficients in calcite: Examination of factors influencing the validity of experimental results and their application to natural systems. Chem. Geol. 82, 265–277.

Morse, J.W., MacKenzie, F.T., 1990. Geochemistry of sedimentary carbonates. Developments in sedimentology 48, 707 p.

Morse, J.W., Luther, G.W., 1999. Chemical influences on trace metal-sulfide interactions in anoxic sediments. Geochim. Cosmochim. Ac. 63 (19/20), 3373–3378.

Morse, J.W., Arvidson, R.A., Lüttge, A., 2007. Calcium carbonate formation and dissolution. Chem. Rev. 197, 342–381.

Mucci, A., Richard, L.-F., Lucotte, M., Guignard, C., 2000. The differential geochemical behavior of arsenic and phosphorus in the water column and sediments of the Saguenay Fjord estuary, Canada. Aquat. Geochem. 6, 293–324.

Müller, G., 1969. Index of geoaccumulation in the sediments of the Rhine River. Geojournal 2, 108–118.

Murnane, R.J., Leslie, B., Hammond, D.E., Stallard, R.F., 1989. Germanium geochemistry in the Southern California Borderlands. Geochim. Cosmochim. Ac. 53, 2873–2882.

Murray, R.W., Ten Brink, M.R.B., Gerlach, D.C., Russ, G.P., Jones, D.L., 1992. Rare earth, major, and trace element composition of Monterey and DSDP chert and associated host sediment: Assessing the influence of chemical fractionation during diagenesis. Geochim. Cosmochim. Ac. 56, 2657–2671.

Murray, R.W.,Ten Brink, M.R.B., Jones, D.L., Gerlach, D.C., Russ, G.P., 1990. Rare earth elements as indicators of different marine depositional environments in chert and shale. Geology, 18, 268–271.

Naehr, T.H., Birgel, D., Bohrmann, G., MacDonald, I.R., Kasten, S., 2009. Biogeochemical controls on authigenic carbonate formation at the Chapopote "asphalt volcano", Bay of Campeche. Chem. Geol. 266, 390–402.

Nagarajan, R., Madhavaraju, J., Armstrong-Atlin, J.S., Nagendra, R., 2011. Geochemistry of Neoproterozoic limestones of the Sahabad Formation, Bhima Basin, Karnataka, southern India. Geosci. J. 15, 9–25.

Nalewajko, G., Lee, K., Jack, T.R., 1995. Effects of vanadium on freshwater phytoplankton photosynthesis. Water Air Soil Poll. 81, 93–105.

Nameroff, T.J., Balistrieri, L.S., Murray, J.W., 2002. Suboxic trace metal geochemistry in the eastern tropical North Pacific. Geochim. Cosmochim. Ac. 66 (7), 1139–1158.

Nance, W.B., Taylor, S.R., 1976. Rare earth elements patterns and crustal evolution – I. Australian post-Archean sedimentary rocks. Geochim. Cosmochim. Ac. 40, 1539–1551.

Nath, B., Jean, J.-S., Lee, M.-K., Yang, H.-J., Liu, C.-C., 2008. Geochemistry of high arsenic groundwater in Chia-Nan plain, Southwestern Taiwan: Possible sources and reactive transport of arsenic. J. Contam. Hydrol. 99, 85–96.

Neubert, N., Nägler, T.F., Böttcher, M.E., 2008. Sulfidity controls molybdenum isotope fractionation into euxinic sediments: Evidence from the modern Black Sea. Geology 36 (10), 775–778.

Neuweiler, F., Gautret, P., Thiel, V., Lange, R., Michaelis, W., Reitner, J., 1999. PEtrology of Lower Cretaceous carbonate mud mounds (Albian, N. Spain): insights into organomineralic deposits of the geological record. Sedimentology 46, 837–859.

Neuweiler, F., Reitner, J., Arp, G., 1996. Controlling factors and environmental significance of organomicrite production and buildup development. In: Reitner, J., Neuweiler, F., Gunkel, F., (Eds.), Global and Regional Controls on Biogenic Sedimentation. I. Reefal Evolution. Research Reports, Göttinger Arb. Geol. Paläont. Sb2, 185–192.

Nöthen, K., Kasten, S., 2011. Reconstructing changes in seep activity by means of pore water and solid phase Sr/Ca and Mg/Ca ratios in pockmark sediments of the Northern Congo Fan. Mar. Geol. 287, 1–13.

Nothdurft, L.D., Webb, G.E., Kamber, B.S., 2004. Rare earth element geochemistry of Late Devonian reefal carbonates, Canning Basin, Western Australia: confirmation of a seawater REE proxy in ancient limestones. Geochim. Cosmochim. Ac. 68, 263–283.

Novikova, S.A., Shnyukov, Y.F., Sokol, E.V., Kozmenko, O.A., Semenova, D.V., Kutny, V.A., 2015. A methane-derived carbonate build-up at a cold seep on the Crimean slope, north-western Black Sea. Mar. Geol. 363, 160–173.

Nozaki, Y., Zhang, J., Amakawa, H., 1997. The fractionation between Y and Ho in the marine environment. Earth Planet. Sci. Lett. 148, 329–340.

Och, L.M., Shields-Zhou, G.A., 2012. The Neoproterozoic oxygenation event: Environmental perturbations and biogeochemical cycling. Earth Sci. Rev. 110, 26–57.

Ohta, A., Kawabe, I., 2001. REE (III) adsorption onto Mn dioxide (MnO_2) and Fe oxyhydroxide: Ce(III) oxidation by MnO_2. Geochim. Cosmochim. Ac. 65, 695–703.

Ohde, S., Ohta, N., Tomura, K., 1978. Determination of trace elements in carbonates by instrumental neutron activation analysis. J. Radiolyt. Chem. 42, 159—167.

Orcutt, B.N., Joye, S.B., Kleindienst, S., Knittel, K., Ramette, A., Reitz, A., Samarkin, V., Treude, T., Boetius, A., 2010. Impact of natural oil and higher hydrocarbons on microbial diversity, distribution, and activity in Gulf of Mexico cold-seep sediments. Deep Sea Res. II: 57, 2008—2021.

Oremland, R.S., Hollibaugh, J.T., Maes, A.S., Presser, T.S., Miller, L.G. , Culbertson, C.W., 1989. Selenate reduction to elemental selenium by anaerobic bacteria in sediments and culture: biogeochemical significance of a novel, sulfate-independent respiration. Appl. Environ. Microbiol. 55, 2333—2343.

Oremland, R.S., Kulp, T.R., Blum, J.S., Hoeft, S.E., Baesman, S., Miller, L.G., Stolz, J.F., 2005. A microbial arsenic cycle in a salt-saturated extreme environment. Science 308, 1305–1308.

Osborne, A.H., Haley, B.H., Hathorne, E.C., Plancherel, Y., Frank, M., 2015. Rare earth element distribution in Caribbean seawater: Continental inputs versus lateral transport of distinct REE compositions in subsurface water masses. Mar. Chem. 177, 172—183.

Ozaki, T., Suzuki, Y., Nankawa, T., Yoshida, T., Ohnuki, T., Kimura, T., Francis, A.J., 2006. Interactions of rare earth elements with bacteria and organic ligands. J. Alloy. Compd. 408–412, 1334–1338.

Pagnanelli, F., Viggi, C.C., Toro, L., 2010. Isolation and quantification of cadmium removal mechanisms in batch reactors inoculated by sulphate reducing bacteria: Biosorption versus bioprecipitation. Biores. Technol. 101, 2981–2987.

Palomares, R.M., Hernández, R.L., Friás, J.M., 2012. Mechanisms of trace metal enrichment in submarine, methane-derived carbonate chimneys from the Gulf of Cadiz. J. Geochem. Explor. 112, 297–305.

Paquette, J., Reeder, R.J., 1995. Relationship between surface structure, growth mechanism, and trace element incorporation in calcite. Geochim. Cosmochim. Ac. 59 (4), 735–749.

Parekh, P.P., Möller, P., Dulski, P., 1977. Distribution of trace elements between carbonate and non-carbonate phases of limestone. Earth Planet. Sci. Lett. 34, 39–50.

Parmar, N., Gorby, Y.A., Beveridge, T.J., Ferris, F.G., 2001. Formation of green rust and immobilization of nickel in response to bacterial reduction of hydrous ferric oxide. Geomicrobiol. J. 184, 375–385.

Pattan, J.N., Pearce, N.J.G., Mislankar, P.G., 2005. Constraints in using Cerium-anomaly of bulk sediments as an indicator of paleo bottom water redox environment: A case study from the Central Indian Ocean Basin. Chem. Geol. 221, 260–278.

Paull, C.K., Chanton, J.P., Neumann, A.C., Coston, J.A., Martens, C.S., 1992. Indicators of methane-derived carbonates and chemosynthetic organic carbon deposits: examples from the Florida escarpment. Palaios 7, 361–375.

Pearce, N. J.G., Perkins, W.T., Fuge, R., 1992. Developments in the quantitative and semiquantitative determination of trace elements in carbonates by laser ablation inductively coupled plasma mass spectrometry. J. Anal. At. Spectrom. 7, 595–598.

Pearson, R.G., 1963. Hard and soft acids and bases. J. Am. Chem. Soc. 85 (22), 3533–3539.

Peckmann, J., Thiel, V., 2004. Carbon cycling at ancient methane–seeps. Chem. Geol. 205, 443–467.

Peckmann, J., Campbell, K.A., Walliser, O.H., Reitner, J., 2007. A Late Devonian hydrocarbon-seep deposit dominated by dimerelloid brachiopods, Morocco. Palaios 22, 114–122.

Peckmann, J., Goedert, J. L., Heinrichs, T., Hoefs, J., Reitner, J., 2003. The Late Eocene'Whiskey Creek'methane-seep deposit (western Washington State): Part II: Petrology, Stable Isotopes, and Biogeochemistry. Facies 48, 241–253.

Peckmann, J., Paul, J., Thiel, V., 1999. Bacterially mediated formation of diagenetic aragonite and native sulfur in Zechstein carbonates (Upper Permian, Central Germany). Sed. Geol. 126, 205–222.

Peketi, A., Mazumdar, A., Joshi, R.K., Patil, D.J., Srinivas, P.L., Dayal, A.M., 2012. Tracing the Paleo sulfate-methane transition zones and H_2S seepage events in marine sediments: An application of C-S-Mo systematics. Geochem. Geophys. Geosys. 13 (10), doi:10.1029/2012GC004288.

Perkins, W.T., Fuge, R., Pearice, N.J.G., 1991. Quantitative analysis of trace elements in carbonates using laser ablation inductively coupled plasma mass spectrometry. J. Anal. Atom. Spectrom. 6, 445—449.

Peterson, M.L., Carpenter, R., 1986. Arsenic distributions in porewaters and sediments of Puget Sound, Lake Washington, the Washington coast and Saanich Inlet, B.C.. Geochim. Cosmochim. Ac. 50, 353–369.

Pettine, M., D'Ottone, L., Campanella, L., Millero, F.J., Passino, R., 1998a. The reduction of chromium (CI) by iron (III) in aqueous solutions. Geochim. Cosmochim. Ac. 62, 1509–1519.

Pettine, M., Barra, I., Campanella, L., Millero, F.J., 1998b. Effects of metals on the reduction of chromium (VI) with hydrogen sulfide. Wat. Res. 32 (9), 2807–2813.

Pierce, M.L., Moore, C.B., 1982. Adsorption of arsenite and arsenate on amorphous iron hydroxide. Water Res. 16, 1247–1253.

Pierre, C., Bayon, G., Blanc-Valleron, M.-M., Mascle, J., Dupré, S., 2014. Authigenic carbonates related to active seepage of methane-rich hot brines at the Cheops mud volcano, Menes caldera (Nile deep-sea fan, eastern Mediterranean Sea). Geo-Mar. Lett. DOI 10.1007/s00367-014-0362-6.

Piepgras, D.J., Wasserburg, G.J., 1985. Strontium and neodymium isotopes in hot springs on the East Pacific Rise and Guaymas Basin. Earth Planet. Sci. Lett. 72, 341–356.

Piper, D.Z., 1974. Rare earth elements in the sedimentary cycle. Chem. Geol. 14, 285–304.

Piper, D.Z., Bau, M., 2013. Normalized rare earth elements in water, sediments, and wine: Identifying sources and environmental redox conditions. Am. J. Anal. Chem. 4, 69–83.

Piper, D.Z., Dean, W.E., 2002. Trace-element deposition in the Cariaco Basin, Venezuela Shelf, under sulfate-reducing conditions – a history of the local hydrography and global climate, 20ka to the present. USGS Prof. Pap. No. 1670, 41 p.

Piper, D.Z., Perkins, R.B., 2004. A modern vs. Permian black shales – the hydrography, primary productivity, and water-column chemistry of deposition. Chem. Geol. 206, 177–197.

Potts, P.J., Thorne, O.W., Watson, J.S., 1981. Determination of the rare-earth element abundances in 29 international rock standards by instrumental neutron activation analysis: A critical appraisal of calibration errors. Chem. Geol. 34, 331–352.

Poulton, S.W., Fralick, P.W., Canfield, D.E., 2004a. The transition to a sulphidic ocean ~1.84 billion years ago. Nature 431, 173–177.

Poulton, S.W., Krom, M.D., Raiswell, R., 2004b. A revised scheme for the reactivity if iron (oxyhydr)oxide minerals towards dissolved sulfide. Geochim. Cosmochim. Ac. 68, 3703–3715.

Pourret, O., Davranche, M., Gruau, G., Dia, A., 2008. New insights into cerium anomalies in organic-rich alkaline waters. Chem. Geol. 251, 120–127.

Pourret, O., Davranche, M., Gruau, G., Dia, A., 2007. Rare earth elements complexation with humic acid. Chem. Geol. 243, 128–141.

Prange, A., Kremling, K., 1985. Distribution of dissolved molybdenum, uranium and vanadium in Baltic Sea waters. Mar. Chem. 16, 259–274.

Premovic, P.I., Pavlovic, M.S., Pavlovic, N.Z., 1986. Vanadium in ancient sedimentary rocks of marine origin. Geochim. Cosmochim. Ac. 50, 1923–1931.

Presley, B.J., Kaplan, I.R., 1968. Changes in dissolved sulfate, calcium and carbonate from interstitial water of near-shore sediments. Geochim. Cosmochim. Act. 32, 1037–1048.

Presley, B.J., Kolodny, Y., Nissenbaum, A., Kaplan, I.R., 1972. Early diagenesis in a reducing fjord, Saanich Inlet, British Columbia—II. Trace element distribution in interstitial water and sediment. Geochim. Cosmochim. Ac. 36, 1073–1090.

Qu, C., Liu, G., Zhao, Y., 2009. Experimental study on the fractionation of yttrium from holmium during the coprecipitation with calcium carbonates in seawater solutions. Geochem. J. 43, 403–414.

Quinn, K.A., Byrne, R.H., Schijf, J., 2006. Sorption of yttrium and rare earth elements by amorphous ferric hydroxide: influence of solution complexation with carbonate. Geochim. Cosmochim. Ac. 70, 4151–4165.

Raiswell, R., Canfield, D.E., 2012. The iron biogeochemical cycle past and present. Geochem. Persp. 1, 1–220.

Ravizza, G., Turekian, K.K., Hay, B.J., 1991. The geochemistry of rhenium and osmium in recent sediments from the Black Sea. Geochim. Cosmochim. Ac. 55, 3741–3752.

Redman, A.D., Macalady, D.L., Ahmann, D., 2002. Natural organic matter affects arsenic speciation and sorption onto hematite. Environ. Sci. Technol. 36, 2889–2896.

Reeder, R.J., Lamble, G.M., Northrup, P.A., 1999. XAFS study of the coordination and local relaxation around Co^{2+}, Zn^{2+}, Pb^{2+}, and Ba^{2+} trace elements in calcite. Am. Mineral. 84, 1049–1060.

Reeder, R J., Nugent, M., Tait, C.D., Morris, D.E., Heald, S.M., Beck, K.M., Hess, W.P., Lanzirotti, A., 2001. Coprecipitation of uranium (VI) with calcite: XAFS, micro-XAS, and luminescence characterization. Geochim. Cosmochim. Ac. 65, 3491–3503.

Reeder, R.J., Nugent, M., Lamble, G.M., Tait, C.D., Morris, D.E., 2000. Uranyl incorporation into calcite and aragonite: XAFS and luminescence studies. Environ. Sci. Technol. 34, 638–644.

Richards, F.A., 1956. On the state of our knowledge of trace elements in the ocean. Geochim. Cosmochim. Ac. 10, 241–243.

Riding, R., 2002. Structure and composition of organic reefs and carbonate mud mounds: concepts and categories. Earth Sci. Rev. 58, 163–231.

Riding, R., 2011. The nature of stromatolites: 3.500 million years of history and a century of research. In: Reitner, J., Quéric, N.-V., Arp, G., Advances in stromatolite geobiology, Springer Berlin Heidelberg, 29–74.

Riley, J.P., Taylor, D., 1968. Chelating resins for the concentration of trace elements from sea waater and their analytical use in conjunction with atomic absorption spectrophotometry. Anal. Chim. Ac. 40, 479–485.

Rimstidt, J D., Balog, A., Webb, J., 1998. Distribution of trace elements between carbonate minerals and aqueous solutions. Geochim. Cosmochim. Ac. 62, 1851–1863.

Ritger, S., Carson, B., Suess, E., 1987. Methane-derived authigenic carbonates formed by subduction-induced pore-water expulsion along the Oregon/Washington margin. Geol. Soc. Am. Bull. 98, 147–156.

Robbins, L.J., Lalonde, S.V., Planavsky, N.J., Partin, C.A., Reinhard, C.T., Kendall, B., Scott, C., Hardisty, D.S., Gill, B. C., Alessi, D.S., Dupont C.L., Saito, M.A., Poulton, S.W., Bekker, A., Lyons, T.W., Konhauser, K.O., 2016. Trace elements at the intersection of marine biological and geochemical evolution. Earth-Sci. Rev. 163, 323–348.

Román-Ross, G., Cuello, G.J., Turrillas, X., Fernández-Martinez, A., Charlet, L., 2006. Arsenite sorption and co-precipitation with calcite. Chem. Geol. 233, 328–336.

Rongemaille, E., Bayon, G., Pierre, C., Bollinger, C., Chu, N.C., Fouquet, Y., Riboulot, V., Voisset, M., 2011. Rare earth elements in cold seep carbonates from the Niger delta. Chem. Geol. 286, 196–206.

Rosenthal, Y., Lam, P., Boyle, E.A., Thomson, J., 1995. Authigenic cadmium enrichments in suboxic sediments: Precipitation and postdepositional mobility. Earth Planet. Sci. Lett. 132, 99–111.

Rousseau, T.C.C., Sonke, J.E., Chmeleff, J., Candaudap, F., Lacan, F., Boaventura, G., Seyler, P., Jeandel, C., 2013. Rare earth element analysis in natural waters by multiple isotope dilution – sector field ICP-MS. J. Anal. At. Spectrom. 28, 573–584.

Rovira, M., Giménez, J., Martínez, M., Martínez-Lladó, X., de Pablo, J. Martí, V., Duro, L., 2008. Sorption of selenium(IV) and selenium(VI) onto natural iron oxides: Goethite and hematite. J. Hazard. Mater. 150, 279–284.

Rudnick, R.L., Gao, S., 2003. Composition of the continental crust. In: Treatise on Geochemistry (Holland, H.D., Turekian, K.K., Eds.), Elsevier, New York, 1–64.

Rudnicki, M.D., Elderfield, H., 1993. A chemical model of the buoyant and neutrally buoyant plume above the TAG vent field, 26N, Mid-Atlantic Ridge. Geochim. Cosmochim. Ac. 57, 2939–2958.

Russell, A.D., Morford, J.L., 2001. The behavior of redox-sensitive metals across a laminated-massive-laminated transition in Saanich Inlet, British Columbia. Mar. Geol. 174, 341–354.

Sabau, A., Pipon, Y., Toulhoat, N., Lomenech, C., Jordan, N., Moncoffre, N., Barkleit, A., Marmier, N., Brendler, V., Surblé, S., Giffuat, E., 2014. Interaction of europium and nickel with calcite studied by Rutherford backscatter spectrometry and time-resolved laser fluorescence spectroscopy. Nucl. Instr. Meth. Phys. Res. B. 332, 111–116.

Sahling, H., Rubin Blum, M., Borowski, C., Escobar-Briones, E., Gaytán Caballero, A., Hsu, C.-W., Loher, M., MacDonald, I.M., Marcon, Y., Pape, T., Römer, M., Schubotz, F., Smrzka, D., Wegener, G., Bohrmann, G., 2016. Massive asphalt deposits, oil seepage, and gas venting support abundant chemosynthetic communities at the Campeche Knolls, southern Gulf of Mexico. Biogeosciences 13, 4491–4512.

Salomons, W., Förstner, U., 1984. Metals in the hydrocycle. Springer, Berlin Heidelberg Tokyo.

Sato, H., Hayashi, K.-I., Ogawa, Y., Kawamura, K., 2012. Geochemistry of deep sea sediments at cold seep sites in the Nankai Trough: insights into the effect of anaerobic oxidation of methane. Mar. Geol. 323, 47–55.

Saito, M.A., Moffett, J.W., 2002. Temporal and spatial variability of cobalt in the Atlantic Ocean. Geochim. Coscmochim. Ac. 66 (11), 1943–1953.

Saito, M.A., Moffett, J.W., DiTullio, G.R., 2004. Cobalt and nickel in the Peru upwelling region: A major flux of labile cobalt utilized as a micronutrient. Glob. Biogeochem. Cyc. 18, DOI: 10.1029/2003GB002216.

Sandberg, P.A., 1983. An oscillating trend in Phanerozoic non-skeletal carbonate mineralogy. Nature 305, 19–22.

Savard, M.M., Beauchamp, B., Veizer, J., 1996. Significance of aragonite cements around Cretaceous marine methane seeps. J. Sed. Res. 66, 430–438.

Sawada, K., Abdel-Aal, K., Tan, K., Satoh, K., 2005. Adsorption of lanthanoid ions on calcite. Dalton Trans. 20, 3291–3296.

Scheller, S., Goenrich, M., Boecher, R., Thauer, R.T., Jaun, B., 2012. The key nickel enzyme of methanogenesis catalyses the anaerobic oxidation of methane. Nature 465, 606–608.

Scherer, M., Seitz, H., 1980. Rare-earth element distribution in Holocene and Pleistocene corals and their redistribution during diagenesis. Chem. Geol. 28, 279–289.

Schieber, J., 1988. Redistribution of rare-earth elements during diagenesis of carbonate rocks from the mid Proterozoic Newland Formation, Montana, U.S.A. Chem. Geol. 69, 111–126.

Schijf, J., Byrne, R.H., 2004. Determination of $SO_4\beta 1$ for yttrium and the rare earth elements at I = 0.66m and t = 25°C – Implications for YREE solution speciation in sulfate-rich waters. Geochim. Cosmochim. Ac. 68, 2825–2837.

Schijf, J., De Baar, H.J.W., Millero, F.J., 1995. Vertical distributions and speciation of dissolved rare earth elements in the anoxic brines of Bannock Basin, eastern Mediterranean Sea. Geochim. Cosmochim. Ac. 59 (16), 3285–3299.

Schlautman, M.A., Han, I., 2001. Effects of pH and dissolved oxygen on the reduction of hexavalent chromium by dissolved ferrous iron in poorly buffered aqueous systems. Water Res. 35, 1534–1546.

Schmitt, R.A., Smith, R.H., Lasch, J.E., Mosen, A.W., Olehy, D.A., Vasilevskis, J., 1963. Abundances of the fourteen rare-earth elements, scandium, and yttrium in meteoritic and terrestrial matter. Geochim. Cosmochim. Ac. 27 (6), 577–622.

Schöne, B.R., Zhang, Z., Jacob, D., Gillikin, D.P., Tütken, T., Gabre-Schönberg, D., McConnaughey, T., Soldati, A., 2010. Effect of organic matrices on the determination of the trace element chemistry (Mg, Sr, Mg/Ca, Sr/Ca) of aragonitic bivalve shells (*Arctica islandica*) – Comparison of ICP-OES and LA-ICP-MS data. Geochem. J. 44, 23–37.

Schopf, J.W., Kudryavtsev, A.B., Czaja, A.D., Tripathi, A.B., 2007. Evidence of Archaean life: Stromatolites and microfossils. Precambrian Res. 158, 141–155.

Schrag, D.P., Higgins, J.A., Macdonald, F.A., Johnston, D.T., 2013. Authigenic carbonate and the history of the global carbon cycle. Science 339, 540–543.

Schutz, D.F., Turekian, K.K., 1965. The investigation of the geographical and vertical distribution of several trace elements in sea water using neutron activation analysis. Geochim. Cosmochim. Ac. 29, 259–313.

Scott, C., Lyons, T.W., 2012. Constraining molybdenum cycling and isotopic properties in euxinic versus non-euxinic sediments and sedimentary rocks: Refining the paleoproxies. Chem. Geol. 324–325, 19–27.

Seby, F., Potin-Gautier, M., Giffaut, E., Borge, G., Donard, O.F.X., 2001. A critical review of thermodynamic data for selenium species at 25°C. Chem. Geol. 171, 173–194.

Selby, D., Creaser, R.A., 2003. Re–Os geochronology of organic rich sediments: an evaluation of organic matter analysis methods. Chem. Geol. 200, 225–240.

Shaw, H.F., Wasserburg, G.J., 1985. Sm-Nd in marine carbonates and phosphates: Implications for Nd isotopes in seawater and crustal ages. Geochim. Cosmochim. Ac. 49, 503–518.

Shen, G.T., Boyle, E.A., 1988. Determination of lead, cadmium and other trace metals in annually-banded corals. Chem. Geol. 67, 47–62.

Shen, G.T., Dunbar, R.B., 1995. Environmental controls on uranium in reef corals. Geochim. Cosmochim. Ac. 59 (10), 2009–2024.

Shields, G., Stille, P., 2001. Diagenetic constraints on the use of cerium anomalies as palaeoseawater redox proxies: an isotopic and REE study of Cambrian phosphorites. Chem. Geol. 175, 29–48.

Shields, G.A., Webb, G.E., 2004. Has the REE composition of seawater changed over geological time? Chem. Geol. 204, 103–107.

Sholkovitz, E.R., Elderfield, H., 1988. The cycling of dissolved rare earth elements in Chesapeake Bay. Global Biogeochem. Cy. 2, 157–176.

Sholkovitz, E., Shen, G.T., 1995. The incorporation of rare earth elements in modern coral. Geochim. Cosmochim. Ac. 59 (13), 2749–2756.

Sholkovitz, E.R., Elderfield, H., Szymczak, R., Casey, K., 1999. Island weathering: river sources of rare earth elements to the Western Pacific Ocean. Mar. Chem. 68, 39–57.

Sholkovitz, E.R., Landing, W.M., Lewis, B.L., 1994. Ocean particle chemistry: The fractionation of rare earth elements between suspended particles and seawater. Geochim. Cosmochim. Ac. 58, 1567–1579.

Sholkovitz, E.R., Piepgras, D.J., Jacobsen, S.T., 1989. The pore water chemistry of rare earth elements in Buzzards Bay sediments. Geochim. Cosmochim. Ac. 53, 2847–2856.

Sholkovitz, E.R., Shaw, T.J., Schneider, D.L., 1992. The geochemistry of rare earth elements in the seasonally anoxic water column and porewaters of Chesapeake Bay. Geochim. Cosmochim. Ac. 56, 3389–3402.

Slawson, R.M., Van Dyke, M.I., Lee, H., Trevors, J.T., 1992. Germanium and silver resistance, accumulation, and toxicity in microorganisms. Plasmid 27 (1), 72–79.

Smedly, P.L., Kinniburgh, D.G., 2002. A review of the source, behaviour and distribution of arsenic in natural waters. Appl. Geochem. 17, 517–568.

Smrzka, D., Zwicker, J., Klügel, A., Monien, P., Bach, W., Bohrmann, G., Peckmann, J., 2016. Establishing criteria to distinguish oil-seep from methane-seep carbonates. Geology 44, 667–670.

Sø, H.U., Postma, D., Jakobsen, R., Larsen, F., 2009. Sorption and desorption of arsenate and arsenite on calcite. Geochim. Cosmochim. Ac. 72, 5871–5884.

Sonke, J.E., Salters, V.J.M., 2006. Lanthanide-humic substances complexation. I. Experimental evidence for a lanthanide contraction effect. Geochim. Cosmochim. Ac. 70, 1495–1506.

Spear, J.R., Figueroa, L.A., Honeyman, B.D., 2000. Modeling reduction of uranium(VI) under variable sulfate concentrations by sulfate-reducing bacteria. Appl. Environ. Microbiol. 3711–3721.

Spencer, D.W., Brewer, P.G., Sachs, P.L., 1973. Aspects of the distribution and trace element composition of suspended matter in the Black Sea. Geochim. Cosmochim. Ac. 36 (1), 71–86.

Stakes, D.S., Orange, D., Paduan, J.B., Salamy, K.A., Maher, N., 1999. Cold-seeps and authigenic carbonate formation in Monterey Bay, California. Mar. Geol. 159, 93–109.

Stauder, S., Raue, B., Sacher, F., 2005. Thioarsenates in sulfidic waters. Environ. Sci. Technol. 39, 5933–5939.

Steinberg, N.A., Blum, J.S., Hochstein, L., Oremland, R.S., 1992. Nitrate is a preferred electron acceptor for growth of freshwater selenate-respiring bacteria. Appl. Environ. Microbiol. 58, 426—428.

Stipp, S.L.S., Christensen, J.T., Lakshtanov, L.Z., Baker, J.A., Waight, T.E., 2006. Rare earth element (REE) incorporation in natural calcite: upper limits for actinide uptake in a secondary phase. Radiochem. Ac. 94, 523–528.

Stipp, S., Hochella, M.F.J., 1991. Structure and bonding environments at the calcite surface observed with X-ray photoelectron spectroscopy (XPS) and low energy diffraction (LEED). Geochim. Cosmochim. Ac. 55, 1723–1736.

Stipp, S., Hochella, M.F.J., Parks, G.A., Leckie, J.O., 1992. Cd^{2+} uptake by calcite: solid-state dussution and the formation of solid-solution: Interface processes observed with near-surface sensitive techniques (XPS, LEED, and AES). Geochim. Cosmochim. Ac. 56, 1941–1954.

Stipp, S.L.S., Lakshtanov, L.Z., Jensen, J.T., Baker, J.A., 2003. Eu^{3+} uptake by calcite: Preliminary results from coprecipitation experiments and observations with surface-sensitive techniques. J. Contam. Hydrol. 61, 33–43.

Stockdale, A., Davison, W., Zhang, H., Hamilton-Taylor, J., 2010. The association of cobalt with iron and manganese (oxyhydr)oxides in marine sediments. Aquat. Geochem. 16, 575–585.

Stolz, J.F., Basu, P., Santini, J.M., Oremland, R.S., 2006. Arsenic and selenium in microbial metabolism. Annu. Rev. Microbiol. 60, 107–130.

Stolz, J.F., Oremland, R.S., 1999. Bacterial respiration of arsenic and selenium. FEMS Microbiol. Rev. 23, 615–627.

Sturchio, N.C., Antonio, M.R., Soderholm, L., Sutton, S.R., Brannon, J.C., 1998. Tetravalent uranium in calcite. Science 281, 971–973.

Sullivan, K.A., Aller, R.C., 1996. Diagenetic cycling of arsenic in Amazon shelf sediments. Geochim. Cosmochim. Ac. 60 (9), 1465–1477.

Sunda, W.G., 1989. Trace metal interactions with marine phytoplankton. Biol. Oceanogr. 6, 411–442.

Sundby, B., Martinez, P,. Gobeil, C., 2004. Comparative geochemistry of cadmium, rhenium, uranium, and molybdenum in continental margin sediments. Geochim. Cosmochim. Ac. 68 (11), 2485–2493.

Sverjensky, D.A., 1984. Europium redox equilibria in aqueous solution. Earth Planet. Sci. Lett. 67, 70–78.

Swanson, V.E., Swanson, V.E., 1961. Geology and geochemistry of uranium in marine black shales: a review, Washington, DC: US Government Printing Office, 110 p.

Swarzenski, P.W., McKee, B.A., Skei, J.M., Todd, J.F., 1999. Uranium biogeochemistry across the redox transition zone of a premanently stratified fjord: Framvaren, Norway. Mar. Chem. 67, 181–198.

Sylvester, P.J., 2008. Matrix effects in laser ablation-ICP-MS. In: Laser ablation ICP-MS in the earth sciences. Current practices and oustanding issues 40, 67–78.

Takahashi, Y., Chatellier, X., Hattori, K.H., Kato, K., Fortin, D., 2005. Adsorption of rare earth elements onto bacterial cell walls and its implication for REE sorption onto natural microbial mats. Chem. Geol. 219, 53–67.

Takahashi, Y., Hirata, T., Shimizu, H., Ozaki, T., Fortin, D., 2007. A rare earth element signature of bacteria in natural waters? Chem. Geol. 244, 569–583.

Takahashi, Y., Yamamoto, M., Yamamoto, Y., Tanaka, K., 2010. EXAFS stury on the cause of enrichment of heavy REEs on bacterial cell surfaces. Geochim. Cosmochim. Ac. 74, 5443–5462.

Tanaka, K., Kawabe, I., 2006. REE abundances in ancient seawater inferred from marine limestones and experimental REE partition coefficients between calcite and aqueous solution. Geochem. J. 40, 425–435.

Tanaka, K., Miura, N., Asahara, Y., Kawabe, I., 2003. Rare earth element and strontium isotopic study of seamount-type limestones in Mesozoic accretionary complex of Southern Chichibu Terrane, central Japan: Implication for incorporation process of seawater REE into limestones. Geochem. J. 37, 163–180.

Tanaka, K., Ohta, A., Kawabe, I., 2004. Experimental REE partitioning between calcite and aqueous solution at 25°C and 1 atm: Constraints on the incorporation of seawater REE into seamount-type limestones. Geochem. J. 38, 19–32.

Tanaka, K., Takahashi, Y., Shimizi, H., 2008. Local structure of Y and Ho in calcite and its relevance to Y fractionation from Ho in partitioning between calcite and aqueous solution. Chem. Geol. 248, 104–113.

Tang, J., Johannesson, K.H., 2003. Speciation of rare earth elements in natural terrestrial waters: Assessing the role of dissolved organic matter from the modeling approach. Geochim. Cosmochim. Ac. 67, 2321–2339.

Tang, J., Johannesson, K.H., 2010a. Ligand extraction of rare earth elements from aquifer sediments: Implications for rare earth element complexation with organic matter in natural waters. Geochim. Cosmochim. Ac. 74, 6690–6705.

Tang, J., Johannesson, K.H., 2010b. Rare earth elements adsorption onto Carizzo sand: Influence of strong solution complexation. Chem. Geol. 279, 120–133.

Taylor, S.R., McLennan, S.M., 1985. The Continental Crust: Its composition and evolution. Blackwell, Malden, Mass.

Tella, M., Pokrovski, G.S., 2009. Antimony(III) complexing with O-bearing organic ligands in aqueous solutions: An X-ray absorption fine structure spectroscopy and solubility study. Geochim. Cosmochim. Ac. 73, 268–290.

Temmam, M., Paquette, J., Vali, H., 2000. Mn and Zn incorporation into calcite as a function of chloride aqueous concentration. Geochim. Cosmochim. Ac. 64, 2417–2430.

Terakado, Y., Masuda, A., 1988. The coprecipitation of rare-earth elements with calcite and aragonite. Chem. Geol. 69, 103–110.

Tesoriero, A.J., Pankow, J.F., 1996. Solid solution partitioning of Sr^{2+}, Ba^{2+}, and Cd^{2+} to calcite. Geochim. Cosmochim. Ac. 60, 1053–1063.

Tessier, A., Campbell, P.G.C., Bisson, M., 1979. Sequential extraction procerude for the speciation of particulate trace metals. Anal. Chem. 51, 844–851.

Thomson, J., Higgs, N.C., Croudace, I.W., Colley, S., Hydes, D.J., 1993. Redox zonation ef elements at an oxic/post-oxic boundary in deep-sea sediments. Geochim. Cosmochim. Ac. 57, 579–595.

Thomson, J., Higgs, N.C., Wilson, T.R.S., Croudace, W., De Lange, G.J., Van Santvoort, P.J.M., 1995. Redistribution and geochemical behavior of redox-sensitive elements around S1, the most recent eastern Mediterranean sapropel. Geochim. Cosmochim. Ac. 59 (17), 3487–3501.

Thomson, J., Jarvis, I., Green, R.H., Green, D.A., Clayton, T., 1998. Mobility and immobility of redox-sensitive elements in deep-sea turbidites during shallow burial. Geochim. Cosmochim. Ac. 62 (4), 643–656.

Tostevin, R., Shields, G.A., Tarbuck, G.M., He, T., Clarkson, M.O., Wood, R.A., 2016. Effective use of cerium anomalies as a redox proxy in carbonate-dominated marine settings. Chem. Geol. 438, 146–162.

Tourtelot, H.A., 1956. Radioactivity and uranium content of some Cretaceous shales, Central Great Plains. Am. Assoc. Petrol. Geol. Bull. 40, 62–83.

Toyama, K., Terakado, Y., 2014. Experimental study of rare earth element partitioning between calcite and sodium chloride solution at room temperature and pressure. Geochem. J. 48, 463–477.

Trefry, J.H., Metz, S., 1989. Role of hydrothermal precipitates in the geochemical cycling of vanadium. Nature 342, 531–533.

Tribovillard, N., Algeo, T.J., Baudin, F., Riboulleau, A., 2012. Analysis of marine environmental conditions based on molybdenum-uranium covariation – Applications to Mesozoic paleoceanography. Chem. Geol. 324–325, 46–58.

Tribovillard, N., Algeo, T.J., Lyons, T., Riboulleau, A., 2006. Trace metals as paleoredox and paleoproductivity proxies: An update. Chem. Geol. 232, 12–32.

Tribovillard, N., Bout-Roumazeilles, V., Riboulleau, A., Baudin, F., Danelian, T., Riquier, L., 2011. Transfer of germanium to marine sediments: Insights from its accumulation in radiolarites and authigenic capture under reducing conditions. Some examples through geological ages. Chem. Geol. 282, 120–130.

Tribovillard, N.P., Desprairies, A., Lallier-Vergès, E., Bertrand, P., Moureau, N., Ramdani, A., Ramanampisoa, L., 1994. Geochemical study of organic-matter rich cycles from the Kimmeridge Clay Formation of Yorkshire (UK): productivity versus anoxia. Palaeogeogr. Palaeoclim. Palaeoecol. 108, 165–181.

Tribovillard, N., du Châtelet, E.A., Gay, A., Barbecot, F., Sansjofre, P., Potdevin, J.-L., 2013. Geochemistry of cold seepage-impacted sediments: Per-ascensum or per-descensum trace metal enrichment? Chem. Geol. 340, 1–12.

Tucker, M.D., Barton, L.L., Thomson, B.M. 1997. Reduction and immobilization of molybdate by *Desulfovibrio desulfuricans*. J. Environ. Qual. 26, 1146–1152.

Tucker, M.D., Barton, L.L., Thomson, B.M., 1998. Reduction of Cr, Mo, Se and U by *Desulfovibrio desulfuricans* immobilized in polyacrylamide gels. J. Ind. Microbiol. Biotechnol. 20, 13–19.

Turekian, K.K., Imbrie, J., 1966. The distribution of trace elements in deep-sea sediments of the Atlantic Ocean. Earth Planet. Sci. Lett. 1, 161–168.

Ulrich, K.-U., Veeramani, H., Latmani-Bernier, R., Giammar, D.E., 2011. Speciation-dependent kinetics of uranium(VI) bioreduction. Geomicrobiol. J. 28, 396–409.

Valdivieso-Ojeda, J.A., Huerta.Diaz, M.A., Delgadillo-Hinojosa, F., 2014. High enrichment of molybdenum in hypersaline microbial mats of Guerrero Negro, Baja California Sur, Mexico. Chem. Geol. 363, 341–354.

Vallee, B.L., Auld, D.S., 1993. Zinc: biological functions and coordination motifs. Acc. Chem. Res. 26, 543–551.

van Dover, C.L., Aharon, P., Bernhard, J.M., Caylor, E., Doerries, M., Flickinger, W., Gilhooly, W., Goffredi, S.K., Knick, K.E., Macko, S.A., Rapoport, S., Raulfs, E.C., Ruppel, C., Salerno, J.L., Seitz, R.D., Sen Gupta, B.K., Shank, T., Turnipseed, M., Vrijenhoek, R., 2003. Blake Ridge methane seeps: characterization of a soft-sediment, chemosynthetically based ecosystem. Deep Sea Res. I 50, 281–300.

Van Kranendonk, M.J., Webb, G.E., Kamber, B.S., 2003. Geological and trace element evidence for a marine sedimentary environment of deposition and biogenicity of 3.45 Ga stromatolitic carbonates in the Pilbara Craton, and support for a reducing Archaean ocean. Geobiology 1, 91–108.

Van der Weijden, R.D., Meina, J., Comans, R.N.J., 1997. Sorption and sorption reversibility of cadmium on calcite in the presence of phosphate and sulfate. Mar. Chem. 57, 119–132.

Van der Weijden, C.H., 2002. Pitfalls of normalization of marine geochemical data using a common divior. Mar. Geol. 184, 167–187.

Van Dyke, M.I., Lee, H., Trevors, J.T., 1989. Germanium accumulation by bacteria. Arch. Microbiol. 152, 533–538.

Vega, M., Van den Berg, C.M.G., 1997. Determination of Cobalt in seawater by catalytic adsorptive cathodic stripping voltammetry. Anal. Chem. 60, 874–881.

Veizer, J., 1983. Chemical diagenesis of carbonates: theory and application of trace element technique. In: Stable Isotope in Sedimentary Geology. SEPM short course 10, 3–100.

Veizer, J., Democvic, R., Turan, J., 1971. Possible use of strontium in sedimentary carbonate rocks as a paleoenvironmental indicator. Sediment. Geol. 5, 5–22.

Vig, K., Megharaj, M., Sethunathan, N., Naidu, R., 2003. Bioavailability and toxicity of cadmium to microorganisms and their activities in soil: a review. Adv. Environ. Res. 8, 121–135.

Vine, J.D., Tourtelot, E.B., 1970. Geochemistry of black shale deposits; a summary report. Econom. Geol. 65, 253–272.

Vink, B.W., 1996. Stability relations of antimony and arsenic compounds in the light of revised and extended Eh-pH diagrams. Chem. Geol. 130, 21–30.

Visscher, P.T., Prins, R.A., van Gemerden, H., 1992. Rates of sulfate reduction and thiosulfate consumption in a marine microbial mat. FEMS Microbiol. Lett. 86, 283–288.

Voigt, M., Mavromatis, V., Oelkers, E.H., 2017. The experimental determination of REE partition coefficients in the water-calcite system. Chem. Geol. 462, 30–43.

Von Blanckenburg, F., Marnberti, M., Schoenberg, R., Kamber, B.S., Webb, G.E., 2008. The iron isotope composition of microbial carbonate. Chem. Geol. 249, 113–128.

Vorlicek, T.P., Kahn, M.D., Kasuya, Y., Helz, G.R., 2004. Capture of molybdenum in pyrite-forming sediments: role of ligand-induced reduction by polysulfides. Geochim. Cosmochim. Ac, 68, 547–556.

Vroon, P.Z., van der Wagt, B., Koornneef, J.M., Davies, G.R., 2008. Problems in obtaining precise and accurate Sr isotope analysis from geological materials using laser ablation MC-ICPMS. Anal. Bioanal. Chem. 390, 465–476.

Wallmann, K., Aloisi, G., Haeckel, M., Obzhirov, A., Pavlova, G., Tishchenko, P., 2006. Kinetics of organic matter degradation, microbial methane generation, and gas hydrate formation in anoxic marine sediments. Geochim. Cosmochim. Ac. 70, 3905–3927.

Wallmann, K., Linke, P., Suess, E., Bohrmann, G., Sahling, H., Schlüter, M., Dählmann, A., Lammers, S., Greinert, J., von Mirbach, N., 1997. Quantifying fluid flow, solute mixing, and biogeochemical turnover at cold vents of the eastern Aleutian subduction zone. Geochim. Cosmochim. Ac. 61, 5209–5219.

Wang, Y., Xu, H., 2001. Prediction of trace metal partitioning between minerals and aqueous solutions: A linear free energy correlation approach. Geochim. Cosmochim. Ac. 65, 1529–1543.

Wang, S., Yan, W., Chen, Z., Zhang, N., Chen, H., 2014. Rare earth elements in cold seep carbonates from the southwestern Dongsha area, northern South China Sea. Mar. Petrol. Geol. 57, 482–493.

Wanty, R.B., Goldhaber, M.B., 1992. Thermodynamics and kinetics of reactions involving vanadium in natural systems: Accumulation of vanadium in sedimentary rocks. Geochim. Cosmochim. Ac. 56, 1471–1483.

Watson, E.B., 1996. Surface enrichment and trace-element uptake during crystal growth. Geochim. Cosmochim. Ac. 60 (24), 5013–5020.

Webb, G.E., Kamber, B.S., 2000. Rare earth elements in Holocene reefal microbialites: a new shallow seawater proxy. Geochim. Cosmochim. Ac. 64, 1557–1565.

Webb, G.E., Kamber, B.S., 2004. Biogenicity inferred from microbialite geochemistry. Microbiol. Aust. 25, 34–35.

Webb, G.E., Nothdurft, L.D., Kamber, B.S., Kloprogge, J.T., Zhao, J.-X., 2009. Rare earth element geochemistry of scleractinitan coral skeleton during meteoric diagenesis: a sequence through neomorphism of aragonite to calcite. Sedimentology 56, 1443–1463.

Weber, J.N., 1964. Trace element composition of dolostones and dolomites and its bearing on the dolomite problem. Geochim. Cosmochim. Ac. 28, 1817–1868.

Wedepohl, K.H., 1971. Environmental influences on the chemical composition of shales and clays. Phys. Chem. Earth 8, 305–333.

Wedepohl, K.H., 1995. The composition of the continental crust. Geochim. Cosmochim. Ac. 59 (7), 1217–1232.

Wendt, J., Belka, Z., Kaufmann, B., Kostrewa, R., Hayer, J., 1997. The world's most spectacular carbonate mud mounds (Middle Devonian, Algerian Sahara). J. Sed. Res.67, 424–436.

Wenger, L.M., Baker, D.R., 1986. Variations in organic geochemistry of anoxic-oxic black shale-carbonate sequences in the Pennsylvanian of the Midcontinent, U.S.A.. Org. Geochem. 10, 85–92.

White, C., Gadd, G.M., 1998. Accumulation and effects of cadmium on sulphate-reducing bacterial biofilms. Microbiology 144, 1407–1415.

Widerlund, A., 1996. Early diagenetic remobilization of copper in near-shore marine sediments: a quantitative pore-water model. Mar. Chem. 54, 41–53.

Widerlund, A., Ingri, J., 1995. Early diagenesis of arsenic in sediments of the Kalix River estuary, northern Sweden. Chem. Geol. 125, 185–196.

Wildeman, T.R., Haskin, L., 1965. Rare-earth elements in ocean sediments. J. Geophys. Res. 70, 2905–2910.

Wilkin, R.T., Barnes, H.L., 1996. Pyrite formation by reactions of ion monosulfides with dissolved inorganic and organic sulfur species. Geochim. Cosmochim. Ac. 60, 4167–4179.

Wilkin, R.T., Wallschläger, D., Ford, R.G., 2003. Speciation of arsenic in sulfidic waters. Geochem. Trans. 4, 1–7.

Williams-Jones, A.E., Migdisov, A.A., Samson, J.M., 2012. Hydrothermal mobilisation of the rare earth elements – a tale of "ceria" and "yttria". Elements 8, 355–360.

Withers, S.H., Peale, R.E., Schulte, A.F., Braunstein, G., Beck, K.M., Hess, W.P., Reeder, R.J., 2003. Broad distribution of crystal-field environments for Nd^{3+} in calcite. Phys. Chem. Min. 30, 440–448.

Wood, S.A., 1993. The aqueous geochemistry of the rare-earth elements: Critical stability constants for complexes with simple carboxylic acids at 25°C and 1 bar and their application to nuclear waste management. Eng. Geol. 34, 229–259.

Woodhead, J., Swearer, S., Hergt, J., Maas, R., 2004. In situ Sr-isotope analysis of carbonates by LA-MC-ICP-MS: interference corrections, high spatial resolution and an example from otolith studies. J. Anal. At. Spectrom. 20, 22–27.

Wright, J., Schrader, H., Holser, W.T., 1987. Paleoredox variations in ancient oceans recorded by rare earth elements in fossil apatite. Geochim. Cosmochim. Ac. 51, 631–644.

Wu, C.-H., Lo, S.-L., Lin, C.-F., Kuo, C.-Y., 2001. Modeling competitive adsorption of molybdate, sulfate, and selenate on γ-Al_2O_3 by the triple layer model. J. Colloid. Interf. Sci. 233, 259–264.

Wyndham, T., McCulloch, M., Tallon, S., Alibert, C., 2004. High-resolution coral records of rare earth elements in coastal seawater: Biogeochemical cycling and a new environmental proxy. Geochim. Cosmochim. Ac. 68, 2067–2080.

Xiong, G., Wnag, J., Wu, H., Zhang, H., Yu, Q., Yan, J., Jiang, X., Cui, X., Wang, Z., 2014. Trace element and REE geochemistry of the Ediacaran Doushantuo Formation from Fanjingshan area, northeast Guizhou province, China. Carbon. Evapor., doi 10.1007/s13146-014-0217-2.

Xu, Z., Han, G., 2009. Rare earth elements (REE) of dissolved and suspended loads in the Xijiang River, South China. Appl. Geochem. 24, 1803–1816.

Xu, N., Hochella, M.F.J., Brown, G.E., Parks, G.A., 1996. Co(II) sorption at the calcite-water interface: I. X-ray photoelectron spectroscopic study. Geochim. Cosmochim. Ac. 60, 2801–2815.

Yang, J., Haley, B., 2016. The profile of the rare earth elements in the Canada Basin, Arctic Ocean, Geochem. Geophys. Geosyst., 17, 3241–3253, doi:10.1002/2016GC006412.

Zachara, J.M., Kittrick, J.A., Harsch, J.B., 1988. The mechanism of Zn^{2+} adsorption on calcite. Geochim. Cosmochim. Ac. 52, 2281–2291.

Zachara J. M., Cowan C. E., Resch C. T., 1991. Sorption of divalent metals on calcite. Geochim. Cosmochim. Ac. 55, 1549–1562.

Zachara, J.M., Kittrick, J.A., Harsh, J.B., 1988. The mechanism of Zn^{2+} adsorption on calcite. Geochim. Cosmochim. Ac. 52, 2281–2291.

Zaky, A.H., Brand, U., Azmy, K., 2015. A new sample processing protocol for procuring seawater REE signatures in biogenic and abiogenic carbonates. Chem. Geol. 416, 36–50.

Zehr, J.P., Oremland, R.S., 1987. Reduction of selenate to selenide by sulfate-respiring bacteria: experiments with cell suspensions and estuarine sediments. Appl. Environ. Microbiol. 53, 1365–1369.

Zerkle, A.L., Claire, M.W., Goldmann-Domagal, S.D., Farquhar, J., Poulton, S.W., 2012. A bistable organic-rich atmosphere on the Neoarchaean Earth. Nat. Geosci. 5, 359–363.

Zhang, H., Van den Berg, C.M.G,. Wollast, R., 1990. The determination of interactions of Cobalt (II) with organic compounds in seawater using cathodic stripping voltammetry. Mar. Chem. 28, 285–300.

Zhang, J., Nozaki, Y., 1998. Behavior of rare earth elements in seawter at the ocean margin: A study along the slopes of the Sagami and Nankai troughs near Japan. Geochim. Cosmochim. Ac. 62, 1307–1317.

Zhang, J., Dong, H., Zhao, L., McCarrick, R., Agrawal, A., 2014. Microbial reduction and precipitation of vanadium by mesophilic and thermophilic methanogens. Chem. Geol. 370, 29–39.

Zhang, J., Amakawa, H., Nozaki, Y., 1994. The comparative behaviors of Yttrium and Lanthanides in the seawater of the North Pacific. Geophys. Res. Lett. 21, 2677–2680.

Zhang, K., Zhu, X.-K., Yan, B., 2015. A refined dissolution method for rare earth element studies of bulk carbonate rocks. Chem. Geol. 412, 82–91.

Zhao, L., Chen, Z.-Q., Algeo, T.J., Chen, J., Chen, Y., Tong, J., Gao, S., Zhou, L., Hu, Z., Liu, Y., 2013. Rare-earth element patterns in conodont albid crowns: Evidence for massive inputs of volcanic ash during the latest Permian biocrisis? Global Planet. Change 105, 135–151.

Zhan, Y.-Y., Zheng, Y.-F., 2013. Geochemical constraints on the origin of post-depositional fluids in sedimentary carbonates of the Ediacaran system in South China. Precambrian Res. 224, 341–363.

Zhao, Y., Vance, D., abouchami, W., de Baar, H.J.W., 2014. Biogeochemical cycling of zinc and its isotopes in the Southern Ocean. Geochim. Cosmochim. Ac. 125, 653–672.

Zhao, Y.-Y., Zheng, Y.-F., Chen, F., 2009. Trace element and strontium isotope constraints on sedimentary environment of Ediacaran carbonates on southern Anhui, South China. Chem. Geol. 265, 345–362.

Zheng, Y., Anderson, R.F., Van Geen, A., Fleischer, M.Q., 2002. Remobilization of authigenic uranium in marine sediments by bioturbation. Geochim. Cosmochim. Ac. 66 (10), 1759–1772.

Zheng, Y., Anderson, R.F., Van Geen, A., Kuwabara, J., 2000. Authigenic molybdenum formation in marine sediments: A link to pore water sulfide in the Santa Barbara Basin. Geochim. Cosmochim. Ac. 64 (24), 4165–4178.

Zheng, X.-Y., Plancherel, Y., Saito, M.A., Scott, P.M., Henderson, G.M., 2016. Rare earth elements (REEs) in the tropical South Atlantic and quantitative deconvolution of their non-conservative behavior. Geochim. Cosmochim. Ac. 177, 217–237.

Zheng, X.-Y., Yang, J., Henderson, G.M., 2014. A robust procedure for high-precision determination of rare earth element concentrations in seawater. Geostan. Geoanal. Res. 39, 277–292.

Zhong, S., Mucci, A., 1995. Partitioning of rare earth elements (REEs) between calcite and seawater solutions at 25 °C and 1 atm, and high dissolved REE concentrations. Geochim. Cosmochim. Ac. 59, 443–453.

Zobrist, J., Dowdle, P.R., Davis, J.A., Oremland, R.S., 2000. Mobilization of arsenite by dissimilatory reduction of adsorbed arsenate. Environ. Sci. Technol. 34, 4747–4753.

Zwicker, J., Smrzka, D., Gier, S., Goedert, J.L., Peckmann, J., 2015. Mineralized conduits are part of the uppermost plumbing system of Oligocene methane-seep deposits, Washington State (USA). Mar. Petrol. Geol. 66 (3), 616–630.

Summary

This thesis presents a comprehensive study on the applications, potentials, and limitations of trace and rare earth element geochemistry in the framework of inorganic geochemistry of natural marine carbonates with specific focus on methane- and oil-seepage derived authigenic carbonates. Natural hydrocarbon and methane seepage from seafloor sediments represent a significant source of organic carbon from the geosphere to the hydrosphere and, potentially, the atmosphere. The discharging organic compounds are metabolized by an anaerobic consortium of archaea and bacteria. The metabolic products of such redox reactions include dissolved carbon compounds that induce the in situ precipitation of carbonate minerals by increasing saturation state with respect to these minerals. Therefore, such authigenic, seepage-derived preciptiates can be used as a potent archive for past biogeochemical and geomicrobiological processes. In recent years the use of trace and rare earth element geochemistry has seen a significant boom, especially due to the fact that many of these metals are redox sensitive and are involved in biological cycling in the oceans. High-resoluition phase-specific trace and rere earth element analyses of carbonate cements yield surprisingly detailed information on past and present element cycling, and can help reconstruct past environmental conditions, as well as fluid composition at ancient hydrocarbon seeps.

This study, in three parts, gives a detailed rendition on how such trace metals can be put to use and what new information can be derived from their analysis. The first part shows how a combination of molybdenum to uranium ratios combined with total rare earth element contents of carbonate cements can help identify oil seepage in the geologic past; a question that has so far eluded scientists interested in the Phanerozoic evolution of chemosynthesis-based macrofaunal communities. As oil has a significant impact on physiology, behavior, and benthic ecology of various types of macrofauna at seeps, being able to confidently identify seepage of oil in Earth's history offers new frontiers into the interpretation of life styles and macroevolution of chemosynthesis-based marine life.

The second part investigates modern oil seepage in the southern Gulf of Mexico in the course of a highly detailed analysis of carbonate cements from recently discovered carbonates at the Campeche Knolls. A systematic and comprehensive approach shows how trace and rare earth metals can distinguish redox conditions, fluid composition, and fluid flux at three different seafloor sites. Together with the analyses of trace and rare earth metals in oil and bitumen itself – an undertaking not yet accomplished on

such samples – it can be shown how a genetic connection exists between oil seepage, oil oxidation, and carbonate precipitation.

The third part offers a large and detailed overview on the current state-of-the-art knowledge of trace metals and their relationship to marine carbonates. This part is in itself split into four parts, dealing with aquatic chemistry of trace metals, their incorporation into solid minerals, their uses in the Earth Sciences, and a more detailed focus on their applicational potentials specifically in hydrocarbon seepage-derived authigenic carbonates. This study as a whole gives new insights on how trace and rare earth elements can be effectively put to use to disentangle some of the complex processes governing environments that enable chemotrophic life.

Zusammenfassung

Diese Doktorarbeit präsentiert eine zusammenfassende Studie über die Anwendung, Potenziale, und Limitierungen der Spurenmetallgeochemie von marinen Karbonaten, mit speziellem Augenmerk auf Karbonate, die an Methanaustritte am Meeresboden gebunden sind. Natürliche Kohlenwasserstoffaustritte aus marinen Sedimenten sind eine sigifikante Quelle von organischem Kohlenstoff der Geosphäre in die Hydrosphäre, sowie in die Atmosphäre. Diese organischen Stoffe werden im Zuge ihres Austritts von anaeroben Bakterien und Archaeen im Zuge von Stoffwechselreaktionen umgewandelt. Die Stoffwechselprodukte dieser Redoxreaktionen sind chemische Verbindungen, deren erhöhte Konzentrationen in sedimentären Porenwässern zu einer erhöhten Karbonatfällung führen, indem diese Stoffe die Löslichkeit von Karbonatmineralen herabsetzen. Deshalb stellen solche authigen im Sediment gegbildete Karbonatpräzipitate ein wichtiges Archiv für fossile biogeochemische und geomikrobiologische Prozesse dar und können bei der Rekonstruktion vergangener Umweltbedingungen und Fluidchemismus helfen.

Diese Studie, gegliedert in drei Teile, stellt eine detaillierte Abhandlung dar wie solche Spurenmetalle angewendet werden können und welchen Informationen man durch deren Analyse gewinnen kann. Der erste Teil zeigt wie eine Kombination von Molybdän- und Uran-Verhältnissen kombiniert mit Gehalten an Seltenen Erden in Karbonatzementen Ölquellen in der geologischen Vergangenheit identifizieren können. Dies ist eine Fragestellung, die schon lange unbeantwortet blieb und vor allem für eine grundlegende paläontoloogische Rekonstruktion der Evolution von chemosynthetischem Leben notwendig ist. Rohöl wirkt sich massiv auf die Zusammensetzung, Physiologie und Ökologie von Mikro- und Makrofauna an kalten Quellen aus. Aus diesem Grund kann eine sichere Identifizierung von Ölquellen im Phanerozoikum neue Erkenntnisse in die Interpretation von chemosynthetischem Leben ermöglichen.

Der zweite Teil beschäftigt sich mit rezenten Ölquellen im südlichen Golf von Mexiko im Rahmen einer detaillierten Studie von Karbonatzementen aus Gesteinen, die unlängst in der Campeche Bucht beprobt wurden. Ein systematischer und umfassender Ansatz zeigt wie mit Spurenmetallen und Seltene Erden Redoxbedingungen, Fluidzusammensetzung und Fluidfluss bestimmt werden können. Gemeinsam mit der Analyse von Spurenmetallen und Seltenen Erden im Rohöl und Bitumen selbst – ein Ansatz der

zum ersten Mal an solchen Proben angewendet wird – zeigt sich wie ein genetischer Zusammenhang zwischen Ölaustritten, Öloxidation, und Karbonatbildung am Meeresboden besteht.

Der dritte Teil bietet eine breit angelegte Zusammenfassung über den momentanen Wissensstand über Spurenmetalle und ihr Verhältnis zu marinen Karbonaten. Dieser Teil ist in sich in vier Teile gegliedert und befasst sich mit der aquatischen Chemie von Spurenmetallen, ihr Einbau in Karbonatminerale, ihre Anwendungen auf geologische Systeme, und liefert einen Einblick auf deren Anwendung bezüglich Karbonaten, die durch die Oxidation von Kohlenwasserstoffen und Methan enstehen. Diese Studie bietet neue Einblicke, wie Spurenmetalle und Seltene Erden effktiv genutzt werden können, um verschiedenste komplexe und miteinander gekoppelte Prozesse zu beschreiben, die Umweltbedingungen generieren unter denen Chemosythese basiertes Leben möglich ist.

Appendix

(Published manuscripts)

Mineralized conduits are part of the uppermost plumbing system of Oligocene methane-seep deposits, Washington State (USA)

J. Zwicker[a], D. Smrzka[a], S. Gier[a], J.L. Goedert[a], J. Peckmann[a]

[a]*Department für Geodynamik und Sedimentologie, Erdwissenschaftliches Zentrum, Universität Wien, 1090 Wien, Austria*

[b]*Burke Museum of Natural History and Culture, University of Washington, Seattle, WA 98195, USA*

Article published in Marine and Petroleum Geology 66, 616-630

Article history:
Received 31 January 2015
Received in revised form
27 April 2015
Accepted 6 May 2015
Available online 5 August 2015

Keywords:
Methane seeps
Fluid conduits
Authigenic minerals
Bioturbation
Lincoln Creek Formation

Abstract

Plumbing systems of marine seeps are complex pathways along which hydrocarbon-rich fluids move upward through the sedimentary column. In the shallow subsurface, seep plumbing systems may become successively filled by methane-derived authigenic carbonates resulting in mineralized conduits.

This work investigates mineralized conduits in the uppermost plumbing network of Oligocene seep deposits from the Lincoln Creek Formation in Washington State that consist of a paragenetic sequence of authigenic mineral phases. At two study sites the pipes grade into the base of seep deposits. The studied samples of concentrically-mineralized conduits are cylindrical in shape, measure 2-3 cm in diameter, and are up to 15 cm in length; the mineralized conduits are referred to as pipes hereafter. The earliest mineral phase in the paragenetic sequence is matrix micrite, making up the outer part of the pipes. Toward their centers the pipes are filled by two intercalated cement phases, (1) clear, banded and botryoidal aragonite and (2) micro-to cryptocrystalline yellow aragonite. The innermost portions of the pipes are filled by brownish calcite, microspar, or pipe-filling micrite. The observed paragenetic sequences archive successions of biogeochemical processes. The $\delta^{13}C$ values of clear and yellow aragonite cements range from −50.6 to −41.2‰, suggesting that their main carbonate source was provided by anaerobic oxidation of methane. In contrast, the later phases (brownish calcite, microspar, pipe-filling micrite) are relatively enriched in ^{13}C ($\delta^{13}C$ values: −2.3 to 3.9‰), pointing to carbonate precipitation from fluids affected by methanogenesis. The size and morphology of the pipes suggest that initial excavation was caused by burrowing organisms. The burrows subsequently acted as preferred fluid pathways, suggesting that the transport of fluids within near-surface sediments at the Oligocene seeps was strongly influenced by the activity of the local fauna. Possible producers of the burrows were sediment-dwelling crustaceans, specifically callianassid decapods, as well as bivalves.

1. Introduction

Seepage of cold, reduced fluids and gases containing a mixture of hydrocarbon compounds has been recognized at numerous sites along active and passive continental margins (e.g. Stakes et al., 1999; Bohrmann et al., 2002, 2003; Campbell et al., 2002; Judd et al., 2002; Peckmann et al., 2002; Torres et al., 2002; Sassen et al., 2004; Campbell, 2006; Judd and Hovland, 2007). Except for oil seeps, cold seeps are dominated by methane-rich fluids and gases, accompanied by small amounts of C_2 to C_5 hydrocarbons and carbon dioxide (Claypool and Kvenvolden, 1983; Joye et al., 2004; Pape et al., 2010, 2011). Some of the methane at cold seeps is produced biologically by methanogenic archaea (Jørgensen and Kasten,

2006; Reeburgh, 2007). The remineralization of complex organic matter results in the production of carbon dioxide, molecular hydrogen, and acetic acid (Kiene, 1991; Rullkötter, 2006; Reeburgh, 2007). Methanogenic archaea utilize these compounds to generate methane via carbon dioxide reduction with hydrogen and acetate fermentation (Rudd and Taylor, 1980; Whiticar, 1999). Thermogenic methane is produced at higher temperatures and pressures during thermocatalytic breakdown of organic matter deeper within the sediments (Claypool and Kaplan, 1974; Sassen et al., 1999). Different intensities of seepage are expressed by corresponding geological features such as large mound or pinnacle-shaped structures associated with accretionary ridges (Suess et al., 1999; Hensen and Wallmann, 2005; Teichert et al., 2005), mud volcanoes (Kopf, 2002), seafloor depressions known as pockmarks (Hovland et al., 2010), and large, tubular carbonate concretions (Kulm and Suess, 1990; Nyman et al., 2010).

Although seepage intensity may substantially vary with time (e.g. Solomon et al., 2008; Feng et al., 2009), hydrocarbon seeps may maintain fluid flow over long periods of time due to long-term accumulation and compaction of sediments rich in organic matter and pore waters overpressure (Sibuet and Olu, 1998). The network of complex pathways along which methane-rich fluids migrate is collectively known as the plumbing system of seeps, which allows fluid flux over long distances upward through the marine sedimentary column (Judd and Hovland, 2007). At greater depths corresponding to several hundreds of meters, fluid flow is enabled by tectonic faulting and fracturing of compacted marine sediments (Hooper, 1991; Talukder, 2012). At shallower depths, several meters below the sediment-water interface, fluid and gas seepage is facilitated by various types of conduits. Orpin (1997) discussed the possibility that large tubular carbonate concretions from New Zealand represent ancient carbonate chimneys. The formation of methane-derived carbonates is restricted to anoxic environments, which are commonly confined to sediments and do not extend into the water column (cf. Ritger et al., 1987; Peckmann et al., 2001; Reitner et al., 2005). Consequently, the term chimney fell out of favor for subsurface plumbing systems, as it suggests primary projection of carbonate structures into the water column. Over the past decade several studies have investigated subsurface carbonate structures of various shapes and sizes that are associated with methane seepage (Table 1). All of the described tubular structures are composed of authigenic carbonates, preserving subsurface plumbing systems.

Carbonate precipitation at seeps is triggered by sulfate-dependent anaerobic oxidation of methane (AOM, Ritger et al., 1987; Suess and Whiticar, 1989; Peckmann and Thiel, 2004), leading to an increase in pore water alkalinity in the sulfate methane transition zone (SMTZ). This process is carried out by a

consortium of methane-oxidizing archaea and sulfate-reducing bacteria (Hinrichs et al., 1999; Boetius et al., 2000; Milucka et al., 2012). The most common ^{13}C-depleted mineral phases forming AOM-derived seep limestones are micrite (i.e. microcrystalline calcite) and fibrous aragonite cement (e.g. Ritger et al., 1987; Beauchamp and Savard, 1992; Savard et al., 1996; Campbell et al., 2002; Peckmann et al., 2002, 2003; Canet et al., 2013). The mineral phases associated with plumbing systems described to date consist exclusively of microcrystalline carbonate, mostly micrite (Aiello et al., 2001; Schwartz et al., 2003; Mazzini et al., 2008; De Boever et al., 2009, 2011), some dolomite (Orpin, 1997; Stakes et al., 1999; Lédesert et al., 2003; Clari et al., 2004; Nyman et al., 2010), as well as iron-bearing dolomite and ankerite (Díaz-del-Rio et al., 2003).

While most studies have dealt with large concretions representing the deeper plumbing system within meters to probably a few tens of meters below the seafloor, the uppermost part of plumbing systems has received less attention (Campbell et al., 2008). Krause et al. (2009) described tubular cavities within Cretaceous seep limestones, and interpreted them as evidence for the transport of methane gas through the seep deposit. Wetzel (2013) investigated seep carbonate nodules collected from the South China Sea. These nodules, typified by a network of open and partly filled channels, resulted from the precipitation of methane-derived carbonates in a zone of active bioturbation. The pipes and tubular concretions were interpreted to represent burrows of seep-dwelling decapod crustaceans. Similarly, putative decapod burrows lithified by authigenic carbonates have been reported from the Gela pockmark basin in the Strait of Sicily (Taviani et al., 2013). Decapod burrows represent preferred migration pathways for methane-rich fluids at seeps (Peckmann et al., 2007; Wetzel, 2013; Wiese et al., this issue), as seeping fluids tend to take the path of lowest resistance through the sediment column (cf. Hovland et al., 2010).

Here we report for the first time small- to medium sized pipes that occur directly below Oligocene seep deposits from the Lincoln Creek Formation in Washington State, northwestern USA, characterized by a distinct paragenetic sequence. They are interpreted as former fluid conduits, representing parts of the uppermost plumbing system. We describe a spatial and temporal sequence of authigenic minerals forming the pipes and relate the individual mineral phases on the basis of microfabrics, elemental composition, and stable isotope geochemistry to successive biogeochemical processes that fostered their formation. Finally, we evaluate what might have formed the conduits in the first place. The outcome of

this study contributes to the understanding of the factors that steer fluid migration in the shallow subsurface at seeps.

Locality	Age	Size		Morphology	Mineralogy	Reference
		Diameter	Length			
Monterey Bay Formation, California	Miocene	2 - 20 cm	40 cm	Cylindrical to tubular, pipe and funnel-shaped	Pyrite-bearing, low Mg-Calcite	Aiello et al., 2001
Panoche Hills, California	Upper Cretaceous	0.5 - 5 m	0.5 - 6 m	Mound-shaped, spherical to ellipsoidal concrections	Mg-Calcite (~80%), dolomite, calcite	Schwartz et al., 2003
Monferrato, Italy	Miocene	8 - 15 cm	1 m	Cylindrical	Calcite	Clari et al., 2004
Hikurangi Margin, New Zealand	Miocene	5 - 10 cm	20 - 30 cm	Tubular, circular	Calcite	Campbell et al., 2008
Dolgovskii Mound, Black Sea	Recent	5 cm	up to 60 cm wide	Slab and tabular-shaped; chimney and tubular-shaped	Calcite, Pyrite	Mazzini et al., 2008
Varna, Bulgaria	Lower Eocene	1.5 cm	up to 15 m	Tubular	Low Mg, non ferroan Calcite	De Boever et al., 2009, 2011
Hikurangi Margin, New Zealand	Miocene	5 cm to 1 m	0.5 to 5 m	Tubular, cylindrical; conical, bulbous and pipe-shaped	Mg-Calcite, Dolomite	Nyman et al., 2010

Table 1. Selected examples of tubular carbonate concretions interpreted as part of seep plumbing systems.

2. Geological setting and studied rock samples

The study area is located on the southern side of the Olympic Mountains on the Olympic Peninsula, western Washington State, USA (Fig. 1). Induced through thrust faulting and followed by the subduction of the oceanic Juan de Fuca plate beneath the continental North American plate approximately 35 million years ago, basaltic units docked on the North American continent and built up the Coast Range Terranes. In the course of these events the Cascadia accretionary wedge started to form. The accretionary wedge belongs to a tectonic unit called the Olympic Subduction Complex (Brandon and Calderwood, 1990) or Olympic Structural Complex (Stewart and Brandon, 2004). It is exposed in the Olympic Mountains and developed through frontal accretion and underplating. The overlying "Coast Range Terrane" (Stewart and Brandon, 2004) is a unit informally called the Peripheral Sequence (Brandon and Vance, 1992; Brandon et al., 1998), or the Peripheral Rocks (Tabor and Cady, 1978a, b), or the Crescent Terrane (*sensu* Babcock et al., 1994). The rocks that are the focus of this study were deposited during rifting and subsidence of marginal marine basins along this part of North America during the Paleogene. These deposits were later locally uplifted by ongoing subduction of the Juan de Fuca plate. The lowest unit of the Coast Range Terrane is the early to middle Eocene Crescent Formation, consisting of pillow and massive basalts (Rau, 1967). This formation is locally overlain by middle to late Eocene marine sedimentary rocks (Rau, 1967; Dragovich et al., 2002), followed by mostly marine Oligocene through lower Miocene marine clastic rocks that make up the Lincoln Creek Formation (Fig. 1A).

The carbonate samples studied herein derive from the latest Eocene to earliest Miocene Lincoln Creek Formation (Beikman et al., 1967; Fig. 1). The Lincoln Creek Formation crops out widely in western Washington (Dragovich et al., 2002), is exposed best in various river valleys on the south side of the Olympic Mountains, and is mapped in various places southward all the way to the north shore of the Columbia River (e.g., Wells, 1989; Kiel, 2010). The Lincoln Creek Formation consists mostly of tuffaceous siltstone and minor amounts of feldspathic sandstone as well as calcareous concretions. In the lower part of the Lincoln Creek Formation thin bedded, laminated, locally bioturbated, fine to medium grained and graded micaceous sandstone is present. The upper part has massive, nearly structureless to laminated bedding with bioturbation, and contains poorly bedded siltstones and mudstones (Rau, 1967; Wells, 1989).

2.1. Studied seep deposits and sampling

The samples discussed here are from outcrops of the early and late Oligocene parts of the Lincoln Creek Formation along the Satsop and Canyon rivers, where the Lincoln Creek Formation is approximately 3000 m thick (Rau, 1966; Prothero and Armentrout, 1985). Seep deposits in the Lincoln Creek Formation originate from an active subduction-related setting and are now exposed in a coherent unit. Some deposits are less than 2 m in their largest dimension (cf. Peckmann et al., 2002; Kiel, 2006), whereas others are many meters across (Campbell and Bottjer, 1993; Kiel and Amano, 2013). One of the Satsop River sites studied here (Fig. 1B; 47°16'18.0"N, 123°28'56.2"W) is the SR4 deposit of Peckmann et al. (2002). Carbonate pipes were collected below the base of the autochthonous SR4 deposit when the river level was particularly low. Fossils of callianassid crustaceans and small, 10 mm long vesicomyid bivalves are most abundant in the lower part of this deposit around the pipes and where the pipes grade into more massive, dense carbonate (Fig. 2). The SR4 deposit has a greater taxonomic diversity than the other seep deposits nearby, containing bivalves, gastropods, cephalopods, decapods, and a coral (Peckmann et al., 2002; Goedert and Peckmann, 2005). The other Satsop River site studied here, SR5 (Fig. 1B; 47°17'40.5"N, 123°28'48.9"W), is located stratigraphically between SR1 and SR2 of Peckmann et al. (2002). This site has numerous carbonate pipes interspersed with and grading into discontinuous, and scattered seep deposits cropping out as tabular to blocky masses, measuring up to 0.5 m across laterally and vertically as exposed in the riverbank. In places the carbonate pipes form tangles and some branch upward, and lengths can exceed 1 m as exposed along the riverbank. The outcrop with scattered seep deposits is approximately 2 m thick and exposed for about 30 m along the south side of the Middle Fork of the Satsop River. One large pipe from SR5 was found oriented parallel to bedding. Smaller sinuous pipes were situated approximately 1.5 m stratigraphically above the horizontal tube, and ended at the base of a small seep limestone (University of Washington Burke Museum [UWBM] loc. B7897) with a few, less than 10 mm long specimens of the vesicomyid bivalve *Archivesica* sp., a small nuculanid bivalve, and several different small to minute gastropods. The Canyon River samples were collected from the CRB site of Nesbitt et al. (2013; Fig.1B; 47°18'7.6"N, 123°30'31.7"W), and this is stratigraphically equivalent to the SR5 deposit according to the sections measured by Rau (1966).

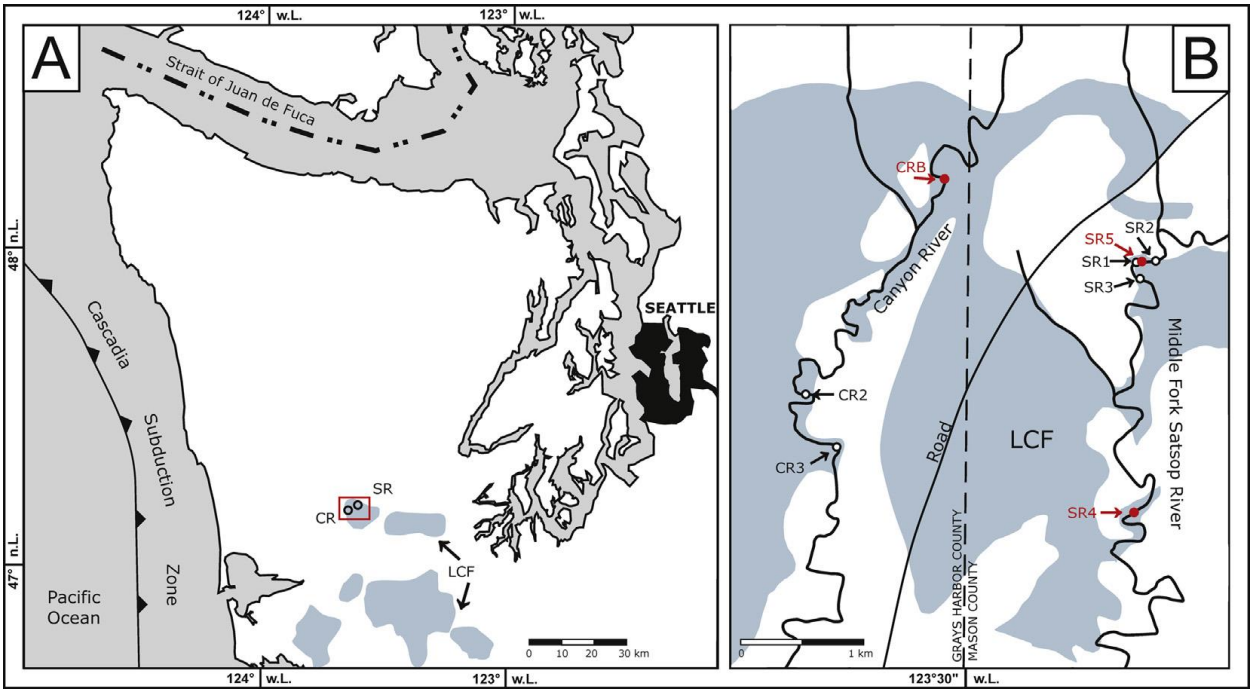


Fig. 1. (A) Tectonic and geologic overview of the study area with the Lincoln Creek Formation (LCF). Locations of the studied seep deposits from Satsop River (SR) and Canyon River (CR) modified after Peckmann et al. (2002). (B) Close up view of red box in (A). Sampling sites marked in red (SR4, SR5, and CRB); designation of seep deposits follows Peckmann et al. (2002) and Nesbitt et al. (2013).

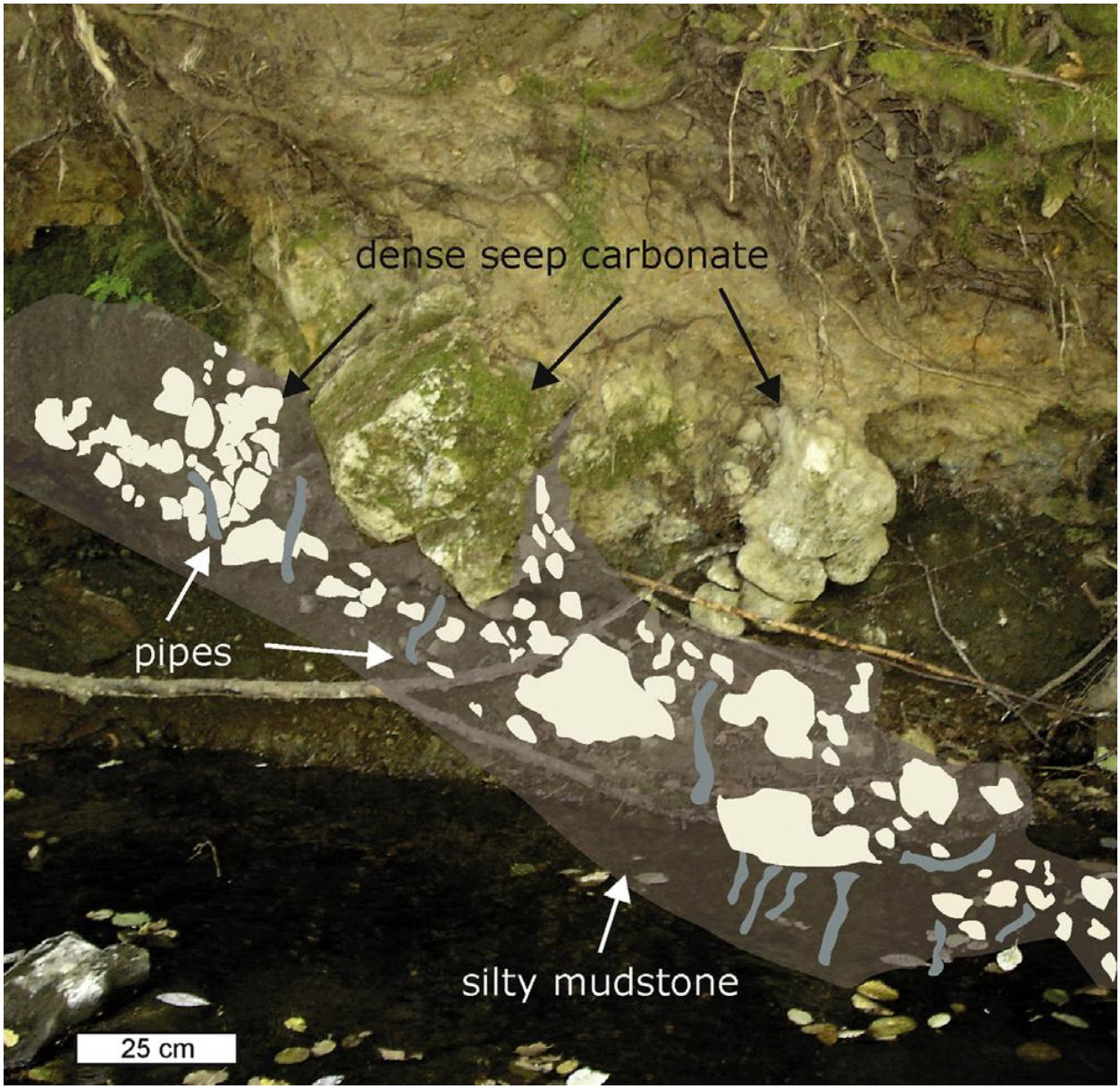


Fig. 2. Combined sketch of the SR4 riverside outcrop (based on an outcrop sketch drawn in 1995 when water-level was low and pipes were exposed) and field photograph (taken in 2007) of the SR4 deposit, showing the position of pipes (gray) directly below the dense seep carbonate (white) surrounded by dark silty mudstone of the Lincoln Creek Formation.

3. Material and Methods

Pipe samples showing obvious concentric mineralization were collected along riverbeds when water levels were low; seven were collected from the SR4 deposit, four from the SR5 deposit and one from the CRB deposit. In order to determine the paragenetic sequence of the pipes, petrographic microscopy was conducted on thin sections (7.4 x 9.7 to 5 x 5 cm) using a Leica DM4500 P polarization microscope. Photographs were taken with Leica DFC 420 and DFC 450 C cameras using the Leica Application Suite 3.2.0 and 4.4.0 software. Additionally, a Nikon SMZ 1500 stereomicroscope with a Prog.Res Speed XT core 5 camera as well as a Nikon Optiphot-2 optical microscope were used for petrographic observations. The software Prog.Res Capture pro 2.8.8. was applied for image analysis. To discriminate carbonate minerals, some thin sections were partly stained with a mixture of potassium ferricyanide and alizarin red solution, dissolved in 0.1% HCl (cf. Dickson, 1966). Some other thin sections were stained with Feigl's solution (cf. Füchtbauer, 1988) to distinguish aragonite from calcite. Powdered samples of two pipes (SR4 deposit) were obtained with a hand-held microdrill for powder X-ray diffraction. The powdered samples were analyzed with a Panalytical PW 3040/60 X'Pert PRO (CuKα radiation, 40 kV, 40 mA, step size 0.0167.5 s per step) diffractometer. X-ray diffraction patterns were interpreted using the Panalytical software "X´Pert High score plus". To determine its iron content, brownish calcite was analyzed by laser ablation inductively coupled plasma mass spectrometry on a ThermoFinigan Element2 mass spectrometer at the University of Bremen. The laser (NewWave UP193ss) was operated with a 5 to 10 Hz pulse rate for point and line ablation, respectively. Two SR4 samples were analyzed, whereby the beam diameter was set to 75 µm for the first and to 100 µm for the second sample. Pre-ablation was made with a 120 µm beam diameter and 5 Hz pulse rate before analysis. The produced data were calibrated against the synthetic SRM (Standard Reference Material) 610 and 612 silicate glasses from the National Institute of Standards and Technology (NIST; Jochum et al., 2012), and BCR-2G basalt glass from the USGS and BHVO-2G basalt glass were used as unknown measured standards. Due to different ablation yields of samples and calibration standards, ^{43}Ca was used as an internal standard. This practice also balanced temporal variations of the ablation signal. Iron was referred to the internal standard to allow quantitative analyses. Samples for carbon and oxygen stable isotope analysis were taken from the surface of sliced pipes (SR4 deposit) using a hand-held microdrill. Sample powders were reacted with 100% orthophosphoric acid in a vacuum at 75°C, and the evolved CO_2 gas was analyzed with a Finnigan MAT

251 mass spectrometer at the University of Bremen. The $\delta^{13}C$ and $\delta^{18}O$ values are reported relative to the Vienna Peedee-Belemnite standard (VPDB; standard deviation smaller than 0.04‰), and appropriate correction factors were applied.

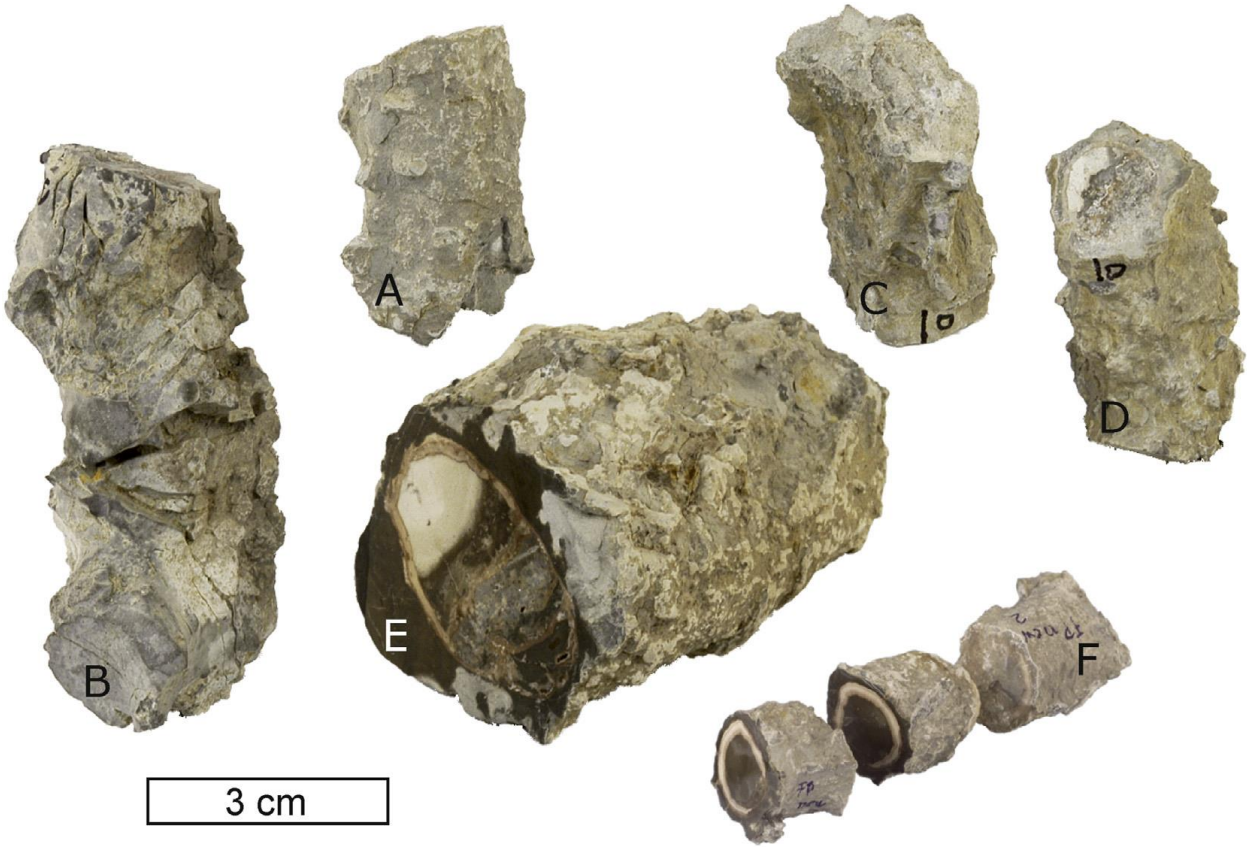


Fig. 3. Hand samples of pipes from the SR4 (A), SR5 (B-E), and CRB (F) deposits.

4. Results

4.1. Petrography and mineralogy

Carbonate pipes from the seep deposits SR4, SR5, and CRB were analyzed to describe internal fabrics and mineral phases. The pipes have mean diameters of 2.3, 3.3, and 2.3 cm, respectively (Figs. 3, 4). The lengths of fragments range from 6 to 10 cm, depending on the size of pieces that could be retrieved during sampling without breaking the pipes (Fig. 3). All studied pipes from the Satsop and Canyon River areas were enclosed by background sediments consisting of dark siltstones and mudstones. The pipes are

formed of a succession of authigenic mineral phases (Fig. 4). Matrix micrite forms the outer part of pipes (Fig. 5). It is dark brown in color and rich in detritus consisting of carbonate fragments, benthic foraminiferans, monaxon and triod sponge spiculae, clay minerals such as glauconite, pieces of wood and organic material, as well as quartz and feldspar (Fig. 5A). Authigenic pyrite mainly occurs as framboids and spherical aggregates (Fig. 5A), or subordinate as dispersed grains. Matrix micrite of all samples contains oval to spherically-shaped fecal pellets (e.g., SR5 deposit in Fig. 5B), some of which are identified as the ichnogenus *Palaxius*, commonly assigned to callianassid decapod crustaceans. Structured crustacean microcoprolites are 200 to 600 μm in diameter. Their typical crescent-shaped canals are not well preserved.

The phase post-dating matrix micrite in the paragenetic sequence is yellow aragonite cement (Fig. 6A, B). The contact between matrix micrite and yellow aragonite is commonly gradational rather than sharp. Yellow aragonite shows a micro- to cryptocrystalline texture and is pervaded by pyrite and dark inclusions, interpreted to represent organic matter. Yellow aragonite forms irregular layers, measuring 10 to 1500 μm in thickness in SR4 samples and 50 to 1550 μm in CRB samples (Fig. 6A, B). It is always closely associated with clear aragonite, which is the next phase in the paragenetic sequence and the volumetrically most abundant phase after matrix micrite in all samples. Clear aragonite forms banded and botryoidal crystal aggregates consisting of fibrous crystals (Fig. 6A, B). Crystal growth proceeded toward the center of pipes, and the isopachous crystal bands show a thickness of 235 to 3000 μm in SR4 pipes, 1000 to 3200 μm in SR5 samples, and 300 to 3400 μm in CRB samples. Botryoids and isopachous bands reveal a layered growth habit, with alternation of inclusion-rich and inclusion-poor layers. Yellow and clear aragonite cements are commonly intercalated. Small portions of the clear aragonite are locally replaced by silica (cf. Smrzka et al., 2015) and ferroan calcite (Fig. 6C).

The three diagenetic mineral phases present in the center of the pipes formed at a later stage. These are brownish calcite, microspar, and pipe-filling micrite (Fig. 4). Brownish calcite and microspar are the latest phases in the SR4 pipes. Brownish calcite occurs in contact with clear aragonite cement and exhibits rod-shaped and, in some cases, dumbbell-shaped crystal aggregates (Fig. 7). These aggregates are up to 50 μm in length. Unidentified brownish linings cover the crystal aggregates of brownish calcite in most places (Fig. 7B). Glauconite and minor pyrite also occur in association with brownish calcite. Brownish calcite revealed a blue stain after treatment with the combined potassium ferricyanide and alizarin red stain, indicating the presence of ferrous iron within its crystal lattice (Fig. 7C). This staining method is

very sensitive to even low contents of ferrous iron in calcite and stains the mineral mauve to blue at only a few ppm of iron (Dickson, 1966; Lindholm and Finkelman, 1972). Laser ablation ICP-MS data from one thin section revealed a ^{57}Fe:^{25}Mg ratio of 7.15:1 for brownish calcite, using ^{43}Ca as the internal standard. Based on the assumption that the sample corresponds to 100 mol% of $CaCO_3$ (i.e. pure calcium carbonate, cf. Himmler et al., 2010; Della Porta et al., 2015), the calculated mole fractions correspond to 8.74 mol% of $FeCO_3$ and 1.04 mol% of $MgCO_3$ in brownish calcite. This is in good agreement with X-Ray diffraction analyses, which yielded a d-spacing of 3.025 Å for the major (104) reflection of calcite. When plotted into a $MgCO_3$ + $FeCO_3$ vs. spacing diagram of Nash and Pittman (1975), this d-spacing value corresponds to a composite $MgCO_3$ + $FeCO_3$ content of approximately 8 mol%.

Microspar is light brown to grayish in color and contains minor pyrite, quartz, and glauconite grains. Microspar crystals are more or less uniformly sized, subhedral to euhedral, measuring 10 to 15 μm in diameter (Fig. 8). In CRB samples, the latest phase is pipe-filling micrite containing detrital grains (Fig. 9A). However, when compared to matrix micrite, the later stage pipe-filling micrite is more homogeneous, exhibits fewer detrital grains and is lighter in color (Fig. 9A, B). Scattered aggregates of pyrite are scarce.

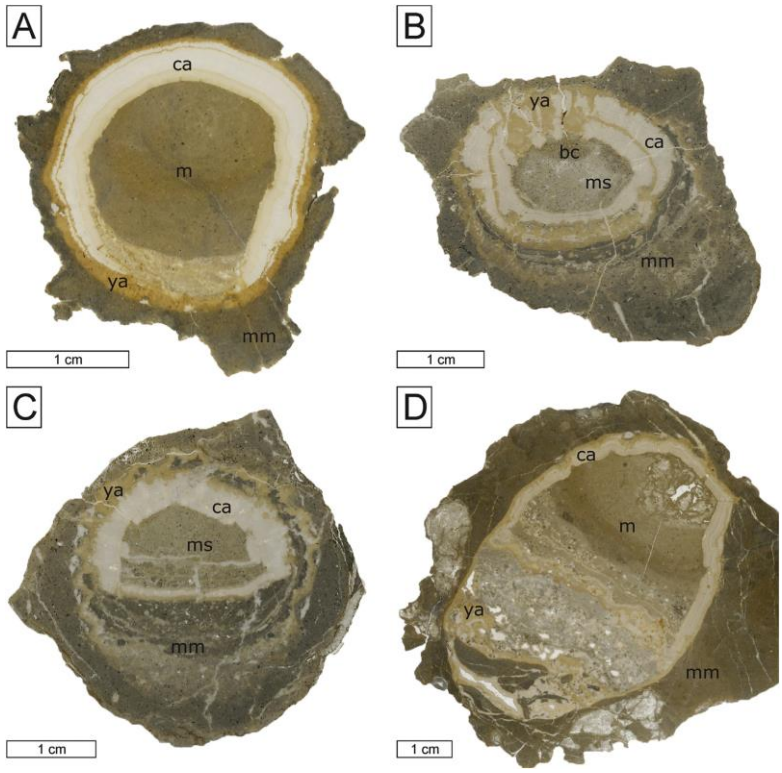


Fig. 4. Scanned thin sections of the pipes; mm = matrix micrite, ya = yellow aragonite, ca = clear aragonite, bc = brownish calcite, ms = microspar, m = pipe-filling micrite. (A) Sample from CRB deposit (cf. Fig. 3F). (B) Sample from SR4 deposit (cf. Fig. 3B). (C) Sample from SR4 deposit with geopetal filling. (D) Sample from SR5 deposit showing geopetal filling (cf. Fig. 3E).

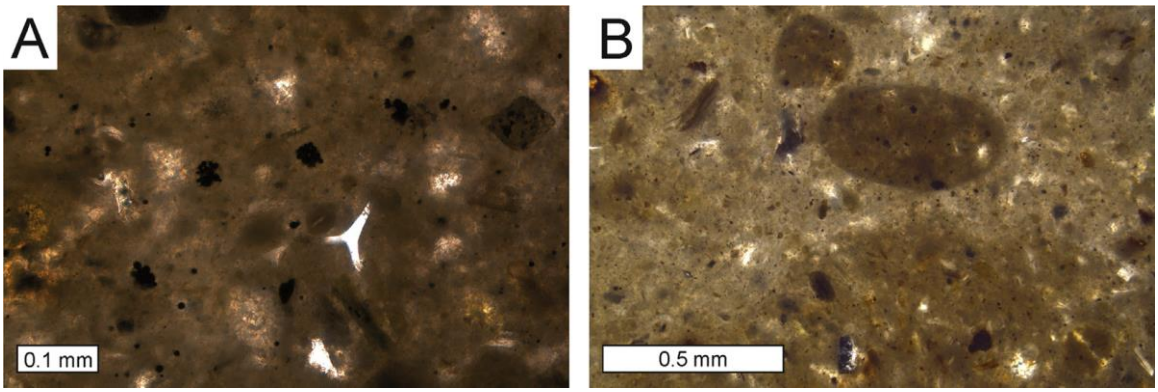


Fig. 5. Matrix micrite, thin section photomicrographs, all plane-polarized light. (A) Micrite of the SR4 deposit containing framboidal pyrite (black) and a triod sponge spicule (white). (B) Detritus-rich micrite of the SR5 deposit and an oval fecal pellet.

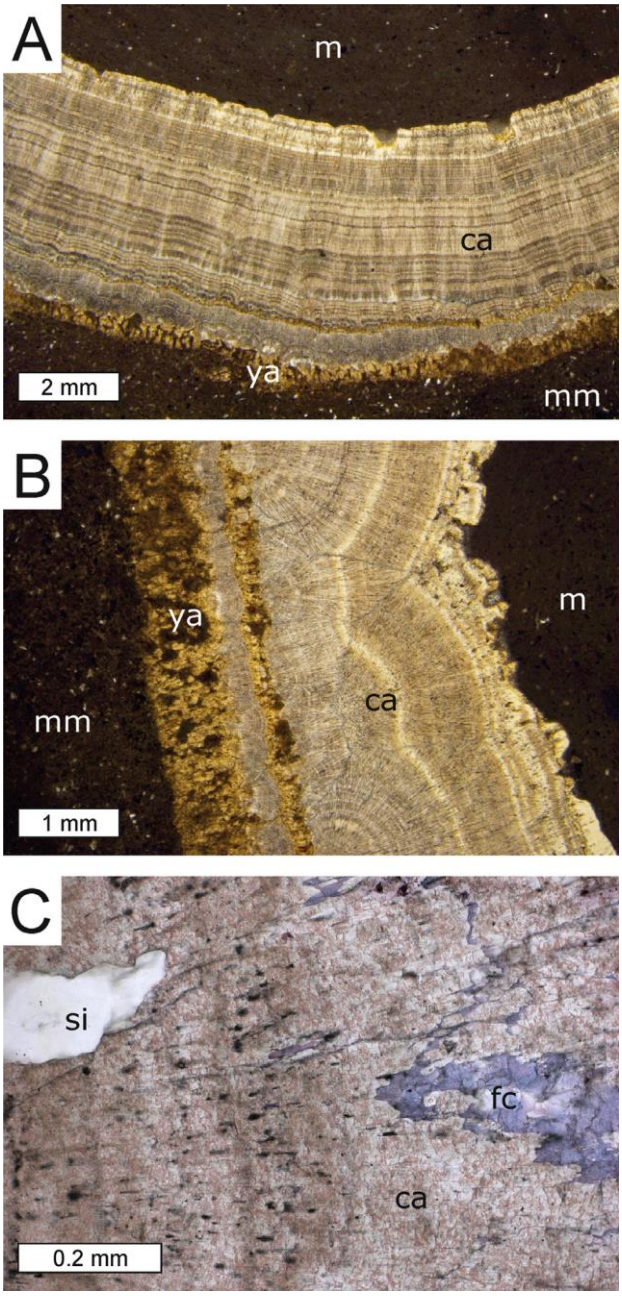


Fig. 6. Yellow and clear aragonite, thin section photomicrographs, all plane-polarized light; mm = matrix micrite, ya = yellow aragonite, ca = clear aragonite, m = pipe-filling micrite, si = silica, fc = ferroan calcite. (A) Paragenetic sequence of a pipe from the CRB deposit represented by matrix micrite, yellow aragonite, clear aragonite, and later stage pipe-filling micrite. (B) Yellow aragonite intercalated with banded clear aragonite, CRB deposit. (C) Clear aragonite (pink) partially replaced by silica (clear) and ferroan calcite (blue), thin section stained with a mixture of potassium ferricyanide and alizarin red solution, SR4 deposit.

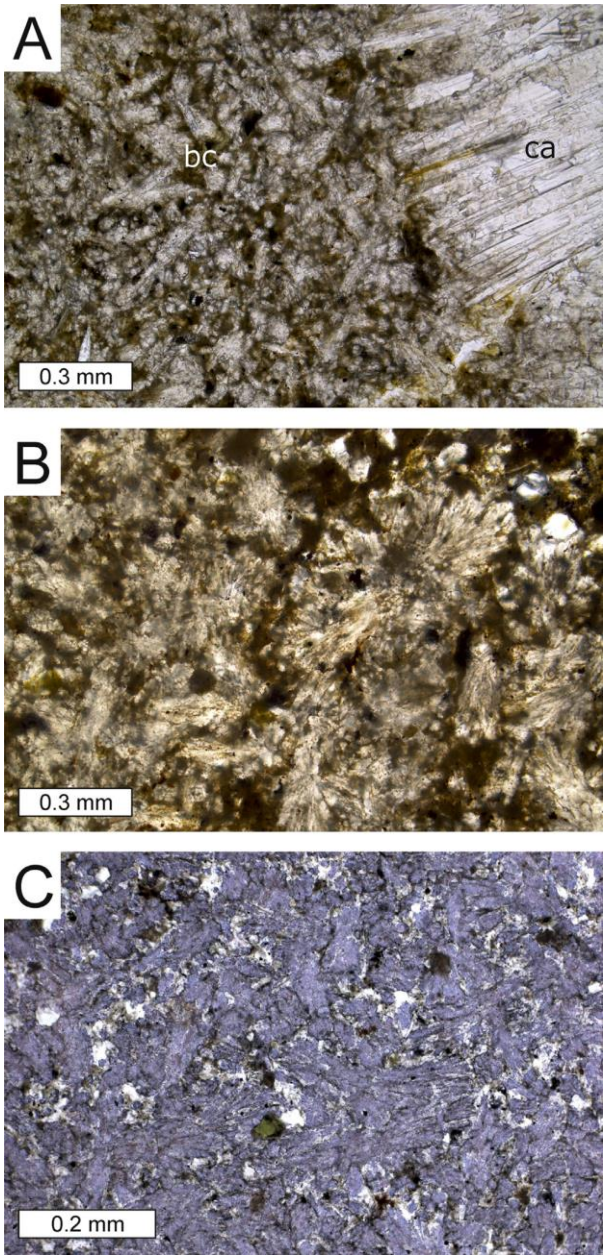


Fig. 7. Brownish calcite, SR4 deposit, thin section photomicrographs, all plane-polarized light; ca = clear aragonite, bc = brownish calcite. (A) Clear aragonite crystals predating brownish calcite. (B) Botryoidal to dumbbell-shaped crystal aggregates of brownish calcite. (C) Brownish calcite stained with potassium ferricyanide and alizarin red solution, resulting in a blue to mauve color. Green grain in the lower center is glauconite.

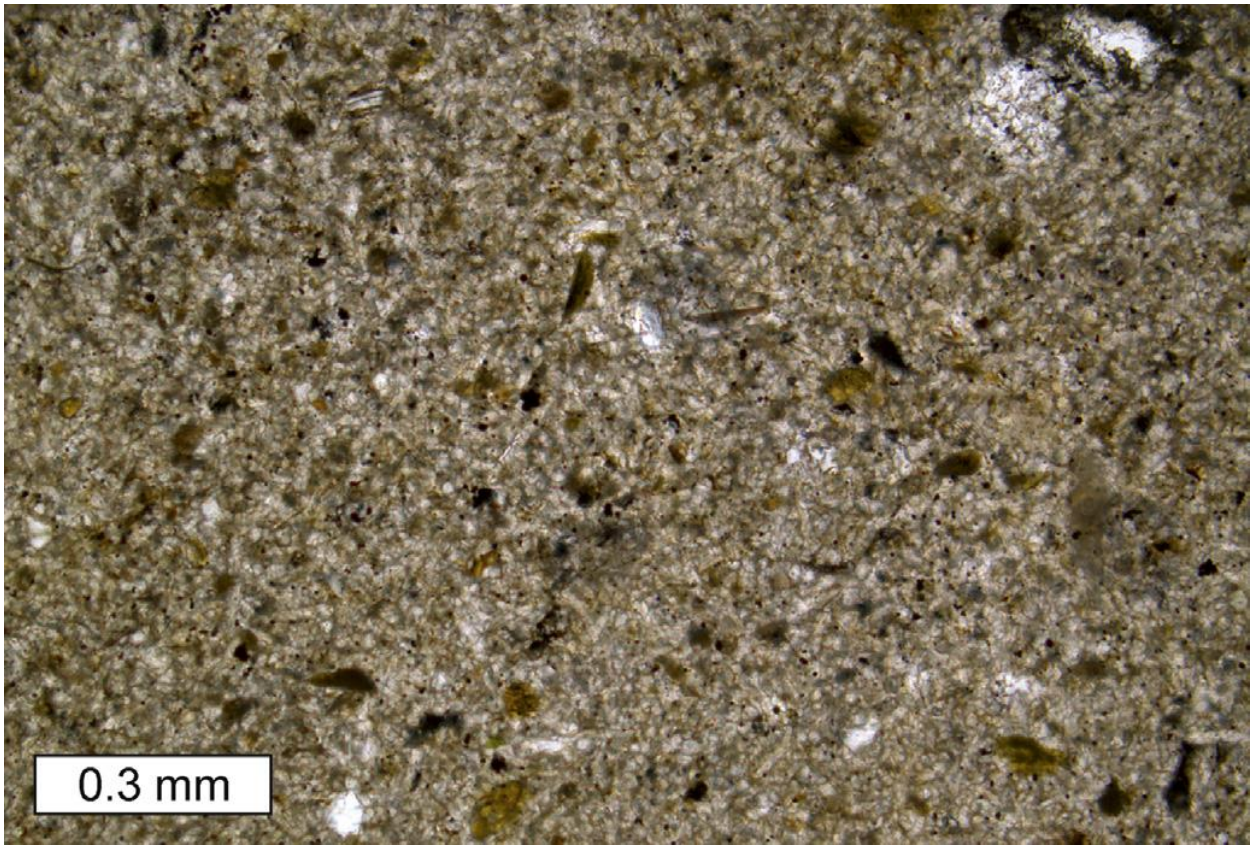


Fig. 8. Microspar, SR4 deposit, thin section photomicrograph; plane-polarized light.

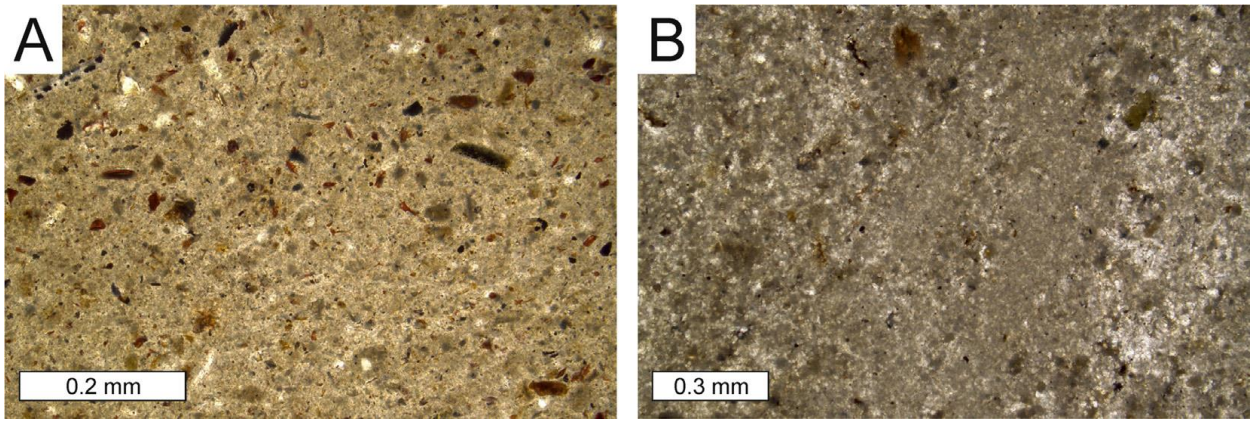


Fig. 9. Pipe-filling micrite, thin section photomicrographs, all plane-polarized light. (A) Pipe-filling micrite from the CRB deposit containing detritus. (B) Pipe-filling micrite from the SR4 deposit.

4.2. Isotope geochemistry of carbonate phases

Forty-two sample powders from five SR4 samples of early and later diagenetic carbonate phases were analyzed for their stable carbon and oxygen isotope compositions (Fig. 10). The $\delta^{13}C$ values of aragonite are lowest, with values of clear aragonite ranging from −50.6 to −42.1‰, and values of yellow aragonite ranging from −47.9 to −41.2‰. Matrix micrite also revealed exclusively negative $\delta^{13}C$ values, ranging from −40.5 to −19.2‰. The $\delta^{13}C$ values of microspar (−0.4 to 3.9‰) and pipe-filling micrite (−2.3 and −0.3‰) are considerably higher. The only phase that yielded exclusively positive $\delta^{13}C$ values is brownish calcite, spanning from 0.3 to 2.5‰. Stable oxygen isotope compositions vary noticeably among phases. Clear and yellow aragonite revealed overall positive $\delta^{18}O$ values, ranging from 0.9 to 1.8 and 0.9 to 1.6‰, respectively. Matrix micrite yielded values from −3.9 to 0.1‰, whereas pipe-filling micrite exhibits values from −4.4 to −4.1‰. Brownish calcite and microspar yielded negative $\delta^{18}O$ values, spanning from −6.5 to −5.6‰ and from −5.0 to −4.5‰, respectively.

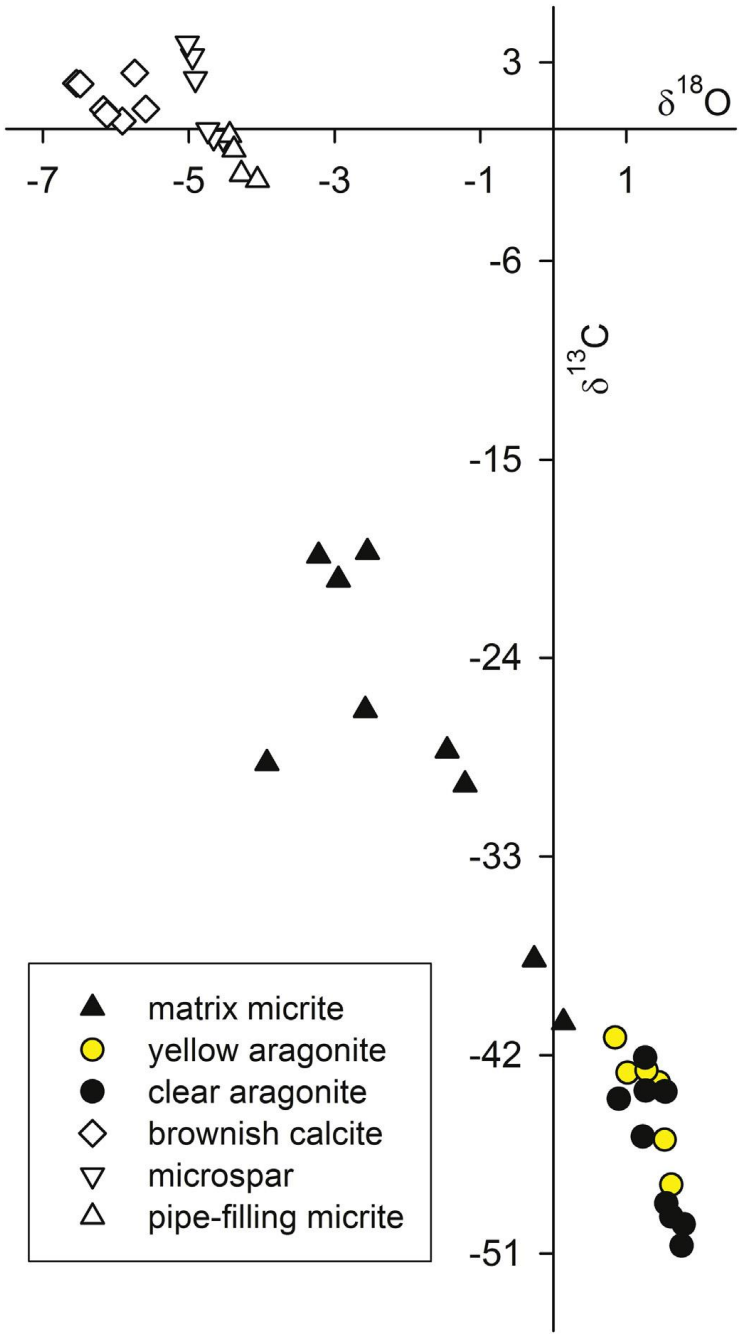


Fig. 10. Carbon and oxygen stable isotope plot of carbonate phases of five of the SR4 pipes. Values are relative to VPDB standard.

5. Discussion

5.1. Zoned mineralization of conduits as an archive of biogeochemical processes at seeps

The previously described tubular structures interpreted as the preserved subsurface plumbing systems of seeps consist predominantly of more or less homogenous microcrystalline carbonate phases (e.g., Aiello et al., 2001; Clari et al., 2004; De Boever et al., 2006; Campbell et al., 2008). Such pipes consequently lack an internal zonation caused by successive mineralization events. In contrast to this, the pipes of the studied Oligocene seep deposits consist of a concentric paragenetic sequence of mineral phases. In chronological sequence the succession of mineral phases is represented by (1) matrix micrite followed by (2) yellow and clear aragonite, and later formed (3) brownish calcite, microspar, and pipe-filling micrite (Fig. 11). In some samples brownish calcite and microspar co-occur, whereby the former precedes the latter phase. However, the timing of the formation of these two phases cannot be put into perspective to the formation the pipe-filling micrite, as the latter has never been found in association with the former. Deviations from the common paragenetic sequence occur where pipes contain geopetal fillings (Fig. 4C, D), indicating that the original orientation of pipes within the sediment was not exclusively vertical.

5.1.1. The early stage diagenetic phases – AOM driven precipitation close to the seafloor

Micrite is the most common carbonate phase of marine seep limestones (Beauchamp and Savard, 1992; Campbell et al., 2002; Peckmann et al., 2003, 2011; Bahr et al., 2009; Kuechler et al., 2012). Matrix micrite represents the first phase in the paragenetic sequence of the studied samples. Low $\delta^{13}C$ values indicate that its formation was induced by AOM with a possible contribution from the microbial decomposition of organic matter. These processes triggered chemical changes of the microenvironment that lead to calcium carbonate precipitation (cf. Ritger et al., 1987; Suess and Whiticar, 1989; Paull et al., 1992; Peckmann et al., 2001; Aloisi et al., 2002). Seep carbonates resulting from the oxidation of biogenic methane are typified by pronounced depletion in ^{13}C (e.g. Ritger et al., 1987; Peckmann and Thiel, 2004; Teichert et al., 2005). This signature is caused by strong fractionation during archaeal methanogenesis, which may result in $\delta^{13}C$ values of methane as low as –110‰ (Whiticar et al., 1986). During AOM, bicarbonate is produced that inherits a negative isotope signature, and the resulting calcium carbonate

precipitates are also depleted in ^{13}C (e.g. Teichert et al., 2005). However, the extent of the actual ^{13}C depletion in carbonate minerals depends on the degree of mixing of carbonate ions from different sources including marine bicarbonate (Peckmann and Thiel, 2004). Carbonate resulting from the oxidation of thermogenic methane or higher hydrocarbons and organic matter exhibit less negative $\delta^{13}C$ values than carbonate resulting from the oxidation of biogenic methane (Roberts and Aharon, 1994; Whiticar, 1999; Peckmann and Thiel, 2004). The heterogeneity of $\delta^{13}C$ values of the matrix micrite ranging from −40.5 to −19.2‰ probably results from a mixing of carbonate derived from different carbon sources (cf. Peckmann and Thiel, 2004). In the course of micrite precipitation at the active Oligocene seeps, the host sediments were increasingly consolidated, favoring the stabilization of the conduits and allowing for a virtually undisturbed growth of the authigenic phases within the conduits. The formation of authigenic pyrite within the matrix micrite indicates bacterial sulfate reduction (Schieber, 2002, but see Ohfuji and Rickard, 2005). Pyrite at seeps is largely the product of sulfate-dependent AOM, but at some seeps organiclastic sulfate reduction may also significantly contribute to the production of sulfide (Joye et al., 2004; Orcutt et al., 2005; Lapham et al., 2008).

Early diagenetic yellow aragonite cement and its putative product yellow calcite cement occur in many ancient seep limestones (e.g. Beauchamp and Savard, 1992; Savard et al., 1996; Campbell et al., 2002; Peckmann et al., 2002, 2003; Himmler et al., 2008; Hagemann et al., 2012; Kuechler et al., 2012). Like the examples of this mineral phase from other seep limestones, yellow aragonite cement of the pipes, as well as the associated clear variety of fibrous aragonite cement, are methane-derived, early diagenetic phases. This is revealed by their low $\delta^{13}C$ values (−50.6 to −41.2‰), indicating that precipitation was triggered by AOM. Although not detailed by Birgel et al. (2008), the samples of the SR4 deposit used for comparison in their biomarker study were the pipes described here. The detection of ^{13}C-depleted bicyclic biphytanic diacids along with other ^{13}C-depleted biomarkers of methanotrophic prokaryotes confirms that AOM occurred in the conduits and resulted in the formation of authigenic carbonate minerals (Birgel et al., 2008). Because aragonite precipitation is favored over calcite precipitation in seawater due to the inhibiting effect of hydrated magnesium ions and the purported inhibition by sulfate ions on the growth of the calcite crystal lattice (Berner et al., 1978; Busenberg and Plummer, 1985; Morse et al., 1997; Arvidson and Morse, 2002), yellow and clear aragonite probably precipitated from waters with a composition similar to that of seawater. It should, however, be noted that the common hypothesis that sulfate ions inhibit the precipitation of calcite has been challenged (Brady et al., 1996). Instead, dolomite

and magnesian calcite precipitation is rather catalyzed by sulfide ions, which reduce the amount of energy required for the dehydration of magnesium ions from aqueous solution (Zhang et al., 2012, 2013). Nonetheless, this finding does not affect the concept that aragonite preferentially precipitates from waters of a seawater composition, whereas calcite precipitation tends to be favored under more reducing conditions.

Given that an at least episodic preferred upward movement of fluids must be assumed in the conduits when the Oligocene seeps were active, it seems very likely that the conduits were still positioned close to the seafloor when aragonite cement precipitated. Aragonite is the dominant carbonate mineral close to the sediment-water interface at modern seeps (e.g. Bohrmann et al., 1998; Luff et al., 2004; Haas et al., 2010). Oxygen isotopes of seep carbonates are more challenging to interpret than carbon isotopes. This is mainly due to the ease of oxygen isotope exchange during diagenesis, as the oxygen pool of waters (as part of the water molecule) involved in late diagenesis is much larger than their carbon pool (e.g. Peckmann et al., 2003). Because the early diagenetic aragonite cements show slightly positive $\delta^{18}O$ values (0.9 to 1.8‰) similar to modern seep carbonates (cf. Teichert et al., 2005), agreeing with precipitation in equilibrium or close to equilibrium with Oligocene seawater (cf. Veizer et al., 1999), the presumption that the aragonite cements formed close to the seafloor from waters with a seawater-like composition is supported by the oxygen isotope data.

5.1.2. The later stage diagenetic phases – precipitation from fluids affected by methanogenesis

The later stage phases that fill the inner part of pipes include brownish calcite, microspar, and pipe-filling micrite, reflecting changes in the diagenetic regime. Peckmann et al. (2002) documented the characteristic crystal morphology of brownish calcite. The formation of the dumbbell-shaped crystal aggregates may have been induced by bacterial activity (cf. Warthmann et al., 2000), but other factors (e.g. silicate weathering; Meister et al., 2011) may also have caused or at least contributed to the generation of the high degree of supersaturation that is required for the precipitation of this type of crystal aggregate (cf. Fernandez-Diáz et al., 1996). Microspar is commonly assumed to either represent an abiotically generated cement, or a neomorphic phase that formed during burial (Flügel, 2004). Because of the lack of evidence that it is replacive in the studied pipes, it is interpreted to represent a cement rather than a neomorphic phase. This interpretation is in accord with its carbon and oxygen stable isotope

composition distinct from that of matrix micrite and pipe-filling micrite (see Fig. 10) as discussed below. Like brownish calcite and microspar, pipe-filling micrite is interpreted as a later stage cement. Its homogenous fabric and the scarcity of detrital grains argue for an authigenic formation rather than placement in the center of the pipe after transportation. Similarly, Campbell et al. (2002) and Kiel et al. (2013) reported later stage, detrital-poor micrite filling cavities and pore spaces in Mesozoic seep limestones, demonstrating that micrite phases poor in detritus postdating matrix micrite are common in seep deposits.

All these later stage diagenetic phases are relatively enriched in ^{13}C compared to the early diagenetic phases of the pipes (see Fig. 10). Positive $\delta^{13}C$ values of methane-seep carbonates, particularly when found in phases post-dating AOM-derived phases, have been ascribed to methanogenesis rather than methane oxidation (Gaillard et al., 1992; Peckmann et al., 2002). The ^{13}C enrichment of pore fluids is caused by the preferential uptake of ^{12}C during archaeal methanogenesis, leaving the residual carbon pool enriched in ^{13}C (Irwin et al., 1977). During burial and on-going sedimentation or episodic changes in fluid flux, the pipes may have shifted into the zone of methanogenesis. Subsequently brownish calcite, microspar, and pipe-filling micrite precipitated. During this stage the pore fluids were depleted in ^{12}C, which was probably caused by the local production of methane and resulted in ^{13}C-enriched precipitates. Apart from continued sedimentation resulting in a continuous displacement of biogeochemical zones on longer timescales, variations in seepage flux control the position of the SMTZ and, accordingly, the zone of AOM within the sediment column on shorter timescales. Due to flux changes, the SMTZ and consequently the AOM zone may move upward or downward (e.g. Lapham et al., 2008; Feng et al., 2009). Alternatively, brownish calcite, microspar, and pipe-filling micrite may not have precipitated in the zone of archaeal methanogenesis but at shallower depth. In this scenario AOM locally ceased and the fluids from which the late stage cements precipitated ascended from a zone of methanogenesis below.

The high iron content of brownish calcite of approximately 8 mol% $FeCO_3$ suggests its formation in the zone of methanogenesis (e.g. Irwin, 1980; Coleman, 1985; Mazzullo, 2000). Carbonate minerals forming in the zone of bacterial sulfate reduction have very low iron contents due to the high affinity of ferrous iron to sulfide ions, resulting in the formation of iron sulfide (Berner 1984; Raiswell and Berner, 1985). Alternatively, high iron contents are typical of carbonate minerals forming in the zone of iron reduction (Coleman, 1985). Nonetheless, $\delta^{13}C$ values of brownish calcite of 0.3 to 2.5‰ render precipitation within the iron reduction zone unlikely, as the diagenetic carbonate minerals of this

biogeochemical zone are typified by lower $\delta^{13}C$ values (Coleman, 1985, 1993). Based on its high $\delta^{13}C$ values and its relatively high iron content, it seems unlikely that brownish calcite formed in the zone of bacterial sulfate reduction. Yet, scarce pyrite occurs intermingled between the crystal aggregates of brownish calcite. It is possible that the accessory pyrite is of a detrital origin and does not reflect the geochemical environment during the formation of brownish calcite. If, however, pyrite formed in situ, this mutually exclusive mineral assemblage would indicate a change of environmental conditions on a spatial microscale or a succession of variable biogeochemical processes during later stage diagenesis.

Brownish calcite, microspar, and pipe-filling micrite are characterized by much lower $\delta^{18}O$ values than the earlier stage cements. A decrease of the ^{18}O content of later diagenetic mineral phases of seep carbonates has been documented in previous studies (e.g. Campbell et al., 2002; Peckmann et al., 2002, 2003; Himmler et al., 2008). The common overall trend from positive towards more negative $\delta^{18}O$ values in seep carbonates along with an inverse trend in stable carbon isotopes has been attributed to progressive diagenesis including changes in the composition of pore fluids and a concomitant increase in formation temperatures during burial (Campbell et al., 2002; Peckmann et al., 2002), a scenario that also applies to the pipes. With respect to the formation scenario of the later diagenetic minerals, the ^{18}O depletion of these phases suggests precipitation at greater depth, some distance from the sediment-water interface. However, as stated above, it cannot be excluded that ^{18}O depleted fluids ascended from a deeper zone of methanogenesis to the depth of the sedimentary column in which the later stage diagenetic phases formed within the pipes (cf. Campbell, 2006, her Fig. 9A).

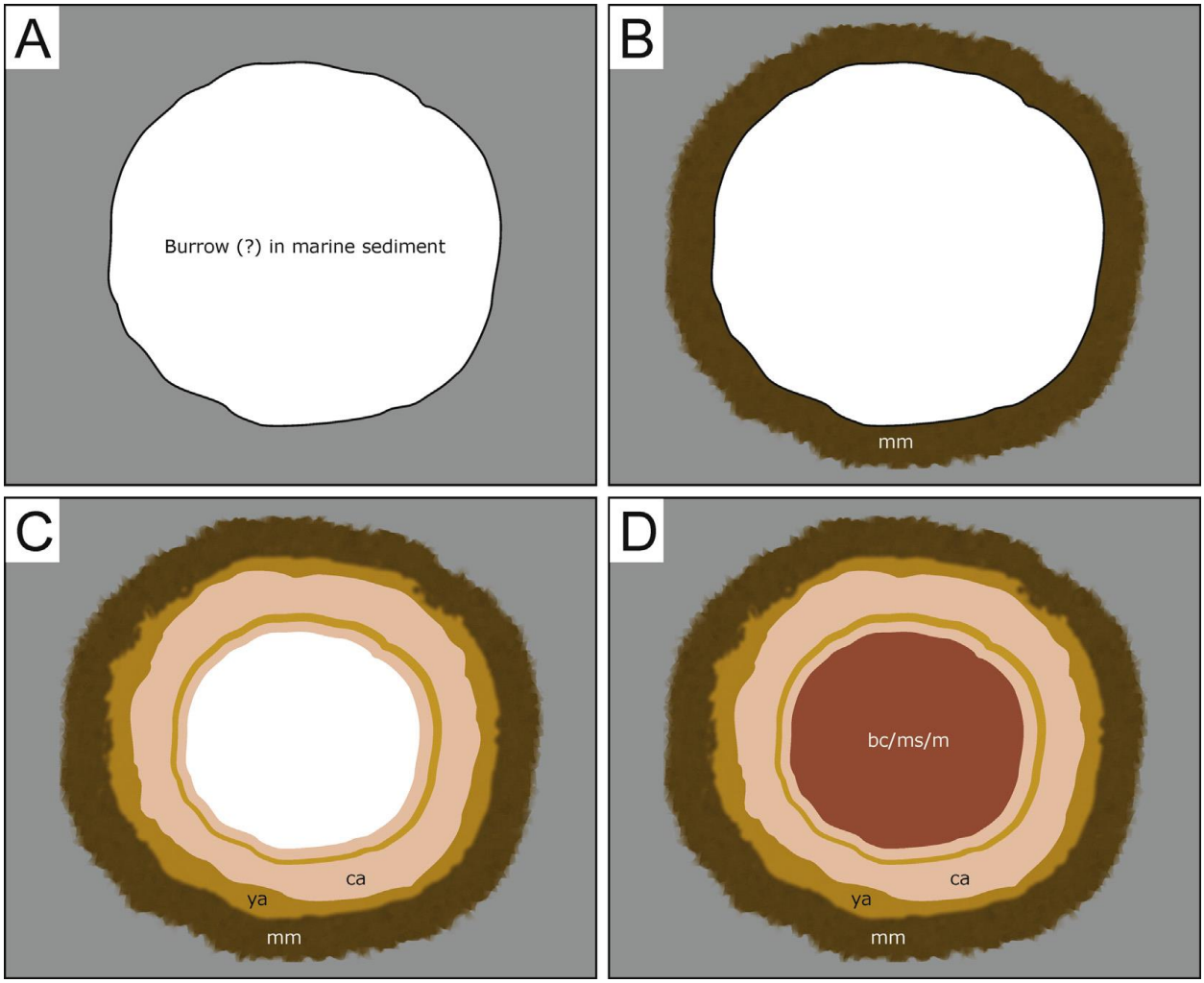


Fig. 11. Cartoon illustrating the paragenetic sequence of the Lincoln Creek Formation pipes, not to scale; mm = matrix micrite, ya = yellow aragonite, ca = clear aragonite, bc = brownish calcite, ms = microspar, m = pipe-filling micrite. (A) Open channel interpreted to represent a burrow within the host sediment (gray background). (B) Precipitation of methane-derived matrix micrite stabilizes the channel. (C) Methane-derived yellow and clear aragonite cements precipitate consecutively on the inner walls of the channel. (D) Precipitation of later stage pipe-filling phases (brownish calcite, microspar, pipe-filling micrite) from a carbonate pool affected by methanogenesis. See text for further details.

5.2. Possible origins of conduits

In contrast to the large subsurface tubular carbonate concretions that have been interpreted to represent the subsurface plumbing system of methane seeps (e.g. Nyman et al., 2010), the much smaller pipes from the Lincoln Creek Formation formed much shallower in the sediment and directly merge into the massive seep deposits. It is inferred that the pipes were originally burrows produced by organisms that dwelled at the ancient seep sites. Seep-endemic megafauna preserved in the studied seep deposits include hexactinellid sponges, corals, bivalves, gastropods, and decapod crustaceans (cf. Peckmann et al., 2002). Among those, some of the bivalves and decapods could have produced burrows that later served as fluid migration pathways and were successively filled by authigenic carbonate phases (e.g. Campbell et al., 2008).

Semi-infaunal to infaunal seep-dwelling bivalves include vesicomyids such as *Calyptogena sp*. (e.g. Nobuhara, 2003; Campbell, 2006), solemyids including *Acharax sp*. (Seike et al., 2012), and several lucinid (Kiel, 2013) and thyasirid (Kiel et al., 2008) species. The bivalves listed above are known to live in symbiosis with chemoautotrophic bacteria (e.g. Distel et al., 1988; Dando et al., 1993; Imhoff et al., 2003; Taylor and Glover, 2010). By extending their foot into the sediment (e.g. the vesicomyid clam *Calyptogena sp*.) or by repetitively migrating from the oxic to the anoxic zone in their burrows (e.g. solemyids like *Acharax johnsoni*), the chemosymbiotic bivalves obtain access to reduced compounds (Childress and Girguis, 2010; Seike et al., 2012), allowing the bivalves to supply their bacterial symbionts with sulfide while still accessing oxygen from seawater (Levin, 2005; Childress and Girguis, 2010). *Acharax johnsoni* has been described to reach shell lengths of up to 8.7 cm at seeps and produces burrows of up to 2 cm in diameter (Seike et al., 2012). Lucinid bivalves can extend their foot up to five times the length of their shell, thyasirids even up to fifteen times (Dufour and Felbeck, 2003). Lucinid and thyasirid bivalves described from ancient seeps reach shell sizes from 6 to 20 cm and 0.5 to 1.5 cm, respectively (Kiel et al., 2008; Kiel, 2013), suggesting that these species could have penetrated 30 to 50 cm deep into the sediment. Solemyid bivalves from the Neogene Quinault seep deposit, western Olympic Peninsula, reach a length of approximately 1.5 cm; their burrows have been found to extend 20 cm into the sediment (Campbell, 1992). Considering the size of burrows and tracks made by bivalves, the studied pipes could well have been formed by bivalve mollusks. The shape of bivalve burrow and track structures ranges from straight (Dufour and Felbeck, 2003), to Y and U shaped (e.g. Campbell, 1992; Seike et al., 2012). Solemyid

bivalves are known to produce very distinctive burrows with ovate to chalice-shaped cross-sections (e.g. Frey, 1968). As the pipes exhibit circular cross-sections, solemyid bivalves can probably be excluded as producers. Moreover, none of the bivalves recognized in the SR4 deposit are large enough to have produced the pipes described here. Bivalves from SR5 and the Canyon River site are possible producers of the pipes, because fossils of thyasirids up to 5.5 cm long, and lucinids up to 5.0 cm long are found in strata a few meters above both sites, but not in direct association with the carbonate pipes. Yet another problem with the interpretation that the pipes represent former structures generated by chemosymbiotic bivalves concerns the unknown permanence of bivalve burrows and tracks. It can be excluded that the burrows were completely filled by authigenic mineral phases while the bivalves where still alive, and it is questionable whether or not bivalve burrows maintain their structural integrity after the death of their producers.

Channeling of fluid flow at seeps due to the burrowing activity of bivalves has been suggested previously. When describing the burrows from the Neogene Quinault deposit, Campbell (1992) invoked that they may have served as pathways for seeping fluids. Dufour and Felbeck (2003) showed that tracks of thyasirid and lucinid bivalves act as conduits allowing for enhanced sulfide flux toward the seafloor during the life span of the bivalves. Similarly, Nobuhara (2003) considered the effects of bivalve bioirrigation and pumping activity that promotes upward fluid flow. He even mentioned the occurrence of rims of aragonite cement on the inner walls of open burrows, similar to what is found for the pipes in this study. Such an early lining of burrow walls by aragonite cement may well stabilize the burrow integrity and allow for a subsequent filling of the tubular cavity. In a modeling approach, Wallmann et al. (1997) showed that the activity of burrowing organisms, including bioirrigation, plays a vital role for solute transport in the surficial sediments at seeps, accelerating carbonate authigenesis.

Another feasible scenario for a biological origin of the studied pipes is bioturbation by sediment-dwelling crustaceans including callianassid decapods. These crustaceans construct straight to branched, vertical to horizontal burrows (Griffis and Suchanek, 1991; Papaspyrou et al., 2005), which are frequently preserved as trace fossils such as *Spongeliomorpha, Ophiomorpha*, and *Thalassinoides* (Neto de Carvalho et al., 2007; Peckmann et al., 2007; Campbell et al., 2008, 2010; Chien et al., 2012; Wetzel, 2013). It has long been suggested that some crustaceans inhabit sediments with anoxic pore waters (Bromley, 1996). They can apparently tolerate anoxia for some time and are capable of ventilating parts of their burrows with oxygenated seawater (Forster and Graf, 1992; Anderson et al., 1994). Callianassid

decapods excrete mucus, which stabilizes burrow walls and acts as organic substrate for the growth of bacteria, representing an additional food source for the crustaceans (Bertics et al., 2010; Griffis and Suchanek, 1991). Due to such stabilization, decapod burrows remain stable for extended periods of time (Dworschak, 1983; Aller and Aller, 1986; de Vaugelas and Buscail, 1990; Papaspyrou et al., 2005). The occurrence of crustacean microcoprolites of the ichnogenus *Palaxius* in the pipes provides evidence that decapod crustaceans lived at the studied seeps. It has been suggested that burrowing activity of crustaceans at seeps promotes the seepage of methane-rich fluids (Peckmann et al., 2007; Wetzel, 2013; Wiese et al., this issue).

The burrow systems of callianassids are built up by shafts and chambers, which measure 1 and 2 cm in diameter, respectively, and can extend up to 3 m into the sediment (Bertics et al., 2010). *Spongeliomorpha* burrows may reach up to 5 cm in diameter (De Gibert and Ekdale, 2010a), revealing that diameter and overall size of the burrows may vary considerably. The surfaces of these trace fossils are often characterized by distinct morphological features known as bioglyphs (De Gibert and Ekdale, 2010b). *Thalassinoides*, unlike *Spongeliomorpha*, does not exhibit such bioglyphs on the inner walls of the burrows (De Gibert and Ekdale, 2010a). Unfortunately, we could not identify bioglyphs with certainty on the pipes. However, based on their size, shape, branching, and the preferred subvertical but also subhorizontal orientation, it is feasible that the pipes resulted from the burrowing activity of decapod crustaceans. Fossils of callianassid crustaceans are abundant at the SR4 locality in direct association with the pipes, but not enclosed within them. We did not detect any crustacean fossils at the SR5 or CRB localities, although they do occur a few meters stratigraphically above both sites. Bivalves cannot be excluded as alternative producers, however, the documented persistence of crustacean burrows argues in favor of crustaceans as producers of the conduits. Although a completely abiogenic origin of the pipes also cannot be excluded, it seems more likely that they resulted from the burrowing activity of sediment-dwelling metazoans. Regardless of how the pipes were originally formed, they subsequently regulated fluid flow in the uppermost part of the plumbing systems of the Oligocene seeps.

An envisioned scenario of the formation of the pipes is shown in Fig. 12. The study site was located at an active continental margin where methane seepage occurred. The seeps were colonized by megafauna causing bioturbation (burrowing) of the unconsolidated host sediment (Fig. 12A). Concomitant with the burrowing activity or slightly later, methane migrated upwards through the burrows (Fig. 12A). Henceforth the burrows acted as conduits for focused methane flux and AOM was not restricted to the

host sediment, but also occurred within the conduits (Fig. 12B). Precipitation of matrix micrite stabilized the conduits in the host sediment before methane-derived carbonate cements started to precipitate on the inner walls of the conduits (Fig. 12B). Due to enhanced supply of dissolved sulfate from above and directed transport of methane from below, the zone of AOM was widened in the periphery of the conduits and biogeochemical activity flourished within the conduits (Fig. 12B). For the formation of the later diagenetic phases (brownish calcite, microspar, and pipe-filling micrite) two scenarios seem equally plausible. (1) Enhanced upward flux of deeper burial fluids imprinted by methanogenesis resulted in the displacement of the SMTZ closer to the sediment-water interface, leading to the precipitation of the later stage carbonate phases within the conduits (Fig. 12C). (2) Ongoing sedimentation and burial resulted in the displacement of the conduits into the zone of methanogenesis (Fig. 12D), where the later stage phases formed.

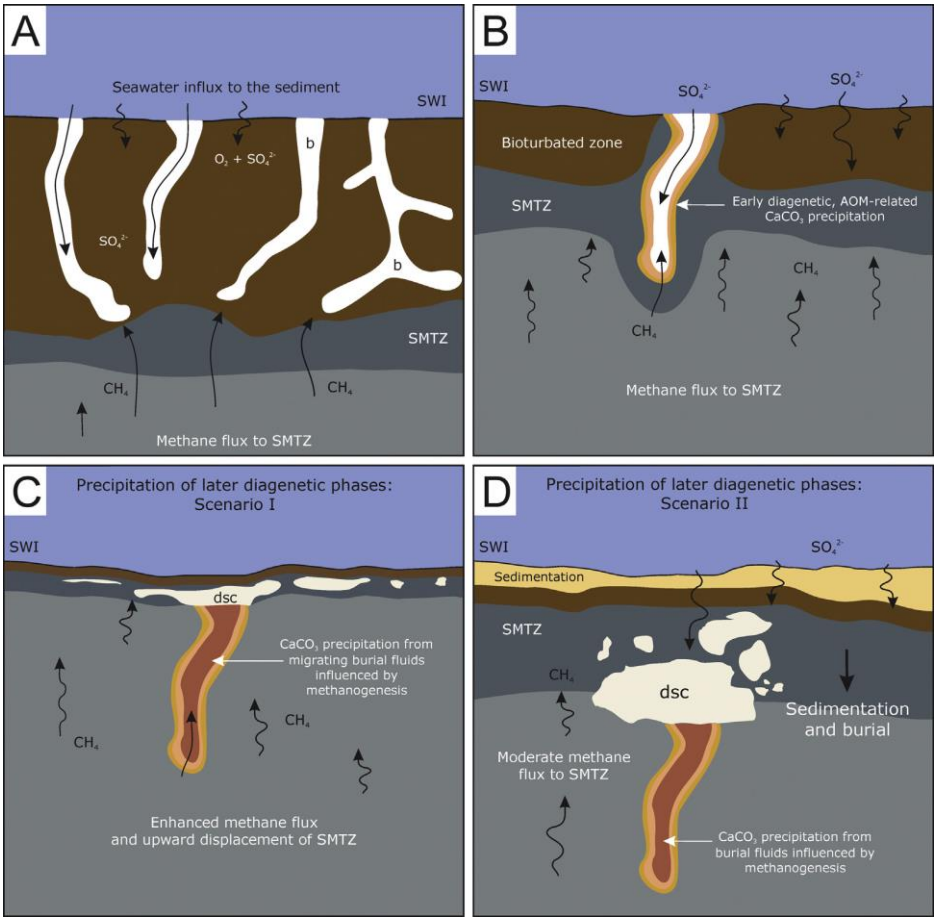


Fig. 12. Cartoon illustrating the envisioned temporal and spatial sequence of events responsible for the formation of the mineralized conduits from the Lincoln Creek Formation, not to scale, SWI = sediment-water interface, b = burrow, SMTZ = sulfate methane transition zone, dsc = dense seep carbonate. (A) Active methane seepage in a convergent margin setting. Seepage towards the oxic bioturbated zone (dark brown). Burrows offer preferred migration pathways for sulfate and methane, enabling focused fluid flow through the sediment. (B) Methane seepage from the zone of methanogenesis (light gray) reaches the zone of AOM (dark gray). Methane and sulfate flux are enhanced within the burrow, triggering the precipitation of AOM-related aragonite cements (cf. Fig. 11C). (C) Scenario I: Local cessation of AOM and upward displacement of the SMTZ lead to precipitation of later stage diagenetic minerals (brownish calcite, microspar, pipe-filling micrite) within the pipe from a carbonate pool affected by methanogenesis (cf. Fig. 11D). (D) Scenario II: On-going sedimentation (beige) and subsequent burial lead to placement of the burrows into the zone of methanogenesis, inducing precipitation of later stage diagenetic phases. See text for further details.

6. Conclusions

The Lincoln Creek Formation in Washington State contains small- to medium sized carbonate pipes that directly grade into the base of methane-seep deposits. The pipes are characterized by an inward directed paragenetic sequence of authigenic carbonate phases, which reflects a succession of biogeochemical processes. The early stage phases including micrite, yellow aragonite, and clear aragonite cement resulted from anaerobic oxidation of methane. Biogenic methane was most probably the dominant carbon source, as indicated by biomarker patterns (Birgel et al., 2008) and $\delta^{13}C_{carbonate}$ values as low as −51‰. The inner portions of the pipes are filled by later stage carbonate phases that apparently reflect methanogenesis, agreeing with the more positive $\delta^{13}C$ values of brownish calcite, microspar, and pipe-filling micrite and the high iron content of brownish calcite.

The pipes from the Lincoln Creek formation probably resulted from bioturbation of seep-dwelling decapod crustaceans or bivalves. This notion is supported by pipe size and morphology, which agree with both invertebrate groups as potential producers of the burrows that acted as fluid conduits. Based on the occurrence of abundant authigenic, methane-derived carbonate phases within the pipes, the formerly open conduits apparently facilitated seepage of methane-rich fluids to the sediment-water interface. Our findings are in accord with observations made at modern seeps and agree with modeling approaches, highlighting that the transport of fluids within near-surface sediments at seeps is dominated by the activity of the local fauna.

Acknowledgments

We thank S. Flotow for preparation of thin sections, Monika Segl for stable isotope analysis, as well as Wolfgang Bach and Andreas Klügel (all Bremen, Germany) for help with LA-ICP-MS analysis. This study would not have been possible without Green Diamond Resource Company (Seattle, Washington) kindly allowing access to the localities on their land. Comments by Kathleen Campbell (Auckland, New Zealand), Carles Canet (Mexico City, Mexico), an anonymous referee, as well as Steffen Kiel and Frank Wiese (both Göttingen, Germany) are gratefully acknowledged.

References

Aiello, I.W., Garrison, R.E., Moore, J.C., Kastner, M., Stakes, D.S., 2001. Anatomy and origin of carbonate structures in a Miocene cold-seep field. Geology 29, 1111–1114.

Aller, J.Y., Aller, R.C., 1986. Evidence for localized enhancement of biological activity associated with tube and burrow structures in deep-sea sediments at the HEBBLE site, western North Atlantic. Deep-Sea Research Part A. Oceanographic Research Papers 33, 755–790.

Aloisi, G., Bouloubassi, I., Heijs, S.K., Pancost, R.D., Pierre, C., Sinninghé Damste, J.S., Gottschal, J.C., Forney, L.J., Rouchy, J-M., 2002. CH_4-consuming microorganisms and the formation of carbonate crusts at cold seeps. Earth and Planetary Science Letters 203, 195–203.

Anderson, S.J., Taylor, A.C., Atkinson, R.J.A., 1994. Anaerobic metabolism during anoxia in the burrowing shrimp *Calocaris macandraea* Bell (Crustacea: Thalassinidea). Comparative Biochemistry and Physiology 108, 515–522.

Arvidson, R.A., Morse, J.W., 2002. The dissolution kinetics of major sedimentary carbonate minerals. Earth-Science Reviews 58, 51–84.

Babcock, R.S., Suczek, C.A., Engebretson, D.C., 1994. The Crescent "terrane", Olympic Peninsula and southern Vancouver Island. In: Lasmanis, R., Cheney, E.S. (Eds.), Regional Geology of Washington State. Washington Division of Geology and Earth Resources Bulletin 80, 141–157.

Bahr, A., Pape, T., Bohrmann, G., Mazzini, A., Haeckel, M., Reitz, A., Ivanov, M., 2009. Authigenic carbonate precipitates from the NE Black Sea: a mineralogical, geochemical, and lipid biomarker study. International Journal of Earth Sciences 98, 677–695.

Beauchamp, B., Savard, M., 1992. Cretaceous chemosynthetic carbonate mounds in the Canadian Arctic. Palaios 7, 434–450.

Beikman, H.M., Rau, W.W., Wagner, H.C., 1967. The Lincoln Creek Formation, Grays Harbor Basin, Southwestern Washington. U.S. Geological Survey Bulletin 1244–I, 20 p.

Berner, R.A., 1984. Sedimentary pyrite formation: An update. Geochimica et Cosmochimica Acta 48, 605–615.

Berner, R.A., Westrich, J.T., Graber, R., Smith, J., Martens, C.E., 1978. Inhibition of aragonite precipitaiton from supersaturated seawater: A laboratory and field study. American Journal of Science 278, 816–837.

Bertics, V.J., Sohm, J.A., Treude, T., Chow, C.E.T., Capone, D.G., Fuhrman, J.A., Ziebis, W., 2010. Burrowing deeper into benthic nitrogen cycling: the impact of bioturbation on nitrogen fixation coupled to sulfate reduction. Marine Ecology Progress Series 409, 1–15.

Birgel, D., Elvert, M., Han, X., Peckmann, J., 2008. ^{13}C-depleted biphytanic diacids as tracers of past anaerobic oxidation of methane. Organic Geochemistry 39, 152–156.

Boetius, A., Ravenschlag, K., Schubert, C.J., Rickert, D., Widdle, F., Gieseke, A., Amann, R., Jørgensen, B.B., Witte, U., Pfannkuche, O., 2000. A marine microbial consortium apparently mediating anaerobic oxidation of methane. Nature 407, 623–626.

Bohrmann, G., Greinert, J., Suess, E., Torres, M., 1998. Authigenic carbonates from the Cascadia subduction zone and their relation to gas hydrate stability. Geology 26, 647–650.

Bohrmann, G., Heeschen, K., Jung, C., Weinrebe, W., Baranov, B., Cailleu, B., Heath, R., Hühnerbach, V., Hort, M., Masson, D., Trummer, I., 2002. Widespread fluid expulsion along the seafloor of the Costa Rica convergent margin. Terra Nova 14, 69–79.

Bohrmann, G., Ivanov, M., Foucher, J.-P., Spiess, V., Bialas, J., Greinert, J., Weinrebe, W., Abegg, F., Aloisi, G., Artemov, Y., Blinova, V., Drews, M., Heidersdorf, F., Krabbenhoft, A., Klaucke, I., Krastel, S., Leder, T., Polikarpov, I., Saburova, M., Schmale, O., Seifert, R., Volkonskaya, A., Zillmer, M., 2003. Mud volcanoes and gas hydrates in the Black Sea: new data from Dvurechenskii and Odessa mud volcanoes. Geo-Marine Letters 23, 239–249.

Brady, P.V., Krumhansl, J.L., Papenguth, H.W., 1996. Surface complexation clues to dolomite growth. Geochimica et Cosmochimica Acta 60, 727–731.

Brandon, M.T., Calderwood, A.R., 1990., High-pressure metamorphism and uplift of the Olympic subduction complex. Geology 18, 1252–1255.

Brandon, M.T., Vance, J.A., 1992. Tectonic evolution of the Cenozoic Olympic subduction complex, Washington State, as deduced from fission track ages for detrital zircons. American Journal of Science 292, 565 –636.

Brandon, M.T., Roden-Tice, M.K., Garver, J.I., 1998. Late Cenozoic exhumation of the Cascadia accretionary wedge in the Olympic Mountains, northwest Washington State. Geological Society of America Bulletin 110, 985–1009.

Bromley, R.G., 1996. Trace fossils: Biology, Taphonomy and Applications. Second edition. Chapman and Hall, London, 361 p.

Busenberg, E., Plummer, N.L., 1985. Kinetic and thermodynamic factors controlling the distribution of SO_3^{2-} and Na^+ in calcites and selected aragonites. Geochimica et Cosmochimica Acta 49, 713–725.

Campbell, K.A., 1992. Recognition of a Mio-Pliocene cold seep setting from the northeast Pacific convergent margin, Washington, USA. Palaios 7, 422–433.

Campbell, K.A., 2006. Hydrocarbon seep and hydrothermal vent paleoenvironments and paleontology: Past developments and future research directions. Palaeogeography, Palaeoclimatology, Palaeoecology 232, 362–407.

Campbell, K.A., Bottjer, D.J., 1993. Fossil cold seeps. National Geographic Research and Exploration 9, 326–343.

Campbell, K.A., Farmer, J.D., Des Marais, D., 2002. Ancient hydrocarbon seeps from the Mesozoic convergent margin of California: carbonate geochemistry, fluids and palaeoenvironments. Geofluids 2, 63–94.

Campbell, K.A., Francis, D.A., Collins, M., Gregory, M.R., Nelson, C.S., Greinert, J., Aharon, P., 2008. Hydrocarbon seep-carbonates of a Miocene forearc (East Coast Basin), North Island, New Zealand. Sedimentary Geology 204, 83–105.

Campbell, K.A., Nelson, C.S., Alfaro, A.C., Boyd, S., Greinert, J., Nyman, S., Grosjean, E., Logan, G.A., Gregory, M.R., Cooke, S., Linke, P., Milloy, S., Wallis, I., 2010. Geological imprint of methane seepage on the seabed and biota of the convergent Hikurangi Margin, New Zealand: Box core and grab carbonate results. Marine Geology 272, 285–306

Canet, C., Anadón, P., Alfonsi, P., Prol-Ledesma, R.M., Villanueva-Estrada, R.E., García-Valles, M., 2013. Gas-seep related carbonate and barite authigenic mineralization in the Northern Gulf of California. Marine and Petroleum Geology 43, 147–165.

Chien, C.W., Huang, C.Y., Chen, Z., Lee, H.C., Harris, R., 2012. Miocene shallow-marine cold seep carbonate in fold-and-thrust Western Foothills, SW Taiwan. Journal of Asian Earth Sciences 56, 200–211.

Childress, J.J., Girguis, P.R., 2010. The metabolic demands of endosymbiotic chemoautotrophic metabolism on host physiological capacities. The Journal of Experimental Biology 214, 312–325.

Clari, P., Cavagna, S., Martire, L., Hunziker, J., 2004. A Miocene mud volcano and its plumbing system: A chaotic complex revisited (Monferrato, NW Italy). Journal of Sedimentary Research 74, 662–676.

Claypool, G.E., Kaplan, I.R., 1974. The origin and distribution of methane in marine sediments. In: Natural Gases in Marine Sediments. Springer US, 99–139.

Claypool, G.E., Kvenvolden, K.A., 1983. Methane and other hydrocarbon gases in marine sediment. Annual Reviews in Earth and Planetary Sciences 11, 299–327.

Coleman, M.L., 1985. Geochemistry of diagenetic non-silicate minerals: kinetic considetations. Philosophical Transactions of the Royal Society of London 315, 39–56.

Coleman, M.L., 1993. Microbial processes: Controls on the shape and composition of carbonate concretions. Marine Geology 113, 127–140.

Dando, P.R., Spiro, B., 1993. Varying nutritional dependence of the thyasirid bivalves *Thyasira sarsi* and *T. equalis* on chemoautotrophic symbiotic bacteria, demonstrated by isotope ratios of tissue carbon and shell carbonate. Marine Ecology Progress Series 92, 151–158.

De Boever, E., Birgel, D., Muchez, P., Peckmann, J., Dimitrov, L., Swennen, R., 2011. Fabric and formation of grapestone concretions within an unusual ancient methane seep system (Eocene, Bulgaria). Terra Nova 23, 56–61.

De Boever, E., Birgel, D., Thiel, V., Muchez, P., Peckmann, J., Dimitrov, L., Swennen, R., 2009. The formation of giant tubular concretions triggered by anaerobic oxidation of methane as revealed by archaeal molecular fossils (Lower Eocene, Varna, Bulgaia). Palaeogeography, Palaeoclimatology, Palaeoecology 280, 23–36.

De Boever, E., Swennen, R., Dimitrov, L., 2006. Lower Eocene carbonate chimneys (Varna, NE Bulgaria): Formation mechanisms and the (a)biological mediation of chimney growth? Sedimentary Geology 185, 159–173.

De Gibert, J.M., Ekdale, A.A., 2010a. Paleobiology of the crustacean trace fossil *Spongeliomorpha iberica* in the Miocene of southeastern Spain. Acta Palaeontologica Polonica 55, 733–740.

De Gibert, J.K., Ekdale, A.A., 2010b. Paleoethologic significance of bioglyphs: fingerprints of the subterranean. Palaios 25, 540–545.

de Vaugelas, J., Buscail, R., 1990. Organic matter distribution in burrows of the thalassinid crustacean *Callichirus laurae*, Gulf of Aqaba (Red Sea). Hydrobiologia 207, 269–277.

Della Porta, G., Webb, G.E., McDonald, I., 2015. REE patterns of microbial carbonate and cements from Sinemurian (Lower Jurassic) siliceous sponge mounds (Djebel Bou Dahar, High Atlas, Morocco). Chemical Geology 400, 65–86.

Díaz-del-Río, V., Somoza, L., Martínez-Frias, J., Mata, M.P., Delgado, A., Hernandez-Molina, F.J., Lunar, R., Martín-Rubí, J.A., Maestro, A., Fernández-Puga, M.C., León, R., Llave, E., Medialdea, T., Vázquez, J.T., 2003. Vast fields of hydrocarbon-

derived carbonate chimneys related to the accretionary wedge/olistostrome of the Gulf of Cádiz. Marine Geology 195, 177–200.

Dickson, J.A.D., 1966. Carbonate identification and genesis as revealed by staining. Journal of Sedimentary Petrology 36, 491–505.

Distel, D.L., Lane, D.J., Olsen, G.J., Giovannoni, S.J., Pace, B., Pace, N.R., Stahl, D.A., Felbeck, H., 1988. Sulfur-oxidizing bacterial endosymbionts: Analysis of phylogeny and specificity by 16S rRNA sequences. Journal of Bacteriology 170, 2506–2510.

Dragovich, J.D., Logan, R.L., Schasse, H.W., Walsh, T.J., Lingley Jr., W.S., Norman, D.K., Gerstel, W.J., Lapen, T.J., Schuster, E., Meyers, K.D., 2002. Geologic map of Washington – Northwest Quadrant. Washington Division of Geology and Earth Resources, Geologic Map GM-50.

Dufour, S.C., Felbeck, H., 2003. Sulphide mining by the superextensile foot of symbiotic thyasirid bivalves. Nature 426, 65–67.

Dworschak, P.C., 1983. The biology of *Upogebia pussila* (Petagna) (Decapoda, Thalassinidea). I.: the burrows. PSZN I: Marine Ecology 4, 19–43.

Feng, D., Chen, D., Peckmann, J., 2009. Rare earth elements in seep carbonates as tracers of variable redox conditions at ancient hydrocarbon seeps. Terra Nova 21, 49–56.

Fernandez-Dıáz, L., Putnis, A., Prieto, M., Putnis, C.V., 1996. The role of magnesium in the crystallization of calcite and aragonite in a porous medium. Journal of Sedimentary Research 66, 482–491.

Flügel, E., 2004. Microfacies of Carbonate Rocks. Springer Verlag Berlin-Heidelberg, 976 p.

Forster, S., Graf, G., 1992. Continuously measured changes in redox potential influenced by oxygen penetrating from burrows of *Callianassa subterranea*. Hydrobiologia 235, 527–532.

Frey, R.W., 1968. The lebensspuren of some common marine invertebrates near Beaufort, North Carolina. I. Pelecypod burrows. Journal of Paleontology 42, 570–574.

Füchtbauer, H., 1988. Sedimentpetrologie, Teil II. Sedimente und Sedimentgesteine. Schweizerbart'sche Verlagsbuchhandlung, 1141 p.

Gaillard, C., Rio, M., Rolin, Y., Roux, M., 1992. Fossil chemosynthetic communities related to vents or seeps in sedimentary basins: The pseudobioherms of southeastern France compared to other world examples. Palaios 7, 451–465.

Goedert, J.L., Peckmann, J., 2005. Fossil deep-water corals from Paleogene hydrocarbon-seep deposits, western Oregon and Washington, northwestern USA. In: Freiwald, A., Roberts, J.M. (Eds.), Cold-water Corals and Ecosystems. Springer-Verlag, Berlin, Heidelberg, 27–40.

Griffis, R.B., Suchanek, T.H., 1991. A model of burrow architecture and trophic modes in thalassinidean shrimp (Decapoda: Thalassinidea). Marine Ecology Progress Series 79, 171–183.

Haas, A., Peckmann, J., Elvert, M., Sahling, H., Bohrmann, G., 2010. Patterns of carbonate authigenesis at the Kouilou pockmarks on the Congo deep sea fan. Marine Geology 268, 129–136.

Hagemann, A., Leefmann, T., Peckmann, J., Hoffmann, V.-E., Thiel, V., 2012. Biomarkers from individual carbonate phases of an Oligocene cold-seep deposit, Washington State, USA. Lethaia 46, 7–18.

Hensen, C., Wallmann, K., 2005. Methane formation at Costa Rica continental margin – constraints for gas hydrate inventories and cross-décollement fluid flow. Earth and Planetary Science Letters 236, 41–60.

Himmler, T., Freiwald, A., Stollhofen, H., Peckmann, J., 2008. Late Carboniferous hydrocarbon-seep carbonates from the glaciomarine Dwyka Group, southern Namibia. Palaeogeography, Palaeoclimatology, Palaeoecology 257, 185–197.

Himmler, T., Bach, W., Bohrmann, G., Peckmann, J., 2010. Rare earth elements in authigenic methane-seep carbonates as tracers for fluid composition during early diagenesis. Chemical Geology 277, 126–136.

Hinrichs, K.-U., Hayes, J.M., Sylva, S.P., Brewert, P.G., DeLong, E.F., 1999. Methane-consuming archaebacteria in marine sediments. Nature 398, 802–805.

Hooper, E.C.D., 1991. Fluid migration along growth faults in compacting sediments. Journal of Petroleum Geology 14, 161–180.

Hovland, M., Heggland, R., De Vries, M.H., Tjelta, T.I., 2010. Unit-pockmarks and their potential significance for predicting fluid flow. Marine and Petroleum Geology 27, 1190–1199.

Imhoff, J.F., Sahling, H., Süling, J., Kath, T., 2003. 16S rDNA-based phylogeny of sulfur-oxidising bacterial endosymbionts in marine bivalves from cold-seep habitats. Marine Ecology Progress Series 249, 39–51.

Irwin, H., Curtis, C., Coleman, M., 1977. Isotopic evidence for source of diagenetic carbonates formed during burial of organic-rich sediments. Nature 269, 209–213.

Irwin, H., 1980. Early diagenetic carbonate precipitation and pore fluid migration in the Kimmeridge Clay of Dorset, England. Sedimentology 27, 577–591.

Jochum, K.P., Scholz, D., Stoll, B., Weis, U., Wilson S.T., Yang, Q., Schwalb, A., Börner, N., Jacob, D.E., Anrdeae, M.O., 2012. Accurate trace element analysis of speleotherms and biogenic calcium carbonates by LA-ICP-MS. Chemical Geology 318–319, 31–44.

Jørgensen, B.B., Kasten, S., 2006. Sulfur cycling and methane oxidation. In: Marine Geochemistry, Schulz, H., Zabel, M. (Eds.), Springer-Verlag Berlin Heidelberg, 271–309.

Joye, S.B., Boetius, A., Orcutt, B.N., Montoya, J.P., Schulz, H.N., Erickson, M.J., Lugo, S.K., 2004. The anaerobic oxidation of methane and sulfate reduction in sediments from Gulf of Mexico cold seeps. Chemical Geology 205, 219–238.

Judd, A.G., Hovland, M., 2007. Seabed Fluid Flow – The Impact of Geology, Biology and the Marine Environment. Cambridge University Press, 492 p.

Judd, A.G., Hovland, M., Dimitrov, L.I., Gil, S.G., Jukes, V., 2002. The geological methane budget at continental margins and its influence on climate change. Geofluids 2, 109–126.

Kiel, S., 2006. New records and species of mollusks from Tertiary cold-seep carbonates in Washington State, U.S.A. Journal of Paleontology 80, 121–137.

Kiel, S., 2010. An eldorado for paleontologists: The Cenozoic seeps of western Washington State, USA. In: Kiel, S. (Ed.), Vent and Seep Biota: Aspects from Microbes to Ecosystems, 433–448.

Kiel, S., 2013. Lucinid bivalves from ancient methane seeps. Journal of Molluscan Studies 79, 346–363.

Kiel, S., Amano, K. 2013. The earliest bathymodiolin mussels: An evaluation of Eocene and Oligocene taxa from deep-sea methane seep deposits in western Washington State, USA. Journal of Paleontology 87, 589–602.

Kiel, S., Amano, K., Jenkins, R.G., 2008. Bivalves from Cretaceous cold-seep deposits on Hokkaido, Japan. Acta Palaeontologica Polonica 53, 525–537.

Kiel, S., Birgel, D., Campbell, K.A., Crampton, J.S., Schiøler, P., Peckmann, J., 2013. Cretaceous methane-seep deposits from New Zealand and their fauna. Palaeogeography, Palaeoclimatology, Palaeoecology 390, 17–34.

Kiene, R.P., 1991. Production and consumption of methane in aquatic systems. In: Rogers, J.E., Whitman, W.B. (Eds.), Microbial Production and Consumption of Greenhouse Gases: Methane, Nitrogen Oxides, and Halomethanes. Washington, DC: American Society for Microbiology, 111–146.

Kopf, A.J., 2002. Significance of mud volcanism. Reviews of Geophysics 40, 1–52.

Krause, F.F., Clark, J., Sayegh, G., Perez, R.J., 2009. Tube worm fossils or relic methane expulsion conduits? Palaios 24, 41–50.

Kuechler, R.R., Birgel, D., Kiel, S., Freiwald, A., Goedert, J.L., Thiel, V., Peckmann, J., 2012. Miocene methane-derived carbonates from southwestern Washington, (USA) and a model for silicification at seeps. Lethaia 45, 259–273.

Kulm, L.D., Suess, E., 1990. Relationship between carbonate deposits and fluid venting: Orgeon accretionary prism. Journal of Geophysical Research 95, 8899–8915.

Lapham, L.L., Chanton, J.P., Martens, C.S., Sleeper, K., Woosley, R., 2008. Microbial activity in surficial sediments overlying acoustic wipeout zones at a Gulf of Mexico cold seep. Geochemistry, Geophysics, Geosystems 9, doi:10.1029/2008GC001944.

Lédesert, B., Buret, C., Chanier, F., Fèrriere, J., Recourt, P., 2003. Tubular structures of northern Wairarapa (New Zealand) as possible examples of ancient fluid expulsion in an accretionary prism: evidence from field and petrographical observations. Geological Society of London Special Publication 216, 95–107.

Levin, L.A., 2005. Ecology of cold seep sediments: Interactions of fauna with flow, chemistry and microbes. Oceanography and Marine Biology: An Annual Review 43, 1–46.

Lindholm, R.C., Finkelman, R.B., 1972. Calcite staining: Semiquantitative determination of ferrous iron. Journal of Sedimentary Petrology 42, 239–242.

Luff, R., Wallmann, K., Aloisi, G., 2004. Numerical modeling of carbonate crust formation at cold vent sites: significance for fluid and methane budgets and chemosynthetic biological communities. Earth and Planetary Science Letters 221, 337–353.

Mazzini, A., Ivanov, M.K., Nermoen, A., Bahr, A., Bohrmann, G., Svensen, H., Planke, S., 2008. Complex plumbing systems in the near subsurface: Geometries of authigenic carbonates from Dolgovsky Mound (Black Sea) constrained by analogue experiments. Marine and Petroleum Geology 25, 457–472.

Mazzullo, S.J., 2000. Organogenic dolomitization in peritidal to deep-sea sediments. Journal of Sedimentary Research 70, 10–23.

Meister, P., Gutjahr, M., Frank, M., Bernasconi, S.M., Vasconcelos, C., McKenzie, J.A., 2011. Dolomite formation within the methanogenic zone induced by tectonically driven fluids in the Peru accretionary prism. Geology 39, 563–566.

Milucka, J., Ferdelman, T.G., Polerecky, L., Franzke, D., Wegener, G., Schmid, M., Lieberwirth, I., Wagner, M., Widdel, F., Kuypers, M.M.M., 2012. Zero-valent sulphur is a key intermediate in marine methane oxidation. Nature 491, 541–546.

Morse, J.W., Wang, Q., Tsio, M.Y., 1997. Influences of temperature and Mg:Ca ratio on $CaCO_3$ precipitates from seawater. Geology 25, 85–87.

Nash, A.J., Pittman, E.D., 1975. Ferro-magnesian calcite cement in sandstones. Journal of Sedimentary Petrology 45, 258–265.

Nesbitt, E.A., Martin, R.A., Campbell, K.A., 2013. New records of Oligocene diffuse hydrocarbon seeps, northern Cascadia margin. Palaeogeography, Palaeoclimatology, Palaeoecology 390, 116–129.

Neto de Carvalho, C., Andrade Viegas, P., Cachao, M., 2007. *Thalassinoides* and its producer: populations of *Mecochirus* buried within their burrow systems, Boca do Chapim Formation (Lower Cretaceous), Portugal. Palaios 22, 104–107.

Nobuhara, T., 2003. Cold seep carbonate mounds with *Vesicomya* (*Calyptogena*) *kawamurai* (Bivalvia: Vesicomyidae) in slope-mud facies of the Pliocene forearc basin of the Sagara-Kakegawa area, central Japan. Paleontological Research 7, 313–328.

Nyman, S.L., Nelson, C.S., Campbell, K.A., 2010. Miocene tubular concretions in East Coast Basin, New Zealand: Analogue for the subsurface plumbing system of cold seeps. Marine Geology 272, 319–336.

Ohfuji, H., Rickard, D., 2005. Experimental syntheses of framboids – a review. Earth Science Reviews 71, 147–170.

Orcutt, B., Boetius, A., Elvert, M., Samarkin, V., Joye, S.B., 2005. Molecular biogeochemistry of sulfate reduction, methanogenesis and the anaerobic oxidation of methane at Gulf of Mexico cold seeps. Geochimica et Cosmochimica Acta 69, 4267–4281.

Orpin, A.R., 1997. Dolomite chimneys as possible evidence of coastal fluids expulsion, uppermost Otago continental slope, southern New Zealand. Marine Geology 138, 51–67.

Papaspyrou, S., Gregersen, T., Cox, R.P., Thessalou-Legaki, M., Kristensen, E., 2005. Sediment properties and bacterial community in burrows of the ghost shrimp *Pestarella tyrrhena* (Decapoda: Thalassinidea). Aquatic Microbial Ecology 38, 181–190.

Pape, T., Bahr, A., Klapp, S.A., Abegg, F., Bohrmann, G., 2011. High-intensity gas seepage causes rafting of shallow gas hydrates in the southeastern Black Sea. Earth and Planetary Science Letters 307, 35–46.

Pape, T., Bahr, A., Rethemeyer, J., Kessler, J.D., Sahling, H., Hinrichs, K.-U., Klapp, S.A., Reeburgh, W.S., Bohrmann, G., 2010. Molecular and isotopic partitioning of low-molecular-weight hydrocarbons during migration and gas hydrate precipitation in deposits of a high-flux seepage site. Chemical Geology 269, 350–363.

Paull, C.K., Chanton, J.P., Neumann, A.C., Coston, J.A., Martens, C.S., Showers, W., 1992. Indicators of methane-derived carbonates and chemosynthetic organic carbon deposits: examples from the Florida escarpment. Palaios 7, 361–375.

Peckmann, J., Thiel, V., 2004. Carbon cycling at ancient methane-seeps. Chemical Geology 205, 443–467.

Peckmann, J., Goedert, J.L., Heinrichs, T., Hoefs, J., Reitner, J., 2003. The Late Eocene 'Whiskey Creek' methane-seep deposit (western Washington State). Part II: Petrology, stable isotopes, and biogeochemistry. Facies 48, 241–254.

Peckmann, J., Goedert, J.L., Thiel, V., Michaelis, W., Reitner, J., 2002. A comprehensive approach to the study of methane-seep deposits from the Lincoln Creek Formation, western Washington State, USA. Sedimentology 49, 855–873.

Peckmann, J., Kiel, S., Sandy, M.R., Taylor, D.G., Goedert, J.L., 2011. Mass occurrences of the brachiopod *Halorella* in Late Triassic methane-seep deposits, eastern Oregon. Journal of Geology 119, 207–220.

Peckmann, J., Reimer, A., Luth, U., Luth, C., Hansen, B.T., Heinicke, C., Hoefs, J., Reitner, J., 2001. Methane-derived carbonates and authigenic pyrite from the northwestern Black Sea. Marine Geology 177, 129–150.

Peckmann, J., Senowbari-Daryan, B., Birgel, D., Goedert, J.L., 2007. The crustacean ichnofossil *Palaxius* associated with callianassid body fossils in an Eocene methane-seep limestones, Humptulips Formation, Olympic Peninsula, Washington. Lethaia 40, 273–280.

Prothero, D.R., Armentrout, J.M., 1985. Magnetostratigraphic correlation of the Lincoln Creek Formation, Washington: Implications for the age of the Eocene/Oligocene boundary. Geology 13, 208–211.

Raiswell, R., Berner, R.A., 1985. Pyrite formation in euxinic and semi-euxinic sediments. American Journal of Science 285, 710–724.

Rau, W.W., 1966. Stratigraphy and Foraminifera of the Satsop River Area, southern Olympic Peninsula, Washington. State of Washington Division of Mines and Geology Bulletin 53, 1–66.

Rau, W.W., 1967. Geology of the Wynoochee Valley quadrangle, Grays Harbor County, Washington. Washington Division of Mines and Geology Bulletin 56, 51 p.

Reeburgh, W.S., 2007. Oceanic methane biogeochemistry. Chemical Reviews 107, 486–513.

Reitner, J., Peckmann, J., Reimer, A., Schumann, G., Thiel, V., 2005. Methane-derived carbonate build-ups and associated microbial communities at cold seeps on the lower Crimean shelf (Black Sea). Facies 51, 66–79.

Ritger, S., Carson, B., Suess, E., 1987. Methane-derived authigenic carbonates formed by subduction-induced pore-water expulsion along the Oregon/Washington margin. Bulletin of the Geological Society of America 98, 147–156.

Roberts, H.H., Aharon, P., 1994. Hydrocarbon-derived carbonate buildups of the northern Gulf of Mexico continental slope: A review of submersible investigations. Geo-Marine Letters 14, 135–148.

Rudd, J.W.M., Taylor, C.D., 1980. Methane cycling in aquatic environments. Advances in Aquatic Microbiology 2, 77–150.

Rullkötter, J., 2006. Organic Matter: The driving force for early diagenesis. In: Marine Geochemistry, Schulz, H., Zabel, M., (Eds.), Springer-Verlag Berlin Heidelberg, 125–162.

Sassen, R., Joye, S., Sweet, S.T., DeFreitas, D.A., Milkov, A.V., MacDonald, I.R., 1999. Thermogenic gas hydrates and hydrocarbon gases in complex chemosynthetic communities, Gulf of Mexico continental slope. Organic Geochemistry 30, 485–497.

Sassen, R., Roberts, H.H., Carney, R., Milkov, A.V., DeFreitas, D.A., Lanoil, B., Zhang, C., 2004. Free hydrocarbon gas, gas hydrate, and authigenic minerals in chemosynthetic communities of the northern Gulf of Mexico continental slope: relation to microbial processes. Chemical Geology 205, 195–217.

Savard, M.M., Beauchamp, B., Veizer, J., 1996. Significance of aragonite cements around Cretaceous marine methane seeps. Journal of Sedimentary Research 66, 430–438.

Schieber, J., 2002. Sedimentary pyrite: A window into the microbial past. Geology 30, 531–534.

Schwartz, H., Sample, J., Weberling, K.D., Minisini, D., Moore, C.J., 2003. An ancient linked fluid migration system: cold-seep deposits and sandstone intrusions in the Panoche Hills, California, USA. Geo-Marine Letters 23, 340–350.

Seike, K., Jenkins, R.G., Watanabe, H., Nomaki, H., Sato, K., 2012. Novel use of burrow casting as a research tool in deep-sea ecology. Biology Letters 8, 648–651.

Sibuet, M., Olu, K., 1998. Biogeography, biodiversity and fluid dependence of deep-sea cold-seep communities at active and passive margins. Deep-Sea Research Part II: Topical Studies in Oceanography 45, 517–567.

Smrzka, D., Kraemer, S.M., Zwicker, J., Birgel, D., Fischer, D., Kasten, S., Goedert, J.L., Peckmann, J., 2015. Constraining silica diagenesis in methane-seep deposits. Palaeogeography, Palaeoclimatology, Palaeoecology 420, 13–26.

Solomon, E.A., Kastner, M., Jannasch, H., Robertson, G., Weinstein, Y., 2008. Dynamic fluid flow and chemical fluxes associated with a seafloor gas hydrate deposit on the northern Gulf of Mexico slope. Earth and Planetary Science Letters 270, 95–105.

Stakes, D.S., Orange, D., Paduan, J.B., Salamy, K.A., Maher, N., 1999. Cold-seeps and authigenic carbonate formation in Monterey Bay, California. Marine Geology 159, 93–109.

Stewart, R.J., Brandon, M.T., 2004. Detrital-zircon fission-track ages for the “Hoh Formation”: Implications for late Cenozoic evolution of the Cascadia subduction wedge. Geological Society of America Bulletin 116, 60–75.

Suess, E., Whiticar, M.J., 1989. Methane-derived CO_2 in pore fluids expelled from the Oregon subduction zone. Palaeogeography, Palaeoclimatology, Palaeoecology 71, 119–136.

Suess, E., Torres, M.E., Bohrmann, G., Collier, R.W., Greinert, J., Linke, P., Rehder, G., Trehu, A., Wallmann, K., Winckler, G., Zuleger, E., 1999. Gas hydrate destabilization: enhanced dewatering, benthic material turnover and large methane plumes at the Cascadia convergent margin. Earth and Planetary Science Letters 170, 1–15.

Tabor, R.W., Cady, W.M. 1978a. Geologic map of the Olympic Peninsula, Washington. U.S. Geological Survey Miscellaneous Investigations Series Map I-994.

Tabor, R.W., Cady, W.M. 1978b. The structure of the Olympic Mountains, Washington – Analysis of a subduction zone. U.S. Geological Survey Professional Paper 1033, 1–38.

Talukder, R.A., 2012. Review of submarine cold seep plumbing systems: leakage to seepage and venting. Terra Nova 24, 255–272.

Taviani, M., Angeletti, L., Ceregato, A., Foglini, F., Froglia, C., Trincardi, F., 2013. The Gela Basin pockmark field in the strait of Sicily (Mediterranean Sea): chemosymbiotic faunal and carbonate signatures of postglacial to modern cold seepage. Biogeosciences 10, 4653–4671.

Taylor, J.D., Glover, E.A., 2010. Chemosynthetic bivalves, in: In: Kiel, S. (Ed.), Vent and Seep Biota: Aspects from Microbes to Ecosystems, 107–135.

Teichert, B.M.A., Bohrmann, G., Suess, E., 2005. Chemoherms on Hydrate Ridge – Unique microbially-mediated carbonate build-ups growing into the water column. Palaeogeography, Palaeoclimatology, Palaeoecology 227, 67–85.

Torres, M.E., McManus, J., Hammond, D.E., de Angelis, M.A., Heeschen, K.U., Colbert, S.L., Tryon, M.D., Brown, K.M., Suess, E., 2002. Fluid and chemical fluxes in and out of sediments hosting methane hydrate deposits on Hydrate Ridge, OR, I: Hydrological provinces. Earth and Planetary Science Letters 201, 525–540.

Veizer, J., Ala, D., Azmy, K., Bruckschen, P., Buhl, D., Bruhn, F., Carden,G.A.F., Diener, A., Ebneth, S., Godderis, Y., Jasper, T., Korte, Pawellek, F., Podlaha, O.G., Strauss, H., 1999. $^{87}Sr/^{86}Sr$, $\delta^{13}C$ and $\delta^{18}O$ evolution of Phanerozoic seawater. Chemical Geology 161, 59–88.

Wallmann, K., Linke, P., Suess, E., Bohrmann, G., Sahling, H., Schlüter, M., Dählmann, A., Lammers, S., Greinert, J., von Mirbach, N., 1997. Quantifying fluid flow, solute mixing, and biogeochemical turnover at cold vents of the eastern Aleutian subduction zone. Geochimica et Cosmochimica Acta 61, 5209–5219.

Warthmann, R., Van Lith, Y., Vasconcelos, C., McKenize, J.A., Karpoff, A.M., 2000. Bacterially induced dolomite precipitation in anoxic culture experiments. Geology 28, 1091–1094.

Wells, R.E., 1989. Geologic map of the Cape Disappointment – Naselle River area, Pacific and Wahkiakum counties, Washington. USGS Miscellaneous Investigations Series I.

Wetzel, A., 2013. Formation of methane-related authigenic carbonates within the bioturbated zone – An example from the upwelling area off Vietnam. Palaeogeography, Palaeoclimatology, Palaeoecology 386, 23–33.

Whiticar, M.J., 1999. Carbon and hydrogen isotope systematics of bacterial formation and oxidation of methane. Chemical Geology 161, 291–314.

Whiticar, M.J., Faber, E., Schoell, M., 1986. Biogenic methane formation in marine and freshwater environments: CO_2 reduction vs. acetate fermentation – Isotope evidence. Geochimica et Cosmochimica Acta 50, 693–709.

Wiese, F., Kiel, S., Pack, A., Walliser, E.O., Agirrezabala, L.M., 2015. The beast burrowed, the fluid followed – Crustacean burrows as methane conduits. Marine and Petroleum Geology, this issue

Zhang, F., Xu, H., Konishi, H., Kemp, J.M., Roden, E.E., Shen, Z., 2012. Dissolved sulfide-catalyzed precipitation of disordered dolomite: Implications for the formation mechanism of sedimentary dolomite. Geochimica et Cosmochimica Acta 97, 148–165.

Zhang, F., Yan, C., Teng, H.H., Roden, E.E., Xu, H., 2013. In situ AFM observations of Ca-Mg carbonate crystallization catalyzed by dissolved sulfide: Implications for sedimentary dolomite formation. Geochimica et Cosmochimica Acta 105, 44–55.

Biogeosciences, 13, 4491–4512, 2016
www.biogeosciences.net/13/4491/2016/
doi:10.5194/bg-13-4491-2016
© Author(s) 2016. CC Attribution 3.0 License.



Biogeosciences Open Access EGU

Massive asphalt deposits, oil seepage, and gas venting support abundant chemosynthetic communities at the Campeche Knolls, southern Gulf of Mexico

Heiko Sahling[1,2], Christian Borowski[2,3], Elva Escobar-Briones[4], Adriana Gaytán-Caballero[4], Chieh-Wei Hsu[1], Markus Loher[2], Ian MacDonald[5], Yann Marcon[6], Thomas Pape[1,2], Miriam Römer[1,2], Maxim Rubin-Blum[3], Florence Schubotz[2], Daniel Smrzka[7], Gunter Wegener[2,3], and Gerhard Bohrmann[1,2]

[1]Department of Geosciences at the University of Bremen, Klagenfurter Str., 28359 Bremen, Germany
[2]MARUM Center for Marine Environmental Sciences, Leobener Str., 28359 Bremen, Germany
[3]Max-Planck Institute for Marine Microbiology, Celsiusstr. 1, 28359 Bremen, Germany
[4]Universidad Nacional Autónoma de México, Instituto de Ciencias del Mar y Limnología, A. P. 70-305 Ciudad Universitaria, 04510 Mexico City, México
[5]Florida State University, P.O. Box 3064326, Tallahassee, FL 32306, USA
[6]Alfred Wegener Institute Helmholz Centre for Polar and Marine Research, HGF-MPG Group for Deep Sea Ecology and Technology, Am Handelshafen 12, 27570 Bremerhaven, Germany
[7]Center for Earth Sciences, University of Vienna, Althanstr. 14, 1090 Vienna, Austria

Correspondence to: Heiko Sahling (hsahling@marum.de)

Received: 17 March 2016 – Published in Biogeosciences Discuss.: 24 March 2016
Revised: 29 June 2016 – Accepted: 19 July 2016 – Published: 11 August 2016

Abstract. Hydrocarbon seepage is a widespread process at the continental margins of the Gulf of Mexico. We used a multidisciplinary approach, including multibeam mapping and visual seafloor observations with different underwater vehicles to study the extent and character of complex hydrocarbon seepage in the Bay of Campeche, southern Gulf of Mexico. Our observations showed that seafloor asphalt deposits previously only known from the Chapopote Knoll also occur at numerous other knolls and ridges in water depths from 1230 to 3150 m. In particular the deeper sites (Chapopopte and Mictlan knolls) were characterized by asphalt deposits accompanied by extrusion of liquid oil in form of whips or sheets, and in some places (Tsanyao Yang, Mictlan, and Chapopote knolls) by gas emission and the presence of gas hydrates in addition. Molecular and stable carbon isotopic compositions of gaseous hydrocarbons suggest their primarily thermogenic origin. Relatively fresh asphalt structures were settled by chemosynthetic communities including bacterial mats and vestimentiferan tube worms, whereas older flows appeared largely inert and devoid of corals and anemones at the deep sites. The gas hydrates at Tsanyao Yang and Mictlan Knolls were covered by a 5-to-10 cm-thick reaction zone composed of authigenic carbonates, detritus, and microbial mats, and were densely colonized by 1–2 m-long tube worms, bivalves, snails, and shrimps. This study increased knowledge on the occurrences and dimensions of asphalt fields and associated gas hydrates at the Campeche Knolls. The extent of all discovered seepage structure areas indicates that emission of complex hydrocarbons is a widespread, thus important feature of the southern Gulf of Mexico.

1 Introduction

Asphalt volcanism in the Campeche Knolls, southern Gulf of Mexico (GoM) has been described as a distinct form of natural hydrocarbon seepage (MacDonald et al., 2004). Heavy oil is extruded and forms lava-like flows that cover $\sim$100 to $\sim$1000 m^2 of abyssal knolls and ridges (Brüning et al., 2010). The flows consist of high-density oil with an abundant asphaltene fraction (MacDonald et al., 2004) with a terpane composition similar to what has been reported from some crude oils in the Bay of Campeche (Scholz-Böttcher

et al., 2008; Schubotz et al., 2011b). As described by Brüning et al. (2010), the heavy oil is at a transition point between mobile and immobile when it flows; fluid-phase material can spread smoothly over the seafloor and, because its density is initially less than seawater, local bulges and "whips" occur due to buoyancy. After exposure to seawater, the heavy oil solidifies to brittle layers because of weathering processes and loss of volatile hydrocarbons. Fissures and cracks through the solidified asphalt deposits were observed to develop with time. Fragmentation of brittle asphalt proceeds until cobble-to-boulder-sized pieces become buried by sedimentation (Brüning et al., 2010).

Most of the research conducted so far concentrated on the type locality, Chapopote Knoll, which was named after the Aztec word for tar. Because it forms a knoll with a central crater-like depression with extensive hard substrata, the term "asphalt volcano" was introduced for Chapopote Knoll (MacDonald et al., 2004). Chapopote Knoll is suggested to overlie a reservoir–seal system for hydrocarbons. From seismic studies it was inferred that coarse-grained sediments sealed by a thin (100–200 m) veneer of fine-grained sediments within the core of the knoll act as a temporal hydrocarbon reservoir (Ding et al., 2008). Ding et al. (2008) speculated that the shallow reservoir plays a role in creating a heavy oil prior to its seafloor discharge: the oil in the region forms from Jurassic source material that has solidified within the hydrocarbon generation window over an extended time period (Magoon et al., 2001). Processes such as biodegradation, water washing, or gas injection in the shallow reservoir could further increase its specific gravity (Tissot and Welte, 1984). However, Schubotz et al. (2011b) did not find evidence for biodegradation in ductile (fresh) asphalts, so the sequence leading to the characteristic asphalt deposition remains speculative. In the Campeche Knolls, oil seepage is widespread as evidenced by sea surface oil slicks detected by synthetic aperture radar satellite images (Fig. 1; Williams et al., 2006). The sea surface slicks occur above dozens of knolls and ridges (Ding et al., 2010) and are thus a significant component of natural seepage in the south-western Gulf of Mexico (MacDonald et al., 2015). Seismic studies at the knolls and ridges indicate shallow subsurface hydrocarbon accumulation as well (Ding et al., 2010) but prior to the present study it was unclear whether these systems also produced asphalt deposits at the seafloor.

The natural hydrocarbon seeps at Chapopote Knoll comprise typical seep components that provide habitat for diverse biological communities. For example, in addition to asphalt deposits, there are reports of oil-soaked sediments (MacDonald et al., 2004; Schubotz et al., 2011a, b), gas hydrate occurrences (MacDonald et al., 2004, Schubotz et al., 2011b, Klapp et al., 2010a, b), gas venting (Brüning et al., 2010), and authigenic carbonates (Naehr et al., 2009). The asphalt deposits sustain hydrocarbon-degrading and sulfate-reducing bacteria within their interiors (Schubotz et al., 2011b), as well as surface bacterial mats and vestimentiferan tube worms that colonize fissures in the asphalt deposits (MacDonald et al., 2004; Brüning et al., 2010). Oil-impregnated sediments were found to harbour a complex microbial community which sustained both methanotrophy and methanogenesis (Schubotz et al., 2010a, b). The stable isotopes of methane in gas hydrates associated with asphalt suggested methanogenesis (Schubotz et al., 2011b). Two species of mytilid mussel (*Bathymodiolus brooksi* and *B. haeckerae*) occurred close to an oil and gas seep, harbouring different endosymbiotic communities (Raggi et al., 2013). A novel symbiont related to the hydrocarbon-degrading bacteria genus *Cycloclasticus* was verified in the seep-associated mussel *B. haeckerae* (Raggi et al., 2013).

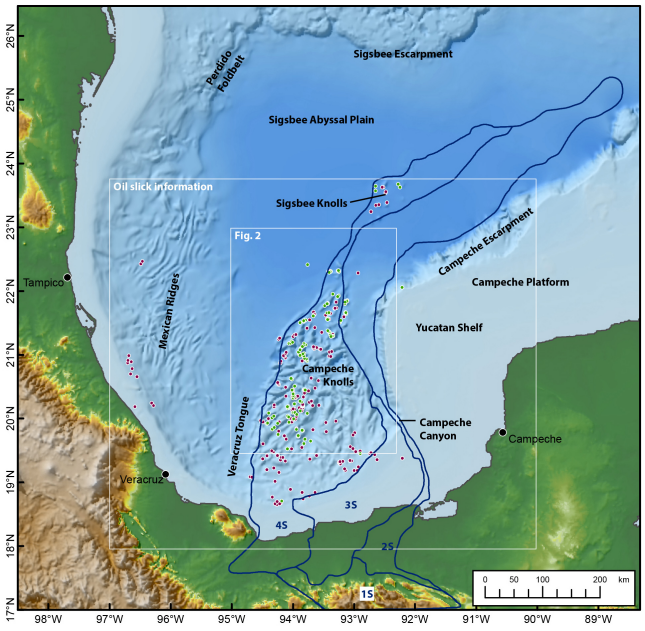


Figure 1. Geomorphological setting of the southern Gulf of Mexico based on shaded GEBCO (General Bathymetric Chart of the Oceans) bathymetry. The Campeche Knolls and Sigsbee Knolls are located within the subprovince 4S, which is part of the South Gulf Salt Province (outlined in blue) as suggested by Cruz-Mercado et al. (2011). Locations of definite (green dots) and probable (purple dots) oil slick origins at the sea surface according to Williams et al. (2006) and the extent of the respective study area (outer rectangle) are shown.

Subsequent to the initial discovery at Chapopote Knoll (MacDonald et al., 2004) asphalt deposits were found at other continental margin settings as well. In the Santa Barbara Basin off California, asphalt volcanoes about 15 and 20 m high formed 31 to 44 kyr ago (Valentine et al., 2010). These structures occur at water depths of around 150 to 180 m in a region additionally comprising tar mounds at ∼ 30 m depths (Vernon and Slater, 1963). In the northern Gulf of Mexico, asphalt mounds about 1 m in height and up to several metres in basal diameter exist in the Puma appraisal area (Weiland et al., 2008) and the Shenzi field

(Williamson et al., 2008) at water depths of about 1500 m. In addition, more than 2000 asphalt mounds with diameters ranging from less than a metre up to 50 m were observed on the Angolan margin at a water depth between 1350 and 2150 m (Jones et al., 2014). Based on their morphological appearance, their partial coverage by sediments, and the general lack of chemosynthetic organisms growing on the asphalt, the asphalt deposits in other regions seem to be older than those described in the southern GoM (Brüning et al., 2010). Moreover, in contrast to those in the southern GoM, asphalt deposits in the other regions are populated by regular, heterotrophic deep-sea organisms growing on hard substrate. Old asphalt deposits have therefore been suggested to foster the deep-sea habitat heterogeneity and provide additional settling grounds for species dispersal, which results in an increase in overall diversity (Jones et al., 2014). The Campeche Knoll asphalt region remains the deepest example known to date. The potential influence of pressure and temperature on emission of asphalt, liquid oil, and gas and their interaction with microbial and metazoan communities warrants further investigation.

We conducted an interdisciplinary research campaign at the Campeche Knolls in spring 2015 on board the R/V *Meteor*. Sites for investigation were developed following a nested approach. We used the information of oil slicks at the sea surface (Williams et al., 2006; MacDonald et al., 2015; Suresh, 2015) to systematically identify potential targets with active hydrocarbon systems. To further focus our activities, we looked for evidence of gas bubble emissions by scanning the water column with a ship-based hull-mounted multibeam echosounder. High-resolution bathymetry of the most promising sites was acquired by the SEAL 5000 autonomous underwater vehicle (AUV) mapping. Finally, we conducted seafloor observations and sampling by QUEST 4000 m remotely operated vehicle (ROV), concentrating on three sites at depths > 2900 m. Specifically, we were interested in disentangling the various seafloor manifestations resulting from the geochemically diverse seepage of heavy oil (leading to asphalt deposits), oil (leading to sea surface slicks), and gas (as bubbles and hydrate deposits). By concentrating on the description of the different environments that we encountered at the hydrocarbon seeps, we provide an overview for more detailed studies that will focus on the geochemistry of different oils, authigenic carbonate composition, microbiology, and fauna. We additionally show, based on our recent findings and results obtained during three precursor cruises (Bohrmann and Schenk, 2004; Bohrmann et al., 2008; MacDonald et al., 2007), that asphalt deposits are not limited to the type locality Chapopote Knoll, but are inherent to natural hydrocarbon seepage in the entire Campeche Knolls.

2 Geological setting of the Campeche Knolls

The Campeche Knolls (Fig. 1) are part of the large South Gulf Salt Province that stretches from the southern land margin across the shelf and the Campeche Knolls to the Sigsbee Knolls in the north. The Sigsbee Abyssal Plain separates the salt province in the southern GoM from the Mississippi–Texas–Louisiana salt province in the north. Salt tectonism in the southern deep GoM basin is believed to be an analogue to that of the Texas–Louisiana slope (Garrison and Martin, 1973). Because the basins share similar salt deposition histories, it is inferred that most of the salt was deposited during the rifting stage of the gulf in the Late Jurassic, equivalent to the Louann salt of the Texas–Louisiana slope (Salvador, 1991).

The Campeche Knolls comprise knolls and ridges that are limited to the west by smooth abyssal seafloor of the salt-free Veracruz tongue (Bryant et al., 1991). The Campeche Canyon, which is not a canyon in erosional sense, formed through the development of the eastern limit of the Campeche Knolls and the carbonate Campeche Platform. Northward, smooth seafloor separates the Campeche Knolls from the Sigsbee Knolls. The Campeche Knolls are covered by a 5–10 km sediment column that hosts prolific petroleum source rocks, with the most productive being of Late Jurassic and Cretaceous age (Magoon et al., 2001). Most of the sediment thickness results from deposition during Cenozoic times and was controlled by orogenic events in the Mexican region and sea-level changes.

The distribution of oil slicks at the sea surface (Williams et al., 2006; MacDonald et al., 2015; Suresh, 2015) aggregates along the north-western sector of the Campeche Knolls (Fig. 1). Interpretation of seismic lines and basin modelling carried out by the Mexican petroleum company PEMEX led to the conclusion that the subprovince designated as 4S (Fig. 1) contains the largest allochthonous and autochthonous salt deposits (Cruz-Mercado et al., 2011; Sánchez-Rivera et al., 2011). The actual density of salt bodies increases from the south-east to the north-western region of the Campeche Knolls. It is proposed that gravitational forces toward the north-west cause contraction and compression in the north-western distal part of the system in which structural folds, high-angle reverse faults, and numerous allochthonous salt bodies developed since the late Miocene (Cruz-Mercado et al., 2011; Sánchez-Rivera et al., 2011).

3 Material and methods

Natural oil slicks at the sea surface were detected by synthetic aperture radar in the region of the southern GoM by Williams et al. (2006). Based on their analyses of repeated observations, they postulated seep locations on the seafloor that could be the origins of the oil slicks. With regard to interpretation limits of the remotely sensed data they distin-

guished between definite, probable, and possible seep locations. Figures 1 and 2 show the inferred seep locations they classified as definite or probable. We excluded the numerous possible seep locations for clarity and because many of the possible seeps were located outside of Campeche Knolls, suggesting that the corresponding oil slicks might not be caused by natural oil seepage. Those sea surface patterns might have been caused by other processes, i.e. algae blooms, local wind fields, or anthropogenic activity.

Ship-based hydroacoustic surveys and dives with an autonomous underwater vehicle (AUV) and a remotely operated vehicle (ROV) were conducted during cruise R/V *Meteor* (M 114) from 12 February to 28 March 2015.

The multibeam echosounder (MBES) Kongsberg EM122 operating at 12 kHz was used for bathymetric mapping. Together with bathymetry data collected during two earlier cruises with R/V *Sonne* in 2003 (SO 174; Bohrmann and Schenk, 2004) and R/V *Meteor* (M67/2; Bohrmann et al., 2008), good bathymetric coverage was acquired in the entire north-western sector of the Campeche Knolls (Fig. 2).

We additionally examined the water column data of the MBES systematically for evidence of gas emissions along the entire cruise track of M 114 (Fig. 2, inset). Water column imaging for the detection of gas bubble plumes was conducted with the Fledermaus Midwater software programme (company: Quality Positioning Services B. V., the Netherlands). Gas bubble plumes cause high backscatter in the water column. In this paper we assume that all acoustic anomalies were related to gas venting and will refer to them as "flares". Flares were traced through the water column by analysing swath by swath, which results in a three-dimensional representation of the bubble streams. We detected numerous gas bubble flares, some of which could be traced completely from the water column down to the seabed. Most flares, however, were only observed in the midwater column and the point of origin at the seabed could not be traced. In those instances, we projected the flares down to the seafloor and give this point as a coordinate. We assume that this lack of backscatter from gas bubbles in great water depths results from the pressure dependence of the backscatter strength (Greinert et al., 2006). Further in-depth studies are required to confirm this. For the objectives of this study, we linearly projected flares from midwater depths to the seabed and assumed that bubbles were escaping the seafloor around these sites. We defined survey areas at the seafloor, which included the putative gas emission sites, and conducted AUV-based micro-bathymetric mapping and ROV-mounted horizontally scanning sonar to locate gas emission sites.

High-resolution bathymetry data were acquired with the MBES Kongsberg 2040 during dives with the AUV SEAL 5000 at an altitude of 80 m. Ship-based and AUV-based bathymetry data were processed with MB-Systems (Caress and Cheyes, 2014).

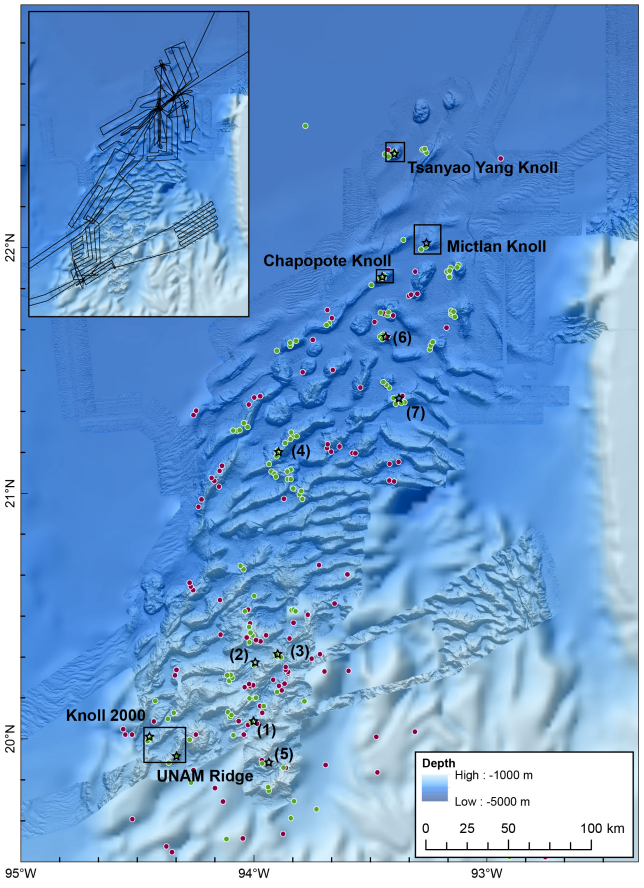


Figure 2. Swath bathymetry draped over GEBCO bathymetry of the Campeche Knolls and cruise track of M 114 (inset). Indicated are oil slick origins as inferred from oil slicks at the sea surface according to Williams et al. (2006), classified as definite (green dots) and probable (purple dots). Seafloor locations of hydrocarbon seepage sites investigated in this study are also shown (open stars, number in brackets). Specifics of those sites are given in Table 1.

The Kongsberg 675 kHz Type 1071 forward-looking sonar on ROV QUEST 4000 m was used for the localization of bubble plumes following the method described in Nikolovska et al. (2008). Seafloor images shown in this study were taken either with the digital Inside Pacific Scorpio 3.3 megapixel still camera or frame-grabbed (Adobe Premiere Pro) from video footage gained with the Insite Pacific Zeus 3CCD HDTV video camera.

In order to geochemically characterize the different hydrocarbon components, gas bubbles (clear and oil coated) and oil drops released from the seafloor were captured with the pressure-tight gas bubble sampler (GBS) at four different knolls and ridges (Supplement Table 1). Two bubble streams were sampled at Tsanyao Yang Knoll whereas at all other investigated sites only one bubble stream was sampled. Gas bubble samples were not recovered from Knoll 2000. Repeated sampling was conducted at Mictlan Knoll during different dives and at different heights above the seafloor. Oil

drops were captured together with chimney-like structures at Marker M114-5 at a site similar in appearance to that shown in Fig. 6d. The samples were analysed for molecular compositions and δ^{13}C-CH_4 signatures according to Pape et al. (2010) and Römer et al. (2012). Biological samples were taken by push corer, scoop net, manipulator, or baited trap with the help of the ROV. Based on the video footage and studies of the animals on board, we identified the fauna to various taxonomic levels but detailed onshore studies are needed to fully explore their taxonomy.

Underwater navigation of AUV and ROV were achieved by use of the IXSEA Posidonia ultrashort baseline system. Spatial data were integrated into the Arc-GIS programme (ESRI) and maps were produced by combined usage of the Arc-GIS and Adobe Illustrator programmes.

Camera sled surveys were conducted during cruises SO 174 (Bohrmann and Schenk, 2004), M 67/2 (Bohrmann et al., 2008), and Chapopote III with R/V *Justo Sierra* in 2007 (MacDonald et al., 2007). Three different camera systems were used for taking video images (M 67/2 and Chapopote III) and photographs (SO 174) at the seafloor. The locations of camera sled observations given in Table 1 are approximated based on ship position.

4 Results

4.1 Site descriptions

4.1.1 Tsanyao Yang Knoll (about 3400 m water depth)

Tsanyao Yang Knoll is a dome approximately 400 m high and 6 km wide (Fig. 3a), which we named after Prof. Tsanyao Yang from the Department of Geosciences, National University of Taiwan. "Frank" Yang dedicated his life to studying mud volcanoes and hydrocarbon seeps on- and offshore Taiwan; he sadly passed away while we were conducting this present study at sea.

Gas emissions were recorded as flares with the echosounder from the seafloor at water depths as great as 3500 m at the plateau-like summit (Fig. 3a). Figure 3b shows the ROV dive track within a depression about 150 to 200 m wide and 30 m deep. Here, we discovered spectacular gas-hydrate exposures at three sites (Site 1, 2, and 3) at depths of about 3420 m. In contrast to the knolls and ridges further south, we did not observe widespread asphalt deposits during the dives at Tsanyao Yang Knoll.

The gas hydrates were found in mounds that were 1–2 m high and 3–10 m wide at their bases and densely colonized by vestimentiferan tube worms, probably of the genus *Escarpia* (Fig. 4a). The mounds had regular borders of gravel-to-boulder-sized rock clasts and shells that separated seep-influenced sediments from normal deep-sea sediments. In some locations, clusters of living vesicomyid clams (*Abyssogena southwardae*) were observed in the transition zone. In several instances, the mounds were fractured, exposing 1–2 m hanging walls of gas hydrate with vigorous gas bubble streams observed emitting from the base (Fig. 4b). Exposed hydrate preserved a fabric of frozen bubbles, which indicated rapid formation (Suess et al., 2001). Some bubble-fabric gas hydrate formed from rising bubbles when they attached to the vertical wall due to adhesion or were captured by overhanging structures. Many bubble streams were composed of transparent bubbles forming white gas hydrates but some streams contained oil-coated bubbles forming blackish-coloured hydrates. We additionally observed dense hydrate cropping out over most of the visible exposed fracture, as exemplified in Fig. 4b. Most of the hydrate was white, but blackish-stained hydrate was also observed.

The outermost 5 to 10 cm-thick layer of the mounds were composed of authigenic carbonates entangled with the posterior parts of the vestimentiferan tubes and other detritus. For convenience, we term these tube worm parts the "rhizosphere" hereafter. Fleshy, thick microbial mats were attached to the carbonates in the lower portion of the rhizosphere. We hypothesize that the carbonates were formed under anoxic conditions in the interior of the rhizosphere, similar to those authigenic carbonates growing in the sediments within the sulfate–methane transition zone at other seeps (Formolo et al., 2004). A flourishing ecosystem of seep-typical fauna (e.g. living mytilid mussels, gastropods, *Alvinocaris* sp. shrimp) occupied the top of the carbonates at the base of the vestimentiferan tubes (Fig. 4c). The vestimentiferan tubes were densely overgrown by colonies of epifaunal suspension feeders (e.g. hydrozoans and anemones).

At site 3, we observed a mound composed of reworked sediment components and gravel-to-pebble-sized rocks (Fig. 4d). An exposed lens-shaped chunk of hydrate (1.5 m wide and 0.5 m high) was present at the top of the mound (Fig. 4f). The upper part of the hydrate showed a dense fabric while the lower part was porous, suggesting that it formed from frozen gas bubbles (Fig. 4f). The two hydrate fabrics were separated by a layer that looked like organic material. Ice worms (cf. *Hesiocaeca methanicola*) were observed living in the bubble-fabric hydrate.

4.1.2 Mictlan Knoll (about 3100 m water depth)

Mictlan Knoll features the characteristics of an asphalt volcano (sensu MacDonald et al., 2004) with a crater-like summit area on top of an approximately 250 m-high circular knoll, which is about 10 km wide at its base (Fig. 5a). This knoll contained diverse and widespread structures related to heavy oil seepage. We named it Mictlan, which means underworld in the Aztec language.

The MBES surveys revealed evidence for gas emission along the crater rim. We conducted five ROV dives on different areas of the crestal region (Fig. 5b) and illustrate our findings with images from four sites: Hydrate Hill, Marker M114-5, Marker M114-1, and "fresh asphalts".

Table 1. Summary of evidence for hydrocarbon seepage in the southern Gulf of Mexico based on AUV SEAL 5000, ROV QUEST 4000 m, and camera sled observations obtained during cruises R/V *Sonne* cruise 174, R/V *Meteor* cruise 67/2, R/V *Justo Sierra* cruise Campeche III, and R/V *Meteor* cruise 114/2. The positions marked with an asterisk are based on ship positions.

Seafloor Structure	Location	Depth	Tools	Observation
Tsanyao Yang Knoll	22°23.55′ N; 93°24.33′ W	3420 m	M 114/2 ROV Dive 358 (15 Mar 2015), Dive 361 (19 Mar 2015), AUV Dive 69 (24 Feb 2015)	Vestimentifera on hydrate outcrops, gas bubble, and oil emission, carbonates, mytilid and vesicomyid bivalves
Mictlan Knoll	22°1.4′ N; 93°14.9′ W	3180 m	M 114/2 ROV Dive 355 (11 Mar 2015), Dive 357 (14 Mar 2015), Dive 360 (18 Mar 2015), Dive 363 (21 Mar 2015), Dive 364 (22 Mar 2015), AUV Dive 68 (23 Feb 2015)	Asphalt deposits, gas bubble, and oil emission, vestimentifera, white bacterial mats, mytilid, and vesicomyid bivalves
Chapopote Knoll	21°53.95′ N; 93°26.25′ W	2920 m	SO 174 OFOS 13 (1 Nov 2003), OFOS 14 (2 Nov 2013); M 67/2 ROV Dive 80 (10 Apr 2006), Dive 81 (11 Apr 2006), Dive 82 (12 Apr 2016), Dive 83 (14 Apr 2006), Dive 84 (15 Apr 2006); M 114/2 ROV Dive 354 (10 Mar 2015), Dive 356 (13 Mar 2015), Dive 359 (16 Mar 2015), Dive 363 (21 Mar 2015), AUV Dive 70 (25 Feb 2015)	Asphalt deposits, gas bubble, and oil emission, vestimentifera, white bacterial mats, mytilid, and vesicomyid bivalves
UNAM ridge	19°55.90′ N; 94°20.89′ W	1230 m	M 114/2 ROV Dive 351 (4 Mar 2015), Dive 352 (5 Mar 2015)	Asphalt deposits, carbonates, vestimentifera, mytilidae, gas bubble emission
Knoll 2000	20°01.12′ N; 94°26.20′ W	1860 m	M114/2 ROV Dive 353 (8 Mar 2015)	Carbonates and possibly asphalts, white bacterial mats on blackish seafloor, pogonophoran tube worms
1	20°4.95′ N; 93°57.85′ W*	1300 m	R/V *Justo Sierra* camera survey, Site L89 (18 Sep 2007)	Asphalt, vestimentifera, soft coral
2	20°19.55′ N; 93°59.15′ W*	1780 m	R/V *Justo Sierra* camera survey, Site L87 (20 Sep 2007)	Asphalt or carbonate pieces, sparse bacterial mats
3	20°22.02′ N; 93°54.28′ W*	1700 m	R/V *Justo Sierra* camera survey, Site L86 (21 Sep 2007)	Asphalt, tube worm, mussels
4	21°11.45′ N; 93°53.40′ W*	2335 m	R/V *Justo Sierra* camera survey, Site L97 (22 Sep 2007)	Asphalt or carbonate
5	19°54.917′ N; 93°56.366′ W*	1100 m	R/V *Justo Sierra* camera survey, Site L94 (19 Sep 2007)	Asphalt or carbonate, bacterial mats
6	21°39.5′ N; 93°26.1′ W*	2980 m	M 67/2 TV-Sled survey (9 Apr 2006)	Asphalt deposits some 10 m in diameter
7	Ca. 21°25′ N; 93°22′ W* and 21°23.8′ N; 93°23.3′ W*	2400–2440 m	SO 174/2 OFOS 10 (29 Oct 2003), OFOS 12 (31 Oct 2003)	Sediment covered, outcropping asphalts, scattered living vesicomyid clams, vestimentifera, bacterial mats

Hydrate Hill is a 30 m-high elevation with a densely populated vestimentiferan tube worm field (cf. *Escarpia* spp.) on its top which was 20 to 30 m wide (Fig. 6a–c). At the summit, gas escaped the seafloor and gas hydrates occurred below an overhanging protrusion consisting of carbonates and vestimentifera. Exposed rocks at the base of the hill appeared to be fragmented asphalts (Fig. 6c) but no samples were recovered. We therefore suggest that the entire hill is an ac-

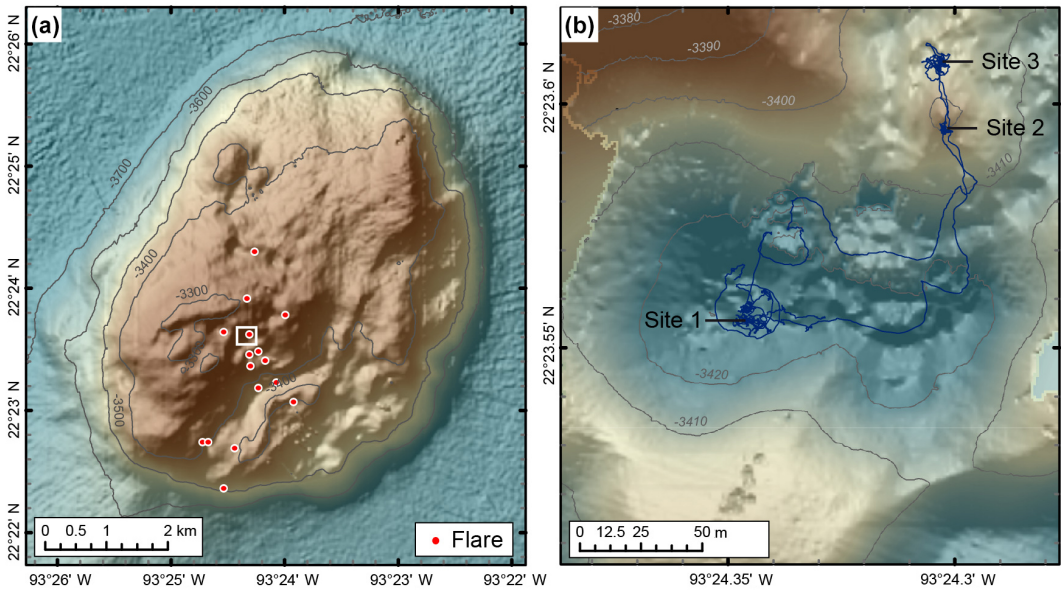


Figure 3. (a) Ship-based swath bathymetry of Tsanyao Yang Knoll (see Fig. 2 for location), flare locations (red dots), and the area shown in **(b)** (box). **(b)** ROV QUEST Dive 361 track and the main study sites plotted on AUV swath bathymetry.

cumulation of asphalt talus that is covered at its summit by authigenic carbonates and vestimentifera.

At Marker M114-5, we observed 1–2 m-sized asphalt humps with small colonies of vestimentiferan tube worms that were less than 1 m long. Remarkably, at this site viscous oil was slowly seeping (about one drop every few minutes) through slender, white-coated chimneys some 10–30 cm in height (Fig. 6d). In the area around Marker M114-5 about 10 sites with chimney clusters were observed.

At Marker M114-1, oil seepage occurred through a flat-topped mound about 1 m-high and tens of metres wide, which was composed of fragmented asphalt and soft sediments. The mound surface was covered by a highly patchy community of 50 cm-long vestimentiferan tube worms, mytilid bivalves (*Bathymodolus brooksi*), bacterial mats, and various epizoic groups of suspension feeders such as sponges, hydrozoa, and anemones (Fig. 6e, f). Oil drops escaped the sediments at a low rate (one drop of oil every 1–5 min). Rising drops at first remained attached to the seafloor by elongating threads and only eventually broke loose, leaving behind strands of oil that floated or adhered to the nearby organisms. Oil was also released from the sediments during sampling of sediments and organisms collected with the ROV and the sample material was heavily soaked with oil when recovered aboard ship.

In the area denoted "fresh asphalts" (Fig. 5b), we observed a variety of structures that provide insight into the flow behaviour of heavy oil deposition at the seafloor. Although the extrusion process of heavy oil was not directly observed by us at the seafloor, the resulting flow structures are illustrative. Based on our observations, two main types of heavy-oil emission and post-emission behaviour may be distinguished. The first type includes extrusion of heavy oil forming strands or sheets that float into the water due to positive buoyancy while they remain attached to the seabed owing to cohesion (Fig. 7a–c). Over time, the strands and sheets apparently lose buoyancy and pile up on the seafloor forming decimetre-to-metre-high accumulations. The second type comprises extrusion of oil that is heavier than seawater and spreads on the seabed following gravity (Fig. 7d–f). These flows solidify over time and, subsequently, accumulate sediments on their surface as illustrated in Fig. 7e and f. Dimensions of flows observed in this study ranged between decimetre and tens of metres in diameter.

4.1.3 Chapopote Knoll (about 2900 m water depth)

Flare mapping with the ship-based MBES system revealed that plumes interpreted to be due to gas emission at this site were widespread along the crater rim (Fig. 8a). Flares were rather dispersed; consequently, we mapped areas with gas emissions rather than individual emission sites. Subsequent ROV dives focused on the 50 m-wide flow of the main asphalt field and a location that had been named the "bubble site" during previous visits (Fig. 8b; Brüning et al., 2010).

The first analysis of the results obtained during our return visit in 2015 revealed that the appearance of the main asphalt field was little altered from what was observed during the first exploration in 2006 (Brüning et al. 2010). The extent of the flow and distributions of bacterial mats and vestimentiferan tube worm remained largely unchanged. While expanding the mapped area in the course of this study, it became apparent that the main asphalt flows terminated on soft sediments in the north and west (Fig. 9a), but overlaid older

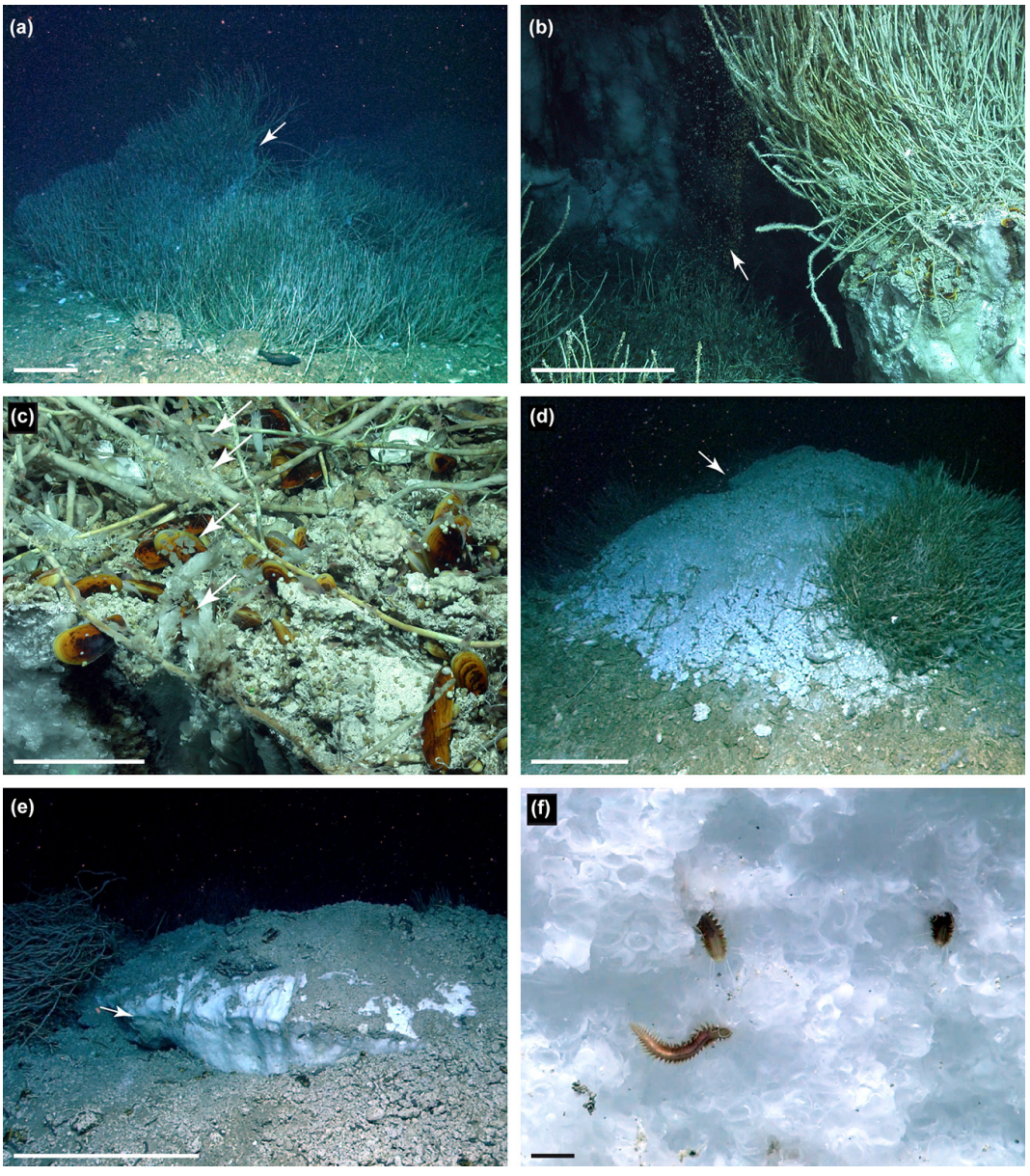


Figure 4. Seafloor images taken at Tsanyao Yang Knoll during ROV QUEST Dive 361. **(a)** Vestimentiferan tube worm bushes on a fractured mound (arrow). Scale bar 50 cm in foreground. **(b)** Gas bubble plume (arrow) rose through the gap of a fractured mound. Hydrates formed at the hanging walls. Scale bar 50 cm. **(c)** Close-up of the mound surface with bubbles emitted into the water column (arrows) from the same spot. Gas hydrate occurred below a layer of authigenic carbonates with mytilids, vestimentifera, gastropods, and shrimps on top. Scale bar 10 cm. **(d)** Mound with exposed gas hydrate (arrow) detailed in **(e)**, **(f)**. Scale bar 50 cm. **(e)** Lens-shaped, exposed gas hydrate composed of bubble-fabric hydrate below and dense hydrate above the arrow. Scale bar 50 cm. **(f)** Bubble-fabric hydrate inhabited by ice worms (cf. *Hesiocaeca methanicola*). Scale bar 1 cm. All images courtesy of MARUM.

flows characterized by fragmented asphalts (Fig. 9b) toward the south and east. Noting significant sediment cover on older asphalts, we conjecture that the main asphalt flow represents the most recent stage of several flow events.

The bubble site is located on a ridge several metres high, formed of fragmented asphalts with soft sediments interspersed between the flow breccia. Gas bubbles escaped the seafloor and gas hydrates were present below a seafloor protrusion (Fig. 9c, d). Recovered sediments and rocks were heavily impregnated with oil. The fauna comprised mytilid bivalves including *Bathymodiolus heckerae*, *B. brooksii*, vestimentiferan tube worms, and a variety of organisms attracted by the seep system, such as *Munidopsis geyeri* and *Alvinocaris muricola* crustaceans (Gaytán-Caballero, 2009),

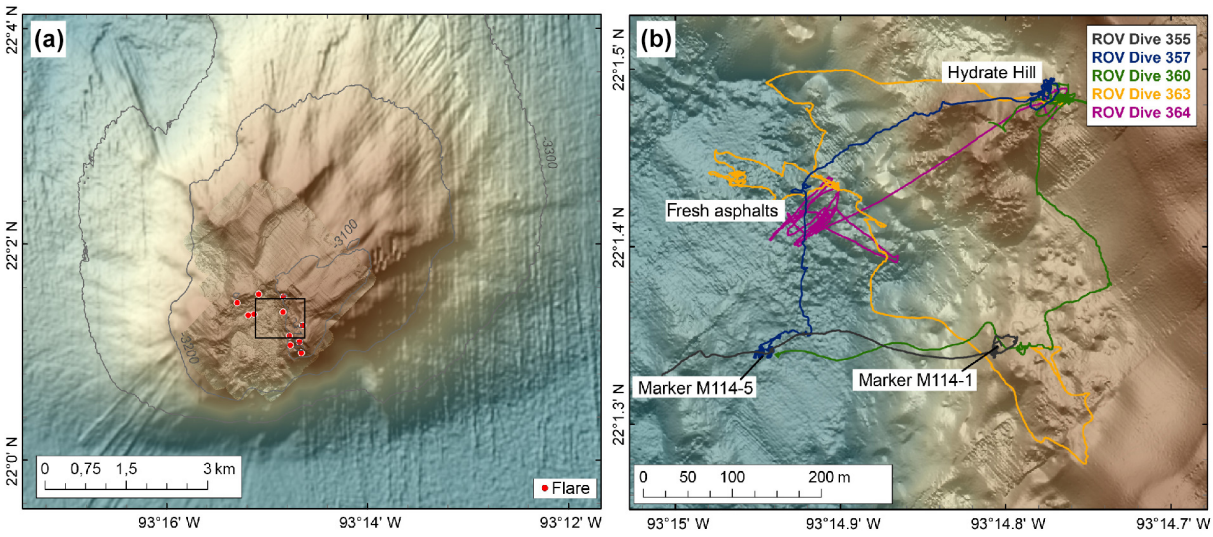


Figure 5. Maps of Mictlan Knoll (see Fig. 2 for location): **(a)** AUV-based bathymetry draped over ship-based bathymetry and positions of flares (red dots). The box defines the area illustrated in **(b)**. **(b)** ROV QUEST dive tracks and main study sites plotted on AUV-based bathymetry.

gastropods, and sponges (Fig. 9d, e). A few metres away from the bubble site, oil drops or oil-coated bubbles were released from the seafloor (Fig. 9f) and dark orange, oil coated hydrate masses were exposed.

4.1.4 Knoll 2000 (about 1850 m water depth)

Knoll 2000 is an elongated feature next to a ridge with two faint flares that originated on the eastern flank of the knoll (Fig. 10). During an ROV dive, authigenic carbonates and dark-stained sediments with whitish patches, interpreted to be bacterial mats, were observed (Fig. 11e, f). Some of the authigenic carbonates were dark-stained and may have contained asphalt. The recovery of frenulate tube worms (Siboglinidae; Frenulata) in whitish-stained sediments (Fig. 11e) was noteworthy because species of this group were not observed at the other sites investigated in this study. However, because of their thin tubes, the tube worms were invisible for the camera systems during the dive. Gas bubble emissions were not observed during the one ROV dive to Knoll 2000.

4.1.5 UNAM ridge (about 1230 m water depth)

UNAM ridge is an approximately 500 m-high ridge named after the Universidad Nacional Autónoma de México in appreciation of the collaborative effort to study the deep-water hydrocarbon seeps off Mexico. This was the shallowest site visited during this study. At least five flares were detected above the crest (Fig. 10). Two ROV dives revealed evidence for an active, albeit senescent seep system. Remarkably, soft corals and other hard-ground suspension feeders were found to settle on iron/manganese-stained carbonates and weathered asphalts (Fig. 11a). The occurrence of vestimentiferans tube worms was limited to a few bushes. Recumbent tube worms were dominant (Fig. 11b), which is generally considered as an indicator for a senescent community. Iron/manganese-stained carbonates were observed along with debris of mytilid shells (Fig. 11c). The most active seep site was situated on the side of a pockmark-like depression and comprised a relatively small bubble stream with only few specimens of living mytilid mussels on carbonates (Fig. 11d). On a small 20 cm-high and 1 m-wide sediment mound we observed a white, hydrate-like texture through a drape of sediment, suggesting the presence of gas hydrates but as we did not attempt any sampling, we cannot prove the occurrence of hydrates.

4.2 Seafloor observations by camera sled

In addition to the findings during M 114, camera sled deployments during the preceding cruises SO 174, M 67/2, and Chapopote III revealed evidence for the presence of asphalts and chemosynthetic communities at seven further knolls and ridges as summarized in Table 1 and Fig. 2. We realized that the identification of asphalts on the basis of images alone is ambiguous because the appearance of iron/manganese-stained carbonates is similar to that of weathered asphalts as shown in Figs. 11a, c and 9b respectively. Nevertheless, the camera sled observations suggests that natural hydrocarbon seepage is widespread in the area of the Campeche Knolls.

4.3 Gas composition and isotopes

Hydrocarbons analysed from all gas bubble samples collected with the gas bubble sampler from Tsanyao Yang

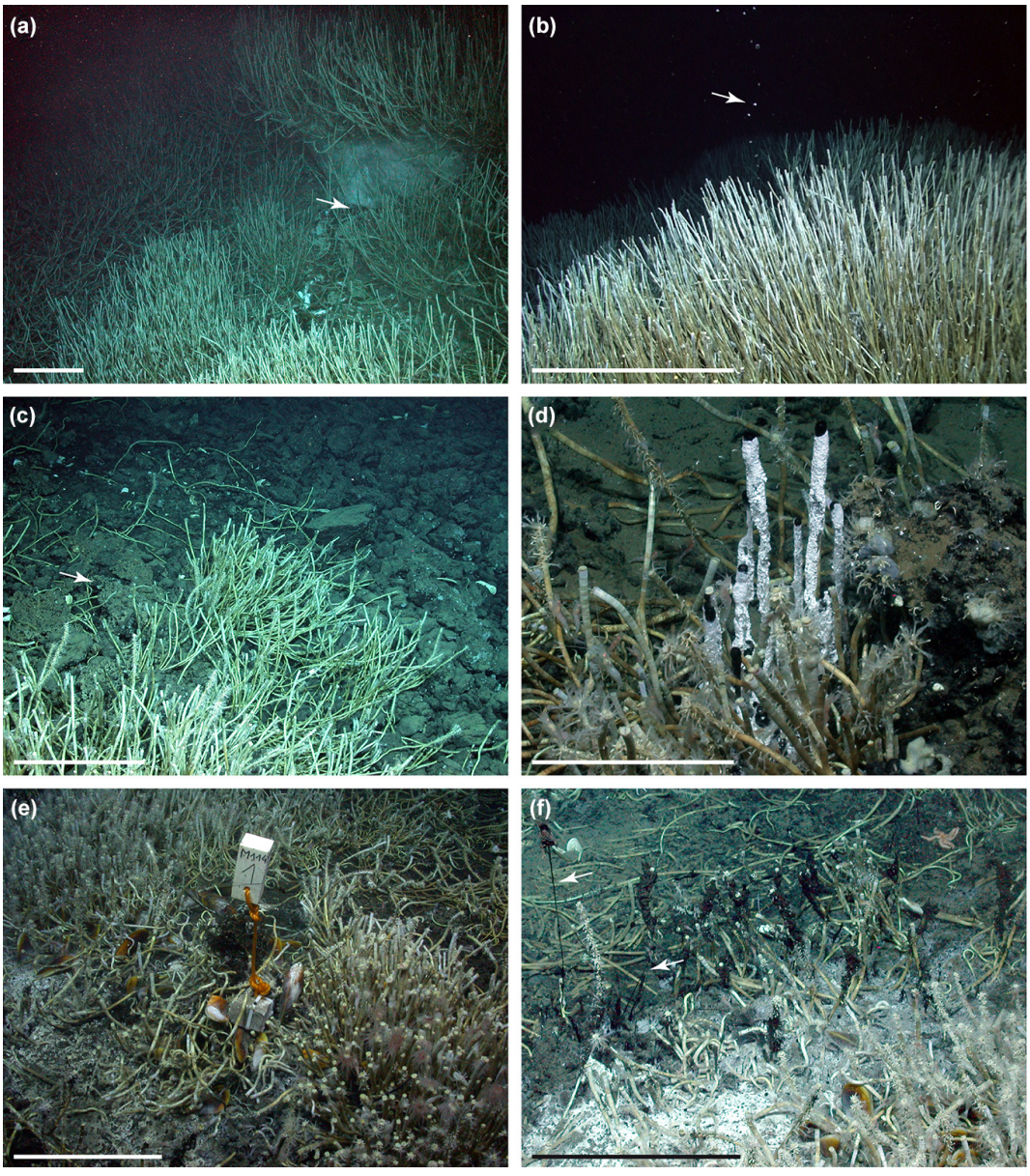


Figure 6. Seafloor images taken at Mictlan Knoll during ROV QUEST Dives 357 **(a–d)** and 360 **(e, f)**. **(a)** Hydrate below overhanging vestimentiferan tube worms (arrow). Scale bar 50 cm. **(b)** Gas bubble stream (arrow) rose through the hydrates and vestimentifera shown in **(a)**. Scale bar 50 cm. **(c)** Fragmented asphalt, authigenic carbonates (arrow), and vestimentifera. Scale bar 50 cm. **(d)** Oil drops released through white-coated chimneys. Scale bar 20 cm. **(e)** Flourishing ecosystem (mytilids, vestimentifera with epizoic suspension feeders, bacterial mats) next to oil-soaked sediments shown in **(f)**. **(f)** Viscous oil drops emanated from the sediments leaving strands behind (arrow). Scale bar 20 cm. All images courtesy of MARUM.

Knoll, Mictlan Knoll, Chapopote Knoll, and UNAM ridge were dominated by methane with a C_1/C_2 ratio varying between 14 and 185 (Fig. 12). The methane stable carbon isotope composition (δ^{13}C-CH_4) ranged between −45.1 and −49.8 ‰ V-PDB. The oil drop sample revealed a relative CH_4-depletion ($C_1 / C_2 = 2$) compared to the gas samples and the δ^{13}C-CH_4 value (−56.4 ‰ V-PDB) was more negative.

5 Discussion

5.1 Natural hydrocarbon seepage in the Campeche Knolls

The region of the Campeche Knolls shows evidence of abundant natural hydrocarbon seepage. This was already evident by the widespread presence of oil slicks at the sea surface (Williams et al., 2006; MacDonald et al., 2015; Suresh,

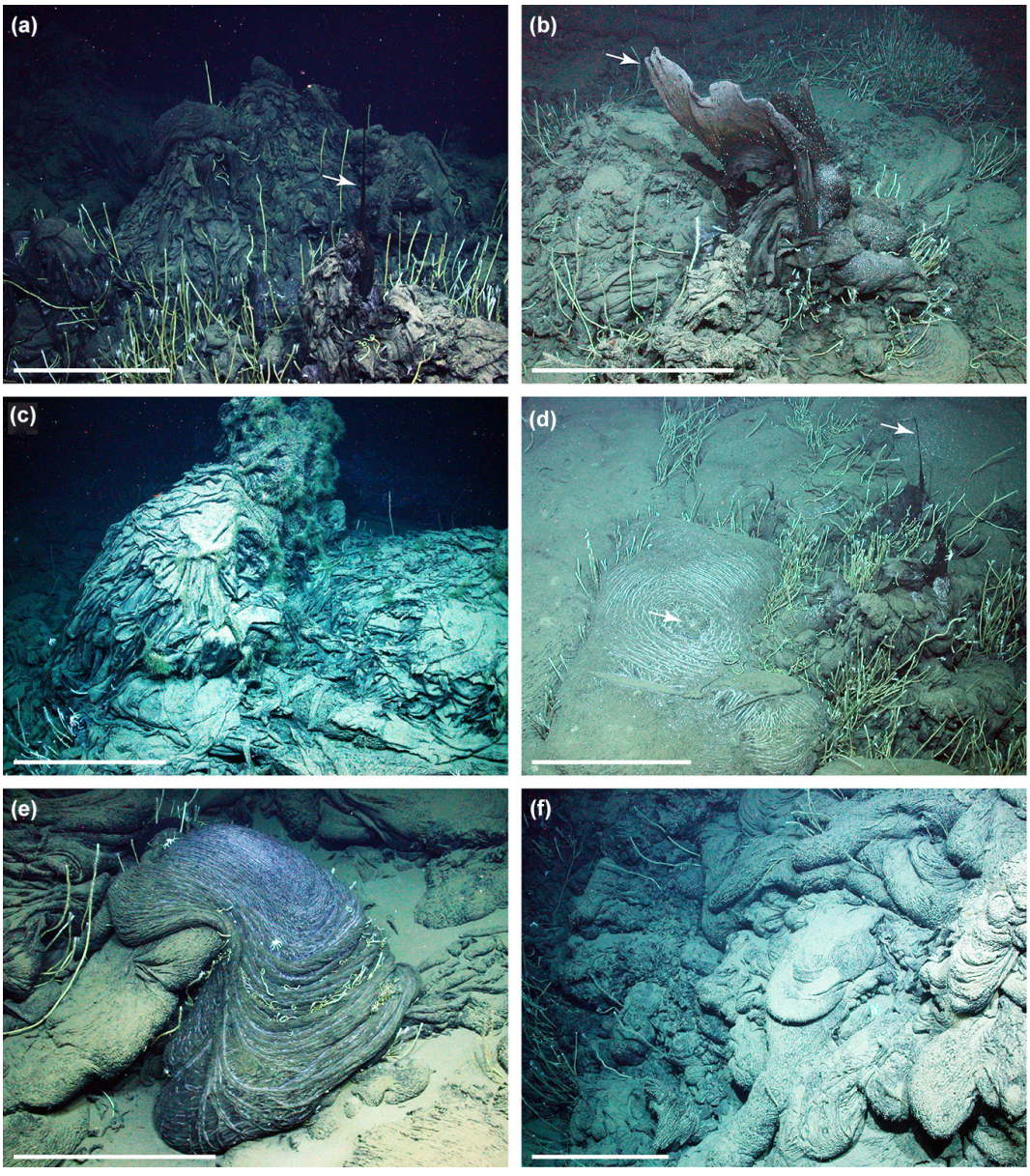


Figure 7. Seafloor images taken at Mictlan Knoll during ROV QUEST Dives 357 **(b, c)**, 363 **(a, e)**, and 364 **(d–f)**. **(a–c)** Oil whips and sheets (arrows) floating in the water. Old whips and sheets apparently lost buoyancy and pile-up at the seafloor. **(d–f)** Flow structures of heavy oil. Scale bar all images 50 cm. All images courtesy of MARUM.

2015). Knolls and ridges in Campeche Knolls are generally the seabed expressions of salt diapirism that causes hydrocarbons to accumulate and, eventually, to migrate though the sediments to the seafloor (Ding et al., 2008, 2010). More than 50 knolls and ridges in our study area exhibited single or multiple oil slick origins (Fig. 2), which suggests that they are as naturally prolific an oil seepage area as the salt province in the much better-studied northern Gulf of Mexico (GoM; e.g. MacDonald et al., 1993, 1996). In the Campeche Knolls, hydrocarbon seepage occurs in water depths down to about 3500 m, which is considerably deeper than seeps discovered at the middle–lower continental slope in the northern GoM (∼ 2750 to ∼ 970 m; Roberts et al., 2010). Only the seeps at the Florida Escapment are located in comparable water depths at 3300 m (Paull et al., 1984; Cordes et al., 2007b).

While previous studies focused on Chapopote Knoll, we summarize in this study hydrocarbon seepage at the seafloor at five sites by ROV observations (including Chapopote Knoll) and, in addition, at seven sites by camera sled surveys at knolls and ridges (Fig. 2, Table 1). These sites range from depths around 1100 m in the south to 3420 m in the north of the study area. At all 12 sites we found evidence

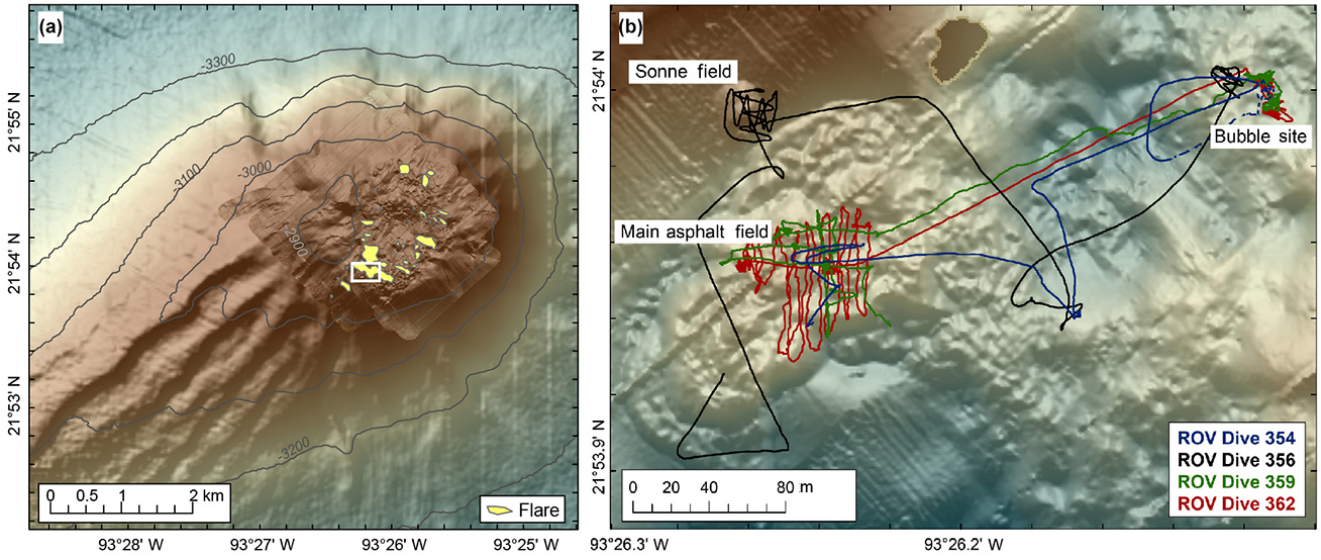


Figure 8. Maps of Chapopote Knoll (see Fig. 2 for location): **(a)** AUV-based bathymetry draped over ship-based bathymetry and areas of flares (yellow). The box shows the area in **(b)**. **(b)** ROV QUEST dive tracks and main study sites plotted on AUV-based bathymetry.

of natural hydrocarbon seepage as indicated by the presence of chemoautotrophic communities, authigenic carbonates, or asphalt deposits, confirming that hydrocarbon seepage is a widespread process in the region of the Campeche Knolls. All of the 12 sites are located at the seafloor below sea surface oil slicks detected by satellite imagery (Williams et al., 2006). However, it should be noted that we only studied the seafloor close to oil slicks and that our method is biased, i.e. it does not provide a correlation between sea surface slicks and seafloor seepage.

Asphalt deposits were visually identified at seven sites (UNAM ridge, Chapopote Knoll and Mictlan Knoll; Sites 1, 3, 6, and 7; Table 1) and they probably also occur at four more sites (Knoll 2000, Sites 2, 4, and 5; Table 1). This clearly shows that seepage of heavy oil is an intrinsic property of the Campeche Knolls (Fig. 2). A possible reason for this is that the crude oil in the Campeche salt province is generally heavy (Magoon et al., 2001) in terms of API gravity (American Petroleum Institute gravity). For now we can only speculate on the mechanisms that lead to the expulsion and deposition of heavy oil on the seafloor, but we assume it is a combination of salt tectonic movements and high gas content that lead to the rise of this heavy oil to the seafloor, where it is then subjected to postdepositional weathering processes.

Out of the about ten sites with asphalt deposits at the seafloor, only three knolls (Chapopote Knoll, Mictlan Knoll, and Site 3; Table 1) exhibit features characteristic of asphalt volcanism (sensu MacDonald et al., 2004), which forms conical mounts with crater-like depressions and extensive hard substrata. The other sites either form ridges or the asphalts are associated with more complex morphologies. Tsanyao Yang Knoll is a noteworthy exception, because we did not find indications for the presence of extensive asphalt deposits, although seepage of oil was observed. The fact that we did not observe large asphalt deposits might be the result of a too-limited survey effort. Alternatively, we speculate that the absence of asphalt deposits at Tsanyao Yang Knoll are related to its unique shape as it is the only flat-topped knoll analysed in this study: its morphology resembles that of passive-type salt diapirs (Ding et al., 2010), where salt intruding very close to the seafloor caused bending-up of hydrocarbon-bearing strata to the seabed. The structural framework of passive-type salt diapirs may not provide the necessary shallow hydrocarbon reservoir typical for the other knolls and ridges (Ding et al., 2008; 2010).

During our investigations it became clear that in most instances gas venting, oil seepage, and flows of heavy oil (leading to asphalt deposits) were temporally and spatially segregated. Oil and gas seepage occurred separately from asphalt occurrences (e.g. at Mictlan Knoll) but also through fractures in asphalts that probably act as conduits for gas/oil migration (e.g. at Hydrate Hill, Marker M114-5, Marker M114-1, and the bubble site at Chapopote). Different chemical compositions of oil and gas result in different manifestations at the seafloor, which we discuss in the following section.

5.2 Geochemical characterization of gas, hydrate, and oil

In order to characterize the origin of hydrocarbons generated in the deep subsurface below the emission sites, we analysed bubble-forming gas escaping the seafloor. Compared to the other hydrocarbon-containing organic substances discharged at the Campeche Knolls (e.g. oil, heavy oil), rapidly

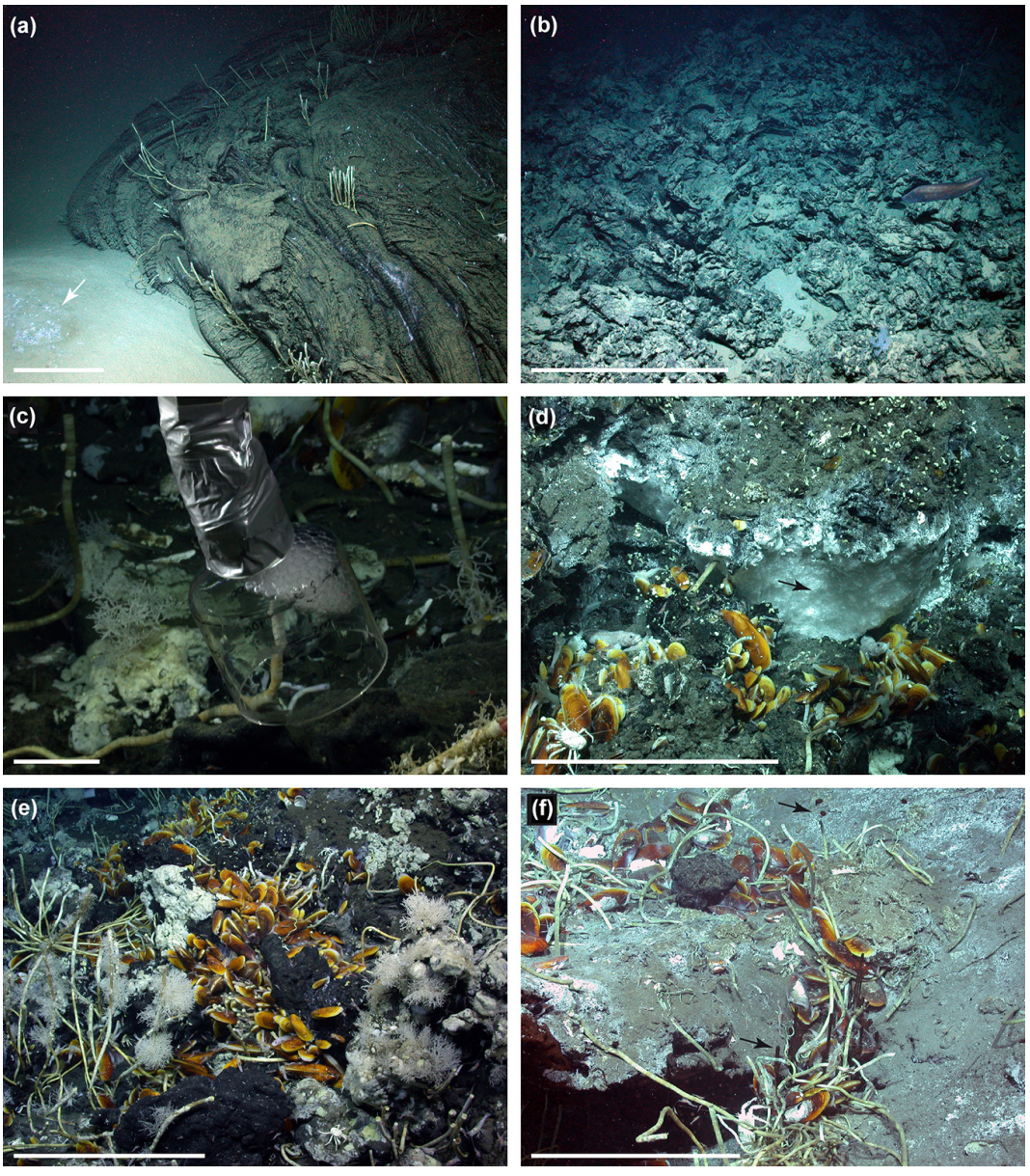


Figure 9. Seafloor images taken at Chapopote Knoll during ROV QUEST Dives 354 **(c, e)**, 362 **(a, f)**, and 365 **(b, d)**. **(a)** Main asphalt field with vestimentifera bordering a bacterial mat (arrow) on soft sediments. Scale bar 50 cm. **(b)** Older flow characterized by fragmented asphalt. Scale bar 50 cm. **(c)** Catching hydrate-coated bubbles at the bubble site. Scale bar 10 cm. **(d)** Gas hydrate outcrop (arrow) with mytilids, gastropods, galatheid crab. Note bubble fabric of exposed hydrate. Scale bar 50 cm. **(e)** Sponges, hydrozoans, mytilids at the bubble site. Scale bar 50 cm. **(f)** Oil drops and oil whips (arrows) close to the bubble site. Scale bar 50 cm. All images courtesy of MARUM.

emitted vent gas is believed to be less affected by alteration in the course of upward migration in the sediment, thus it can provide an insight into the chemical characteristics of the subsurface reservoir of light hydrocarbons. Considering the molecular compositions of light hydrocarbons (expressed as C_1 / C_2 ratios) and stable carbon isotopic signatures of methane (δ^{13}C-CH_4), most samples plot within or close to the empirical field proposed for a thermocatalytic origin (Fig. 12).

The variability of δ^{13}C-CH_4 values in gas bubbles was noticeably small ($\Delta\delta^{13}$C-$CH_4 = 4.7$ ‰ V-PDB), given the fact that sampling was conducted at four different knolls and ridges positioned at some tens to hundreds of kilometres distance from each other. In contrast, C_1 / C_2 ratios appear to be more variable with the highest values determined for apparently pure gas bubbles from Hydrate Hill at Mictlan Knoll (185, GeoB19336-15) and lowest values for oil-coated bubbles at Tsanyao Yang Knoll (14, GeoB19337-2). A vari-

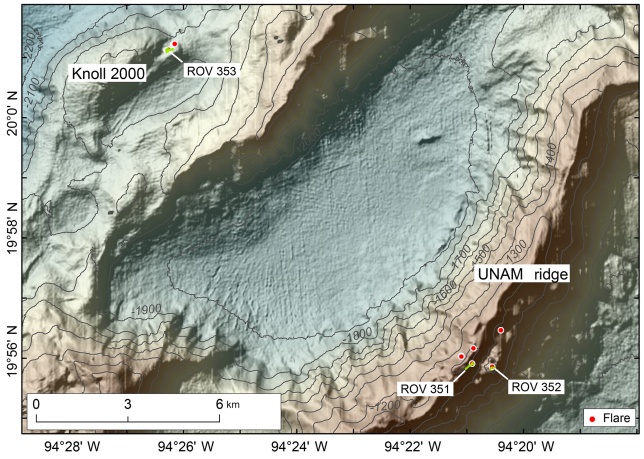


Figure 10. Ship-based bathymetry of Knoll 2000 and UNAM ridge (see Fig. 2 for location), locations of flares (red dots), and ROV QUEST dive tracks (green).

ety of possible post-genetic processes can affect the distributions of light hydrocarbons, e.g. abiotic molecular fractionation during migration (Leythaeuser et al., 1980), admixture with oil-derived components or secondary methane (Milkov and Dzou, 2007), and microbial oxidation of methane and non-methane hydrocarbons (Hoehler et al., 1994; Joye et al., 2004; Kniemeyer et al., 2007). However, the causes for the variations in C_1 / C_2 ratios observed in this study remain unexplained.

Methane in the gas bubbles sampled during this study was enriched in ^{13}C relative to oil samples ($\delta^{13}C\text{-}CH_4 < -50.3\,‰$), which were either collected during this study (one sample) or in the course of previous studies (Fig. 12) (MacDonald et al., 2004; Schubotz et al., 2011b). The variability in the $\delta^{13}C\text{-}CH_4$ and C_1 / C_2 ratios of the oil samples either reflects site-specific properties of the oil source or indicates alteration processes during migration to variable extents. More negative values $\delta^{13}C\text{-}CH_4$ of the oil samples in general may result from admixture by microbial-produced ^{13}C-depleted secondary methane from the oxidation of higher short-chained hydrocarbons at shallow sediment depth (Milkov and Dzou, 2007; Schubotz et al., 2011b).

We failed to sample gas hydrates during this study, but shallow hydrates were collected from two sites at Chapopote Knoll during previous investigations (MacDonald et al., 2004; Schubotz et al., 2011b). Hydrate-bound methane in these studies was depleted in ^{13}C by $>3\,‰$ compared to methane in bubbles collected in our study. It should be stressed that sampling was conducted in different years and not at exactly the same sites. Nevertheless, $\delta^{13}C\text{-}CH_4$ differences between gas bubbles and hydrates within Chapopote Knoll are an interesting result, as hydrate deposits close to the seafloor are considered to form from gas bubbles (see below) without significant isotopic fractionation of methane (Bourry et al., 2009; Pape et al., 2010; Sassen et al., 2004). The difference in $\delta^{13}C$ of $>3\,‰$ between methane in bubble streams and in shallow hydrates at Chapopote Knoll, therefore, suggests some contribution of microbial-generated methane to the hydrate.

5.3 Gas venting, hydrate occurrence, and the vestimentifera-gas/hydrate habitat

Gas emissions are integral parts of submarine seep systems in various geological settings worldwide but hydrate-containing mounds overgrown by dense vestimentiferan tube worm fields probably belonging to the genus *Escarpia* are, to our knowledge, unique to the Campeche Knolls. Massive hydrate deposits close to the seafloor are considered to result from gas bubble migration through the sediments (Haeckel et al., 2004; Smith et al., 2014). Part of the gas can be sequestered as gas hydrate at shallow sediment depths in case the crystallization force overcomes the effective overburden stress (Torres et al., 2004). Shallow hydrate deposits typically form a mounded topography of soft sediment at the seafloor as observed at Hydrate Ridge (Cascadia Margin; Suess et al., 2001; Sahling et al., 2002) and Bush Hill in the northern GoM (MacDonald et al., 1994). At Hydrate Ridge, intensive anaerobic oxidation of methane (AOM) in sediments overlying hydrates results in production of hydrogen sulfide that is consumed by sulfide-oxidizing bacteria that form mats draping the mounds (Boetius et al., 2000; Treude et al., 2003). Sulfate reduction coupled to the degradation of higher-order hydrocarbons brought along with oil propagating in the sediments was additionally proposed to occur in the northern GoM (Formolo et al., 2004; Joye et al., 2004).

In our study, we found vestimentiferan tube worms capping hydrate deposits, which has not been observed before in such a clear association. In order to illustrate the relevant processes, we illustrate the two different situations encountered at Tsanyao Yang Knoll and Mictlan Knoll in Fig. 13. At both knolls, gas bubbles percolated through the mounds and we propose that the continuous gas supply from below drives hydrate formation in the shallow subsurface. At Tsanyao Yang Knoll, hydrate formed as massive layers in the sediments within the mound (Fig. 4b), whereas for Mictlan Knoll we speculate that hydrates occupy voids between fragmented asphalt (Fig. 6a–c). In both cases, hydrates serve as methane reservoir (e.g. Sahling et al., 2002) from which methane and other short-chained hydrocarbons are constantly diffusing towards the overlaying seawater. We further propose that AOM dominates in the rhizosphere, which is a distinct 5–10 cm-thick layer consisting of the posterior tubes of the vestimentiferan tube worms. Vestimentiferan tube worms can release sulfate through their posterior tubes (Dattagupta et al., 2006, 2008) and we therefore suggest that the rhizosphere in particular is supporting AOM. Due to the fact that AOM efficiently produce alkalinity necessary for carbonate precipitation, we propose that vestimentifera in the southern GoM largely rely on sulfide produced by sulfate reduction coupled

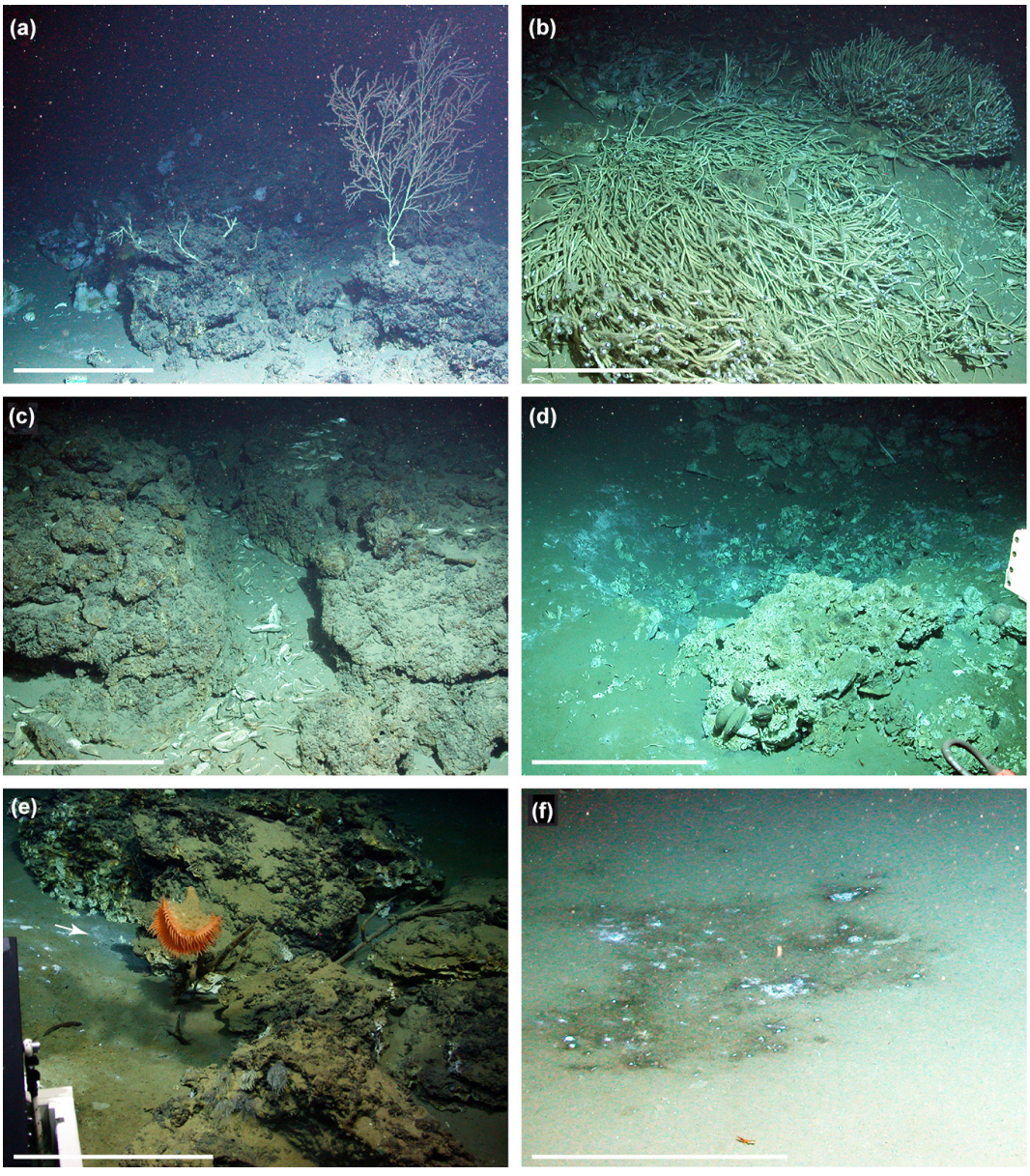


Figure 11. Seafloor images taken at UNAM ridge **(a–d)** and Knoll 2000 **(e, f)** during ROV QUEST dives 352 and 353 respectively. **(a)** Soft coral and other suspension feeders on iron-/manganese-stained authigenic carbonates. **(b)** Recumbent vestimentifera. **(c)** Authigenic carbonates and mytilid shells. **(d)** A few living mytilids attached to carbonates (foreground) and a 1 m-wide circular depression. **(e)** Frenulate tube worms were recovered from samples of whitish-stained sediments (arrow) next to carbonates inhabited by suspension feeders (*Actinoscyphia* sp., anemones, sponges). **(f)** Whitish patches at seafloor interpreted to be bacterial mats on dark-stained sediments. Scale bar all images 50 cm. All images courtesy of MARUM.

to methane oxidation. This is further supported by the composition of the gas that forms the hydrate, which is dominated by methane (Fig. 12). The geochemistry in the southern GoM is in contrast to that for vestimentifera in the northern GoM, which rely on sulfide produced by sulfate-reduction coupled to methane oxidation and likely augmented by degeneration of organic carbon that may include higher hydrocarbons (e.g. Joye et al., 2004). We favour the concept that considers the vestimentifera as ecosystem engineers (sensu Cordes et al., 2003, 2005) that play a pivotal role for this particular gas/hydrate habitat as they intensify chemical turnover processes within the rhizosphere, and the space at and in between the tubes provides habitat for numerous other seep-typical species. Moreover, the thick blanket of the rhizosphere shields gas hydrate from direct contact with seawater

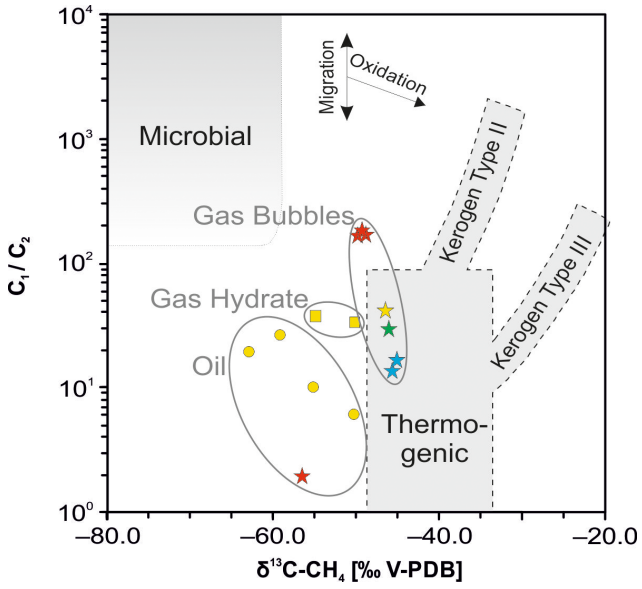


Figure 12. Molecular (C_1 / C_2) vs. stable C isotopic composition of methane (δ^{13}C-CH_4) sampled by gas bubble sampler at Tsanyao Yang Knoll (blue), Mictlan Knoll (red), Chapopote Knoll (yellow), and UNAM ridge (green) and a single oil-associated gas sample (Mictlan Knoll) collected during this study with the GBS. Stars indicate samples analysed in this study, dots and squares are values according to results for methane in hydrates and oil collected during previous campaigns (MacDonald et al., 2004; Schubotz et al., 2011b). Classification according to the Bernard diagram, modified after Whiticar (1990). Gas samples studied herein are plotted close to the empirical field of thermogenic methane.

and may impede its dissolution, thereby preserving the driver of AOM.

With regard to our discovery of the vestimentifera-gas/hydrate habitat, we attempted to characterize differences in environmental parameters in the Campeche Knolls and areas where bacterial mats drape soft sediments covering hydrates (MacDonald et al., 1994; Suess et al., 2001). First, seeps in the southern GoM occur at greater water depth (∼ 3000 m) than the hydrate mounds at Hydrate Ridge (∼ 780 m) and at Bush Hill in the northern GoM (∼ 540 m). The higher pressure at greater water depth in conjunction with very vigorous gas bubble emission could lead to more voluminous and more rapid formation of gas hydrate close to the seafloor. In addition, the deep-water physical environment is more stable compared to at the upper slope, where temperature is higher and pressure changes are considerably larger (MacDonald et al., 1994, 2005). Further, with respect to the mature vestimentiferan communities and authigenic carbonates within the rhizosphere we speculate that gas seepage at our study sites was stable on extended timescales. Vestimentifera are considered to be long-living organisms, with estimated lifespans of 170–250 years for 2 m-long species in the northern GoM (Bergquist et al., 2000; Cordes et al., 2007a). Although the vestimentiferan species present in the southern GoM probably belong to the genus *Escarpia* and are thus different from those in the northern GoM, it is possible that slow growth is a general characteristic of vestimentifera at seeps and that the vestimentifera observed in our study (with tube length of ∼ 2 m) might be considerably old as well. Independent support comes from a modelling study that suggested timescales of 100 to 500 years for the formation of authigenic carbonate crust which are a few centimetres thick (Luff et al., 2004).

5.4 Heavy oil flows leading to asphalt deposits and asphalt as habitat

Our ROV-based observations revealed numerous examples for voluminous asphalt deposits at Chapopote Knoll and Mictlan Knoll. Their formation has been explained by a model proposed by Brüning et al. (2010), which takes the API gravity into account. Oil that floats in the water while still being attached to the seabed has an API gravity slighter higher than 10° API, which corresponds to a density close to seawater. This places it at the boundary between heavy oil (10–12 to 20° API) and very heavy oil (< 10–12° API), that are mobile and immobile at reservoir conditions respectively (Tissot and Welte, 1984). Oil whips and sheets were observed (Fig. 7a–c) indicating seepage of heavy oil that has slight positive buoyancy (> 10° API) but is sufficiently cohesive to remain attached to the point of extrusion. In contrast, the extensive asphalt deposits must have been negatively buoyant (< 10° API) when they exited because they clearly flowed at the seafloor (Figs. 7d–f, 9a). Incorporation of sediments into and accumulation of sediments onto flowing asphalts will also contribute to their negative buoyancy. Formation of asphalt deposits thus depends on the viscosity of the extruded heavy-to-very-heavy oil (∼ 10° API) and the duration for which it is exposed to weathering processes at the seafloor that lead to a transition from mobile to immobile; i.e. the viscosity is high enough to allow the ascent through the sediment, but after emission at the seafloor, it rapidly becomes immobile, probably due an increase in viscosity due to the loss of volatile compounds.

In spite of this, additional possibly post-depositional processes lead to a decrease in bulk density, which can be deduced from observations at the main asphalt field at Chapopote Knoll. Pure gas hydrate, which typically exhibits a specific density less than seawater (ca. 0.9 g cm^{-3}), was present below and within fresh asphalts (Schubotz et al., 2011b; Klapp et al., 2010a, b) and asphalt pieces floated up when extracted from an intact flow (Brüning et al., 2010). The elevated gas content might be explained by post-depositional hydrate formation and gas invasion into the pore space of the asphalts resulting from gas supply from below. However, with respect to the considerable difference in δ^{13}C signatures between hydrate methane below the asphalts (−54.8 ‰; Schubotz et al., 2011b) and the vent gas methane

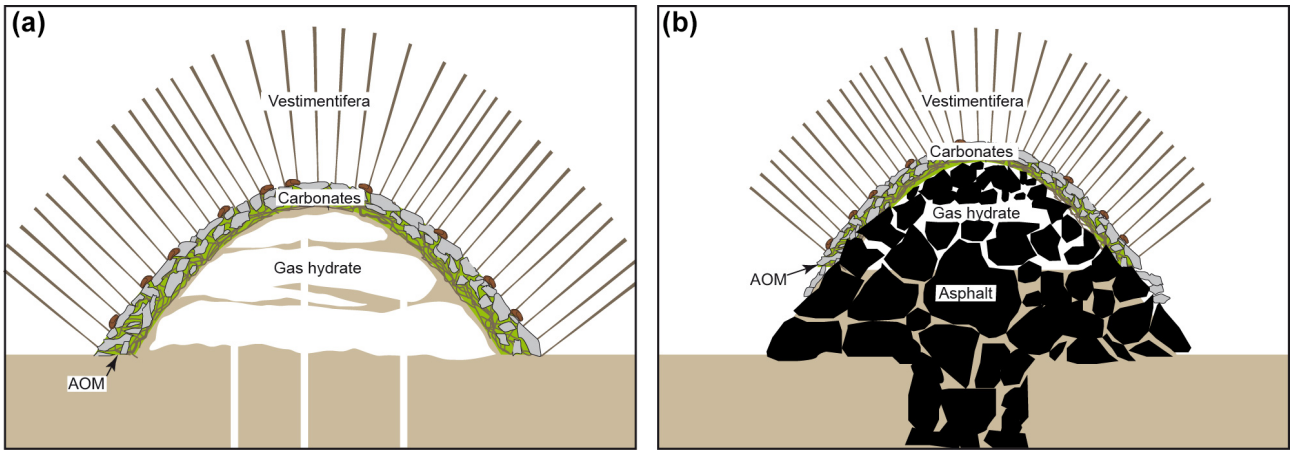


Figure 13. Sketch depicting the interpreted vestimentifera-gas/hydrate habitat encountered at **(a)** Tsanyao Yang Knoll and **(b)** Mictlan Knoll. Drawing not to scale. The mounds at Tsanyao Yang Knoll were a few metres wide whereas Hydrate Hill at Mictlan Knoll was about 30 m in diameter. AOM is anaerobic oxidation of methane (green).

(−46.5 ‰; Fig. 12), it is unlikely that these gases share the same source. A possible interpretation for the more negative δ^{13}C-signature of hydrate-bound methane could be that microbial methane is produced in sufficient amounts in shallow, hydrocarbon-soaked sediments below or within the asphalts.

As we did not observe active extrusion of heavy oil during the ROV dives, discharge rates of heavy oil at the seafloor remain unknown but could possibly be in the range of weeks to years. The heavy oil apparently serves as energy source for chemosynthesis-based organisms like whitish bacterial mats and vestimentiferan tube worms that generally depend on the supply of reduced sulfur compounds (Hilario et al., 2011; Teske and Nelson, 2006). If the outflow of heavy oil is a slow process, chemosynthetic organisms may grow while the oil is still in motion. Alternatively, the chemosynthetic organism may settle after deposition. Chemosynthetic organisms may thrive on reduced sulfur compounds contained in the heavy oil or on sulfide produced during microbial oil degradation coupled to sulfate reduction (Schubotz et al., 2011b).

Based on their distribution at the seafloor exemplified in Fig. 7d and e, we propose that predominantly relatively young ejections, such as whips and sheets in the water column, and those in the central parts of asphalt flows, are populated by whitish bacterial mats. Moreover, the spatial extent of bacterial mats at the main asphalt field at Chapopote Knoll during this study in 2015 was very similar to that observed during its initial documentation in 2006 (Brüning et al., 2010), demonstrating considerable ecosystem stability over a decade. This is remarkable as we observed holothurians, galatheid crabs, and myriads of small crustaceans inferred to be grazing on the bacteria. This indicates a high primary production by chemosynthetic microbes. At more distal parts of the most recent asphalt deposits, bacterial mats were absent, while tube worms occurred nestling in fissures (Figs. 7e and 9a). Considering the relatively low growth rates of vestimentiferan tube worms (Bergquist et al., 2000), we propose that even the most recent asphalt deposits discovered in this study have already existed for decades. The ostensible absence of bacteria on asphalt surface and the presence of vestimentifera growing posteriorly into the substrate suggest that the sulfide source progresses towards deeper parts of the asphalts with time. This would be in line with our concept of successive stages being represented by bacteria and tube worms.

The most common asphalt deposits in our study were in an inert stage. It was devoid of any macro- or megafauna and ranged in terms of appearance from solid asphalt flows to partly or entirely fragmented asphalt deposits (e.g. Fig. 9b). We suggest that these asphalts no longer serve as habitats for chemosynthesis-based bacteria or tube worms because a greater portion of volatiles has already escaped to the water column. Furthermore, we point out that authigenic carbonates were virtually absent where fragmented asphalts occurred alone, i.e. without oil or gas seepage (Naehr et al., 2009). This observation suggests that microbial degradation of heavy oil does not produce sufficient alkalinity for authigenic carbonate formation. Based on our findings we may refer to the asphalt deposits without visible chemosynthetic fauna prevailing in the Campeche Knolls as being in an inert stage. Heterotrophic suspension feeders that are common in other regions with asphalt deposits (Weiland et al., 2008; Williamson et al., 2008; Valentine et al., 2010; Jones et al., 2014) were also absent at the inert stage at the Campeche Knolls. In our study area soft corals attached to asphalts were only found at the shallowest site investigated, UNAM ridge at 1230 m water depth (Fig. 11a). Therefore, the paucity of suspension feeders in the region of the Campeche Knolls might be caused by a limited food supply at the deep-water asphalt deposits, Mictlan Knoll and Chapopote Knoll (3420 to 2900 m water depth respectively).

In contrast to seafloor asphalt deposits in other regions (Weiland et al., 2008; Williamson et al., 2008; Valentine et al., 2010; Jones et al., 2014), those in the Campeche Knolls are sourced by geologically recent emissions of heavy oil. However, given that lobate flow patterns are still discernible for asphalts in the Santa Barbara Basin 31 to 44 kyr after seafloor deposition (Valentine et al., 2010), asphalt deposits sourced by emission of heavy oil in the Campeche Knolls may have existed for tens to probably hundreds of thousands of years while being fragmented and draped by sediments. The Campeche Knolls asphalts provide a natural laboratory for studying their more recent genesis as well as their alteration through time.

5.5 Oil seepage and oil-soaked sediments as habitat

Because oil seepage is an integral component of the hydrocarbon seepage system at the Campeche Knolls, as revealed by numerous oil slicks at the sea surface (Fig. 1), we concentrated on identifying oil seepage sites at the seafloor. In general, oil may rise as oil-coated gas bubbles or as oil drops (De Beukelaer et al., 2003; Leifer and MacDonald, 2003). Oily bubbles are difficult to identify visually during ascent through the water column, as they can appear as transparent as pure gas bubbles. Therefore, oil might have been a significant component of the observed gas bubble streams. Only in a few instances, the coating of gas bubbles was dark and the hydrate forming from the bubbles was dark stained. In contrast, a release of oil drops was clearly observed and occurred in association with two different seafloor manifestations: white-coated chimneys (Fig. 6d) and oil-soaked sediments inhabited by *Bathymodiolus heckerae* (Fig. 9f). These observations demonstrate that a seep system of oil exists next to a seep system of heavy oil leading to asphalt deposits. Seepage of oil was associated with old asphalt deposits (sediment-covered asphalt mounds and fragmented asphalt pieces) at three sites (Marker M114-1 and M115-5 at Mictlan Knoll; bubble site at Chapopote Knoll), suggesting that the oil migrated through the sediments along pre-existing pathways.

At Chapopote Knoll and Mictlan Knoll biological communities were physically exposed to oil (Figs. 6f, 9f). As found in the northern GoM, degradation of oil-derived components in sediments, like non-methane hydrocarbons, can be performed by sulfate-reducing bacteria (belonging to the δ-proteobacteria group) while producing hydrogen sulfide (e.g. Joye et al., 2004; Kniemeyer et al., 2007). This is used as an energy source for chemosynthesis-based organisms such as mat-forming, sulfide-oxidizing bacteria, and vestimentifera living in symbiosis with chemosynthetic bacteria. The two mytilid species studied in our area harbour symbionts that are capable of oxidizing sulfides as well as methane (Raggi et al., 2013). In addition, the mussel *Bathymodiolus heckerae* from the bubble site at Chapopote Knoll evidenced a unique symbiosis with a proteobacterium of the genus *Cycloclasticus*, which is supposed to degrade hydrocarbons (Raggi et al., 2013). This symbiosis is unique to that site where the animals are virtually bathed in oil.

6 Summary

Natural oil seepage is inherent to the Campeche Knolls, as revealed by our new findings obtained during cruise M114 in 2015, and by a reanalyses of seafloor images gathered during previous cruises. Unique to the Campeche Knolls is the widespread occurrence of asphalt deposits, which was definitely confirmed at seven sites. The flow structures of heavy oil encountered at Chapopote Knoll and Mictlan Knoll are noteworthy, as they represent more recent asphalt deposits compared to those described from other continental margin settings. The recently discharged asphalts sustain chemosynthetic organisms such as bacterial mats and vestimentifera as well as a suite of heterotrophic organisms that warrant further taxonomic studies. Based on our preliminary observations, and in contrast to the asphalt deposits at other continental margins, those at the deeper Campeche Knolls (> 2900 m water depth) are generally not utilized by sessile, filter-feeding organisms that attach to hard substrates.

Seepage of oil and gas bubbles co-occurs next to and through the asphalt deposits. Most intriguing was our finding of vigorous gas bubble streams forming hydrate mounds (Tsanyao Yang Knoll) or percolating through old, fragmented asphalts leading to hydrate precipitation in the voids between the asphalt breccia (Mictlan Knoll). The hydrates likely serve as a shallow methane reservoir underlying dense communities of vestimentiferan tube worms, which then act as ecosystem engineers, facilitating AOM, and preserving the hydrate. We further suggest that in the tube worms rhizosphere, intense microbially mediated turnover processes are probably taking place, which facilitated the precipitation of authigenic carbonates. Our observation of the closely associated hydrate and vestimentiferan tube worm is unparalleled, but this relationship and the involved biogeochemical processes could also be relevant in other hydrocarbon settings with shallow hydrate deposits. The healthy-appearing vestimentifera growing on hydrate suggest considerable stability of these habitats over extended time spans, required for establishment of the slow-growing vestimentifera and formation of authigenic carbonates.

Oil drops escaped the seafloor through small chimney-like structures or, together with gas bubbles, through a mixture of fragmented, old asphalt and sediments. In the latter case, sediments were heavily impregnated by oil. The seep-associated communities appeared very diverse, with two chemosynthetic mussel species and various other heterotrophic organisms.

7 Data availability

The data will be freely accessible through the world data center PANGAEA after publishing the major results in peer-reviewed publications. The data will become available at: https://doi.pangaea.de/10.1594/PANGAEA.860373.

The Supplement related to this article is available online at doi:10.5194/bg-13-4491-2016-supplement.

Author contributions. Maxim Rubin Blum, Gerhard Bohrmann, Christian Borowski, Chieh-Wei Hsu, Markus Loher, Ian MacDonald, Yann Marcon, Miriam Römer, Heiko Sahling, Florence Schubotz, Daniel Smrzka, and Gunter Wegener conducted the ROV dives as scientific advisors on which this present study is largely based on. Chieh-Wei Hsu, Markus Loher, and Miriam Römer detected the gas emissions by hydroacoustic means. Thomas Pape analysed the gas. Adriana Gaytán-Caballero assisted in taxonomic determination of fauna at sea. Elva Escobar-Briones supported the application procedure to acquire the Mexican research permission and supervised the participation of three Mexican scientists and students in the cruise. Heiko Sahling prepared the manuscript with contributions of all co-authors.

Acknowledgements. We are grateful to the Mexican authorities for granting permission to conduct the research in the southern Gulf of Mexico (permission of DGOPA: 02540/14 from 5 November 2014). We thank the master and crew of R/V *Meteor* for their highly professional assistance at sea. Thanks to MARUM AUV SEAL 5000 and ROV QUEST 4000 m teams for providing and handling of the indispensable equipment at sea. Various people have contributed to the successful cruise, we namely thank Monika Breitzke, Stefanie Buchheister, Christian Ferreira, Patrizia Geprägs, Jan-Derk Groeneveld, Elvira Jiménez Guadarrama, Ingo Klaucke, Sven Klüber, Esmeralda Morales Dominguez, Gopika Suresh, Marta Torres, Monika Wiebe, Paul Wintersteller, and Jennifer Zwicker. We thank three anonymous reviewers and Daniel Orange for their constructive comments that improved the manuscript. The cruise was core funded by the German Research Foundation (DFG – Deutsche Forschungsgemeinschaft) through the cruise proposal "Hydrocarbons in the southern Gulf of Mexico". Additional support was provided through the DFG-Research Center/Excellence Cluster "The Ocean in the Earth System".

The article processing charges for this open-access publication were covered by the University of Bremen.

Edited by: H. Niemann
Reviewed by: three anonymous referees

References

Bergquist, D. C., Williams, F. M., and Fisher, C. R.: Longevity record for deep-sea invertebrate, Nature, 403, 499–500, 2000.

Boetius, A., Ravenschlag, K., Schubert, C. J., Rickert, D., Widdel, F., Gieseke, A., Amann, R., Jørgensen, B. B., Witte, U., and Pfannkuche, O.: A marine microbial consortium apparently mediating anaerobic oxidation of methane, Nature, 407, 623–626, 2000.

Bohrmann, G. and Schenk, S.: RV *Sonne*, Cruise report SO 174, OTEGA II: (Lotus-Omega-Mumm), Balboa-Corpus Christi-Miami, 1 October–12 November 2003, 117 pp., 2004.

Bohrmann, G., Spiess, V., and cruise participants: Report and preliminary results of R/V *Meteor* Cruise M67/2a and 2b, Balboa – Tampico – Bridgetown, 15 March–24 April 2006, Fluid seepage in the Gulf of Mexico., Berichte Fachbereich Geowissenschaften, Universität Bremen, Bremen, 263, 119 pp., 2008.

Bourry, C., Chazallon, B., Charlou, J. L., Donval, J. P., Ruffine, L., Henry, P., Geli, L., and Cagatay, M. N.: Free gas and gas hydrates from the Sea of Marmara, Turkey, Chemical and strucural characterization, Chem. Geol., 264, 192–206, 2009.

Brüning, M., Sahling, H., MacDonald, I. R., Ding, F., and Bohrmann, G.: Origin, distribution, and alteration of asphalts at Chapopote Knoll, Southern Gulf of Mexico, Mar. Petrol. Geol., 27, 1093–1106, 2010.

Bryant, R. B., Lugo, J., Córdova, C., and Salvador, A.: Physiography and bathymetry, in: The Geology of Northern America, The Gulf of Mexico Basin, edited by: Salvador, A., Geological Society of America, Boulder, Colorado, 1991.

Caress, D. W. and Cheyes, D. N.: MB-System Seafloor Mapping Software, http://www.mbari.org/data/mbsystem/, last access: 31 January 2014.

Cordes, E. E., Bergquist, D. C., Shea, K., and Fisher, C. R.: Hydrogen sulphide demand of long-lived vestimentiferan tubeworm aggregations modifies the chemical environment at deep-sea hydrocarbon seeps, Ecol. Lett., 6, 212–219, 2003.

Cordes, E. E., Hourdez, S., Predmore, B. L., Redding, M. L., and Fisher, C. R.: Succession of hydrocarbon seep communities associated with the long-lived foundation species *Lamellibrachia luymesi*, Mar. Ecol. Prog. Ser., 305, 17–29, 2005.

Cordes, E. E., Bergquist, D. C., Redding, M. L., and Fisher, C. R.: Patterns of growth in cold-seep vestimenferans including *Seepiophila jonesi*: a second species of long-lived tubeworm, Mar. Ecol., 28, 160–168, 2007a.

Cordes, E. E., Carney, S. L., Hourdez, S., Carney, R. S., Brooks, J. M., and Fisher, C. R.: Cold seeps of the deep Gulf of Mexico: Community structure and biogeographic comparison to Atlantic equatorial belt seep communities, Deep-Sea Res. Pt. I, 54, 637–653, 2007b.

Cruz-Mercado, M. Á., Flores-Zamora, J. C., León-Ramirez, R., López-Céspedes, H. G., Peterson-Rodríguez, R. H., Reyes-Tovar, E., Sánchez-Rivera, R. S., and Barrera-Gonzáles, D.: Salt provinces in the Mexican portion of the Gulf of Mexico – structural characterization and evolutionary model, Gulf Coast Assoc. Geol. Soc. Trans., 61, 93–103, 2011.

Dattagupta, S., Miles, L. L., Barnabei, M. S., and Fisher, C. R.: The hydrocarbon seep tubeworm *Lamellibrachia luymesi* primarily eliminates sulfate and hydrogen ions across its roots to conserve energy and ensure sulfide supply, J. Exp. Biol., 209, 3795–3805, 2006.

Dattagupta, S., Arthur, M. A., and Fisher, C. R.: Modification of sediment geochemistry by the hydrocarbon seep tubeworm

Lamellibrachia luymesi: A combined empirical and modeling approach, Geochim. Cosmochim. Ac., 72, 2298–2315, 2008.

De Beukelaer, S. M., MacDonald, I. R., Guinnasso, N. L., and Murray, J. A.: Distinct side-scan sonar, RADARSAT SAR, and acoustic profiler signatures of gas and oil seeps on the Gulf of Mexico slope, Geo-Mar. Lett., 23, 177–186, 2003.

Ding, F., Spiess, V., Brüning, M., Fekete, N., Keil, H., and Bohrmann, G.: A conceptual model for hydrocarbon accumulation and seepage processors around Chapopote asphalt site, southern Gulf of Mexico: From high resolution seismic point of view, J. Geophys. Res., 113, B08404, doi:10.1029/2007JB005484, 2008.

Ding, F., Spiess, V., MacDonald, I. R., Brüning, M., Fekete, N., and Bohrmann, G.: Shallow sediment deformation styles in northwest Campeche Knolls, Gulf of Mexico and their controls on the occurrence of hydrocarbon seepage, Mar. Petrol. Geol., 27, 959–972, 2010.

Formolo, M. J., Lyons, T. W., Zhang, C., Kelley, C., Sassen, R., Horita, J., and Cole, D. R.: Quantifying carbon sources in the formation of authigenic carbonates at gas hydrate sites in the Gulf of Mexico, Chem. Geol., 205, 253–264, 2004.

Garrison, L. E. and Martin, R. G. J.: Geologic structure in the Gulf of Mexico, US Government Printing Office, Washington, DC, 85 pp., 1973.

Gaytán-Caballero, A.: *Munidopsis geyeri* Pequegnat & Pequegnat, 1970 asociado al volcán de asfalto (sur del Golfo de México) y su vinculación con las poblaciones del Atlántico, master thesis, Universidad Nacional Autónoma de México, Mexico City, 146 pp., 2009.

Greinert, J., Artemov, Y., Egorov, V., Debatist, M., and McGinnis, D.: 1300-m-high rising bubbles from mud volcanoes at 2080m in the Black Sea: Hydroacoustic characteristics and temporal variability, Earth Planet. Sci. Lett., 244, 1–15, 2006.

Haeckel, M., Suess, E., Wallmann, K., and Rickert, D.: Rising methane gas bubbles form massive hydrate layers at the seafloor, Geochim. Cosmochim. Ac., 68, 4335–4345, 2004.

Hilario, A., Capa, M., Dahlgren, T. G., Halanych, K. M., Little, C. T., Thornhill, D. J., Verna, C., and Glover, A. G.: New perspectives on the ecology and evolution of siboglinid tubeworms, PLoS One, 6, e16309, doi:10.1371/journal.pone.0016309, 2011.

Hoehler, T. M., Alperin, M. J., Albert, D. B., and Martens, C. S.: Field and laboratory studies of methane oxidation in an anoxic marine sediment: evidence for methanogenic-sulfate reducer consortium, Global Biogeochem. Cy., 8, 451–463, 1994.

Jones, D. O. B., Walls, A., Clare, M., Fiske, M. S., Weiland, R. J., O'Brien, R., and Touzel, D. F.: Asphalt mounds and associated biota on the Angolan margin, Deep-Sea Res. Pt. I, 94, 124–136, 2014.

Joye, S. B., Boetius, A., Orcutt, B. N., Montoya, J. P., Schulz, H. N., Erickson, M. J., and Lugo, S. K.: The anaerobic oxidation of methane and sulfate reduction in sediments from Gulf of Mexico cold seeps, Chem. Geol., 205, 219–238, 2004.

Klapp, S. A., Bohrmann, G., Kuhs, W. F., Mangir Murshed, M., Pape, T., Klein, H., Techmer, K. S., Heeschen, K. U., and Abegg, F.: Microstructures of structure I and II gas hydrates from the Gulf of Mexico, Mar. Petrol. Geol., 27, 116–125, 2010a.

Klapp, S. A., Murshed, M. M., Pape, T., Klein, H., Bohrmann, G., Brewer, P. G., and Kuhs, W. F.: Mixed gas hydrate structures at the Chapopote Knoll, southern Gulf of Mexico, Earth Planet. Sci. Lett., 299, 207–217, 2010b.

Kniemeyer, O., Musat, F., Sievert, S. M., Knittel, K., Wilkes, H., Blumenberg, M., Michaelis, W., Classen, A., Bolm, C., Joye, S. B., and Widdel, F.: Anaerobic oxidation of short-chain hydrocarbons by marine sulphate-reducing bacteria, Nature, 449, 898–902, 2007.

Leifer, I. and MacDonald, I.: Dynamics of the gas flux from shallow gas hydrate deposits: interaction between oily hydrate bubbles and the oceanic environment, Earth Planet. Sci. Lett., 210, 411–424, 2003.

Leythaeuser, D., Schaefer, R. G., and Yukler, A.: Diffusion of light hydrocarbons through near-surface rocks, Nature, 284, 522–525, 1980.

Luff, R., Wallmann, K., and Aloisi, G.: Numerical modeling of carbonate crust formation at cold vent sites: Significance for fluid and methane budgets and chemosynthetic biological communities, Earth Planet. Sci. Lett., 221, 337–353, 2004.

MacDonald, I., Bender, L., Vardaro, M., Bernard, B., and Brooks, J.: Thermal and visual time-series at a seafloor gas hydrate deposit on the Gulf of Mexico slope, Earth Planet. Sci. Lett., 233, 45–59, 2005.

MacDonald, I. R., Guinasso jr., N. L., Ackleson, S. G., Amos, J. F., R., D., Sassen, R., and Brooks, J. M.: Natural oil slicks in the Gulf of Mexico visible from space, J. Geophys. Res., 98, 16351–16364, 1993.

MacDonald, I. R., N. L. Guinasso, J., Sassen, R., Brooks, J. M., Lee, L., and Scott, K. T.: Gas hydrate that breaches the sea floor on the continental slope of the Gulf of Mexico, Geology, 22, 699–702, 1994.

MacDonald, I. R., Reilly Jr., J. F., Best, S. E., Venkataramaiah, R., Sassen, R., and Guinasso Jr., N. L.: Remote sensing inventory of active oil seeps and chemosynthetic communities in the northern Gulf of Mexico, in: Hydrocarbon migration and its near-surface expression, edited by: Schumacher, D. and Abrams, M. A., American Association of Petroleum Geologists, 27–37, 1996.

MacDonald, I. R., Bohrmann, G., Escobar, E., Abegg, F., Blanchon, P., Blinova, V., Brückmann, W., Drews, M., Eisenhauer, A., Han, X., Heeschen, K., Meier, F., Mortera, C., Naehr, T., Orcutt, B., Bernard, B., Brooks, J., and de Farágo, M.: Asphalt volcanism and chemosynthetic life in the Campeche Knolls, Gulf of Mexico, Science, 304, 999–1002, 2004.

MacDonald, I. R., Escobar, E., Naehr, T., Joye, S., and Spiess, V.: The asphalt ecosystem of the Gulf of Mexico: Results from the Chapopte III Cruise, Fall Meet. Suppl., Abstract B43E-1660, 2007.

MacDonald, I. R., Garcia-Pineda, O., Beet, A., Daneshgar Asl, S., Feng, L., Graettinger, G., French-McCay, D., Holmes, J., Hu, C., Huffer, F., Leifer, I., Muller-Karger, F., Solow, A., Silva, M., and Swayze, G.: Natural and unnatural oil slicks in the Gulf of Mexico, J. Geophys. Res.-Ocean., 120, 8364–8380, 2015.

Magoon, L. B., Hudson, T. L., and Cook, H. E.: Pimienta-Tamabra (!) – A giant supercharged petroleum system in the southern Gulf of Mexico, onshore and offshore Mexico, in: The western Gulf of Mexico basin: Tectonics, sedimentary basins, and petroleum systems, edited by: Bartolini, C., Biuffler, R. T., and Cantú-Chapa, A., AAPG Memoir, 75, 83–125, 2001.

Milkov, A. V. and Dzou, L.: Geochemical evidence of secondary microbial methane from very slight biodegradation of undersaturated oils in a deep hot reservoir, Geology, 35, 455–458, 2007.

Naehr, T. H., Birgel, D., Bohrmann, G., MacDonald, I. R., and Kasten, S.: Biogeochemical controls on authigenic carbonate formation at the Chapopote "asphalt volcano", Bay of Campeche, Chem. Geol., 266, 390–402, 2009.

Nikolovska, A., Sahling, H., and Bohrmann, G.: Hydroacoustic methodology for detection, localization, and quantification of gas bubbles rising from the seafloor at gas seeps from the Black Sea, Geochem. Geophys. Geosys., 9, Q10010, doi:10.1029/2008GC002118, 2008.

Pape, T., Bahr, A., Rethemeyer, J., Kessler, J. D., Sahling, H., Hinrichs, K.-U., Klapp, S. A., Reeburgh, W. S., and Bohrmann, G.: Molecular and isotopic partitioning of low-molecular-weight hydrocarbons during migration and gas hydrate precipitation in deposits of a high-flux seepage site, Chem. Geol., 269, 350–363, 2010.

Paull, C. K., Hecker, B., Commeau, R., Freeman-Lynde, R. P., Neumann, C., Corso, W. P., Golubic, S., Hook, J. E., Sikes, E., and Curray, J.: Biological communities at the Florida Escarpment resemble hydrothermal vent taxa, Science, 226, 965–967, 1984.

Raggi, L., Schubotz, F., Hinrichs, K. U., Dubilier, N., and Petersen, J. M.: Bacterial symbionts of *Bathymodiolus* mussels and *Escarpia* tubeworms from Chapopote, an asphalt seep in the southern Gulf of Mexico, Environ. Microbiol., 15, 1969–1987, 2013.

Roberts, H. H., Shedd, W., and Hunt Jr, J.: Dive site geology: DSV ALVIN (2006) and ROV JASON II (2007) dives to the middle-lower continental slope, northern Gulf of Mexico, Deep-Sea Res. Pt. II, 57, 1837–1858, 2010.

Römer, M., Sahling, H., Pape, T., Bahr, A., Feseker, T., Wintersteller, P., and Bohrmann, G.: Geological control and magnitude of methane ebullition from a high-flux seep area in the Black Sea-the Kerch seep area, Mar. Geol., 319–322, 57–74, 2012.

Sahling, H., Rickert, D., Lee, R. W., Linke, P., and Suess, E.: Macrofaunal community structure and sulfide flux at gas hydrate deposits from the Cascadia convergent margin, NE Pacific, Mar. Ecol. Prog. Ser., 231, 121–138, 2002.

Sahling, H. and Bohrmann, G.: Seafloor images along 9 ROV profiles during METEOR cruise M114/2, unpublished dataset #860373, available at: https://doi.pangaea.de/10.1594/PANGAEA.860373, last access: 10 August 2016.

Salvador, A. (Ed.): The Gulf of Mexico basin, Geology of North America, Geological Society of America, Boulder, Colorado, 568 pp., 1991.

Sánchez-Rivera, R. S., Cruz-Mercado, M. Á., Reyes-Tovar, E., López-Céspedes, H. G., Peterson-Rodriguez, R. H., Flores-Zamora, J. C., Ramirez, R. L., and Barrera-Gonzáles, D.: Tectonic evolution of the South Gulf Salt Province in the Gulf of Mexico, Gulf Coast Assoc. Geol. Soc. Trans., 61, 421–427, 2011.

Sassen, R., Roberts, H. H., Carney, R., Milkov, A. V., DeFreitas, D. A., Lanoil, B., and Zhang, C.: Free hydrocarbon gas, gas hydrate, and authigenic minerals in chemosynthetic communities of the northern Gulf of Mexico continental slope: relation to microbial processes, Chem. Geol., 205, 195–217, 2004.

Scholz-Böttcher, B. M., Ahlf, S., Vazquez-Gutierrez, F., and Rullkötter, J.: Sources of hydrocarbon pollution in surface sediments of the Campeche Sound, Gulf of Mexico, revealed by biomarker analysis, Org. Geochem., 39, 1104–1108, 2008.

Schubotz, F., Lipp, J. S., Elvert, M., and Hinrichs, K.-U.: Stable carbon isotopic compositions of intact polar lipids reveal complex carbon flow patterns among hydrocarbon degrading microbial communities at the Chapopote asphalt volcano, Geochim. Cosmochim. Ac., 75, 4399–4415, 2011a.

Schubotz, F., Lipp, J. S., Elvert, M., Kasten, S., Mollar, X. P., Zabel, M., Bohrmann, G., and Hinrichs, K.-U.: Petroleum degradation and associated microbial signatures at the Chapopote asphalt volcano, Southern Gulf of Mexico, Geochim. Cosmochim. Ac., 75, 4377–4398, 2011b.

Smith, A. J., Flemings, P. B., Liu, X., and Darnell, K.: The evolution of methane vents that pierce the hydrate stability zone in the world's oceans, J. Geophys. Res.-Solid Earth, 119, 6337–6356, 2014.

Suess, E., Torres, M. E., Bohrmann, G., Collier, R. W., Rickert, D., Goldfinger, C., Linke, P., Heuser, A., Sahling, H., Heeschen, K., Jung, C., Nakamura, K., Greinert, J., Pfannkuche, O., Trehu, A., Klinkhammer, G., Whiticar, M. J., Eisenhauer, A., Teichert, B., and Elvert, M.: Sea floor methane hydrates at Hydrate Ridge, Cascadia Margin, in: Natural gas hydrates: Occurrence, distribution, and detection, edited by: Paull, C., Geophysical Monograph 124, American Geophysical Union, 87–98, 2001.

Suresh, G.: Offshore oil seepage visible from space: A Synthetic Aperture Radar (SAR) based automatic detection, mapping and quantification system, Dissertation Thesis, Department of Geosciences, University of Bremen, 180 pp., 2015.

Teske, A. and Nelson, B. W.: The genera *Beggiatoa* and *Thioploca*, Prokaryotes, 6, 784–810, 2006.

Tissot, B. P. and Welte, D. H.: Petroleum formation and occurrence, Springer, Berlin, 699 pp., 1984.

Torres, M. E., Wallmann, K., Tréhu, A. M., Bohrmann, G., Borowski, W. S., and Tomaru, H.: Gas hydrate growth, methane transport, and chloride enrichment at the southern summit of Hydrate Ridge, Cascadia margin off Oregon, Earth Planet. Sci. Lett., 226, 225–241, 2004.

Treude, T., Boetius, A., Knittel, K., Wallmann, K., and Jorgensen, B. B.: Anaerobic oxidation of methane above gas hydrates at Hydrate Ridge, NE Pacific Ocean, Mar. Ecol. Prog. Ser., 264, 1–14, 2003.

Valentine, D. L., Reddy, C. M., Farwell, C., Hill, T. M., Pizarro, O., Yoerger, D. R., Camilli, R., Nelson, R. K., Peacock, E. E., Bagby, S. C., Clarke, B. A., Roman, C. N., and Soloway, M.: Asphalt volcanoes as a potential source of methane to late Pleistocene coastal waters, Nat. Geosci., 3, 345–348, 2010.

Vernon, J. W. and Slater, R. A.: Submarine tar mounds, Santa Barbara County, Calinfornia, Bull. Am. Assoc. Petrol. Geol., 47, 1624–1627, 1963.

Weiland, R. J., Adams, G. P., McDonald, R. D., Rooney, T. C., and Wills, L. M.: Geological and biological relationships in the Puma appraisal area: From salt diapirism to chemosynthetic communities, Offshore Technology Conference, Houston, Texas, USA, 5–8 May 2008, OTC-19360-PP, 2008.

Whiticar, M. J.: A geochemial perspective of natural gas and atmospheric methane, Org. Geochem., 16, 531–547, 1990.

Williams, A. K., Lawrence, G. M., and King, M.: Exploring for deepwater petroleum systems with satellite SAR (Synthetic Aperture RADAR). Fact or Fiction? Comparing results from two of today's hotspots (Congo and Santos) with two of tomorrow's (Campeche and Cariaco) (2 Poster), Adapted

from poster presentation of the AAPG Annual Convention, Houston, 2006, available at: http://www.searchanddiscovery.com/documents/2006/06100williams/index.htm (last access: 10 March 2016), 2006.

Williamson, S. C., Zois, N., and Hewitt, A. T.: Integrated site investigation of seafloor features and associated fauna, Shenzi field, deepwater Gulf of Mexico, Offshore Technology Conference, Houston, Texas, USA, 5–8 May 2008, OTC 19356, 2008.

The Depositional Record
The journal of the International Association of Sedimentologists
Open Access

ORIGINAL RESEARCH ARTICLE

Methane seepage in a Cretaceous greenhouse world recorded by an unusual carbonate deposit from the Tarfaya Basin, Morocco

DANIEL SMRZKA*, JENNIFER ZWICKER*, SADAT KOLONIC†, DANIEL BIRGEL‡, CRISPIN T.S. LITTLE§, AKMAL M. MARZOUK¶, EL HASSANE CHELLAI**, THOMAS WAGNER†† and JÖRN PECKMANN*,‡

*Department für Geodynamik und Sedimentologie, Universität Wien, 1090 Wien, Austria
†Shell Petroleum Development Company of Nigeria, Port Harcourt, Nigeria
‡Institut für Geologie, Universität Hamburg, Bundesstraße 55, 20146 Hamburg, Germany (E-mail: joern.peckmann@uni-hamburg.de)
§School of Earth and Environment, University of Leeds, Leeds, LS2 9JT, UK
¶Geology Department, Faculty of Science, Tanta University, 31527 Tanta, Egypt
**Department of Geology, Faculty of Sciences Semlalia, Cadi Ayyad University, Marrakech, Morocco
††Lyell Centre, Heriot-Watt University, Edinburgh, EH14 4AS, UK

Keywords
Black shales, carbonate authigenesis, cold seeps, oceanic anoxic events, Tarfaya Basin.

Manuscript received: 30 November 2016; Accepted: 8 February 2017

The Depositional Record 2017; 3(1): 4–37

doi: 10.1002/dep2.24

ABSTRACT

During the Cretaceous major episodes of oceanic anoxic conditions triggered large scale deposition of marine black shales rich in organic carbon. Several oceanic anoxic events (OAEs) have been documented including the Cenomanian to Turonian OAE 2, which is among the best studied examples to date. This study reports on a large limestone body that occurs within a black shale succession exposed in a coastal section of the Tarfaya Basin, Morocco. The black shales were deposited in the aftermath of OAE 2 in a shallow continental sea. To decipher the mode and causes of carbonate formation in black shales, a combination of element geochemistry, palaeontology, thin section petrography, carbon and oxygen stable isotope geochemistry and lipid biomarkers are used. The ^{13}C-depleted biphytanic diacids reveal that the carbonate deposit resulted, at least in part, from microbially mediated anaerobic oxidation of methane in the shallow subseafloor at a hydrocarbon seep. The lowest obtained $\delta^{13}C_{carbonate}$ values of $-23{\cdot}5‰$ are not low enough to exclude other carbon sources than methane apart from admixed marine carbonate, indicating a potential contribution from *in situ* remineralization of organic matter contained in the black shales. Nannofossil and trace metal inventories of the black shales and the macrofaunal assemblage of the carbonate body reveal that environmental conditions became less reducing during the deposition of the background shales that enclose the carbonate body, but the palaeoenvironment was overall mostly characterized by high productivity and episodically euxinic bottom waters. This study reconstructs the evolution of a hydrocarbon seep that was situated within a shallow continental sea in the aftermath of OAE 2, and sheds light on how these environmental factors influenced carbonate formation and the ecology at the seep site.

INTRODUCTION

The Cretaceous was a period in Earth history when major episodes of oceanic anoxic conditions led to large scale accumulation of organic matter in marine sediments (Arthur & Sageman, 1994; Larson & Erba, 1999; Jones & Jenkyns, 2001). These organic-rich deposits have been termed black shales, and phases of their coeval and repeated occurrence in the Phanerozoic rock record have been referred to as oceanic anoxic events (OAEs, Schlanger & Jenkyns, 1976; Weissert *et al.*, 1979; Schlanger *et al.*, 1987; Kerr, 1998; Jenkyns, 2003; Meyer & Kump, 2008). Sea-level was markedly elevated during some periods of the Cretaceous compared to the present due to the

© 2017 The Authors. *The Depositional Record* published by John Wiley & Sons Ltd on behalf of International Association of Sedimentologists. This is an open access article under the terms of the Creative Commons Attribution License, which permits use, distribution and reproduction in any medium, provided the original work is properly cited.

warm, equable climate (Sames *et al.*, 2016 and references therein). The expansion of shallow epicontinental seas, where upwelling and enhanced nutrient flux from the continents increased primary production, enabled the accumulation of organic carbon-rich sediments in water depths of several hundreds of metres (Hallam & Bradshaw, 1977; Weissert, 1981; Kuhnt *et al.*, 1990; Arthur & Sageman, 1994). Two processes held primarily responsible for the deposition of black shales are (1) pulses of enhanced primary productivity accompanied by elevated atmospheric carbon dioxide concentrations and sea surface temperatures (Barron, 1983; Ingall *et al.*, 1993; Forster *et al.*, 2007), and (2) the increased preservation of organic matter within restricted, stratified, oxygen-deficient basins (Mascle *et al.*, 1997; Meyer & Kump, 2008). With supporting evidence for both scenarios, it is likely that both production and preservation in stratified basins increased sequestration rates of organic carbon in Cretaceous marine sediments (Jenkyns *et al.*, 2007; Owens *et al.*, 2013).

Several OAEs have been documented during the Cretaceous including the Aptian to Albian OAE 1, the Cenomanian to Turonian OAE 2 and the Coniacian to Santonian OAE 3 (Jenkyns, 2010 and references therein). The OAE 2, or Bonarelli event (Bonarelli, 1891; Schlanger *et al.*, 1987), is among the best studied examples to date. High rates of sea floor spreading and volcanic activity – both linked to the breakup of Gondwana with the formation of early ocean basins as carbon sinks and the evolution of ocean gateways – led to increasing atmospheric carbon dioxide concentrations followed by a significant turnover of ocean chemistry and extinctions of marine biota (Brumsack, 1980; Arthur *et al.*, 1985; Larson, 1991; Kaiho, 1994; Wagner & Pletsch, 1999; Gale *et al.*, 2000; McAnena *et al.*, 2013). Black shales related to OAE 2 have been reported from many parts of the world including the proto southern North Atlantic and eastern Tethys Oceans (Lüning *et al.*, 2004). During OAE 2 the Tethys and Atlantic Oceans were affected by sluggish circulation of bottom waters caused by the shallow and partly closed connections to neighbouring oceans (Kuypers *et al.*, 2002). Replenishment of oxygen was impeded within these partially isolated basins, favouring the development of anoxic and, possibly, euxinic conditions even in the photic zone (Herbin *et al.*, 1986; Baudin, 1995; Sinninghe Damsté & Köster, 1998; Handoh *et al.*, 1999). Large areas of the continental shelf and slope along the northern parts of Algeria, Libya, Tunisia and Morocco were deprived of oxygen, and enabled the rapid accumulation of shales and limestones rich in organic carbon linked to cyclic perturbations of redox-nutrient cycles and orbital forcing (Leine, 1986; El Albani *et al.*, 1999a; Nederbragt & Fiorentino, 1999; Kolonic *et al.*, 2005; Poulton *et al.*, 2015; for Atlantic-wide teleconnections see Wagner *et al.*, 2013 and references therein).

The Cretaceous has yielded several unusual carbonate deposits occurring before, during and after the OAEs. Some of these deposits have been ascribed to carbonate precipitation related to chemosynthesis-based microbial activity, and include examples from the Western Interior Seaway (Kauffman *et al.*, 1996; Metz, 2010; Kiel *et al.*, 2012) and the northern Tethyan and North African continental margins (Layeb *et al.*, 2012, 2014). Limestones from the Western Interior Seaway feature shallow-water methane-seep deposits that formed during OAE 2 in warm bottom waters (Kiel *et al.*, 2012), and are characterized by ^{13}C-depleted carbonate mineral phases and a high-abundance but low-diversity faunal assemblage. The Campanian organic-rich Pierre Shales comprise numerous peculiar carbonate bodies, collectively known as the Tepee Buttes (Shapiro & Fricke, 2002; Metz, 2010). These deposits are rich in chemosymbiotic macrofaunal communities and exhibit diagnostic ^{13}C-depleted mineral fabrics and ^{13}C-depleted molecular fossils of the anaerobic oxidation of methane (AOM) consortium, confirming that carbonate precipitation was driven by microbial oxidation of methane (Kauffman *et al.*, 1996; Birgel *et al.*, 2006). The fossiliferous Tepee Butte limestones possibly formed during periods of enhanced bottom water oxygenation, supported by the presence of molecular fossils of aerobic methanotrophic bacteria (Birgel *et al.*, 2006). Layeb *et al.* (2012) documented carbonate build-ups from the Lower Cretaceous Fahdene Basin in Tunisia. These limestones reveal a thrombolitic fabric and formed within organic-rich black shales deposited during the Late Albian OAE 1d. The fabric and texture of these limestones suggest the involvement of microbes during their formation below a water body with eutrophic, anoxic waters. Layeb *et al.* (2014) further reported on mound-shaped carbonate structures associated with OAE 2 within Late Cenomanian black shales from the Bahloul Formation in Northern Tunisia. The genesis of the Tunisian limestones possibly involved microorganisms mineralizing large amounts of organic matter, as suggested by ^{13}C-depleted carbonate cements and thrombolitic fabrics (Layeb *et al.*, 2014).

This study reports on a large limestone body associated with black shales deposited in the aftermath of OAE 2 exposed along a coastal section of the Tarfaya Basin, Morocco. A combination of petrography, macro- and micropalaeontology, carbon and oxygen stable isotope and trace element geochemistry, as well as lipid biomarkers has been used to decipher the mode of carbonate accretion that led to the unusual morphology of this limestone body. The potential triggers for carbonate precipitation within the mid-Cretaceous organic-rich

© 2017 The Authors. *The Depositional Record* published by John Wiley & Sons Ltd on behalf of International Association of Sedimentologists.

deposits, and the impact of the prevailing oceanographic and geochemical conditions on the benthonic environment and faunal communities are assessed. Although the Amma Fatma limestone body reveals only a limited number of lithological features typical of hydrocarbon seep carbonates and apparently no endemic seep fauna, it is shown to have resulted from methane seepage. The lack of obligate, endemic seep fauna is interpreted to have been caused by (1) shallow water depth – a factor known to discriminate against seep taxa (Kiel, 2010) – and (2) the eutrophic palaeoenvironment in the aftermath of OAE 2 that favoured photosynthetic primary production and subsequent consumption of organic matter by heterotrophs. This work reveals that seep deposits are difficult to identify in high productivity settings, where chemosynthesis-based seep fauna is likely to be outcompeted by heterotrophic background fauna.

GEOLOGICAL SETTING

Deposits from the Cenomanian–Turonian (C/T) boundary in Northern Africa have been intensively studied in Tunisia and Morocco. This is partly due to the fact that these regions feature up to 800 m thick successions of organic-rich shales and limestones (Kuhnt *et al.*, 2001; Kolonic *et al.*, 2002), making them prolific petroleum source rocks (Leine, 1986) and high resolution climate archives (Kolonic *et al.*, 2005; Kuhnt *et al.*, 2005). The southern Moroccan passive continental margin includes the Tarfaya Basin, one of several palaeo-shelf basins located on the coasts of Senegal, Morocco and Tunisia (Figs 1 and 2A; Lüning *et al.*, 2004; Kolonic *et al.*, 2005). It covers an area of around 170 000 km^2 and features the highest accumulation rates of organic matter from the C/T boundary known to date, as well as one of the largest oil shale deposits in the world (Amblés *et al.*, 1994; Kuhnt *et al.*, 2001). The Tarfaya Basin is situated to the south of the Anti-Atlas Mountains and extends into the Tindouf Basin to the East, the Senegal Basin to the South, and is bordered by the East Canary Ridge to the West (Kolonic *et al.*, 2002). It has been suggested that the basin was a distal section of the proto southern North Atlantic with outer shelf to upper bathyal water depths of 200 to 300 m (Figs 1 and 2B; El Albani *et al.*, 1999b; Kuhnt *et al.*, 2001). It experienced intense upwelling, extended oxygen minimum zones and recurrent pulses of high primary production since at least the Late Cenomanian (Kuhnt & Wiedmann, 1995; El Albani *et al.*, 1999a,b; Kolonic *et al.*, 2002, 2005), leading to pronounced redox cycles on orbital time scales that alternated between sulphidic and anoxic ferruginous water-column conditions (Poulton *et al.*, 2015).

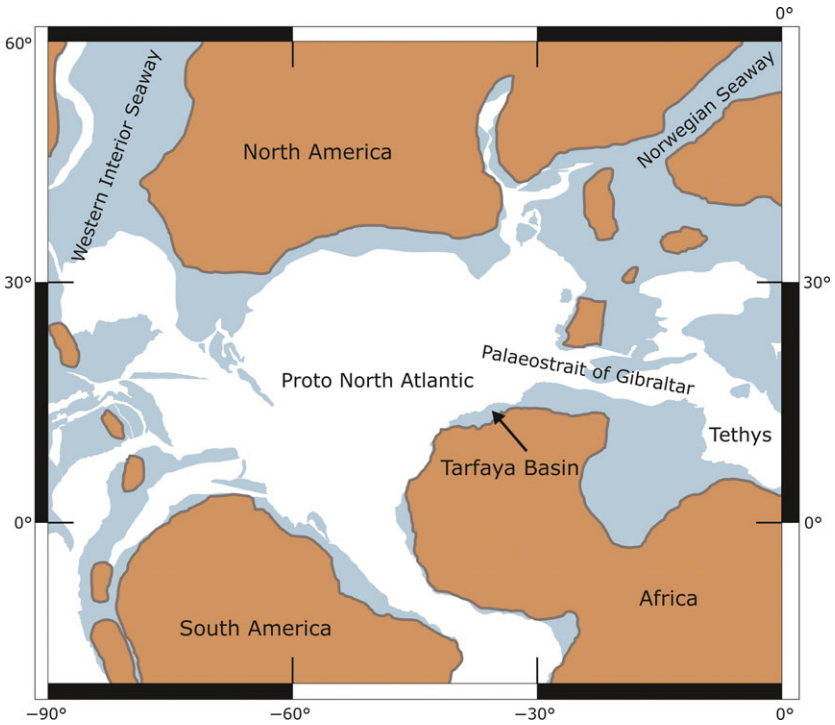


Fig. 1. Palaeogeographical map of the mid-Cretaceous (*ca* 94 Ma) showing the study site within the Tarfaya Basin, Morocco. Light blue areas represent continental plates covered by shallow epicontinental seas, brown areas represent dry land. Brown, thick lines delineate palaeocoastlines (modified from Kuypers *et al.*, 2002).

© 2017 The Authors. *The Depositional Record* published by John Wiley & Sons Ltd on behalf of International Association of Sedimentologists.

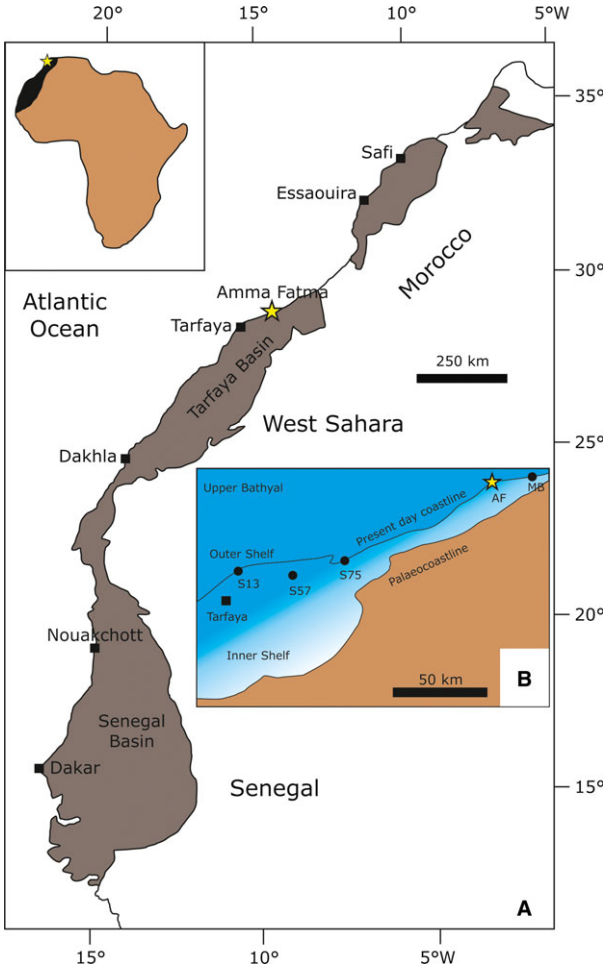


Fig. 2. (A) Locality map showing the distribution of unfolded Mesozoic and Cenozoic Basins containing black shales (grey) from the C/T boundary along the northwestern African continental margin (modified from Kolonic *et al.*, 2005). Yellow stars indicating the Amma Fatma section in (A), (B) and the small inset map in the upper left, which indicates the location of the studied section in Africa. (B) Palaeogeographic map of the Tarfaya Basin (modified from Kolonic *et al.*, 2005); AF = Amma Fatma, MB = Mohammed Plage, S13, S57 and S75 = drill cores described by Leine (1986) and Kolonic *et al.* (2005).

The carbonate body studied here crops out at Amma Fatma Plage, which is a coastal to middle shelf section at the northern edge of the Tarfaya Basin (Fig. 2). Amma Fatma Plage is located *ca* 8 km to the south-west of Mohammed Plage, the latter being a well-studied coastal section of the basin where deposition of organic-rich shales and carbonate beds occurred close to the palaeocoastline (El Albani *et al.*, 1999b; Kolonic *et al.*, 2005). Both sites experienced a series of transgressional cycles during the mid to late Cretaceous that caused repeated and widespread flooding, and initiated the deposition of laminated biogenic sediments associated with OAE 2 (Kolonic *et al.*, 2002, 2005; Gebhardt *et al.*, 2004; Kuhnt *et al.*, 2009; Gertsch *et al.*, 2010). Amma Fatma Plage lies along a 175 km long palaeotransect through the Tarfaya Basin, together with shallow exploration wells S13, S57, S75 and Mohammed Plage (cf. Kolonic *et al.*, 2002, 2005). The transect runs in SW to NE direction and connects its deepest and most distal part at wells S13 and S57 to its most proximal part at Mohammed Plage (Fig. 2B). Exploration well S13 is interpreted as an open-marine shelf setting with water depths of 200 to 300 m, whereas Mohammed Plage and Amma Fatma Plage represent shallower, proximal successions deposited at the northwestern margin of the Sahara platform (Kolonic *et al.*, 2002, 2005; Kuhnt *et al.*, 2009).

MATERIAL AND METHODS

Petrography, mineralogy and palaeontology

Rock samples from the carbonate body and from a vertical profile at Amma Fatma Plage were collected during a field trip in 2003. Samples from the studied sedimentary succession were recovered from a fresh coastal exposure in direct proximity to the carbonate body, and taken at regular intervals of 5 to 10 cm across the profile. A total of 20 samples were collected from various zones of the carbonate body, two further samples were collected from a carbonate bank covering the structure (hereafter referred to as cover bed). Thin sections (150 × 100 mm, 100 × 75 mm) were made at the University of Bremen and the University of Vienna. Thin section microscopy was conducted using a Leica DM4500 P polarization microscope (Wetzlar, Germany). Photographs were taken with a Leica DFC 450 C camera using the Leica Application Suite 4.4.0 software. Additionally, a Nikon SMZ 1500 stereomicroscope coupled to a Prog.Res Speed XT core 5 camera, as well as a Nikon Optiphot-2 optical microscope (Tokyo, Japan) were used for petrographic observations using the software Prog.Res Capture pro 2.8 for image analysis and camera control. To discriminate the different carbonate minerals under the microscope, several thin sections were stained with a mixture of potassium ferricyanide and alizarin red S solution dissolved in 0·1% hydrochloric acid (cf. Dickson, 1966). Powdered samples for X-ray diffraction (XRD) and carbon and oxygen stable isotope analyses were obtained from polished rock slabs using a hand-held microdrill at low to medium rotational speed. For XRD analysis, powdered samples were analysed with a Panalytical PW 3040/60 X'Pert PRO (CuKα radiation, 40 kV, 40 mA, step size 0·0167·5 s per step) diffractometer at the University of Vienna. X-ray diffraction patterns were interpreted using the Panalytical software "X'Pert High score plus". Calcareous nannoplankton

© 2017 The Authors. *The Depositional Record* published by John Wiley & Sons Ltd on behalf of International Association of Sedimentologists.

assemblages were studied in 150 samples with a high-resolution spacing of about 4 to 7 cm within the slabbed intervals. For the calcareous nannoplankton, smear slides were prepared using techniques described in Bramlette & Sullivan (1961) and Hay (1961, 1965). The slides were examined at a magnification of about 1250 times under both cross-polarized and phase-contrast illumination.

Inorganic geochemistry – Total organic carbon, carbon and oxygen stable isotopes and trace elements

Total carbon (TC) and total organic carbon (TOC) contents of the Amma Fatma carbonate body were determined using a LECO RC-612 Carbon Analyzer (St. Joseph, MI, USA), equipped with a solid-state infrared detector at the Department of Environmental Geosciences at the University of Vienna. All samples were ground to fine powder in an agate mortar prior to measurements. To measure TC, carbon dioxide was released at a temperature of 1000°C. Prior to sample measurements a pure $CaCO_3$ standard (Co. Merck, Kenilworth, NJ, USA) was measured, revealing a relative standard deviation of 0·06%. The TOC contents were determined at 550°C. A Synthetic Carbon Leco 502-029 (1·01 ± 0·02 carbon%) standard was measured prior to sample analyses and a standard deviation of 0·005% was calculated. Carbonate ($CaCO_3$%) contents were calculated according to the equation: $CaCO_3\% = (TC - TOC) \times 8{\cdot}333$. All black shale samples were carefully dried and ground in an agate mortar. The TIC and TOC contents of black shales were measured using a LECO CS-300 carbon-sulphur analyser at the Geoscience Department, University of Bremen. Before TOC determination, inorganic carbon was carefully removed by repetitive addition of 0·25 N HCl. The $CaCO_3$ contents were calculated as above (precision of measurements ±3%). The $\delta^{13}C_{TOC}$ values (±0·1‰ vs. Vienna Pee Dee belemnite, V-PDB) were determined on decalcified sediment samples using automated on-line combustion followed by conventional isotope-ratio mass spectrometry.

A total of 48 sample powders from 12 different samples throughout the Amma Fatma carbonate body were analysed for their stable carbon and oxygen isotope content. Sample powders were obtained from polished rock slabs using a hand-held microdrill. Stable carbon and oxygen isotope analyses were performed at the light stable isotope laboratory of the Institute of Earth Sciences, Karl-Franzens University, Graz. Effective accuracy was ±0·05 for $\delta^{13}C$ values and ±0·11 for $\delta^{18}O$ values. The $\delta^{13}C$ and $\delta^{18}O$ values are reported relative to V-PDB (standard deviation smaller than 0·04‰), and appropriate correction factors were applied.

Trace metal compositions of black shales and limestones were determined using X-ray fluorescence (XRF) spectrometry on fused-borate glass beads, and by inductively coupled plasma atomic emission spectrometry (ICP-AES). The XRF calibration curves were based on international standard reference material. For ICP-AES, about 50 mg of sample powder was digested in a mixture of 3 ml HNO_3 (65%), 2 ml HF (40%) and 2 ml HCl (36%) of suprapure quality at 200°C and 30 kbar in closed Teflon vessels (Heinrichs *et al.*, 1986). Sample powders were then dried by evaporation, and the residue was re-dissolved in 0·5 ml HNO_3 (65%) and 4·5 ml deionized water. The solutions were analysed with ICP-AES, and the results were checked with international standard reference material. Relative standard deviations in duplicate measurement were below 3%. Enrichment factors (EFs) of trace elements were calculated according to Brumsack (2006):

$$EF_{element} = (element/Al)_{sample}/(element/Al)_{average\ shale}$$

Average shale refers to the composition of collected shale samples compiled by Wedepohl (1969). An element with an EF either above or below 1 is considered to be enriched or depleted compared to average shale, respectively.

Organic geochemistry – Lipid biomarkers

Four carbonate rock samples were chosen for biomarker analysis, one from the cover bed and one from each of the zones 4, 3 and 1. The samples were cleaned repeatedly by washing with 10% hydrochloric acid (HCl) and then dichloromethane (DCM) to avoid any contamination, and then ground to fine powder. All carbonates were treated with a 'two-step extraction procedure' to discriminate preferentially intercrystalline-bound from preferentially intracrystalline-bound molecular fossils (cf. Thiel *et al.*, 1999; Guido *et al.*, 2013), and to separate compounds tightly associated with the carbonate matrix from easily extractable compounds. To obtain preferentially intercrystalline-bound compounds, the ground samples were extracted by ultrasonication in DCM : MeOH (3 : 1) nine times until the solvents became colourless to get the first total lipid extract (TLE). This extract is referred to as the extract before decalcification below. To obtain preferentially intracrystalline-bound molecular fossils, the residual sediment of the first extraction step was decalcified and then extracted again. In detail, doubly distilled water was added and 10% HCl was slowly poured onto the samples. To avoid transesterification reactions at low pH, HCl addition was stopped when *ca* 75% of the carbonate was dissolved. The remaining sample powder was centrifuged and extracted as described above to

 © 2017 The Authors. *The Depositional Record* published by John Wiley & Sons Ltd on behalf of International Association of Sedimentologists.

obtain a second TLE. This extract is referred to as the extract after decalcification below. From here on, the extracts before and the extract after decalcification are treated in the same fashion. After washing with clean water, the samples were saponified with 6% potassium hydroxide (KOH) in methanol (MeOH) to release bond carboxylic acids. The supernatants were decanted and the residues were subsequently extracted via ultrasonication in DCM/MeOH (3 : 1; v : v) four times until the solvents became colourless. The combined extracts were then treated with 10% HCl to transfer the free fatty acids (FAs) to the organic solvent phase. For gas chromatography (GC) analyses the extracts were dried with sodium sulphate and the TLE of both extraction procedures were separated by column chromatography. Alcohols were derivatized by adding 100 µl pyridine and 100 µl N,O-bis(trimethylsilyl) trifluoracetamide (BSTFA) to the alcohol fraction at 70°C for 30 min. The derivatized fraction was dried under a stream of nitrogen (N_2) and dissolved in *n*-hexane prior to injection. The alcohol fractions are not described below due to the lack of pristine compounds. Free carboxylic acids were reacted with 1 ml 14% boron trifluoride (BF_3) in MeOH at 70°C for 1 h to form FA methyl esters. After cooling, the mixture was extracted four times with 2 ml *n*-hexane. Combined extracts were evaporated under a stream of N_2 and redissolved in *n*-hexane before injection. The derivatized carboxylic acid fractions were analysed using GC-mass spectrometry (GC-MS) with an Agilent 7890 A GC system coupled to an Agilent 5975C inert MSD mass spectrometer. Quantification was done using GC-flame ionization detection (GC-FID) with an Agilent 7820 A GC system. Internal standards used were 5α-cholestane for the hydrocarbon and 2-Me-C_{18} FA for the carboxylic acid fractions. Both GC systems were equipped with HP-5 MS UI fused silica columns (30 m × 0·25 mm i.d., 0·25 µm film thickness). Helium was used as the carrier gas. The GC temperature program for hydrocarbons and carboxylic acids was 60°C (1 min) to 150°C at 10°C min^{-1}, then to 320°C (held 25 min) at 4°C min^{-1}. Compound assignment was based on retention times and published mass spectra.

Compound-specific stable carbon isotope analysis was performed using a Thermo Fisher Trace GC Ultra connected via a Thermo Fisher GC Isolink interface to a Thermo Fisher Delta V Advantage spectrometer at the Department of Terrestrial Ecosystem Research, University of Vienna. Compound-specific carbon isotope values are given as δ values in per mil (‰) relative to V-PDB. The $\delta^{13}C$ values of carboxylic acids (methyl esters) were corrected for additional carbon introduced after derivatization. Each measurement was calibrated using several pulses of carbon dioxide (CO_2) of known isotopic composition prior to and after the run. Precision was checked with an *n*-alkane mixture (C_{14} to C_{38}) of known isotopic composition. Analytical standard deviation was <0·7‰.

RESULTS

Amma Fatma section – Lithology, biostratigraphy and inorganic geochemistry

The complete section at Amma Fatma Plage measures *ca* 14 m from top to bottom and features cyclic alternations of black shales, siltstones and organic-rich, marly limestone beds (Figs 3 and 4). The limestones are represented by (1) carbonate nodules mainly composed of mudstones and wackestones that are aligned parallel to stratification and (2) discontinuous bioclastic storm beds with hummocky cross-stratification (cf. El Albani *et al.*, 1999b). The limestones contain Foraminifera, calcispheres, molluscs including ammonites, brachiopods, variable amounts of quartz grains and are partly bioturbated. A detailed microfacies analysis is included in El Albani *et al.* (1997, 1999a). The succession of 22 beds is shown by the stratigraphic chart of the outcrop in Figs 3 and 5. Limestone and black shale beds alternate regularly, whereby their thicknesses measure 20 to 80 cm and 60 to 300 cm, respectively. Beds comprising limestone nodules with chert measure up to 20 cm in thickness. One exception is a 1 m thick bed 3 m above the base of the profile featuring large carbonate nodules with a corona made of chert. Calcium carbonate and TOC contents of the black shale beds vary from 60 to 90% and 4 to 9%, respectively. Calcium carbonate and TOC values throughout the section are shown in Table 1. The characteristic positive $\delta^{13}C_{TOC}$ excursion that is prominently observed across the C/T boundary in adjacent sites is not found at Amma Fatma Plage, supporting a post OAE period of deposition. The measured $\delta^{13}C_{TOC}$ values vary slightly between −26·2 and −27·8‰.

Biostratigraphic data confirm the positioning relative to the OAE 2 carbon isotope excursion, placing the investigated sedimentary succession within the *H. helvetica* planktonic foraminiferal zone and the *coloradoense* and *nodosoides* ammonite zone of the upper part of the Lower Turonian stage (cf. Marzouk & Lüning, 2005). The position of the nannofossil zonal datum marker CC11/CC12 is placed at about 9·5 m above the *helvetica* and *nodosoides* zones. Planktonic Foraminifera are present in very high numbers and benthonic foraminiferal faunas are of low diversity. A highly diverse and highly abundant calcareous nannofossil flora was observed in all samples studied. Preservation is moderate, except in the uppermost part of the section (from 13·5 m onwards), where preservation is good. *Watznaueria barnesae* and *Eiffelithus turriseffeilii* are abundant throughout the section (except

© 2017 The Authors. *The Depositional Record* published by John Wiley & Sons Ltd on behalf of International Association of Sedimentologists.

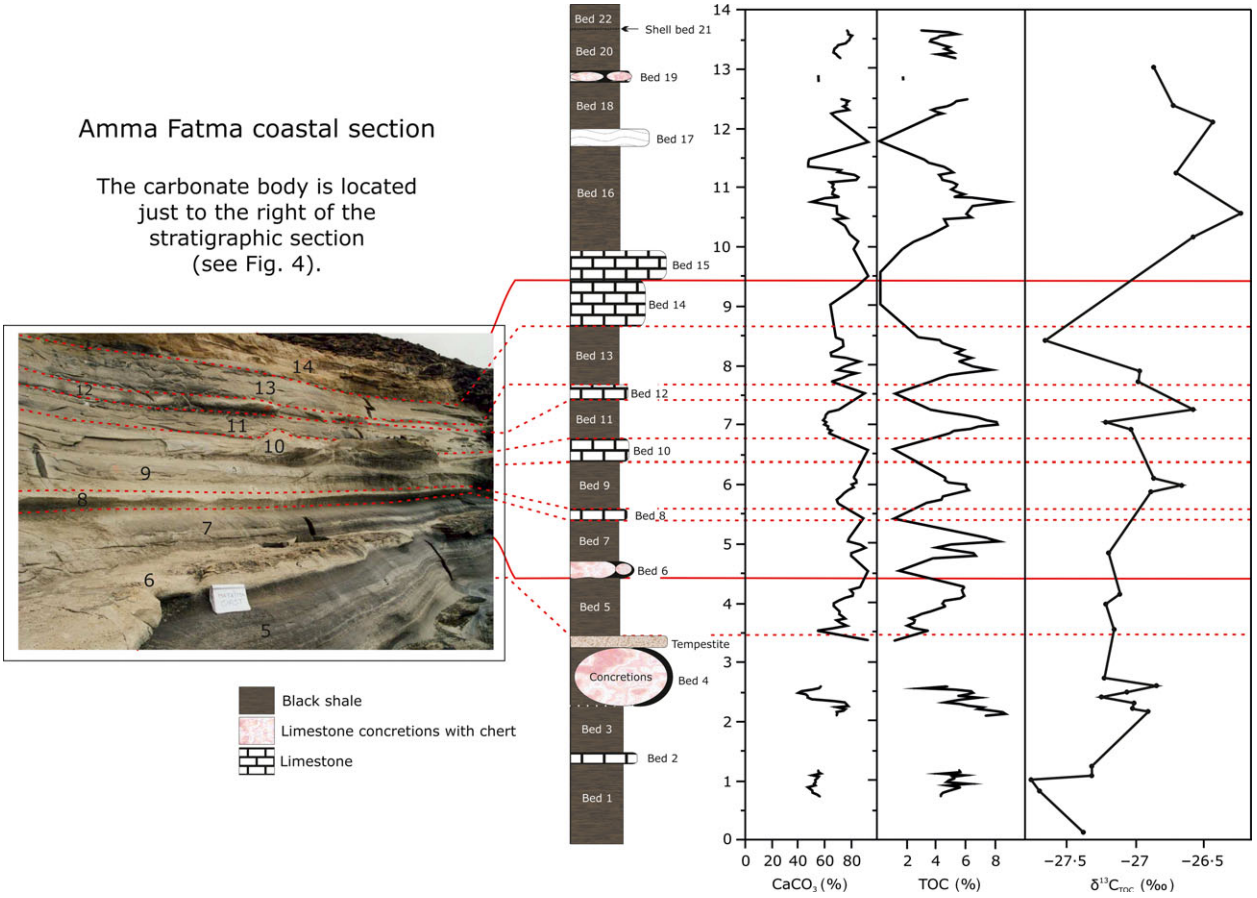


Fig. 3. (Left) Photograph of the Amma Fatma outcrop section showing beds 5 to 14 separated by dashed red lines; the Amma Fatma carbonate body lies within beds 6 to 14 delimited by the thick red lines (cf. Fig. 4). (Centre) Lithostratigraphic chart of the Amma Fatma coastal section showing lithologies and their corresponding thickness. (Right) $CaCO_3$ content, total organic carbon (TOC) content and its carbon stable isotope composition within the corresponding beds.

in two carbonate beds), and are known to be very resistant to solution. Although frequent, the abundance of *Watznaueria barnesae* does not surpass 40%, a cut-off value proposed by Roth & Krumbach (1986) to indicate that nannofossil distribution patterns can still largely be used for palaeoecological interpretations, despite diagenetic and syndepositional dissolution. Notably, *Cyclagelosphaera margerelii* shows a similarly abundant distribution and, therefore, appears to be also solution resistant.

The nannofossil distribution in the Amma Fatma section is characterized by many species having longer term, gradual changes, with only some species exhibiting stronger, high-frequency abundance fluctuations over a few centimetres (*Tranolithus orionatus*, *Zeugrhabdus diplogrammus*). Abundant species throughout the section include *Zygodiscus erectus*, *Rhagodiscus splendens* and *Eprolithus floralis*. *R. splendens* occurs in moderate and high abundances in the lowermost and uppermost parts of the studied section, and is absent in the interval in-between. Notably, the distribution of *E. floralis* in the section is characterized by similar abundance peaks at the base and top of the section. Other identified species *Broisonia* spp. (except *B. enormis*) and *Gartnerago* spp. (Thierstein, 1976; Hattner *et al.*, 1980) are notably rare throughout the section. An exception is a *Gartnerago segmentatum* abundance peak between 7·5 and 8 m. Abundance and distribution of all identified nannofossil species and phosphorus content throughout the Amma Fatma section are shown in Fig. 5.

Total contents of all measured elements are shown in Table 1. Prominent trace metal enrichment is restricted to stratigraphic intervals that correspond to the organic carbon-rich black shales. Trace metal patterns vary across the section between alternating black shales and limestone beds, and also within the black shale successions themselves. Calculated EFs of trace metals whose deposition is influenced by bottom and pore water redox conditions are plotted with depth in Fig. 6. Mean trace metal

 © 2017 The Authors. *The Depositional Record* published by John Wiley & Sons Ltd on behalf of International Association of Sedimentologists.

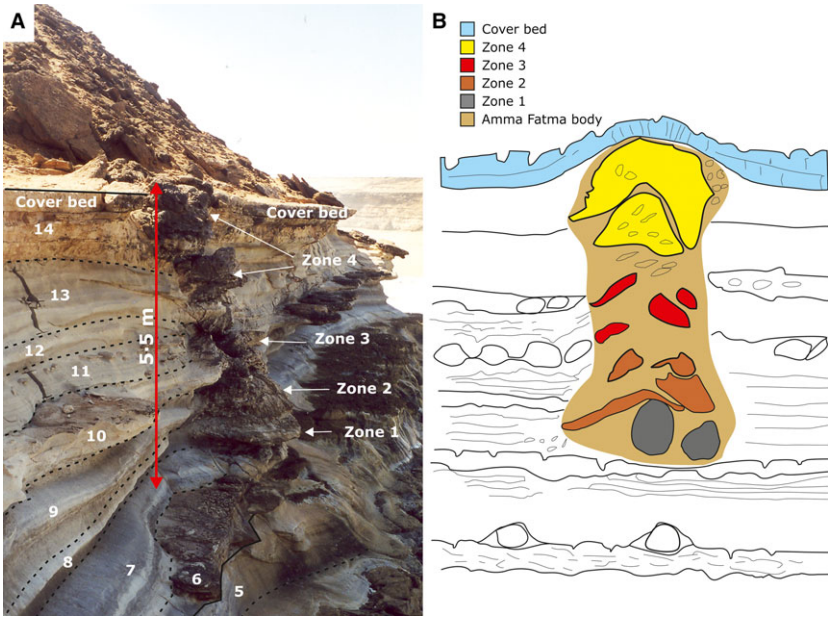


Fig. 4. (A) Photograph of the Amma Fatma carbonate body with its four zones highlighted by arrows amongst the beds shown in Fig. 3. (B) Schematic sketch of the Amma Fatma body highlighting the four zones from bottom to top and the cover bed capping the body.

concentrations and EFs of black shale and limestone beds that correspond to zones 1 to 4 and the cover bed are shown in Tables 2 and 3, respectively. Zone 1 shows the lowest concentration of several major elements including Al, Mg, Fe and Mn (Tables 1 and 2). Particularly, zone 1 has an Al content that is half that of zone 4, which has a considerable effect on calculated EFs. Zone 4 reveals relatively high Al contents, and all EFs are higher in the lower zones 1 and 2 compared to zone 4 (Table 3). As EFs may be exaggerated due to varying Al content, they must be considered together with absolute contents of the respective elements. This is particularly the case for bed 14, which consists mainly of marly limestone and exhibits low Al concentrations. Chromium, Co and U are the only trace metals whose concentrations increase from zone 1 to 4 (Table 2), whereas Mo concentrations in zone 1 and 4 are almost equal. There is a distinct peak of all trace metals except Cr and Co in zone 3, which is not as apparent in respective EFs due to high Al contents in this zone. Bed 14 exhibits the lowest contents of most trace metals with the exception of U. Molybdenum/U ratios decrease steadily from bottom to top and fall below unity in bed 14. Correlation coefficients between trace metals and Al, as well as between trace metals themselves were calculated and are shown in Table 4. The only trace metals that exhibit correlation with Al are Cr and Co, with the latter correlated better than the former. Trace metal correlations can be distinguished into three groups of elements that correlate well among each other, these being (1) Cr with Cu, (2) Mo with Ni, Zn and V and (3) Zn with Ni and Cd (Table 4).

The Amma Fatma carbonate body

The carbonate body associated with black shales (Figs 3 and 4) is enclosed by beds 6 to 14 of the Amma Fatma section, and measures 5·5 m in height and 3·6 m in width. The carbonate body was divided into 4 zones, illustrated in a schematic sketch (Fig. 4B). Zones 1 and 2 comprise the base and lowermost part of the structure and feature concretionary and nodular carbonates penetrated by numerous veins made of secondary precipitates (Fig. 7). A carbonate bank measuring 17 to 19 cm in thickness separates zone 1 from 2 (Fig. 7B). Zone 3 comprises the middle part of the body, and features massive limestone blocks and nodules. Zone 4 is the topmost part of the carbonate body and yielded abundant molluscan fossils, as well as cylindrical to tubular trace fossils (Fig. 8C). The top of the body is capped by a 15 to 20 cm thick carbonate bank, referred to as a cover bed (Figs 4 and 8A to C), which corresponds to bed 14 of the section (Figs 3 and 4A).

The Amma Fatma carbonate body – Petrography and mineralogy

Micrite (i.e. microcrystalline calcite with a crystal size below 10 μm) is the dominant primary mineral that

© 2017 The Authors. *The Depositional Record* published by John Wiley & Sons Ltd on behalf of International Association of Sedimentologists.

Table 1. Total concentrations of all measured elements of the Amma Fatma black shale section. All data are given in ppm except depth (in m), $CaCO_3$ and total organic carbon (TOC) content (both in %)

Depth [m]	$CaCO_3$ [%]	TOC [%]	Ti	Al	Ba	Ca	Fe	K	Mg	Mn	P	Cr	Mo	Ni	Zn	Cu	V	Pb	As	Cd	Co	Re	U
13·5	10·0	3·62	342	6342	664	293 386	2946	3567	9149	41·7	716	28·6	10·3	44·6	40·2	10·6	93·1	2·07	7·19	1·36	1·97	0·050	9·93
13·4	34·6	5·66	426	6792	43·7	279 035	3381	4069	8796	35·0	528	35·3	22·6	67·5	139	13·7	154	2·04	7·13	2·55	2·00	0·100	9·05
13·3	18·9	4·13	501	8446	52·3	284 508	4474	4613	10 626	46·1	438	34·5	20·7	53·8	75·5	10·7	183	1·76	7·38	2·14	2·12	0·040	8·73
13·1	19·9	5·47	614	11 928	60·6	252 778	6346	5416	9189	44·7	1419	40·8	23·9	63·1	79·8	11·6	206	2·42	9·41	2·10	2·51	0·060	9·15
13·0	27·7	5·59	421	9278	54·3	264 626	4559	4146	7795	38·4	1103	46·6	23·4	62·4	111	12·7	192	2·32	8·87	3·03	1·95	0·050	8·01
12·9	19·5	2·51	1158	15 361	81·5	211 050	8242	7054	16 448	81·5	735	43·4	23·3	59·8	78·3	11·3	246	3·12	9·04	1·76	3·13	0·020	6·14
12·4	36·4	6·28	550	9047	57·7	263 207	4937	4656	9411	42·4	724	40·6	26·4	78·0	146	13·4	161	2·59	7·31	3·12	2·27	0·110	8·47
12·3	33·3	5·32	473	7043	60·0	276 795	2912	4008	8186	36·3	613	39·7	13·2	55·8	133	11·9	106	2·11	7·11	2·80	1·97	0·060	8·99
12·1	29·7	4·37	833	11 564	64·2	243 988	5638	5432	14 622	58·9	522	46·1	22·7	68·8	119	15·4	160	2·95	9·22	2·39	2·49	0·090	9·39
11·7	2·7	0·231	60·0	967	85·2	363 527	523	513	3699	38·4	122	4·61	3·00	6·89	10·7	1·90	38	1·04	3·06	1·02	1·06	0·020	0·756
11·2	28·8	3·78	1786	22 793	108	188 394	11 925	9355	18 824	102	612	58·8	18·6	56·0	115	15·5	185	4·30	15·1	2·67	4·58	0·030	5·54
11·1	37·6	5·43	1065	13 377	82·4	240 279	6123	6743	14 798	70·0	633	53·9	17·1	54·5	150	17·5	170	3·31	11·4	4·96	2·72	0·040	7·96
10·9	21·2	5·67	1066	14 505	88·5	253 042	6787	6767	12 459	66·6	830	62·2	13·2	45·7	84·9	18·0	127	3·22	11·9	1·70	3·06	0·050	6·34
10·8	28·4	6·07	1006	13 631	85·0	251 781	5493	6760	13 487	65·9	616	59·3	8·54	52·3	114	15·3	97·7	2·73	10·3	2·25	3·05	0·040	5·07
10·7	49·1	6·54	793	12 000	72·1	234 427	6510	5709	12 893	65·3	505	63·9	18·9	82·6	197	23·0	160	4·00	13·3	3·89	3·13	0·060	9·04
10·6	47·4	6·46	647	9490	63·3	244 942	4457	4428	10 286	49·0	557	51·9	15·9	73·2	190	18·4	135	3·06	10·8	3·96	2·48	0·030	9·58
10·4	34·0	5·09	785	10 620	76·2	229 982	4745	5950	17 944	60·0	469	46·9	9·46	56·7	136	12·1	86·2	2·89	12·4	2·97	2·45	0·030	7·31
10·2	14·0	2·37	597	7754	53·4	245 794	3220	4770	30 725	70·2	262	21·7	3·57	26·5	55·9	8·11	31·8	1·54	7·68	1·37	2·13	0·020	6·39
9·91	3·48	0·068	116	1695	76·5	346 508	781	1229	6814	31·5	131	6·61	3·44	5·30	13·9	3·08	13·8	1·17	11·5	1·38	1·13	0·040	1·86
9·35	3·62	0·093	170	2556	37·7	303 607	548	1959	8324	27·7	142	18·2	2·27	5·86	14·5	5·66	48·3	1·56	5·67	1·83	1·14	0·030	5·20
8·67	11·3	0·064	498	7031	55·6	279 359	3260	3950	14 793	54·0	609	31·6	5·18	19·2	45·2	5·28	127	3·27	9·52	3·07	2·90	0·030	6·37
8·39	21·9	3·45	918	13 497	80·8	239 388	6821	5831	23 383	75·9	613	41·1	13·0	42·5	87·7	11·9	150	2·77	13·0	1·47	2·67	0·020	6·41
8·20	31·7	6·03	779	11 637	76·1	242 917	5315	5620	19 351	59·6	683	59·5	19·1	52·9	127	24·6	148	2·99	11·6	1·62	2·29	0·050	7·67
8·07	21·8	6·51	602	9544	79·3	268 301	3827	4640	9738	43·7	825	51·0	19·2	47·4	87·2	16·5	135	2·69	8·86	1·60	1·90	0·040	9·77
7·87	25·1	7·63	526	10 743	96·0	259 113	4782	4902	8169	41·0	688	59·7	23·6	55·2	101	19·2	167	3·14	10·7	1·69	2·09	0·040	10·1
7·8	17·9	5·20	452	6305	55·8	289 013	2794	3134	7930	36·4	583	38·2	13·1	40·2	71·6	13·2	98·8	2·10	7·82	1·64	1·74	0·020	7·87
7·69	15·4	4·15	995	14 670	81·4	236 752	6152	5843	18 177	68·2	426	53·7	10·8	32·1	61·7	13·0	107	3·10	9·98	1·52	2·56	0·040	5·61
7·45	10·8	1·17	485	7054	134	301 984	2927	3015	9045	43·0	197	19·1	6·01	14·0	43·3	6·67	57·5	2·01	7·05	1·32	1·55	0·002	2·40
7·22	21·3	4·08	846	11 967	84·7	277 504	4594	4909	10 053	52·9	695	46·0	10·6	44·9	85·2	11·8	121	2·48	8·63	5·10	2·87	0·030	5·95
7·13	43·4	5·94	1029	14 959	85·1	245 875	7350	5747	9414	54·0	930	55·8	25·1	85·5	174	19·8	247	4·03	11·9	4·87	3·62	0·080	9·35
7·00	90·3	8·00	969	13 749	79·2	243 523	6853	5450	9233	49·5	1122	59·3	36·7	122·0	361	25·0	403	4·27	12·3	8·24	3·55	0·150	12·2
6·94	70·9	6·45	972	14 450	80·3	246 417	7215	5654	11 185	54·8	857	55·0	31·4	99·2	284	20·3	322	4·21	12·6	6·89	3·42	0·220	9·57
6·88	44·3	5·26	1057	15 136	85·1	247 997	7506	5896	13 140	59·3	1083	55·5	25·4	78·6	177	17·4	254	4·46	13·0	4·32	3·23	0·160	9·70
6·5	5·5	1·00	220	3212	39·5	354 767	1272	1392	5525	40·7	199	11·9	3·74	12·6	22·1	4·29	64·6	1·54	4·88	1·42	1·38	0·020	1·97
6·05	23·2	4·96	422	6315	58·2	303 839	2701	3090	7409	35·6	610	38·2	13·9	52·6	92·9	12·5	88·2	2·53	7·17	2·56	2·16	0·060	7·66
5·93	33·0	6·34	570	8509	61·6	291 161	3829	3824	7684	41·8	550	36·4	15·7	63·4	132	14·7	108	3·14	7·80	3·29	2·31	0·050	6·48
5·82	29·5	4·77	920	13 799	82·0	260 758	6191	5599	14 255	66·6	515	49·1	16·8	53·3	118	13·8	121	3·19	11·1	3·01	3·04	0·030	5·20
5·44	11·7	1·12	509	7378	107	312 712	3433	3224	9423	50·9	250	19·5	5·40	17·2	46·8	5·33	40·4	2·13	6·66	1·90	2·27	0·020	1·70
4·92	61·2	8·09	351	5401	55·4	300 061	2429	2891	8959	32·0	753	48·6	22·7	96·5	245	16·0	173	3·25	7·90	5·75	2·18	0·060	8·54
4·85	38·0	4·48	251	4097	44·5	330 172	1950	2190	7617	31·7	574	38·8	16·9	62·5	152	11·2	161	2·72	5·43	4·80	1·96	0·050	6·80
4·78	72·8	6·73	467	7096	58·7	296 750	3893	3377	10 794	45·8	956	45·1	28·3	94·6	292	15·9	231	3·34	8·76	7·55	2·50	0·050	7·76

(*Continued*)

© 2017 The Authors. *The Depositional Record* published by John Wiley & Sons Ltd on behalf of International Association of Sedimentologists.

Table 1. Continued.

Depth [m]	$CaCO_3$ [%]	TOC [%]	Ti	Al	Ba	Ca	Fe	K	Mg	Mn	P	Cr	Mo	Ni	Zn	Cu	V	Pb	As	Cd	Co	Re	U
4·75	37·1	4·29	506	7904	61·0	304 941	3895	3588	12 375	53·6	662	37·1	19·8	64·1	149	11·9	194	3·08	6·95	5·29	2·39	0·050	5·96
4·55	14·7	1·46	193	3026	56·0	336 650	1400	1634	6612	41·6	358	15·2	3·67	18·5	59·0	4·98	83·2	2·24	4·18	1·72	1·51	0·020	2·54
4·23	37·4	6·10	423	6121	66·4	307 471	2695	2839	7314	33·8	704	41·1	14·2	63·9	150	13·2	124	2·79	7·10	4·57	2·14	0·050	8·24
4·08	29·1	6·10	549	8718	63·0	294 824	3456	3196	7015	33·8	482	40·6	19·0	51·0	117	13·5	150	3·79	8·14	3·02	2·02	0·020	7·12
3·91	36·0	5·01	918	13 538	77·5	258 689	6963	4864	14 672	61·5	604	46·6	21·4	61·4	144	13·8	199	3·67	11·2	4·18	2·93	0·050	6·93
3·62	17·9	3·20	1139	16 723	92·1	280 049	8198	5923	13 293	81·8	504	41·1	14·0	39·9	71·5	12·1	157	3·20	12·9	2·04	3·02	0·010	5·16
3·48	20·6	4·02	1623	23 868	124	209 749	11 962	8254	16 204	93·5	501	80·6	16·2	44·7	82·5	15·4	190	4·00	17·0	2·13	4·05	0·040	5·41
3·14	5·70	1·05	335	4713	124	348 899	2432	1764	7141	40·0	198	13·3	4·46	15·0	22·8	4·10	78·4	1·81	5·71	0·98	1·56	0·020	1·64
2·65	37·8	5·11	1130	16 500	94·2	222 161	8856	6632	15 091	68·3	730	43·7	27·0	73·3	151	16·1	362	4·11	13·8	3·60	3·32	0·030	7·12
2·62	37·9	3·75	888	13 315	81·0	220 796	6738	5278	12 784	58·9	628	35·1	21·4	58·7	152	12·2	296	3·05	10·4	2·79	2·82	0·060	5·86
2·52	57·1	6·61	1557	22 446	114	169 364	12 514	8565	17 283	82·3	974	55·7	35·1	84·4	229	19·3	428	4·76	18·7	6·54	4·18	0·110	9·49
2·47	56·9	5·75	1508	21 271	117	180 611	11 811	8226	16 347	80·2	846	71·7	37·5	84·5	228	18·6	414	4·61	18·4	4·93	4·20	0·030	9·19
2·42	59·3	6·90	1405	20 537	112	180 636	10 620	7893	15 405	70·7	850	55·3	36·7	84·6	238	20·2	389	5·03	17·5	4·93	3·90	0·030	8·98
2·33	29·6	4·99	652	8907	92·3	272 670	4273	4067	10 505	47·3	706	35·4	18·3	44·1	118	11·3	198	2·90	8·26	2·23	2·05	0·050	6·57
2·23	41·7	6·90	624	9153	75·6	268 239	4562	3946	7994	44·6	849	37·5	29·6	67·6	167	16·7	222	3·49	9·78	3·75	2·06	0·070	9·17
2·14	52·1	8·47	649	10 269	74·0	257 396	4016	4293	6995	35·9	510	47·5	30·8	88·5	208	18·6	267	3·22	10·0	4·38	2·34	0·070	8·37
2·09	52·1	7·33	672	10 629	76·6	257 256	39	4515	7951	38·8	484	48·6	22·4	78·4	209	16·6	244	3·21	10·7	3·75	2·27	0·090	8·40
1·24	59·0	5·83	1333	20 823	101	199 540	10 035	6974	19 995	71·9	621	62·8	31·4	67·9	236	18·1	332	4·53	14·6	5·21	3·49	0·010	5·46
1·18	42·6	4·81	1424	22 475	103	203 908	10 222	7184	18 097	65·7	466	59·1	25·1	53·5	170	17·0	299	4·92	17·4	2·80	3·40	0·002	4·49
1·15	87·1	6·10	1479	23 513	108	186 148	11 410	7741	22 088	80·7	722	65·3	36·9	85·6	349	20·0	380	5·02	16·6	7·03	4·18	0·020	6·54
1·02	53·9	5·09	1534	24 136	109	192 277	11 533	7682	19 396	75·2	513	65·4	27·6	71·5	216	18·0	306	4·88	16·9	5·01	4·24	0·020	5·31
0·990	71·5	6·32	1459	23 156	105	186 532	10 952	7669	21 246	75·9	651	63·8	34·9	82·0	286	19·9	343	4·98	16·2	6·46	3·86	0·030	6·20
0·960	42·0	5·15	1538	23 965	109	193 622	10 423	7714	19 272	73·0	473	66·2	30·6	72·6	168	19·1	299	4·99	17·7	3·38	4·39	0·030	5·48
0·920	35·5	5·87	1708	26 651	116	156 833	12 810	8534	20 359	80·0	554	53·4	25·2	68·0	142	16·5	274	4·24	16·3	3·22	3·83	0·040	7·99
0·730	21·5	4·75	1428	21 727	107	184 326	11 082	6854	13 574	72·0	1329	54·8	10·0	47·4	86·0	14·8	106	3·11	12·2	1·70	3·08	0·020	9·73
0·030	44·9	4·43	1148	16 750	89·4	207 076	6587	5357	9817	57·9	440	67·20	28·76	86·6	180	23·2	302	5·74	22·3	4·27	4·70	0·040	6·71

© 2017 The Authors. *The Depositional Record* published by John Wiley & Sons Ltd on behalf of International Association of Sedimentologists.

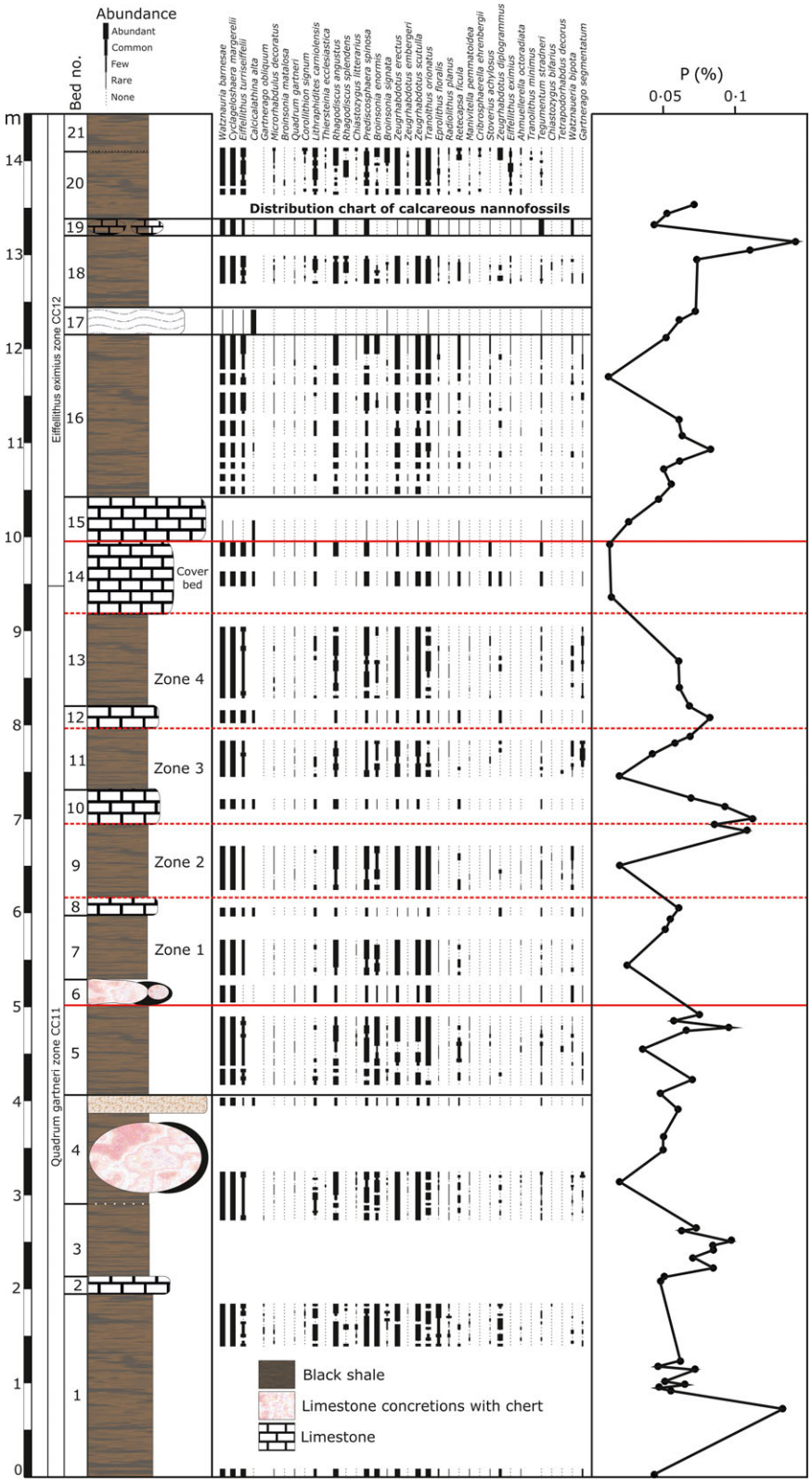


Fig. 5. Distribution chart of nannofossils and phosphorus content across the Amma Fatma section. Solid red lines delineate upper and lower boundaries of the Amma Fatma carbonate body; dashed red lines outline zones 1 to 4 and the cover bed (cf. Fig. 4).

© 2017 The Authors. *The Depositional Record* published by John Wiley & Sons Ltd on behalf of International Association of Sedimentologists.

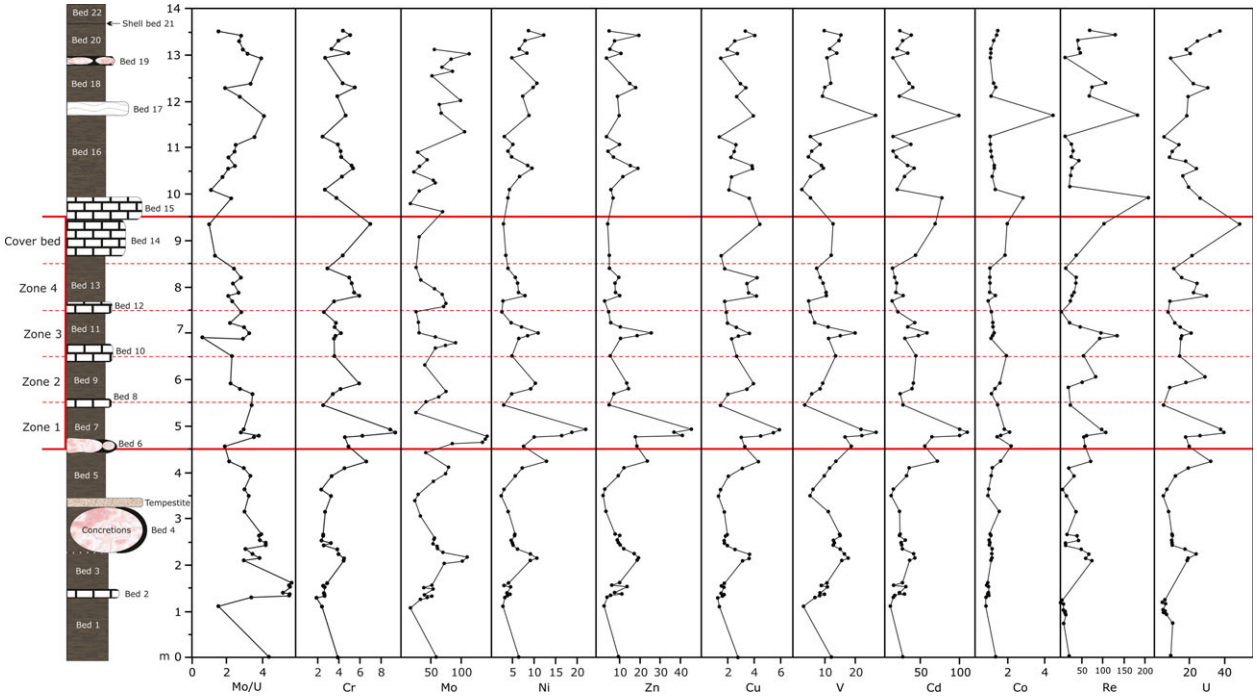


Fig. 6. Trace metal enrichment factors and Mo/U ratios across the Amma Fatma section. Solid red lines delineate upper and lower boundaries of the Amma Fatma carbonate body; dashed red lines outline zones 1 to 4 and the cover bed (cf. Fig. 4, 5).

Table 2. Mean element concentrations in ppm of black shale beds. The stratigraphically corresponding zones of the carbonate body are indicated for comparison

Beds	Zone	Al	Cr	Mo	Ni	Zn	Cu	V	Cd	Co	Re	U	P	Mo/U
14	Cover bed	4794	24·9	3·72	12·5	29·9	5·47	87·4	2·45	2·02	0·030	5·78	376	0·625
13	4	11 066	50·5	16·5	45·1	89·3	16·4	134	1·59	2·21	0·035	7·91	636	2·07
10 to 12	3	11 504	43·2	19·9	65·2	164	15·0	210	4·60	2·81	0·095	7·30	726	2·54
9	2	9541	41·2	15·5	56·5	114	13·6	106	2·96	2·50	0·047	6·45	558	2·49
6 to 8	1	5817	34·0	16·1	58·9	157	10·9	147	4·50	2·13	0·042	5·55	592	2·79

Table 3. Mean major and trace element enrichment factors of black shale beds. The stratigraphically corresponding zones of the carbonate body are indicated for comparison

Beds	Zone	Cr	Mo	Ni	Zn	Cu	V	Cd	Co	Re	U
14	Cover bed	5·67	27·5	3·25	5·61	2·90	12·5	63·4	1·99	70·4	35·0
13	4	4·69	54·3	5·69	7·95	3·09	8·63	17·2	0·956	28·7	18·7
10 to 12	3	3·60	53·7	6·71	11·8	2·50	11·9	43·1	1·22	64·2	14·5
9	2	4·52	59·4	8·48	12·0	3·06	8·00	37·1	1·29	51·5	18·6
6 to 8	1	6·06	94·6	13·6	26·0	3·85	18·2	87·9	1·81	67·5	24·4

makes up the matrix of the Amma Fatma carbonate body. Matrix micrite and peloidal micrite occur, whereby the former is the most abundant carbonate phase in zones 1 and 2, making up at least 80% of the bulk rock volume (Figs 9 and 10A). Matrix micrite is light to dark brown in colour, exhibits a very heterogeneous and partly clotted texture and is rich in detrital material comprising large amounts of recrystallized bivalve and gastropod shell fragments (Fig. 9A), benthonic Foraminifera (Fig. 9B), *Palaxius* faecal pellets (Fig. 10B), radiolarians (Fig. 11A) and

© 2017 The Authors. *The Depositional Record* published by John Wiley & Sons Ltd on behalf of International Association of Sedimentologists.

Table 4. Mean correlation coefficients of major and trace elements of black shale beds. The stratigraphically corresponding zones of the carbonate body are indicated for comparison

Beds	Zone	Al : Cr	Al : Mo	Al : Ni	Al : Zn	Al : Cu	Al : V	Al : Cd	Al : Co	Al : Re	Al : U	Cr : Cu	Mo : Ni	Mo : Zn	Mo : V	Ni : Zn	Zn : V	Zn : Cd
14	Cover bed	0·95	0·85	0·99	0·99	0·51	0·99	0·99	0·99	−0·62	0·80	0·76	0·90	0·91	0·75	1·00	0·96	0·97
13	4	0·35	−0·25	−0·25	0·01	−0·06	0·27	−0·67	0·95	0·29	−0·58	0·77	0·94	0·70	0·75	0·86	0·74	0·38
10 to 12	3	0·98	0·84	0·85	0·74	0·89	0·79	0·79	0·96	0·73	0·91	0·94	0·99	0·97	0·99	0·97	0·99	0·93
9	2	0·91	0·93	−0·18	0·44	0·41	0·93	0·41	0·99	−1·00	−0·98	0·00	0·20	0·74	1·00	0·81	0·73	1·00
6 to 8	1	0·27	0·39	0·24	0·24	0·29	0·26	0·37	0·92	0·19	0·10	0·98	0·97	0·96	0·95	0·97	0·89	0·96

clay minerals. Peloidal micrite is particularly abundant in zones 3 and 4, where it accounts for around 70% of the rock volume (Figs 10C and 11B). This micrite is characterized by abundant oval to spherically shaped peloids, which measure 100 to 500 μm in diameter. The peloids do not show any obvious internal structure and exhibit a cloudy and heterogeneous fabric. The space between the peloids is occupied by fine, dispersed equant calcite cement. Similar to the matrix micrite, the peloidal micrite exhibits scattered occurrences of *Palaxius* faecal pellets, gastropod, bivalve and ammonite shell fragments, as well as Foraminifera and radiolarian tests. The peloids and *Palaxius* faecal pellets are fluorescent under UV light, suggesting that they are enriched in organic matter compared to the surrounding micrite. *Palaxius* faecal pellets are present in all zones but are particularly common in zones 1 and 2 (Fig. 10B). The crescent-shaped canals are arranged in two groups around a symmetry plane, and are oriented in different directions towards and away from the symmetry plane. They are oval to spherical in shape and measure up to 500 μm in diameter. Their internal structure clearly distinguishes them from the aforementioned micritic peloids. Pyrite occurs as very small and finely dispersed grains measuring only several microns in size. In some rare cases pyrite also forms aggregates and clusters of idiomorphic crystals (Fig. 9B). Dolomite occurs within zones 1 and 2. The dolomite crystals are pale grey in colour and show well-defined crystal faces (Figs 9B and 10B).

The Amma Fatma limestone is penetrated by numerous veins, cracks and large cavities throughout zones 1 to 4. Cavities and veins show the same paragenetic mineral sequence in all zones: Matrix micrite or peloidal micrite represents the primary fabric of the rock. Cavities and veins are rimmed by microquartz, followed by equant calcite spar and megaquartz (Figs 10C, D, 11B, C, 12A and B). Microquartz (*sensu* Knauth, 1994) is pale brown to beige in colour (Figs 10C and 11B, C), and typified by very small grain sizes reaching no more than several microns in diameter. In places it can also be found finely dispersed among the equant calcite crystals. Microquartz occasionally forms crystal fans showing oscillatory extinction patterns under crossed polarized light. Volumetrically, equant calcite is the dominant void filling phase in all four zones (Figs 10A, 11C, 12A and B); its crystals measure up to 1 mm in diameter. The last phase in the paragenetic phase sequence is megaquartz (*sensu* Knauth, 1994). Megaquartz crystals reach up to 1 mm or more in diameter (Fig. 10C and D). An accessory peculiar carbonate phase present within fractures and voids is an authigenic rim of microcrystalline calcite referred to as seam micrite (Fig. 12). It is present in all zones and occurs exclusively along the outer rims of veins and cavities,

© 2017 The Authors. *The Depositional Record* published by John Wiley & Sons Ltd on behalf of International Association of Sedimentologists.

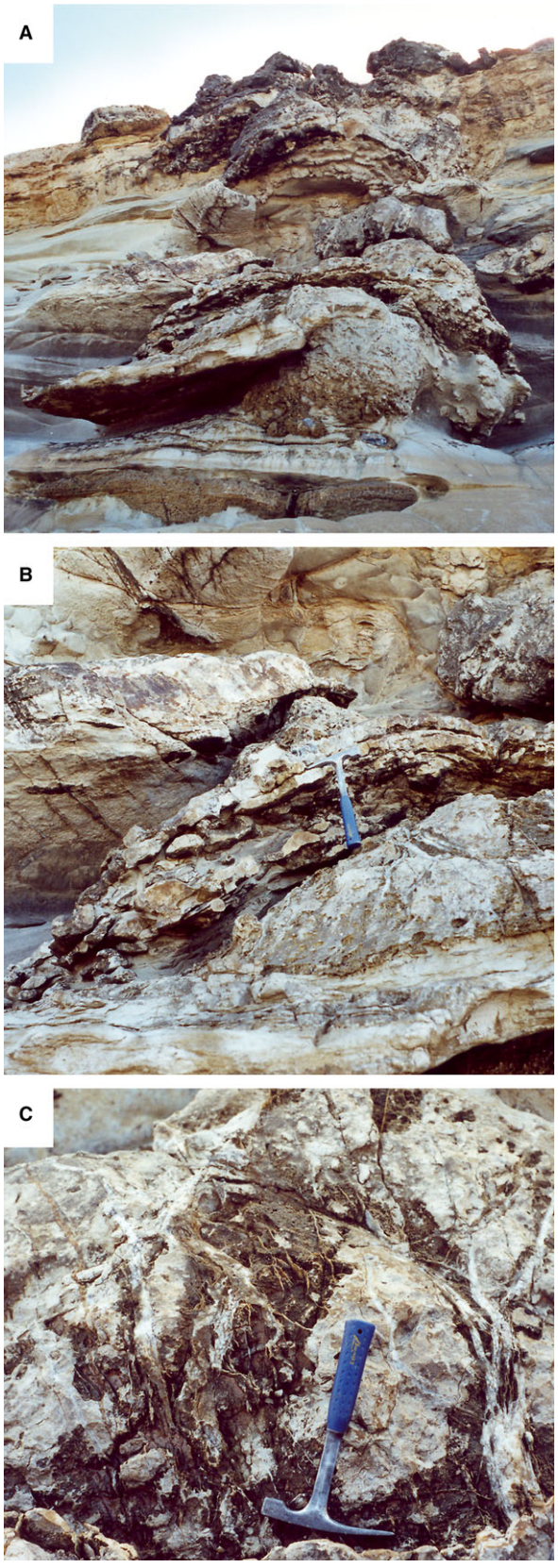


Fig. 7. (A) Bottom view of the Amma Fatma body. The width of the image is 4 m at the base of the carbonate body. (B) A carbonate bank separating zone 2 from zone 1, hammer for scale. (C) Concretionary carbonate from zone 2 penetrated by numerous carbonate veins, hammer for scale.

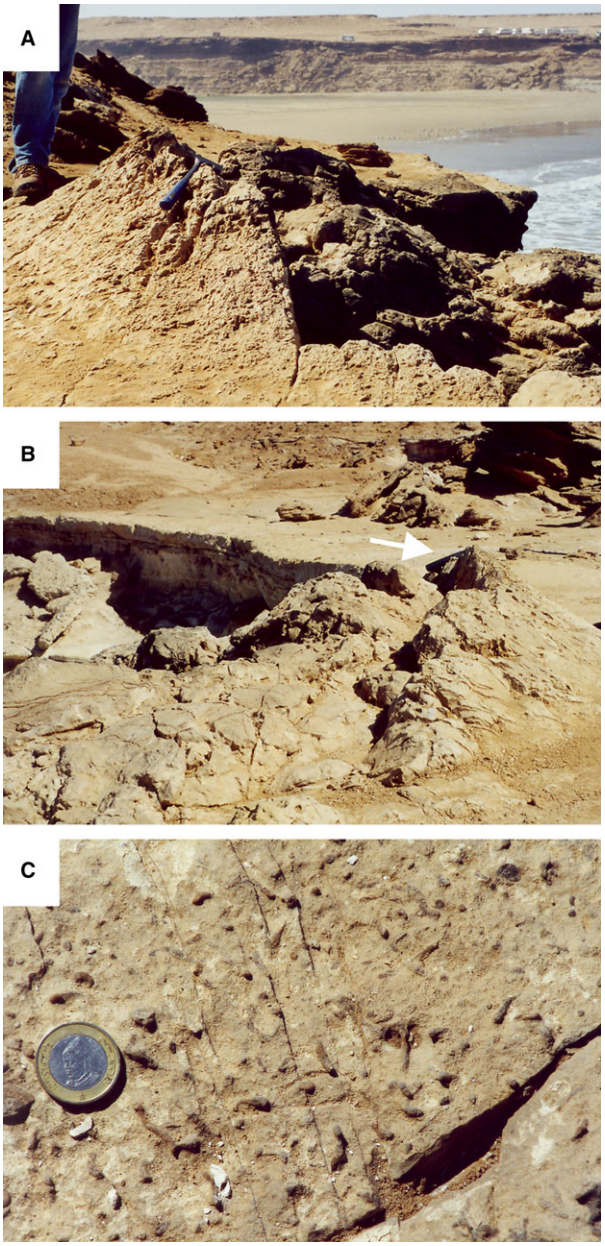


Fig. 8. Photographs from the topmost part of the body. (A) View from northeast, the cover bed capping the body bends upwards, hammer for scale (cf. Fig. 4A). (B) Same as (A), view from south-west, hammer (arrow) for scale. (C) Tubular fossils from zone 4 of the carbonate body, coin for scale.

© 2017 The Authors. *The Depositional Record* published by John Wiley & Sons Ltd on behalf of International Association of Sedimentologists.

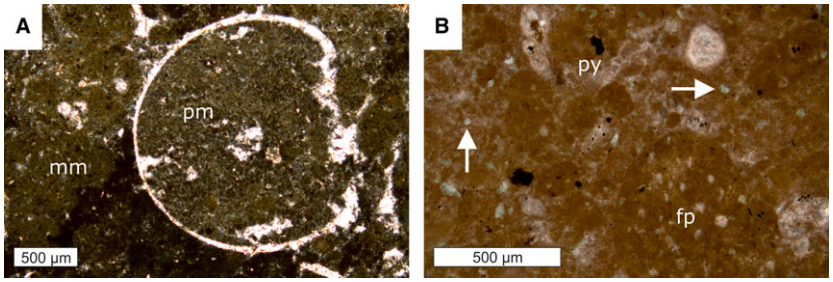


Fig. 9. Photomicrographs of zone 1 limestones; plane-polarized light. (A) Detritus-rich matrix micrite (mm) surrounding a gastropod shell filled by peloidal micrite (pm). (B) Stained thin section showing peloidal micrite with faecal pellets (fp), pyrite aggregates (py) and grey, unstained dolomite crystals (arrows).

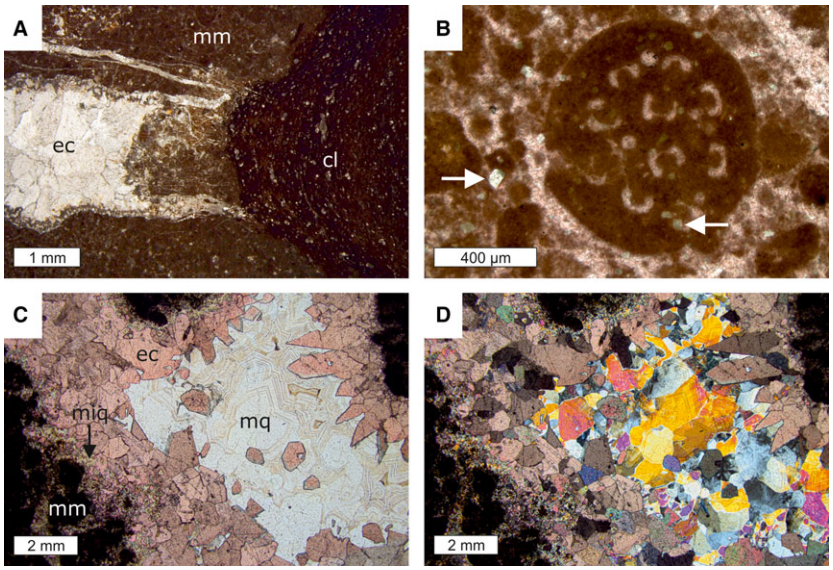


Fig. 10. Photomicrographs of zone 2 limestones. (A) Matrix micrite (mm) surrounding a large cavity filled by equant calcite (ec), several mm thick clay layers (cl) to the left; plane-polarized light. (B) Detailed view of a *Palaxius* faecal pellet with rhombohedral dolomite crystals (arrows); stained thin section, plane-polarized light. (C) Large cavity surrounded by matrix micrite (mm), rimmed by microquartz (miq) and equant calcite (ec); centre of the cavity is filled by large megaquartz crystals (mq); stained thin section, plane-polarized light. (D) Same photograph as (C) in crossed-polarized light.

where it forms highly irregular patches and fringes (Fig. 12A and B). Seam micrite is dark brown, almost black in colour and is very homogenous, showing no detrital inclusions. It shows strong epifluorescence when excited with UV light (Fig. 12C).

The carbonate cover bed (Fig. 4) shows a quite similar paragenetic phase sequence to zones 1 to 4 of the carbonate body (Fig. 4). The matrix comprises micrite, which, compared to the matrix micrite of zones 1 to 4, contains less detrital material. It is relatively homogeneous showing no clotted or peloidal textures and contains minor dolomite crystals (Fig. 13). The fossil content is low, represented by mainly radiolarian and foraminiferan tests (Fig. 13A). Similar to the carbonate body, the cover bed is penetrated by numerous cracks and veins, which have been filled by secondary precipitates. Cavities contain microquartz and later formed equant calcite spar (Fig. 13B and C).

Macrofauna

The macrofossils collected from Zone 4 of the carbonate body comprise a low diversity molluscan assemblage of gastropods, bivalves and ammonites, together with *Palaxius* faecal pellets and burrows. The gastropods comprise 23 specimens of the aporrhaid *Drepanocheilus* sp. (Fig. 14A and B), mostly juveniles, but also a few adults up to 21 mm high, and a single, partially fragmented specimen that might represent a neogastropod belonging to the genera *Drilluta*, *Bellifusus* or *Paleopsephaea* (Fig. 14C). The bivalves belong to three taxa: a single articulated lucinid specimen (Fig. 14E), juvenile

© 2017 The Authors. *The Depositional Record* published by John Wiley & Sons Ltd on behalf of International Association of Sedimentologists.

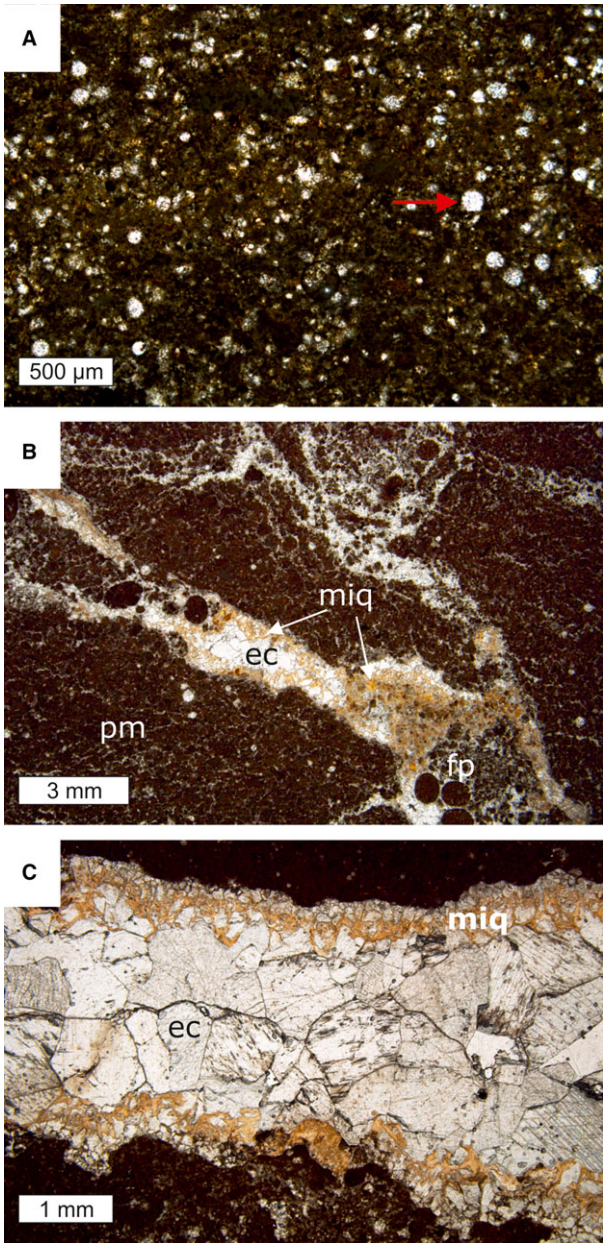


Fig. 11. Photomicrographs of zone 3 limestones; plane-polarized light. (A) Microcrystalline calcite matrix featuring abundant radiolarian tests (arrow). (B) Peloidal micrite with faecal pellets (fp) surrounding veins and cracks rimmed by microquartz (miq) and filled by equant calcite (ec). (C) Close-up view of a vein rimmed by microquartz (miq) and filled by equant calcite (ec).

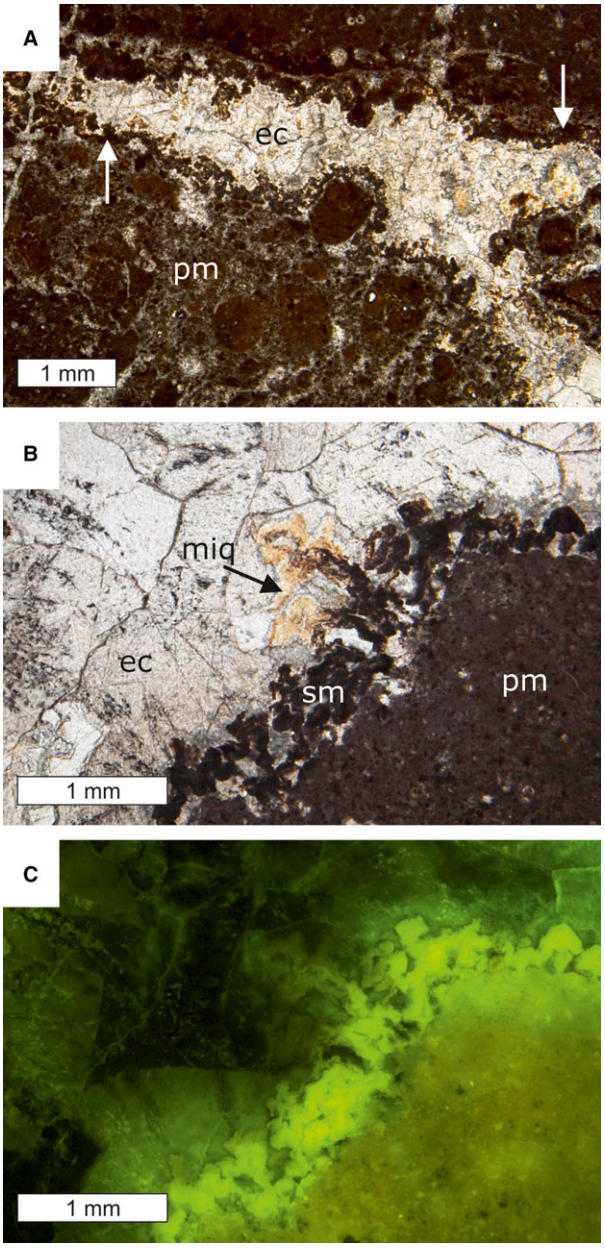


Fig. 12. Photomicrographs of zone 4 limestones. (A) Peloidal micrite (pm) surrounding a void filled by equant calcite (ec), arrows indicate seam micrite (sm) lining the cavity; plane-polarized light. (B) Close-up view of the seam micrite (sm), pm = peloidal micrite, miq = microquartz, ec = equant calcite; plane-polarized light. (C) Same detail as (B) under fluorescent light.

inoceramids (n = 4; Fig. 14D) and gryphaeid oysters (n = 6), which could belong to the genus *Pycnodonte*. The small specimen sizes (<10 mm) of the two latter taxa and the articulation of the lucinid precludes further identification. The ammonites (n = 5) are juveniles and adults belonging to the genus *Benueites*, including *Benueites* cf. *benueensis*.

Isotope geochemistry, TC and TOC

Results of carbon and oxygen stable isotope analyses are shown in Fig. 15. Matrix micrite is ^{13}C-depleted to different degrees throughout all zones of the carbonate body, including the cover bed. It revealed the lowest δ^{13}C values

© 2017 The Authors. *The Depositional Record* published by John Wiley & Sons Ltd on behalf of International Association of Sedimentologists.

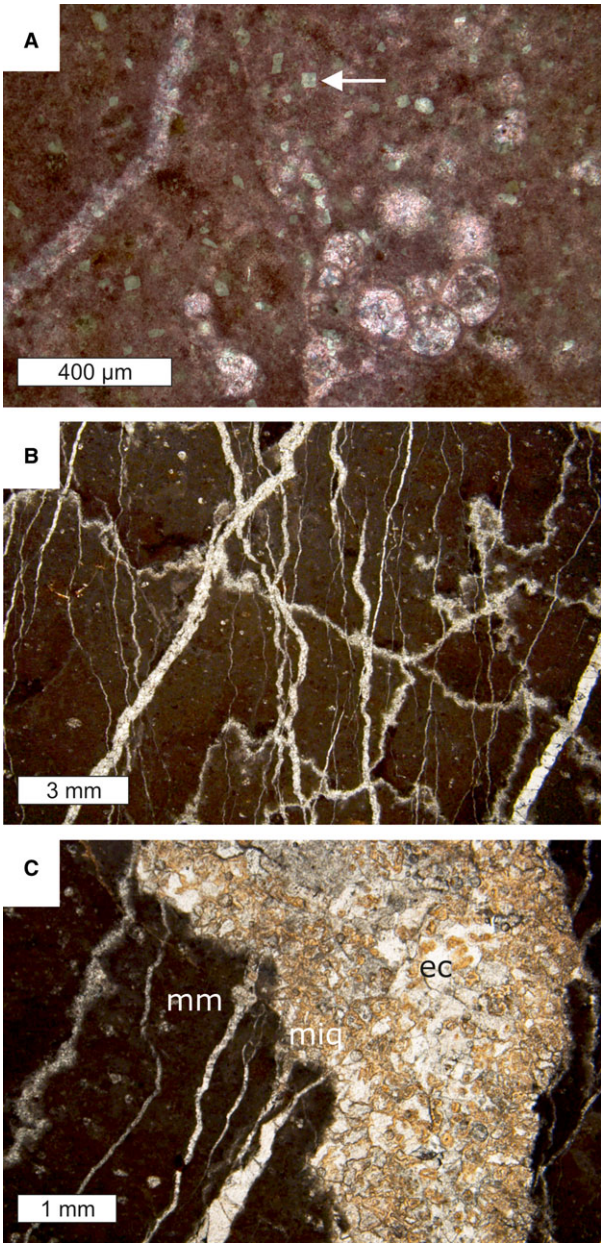


Fig. 13. Photomicrographs of the cover bed; plane-polarized light. (A) Close-up view of matrix micrite featuring dolomite crystals (arrow) and foraminifera tests, stained thin section. (B) Dark brown, fine-grained micrite pervaded by several veins made of secondary equant calcite. (C) Large cavity surrounded by matrix micrite (mm) and filled by microquartz (miq) and equant calcite (ec).

in zone 1, ranging from −23·5 to −21·3‰. Zone 2 micrite yielded a wider range of values from −23·1 to −7·9‰, and zone 3 micrite more positive values between −11·0 to −0·3‰. Zone 4 micrite shows the largest scatter of $\delta^{13}C$ values, falling between −22·9 and −1·3‰. The matrix micrite of the cover bed yielded $\delta^{13}C$ values from −2·3 to −0·4‰. The $\delta^{13}C$ values of equant calcite were analysed from zones 3, 4 and the cover bed. Generally, equant calcite is less ^{13}C-depleted than matrix micrite. A sample from zone 3 revealed the only positive $\delta^{13}C$ value of 1·6‰. Samples from zone 4 and the cover bed show little heterogeneity and fall between −3·7 to −1·5‰ and −0·9 to −0·7‰, respectively.

The $\delta^{18}O$ values of matrix micrite and equant calcite from all sections of the carbonate body are exclusively negative. Matrix micrites from zones 1, 2 and 3 exhibit values from −2·9 to −2·3‰, −3·2 to −2·1‰ and −3·4 to −1·8‰, respectively. Zone 4 matrix micrite displays more scattered $\delta^{18}O$ values from −4·3 to −1·7‰. Matrix micrite of the cover bed yielded values from −3·3 to −2·6‰. The $\delta^{18}O$ value of equant calcite from zone 3 and 2 is −3·4‰. Equant calcite from zone 4 shows the most negative $\delta^{18}O$ values from −6·2 to −2·6. Equant calcite of the cover bed is less ^{18}O depleted (−2·3 and −1·7‰).

A total of six samples from the Amma Fatma carbonate body were analysed for their TC and TOC contents (Table 5). The TOC content increases significantly from top to bottom, from 0·1% in zone 4 to 0·7% in zone 1. The cover bed exhibits a similar TOC content as the top-most zone 4 of 0·1%.

Biomarkers

Hydrocarbons

Organic matter enclosed in the sediments of the Tarfaya Basin has been shown to be of low maturity (Kolonic *et al.*, 2002; Sachse *et al.*, 2012). The hydrocarbon fraction before decalcification from the cover bed is characterized by short and long chain *n*-alkanes that range from C_{16} to C_{34}. The shorter-chain C_{16} to C_{20} *n*-alkanes dominate over longer chain *n*-alkanes, whereby *n*-alkanes peak at *n*-C_{20}. Apart from *n*-alkanes, the only compounds detected are minor amounts of the regular isoprenoids pristane and phytane, with phytane more abundant than pristane. The hydrocarbon fraction after decalcification from the cover bed shows a very similar pattern, except that the contents are much reduced compared to the fraction before decalcification.

Hydrocarbons in the extract before decalcification from zone 1 are characterized by the dominance of *n*-alkanes from C_{16} to C_{30}. In contrast with the cover bed, C_{16} and C_{18} dominate over C_{20}. Pristane and phytane are the only non-alkane compounds detected in zone 1, with phytane slightly more abundant than pristane. The hydrocarbon fraction after decalcification is similar to the fraction before decalcification except that the overall intensities of all compounds are greatly reduced. Very similar results

© 2017 The Authors. *The Depositional Record* published by John Wiley & Sons Ltd on behalf of International Association of Sedimentologists.

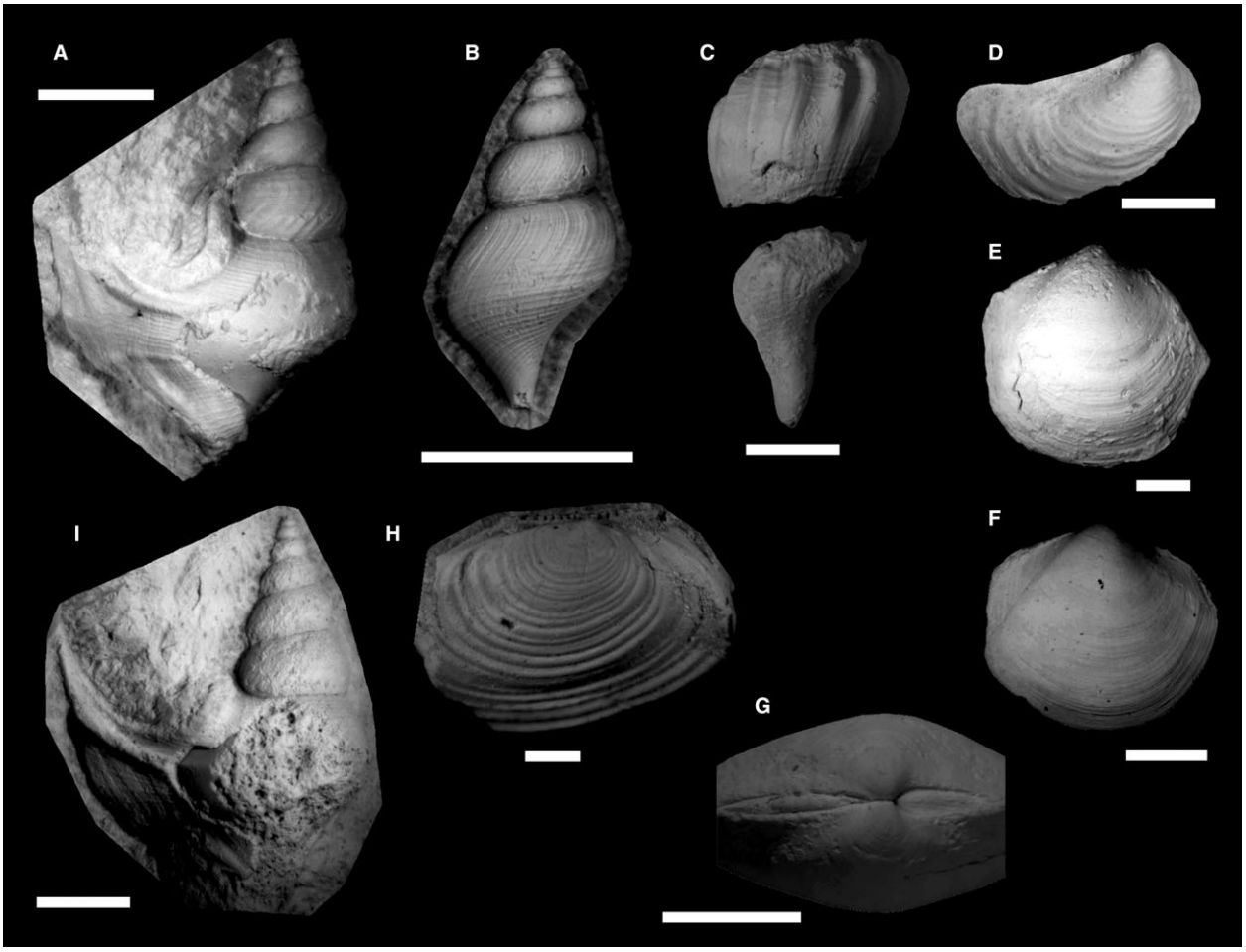


Fig. 14. Representative macrofossils from Amma Fatma Plage. Carbonate body: (A to E); bed 2 Amma Fatma section: (F to I) from collections of the Oxford University Museum, U.K. (KX codes). (A) Adult *Drepanocheilus* sp. (B) Juvenile *Drepanocheilus* sp. (C) Possible neogastropod; specimen at outcrop had siphon broken from (but still closely associated with) the main part of the body whorl. (D) Juvenile inoceramid. (E) Lucinid; right valve with partially fractured anterior margin. (F) Lucinid; right valve (KX.15683). (G) Lucinid; detail of dorsal margin of articulated specimen, anterior to right. Note well-developed lunule and calcified ligament (KX.15684). (H) Inoceramid, oblique dorsal view of right valve (KX.15696). (I) Adult *Drepanocheilus* sp. (KX.15683). All scales = 5 mm.

were obtained for two carbonate samples of zones 3 and 4, and are not further detailed here.

Carboxylic acids

Carboxylic acid fractions before and after decalcification from the cover bed and zone 1 limestone are shown in Fig. 16. The carboxylic acid fraction from the cover bed is dominated by saturated short chain *n*-fatty acids ranging from C_{12} to C_{18}. Most abundant *n*-fatty acids are C_{16} and C_{18}, which dominate over C_{12}. Unsaturated *n*-fatty acids and long-chained saturated *n*-fatty acids are present in very small amounts (Fig. 16A). The carboxylic acid fraction after decalcification varies only slightly from the fraction before decalcification, with medium-chain *n*-fatty acids up to C_{23} more abundant in the former (Fig. 16B). The contents of short chained *n*-fatty acids are markedly decreased (*ca* 50% of all carboxylic acids) compared to the fraction before decalcification (Table 6), however, the distribution of C_{12}, C_{16} and C_{18} is similar.

The carboxylic acid fraction prior to decalcification of zone 1 limestone (Fig. 16C) is characterized by short-chained, C_{12} to C_{18} *n*-fatty acids. The C_{12}, C_{16} and C_{18} *n*-fatty acids are dominant over all other compounds. Additionally, αβ- and ββ-hopanoic acids with 31 and 32 carbon atoms are accessory compounds. The carboxylic acid fraction after decalcification of zone 1 limestone (Fig. 16D) differs markedly from all other samples. Apart from short-chain *n*-fatty acids numerous middle- to long-chain compounds are abundant. These compounds

© 2017 The Authors. *The Depositional Record* published by John Wiley & Sons Ltd on behalf of International Association of Sedimentologists.

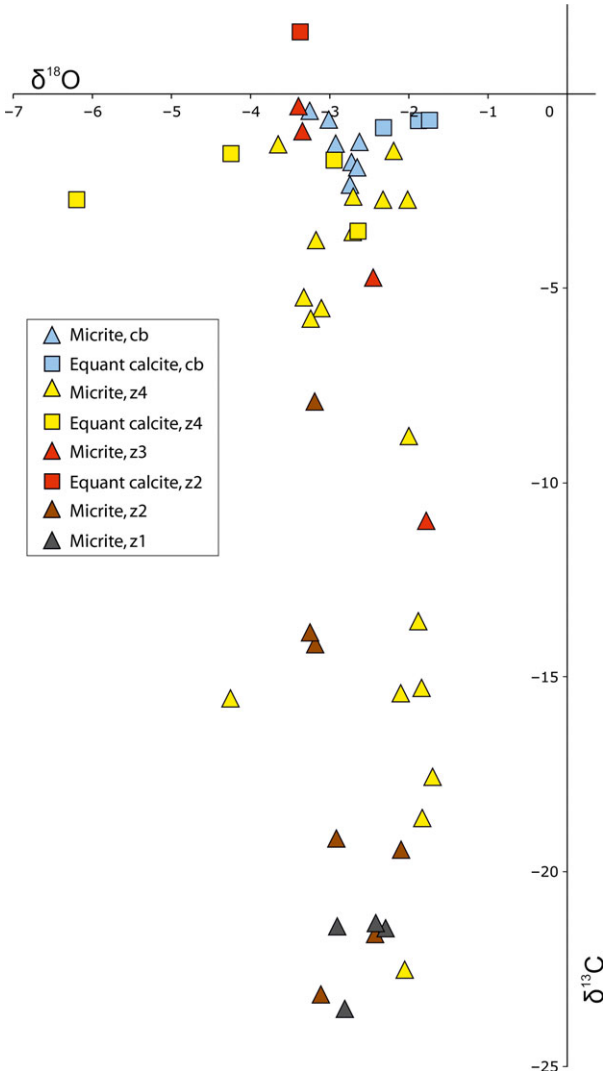


Fig. 15. Carbon and oxygen stable isotope cross-plot of carbonate phases from zones 1 to 4 (z1 to z4) and the cover bed (cb). All values are relative to V-PDB.

include C_{16}, C_{18} and C_{22} α,ω-diacids and minor hopanoic acids, namely C_{32}-17β(H),21β(H)-hopanoic acid. Acyclic to tricyclic biphytanic diacids were only found in zone 1 limestone. The mono- and bicyclic biphytanic diacids only contain cyclopentane rings, whereas the tricyclic biphytanic diacid contains two cyclopentane rings and one cyclohexane ring, according to its mass spectrum and retention time. Of all biphytanic diacids, bicyclic biphytanic diacid (BP-2) dominates over acyclic- (BP-0), monocyclic- (BP-1) and tricyclic- (BP-3) biphytanic diacids. BP-2 is strongly ^{13}C-depleted (−96‰), while BP-3 shows a higher δ^{13}C value of −22‰.

Table 5. Total organic carbon (TOC) content of the zones of the carbonate body including the cover bed

Sample	Zone	TOC%	TIC%	TC%
M-01	Cover Bed	0·12	8·36	8·48
M-03	Zone 4	0·13	8·23	8·36
M-06		0·13	8·02	8·15
M-20	Zone 3	0·45	7·75	8·20
M-11	Zone 1	0·69	7·59	8·28
M-17		0·59	7·65	8·24

The total amount of carboxylic acids varies strongly between the samples. For the cover bed the amount of acids in the extract after decalcification is half that of the fraction before decalcification. For the samples from zones 4, 3 and 1 the ratio is reversed, where the carboxylic acids were found to be more tightly bound to the carbonate lattice. The amount of acids increases from zone 4 to zone 1. Contents and phase-specific stable carbon isotope values of the carboxylic acids are shown in Table 6.

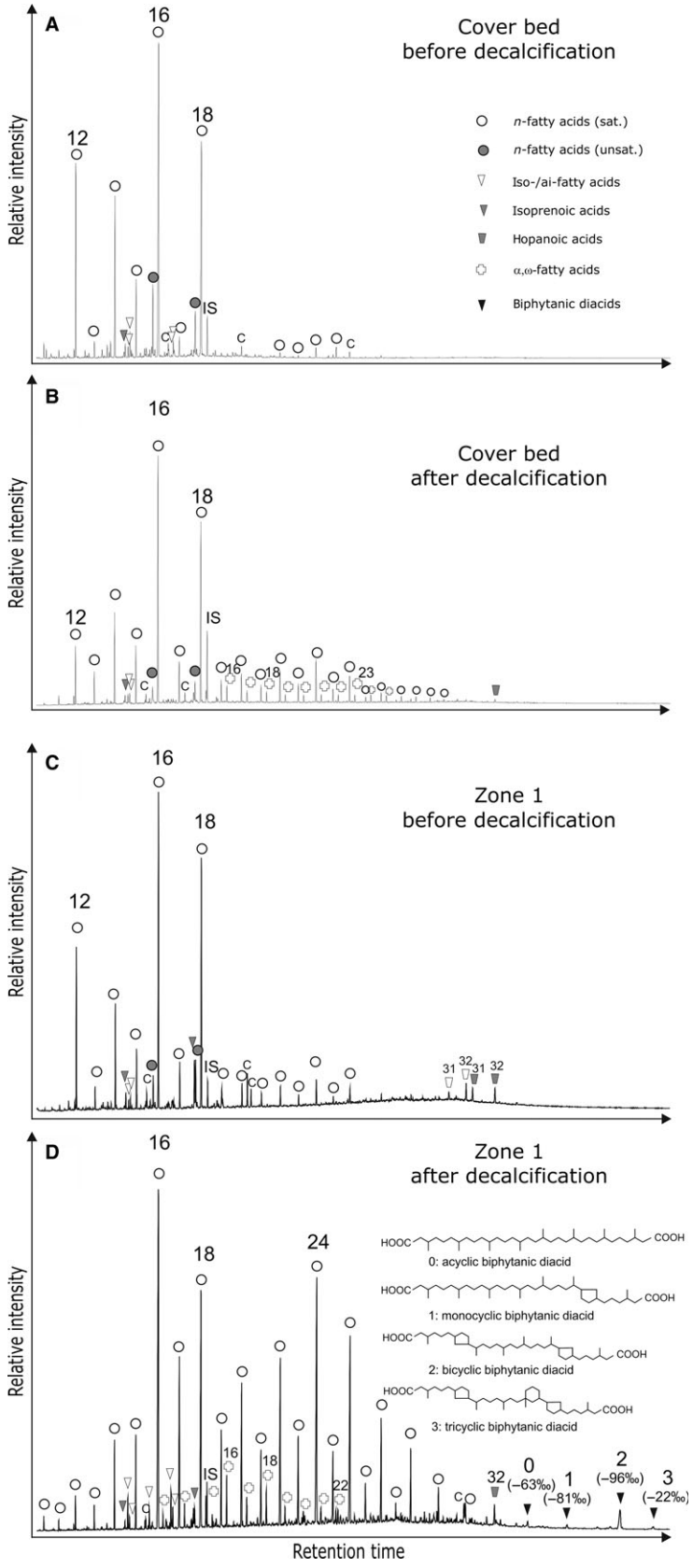
INTERPRETATION AND DISCUSSION

The Amma Fatma carbonate body – A hydrocarbon seep deposit

The comprehensive data set obtained for the Amma Fatma carbonate body allows constraining of the geological setting and the processes that triggered its formation. Although this deposit is unlike many hydrocarbon-seep deposits in terms of its faunal content (cf. Campbell, 2006), there is multiple evidence that it formed at a shallow-water seep in a high productivity realm. The strongest indication for methane seepage is the presence of ^{13}C-depleted biphytanic diacids, which are molecular fossils of anaerobic methane oxidizing archaea (ANMEs; Birgel *et al.*, 2008a). These compounds are putative diagenetic breakdown products of glycerol dibiphytanyl glycerol tetraethers (GDGTs; Liu *et al.*, 2016) and are membrane lipids of archaea including ANMEs (see Schouten *et al.*, 2013 for a review). Biphytanic diacids with extreme ^{13}C-depletions have been reported from various methane-rich environments (Schouten *et al.*, 2003;

Fig. 16. Gas chromatograms (total ion currents) of the carboxylic acid fractions from total rock samples before decalcification (intercrystalline compounds) and from the residual powders after decalcification (intracrystalline compounds), IS = internal standard. (A) Carboxylic acids from the cover bed before decalcification. (B) Carboxylic acids from the cover bed after decalcification. (C) Carboxylic acids from zone 1 before decalcification. (D) Carboxylic acids from zone 1 after decalcification; numbers 0 to 3 refer to the biphytanic diacids BP-0 to BP-3, their δ^{13}C values are indicated in parentheses and are versus V-PDB.

© 2017 The Authors. *The Depositional Record* published by John Wiley & Sons Ltd on behalf of International Association of Sedimentologists.



© 2017 The Authors. *The Depositional Record* published by John Wiley & Sons Ltd on behalf of International Association of Sedimentologists.

Birgel *et al.*, 2008a; De Boever *et al.*, 2009; Natalicchio *et al.*, 2012). GDGTs and biphytanic diacids are uncommon in Mesozoic and Palaeozoic seep limestones, and the more persistent irregular isoprenoids crocetane and pentamethylicosane (PMI) have been used to track methane oxidation in the rock record (Birgel *et al.*, 2008b), but neither of these were found in the Amma Fatma deposit. The most abundant biphytanic diacid in the Amma Fatma limestone is BP-2. Values as low as −96‰ for BP-2 in the Amma Fatma deposit have only been reported from seep-dwelling ANMEs. A similar predominance of ^{13}C-depleted BP-2 among the biphytanic diacids was also reported for other Cenozoic and modern methane-seep carbonates (Birgel *et al.*, 2008a). In contrast with BP-2, BP-3 is derived from other sources, as indicated by its δ^{13}C value similar to that of crenarchaeol-derived tricyclic biphytanes of planktonic Thaumarchaeota (Könneke *et al.*, 2012; Schouten *et al.*, 2013; Pearson *et al.*, 2016).

Interestingly, biphytanic diacids are only present in the lowermost zone 1, suggesting a heterogeneous composition of the Amma Fatma carbonate body. In zones 2 to 4, however, biphytanic diacids and other molecular fossils of hydrocarbon seepage such as isoprenoid hydrocarbons are possibly obscured by hydrocarbons and unresolvable complex mixtures, similar to some modern seep carbonates, particularly oil-seep carbonates (Naehr *et al.*, 2009; Feng *et al.*, 2014). Since biphytanic diacids were only detected within the carboxylic acids fraction after decalcification, these compounds are tightly bound to the carbonate lattice and consequently reflect environmental conditions during authigenesis, consistent with anaerobic methanotrophy contributing to carbonate formation.

Many ancient seep limestones are typified by a distinct paragenetic sequence of mineral phases that enables the reconstruction of processes that governed their formation (Beauchamp & Savard, 1992; Campbell *et al.*, 2002; Peckmann *et al.*, 2002; Hagemann *et al.*, 2013; Zwicker *et al.*, 2015). Microcrystalline calcite (i.e. micrite) forms the matrix of most seep limestones, and several types can be distinguished including clotted (Peckmann *et al.*, 2002), peloidal (Roberts & Aharon, 1994) and detritus-rich matrix micrite (Kiel *et al.*, 2013; Tong *et al.*, 2016). Micrite of the Amma Fatma deposit exhibit a wide range of δ^{13}C values, a pattern commonly found for seep limestones (cf. Greinert *et al.*, 2001). The composition of the carbon pool from which carbonates precipitate at seeps varies over time and depends on the degree of mixing between various carbon sources (Suess & Whiticar, 1989; Peckmann & Thiel, 2004). Biogenic and thermogenic methane, higher hydrocarbon compounds including crude oil and dissolved inorganic carbon from sea water all contribute to the carbon pool of the parent fluid, and determining the contribution of each source to carbonate precipitation at ancient seeps thus remains problematic. Sulphate-dependent AOM is considered to be the main process triggering carbonate precipitation at seeps, whereby the carbonates inherit the ^{13}C-depletion of the organic carbon sources (Ritger *et al.*, 1987; Peckmann & Thiel, 2004; Campbell, 2006). Regardless of the carbon source controlling the isotopic composition of the carbon pool, the carbonates that precipitate at seeps are usually more ^{13}C-enriched than the organic carbon sources due to an admixture of marine carbonate (Peckmann & Thiel, 2004).

The lowest δ^{13}C value of the Amma Fatma matrix micrite of −23·5‰ therefore suggests that AOM did not necessarily contribute substantially to carbonate precipitation, although ^{13}C-depleted biphytanic diacids testify to the presence of microbial communities performing AOM. Slightly lower δ^{13}C values were obtained from seep deposits associated with Jurassic black shales from Kilve, UK, and were attributed to biogenic methane production in the host sediments and its oxidation close to the sea floor (Xu *et al.*, 2016). The oxidation of higher hydrocarbon compounds may have contributed to carbonate formation at Amma Fatma. This notion, however, is rather speculative as evidence for the presence of oil at the ancient seep is missing, and it is only supported by δ^{13}C values that are within the range of carbonates precipitating at modern oil seeps (cf. Anderson *et al.*, 1983; Sassen *et al.*, 1999; Formolo *et al.*, 2004). A new approach using trace and rare earth metal contents may shed light on the composition of fluids of the Amma Fatma seep (cf. Smrzka *et al.*, 2016), and future work may assess the impact of crude oil at ancient seeps with more confidence. Finally, the Amma Fatma black shales themselves might have acted as a readily available source of organic carbon, causing microbially remineralization-driven carbonate formation. The $\delta^{13}C_{TOC}$ values of the Amma Fatma succession are slightly lower than the δ^{13}C values of the authigenic carbonates. Remineralization of large amounts of organic carbon buried during OAE 2 may have consequently contributed to carbonate precipitation, but it does not explain the presence of ^{13}C-depleted biphytanic diacids.

Seam micrite is a peculiar carbonate phase of the Amma Fatma deposit. Peckmann *et al.* (2003) described a similar phase in Eocene seep deposits from Washington State that also lines cavity walls and predates later-stage calcite cements. The purity and microfabric of the Amma Fatma seam micrite are indicative of an *in situ* precipitation, and its intense epifluorescence (Fig. 12C) distinguishes it from matrix and peloidal micrite. The latter observation suggests an increased content of organic residue, agreeing with an involvement of microbial activity in its formation (cf. Peckmann & Thiel, 2004). Equant

 © 2017 The Authors. *The Depositional Record* published by John Wiley & Sons Ltd on behalf of International Association of Sedimentologists.

Table 6. Contents and compound-specific stable carbon isotope values of carboxylic acids. Summed up values are in ng g^{-1} rock, grouped lipid contents are in relative percentages of all carboxylic acids, $\delta^{13}C$ values in parentheses are in ‰ relative to V-PDB

Sample	Cover Bed		Zone 4		Zone 3		Zone 1	
Before/after decalcification	Before	After	Before	After	Before	After	Before	After
Short-chain *n*-fatty acids (14 to 18)	87% (−30‰)	58% (−30‰)	88% (−30‰)	58% (−31‰)	76% (−31‰)	28% (−30‰)	68% (−30‰)	35% (−30‰)
Long-chain *n*-fatty acids (26 to 32)	0	4% (n.m.)	2% (n.m.)	9% (−31‰)	1% (n.m.)	31% (−31‰)	1% (n.m.)	17% (−31‰)
Iso-& *anteiso*-fatty acids (15 and 17)	5% (n.m.)	2% (n.m.)	0	1% (n.m.)	0	0	2% (n.m.)	3% (n.m.)
Short-chain α,ω-diacids (14 to 24)	0	4% (n.m.)	0	3% (n.m.)	0	0	0	5% (n.m.)
Long-chain α,ω-diacids (25 to 28)	0	3% (n.m.)	0	3% (n.m.)	0	0	0	0
Hopanoic acids (αβ 31/32 and ββ 31/32)	0	<1% (n.m.)	0	2% (n.m.)	5% (−32‰)	0	6% (−31‰)	1% (n.m.)
Biphytanic diacids (BP 0 to 3)	0	0	0	0	0	0	0	3% (−66‰)
Others	8%	29%	10%	25%	18%	40%	23%	36%
Sum of all carboxylic acids [ng g^{-1} rock]	2322·2	1117·3	2235·4	4640·5	3149·1	4886·9	3191·8	5925·5

calcite is a typical, later-stage mineral phase of seeps limestones (Campbell *et al.*, 2002; Peckmann *et al.*, 2003), and is interpreted as an abiotically formed cement that precipitated during increasing burial and progressive diagenesis, which agrees with the only moderate ^{13}C-depletion of the Amma Fatma equant calcite.

Authigenic silica minerals typify many Mesozoic and Cenozoic seep limestones (Goedert *et al.*, 2000; Himmler *et al.*, 2008; Peckmann *et al.*, 2011; Kuechler *et al.*, 2012; Kiel *et al.*, 2013; Smrzka *et al.*, 2015). Most of the dissolved silica required for quartz precipitation in seep and non-seep environments is derived from the dissolution of radiolarian tests, diatom frustules and sponge spicules (Lancelot, 1973; Von Rad *et al.*, 1977; Bohrmann *et al.*, 1994; DeMaster, 2002; Kuechler *et al.*, 2012), although dissolution of volcanic glass and clay minerals may also become relevant during late burial diagenesis (Keene, 1975). The abundance of radiolarian tests within the Amma Fatma carbonate body (Fig. 11A) suggests a biogenic source of silica. The sequence of microquartz occurring as thin linings along crack and cavity walls (Figs 11B, C and 12) and later megaquartz occluding large cavities (Fig. 10C and D) is typical of seep limestones (Smrzka *et al.*, 2015). The presence of silica polymorphs suggests that changing silicic acid concentrations controlled the mineralogy of the precipitate over time (Heany, 1993), whereby microquartz precipitated from fluids with higher concentrations of silicic acid and megaquartz formed during a later stage when silica concentrations had decreased.

Although the Amma Fatma deposit features mineral phases that are common in ancient and modern seep limestones, it lacks a carbonate phase that typifies many seep deposits, namely banded and botryoidal aggregates of fibrous aragonite cement. This type of cement typically exhibits low $\delta^{13}C$ values, reflecting its origin from AOM (Beauchamp & Savard, 1992; Roberts *et al.*, 1993; Savard *et al.*, 1996). The lack of this phase together with the dominance of micrite suggests that the Amma Fatma seep was characterized by diffusive rather than advective seepage of hydrocarbon-rich fluids (cf. Peckmann *et al.*, 2009).

Benthonic fauna

The benthonic macrofossil assemblage of the top part of the Amma Fatma carbonate body includes aporrhaid (*Drepanocheilus* sp.) and possible neogastropod gastropods, lucinid, inoceramid and gryphaeid (*Pycnodonte* sp.) bivalves. The small inoceramids and gryphaeids were epifaunal filter feeders, and the lucinid was an infaunal taxon that almost certainly had sulphide-oxidizing chemosymbionts, by comparison with modern members

© 2017 The Authors. *The Depositional Record* published by John Wiley & Sons Ltd on behalf of International Association of Sedimentologists.

of this family (Dando *et al.*, 1986). The aporrhaid was an epifaunal/shallow infaunal suspension or deposit feeder. The possible neogastropod was most likely epifaunal, but without further taxonomic information its diet cannot be inferred. The presence of this fauna suggests that oxygenated conditions were at least episodically present in the water column and sediment during the formation of at least the upper part of the carbonate body, although the absence of large inoceramid and oyster specimens may hint at challenging environmental conditions. A taxonomically very similar low diversity fauna is present in shell-rich micritic carbonate concretions from below the carbonate body in bed 2 at Amma Fatma Plage, collected by Andrew Gale in 2003 and now housed in the collections of the Oxford University Museum, UK. This includes the same species of lucinid (Fig. 14F and G) and *Drepanocheilus* sp. (Fig. 14I), but also much larger inoceramids (up to 35 mm long, Fig. 14H). Furthermore, species of *Pycnodonte*, inoceramids, lucinids and aporrhaid gastropods are common elements in Late Cretaceous faunas from across North Africa (Busson *et al.*, 1999; El Qot, 2006; Ayoub-Hannaa *et al.*, 2014). This indicates that the Amma Fatma seep fauna contains mostly elements of normal marine background faunas, and lacks specialized obligate taxa, possibly apart from the lucinid, which might belong to the seep obligate genus *Nymphalucina* (Kiel, 2013), although is also similar to the lucind figured in El Qot (2006, plate 14, figs 7 to 10) as *Lucina fallax* Forbes, 1846 from the Late Cenomanian of Egypt. This paucity of obligate seep taxa is a common feature of shallow water seep faunas in the Mesozoic and Cenozoic (Kiel, 2010; Little *et al.*, 2015). Other examples include the slightly older Cenomanian Tropic Shale seep faunas from southern Utah, USA (Kiel *et al.*, 2012), which are dominated by mostly small specimens of the bivalve genera *Inoceramus* and *Nymphalucina*, the gastropod genus *Drepanochilus*, rarer examples of the neogastropod *Paleopsephaea* and *Callianassa* decapod claws. A younger example is the Paleocene Panoche Hills seep deposit from California, USA (Schwartz *et al.*, 2003), which contains numerous specimens of *Nymphalucina* and less common aporrhaid gastropods (Kiel, 2013).

The *Palaxius* faecal pellets found throughout the Amma Fatma carbonate body are microcoprolites, which are today produced by callianassid decapod crustaceans. *Palaxius* microcoprolites are common in Palaeozoic and Mesozoic shallow water limestones (Senowbari-Daryan *et al.*, 1992; Schweigert *et al.*, 1997) and other methane-seep deposits (Peckmann *et al.*, 2007; Senowbari-Daryan *et al.*, 2007; Zwicker *et al.*, 2015). The number and shape of the crescent shaped canals in the Amma Fatma microcoprolites strongly resemble *Palaxius decemlunulatus*, which has previously been found in Cretaceous shallow water carbonate deposits of northern Africa (Senowbari-Daryan & Kuss, 1992). The high density of *Palaxius* microcoprolites in the Amma Fatma body suggests high productivity and organic matter availability, sustaining dense populations of crustaceans.

Mode of formation of the Amma Fatma carbonate deposit

The Amma Fatma carbonate body is not older than Lower Turonian in age. The presence of ammonites belonging to the genus *Benueites* in zone 4 shows that the upper part of the seep deposit belongs to the *nodosoides* Zone, the youngest zone of the Lower Turonian, as elsewhere in the Tarfaya Basin. *Benueites* species, including *benueensis*, are associated with *Mammites nodosoides* (Collignon, 1966). El Albani *et al.* (2001) described the laminated marls at Amma Fatma and deduced an early Turonian age based on the ammonite fauna and planktonic Foraminifera. The macrofaunal assemblage of the upper part of the Amma Fatma deposit suggests that the entire water column was at least episodically oxygenated at that time. The absence of the diagnostic $\delta^{13}C$ isotope excursion observed for OAEs confirms that the black shales and the carbonate body formed in the aftermath of OAE 2, and is consistent with biostratigraphic evidence.

The Amma Fatma deposit is a tall, concretionary carbonate body, and in this respect resembles some of the exhumed Oxfordian seep deposits from Beauvoisin (Peckmann *et al.*, 1999) and Miocene deposits of Italy (Conti *et al.*, 2004). Concretions of various shapes and sizes are common in Mesozoic strata, and typically stand out from the host sediment after erosion (Coleman, 1993; Coleman & Raiswell, 1995; Sellés-Martínez, 1996; Seilacher, 2001; Marshall & Pirrie, 2013; Liang *et al.*, 2016). What is most indicative of concretionary growth is that the Amma Fatma carbonate body clearly stands out from the host successions. Apart from this large carbonate deposit, laminated strata from Amma Fatma and Mohammed Plage feature isolated, nodular, diagenetic concretions that precipitated within the organic carbon-rich limestones and black shales (El Albani *et al.*, 1997, 1999a). El Albani *et al.* (2001) described lower Turonian, elongated carbonate concretions in direct proximity to the Amma Fatma carbonate body. These concretions formed during early diagenesis before significant compaction occurred, as fossils were well-preserved and surrounding beds of the host marls wrap above and below the outside of the concretions. The Amma Fatma deposit crosses almost the entire section of laminated shales and limestones, making it difficult to ascertain if the carbonates precipitated during or after their deposition.

 © 2017 The Authors. *The Depositional Record* published by John Wiley & Sons Ltd on behalf of International Association of Sedimentologists.

The cover bed capping the Amma Fatma deposit sheds light on the mode of accretion. It thins out around the top of the carbonate body (Fig. 8A and B), which agrees with the presence of a relief on the sea floor during the time of deposition. Such a scenario is in contrast with a thickening of a cover bed as seen during pockmark formation (cf. Agirrezabala *et al.*, 2013). The circumstance that the cover bed is much thinner directly on top of the seep deposit, and thickens readily away from it, indicates that the deposit was elevated above the sea floor. Given the changing environmental conditions, the carbonate body may have projected into the water column during episodes of sulphidic bottom waters as observed today in the Black Sea (Peckmann *et al.*, 2001). However, there is no evidence for an ancient hardground or firmground, as cementing epifauna are absent. It is conceivable that concretionary growth accompanied by compaction of the host sediment were the main modes of accretion of the Amma Fatma carbonate body, and that carbonate precipitation occurred in the subsurface but close to the sea floor. Large concretionary bodies require a constant and large supply of pore water that transports the necessary solutes to the locus of precipitation (Raiswell & Fischer, 2004; Mozley & Davis, 2005). Diffusive and advective transport of solutes by seeping fluids is the most likely mechanism that sustained concretionary growth over long timescales that subsequently fostered compaction and cementation of the Turonian black shales and marly limestones.

Mean $\delta^{18}O$ values of the predominantly authigenic matrix micrite ranging between $-2{\cdot}6$ and $-2{\cdot}9‰$ also point towards precipitation close to the sea floor, as they are within the range of values for limestones that precipitated in equilibrium with Cretaceous sea water at Mohammed Plage (cf. Kuhnt *et al.*, 2009). They show no appreciable deviation throughout the body, suggesting that pore waters did not experience large temperature shifts or meteoric water input that would have produced more negative $\delta^{18}O$ values (Hudson, 1978; Astin & Scotchman, 1988). Such fairly homogeneous oxygen isotope compositions are common for concretions that grew in shallow sediments close to the sea floor (Hudson & Friedman, 1974; Raiswell & Fisher, 2000). The $\delta^{18}O$ values of the later-stage equant calcite do not differ substantially from those of the matrix micrite, suggesting that neither phase experienced much elevated temperatures during burial diagenesis (cf. Campbell *et al.*, 2002).

In contrast, the trend towards lower $\delta^{13}C$ values from the topmost zone 4 to the lowermost zone 1 (Fig. 15) is interesting. The bottom zone 1 not only shows the highest ^{13}C depletion, but also the sole occurrence of biphytanic diacids and the highest TOC content. Explaining these patterns is challenging, as the preferential growth direction of the Amma Fatma deposit is not obvious. Neither pervasive growth, outward, downward, nor upward growth can be excluded, and assumptions on the mode of accretion remain speculative. Seep carbonate formation is fuelled by a source of reduced, hydrocarbon-rich fluids from below. Zone 1 was possibly affected most by these fluids, which drove microbial activity as evidenced by the occurrence of ^{13}C-depleted biphytanic diacids. Fluid seepage apparently continued during ongoing sedimentation of organic material, and zone 1 remained the hotspot of hydrocarbon-driven authigenesis that clogged up the pore space and reduced permeability. The impact of methane-bearing fluids on carbonate precipitation in the upper zones 3 and 4 was apparently lower, resulting in gradually less negative $\delta^{13}C_{carbonate}$ values as the dominant carbon source changed from isotopically lighter, seepage-derived hydrocarbons to heavier organic matter derived from the host black shales associated with OAE 2.

Methane seepage and carbonate precipitation in the aftermath of OAE 2

The depositional environment of Amma Fatma Plage was most likely an outer shelf setting, as suggested by the foraminiferal assemblages and smectite-dominated clay mineral assemblages (Holbourn *et al.*, 1999) as well as the macrofossil content of the seep deposit (see above). The three palaeoecologically significant Foraminifera species identified at Amma Fatma are *Zygodiscus* (=*Zeugrhabdotus*) *erectus*, *Rhagodiscus splendens* and *Eprolithus floralis*. Generally, temperature and trophic resources are considered the most important factors affecting the distribution of calcareous nannoplankton, whereby ecological preferences of some species are already partly known (Eshet & Almogi-Labin, 1996; Mattioli, 1997; Lüning *et al.*, 1998; Herrle, 2003). The foraminiferal assemblages in combination with the occurrence of radiolarians and diatoms suggest high surface water productivity (El Albani *et al.*, 1999b; Holbourn *et al.*, 1999). Specifically, *Zygodiscus* (=*Zeugrhabdotus*) *erectus* is interpreted as an indicator for high productivity (Roth, 1981; Roth & Krumbach, 1986; Erba *et al.*, 1992; Herrle, 2003). This species is abundant throughout the Amma Fatma section and lacks any systematic distributional changes, suggesting persistent high productivity conditions throughout the entire section consistent with overall high carbon burial. Another species identified as high productivity-prone is *Rhagodiscus splendens*. This may indicate further intensification of upwelling conditions, possibly marking high productivity phases at the base and the top of the section within a generally highly productive setting. An additional argument for upwelling conditions is the presence of

© 2017 The Authors. *The Depositional Record* published by John Wiley & Sons Ltd on behalf of International Association of Sedimentologists.

Eprolithus floralis, which is also considered to be an indicator for cooler waters (Kuhnt *et al.*, 2001). The co-occurrence of these three species suggests that intensified upwelling of relatively cool, intermediate water occurred during the lower Turonian along the Tarfaya shelf. This interpretation is supported by pronounced peaks in phosphorus content that coincide with higher abundances of *Eprolithus floralis* and *Rhagodiscus splendens* at the bottom and top parts of the Amma Fatma section (Fig. 5). These observations, together with the characterization of the macrofaunal assemblage, help to reconstruct the environmental conditions in which the Amma Fatma seep deposit formed.

Carbonates from zone 4 and the cover bed formed under the influence of more prolonged periods of oxygenated conditions. The occurrence of marine background fauna suggests that it dominated and outcompeted any specialized seep-specific taxa in this shallow water and high productivity environment. The absence of benthonic macrofauna in the lower part of the body might suggest lower levels of oxygen compared to the upper part. The presence of *Palaxius* in the lower part does not contradict this notion, as callianassid decapod crustaceans can tolerate extended periods of anoxia (Forster & Graf, 1992; Anderson *et al.*, 1994; Bromley, 1996). The carbonate body formed either during or shortly after deposition of the host strata, and vital information on the environmental conditions can be derived by analysing the trace metal content of host black shales and limestones. Organic-rich shales are distinctly enriched in trace metals including Cr, Mo, U, Ni, Zn, Cu, V, Cd, Co and Re, whereby the modes and mechanisms of enrichment differ somewhat between these elements (Calvert & Pedersen, 1993; Algeo & Maynard, 2004; Brumsack, 2006). The fact that all trace metals – with the exception of Cr and Co – do not correlate with Al confirms that their authigenic enrichment is due to geochemical changes in bottom and pore waters. The use of Cr in palaeoenvironmental analysis has been cautioned, as it is to a large degree of detrital provenance and is highly mobile in marine sediments (Tribovillard *et al.*, 2006). Cobalt mainly resides within the alumosilicate fraction of the black shales as it shows the strongest correlation with Al of all trace metals, and will be consequently omitted from the discussion below. Black shale beds 7 to 13 show EFs of varying magnitudes, which argue for changing environmental conditions during deposition (Table 3). Molybdenum, Cd, Re and U exhibit the highest EFs. Molybdenum behaviour in sedimentary pore waters is linked to the presence of hydrogen sulphide that causes a speciation change from oxidized Mo to reduced thiomolybdate, which can be much more readily deposited either on organic species, or be incorporated and co-precipitated by iron sulphides (Helz *et al.*, 1996). Cadmium exhibits a similar behaviour towards dissolved hydrogen sulphide, except that it accumulates as a separate sulphide phase and can be just as easily enriched in barely reducing conditions at very low hydrogen sulphide concentrations (Rosenthal *et al.*, 1995). The ease of Cd enrichment in anoxic sediments and its high sensitivity towards hydrogen sulphide leads to high EFs, as well as to the large spread in EFs and total concentrations between zones 1 and 4 (Tables 2 and 3). Rhenium EFs are the highest on average of any trace metal. This is due to its very low crustal concentrations and the ease with which it accumulates in anoxic sediments (Crusius *et al.*, 1996). Rhenium enrichment does not require the presence of free hydrogen sulphide or Fe or Mn (oxy)hydroxides, and is solely controlled by the redox potential of the ambient water (Morford *et al.*, 2005). This suggests that the sediments in which carbonates of zones 1 to 4 formed were all characterized by a very shallow oxygen penetration depth or, more likely, periodically anoxic bottom waters.

In modern sediments U enrichment is observed at redox potentials present within the Fe reduction zone, before Mo accumulation occurs under more reducing conditions (Morford & Emerson, 1999). It has been argued that preferential U over Mo uptake is an indicator for suboxic conditions, whereas the reverse is the case when pore waters are strongly sulphidic (Algeo & Tribovillard, 2009). The decrease in Mo/U ratios, total Mo concentrations and Mo, Cd and Re EFs, combined with the concomitant increase in U content from zone 1 to 4 suggests a trend from euxinic conditions in zone 1 to more mildly anoxic conditions in zone 4. Nickel and Zn accumulate most effectively under euxinic conditions and reside in Ni- and Fe-sulphides, respectively (Algeo & Maynard, 2004). Vanadium can also accumulate efficiently within the nitrate reduction zone of marine sediments, and does not necessarily require dissolved sulphide. However, the combined enrichment of V, Zn, Ni and Mo suggest at least temporal euxinia at the sediment-water interface throughout zones 1 to 4 (cf. Hetzel *et al.*, 2009). The notion that ambient water mass chemistry lead to authigenic enrichment of Mo, Ni, Zn, V and Cd is supported by the strong positive correlation between these elements, and their lack of correlation to Al (Table 4).

Trace metal contents of black shales and limestones are governed by bottom water redox conditions, as well as sedimentary redox conditions. Redox-sensitive metals precipitate at redox boundaries in the sediments that often lie substantially below the sediment surface, which may lead to a strong offset between the age of authigenic precipitates and the age of the sediment in which the elements are enriched. It can therefore be difficult to

 © 2017 The Authors. *The Depositional Record* published by John Wiley & Sons Ltd on behalf of International Association of Sedimentologists.

discriminate between enrichment of trace metals via direct precipitation from bottom waters, and enrichment via the precipitation of solid phases within redox zones in the sediment (cf. Kasten *et al.*, 2003; Reitz *et al.*, 2004). However, this age offset between authigenic minerals and the host sediment decreases the more the redox zonation is compressed in the sediment like in the case of anoxic bottom waters. Analyses of trace metal enrichment argue for a formation of black shale and marly limestone beds 7 to 14 under episodic euxinic bottom waters. More importantly, the distribution of Mo, U, Cd and Re implies changes in hydrogen sulphide content of the water mass, from higher contents in zone 1 to lower contents in zone 4. This questions the proposition that the carbonate body grew in its entirety and simultaneously within the shales and limestones. Zone 4 carbonates formed under at least episodically oxygenated conditions, which would have hampered the formation of black shales in bed 13.

Despite the occurrence of macrofossils in zone 4, the Amma Fatma body is poor in fossils compared to most Phanerozoic seep deposits, which are usually replete in shelly macrofauna (Campbell & Bottjer, 1995; Kiel & Peckmann, 2007; Little *et al.*, 2015). Most of the shells identified in thin sections are severely fragmented and were most likely transported to the site over some distance, indicating that most of these molluscs did not live at the seep. Environmental conditions for macrofaunal species at the Amma Fatma seep were at the very least challenging, if not precluding their survival altogether. Euxinic conditions occurred during all stages of carbonate precipitation, interrupted by sporadic oxygenation during formation of zone 4 that enabled macrofaunal assemblages to temporarily colonize the seep. Bottom water conditions were temporarily sulphidic, as were the shallow sediments where carbonate precipitation occurred, consistent with reconstructions for the wider Tarfaya palaeo-shelf area (Kolonic *et al.*, 2005; Poulton *et al.*, 2015). The carbonate mineralogy of the Amma Fatma seep deposits is almost exclusively calcite, lacking any banded and botryoidal aragonite cement. Calcite precipitation at seeps is favoured over aragonite precipitation under the influence of strongly reducing pore waters with low sulphate concentrations (Haas *et al.*, 2010; Nöthen & Kasten, 2011). The environmental conditions as constrained by trace metal analyses of the black shales did consequently not only govern the mode of accretion, but apparently influenced the mineralogy of authigenic carbonate at the Amma Fatma seep as well.

At passive continental margins various processes control the mechanism of fluid flow from sea floor sediments, including tectonic processes, thermohaline convection, sea-level changes and changes in sedimentation rates (Judd & Hovland, 2007; Suess, 2014). Relevant factors that may have influenced the mode of seepage in the Cretaceous Tarfaya Basin include differential compaction and pore water overpressure, both of which are in turn controlled by sedimentation rates and changes in sea-level. Low sea levels promote seepage of fluids through the sediment column (Teichert *et al.*, 2003), as the hydraulic pressure needs to exceed the pressure of the water column to enable upward fluid flow towards the sea floor (Carson & Screaton, 1998). High-frequency sea-level changes at Amma Fatma Plage are indicated by intercalations of bioclastic storm beds into the marly, hemipelagic background sediments (cf. El Albani *et al.*, 1999b). The Amma Fatma coastal section is early Turonian in age, and studies from the Tarfaya Basin have demonstrated that the sea-level rose continuously during the Cenomanian due to a combination of eustatic sea-level rise and shelf subsidence (Gebhardt *et al.*, 2004; Mort *et al.*, 2008; Kuhnt *et al.*, 2009). This sea-level rise culminated during the earliest Turonian where sea-levels were possibly up to 250 m higher than today, the highest during the Cretaceous (Haq, 2014). However, Kuhnt *et al.* (2009) inferred that the lowermost Turonian at Mohammed Plage was characterized by a sea-level lowstand, linked to the ephemeral build-up of Antarctic ice sheets during that time. This is in accord with the inferred outer shelf water depths at Amma Fatma, which should have promoted seepage of hydrocarbon-rich fluids due to the comparatively low pressure of the water column. The presence of shallow water species *Broisonia enormis* and the abundance peak of *Gartnerago segmentatum* (Thierstein, 1976; Hattner *et al.*, 1980) further suggests that a short-term shallowing event may have occurred. Finally, El Albani *et al.* (1997) noted an upward increase in the frequency and thickness of the storm beds, and interpreted this observation as evidence for a falling sea-level through the section corresponding to the eustatic sea-level development during the late Early Turonian also suggested by Hardenbol *et al.* (1998).

Apart from sea-level changes, sedimentation rates also affect seepage dynamics in continental margin sediments. Sedimentation rates in the Tarfaya Basin during OAE 2 were estimated to have been above 10 cm kyr^{-1} (Kuhnt *et al.*, 2005), or correspond to 4·8 cm kyr^{-1} at well S13 (see Fig. 2) and 1·6 cm kyr^{-1} at Mohammed Plage (Kolonic *et al.*, 2005). Despite the differences in these reconstructions, all estimates reflect high sedimentation rates. Such high sedimentation rates increase sediment loading on the continental slope that can lead to pore water overpressure, which squeezes reduced fluids from the underlying organic carbon-rich source rocks towards the sea floor (cf. Suess, 2014). Taken together, favourable conditions for seepage over long timescales were apparently favoured

© 2017 The Authors. *The Depositional Record* published by John Wiley & Sons Ltd on behalf of International Association of Sedimentologists.

by a relative sea-level fall and high sedimentation rates, which facilitated the precipitation of large amounts of authigenic carbonate at the Amma Fatma seep.

CONCLUSIONS

The Amma Fatma carbonate body is an unusual seep deposit, as seep-endemic macrofauna that characterizes many other seep deposits is absent. Nonetheless, lipid biomarkers testify to the presence of microbial communities that performed AOM and contributed to authigenic carbonate formation. With $\delta^{13}C$ values of matrix micrite as low as $-23{\cdot}5‰$ it appears that anaerobic oxidation of methane was not the only trigger for carbonate precipitation. Remineralization of organic matter residing in the host black shales may have been an additional source of carbon for limestone formation. Persistent seepage was probably favoured by a sea-level lowstand and high sedimentation rates. The Amma Fatma deposit formed during the aftermath of OAE 2 over a considerable length of time. High productivity and partly euxinic conditions resulted in the deposition and preservation of black shales rich in organic matter. The Amma Fatma deposit is poor in macrofossils, and those present in the uppermost zone 4 are all Cretaceous shallow water species. Their presence testifies to the sporadic occurrence of oxygenated conditions in the bottom water. However, nannofossil distribution and pronounced enrichments of trace metals within the host strata point towards a high productivity setting with recurrent episodes of euxinia that shaped the shallow marine environment. Identifying seep deposits in such a shallow water setting poses a challenge. Diagnostic signals are masked by high primary production favouring heterotrophic taxa, which take advantage of the vast amounts of organic matter derived from photosynthetic primary production and outcompete obligate, endemic chemosymbiotic seep fauna. The Amma Fatma carbonate body may serve as an example on how to identify seep deposits in high productivity, shallow water settings. In such an environment, only a combination of methods will allow to ascertain that authigenic carbonate deposits formed at hydrocarbon seeps, and to constrain the modes of carbonate formation.

ACKNOWLEDGEMENTS

We thank Lukas Gerdenits for analytical support, Leopold Slawek for the preparation of thin sections, Susanne Gier for XRD measurements, Petra Körner for LECO measurements, Sabine Kasten and Matthias Zabel for help with element analysis and Sylvain Richoz for stable isotope analyses of carbonate samples. CTSL thanks Louella Saul, Annie D'Hondt, Franz Fürsich, Wagih Hannaa, Dick Squires, Andrew Gale, Steffen Kiel and Jim Kennedy for advice about macrofossil identifications, and Eliza Howlett for access to specimens curated in the Oxford University Natural History Museum. Comments by Sabine Kasten and the two journal reviewers Nicolas Tribovillard and an anonymous referee are gratefully acknowledged.

References

Agirrezabala, L.M., Kiel, S., Blumenberg, M., Schäfer, N. and **Reitner, J.** (2013) Outcrop analogues of pockmarks and associated methane-seep carbonates: a case study from the Lower Cretaceous (Albian) of the Basque-Cantabrian Basin, western Pyrenees. *Palaeogeogr. Palaeoclimatol. Palaeoecol.*, **390**, 94–115.

Algeo, T.J. and **Maynard, J.B.** (2004) Trace-element behavior and redox facies in core shales of Upper Pennsylvanian Kansas-type cyclothems. *Chem. Geol.*, **206**, 289–318.

Algeo, T.J. and **Tribovillard, N.** (2009) Environmental analysis of paleoceanographic systems based on molybdenum-uranium covariation. *Chem. Geol.*, **268**, 211–225.

Amblés, A., Halim, M., Jacquesy, J.C., Vitorovic, D. and **Ziyad, M.** (1994) Characterization of kerogen from Timahdit shale (Y-layer) based on multistage alkaline permanganate degradation. *Fuel*, **73**, 17–24.

Anderson, R.K., Scalan, R.S., Parker, R.L. and **Behrens, E.W.** (1983) Seep oil and gas in Gulf of Mexico slope sediments. *Science*, **222**, 619–622.

Anderson, S.J., Taylor, A.C. and **Atkinson, R.J.A.** (1994) Anaerobic metabolism during anoxia in the burrowing shrimp *Calocaris macandraea* Bell (Crustacea: Thalassinidea). *Comp. Biochem. Phys. A*, **108**, 515–522.

Arthur, M.A. and **Sageman, B.** (1994) Marine black shales, depositional mechanisms and environments of ancient deposits. *Annu. Rev. Earth Pl. Sc.*, **22**, 499–551.

Arthur, M.A., Dean, W.E. and **Schlanger, S.O.** (1985) Variations in the global carbon cycle during the Cretaceous related to climate, volcanism, and changes in atmospheric CO_2. In: *The Carbon Cycle and Atmospheric CO_2: Natural Variations Archean to Present* (Eds E.T. Sundquist and W.S. Broecker), *Geophys. Monogr. Ser.*, **32**, 504–529. AGU, Washington, DC.

Astin, T.R. and **Scotchman, T.C.** (1988) The diagenetic history of some septarian concretions from the Kimmeridge clay, England. *Sedimentology*, **35**, 349–368.

Ayoub-Hannaa, W., Fürsich, F.T. and **El Qot, G.M.** (2014) Cenomanian-Turonian bivalves from eastern Sinai, Egypt. *Palaeontogr. Abt. A*, **301**, 63–168.

Barron, E.J. (1983) A warm, equable Cretaceous: the nature of the problem. *Earth Sci. Rev.*, **19**, 305–338.

Baudin, F. (1995) Depositional controls on Mesozoic source rocks in the Tethys. In: *Paleogeography, Paleoclimate, and Source Rock* (Ed. A.Y. Huc), *AAPG Stud. Geol.*, **40**, 191–211.

 © 2017 The Authors. *The Depositional Record* published by John Wiley & Sons Ltd on behalf of International Association of Sedimentologists.

Beauchamp, B. and **Savard, M.** (1992) Cretaceous chemosynthetic carbonate mounds in the Canadian Arctic. *Palaios*, **7**, 434–450.

Birgel, D., Peckmann, J., Klautzsch, S., Thiel, V. and **Reitner, J.** (2006) Anaerobic and aerobic oxidation of methane at late Cretaceous seeps in the Western Interior Seaway, USA. *Geomicrobiol J.*, **23**, 565–577.

Birgel, D., Elvert, M., Han, X. and **Peckmann, J.** (2008a) ^{13}C-depleted biphytanic acids as tracers of past anaerobic oxidation of methane. *Org. Geochem.*, **39**, 152–156.

Birgel, D., Himmler, T., Freiwald, A. and **Peckmann, J.** (2008b) A new constraint on the antiquity of anaerobic oxidation of methane: Late Pennsylvanian seep limestones from southern Namibia. *Geology*, **36**, 543–546.

Bohrmann, G., Abelmann, A., Gersonde, R., Hubberten, H. and **Kuhn, G.** (1994) Pure siliceous ooze, a diagenetic environment for early chert formation. *Geology*, **22**, 207–210.

Bonarelli, G. (1891) *Il territorio di Gubbio*. Notizie Geologiche: Tipografia Economica, Roma, 38 pp.

Bramlette, M.N. and **Sullivan, F.R.** (1961) Coccolithophorids and related nannoplankton of the early Tertiary in California. *Micropaleontology*, **7**, 129–174.

Bromley, R.G. (1996) *Trace Fossils: Biology, Taphonomy and Applications*, 2nd edn. Chapman and Hall, London, 361 pp.

Brumsack, H.J. (1980) Geochemistry of Cretaceous black shales from the Atlantic Ocean (DSDP Legs 11, 14, 36, and 41). *Chem. Geol.*, **31**, 1–25.

Brumsack, H.J. (2006) The trace metal content of recent organic carbon-rich sediments: implications for Cretaceous black shale formation. *Palaeogeogr. Palaeoclimatol. Palaeoecol.*, **232**, 344–361.

Busson, G., Dhondt, A., Amédro, F., Néraudeau, D. and **Cornée, A.** (1999) La grande transgression du Cénomanien supérieur-Turonien inférieur sur la Hamada de Tinrhert (Sahara algérien): datations biostratigraphiques, environnement de dépôt et comparaison d'un témoin épicratonique avec les séries contemporaines à matière organique du Maghreb. *Cretaceous Res.*, **20**, 29–46.

Calvert, S.E. and **Pedersen, T.F.** (1993) Geochemistry of recent oxic and anoxic marine sediments – implications for the geological record. *Mar. Geol.*, **113**, 67–88.

Campbell, K.A. (2006) Hydrocarbon seep and hydrothermal vent paleoenvironments and paleontology: past developments and future directions. *Palaeogeogr. Palaeoclimatol. Palaeoecol.*, **232**, 362–407.

Campbell, K.A. and **Bottjer, D.J.** (1995) Brachiopods and chemosynbiotic bivalves in Phanerozoic hydrothermal vent and cold seep environments. *Geology*, **23**, 321–324.

Campbell, K.A., Farmer, J.D. and **Des Marais, D.** (2002) Ancient hydrocarbon seeps from the Mesozoic convergent margin of California: carbonate geochemistry, fluids and paleoenvionments. *Geofluids*, **2**, 63–94.

Carson, B. and **Screaton, E.J.** (1998) Fluid flow in accretionary prisms: evidence for focused, time-variable discharge. *Rev. Geophys.*, **36**, 329–351.

Coleman, M.L. (1993) Microbial processes: controls on the shape and composition of carbonate concretions. *Mar. Geol.*, **113**, 127–140.

Coleman, M.L. and **Raiswell, R.** (1995) Source of carbonate and origin of zonation in pyritiferous carbonate concretions: evaluation of a dynamic model. *Am. J. Sci.*, **295**, 282–308.

Collignon, M. (1966) Les céphalopodes crétacés du bassin côtier de Tarfaya. *Service Geol. Maroc, Notes et Mem.*, **175**, 1–35.

Conti, S., Fontana, D., Gubertini, A., Sighinolfi, G., Tateo, F., Fioroni, C. and **Fregni, P.** (2004) A multidisciplinary study of middle Miocene seep-carbonates from the northern Apennine foredeep (Italy). *Sed. Geol.*, **169**, 1–19.

Crusius, J., Calvert, S., Pedersen, T. and **Sage, D.** (1996) Rhenium and molybdenum enrichments in sediments as indicators of oxic, suboxic and sulfidic conditions of deposition. *Earth Planet. Sci. Lett.*, **145**, 65–78.

Dando, P.R., Southward, A.J. and **Southward, E.C.** (1986) Chemoautotrophic symbionts in the gills of the bivalve mollusc *Lucinoma borealis* and the sediment chemistry of its habitat. *P. R. Soc. London B. Biol.*, **227**, 227–247.

De Boever, E., Birgel, D., Thiel, V., Muchez, P., Peckmann, J., Dimitrov, L. and **Swennen, R.** (2009) The formation of giant tubular concretions triggered by anaerobic oxidation of methane as revealed by archaeal molecular fossils (Lower Eocene, Varna, Bulgaria). *Palaeogeogr. Palaeoclimatol. Palaeoecol.*, **280**, 23–36.

DeMaster, D.J. (2002) The accumulation and cycling of biogenic silica in the Southern Ocean: revisiting the marine silica budget. *Deep-Sea Res. Pt. II*, **49**, 3155–3167.

Dickson, J.A.D. (1966) Carbonate identification and genesis as revealed by staining. *J. Sed. Petrol.*, **36**, 491–505.

El Albani, A., Caron, M., Deconinck, J.-F., Robazynski, F., Amédro, F., Daoudi, L., Ezaidi, A., Terrab, S. and **Thurow, J.** (1997) Origin of nodules in Lower Turonian organic-rich sediments in Tarfaya Basin (Southwest Morocco). *CR Acad. Sci. Ser. IIA Earth Planet. Sci.*, **324**, 9–16.

El Albani, A., Kuhnt, W., Luderer, F., Herbin, J.P. and **Caron, M.** (1999a) Palaeoenvironmental evolution of the Late Cretaceous sequence in the Tarfaya Basin (Southwest of Morocco). In: *The Oil and Gas Habitats of the South Atlantic* (Eds N.R. Cameron, R.H. Bate and V.S. Clure), *Geol. Soc. London. Spec. Publ.*, **153**, 223–240.

El Albani, A., Vachard, D., Kuhnt, W. and **Chellai, H.** (1999b) Signature of hydrodynamic activity caused by rapid sea level changes in pelagic organic-rich sediments, Tarfaya Basin (southern Morocco). *CR Acad. Sci. Ser. IIA Earth Planet. Sci.*, **329**, 397–404.

El Albani, A., Vachard, D., Kuhnt, W. and **Thurow, J.** (2001) The role of diagenetic carbonate concretions in the

© 2017 The Authors. *The Depositional Record* published by John Wiley & Sons Ltd on behalf of International Association of Sedimentologists.

preservation of the original sedimentary record. *Sedimentology*, **48**, 875–886.

El Qot, G.M. (2006) Late Cretaceous macrofossils from Sinai, Egypt. *Beringeria*, **36**, 3–163.

Erba, E., Castradori, D., Guasti, G. and **Ripepe, M.** (1992) Calcareous nannofossils and Milankovitch cycles: the example of the Albian Gault Clay Formation (Southern England). *Palaeogeogr. Palaeoclimatol. Palaeoecol.*, **93**, 47–69.

Eshet, Y. and **Almogi-Labin, A.** (1996) Calcareous nannofossils as paleoproductivity indicators in Upper Cretaceous organic-rich sequences in Israel. *Mar. Micropaleontol.*, **29**, 37–61.

Feng, D., Birgel, D., Peckmann, J., Roberts, H.H., Joye, S.B., Sassen, R., Liu, X.-L., Hinrichs, K.-U. and **Chen, D.** (2014) Time integrated variation of sources of fluids and seepage dynamics archived in authigenic carbonates from Gulf of Mexico Gas Hydrate Seafloor Observatory. *Chem. Geol.*, **385**, 129–139.

Formolo, M.J., Lyons, T.W., Zhang, C., Kelley, C., Sassen, R., Horita, J. and **Cole, D.R.** (2004) Quantifying carbon sources in the formation of authigenic carbonates at gas hydrate sites in the Gulf of Mexico. *Chem. Geol.*, **205**, 253–264.

Forster, S. and **Graf, G.** (1992) Continuously measured changes in redox potential influenced by oxygen penetrating from burrows of *Callianassa subterranea*. *Hydrobiologia*, **235**, 527–532.

Forster, A., Schouten, S., Moriya, K., Wilson, P.A. and **Sinninghe Damsté, J.S.** (2007) Tropical warming and intermittent cooling during the Cenomanian/Turonian oceanic anoxic event 2: sea surface temperature records from the equatorial Atlantic. *Paleoceanography*, **22**, PA1219. doi:10.1029/2006PA001349.

Gale, A.S., Smith, A.B., Monks, N.E.A., Young, J.A., Howard, A., Wray, D.S. and **Huggett, J.M.** (2000) Marine biodiversity through the Late Cenomanian-Early Turonian: paleoceanographic controls and sequence stratigraphic biases. *J. Geol. Soc. London*, **157**, 745–757.

Gebhardt, H., Kuhnt, W. and **Holbourn, A.** (2004) Foraminiferal response to sea level change, organic flux and oxygen deficiency in the Cenomanian of the Tarfaya Basin, southern Morocco. *Mar. Micropaleontol.*, **53**, 133–157.

Gertsch, B., Adatte, T., Keller, G., Tantawy, A.A.A., Berner, Z., Mort, H.P. and **Fleitmann, D.** (2010) Middle and late Cenomanian oceanic anoxic events in shallow and deeper shelf environments of western Morocco. *Sedimentology*, **57**, 1430–1462.

Goedert, J.L., Peckmann, J. and **Reitner, J.** (2000) Worm tubes in an allochtonous cold-seep carbonate from lower Oligocene rocks of western Washington. *J. Paleontol.*, **74**, 992–999.

Greinert, J., Bohrmann, G. and **Suess, E.** (2001) Gas hydrate-associated carbonates and methane-venting at Hydrate Ridge: classification, distribution, and origin of authigenic lithologies. *Geoph. Monog.*, **124**, 99–113.

Guido, A., Heindel, K., Birgel, D., Rosso, A., Mastandrea, A., Sanfilippo, R., Russo, F. and **Peckmann, J.** (2013) Pendant bioconstructions cemented by microbial carbonate in submerged marine caves (Holocene, SE Sicily). *Palaeogeogr. Palaeoclimatol. Palaeoecol.*, **388**, 166–180.

Haas, A., Peckmann, J., Elvert, M., Sahling, H. and **Bohrmann, G.** (2010) Patterns of carbonate authigenesis at the Kouilou pockmarks on the Congo deep-sea fan. *Mar. Geol.*, **268**, 129–136.

Hagemann, A., Leefmann, T., Peckmann, J., Hoffmann, V.-E. and **Thiel, V.** (2013) Biomarkers from individual carbonate phases of an Oligocene cold-seep deposit, Washington State, USA. *Lethaia*, **46**, 7–18.

Hallam, A. and **Bradshaw, A.** (1977) Bituminous shales and oolitic ironstones as indicators of transgressions and regressions. *J. Geol. Soc. London*, **36**, 57–64.

Handoh, I.C., Bigg, G.R., Jones, E.J.W. and **Inoue, M.** (1999) An ocean modeling study of the Cenomanian Atlantic: equatorial paleoupwelling, organic-rich sediments and the consequences for a connection between the proto-North and South Atlantic. *Geophys. Res. Lett.*, **26**, 223–226.

Haq, B.U. (2014) Cretaceous eustasy revisited. *Global Planet. Change*, **113**, 44–58.

Hardenbol, J., Thierry, J., Farley, M.B., Jacquin, T., De Graciansky, P.C. and **Vail, P.R.** (1998) Mesozoic and Cenozoic sequence chronostratigraphic framework of European Basins. *SEPM Spec. Publ.*, **60**, 3–13.

Hattner, J.G., Wind, F.H. and **Wise, S.W.** (1980) The Santonian-Campanian boundary. Comparison of nearshore-offshore calcareous nannofossil assemblages. *Cah. Micropaléontol.*, **3**, 9–26.

Hay, W.W. (1961) Note on the preparation of samples for discoasterids. *J. Paleontol.*, **35**, 873.

Hay, W.W. (1965) Calcareous nannofossils. In: *Handbook of Paleonological Techniques*(Eds. B. Kummel and D. Raup), pp. 3–7. Freeman, San Francisco, CA.

Heany, P.J. (1993) A proposed mechanism for the growth of chalcedony. *Contrib. Mineral. Petrol*, **115**, 66–74.

Heinrichs, H., Brumsack, H.-J., Loftfield, N. and **König, N.** (1986) Verbessertes Druckaufschlußsystem für biologische und anorganische Materialen. *Z. Pflanzenernähr. Bodenk.*, **149**, 350–353.

Helz, G.R., Miller, C.V., Charnick, J.M., Mosselmans, J.F.W., Pattrick, R.A.D., Garner, C.D. and **Vaughan, D.J.** (1996) Mechanism of molybdenum removal from the sea and its concentration in black shales: EXAFS evidence. *Geochim. Cosmochim. Acta*, **60**, 3631–3642.

Herbin, J.P., Montadert, L., Mueller, C., Gomez, R., Thurow, J. and **Wiedmann, J.** (1986) Organic-rich sedimentation at the Cenomanian–Turonian Boundary in oceanic and coastal basins in the North Atlantic and Tethys. In: *North Atlantic*

 © 2017 The Authors. *The Depositional Record* published by John Wiley & Sons Ltd on behalf of International Association of Sedimentologists.

Palaeoceanography (Eds C. Summerhayes and N.J. Shackleton), *Geol. Soc. London*, **21**, 389–422.

Herrle, J.O. (2003) Reconstructing nutricline dynamics of mid-Cretaceous oceans: evidence from calcareous nannofossils from the Niveau Paquier black shale (SE France). *Mar. Micropalaeontol.*, **47**, 307–321.

Hetzel, A., Böttcher, M.E., Wortmann, U.G. and **Brumsack, H.-J.** (2009) Paleo-redox conditions during OAE 2 reflected in Demarara Rise sediment geochemistry (ODP Leg 207). *Palaeogeogr. Palaeoclimatol. Palaeoecol.*, **273**, 302–328.

Himmler, T., Freiwald, A., Stollhofen, H. and **Peckmann, J.** (2008) Late Carboniferous hydrocarbon-seep carbonates from the glaciomarine Dwyka Group, southern Namibia. *Palaeogeogr. Palaeoclimatol. Palaeoecol.*, **257**, 185–197.

Holbourn, A., Kuhnt, W., El Albani, A., Pletsch, T., Luderer, F. and **Wagner, T.** (1999) Upper Cretaceous palaeoenvironments and benthonic foraminiferal assemblages of potential source rocks from the western African margin, Central Atlantic. In: *The Oil and Gas Habitats of the South Atlantic* (Eds N.R. Cameron, R.H. Bate and V.S. Clure), *Geol. Soc. London. Spec. Publ.*, **153**, 195–222.

Hudson, J.D. (1978) Concretions, isotopes and the diagenetic history of the Oxyford Clay (Jurassic) of central England. *Sedimentology*, **25**, 339–370.

Hudson, J.D. and **Friedman, I.** (1974) Carbon and oxygen isotopes in concretions: relationship to pore water changes during diagenesis. In: *Proceedings of the International Symposium on Water-Rock Interaction*(Eds. J. Cadetm and T. Paces), pp. 331–339. Geological Survey, Prague.

Ingall, E.D., Bustin, R.M. and **Van Cappellen, P.** (1993) Influence of water column anoxia on the burial and preservation of carbon and phosphorus in marine shales. *Geochim. Cosmochim. Acta*, **57**, 303–316.

Jenkyns, H.C. (2003) Evidence for rapid climate change in the Mesozoic-Palaeogene greenhouse world. *Philos. T. R. Soc. London*, **361**, 1885–1916.

Jenkyns, H.C. (2010) Geochemistry of oceanic anoxic events. *Geochem. Geophys. Geosys.*, **11**, 1–30.

Jenkyns, H.C., Matthews, A., Tsikos, H. and **Erel, Y.** (2007) Nitrate reduction, sulfate reduction, and sedimentary iron isotope evolution durint the Cenomanian – Turonian oceanic anoxic event. *Palaeoceanography*, **22**, 1–17.

Jones, C.E. and **Jenkyns, H.C.** (2001) Seawater strontium isotopes, oceanic anoxic events, and seafloor hydrothermal activity in the Jurassic and Cretaceous. *Am. J. Sci.*, **301**, 112–149.

Judd, A.J. and **Hovland, M.** (2007) *Submarine Fluid Flow, the Impact on Geology, Biology, and the Marine Environment*. Cambridge University Press, Cambridge.

Kaiho, K. (1994) Benthic foraminiferal dissolved-oxygen index and dissolved-oxygen levels in the modern ocean. *Geology*, **22**, 719–722.

Kasten, S., Zabel, M., Heuer, V. and **Hensen, C.** (2003) Processes and signals of nonsteady-state diagenesis in deep-sea sediments and their pore waters. *The South Atlantic in the Late Quaternary*, pp. 431–459. Springer, Berlin, Heidelberg.

Kauffman, E.G., Arthur, M.A., Howe, B. and **Scholle, P.A.** (1996) Widespread venting of methane-rich fluids in Late Cretaceous (Campanian) submarine springs (Tepee Buttes), Western Interior seaway, U.S.A. *Geology*, **24**, 799–802.

Keene, J.B. (1975) Cherts and porcellanites from the North Pacific. *Initial Rep. Deep Sea.*, **32**, 429–507.

Kerr, A.C. (1998) Oceanic plateau formation: a cause of mass extinction and black shale deposition around the Cenomanian-Turonian boundary? *J. Geol. Soc. London*, **155**, 619–626.

Kiel, S. (2010) On the potential generality of depth-related ecologic structure in cold-seep communities: evidence from Cenozoic and Mesozoic examples. *Palaeogeogr. Palaeoclimatol. Palaeoecol.*, **295**, 245–257.

Kiel, S. (2013) Lucinid bivalves from ancient methane seeps. *J. Malacol. Soc. London*, **79**, 346–363.

Kiel, S. and **Peckmann, J.** (2007) Chemosymbiotic bivalves and stable carbon isotopes indicate hydrocarbon seepage at four unusual Cenozoic fossil localities. *Lethaia*, **40**, 345–357.

Kiel, S., Wiese, F. and **Titus, A.L.** (2012) Shallow-water methane-seep faunas in the Cenomanian Western Interior Seaway: no evidence for onshore-offshore adaptations to deep-sea vents. *Geology*, **40**, 839–842.

Kiel, S., Birgel, D., Campbell, K.A., Crampton, J.S., Schiøler, P. and **Peckmann, J.** (2013) Crecateous methane-seep deposits from New Zealand and their fauna. *Palaeogeogr. Palaeoclimatol. Palaeoecol.*, **390**, 17–34.

Knauth, P.L. (1994) Petrogenesis of chert. In: *Reviews in Mineralogy, vol. 29: Silica – Physical Behavior, Geochemistry and Materials Applications*(Eds. P.W. Heany, C.T. Prewitt and G.V. Gibbs), pp. 233–258. Mineralogical Society of America, Washington, DC.

Kolonic, S., Sinninghe Damsté, J.S., Böttcher, M.E., Kuypers, M.M.M., Kuhnt, W., Beckmann, B., Scheeder, G. and **Wagner, T.** (2002) Geochemical characterization of Cenomanian/Turonian black shales from the Tarfaya Basin (SW Morocco): relationships between paleoenvironmental conditions and early sulfurization of sedimentary organic matter. *J. Petrol. Geol.*, **25**, 325–350.

Kolonic, S., Wagner, T., Forster, A., Sinninghe Damsté, J.S., Walsworth-Bell, B., Erba, E., Turgeon, S., Brumsack, H.J., Chellai, E.H., Tsikos, H., Kuhnt, W. and **Kuypers, M.M.M.** (2005) Black shale deposition on the northwest African shelf during the Cenomanian-Turonian oceanic anoxic event: climate coupling and global organic carbon burial. *Paleoceanography*, **20**, 1–18.

Könneke, M., Lipp, J.S. and **Hinrichs, K.-U.** (2012) Carbon isotope fractionation by the marine ammonia-oxidizing archaeon *Nitrosopumilus maritimus*. *Org. Geochem.*, **48**, 12–24.

Kuechler, R.R., Birgel, D., Kiel, S., Freiwald, A., Goedert, J.L., Thiel, V. and **Peckmann, J.** (2012) Miocene methane-

© 2017 The Authors. *The Depositional Record* published by John Wiley & Sons Ltd on behalf of International Association of Sedimentologists.

derived carbonates from southwestern Washington (USA) and a model for silicification at seeps. *Lethaia*, **45**, 259–273.

Kuhnt, W. and **Wiedmann, J.** (1995) Cenomanian –Turonian source rocks: paleobiogeographic and paleoenvironmental aspects. In: *Paleogeography, Paleoclimate and Source Rocks* (Ed. A.Y. Huc), *Stud. Geol.*, **40**, 213–232. AAPG, Tulsa, OK.

Kuhnt, W., Herbin, J.P., Thurow, J. and **Wiedmann, J.** (1990) Distribution of Cenomanian–Turonian organic facies in the western Mediterranean and along the adjacent Atlantic margin. In: *Deposition of Organic Facies* (Ed. A.Y. Huc), *AAPG Stud. Geol.*, **30**, 133–160.

Kuhnt, W., El Chellai, H., Holbourn, A., Luderer, F., Thurow, J., Wagner, T., El Albani, A., Beckmann, B., Herbin, J.P., Kawamura, H., Kolonic, S., Nederbragt, S., Street, C. and **Ravilious, K.** (2001) Morocco basin's sedimentary record may provide correlations for Cretaceous paleoceanographic events worldwide. *EOS Trans. Am. Geophys. Union*, **82**, 361–364.

Kuhnt, W., Luderer, F., Nederbragt, A., Thurow, J. and **Wagner, T.** (2005) Millennial resolution record of the Late Cenomanian Oceanic Anoxic Event (OAE2) in the Tarfaya Basin (Morocco). *Int. J. Earth Sci.*, **94**, 147–159.

Kuhnt, W., Holbourn, A., Gale, A., Chellai, E.H. and **Kennedy, W.J.** (2009) Cenomanian sequence stratigraphy and sea-level fluctuations in the Tarfaya Basin (SW Morocco). *Geol. Soc. Am. Bull.*, **121**, 1695–1710.

Kuypers, M.M.M., Pancost, R.D., Nijenhuis, I.A. and **Sinninghe Damsté, J.S.** (2002) Enhanced productivity led to increased organic carbon burial in the euxinic North Atlantic basin during the late Cenomanian oceanic anoxic event. *Paleoceanography*, **17**, 1–13.

Lancelot, Y. (1973) Chert and silica diagenesis in sediments from the central Pacific. *Initial Rep. Deep Sea*, **32**, 429–507.

Larson, R.L. (1991) Latest pulse of Earth; evidence for a mid-Cretaceous super-plume. *Geology*, **19**, 547–550.

Larson, R.L. and **Erba, E.** (1999) Onset of the Mid-Cretaceous greenhouse in the Barremian-Aptian: igneous events and the biological, sedimentary, and geochemical responses. *Paleoceanography*, **14**, 663–678.

Layeb, M., Fadhel, M.B. and **Youssef, M.B.** (2012) Thrombolitic and coral buildups in the Upper Albian of the Fahdene basin (North Tunisia): stratigraphy, sedimentology and genesis. *Bull. Soc. Géol. France*, **183**, 217–231.

Layeb, M., Fadhel, M.B., Layeb-Tounsi, Y. and **Youssef, M.B.** (2014) First microbialites associated to organic-rich facies of the Oceanic Anoxic Event 2 (Northern Tunisia, Cenomanian-Turonian transition). *Arab. J. Geosc.*, **7**, 3349–3363.

Leine, L. (1986) Geology of the Tarfaya oil shale deposit, Morocco. *Geol. Mijnbouw*, **65**, 57–74.

Liang, H., Chen, X., Wang, C., Zhao, D. and **Weissert, H.** (2016) Methane-derived authigenic carbonates of mid-Cretaceous age in southern Tibet: types of carbonate concretions, carbon sources, and formation processes. *J. Asian Earth Sci.*, **115**, 153–169.

Little, C.T.S., Birgel, D., Boyce, A.J., Crame, A.J., Francis, J.E., Kiel, S., Peckmann, J., Pirrie, D., Rollinson, G.K. and **Witts, J.D.** (2015) Late Cretaceous (Maastrichtian) shallow water hydrocarbon seeps from Snow Hill and Seymour Islands, James Ross Basin, Antarctica. *Palaeogeogr. Palaeoclimatol. Palaeoecol.*, **418**, 213–228.

Liu, X.-L., Birgel, D., Elling, F.J., Sutton, P.A., Lipp, J.S., Zhu, R., Zhang, C., Könneke, M., Peckmann, J., Rowland, S., Summons, R.E. and **Hinrichs, K.-U.** (2016) From ether to acid: a plausible degradation pathway of glycerol dialkyl glycerol tetraethers. *Geochim. Cosmochim. Acta*, **183**, 138–152.

Lüning, S., Marzouk, A.M. and **Kuss, J.** (1998) Latest Maastrichtian high frequency litho- and ecocycles from the hemipelagic of Eastern Sinai, Egypt. *J. Afr. Earth Sci.*, **27**, 373–395.

Lüning, S., Kolonic, S., Belhadj, E.M., Belhadj, Z., Cota, L., Baric, G. and **Wagner, T.** (2004) Integrated depositional model for the Cenomanian-Turonian organic-rich strata in North Africa. *Earth Sci. Rev.*, **64**, 51–117.

Marshall, J.D. and **Pirrie, D.** (2013) Carbonate concretions – explained. *Geol. Today*, **29**, 53–62.

Marzouk, A.M. and **Lüning, S.** (2005) Calcareous nannofossil biostratigraphy and distribution patterns in the Cenomanian-Turonian of North Africa. *Grmena*, **1**, 107–122.

Mascle, J., Lohmann, G.P., Clift, P.D. and **Party, S.S.** (1997) Development of a passive transform margin: Cote d'Ivoire–Ghana transform margin — ODP Leg 159 preliminary results. *Geo-Mar. Lett.*, **17**, 4–11.

Mattioli, E. (1997) Nannoplankton productivity and diagenesis in the rhythmically bedded Toarcian-Aalenian Fiuminata sequence (Umbria-Marche Apennine, Central Italy). *Palaeogeogr. Palaeoclimatol. Palaeoecol.*, **130**, 113–134.

McAnena, A., Floegel, S., Hofmann, P., Herrle, J.O., Griesand, A., Pross, J., Talbot, H.M., Rethemeyer, L., Wallmann, K. and **Wagner, T.** (2013) Atlantic opening, million-year cooling and coupled marine biotic crises in the Cretaceous. *Nat. Geosci.*, **6**, 558–561.

Metz, C.L. (2010) Tectonic controls on the genesis and distribution of Late Cretaceous Western Interior Basin hydrocarbon-seep mounds (Tepee Buttes) of North America. *J. Geol.*, **118**, 201–213.

Meyer, K.M. and **Kump, L.R.** (2008) Oceanic euxinia in Earth history: causes and consequences. *Ann. Rev. Earth Planet. Sci.*, **36**, 251–288.

Morford, J.L. and **Emerson, S.R.** (1999) The geochemistry of redox sensitive trace metals in sediments. *Geochim. Cosmochim. Acta*, **63**, 1735–1750.

Morford, J.L., Emerson, S.R., Breckel, E.J. and **Kim, S.H.** (2005) Diagenesis of oxyanions (V, U, R, and Mo) in pore

 © 2017 The Authors. *The Depositional Record* published by John Wiley & Sons Ltd on behalf of International Association of Sedimentologists.

waters and sediments from a continental margin. *Geochim. Cosmochim. Acta*, **69**, 5021–5032.

Mort, H.P., Adatte, T., Keller, G., Bartels, D., Föllmi, K.B., Steinmann, P., Berner, Z. and **Chellai, E.H.** (2008) Organic carbon deposition and phosphorus accumulation during Oceanic Anoxic Event 2 in Tarfaya. *Morocco. Cretaceous Res.*, **29**, 1008–1023.

Mozley, P.S. and **Davis, J.M.** (2005) Internal structure and mode of growth of elongate calcite concretions: evidence for small-scale, microbially induced, chemical heterogeneity in groundwater. *Geol. Sco. Am. Bull.*, **117**, 1400–1412.

Naehr, T.H., Birgel, D., Bohrmann, G., MacDonald, I.R. and **Kasten, S.** (2009) Biogeochemical controls on authigenic carbonate formation at the Chaopopote "asphalt volcano", Bay of Campeche. *Chem. Geol.*, **266**, 390–402.

Natalicchio, M., Birgel, D., Dela Pierre, F., Martire, L., Clari, P., Spötl, C. and **Peckmann, J.** (2012) Polyphasic carbonate precipitation in the shallow subsurface: insights from microbially-formed authigenic carbonate beds in upper Miocene sediments of the Tertiary Piedmont Basin (NW Italy). *Palaeogeogr. Palaeoclimatol. Palaeoecol.*, **329–330**, 158–172.

Nederbragt, A.J. and **Fiorentino, A.** (1999) Stratigraphy and palaeoeoceanography of the Cenomanian-Turonian Boundary Event in Oued Mellegue, north– western Tunisia. *Cretaceous Res.*, **20**, 47–62.

Nöthen, K. and **Kasten, S.** (2011) Reconstructing changes in seep activity by means of pore water and solid phase Sr/Ca and Mg/Ca ratios in pockmark sediments of the Northern Congo Fan. *Mar. Geol.*, **287**, 1–13.

Owens, J.D., Gill, B.C., Jenkyns, H.C., Bates, S.M., Severmann, S., Kuypers, M.M.M., Woodfine, R.G. and **Lyons, T.W.** (2013) Sulfur isotopes track the global extent and dynamics of euxinia during Cretaceous Oceanic Anoxic Event 2. *Proc. Natl Acad. Sci. USA*, **110**, 18407–18412.

Pearson, A., Hurley, S.J., Walter, S.R.S., Kusch, S., Lichtin, S. and **Zhang, Y.G.** (2016) Stable carbon isotope ratios of intact GDGTs indicate heterogenus sources to marine sediments. *Geochim. Cosmochim. Acta*, **181**, 18–35.

Peckmann, J. and **Thiel, V.** (2004) Carbon cycling at ancient methane seeps. *Chem. Geol.*, **205**, 443–467.

Peckmann, J., Thiel, V., Michaelis, W., Clari, P., Gaillard, P., Martire, L. and **Reitner, J.** (1999) Cold seep deposits of Beauvoisin (Oxfordian; southeastern France) and Marmorito (Miocene; northern Italy): microbially induced authigenic carbonates. *Int. J. Earth Sci.*, **88**, 60–75.

Peckmann, J., Reimer, A., Luth, U., Luth, C., Hansen, B.T., Heinicke, C., Hoefs, J. and **Reitner, J.** (2001) Methane derived carbonates and authigenic pyrite from the northwestern Black Sea. *Mar. Geol.*, **177**, 129–150.

Peckmann, J., Goedert, J.L., Thiel, V., Michaelis, W. and **Reitner, J.** (2002) A comprehensive approach to the study of methane–seep deposits from the Lincoln Creek Formation, western Washington State USA. *Sedimentology*, **49**, 855–873.

Peckmann, J., Goedert, J.L., Heinrichs, T., Hoefs, J. and **Reitner, J.** (2003) The late Eocene 'Whiskey Creek' methane-seep deposit (western Washington State). Part II: petrology, stable isotopes, and biogeochemistry. *Facies*, **48**, 241–254.

Peckmann, J., Senowbari-Daryan, B., Birgel, D. and **Goedert, J.L.** (2007) The crustacean ichnofossil *Palaxius* associated with callianassid body fossils in an Eocene methane-seep limestone, Humptulips Formation, Olympic Peninsula, Washington. *Lethaia*, **40**, 273–280.

Peckmann, J., Birgel, D. and **Kiel, S.** (2009) Molecular fossils reveal fluid composition and flow intensity at a Cretaceous seep. *Geology*, **37**, 847–850.

Peckmann, J., Kiel, S., Sandy, M.R., Taylor, D.G. and **Goedert, J.L.** (2011) Mass occurrences of the brachiopod *Halorella* in Late Triassic methane-seep deposits, eastern Oregon. *J. Geol.*, **119**, 207–220.

Poulton, S.W., Henkel, S., März, C., Urquhart, H., Floegel, S., Kasten, S., Sinninghe Damsté, J. and **Wagner, T.** (2015) A continental-weathering control on orbitally driven redox-nutrient cycling during Cretaceous Oceanic Anoxic Event 2. *Geology*, **43**, 963–966.

Raiswell, R. and **Fischer, Q.J.** (2004) Rates of carbonate cementation associated with sulphate reduction in DSDP/ODP sediments: implications for the formation of concretions. *Chem. Geol.*, **211**, 71–85.

Raiswell, R. and **Fisher, Q.J.** (2000) Mudrock-hosted carbonate concretions: a review of growth mechanisms and their influence on chemical and isotopic composition. *J. Geol. Soc. London*, **157**, 239–251.

Reitz, A., Hensen, C., Kasten, S., Funk, J.A. and **De Lange, G.J.** (2004) A combined geochemial and rock-magnetic investigation of a redox horizon at the last glacial/interglacial transition. *Phys. Chem. Earth*, **29**, 921–931.

Ritger, S., Carson, B. and **Suess, E.** (1987) Methane derived authigenic carbonates formed by subduction-induced pore-water expulsion along the Oregon/Washington margin. *Geol. Soc. Am. Bull.*, **98**, 147–156.

Roberts, H.H. and **Aharon, P.** (1994) Hydrocarbon-derived carbonate buildups of the northern Gulf of Mexico contintental slope: a review of submersible investigations. *Geo-Mar. Lett.*, **14**, 135–148.

Roberts, H.H., Aharon, P. and **Walsh, M.M.** (1993) Cold-seep carbonates of the Louisiana continental slope-to-basin floor. In: *Carbonate Microfabrics*(Eds R. Rezak and D.L. Lavoie), pp. 95–104. Springer, Berlin, Heidelberg, New York.

Rosenthal, Y., Lam, P., Boyle, E.A. and **Thomson, J.** (1995) Authigenic cadmium enrichments in suboxic sediments: precipitation and postdepositional mobility. *Earth Planet. Sci. Lett.*, **132**, 99–111.

© 2017 The Authors. *The Depositional Record* published by John Wiley & Sons Ltd on behalf of International Association of Sedimentologists.

Roth, P.H. (1981) Mid-Cretaceous calcareous nannoplankton from the central Pacific: implication for paleoceanography. *Initial Rep. Deep Sea*, **62**, 471–489.

Roth, P.H. and **Krumbach, K.R.** (1986) Middle Cretaceous calcareous nannofossil biogeography and preservation in the Atlantic and Indian Oceans: implications for paleoceanography. *Mar. Micropaleontol.*, **10**, 235–266.

Sachse, V.F., Littke, R., Jabour, H., Schümann, T. and **Kluth, O.** (2012) Late Cretaceous (Late Turonian, Coniacian and Santonian) petroleum source rocks as part of an OAE, Tarfaya Basin, Morocco. *Mar. Petrol. Geol.*, **29**, 35–49.

Sames, B., Wagreich, M., Wendler, J.E., Haq, B.U., Conrad, C.P., Dobrinescu-Melinte, M.C., Hu, X., Wendler, I., Wolfgring, E., Yilmaz, I.Ö. and **Zorina, S.O.** (2016) Review: short-term sea-level changes in a greenhouse world – a view from the Cretaceous. *Palaeogeogr. Palaeoclimatol. Palaeoecol.*, **441**, 393–411.

Sassen, R., Joye, S., Sweet, S.T., DeFreitas, D.A., Milkov, A.V. and **MacDonald, I.R.** (1999) Thermogenic gas hydrates and hydrocarbon gases in complex chemosynthetic communities, Gulf of Mexico continental slope. *Org. Geochem.*, **30**, 485–497.

Savard, M.M., Beauchamp, B. and **Veizer, J.** (1996) Significance of aragonite cements around Cretaceous marine methane seeps. *J. Sed. Res.*, **66**, 430–438.

Schlanger, S.O. and **Jenkyns, H.C.** (1976) Cretaceous oceanic anoxic events: causes and consequences. *Geol. Mijnbouw*, **55**, 179–184.

Schlanger, S.O., Arthur, M.A., Jenkyns, H.C. and **Scholle, P.A.** (1987) The Cenomanian–Turonian oceanic anoxic event, I. Stratigraphy and distribution of organic carbon-rich beds and the marine $\delta^{13}C$ excursion. In: *Marine Petroleum Source Rocks* (Eds J. Brooks and A.J. Fleet), *Geol. Soc. Spec. Publ.*, **26**, 371–399.

Schouten, S., Wakeham, S.T., Hopmans, E.C. and **Sinninghe Damsté, J.S.** (2003) Biogeochemical evidence that thermophilic archaea mediate the anaerobic oxidation of methane. *Appl. Environ. Microb.*, **69**, 1680–1686.

Schouten, S., Hopmans, E.C. and **Sinninghe Damsté, J.S.** (2013) The organic geochemistry of glycerol dialkyl glycerol tetraether lipids: a review. *Org. Geochem.*, **54**, 19–61.

Schwartz, H., Sample, J., Weberling, K.D., Minisini, D. and **Moore, J.C.** (2003) An ancient linked fluid migration system: cold-seep deposits and sandstone intrusions in the Panoche Hills, California, USA. *Geo-Mar. Lett.*, **23**, 340–350.

Schweigert, G., Seegis, D.B., Fels, A. and **Leinfelder, R.R.** (1997) New internally structured decapod microcoprolites from Germany (Late Triassic/Early Miocene), Southern Spain (Early/Middle Jurassic) and Portugal (Late Jurassic): taxonomy, palaeoecology and evolutionary patterns. *Paläontol. Z.*, **71**, 51–69.

Seilacher, A. (2001) Concretion morphologies reflecting diagenetic and epigenetic pathways. *Sed. Geol.*, **143**, 41–57.

Sellés-Martínez, J. (1996) Concretion morphology, classification and genesis. *Earth Sci. Rev.*, **41**, 177–210.

Senowbari-Daryan, B. and **Kuss, J.** (1992) Anomuren-Koprolithen aus der Kreide von Ägypten. *Mitt. Geol.*, **73**, 129–157.

Senowbari-Daryan, B., Weidlich, O. and **Flügel, E.** (1992) Erster Nachweis von, Favreinen' (Crustaceen-Koprolithen) aus dem Perm: Oberperm, Oman-Berge. *Paläontol. Z.*, **6**, 187–196.

Senowbari-Daryan, B., Gaillard, C. and **Peckmann, J.** (2007) Crustacean microcoprolites from Jurassic (Oxfordian) hydrocarbon-seep deposits of Beauvoisin, southeastern France. *Facies*, **53**, 229–238.

Shapiro, R. and **Fricke, H.** (2002) Tepee Buttes: fossilized methane seep ecosystems. *Geol. Soc. Am. Field Guides*, **3**, 94–101.

Sinninghe Damsté, J.S. and **Köster, J.** (1998) A euxinic southern North Atlantic Ocean during the Cenomanian/Turonian oceanic anoxic event. *Earth Planet. Sci. Lett.*, **158**, 165–173.

Smrzka, D., Kraemer, S.M., Zwicker, J., Birgel, D., Fischer, D., Kasten, S., Goedert, J.L. and **Peckmann, J.** (2015) Constraining silica diagenesis in methane-seep deposits. *Palaeogeogr. Palaeoclimatol. Palaeoecol.*, **420**, 13–26.

Smrzka, D., Zwicker, J., Klügel, A., Monien, P., Bach, W., Bohrmann, G. and **Peckmann, J.** (2016) Establishing criteria to distinguish oil-seep from methane-seep carbonates. *Geology*, **44**, 667–670.

Suess, E. (2014) Marine cold seeps and their manifestations: geological control, biogeochemical criteria and evironmental conditions. *Int. J. Earth Sci.*, **103**, 1889–1916.

Suess, E. and **Whiticar, M.J.** (1989) Methane-derived CO_2 in pore fluids expelled from the Orgeon subduction zone. *Palaeogeogr. Palaeoclimatol. Palaeoecol.*, **71**, 119–136.

Teichert, B.M.A., Eisenhauer, A., Bohrmann, G., Haase-Schramm, A., Bock, B. and **Linke, P.** (2003) U/Th Systematics and ages of authigenic carbonates from Hydrate Ridge, Cascadia Margin: recorders of fluid flow variations. *Geochim. Cosmochim. Acta*, **67**, 3845–3857.

Thiel, V., Peckmann, J., Seifert, R., Wehrung, P., Reitner, J. and **Michaelis, W.** (1999) Highly isotopically depleted isoprenoids: molecular markers for ancient methane venting. *Geochim. Cosmochim. Acta*, **63**, 3959–3966.

Thierstein, H.R. (1976) Mesozoic calcareous nannoplankton biostratigraphy of marine sediments. *Mar. Micropaleontol.*, **1**, 325–362.

Tong, H., Wang, Q., Peckmann, J., Cao, Y., Chen, L., Zhou, W. and **Chen, D.** (2016) Diagenetic alteration affecting $\delta^{18}O$, $\delta^{13}C$ and $^{87}Sr/^{86}Sr$ signatures of carbonates: a case study on Cretaceous seep deposits from Yarlung-Zangbo Suture Zone, Tibet, China. *Chem. Geol.*, **444**, 71–82.

Tribovillard, N., Algeo, T.J., Lyons, T. and **Riboulleau, A.** (2006) Trace metals as paleoredox and paleoproductivity proxies: an update. *Chem. Geol.*, **232**, 12–32.

 © 2017 The Authors. *The Depositional Record* published by John Wiley & Sons Ltd on behalf of International Association of Sedimentologists.

Von Rad, U., Riech, V. and **Rösch, H.** (1977) Silica diagenesis in contintental margin sediments off northwest Africa. *Initial Rep. Deep Sea*, **41**, 879–905.

Wagner, T. and **Pletsch, T.** (1999) Tectono-sedimentary controls on Cretaceous black shale deposition along the opening Equatorial Atlantic Gateway (ODP Leg 159). In: *Oil and Gas Habitats of the South Atlantic* (Eds N.R. Cameron, R.H. Bate and V.S. Clure), *Geol. Soc. London. Spec. Publ.*, **153**, 241–265.

Wagner, T., Floegel, S. and **Hofmann, P.** (2013) Marine black shale and Hadley Cell dynamics: a conceptual framework for the Cretaceous Atlantic Ocean. *Mar. Petrol Geol.*, **43**, 222–238.

Wedepohl, K.H. (ed.) (1969) Composition and abundance of common igneous rocks. In: *Handbook of Geochemistry*, **1**, 227–249.

Weissert, H. (1981) The environment of deposition of black shales in the Early Cretaceous: an ongoing controvery. *SEPM Spec. Publ.*, **32**, 547–560.

Weissert, H., McKenzie, J. and **Hochuli, P.** (1979) Cyclic anoxic events in the Early Cretaceous Tethys Ocean. *Geology*, **7**, 147–151.

Xu, W., Ruhl, M., Hesselbo, S.P., Riding, J.B. and **Jenkyns, H.C.** (2016) Orbital pacing of the Early Jurassic carbon cycle, black shale formation and seabed methane seepage. *Sedimentology*, **64**, 127–149.

Zwicker, J., Smrzka, D., Gier, S., Goedert, J.L. and **Peckmann, J.** (2015) Mineralized conduits are part of the uppermost plumbing system of Oligocene methane-seep deposits, Washington State (USA). *Mar. Petrol. Geol.*, **66**, 616–630.

© 2017 The Authors. *The Depositional Record* published by John Wiley & Sons Ltd on behalf of International Association of Sedimentologists.